

Geographia Technica



Technical Geography
an International Journal for the Progress of Scientific Geography

Volume 18, Geographia Technica No. 2/2023

www.technicalgeography.org

Cluj University Press

Editorial Board

Okke **Batelaan**, Flinders University Adelaide, Australia
Yazidhi **Bamutaze**, Makerere University, Kampala, Uganda
Valerio **Baiocchi**, Sapienza University of Rome, Italy
Gabriela **Biali**, "Gh. Asachi" University of Iasi, Romania
Habib **Ben Boubaker**, University of Manouba, Tunisia
Gino **Dardanelli**, University of Palermo, Italy
Qingyun **Du**, Wuhan University, China
Renata **Dulias**, University of Silesia, Poland
Massimiliano **Fazzini**, University of Ferrara, Italy
Edward **Jackiewicz**, California State University, Northridge CA, USA
Shadrack **Kithiia**, University of Nairobi, Kenya
Jaromir **Kolejka**, Masaryk University Brno, Czech Republic
František **Križan**, Comenius University in Bratislava, Slovakia
Muh Aris **Marfai**, Universitas Gadjah Mada, Yogyakarta, Indonesia
Béla **Márkus**, University of West Hungary Szekesfehervar, Hungary
Jean-Luc **Mercier**, Université de Strasbourg, France
Igor **Patrakeyev**, Kyiv University of Construction and Architecture, Ukraine
Cristian Valeriu **Patriche**, Romanian Academy, Iasi, Romania
Dušan **Petrovič**, University of Ljubljana, Slovenia
Hervé **Quénol**, Université de Rennes 2 et CNRS, France
Sanda **Roșca**, Babes-Bolyai University of Cluj-Napoca, Romania
José J. de **Sanjosé Blasco**, University of Extremadura, Spain
Richard R. **Shaker**, Reyson University, Toronto, Canada
Sarintip **Tantane**, Naresuan University, Phitsanulok, Thailand
Gábor **Timár**, Eötvös University Budapest, Hungary
Kinga **Temerdek-Ivan**, Babes-Bolyai University of Cluj-Napoca, Romania
Yuri **Tuchkovenko**, Odessa State Environmental University, Ukraine
Eugen **Ursu**, Université de Bordeaux, France
Changshan **Wu**, University of Wisconsin-Milwaukee, USA
Chong-yu **Xu**, University of Oslo, Norway

Editor-in-chief

Ionel **Haidu**, University of Lorraine, France

Editorial Secretary

Marcel Mateescu, Airbus Group Toulouse, France
George Costea, Yardi Systemes, Cluj-Napoca, Romania

Online Publishing

Magyari-Sáska Zsolt, "Babes-Bolyai" University of Cluj-Napoca, Romania

Geographia Technica



Technical Geography

an International Journal for the Progress of Scientific Geography

2023 – No. 2

Cluj University Press

ISSN: 1842 - 5135 (Printed version)

ISSN: 2065 - 4421 (Online version)

© 2023. All rights reserved. No part of this publication may be reproduced or transmitted in any form or by any means, electronic or mechanical, including photocopy, recording or any information storage and retrieval system, without permission from the editor.

Babeş-Bolyai University
Cluj University Press
Director: Codruța Săcelean
Str. Hașdeu nr. 51
400371 Cluj-Napoca, România
Tel./fax: (+40)-264-597.401
E-mail: editura@editura.ubbcluj.ro
<http://www.editura.ubbcluj.ro/>

Asociatia Geographia Technica
2, Prunilor Street
400334 Cluj-Napoca, România
Tel. +40 744 238093
editorial-secretary@technicalgeography.org
<http://technicalgeography.org/>

Cluj University Press and Asociatia Geographia Technica
assume no responsibility for material, manuscript, photographs or artwork.

Contents

Geographia Technica

Volume 18, Issue 2, autumn 2023

An International Journal of Technical Geography

ISSN 2065-4421 (Online); ISSN 1842-5135 (printed)

2D SIMULATION OF DESIGN DISCHARGE IN FLOOD HAZARD SPATIAL ANALYSIS USING HEC-RAS, (CASE STUDY MATA ALLO SUB-WATERSHED, ENREKANG, INDONESIA)

Uca SIDENG, Hamzah UPU, Nurul Afdal HARIS
& Dwi RAHMAYANA 1
DOI: 10.21163/GT_2023.182.01

QUANTITATIVE AND QUALITATIVE DATA IN DISASTER RISK MANAGEMENT OF FIRES: A CASE STUDY FROM SOUTH AFRICA AT VARIOUS GEOGRAPHICAL LEVELS

Rennifer MADONDO, Roman TANDLICH, Eric Thabo STOCH, Ágoston RESTÁS & Siviwe SHWABABA 14
DOI: 10.21163/GT_2023.182.02

PRODUCTION OF HIGH GEOMETRIC RESOLUTION ORTHOPHOTOS BY PHOTOGRAMMETRIC APPROACH FOR THE ROYAL RACCONIGI CASTEL PARK DOCUMENTATION

Vincenzo Saverio ALFIO, Domenica COSTANTINO, Massimiliano PEPE, Gabriele ROSSI & Massimo LESERRI..... 40
DOI: 10.21163/GT_2023.182.03

TSUNAMI HAZARD MAPPING BASED ON COASTAL SYSTEM ANALYSIS USING HIGH-RESOLUTION UNMANNED AERIAL VEHICLE (UAV) IMAGERY (CASE STUDY IN KUKUP COASTAL AREA, GUNUNGKIDUL REGENCY, INDONESIA)

DANARDONO, Afif Ari WIBOWO, Dewi Novita SARI, Kuswaji Dwi PRIYONO & Ecky Safira Maharani DEWI 51
DOI: 10.21163/GT_2023.182.04

SPATIAL MODEL OF RUNOFF FLOWING INTO THE NEWLY FORMED LAKE AT SINABUNG VOLCANO

Sandy Budi WIBOWO, Polin Mouna TOGATOROP, Tsamara HANINDHIYA, Barandi Sapta WIDARTONO & R. Ibnu ROSYADI .. 68
DOI : 10.21163/GT_2023.182.05

COMPARISON OF TWO SEPARATION MULTIPATH TECHNIQUES IN GNSS REFLECTOMETRY FOR SEA LEVEL DETERMINATION IN INDONESIA

Lisa A. CAHYANINGTYAS, Dudy D. WIJAYA & Nabila S.E. PUTRI 79
DOI : 10.21163/GT_2023.182.06

ASSESSMENT OF INUNDATION SUSCEPTIBILITY IN THE CONTEXT OF CLIMATE CHANGE, BASED ON MACHINE LEARNING AND REMOTE SENSING: CASE STUDY IN VINH PHUC PROVINCE OF VIETNAM

Phan Manh HUNG, Huu Duy NGUYEN & Chien Pham VAN 93
DOI: 10.21163/GT_2023.182.07

A MULTISCALE GEOMATIC APPROACH FOR THE SURVEY OF HISTORIC CENTRES MAIN STREETS: THE CASE STUDY OF CAPITIGNANO, ITALY

Giovanni MATALONI, Donato PALUMBO, Massimiliano PEPE & Claudio VARAGNOLI 113
DOI: 10.21163/GT_2023.182.08

THAI EASTERN ECONOMIC CORRIDOR DROUGHT MONITORING USING TERRA/MODIS SATELLITE-BASED DATA

Phaisarn JEEFOO 123
DOI: 10.21163/GT_2032.182.09

TSUNAMI EVACUATION MODEL IN THE PANIMBANG SUBDISTRICT, BANTEN PROVINCE, INDONESIA: GIS- AND AGENT-BASED MODELING APPROACHES

Dini PURBANI, Marza Ihsan MARZUKI, Budianto ONTOWIRJO, Farhan Makarim ZEIN, Didik Wahyu Hendro TIAHJO, Sri Endah PURNAMANINGTYAS, Rudy AKHWADY, Amran Ronny SYAM, Arip RAHMAN, Yayuk SUGIANTI, Safar DODY, Adriani Sri NASTITI, Andri WARSA, Lismining Pujiyani ASTUTI, YOSMANIAR, Tutik KADARINI, Tri Heru PRIHADI & Ulung Jantama WISHA 132
DOI : 10.21163/GT_2032.182.10

CONTRIBUTION OF SPACE REMOTE SENSING AND NEW GIS TOOLS FOR MAPPING GEOLOGICAL STRUCTURES IN THE MEKKAM REGION OF NORTHEAST MOROCCO

Abdelali GOUISS, Youness TAYBI, Youssef GHARMANE & Souad M'RABET 149
DOI: 10.21163/GT_2023.182.11

IDENTIFICATION OF RETENTION AREAS USING AIRBORNE LIDAR DATA. A CASE STUDY FROM CENTRAL SWEDEN

Jakub SEIDL 158
DOI: 10.21163/GT_2023.182.12

A ROBUST UNIFIED MODEL FOR NATIONAL STREET GAZETTEER BASED ON LAND REGISTER AND GIS FOR THE REPUBLIC OF KOSOVO

Përparim AMETI & Dustin SANCHEZ 170
DOI: 10.21163/GT_2023.182.13

THE LATEST BATHYMETRY AND TOPOGRAPHY EXTRACTION OF LAKE LEDULU FROM MULTI-SOURCE GEOSPATIAL DATA

Atriyon JULZARIKA, Dany Puguh LAKSONO, Luki SUBEHI, Elisa ISWANDONO, Alfred Onisimus Maximus DIMA, Media Fitri Isma NUGRAHA & Kayat KAYAT 180
DOI: 10.21163/GT_2023.182.14

APPLICATION OF GIS TECHNOLOGY TO ASSESS THE ENVIRONMENTAL SUITABILITY FOR RUPICAPRA RUPICAPRA IN ROMANIAN CARPATHIANS

Sanda-Maria ROȘCA & Vasile CEUCA 196
DOI: 10.21163/GT_2023.182.15

CHATEAU BROWNFIELDS IN SELECTED LAU1 REGIONS OF THE CZECH REPUBLIC: SEARCHING FOR REMARKABLE FEATURES WITHIN DESCRIPTIVE LOCALIZATION ANALYSIS

Kamila TURECKOVA 213
DOI: 10.21163/GT_2023.182.16





CHANGES AND TRENDS IN IDEAL HOLIDAY PERIOD BASED ON HOLIDAY CLIMATE INDEX APPLIED TO THE CARPATHIAN BASIN

Zsolt MAGYARI-SÁSKA & Attila MAGYARI-SÁSKA 225
DOI: 10.21163/GT_2023.182.17

INVESTIGATION OF CHLOROPHYLL-A VARIABILITY IN RED SEA USING SATELLITE-BASED METEOROLOGY AND OCEANOGRAPHY DATA

Anton Satria PRABUWONO, KUNARSO, Anindya WIRASATRIYA & Satria ANTONI 238
DOI: 10.21163/GT_2023.182.18

2D SIMULATION OF DESIGN DISCHARGE IN FLOOD HAZARD SPATIAL ANALYSIS USING HEC-RAS, (CASE STUDY MATA ALLO SUB-WATERSHED, ENREKANG, INDONESIA)

Uca SIDENG^{1*}, Hamzah UPU², Nurul Afdal HARIS¹, Dwi RAHMAYANA¹

DOI: 10.21163/GT_2023.182.01

ABSTRACT:

Indonesia is one of the countries frequently hit by hydrometeorological disasters. Flood is one of the disasters that often occurs in Indonesia. Especially for the Enrekang area which is traversed by the Mata Allo River. With topographical characteristics and land use that has the potential to cause flooding and high rainfall. It will harm activities in the watershed area. In reducing the impact that occurs, it is necessary to identify and map flood-prone areas as initial information on flood control. This study aims to determine the distribution and level of vulnerability to flooding in the Mata Allo sub-watershed using 2D HEC-RAS simulations. By utilizing annual rainfall data, the Nakayasu HSU method is applied to generate design discharge values to be used in flood simulations. The simulation results show that there are five classes of flood hazard levels which show the uniformity of flood vulnerability levels in each return period. The average level of vulnerability is in the very low range of ± 9.60 Ha, in the low range of ± 8.8 Ha, medium vulnerability is in the range of ± 13.63 Ha, high vulnerability is ± 23.58 Ha, and extreme vulnerability is ± 25.71 Ha. The area that is mapped is an area that is often affected when a flood occurs. As a result, the use of this approach can provide an overview of the distribution of flood-prone areas.

Key-words: *spatial analysis, flood, Nakayasu HSU, discharge, simulation.*

1. INTRODUCTION

Natural disasters are phenomena significantly impacting either the natural environment or human, with a high chance of damage (Popescu and Bărbulescu, 2023). Indonesia is a country with high potential for natural disasters, influenced by geological conditions and climatic factors (Rauf, 2021). Indonesia's National Disaster Management Agency noted throughout 2022 that natural disasters in Indonesia had occurred $\pm 2,111$ times, be it extreme weather, landslides, drought, earthquakes, fires, tidal waves, abrasion, and floods. In the period of natural disasters that occurred, it was also explained that floods were the most dominant of the other natural disasters that occurred (BNPB, 2022).

Flooding is a condition where a land is submerged because the amount of surface runoff exceeds the capacity of the drainage system (Kodoatie, 2013), often occurring in several areas every rainy season (Pratiwi and Santosa, 2021). Through this situation, it also causes huge losses and even casualties. South Sulawesi Province is an area in Indonesia with a high risk of flood vulnerability, which has a disaster index of 154.87 (BNPB, 2022). Of the several districts/cities that Included in the list of flood-prone areas in the high vulnerability level, Enrekang Regency is one of those that has a high risk of flood vulnerability during 2020-2021. This is based on the convergence of the main sub-watersheds of the Saddang watershed, namely the Saddang sub-watershed and the Mata Allo sub-watershed. These two sub-watersheds meet in the capital of Enrekang Regency and flooding often occurs (Uca *et al.*, 2021). In responding to an area that is prone to a disaster, Flood disaster management efforts need to be made. One of the efforts in flood disaster management is the provision of information about flood risk hazards, especially related to the potential distribution of floods that are expected to occur in an area.

¹ Geography Department, Faculty of Mathematics and Natural Science, State University of Makassar, Makassar, Indonesia, corresponding author ucasideng@unm.ac.id, nurul.afdal.haris@mail.ugm.ac.id, 200110500007@student.unm.ac.id

² Mathematic Department, Faculty of Mathematics and Natural Science, State University of Makassar, Makassar, Indonesia, hamzahupu@gmail.com

The level of regional vulnerability to flooding can be determined by spatial modeling of floods through a review or determined from the prone aspects of flood disasters (Rauf, 2021). The flood prone index is then used to determine the level of disaster vulnerability, which consists of 2 main components, namely the likelihood of a disaster occurring and the magnitude of the disaster impact that occurs.

Geographic Information System (GIS) is one of the evidences or results of the increasing advancement of information and computer technology in supporting spatial analysis (Rajeev and Singh, 2016). The use of this technology has been widely used in modeling hydrological mechanisms (Avinash, Jayappa and Deepika, 2011) such as the level of vulnerability of a disaster and prediction of watershed overflow through hydraulics modeling. The capacity to simulate flood hazard maps is particularly strong when GIS and HEC-RAS (Hydrologic Engineering Center-River Analysis System) are combined. HEC-RAS was created for the management of floodplains and studies evaluating flood inundation, and it can analyze changes to river water and channel profiles (US Army Corps of Engineers, 2016). The assessment of hydrological issues, including flooding, as well as modeling watershed-related issues can both be aided by this application (Sabău and Șerban, 2018; Kim, Tantanee and Suparta, 2020). Over the past decades, many hydraulics models have been developed (Lea, Yeonsu and Hyunuk, 2019). Hydraulic modeling takes into account the prediction of peak discharge and the shape of the flood hydrograph on the river water surface (Bomers *et al.*, 2019). The use of several software such as HEC-RAS is one form of hydraulic model development to address hydraulic problems in detail (Bomers, Schielen and Hulscher, 2019). HEC-RAS is intended for processing geospatial data, and makes it easy for users to create files containing geometric data, and the results of the formed water surface profile can be used and interpreted in determining the depth and extent of flooding (Ahmad *et al.*, 2022). Hydraulic modeling through HEC-RAS can be interpreted into 2-D modeling, the resulting simulation also provides a more accurate average depth value (Ngo *et al.*, 2023).

Efforts to visualize flood events, integration between 2D HEC-RAS simulations and Geographic Information Systems (GIS) have been applied almost all over the world in an effort to develop mitigation strategies (Liu, Merwade and Jafarzadegan, 2019), also applicable to the Saddang watershed area (Mata Allo sub-watershed). Previous research that also applies hydrological modeling such as in surface flow calculations (Haidu and Ivan, 2016), flood simulation (Popescu and Bărbulescu, 2023) and curve number calculation (Khaddor and Alaoui, 2014). This study's aim is to figure out the distribution of flooded areas using simulation results and design discharge analysis in view of the background information. to gather information on the spatial distribution of flood hazard. This is crucial to do as a first step in providing details or an overview of places that are vulnerable to floods and at high risk. As an additional early warning system for the surrounding community.

2. STUDY AREA

This research is located in the Saddang River basin, Mata Allo Sub-watershed located in Enrekang District, Enrekang Regency, South Sulawesi Province (**Fig. 1**). Enrekang regency is located between 3°14'–3°50'S and 119°40'–120°06'E. The Mata Allo sub-watershed is 4.81 km long from upstream (H1) to downstream (H2) as can be seen in Figure 1 below. The location of this study was determined because the area often experiences flooding. One of the causes is a change in land use in the upstream area which causes the rapid concentration of surface runoff into the river area. as well as a confluence with the Saddang river in the downstream area, thus enabling an increase in water volume in the area.

3. DATA AND METHODS

To achieve the objectives of this research, data is needed that can be formed to present a river cross-section model. As well as rainfall data within a period of 10 years to produce river discharge data. The data used to obtain the data are described as follows (a) and (b):

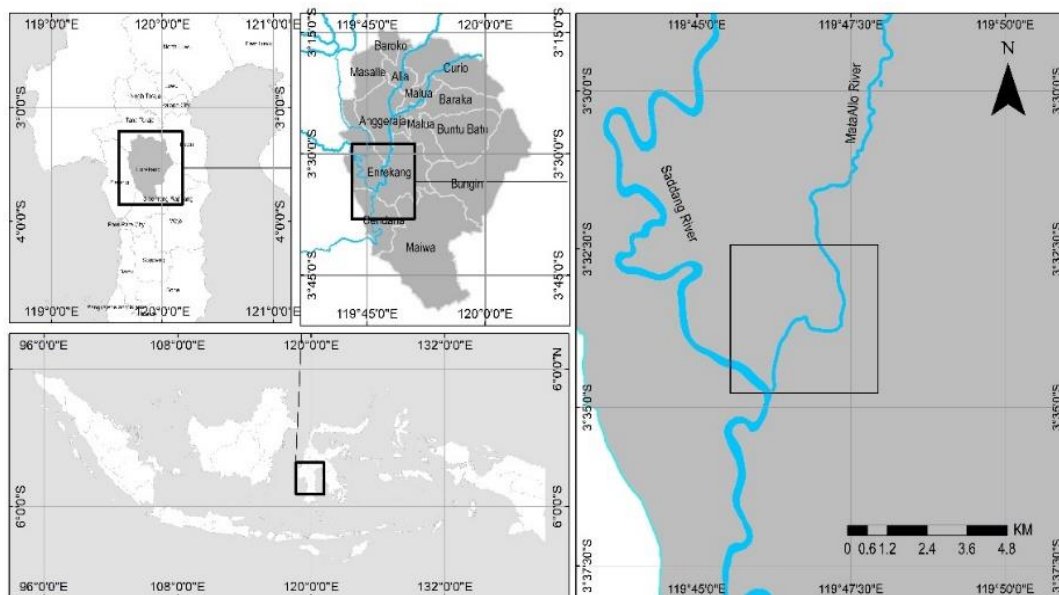


Fig. 1. Map of the Study Area.

- a) DEM (Digital Elevation Model) data with 8.2m resolution, obtained from the Geospatial Information Agency (<https://tanahair.indonesia.go.id/>) was used as the basis for river geometry (Pathan and Agnihotri, 2020). With this resolution DEM data will be able to provide a more detailed formation for the scale of mapping used. So that the results given are close to the real conditions in the field.
- b) Rainfall data (2012 to 2021) was obtained from the Climate Hazards Group InfraRed Precipitation with Station (CHIRPS) through the Google Earth Engine (GEE) platform (<https://earthengine.google.com/>). CHIRPS itself provides daily rainfall data at 0.05° spatial resolution since 1981 to the present, and users can use it for free. CHIRPS data shows good potential accuracy for use in meteorological studies and research related to water resources (Geleta and Deressa, 2021). The rainfall data used has gone through an interpolation process in GEE to cover the study area. In addition, CHIRPS rainfall data can improve the accuracy of runoff and river flow simulations for hydrological modeling (Le and Pricope, 2017)

The data that has been collected is then processed using ArcGIS, HEC-RAS, Matlab Aprob_41, Microsoft Office software.

The stages of data processing and analysis are described as follows (1), (2), (3) and (4):

- 1) The design rainfall was analyzed according to Triatmodjo (2013) which includes the calculation of standard deviation (s), coefficient of variation (Cv), slope coefficient (Cs), and kurtosis coefficient (Ck). The precipitation period uses return periods of 2, 10, 25, 50 and 100 years. The Gumbel, Normal, Normal Log, , and Pearson III methods were used in analyzing the frequency distribution (Harahap, Jeumpa and Hadibroto, 2018). Distribution matching includes analysis of Chi-Square test and Smirnov-Kolmogorov test using Matlab AProb_41 software. From the results of the frequency analysis and the Chi-Square and Smirnov-Kolmogorov tests, the distribution type with the lowest Smirnov-Kolmogorov test value and passing the Chi-Square test was selected for use in further analysis (Steele, Chaseline and Hurst, 2006).
- 2) The calculation of the unit hydrograph is to determine the peak flow based on the maximum rainfall data that occurs in the study area. The Nakayasu HSU (Hydrograf Synthetic Unit) method was used in this study to analyze the peak flow as input from the river flow simulation using the HEC-RAS software. Because the Nakayasu HSU method, in calculating the total

flood discharge also considers the effective rainfall and baseflow discharge (Harahap, Jeumpa and Hadibroto, 2018; Prastica and Fanani, 2021). Thus, the return period flood discharge is the result of the total discharge from multiplying the ordinate of the Nakayasu HSU unit to the effective rainfall distribution which is then summed up with the base flow discharge.

We present below the formulas that are the basis of the study.

Nakayasu HSU formula:

$$Q_p = \frac{1}{3,6} \left(\frac{A R_o}{0,3T_p + T_{0,3}} \right) \quad (1)$$

$$T_p = t_g + 0,8T_r \quad (2)$$

$$t_g = 0,4 + 0,058L \quad (\text{for } L > 15\text{km}) \quad (3)$$

$$t_g = 0,2L^{0,7} \quad (\text{for } L < 15\text{km}) \quad (4)$$

$$T_{0,3} = \alpha t_g \quad (5)$$

$$t_r = 0,5t_g \text{ to } t_g \quad (6)$$

where:

- Q_p - peak flood discharge
- A - watershed area (km²)
- R_o - effective rainfall (1mm)
- T_p - time from the beginning of the flood to the peak of the hydrograph (hours)
- T_{0,3} - time from the flood peak to 0.3 times to peak discharge (hours)
- t_g - time of concentration (hours)
- t_r - time unit of rainfall (hours)
- α - watershed characteristic coefficient (between 1,5 – 3)
- L - main river length (km)

Nakayasu HSU Unit Ordinate Formula:

The curve rises when $0 < t < T_p$

$$Q_a = Q_p \times \left(\frac{t}{T_p} \right)^{2,4} \quad (7)$$

Descending curve $T_p < t < T_{0,3} + T_p$

$$Q_{d1} = Q_p \times (0,3)^{\frac{(t-T_p)}{T_{0,3}}} \quad (8)$$

$$Q_{d2} = Q_p \times (0,3)^{\frac{(t-T_p)+(0,5T_{0,3})}{1,5T_{0,3}}} \quad (9)$$

$$Q_{d3} = Q_p \times (0,3)^{\frac{(t-T_p)+(1,5T_{0,3})}{2,0T_{0,3}}} \quad (10)$$

Effective rainfall formula:

$$R_e = R_h \times C \quad (11)$$

where:

- R_e - Effective rainfall
- R_h - Probability of daily rainfall from Log Pearson III plan rainfall calculation analysis
- C - Flow coefficient total

Flood discharge formula:

$$Q_T = (\sum_{t=1}^n U_t \times Re) + Q_B \quad (12)$$

where:

- Q_T - total flood discharge
- U_t - hydrograph ordinate (Q_a , Q_{d1} , Q_{d2} , Q_{d3})
- Re - effective rainfall
- Q_B - base flow discharge

- 3) Hydrological modeling is carried out using the HEC-RAS application with a 2D model. The 2D hydraulic modeling in question is a model that has two flow directions consisting of flow directions along the main channel and flow directions around the main stream (Indrawan and Siregar, 2018). The continuity equation is used as an unsteady flow simulation using the assumption that the water flow varies with time. The continuity equation (conservation of mass principle) can be written in the form of a partial differential equation.

$$\frac{\partial A}{\partial t} + \frac{\partial Q}{\partial x} - ql = 0 \quad (13)$$

where:

- A - total cross-sectional area of the stream
- Q - flow discharge
- ql - lateral discharge of unity length
- x - distance measured in the direction of flow
- t - time

In the simulation on the HEC-RAS program, the Manning roughness coefficient data is needed to provide the influence of the channel bed surface conditions. The determination of the Manning's roughness coefficient is based on field observations of the characteristics of the Mata Allo sub-watershed study site. The river has a rocky bottom along the flow, especially in the lower reaches of the river and there is little vegetation. The Manning coefficient value is adjusted to the value issued by Gray, 1973. So that the Manning roughness coefficient used based on the characteristics of the study area is 0.05 (Gray, 1973; Liu, Merwade and Jafarzadegan, 2019).

- 4) The 2D simulation data in the form of inundation depth values is then used to identify flood hazards. The discharge results obtained from the calculation of the design discharge are then used as input to the HEC-RAS program in simulating river flow or flooding at certain return times (**Fig. 2**). Using the previous DEM data, river geometry data in the study area can be generated. This is then used as the basis for the river discharge flow analysis model. The simulation is carried out on the Unsteady Flow model because the inputted discharge is not a fixed flow (Gray, 1973; US Army Coprs of Engineers, 2016; Albo-Salih, Mays and Che, 2022). **Table 1** below presents the depth class in the spatial analysis of flood hazard.

Table 1.

Classification of Flood Hazard Levels Based on Depth.

No	Depth Interval (m)	Hazard Level
1	< 0,50	Very Low
2	0,50 – 1,00	Low
3	1,00 – 2,00	Medium
4	2,00 – 5,00	High
5	>5,00	Extreme

Source: (Ahmad et al., 2022)

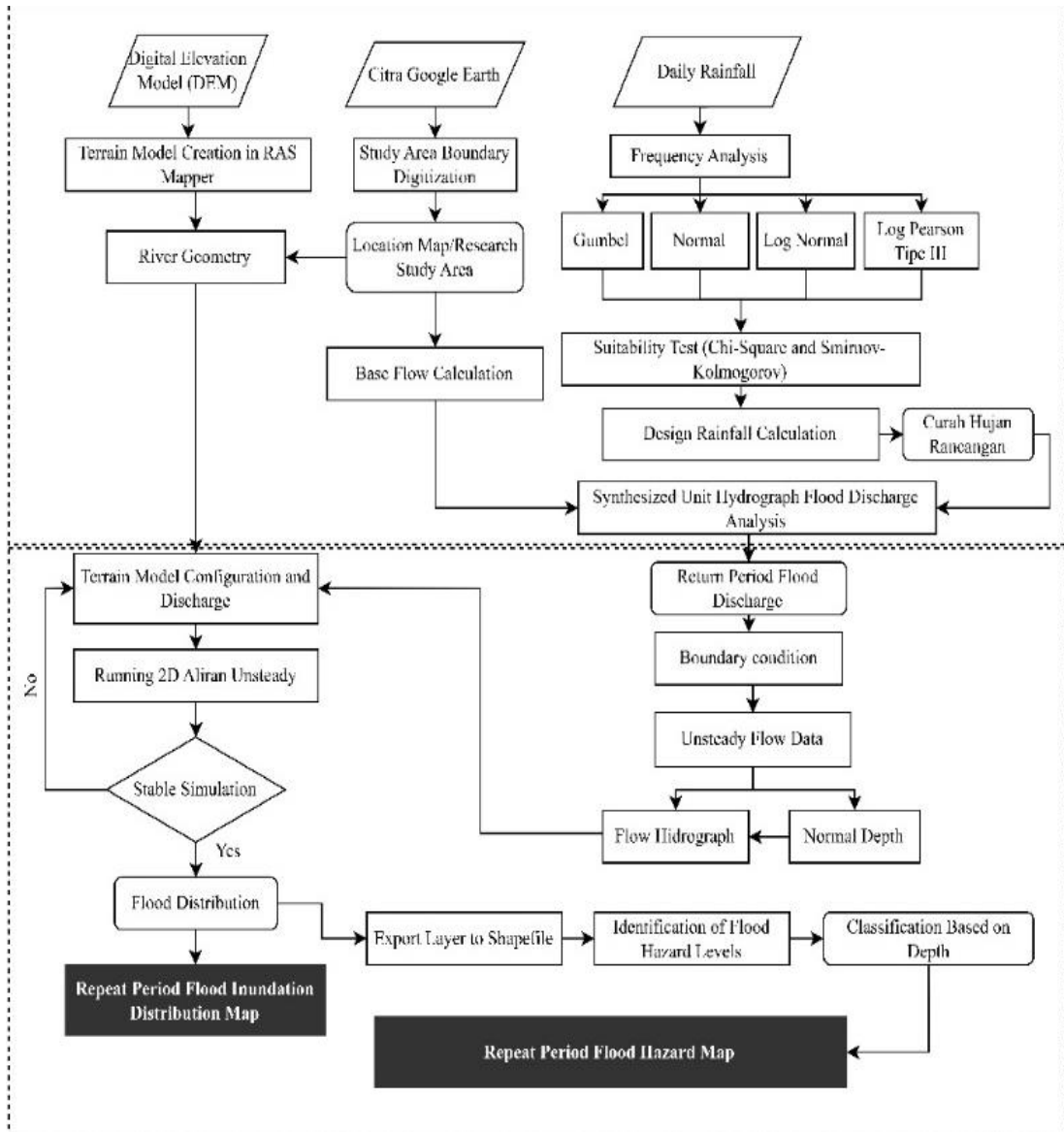


Fig. 2. Flow Chart of 2D Flow Modelling Simulation.

4. RESULTS AND DISCUSSIONS

4.1 Frequency of Rainfall

Calculation of the frequency of rainfall using maximum daily rainfall data in units of 24 hours/mm, as the design rain value (Fig. 3). From this data, statistical parameter calculations are carried out in calculating the dispersion value (Amin, Izwan and Alazba, 2016).

In measuring dispersion to obtain statistical parameters, the Normal Distribution, Gumbel, Normal Log, and Log Pearson III were calculated (Ben Khalfallah and Saidi, 2018; Rauf, 2021). It was found that the Log Pearson III meets the requirements in the calculation of the statistical parameter dispersion and will be used for further analysis. Seen in Fig. 4, it is found that the skewness value for Log Pearson III is 0.416 with the condition that the value must not be equal to zero ($\neq 0$) (Ben Khalfallah and Saidi, 2018).

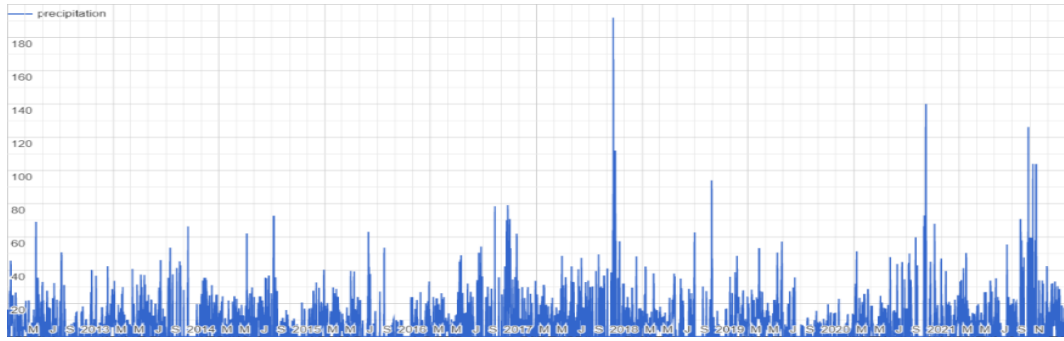


Fig. 3 Daily Rainfall of the Mata Allo Sub-watershed for 2012-2021

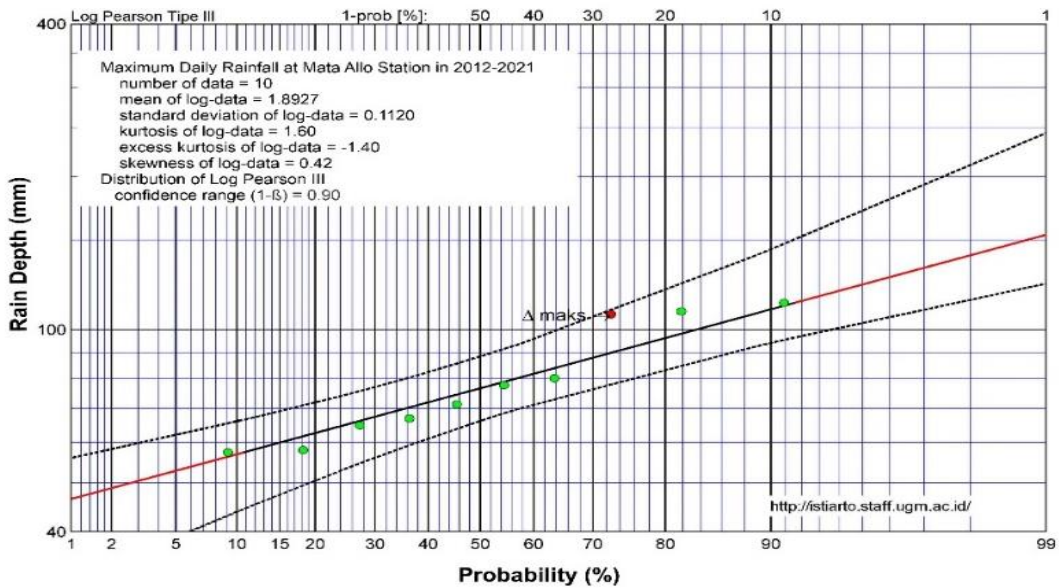


Fig. 4. Probability Distribution of Maximum Rainfall using the Log Pearson III Method

Based on the requirements for selecting the type of distribution and the data distribution suitability test shows that the Log Pearson III method is suitable for use. The results of the calculation of rainfall return periods using the Log Pearson III method can be seen in full in **Table 2** below.

Tabel 2.

Results of rainfall calculation plan

Return Period (year)	Rainfall (mm)
2	76,51
5	96,38
10	109,73
25	127,00
50	140,23
100	153,77

Source: Results of calculations and data processing, 2022.

4.2 Discharge Analysis

By using the planned rainfall value, a flood discharge analysis is obtained using the Nakayasu HSU method. The calculation results show, the peak time (T_p) for the Mata Allo Sub-watershed is 1 hour with a hydrograph shape that can be seen in **Fig. 5**. In addition, the magnitude of the peak flood discharge obtained at the return period of 2 to 100 years is 137,05 m³/det; 148,83 m³/det; 156,75 m³/det; 167,0 m³/det; 174,84 m³/det; 182,87 m³/det.

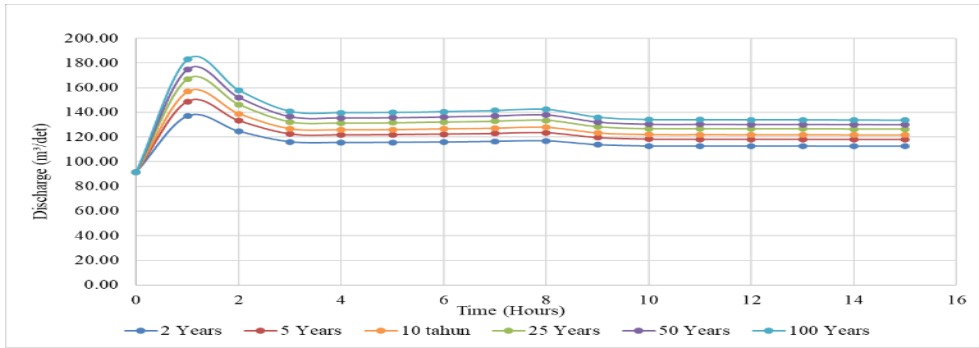


Fig. 5. Flood Hydrograph of Mata Allo Sub-watershed using Nakayasu HSU Method.

The simulated flood inundation area shows 54.9266 Ha at the 2-year return period, 59.3351 Ha at the 5-year return period, 62.1189 Ha at the 10-year return period, 64.8449 Ha at the 25-year return period, 68.734 Ha at the 50-year return period and 69.734 Ha at the 100-year return period. From all simulations of the return period that have been carried out, it can be seen that the areas that experience inundation include Lewaja District, Galonta District, Puserren District, Juppandang District, and Ranga Village (**Fig. 6**).

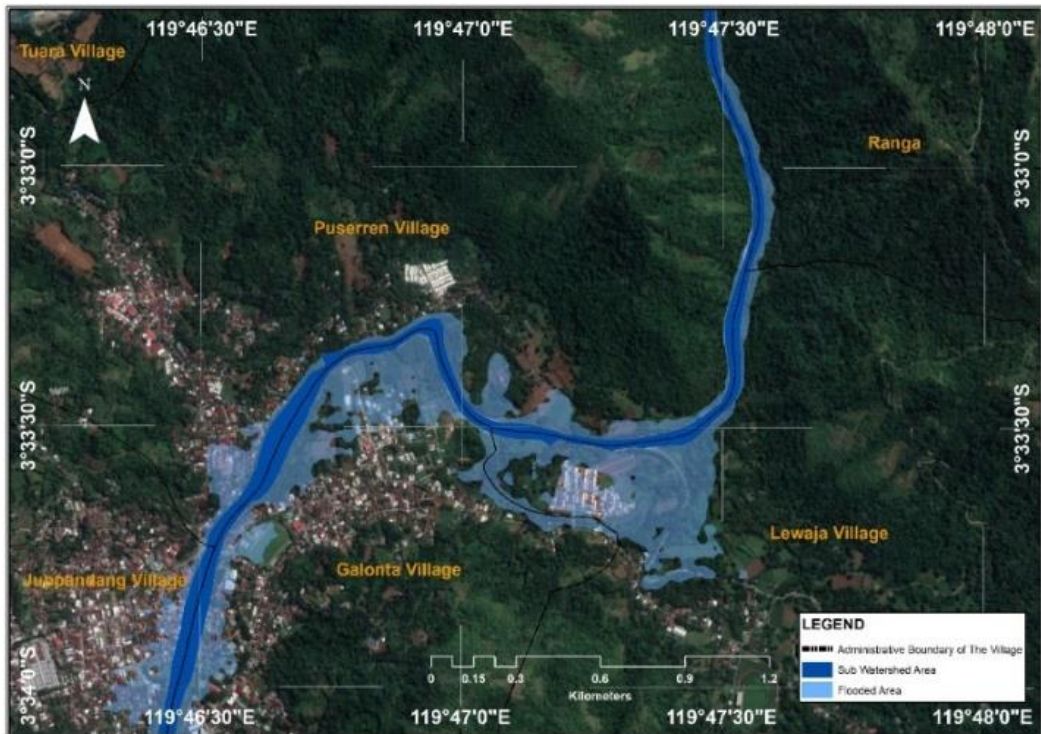


Fig. 6. Flood inundation distribution map of the Mata Allo Sub-watershed at the Q100 year return period.

In addition, the depth value from the simulation results also shows the uniformity of the location of the flood vulnerability level at each return period. The average level of vulnerability in the very low range is ± 9.60 Ha, low range is ± 8.8 Ha, moderate vulnerability range is ± 13.63 Ha, high vulnerability level is ± 23.58 Ha, and the level of vulnerability in the extreme range is ± 25.71 Ha. As for urban villages with a level of flood hazard based on spatial analysis carried out which have high to extreme vulnerability are Lewaja Village and Galonta Village. For clarity, it can be seen in **Fig. 7**.

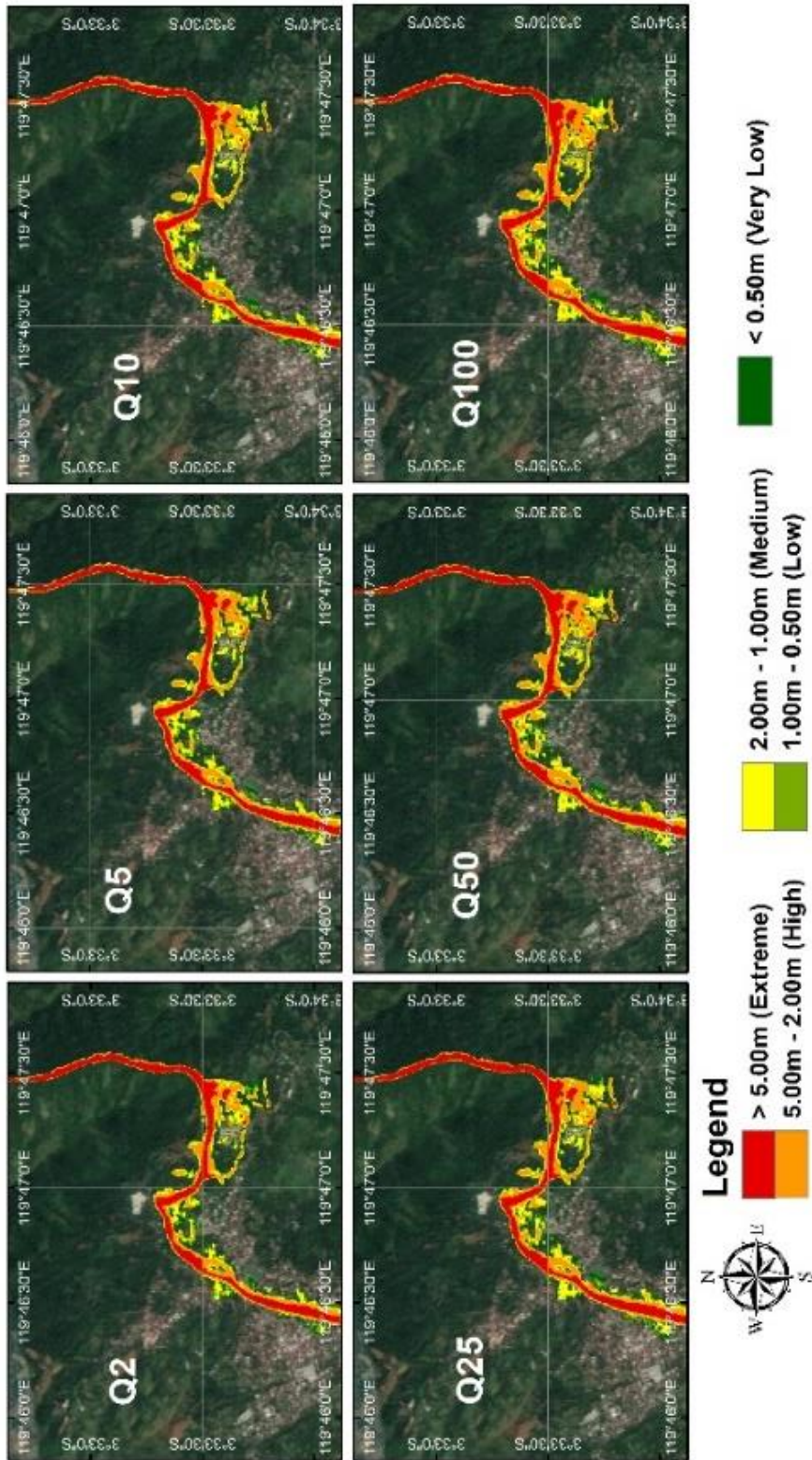


Fig. 7. Flood hazard level of the study area.

4.3 Discussion

Vojtek and Vojteková (2019) explained that the flood phenomenon is influenced by 4 main factors which include hydrography, hydrology, morphometry and permeability that compose an area. The flood phenomenon that occurs at the Mata Allo Sub-watershed research location based on the results of the analysis that has been carried out shows that flood events tend to be influenced by hydrological and morphometric factors of the region.

The hydrological aspect is closely related to river problems, especially the rain that will flow into the river system (Harahap, Jeumpa and Hadibroto, 2018). The amount of rainwater flowed determines the increase in flood runoff (Kang et al., 2013). The design flood analysis uses the maximum value of the planned rainfall (Harahap, Jeumpa and Hadibroto, 2018). The results of the calculation of the rainfall value at the study location for the return period of 2 to 100 years respectively are 76.51mm, 96.51mm, 109.73mm, 127.00mm, 140.23mm, and 153.77mm respectively. The calculation of this rainfall plan uses the distribution of the Log Pearson III. So that the estimated amount of flood discharge for a certain period of the estimated flood discharge does not deviate far from the actual flood event (Harahap, Jeumpa and Hadibroto, 2018). Meanwhile, the peak flood discharge at the return period obtained is 137,05 m³/s; 148,83 m³/s; 156,75 m³/s; 167,0 m³/s; 174,84 m³/s; 182,87 m³/s.

Physical and hydrological characteristics are the main factors that influence the frequency of flooding for different return periods. However, it is known that the slope has a greater influence on the intensity and frequency of flood events (Ben Khalfallah and Saidi, 2018). The morphometric aspect is illustrated from the results of DEM data processing, the topographic conditions of the Mata Allo Sub-watershed area are low relief and gentle slopes which are in line with the research of Uca et al., (2021). Mata Allo watershed has a rounded or elongated rounding ratio where the time required by river water is getting shorter so that river flood fluctuations will be higher and the ratio of low relief and gentle slopes (Uca et al., 2021).

Modeling the distribution of flood inundation that occurs at the research site using 2D HEC-RAS simulation. The simulation results obtained through the HEC-RAS application are given to produce inundation maps to determine the estimated flood hazard areas (Bharath et al., 2021). Determination of the inundation area limit that occurs due to peak flood discharge is carried out with the assumption that the flow is in the form of unsteady flow in the state of the river at the study location. In addition, knowing the flood hazard assessment requires flood propagation that changes over time. This is the basis that steady flow simulations can illustrate how flood hazards through water surface elevations (Albo-Salih, Mays and Che, 2022) and become part of an early warning information system against flooding. Based on the simulation results, the simulated flood inundation area shows 54.9266 Ha at the 2-year return period, 59.3351 Ha at the 5-year return period, 62.1189 Ha at the 10-year return period, 64.8449 Ha at the 25-year return period, 68.734 Ha at the 50-year return period and 69.734 Ha at the 100-year return period. The depth value shows the uniformity of the location of the flood vulnerability level between return periods. Based on the classification of Ahmad *et al.* (2022) to the depth of flood. The average level of vulnerability in the very low range is ±9.60 Ha, low range is ±8.8 Ha, moderate vulnerability range is ±13.63 Ha, high vulnerability level is ±23.58 Ha, and the level of vulnerability in the extreme range is ±25.71 Ha. These results indicate that areas in the Mata Allo Sub-watershed are in the high to extreme range with inundation depths of 2 meters to above 5 meters. This result also includes the value of river depth during flooding according to the HEC-RAS simulation that has been carried out (Ahmad et al., 2022).

6. CONCLUSIONS

This research produced flood inundation maps in the area around the Mata Allo Sub-watershed study site using a hydraulics and Geographic Information System approach, with the help of HEC-RAS software. Based on the results of the research, it was found that flood mapping using 2D HEC-RAS can provide a visualization of the distribution of inundation and the potential level of flood vulnerability that may occur as a result of flood recurrence. This is based on the results of spatial

analysis of the height and flood inundation of the Mata Allo Sub-watershed, which shows that the Lewaja Village and Galonta Village areas are at the highest level of inundation of potential floods and are affected by flood events. In addition, given that the simulations in this flood modeling incorporate peak discharge data obtained from the last 10 years of maximum rainfall data, as well as river geometry data that has a resolution of 8.2 meters, the maps resulting from this modeling may not always represent annual routine events in the Mata Allo Sub-watershed study area.

The use of annual rainfall data in an effort to obtain river discharge data using the Nakayasu HSU method is very helpful in obtaining discharge data. The actual data discharge for rivers in Indonesia is still lacking, especially for rivers in Enrekang (Mata Allo Sub-watershed). With this debit data, the use of the HEC-RAS program can be done by inputting the existing debit data. The results can then describe flood-prone areas by classifying flood areas based on their depth level. But keep in mind, the resolution of the DEM data used is only 8.2m which cannot fully describe the cross-sectional model in detail. So, the results of this study are only limited to an overview in anticipation of floods that often occur in the study area.

REFERENCES

- Ahmad, I., Wang, X., Waseem, M., Zaman, M., Aziz, F., Khan, R.Z.N. and Ashraf, M. (2022) "Flood Management, Characterization and Vulnerability Analysis Using an Integrated RS-GIS and 2D Hydrodynamic Modelling Approach: The Case of Deg Nullah, Pakistan," *Remote Sensing*, 14(9). Available at: <https://doi.org/10.3390/rs14092138>.
- Albo-Salih, H., Mays, L.W. and Che, D. (2022) "Application of an Optimization/Simulation Model for the Real-Time Flood Operation of River-Reservoir Systems with One-and Two-Dimensional Unsteady Flow Modeling," *Water (Switzerland)*, 14(1). Available at: <https://doi.org/10.3390/w14010087>.
- Amin, M.T., Izwan, M. and Alazba, A.A. (2016) "A best-fit probability distribution for the estimation of rainfall in northern regions of Pakistan," *Open Life Sciences*, 11(1), pp. 432–440. Available at: <https://doi.org/10.1515/biol-2016-0057>.
- Avinash, K., Jayappa, K.S. and Deepika, B. (2011) "Prioritization of sub-basins based on geomorphology and morphometric analysis using remote sensing and geographic information system (GIS) techniques," *Geocarto International*, 26(7), pp. 569–592. Available at: <https://doi.org/10.1080/10106049.2011.606925>.
- Bharath, A., Shivapur, A. V., Hiremath, C.G. and Maddamsetty, R. (2021) "Dam break analysis using HEC-RAS and HEC-GeoRAS: A case study of Hidkal dam, Karnataka state, India," *Environmental Challenges*, 5(November), p. 100401. Available at: <https://doi.org/10.1016/j.envc.2021.100401>.
- BNPB (2022) *Kejadian Bencana per Provinsi Tahun 2022*. Available at: <https://gis.bnpb.go.id/> (Accessed: September 7, 2022).
- Bomers, A., Meulen, B. van der, Schielen, R.M.J. and Hulscher, S.J.M.H. (2019) "Historic Flood Reconstruction With the Use of an Artificial Neural Network," *Water Resources Research*, pp. 73–88. Available at: <https://doi.org/10.1029/2019WR025656>.
- Bomers, A., Schielen, R.M.J. and Hulscher, S.J.M.H. (2019) "Decreasing uncertainty in flood frequency analyses by including historic flood events in an efficient bootstrap approach," *Hazards Earth Syst*, pp. 1–23. Available at: <https://doi.org/https://doi.org/10.5194/nhess-19-1895-2019>, 2019.
- Geleta, C.D. and Deressa, T.A. (2021) "Evaluation of Climate Hazards Group InfraRed Precipitation Station (CHIRPS) satellite-based rainfall estimates over Finchaa and Neshe Watersheds, Ethiopia," *Engineering Reports*, 3(6), pp. 1–16. Available at: <https://doi.org/10.1002/eng2.12338>.
- Gray, D.M. (1973) *Handbook on the Principles of Hydrology: With Special Emphasis Directed to Canadian Conditions in the Discussions, Applications, and Presentation of Data*. Water Information Center, Incorporated (A Water Information Center publication). Available at: <https://books.google.co.id/books?id=5P1OAAAAMAAJ>.
- Haidu, I. and Ivan, K. (2016) "Urban runoff pathways and surface water volumes evolution. Case study: Bordeaux 1984-2014, France," *Houille Blanche*, 2016-October(5), pp. 51–56. Available at: <https://doi.org/10.1051/lhb/2016050>.

- Harahap, R., Jeumpa, K. and Hadibroto, B. (2018) "Flood Discharge Analysis with Nakayasu Method Using Combination of HEC-RAS Method on Deli River in Medan City," *Journal of Physics: Conference Series*, 970(1). Available at: <https://doi.org/10.1088/1742-6596/970/1/012011>.
- Indrawan, I. and Siregar, R.I. (2018) "Analysis of flood vulnerability in urban area; A case study in deli watershed," *Journal of Physics: Conference Series*, 978(1). Available at: <https://doi.org/10.1088/1742-6596/978/1/012036>.
- Kang, M.S., Goo, J.H., Song, I., Chun, J.A., Her, Y.G., Hwang, S.W. and Park, S.W. (2013) "Estimating design floods based on the critical storm duration for small watersheds," *Journal of Hydro-Environment Research*, 7(3), pp. 209–218. Available at: <https://doi.org/10.1016/j.jher.2013.01.003>.
- Khaddor, I. and Alaoui, A.H. (2014) "Production of a Curve Number map for Hydrological simulation -Case study: Kalaya Watershed located in Northern Morocco," *International Journal of Innovation and Applied Studies ISSN*, 9(4), pp. 2028–9324. Available at: <http://www.ijias.issr-journals.org/>.
- Ben Khalfallah, C. and Saïdi, S. (2018) "Spatiotemporal floodplain mapping and prediction using HEC-RAS -GIS tools: Case of the Mejerda river, Tunisia," *Journal of African Earth Sciences*, 142, pp. 44–51. Available at: <https://doi.org/10.1016/j.jafrearsci.2018.03.004>.
- Kim, V., Tantance, S. and Suparta, W. (2020) "GIS-Based Flood Hazard Mapping Using HEC_RAS Model: A Case Study of Lower Mekong River, Cambodia," 15(1), pp. 16–26. Available at: https://doi.org/10.21163/GT_2020.151.02.
- Kodoatie, R.J. (2013) *Rekayasa dan Manajemen Banjir Kota*. Yogyakarta: ANDI OFFSET.
- Le, A.M. and Pricope, N.G. (2017) "Increasing the accuracy of runoff and streamflow simulation in the Nzoia Basin, Western Kenya, through the incorporation of satellite-derived CHIRPS data," *Water (Switzerland)*, 9(2). Available at: <https://doi.org/10.3390/w9020114>.
- Lea, D., Yeonsu, K. and Hyunuk, A. (2019) "Case study of HEC-RAS 1D-2D coupling simulation: 2002 Baeksan flood event in Korea," *Water (Switzerland)*, 11(10), pp. 1–14. Available at: <https://doi.org/10.3390/w11102048>.
- Liu, Z., Merwade, V. and Jafarzadegan, K. (2019) "Investigating the role of model structure and surface roughness in generating flood inundation extents using one- and two-dimensional hydraulic models," *Journal of Flood Risk Management*, 12(1). Available at: <https://doi.org/10.1111/jfr3.12347>.
- Ngo, H., Bomers, A., Augustijn, D.C.M., Ranasinghe, R., Filatova, T., van der Meulen, B., Herget, J. and Hulscher, S.J.M.H. (2023) "Reconstruction of the 1374 Rhine river flood event around Cologne region using 1D-2D coupled hydraulic modelling approach," *Journal of Hydrology*, 617(PC), p. 129039. Available at: <https://doi.org/10.1016/j.jhydrol.2022.129039>.
- Pathan, A.K.I. and Agnihotri, P.G. (2020) "2-D unsteady flow modelling and inundation mapping for lower region of Purna basin using HEC-RAS," *Nature Environment and Pollution Technology*, 19(1), pp. 277–285.
- Popescu, C. and Bărbulescu, A. (2023) "Floods Simulation on the Vedea River (Romania) Using Hydraulic Modeling and GIS Software: A Case Study," *Water*, 15(3), p. 483. Available at: <https://doi.org/10.3390/w15030483>.
- Prastica, R.M.S. and Fanani, A.J. (2021) "What causes Ngancar River in Wiroko Temon sub-watershed vulnerable to flooding?," *IOP Conference Series: Earth and Environmental Science*, 847(1). Available at: <https://doi.org/10.1088/1755-1315/847/1/012003>.
- Pratiwi, Z. and Santosa, B. (2021) "Journal of Geospatial Information Science and Engineering," *Journal of Geospatial Information Science and Engineering*, 4(1), pp. 81–86.
- Rajeev and Singh, S. (2016) "Watershed Management - A GIS Approach," *IMPACT: International Journal of Research in Applied, Natural and Social Sciences*, 4(6), pp. 109–116. Available at: <https://oaji.net/articles/2016/491-1468576163.pdf>.
- Rauf, I. (2021) "Analisis Spasial Tingkat Bahaya Banjir Desa Amasing Kali Dengan HEC-RAS 2D," *Jurnal Teknik*, 19(2), pp. 107–119. Available at: <https://doi.org/10.37031/jt.v19i2.188>.
- Sabău, D., and Șerban, G. (2018). Arch dam failure preliminary analysis using HEC-RAS and HEC-GEO RAS modeling. Case study Someșul Rece 1 reservoir. *Forum Geografic*, XVII (1), 44-55. doi:10.5775/fg.2018.058.i

- Steele, M., Chaseline, J. and Hurst, C. (2006) *A comparison of the powers of the Chi-Square test statistic with the discrete Kolmogorov-Smirnov and Cramér-von Mises test statistics.*, *COMPSTAT Proceedings in Computational Statistics*. Available at: <http://eprints.jcu.edu.au/281/>.
- Triatmodjo, B. (2013) *Hidrologi Terapan*. Keempat. Yogyakarta: Beta Offset.
- Uca, Amal, Tabbu, M.A.S., Yusuf, M., Jeddayanti and Sriwahyuni (2021) "Karakteristik Morfometri Sub DAS Saddang dan Mata Allo Provinsi Sulawesi Selatan," *Indonesian Journal Of Fundamental Sciences*, 7(2), pp. 52–66. Available at: <https://doi.org/https://doi.org/10.26858/ijfs.v7i2.26151>.
- US Army Corps of Engineers (2016) "HEC-RAS River Analysis System: User Manual 1D and 2D Version 5.0," *US Army Corps of Engineers*. US ACE IWR Hydrologic Engineering Center, pp. 1–790. Available at: www.hec.usace.army.mil.
- Vojtek, M. and Vojteková, J. (2019) "Flood susceptibility mapping on a national scale in Slovakia using the analytical hierarchy process," *Water (Switzerland)*, 11(2). Available at: <https://doi.org/10.3390/w11020364>.

QUANTITATIVE AND QUALITATIVE DATA IN DISASTER RISK MANAGEMENT OF FIRES: A CASE STUDY FROM SOUTH AFRICA AT VARIOUS GEOGRAPHICAL LEVELS

Rennifer MADONDO¹ , *Roman TANDLICH^{1*}* , *Eric Thabo STOCH²* ,
Ágoston RESTÁS³  and *Siviwe SHWABABA¹* 

DOI: 10.21163/GT_2023.182.02

ABSTRACT. The current paper is aimed at investigating some quantitative and qualitative data, as well as their implications for the space/place/time perspective in terms of fire disaster management in Makana Local Municipality. The working hypothesis of the current article is that fire-fighting under drought conditions will pose severe challenges on the disaster risk management system (DRM) in the study area. Methodology of the article includes a combination of document analysis, modelling using the Google-related tools to track and statistically analyse the public interest in fires, the legislation, and financial/practical implications of the drought on fire disaster management in Makana Local Municipality. Results of the study indicate that there has been a constant and increasing trend in terms of the South African public's interest in fires. That trend is driven by interest in fire-fighting equipment and possibly also by the interest of the South African population in fire-fighting as a career. On causality front, the interest in fires is quantitatively driven by number of fires in South Africa between 2004 and 2017, as well as access to the internet by the South African population.

Key-words: *Fire, Risk, Quantitative data, Qualitative data, Disaster management, South Africa*

1. INTRODUCTION

Disasters are devastating events that lead to disruption of set ways in which humans are used to experience everyday life and situations in it. Between two disasters, the human society or a population at risk are in a stable condition or a steady state of their existence (Madondo et al., 2023). The population at risk exists as part of an open system, where the population members interact with each other, the society outside of the area at hazard interacts with the population at risk and the biosphere and the environment at large do as well. When no disaster has just happened, no response or recovery are unfolding, the population at risk exists by exchanging resources and information with the outside world and the surrounding environment (Madondo et al., 2023). The flow of the materials, energy, information and other everyday necessities of humans and socio-ecological systems lead to humans and the disaster-prone area to be part of a system and a location, where only the GPS coordinates are constant (Madondo et al., 2023). The remainder of the space, humans, the biosphere, and environment are in a constant state of flux. Humans can be stationary, but they can also move freely in and out of the area at hazard as part of an open geographical system. As the disaster hazards are omnipresent, and they continuously interact with the conditions of human existence at the GPS coordinates of a location at hazard. From an anthropocentric point of view, a steady-state population at risk will be experiencing a sense of place through the so-called 'life space', i.e. which is here understood as a combination of everyday activities and place that a human being exists in (Lawton, 1983). This overlaps with the life space of other people through interactions, which can be traced, monitored, and evaluated as a living and fluid structure of space over time (Gong et al., 2020).

¹ *Disaster Management and Ethics Research Group (DMERG), Faculty of Pharmacy, Rhodes University, Grahamstown/Makhanda 6140, South Africa; renniferray@gmail.com, corresponding author* r.tandlich@ru.ac.za, siviwe.shwababa@ru.ac.za.*

² *African Centre for Disaster Studies, Faculty of Natural and Agricultural Sciences, North-West University, Potchefstroom 2520, South Africa; ejstoch@gmail.com.*

³ *Institute of Disaster Management, National University of Public Service, 1441 Budapest, Hungary; Restas.Agoston@uni-nke.hu.*

As a species, humanity has not only been living with disasters, but recent discourse and discoveries in the disaster risk science tend to indicate that humans have become triggering agents of disasters (Mizutori, 2020). Human actions, e.g. the building of settlements on marginal land, not in line with sound construction practices and in the proximity to disaster hazards (Chmutina et al., 2017), drive the occurrence and impact of disasters, they require that we stop using the term ‘natural disasters’ (Mizutori, 2020). All disasters could thus be seen as manmade and impacts of disasters, at least in part, are counteractive to ensuring human wellbeing (Padli et al., 2018). Based on the effects of climate change and other trans-boundary effects, it is the most plausible to say that disasters are manmade. At the same time, the impacts of such manmade disasters are often local based on the extent of human activity. A particular disaster always unfolds in space, affects particular people, and takes place in a given time frame (Meriläinen and Koro, 2021). In the accompanying paper, Madondo et al. (2023) described in detail that the Kant’s definition of the space could be applied as way to interpret the experiences for the population(s), which is impacted by a disaster, or who live in a disaster-prone area, in a proximity to a disaster hazard (Lawton, 1983; Stanford Encyclopedia of Philosophy, 2009-2022). From a disaster risk management (DRM) point of view, a population of humans can be seen as a population at risk, i.e. population which lives or has lived in the vicinity of a disaster hazard for a short or a long period of time. In contrast, a population under disaster is a human population that finds itself existing in a disaster-impacted zone, geographical location at a particular time, in a place that has been impacted by a disaster. That disaster had been triggered by the proximity to a hazard by the population at risk (Madondo et al., 2023). Population at risk can transform into a population under disaster during such conditions, based on the space/place/time perspective (Madondo et al., 2023). Extent of the transformation into population under disaster unfolds and must be studied or understood in the same space across time frame of the disaster management cycle for a given disaster (Daly et al., 2020).

The theoretical perspective, which the authors have compiled as an accompanying paper to this article, provides an outline about the nature and types of data that are used in DRM (Madondo et al., 2023). Data were argued in that paper to be critical in the description of the ‘life space’ of individual humans and communities they are part of. Careful evaluation of quantitative and qualitative data facilitates allocation of the resources along the lines of principles of humanitarian ethics, humanity, impartiality, independence, and neutrality (NRC, 20023). Resources, their types and quantities; and their allocation to the population at risk or under disaster at particular GPS coordinates must be carefully tailored to the needs of the local population (Madondo et al., 2023). Diversity of the DRM practices can be seen at the theoretical and practical levels of engagement of diverse DRM stakeholders in phases of the disaster management cycle. They reflect the local conditions that set the overall scene for the disaster unfolding, the legislative settings in which the phases of the disaster management cycle are carried out, and the interaction among the private citizens, the government, the insurance companies, and the non-governmental/third sector that assists with specific tasks in the DRM landscape (Lee et al., 2014).

Localisation of approaches to DRM manifests in relevant differences between the low-income and middle-income settings (Lee et al., 2014). Data from the local settings, whether quantitative or qualitative in nature, are important as they provide for an ethical, a locally-tailored, and the most efficient foundation for unit operations in the individual stages of the disaster management cycle. It is a foundation to protect the steady state of human ‘life space’ by the country’s DRM system, or to minimise the extent of changes between the steady state of existence at risk and the ‘(un)steady state’ under disaster. In the next section, data sources for DRM in South Africa are outlined here and linked to the theoretical concepts of Madondo et al. (2023).

1.1. Data and the DRM landscape in South Africa

Life space of South Africans and the localisation of the data about it can be demonstrated by outlining the disaster profile of the country (e.g. Vhiriri et al., 2021). As a snapshot of the last 12 months, South Africa has experienced floods and landslides in the Province of KwaZulu-Natal which

led to 448 fatalities and the displacement of 40000 (OCHA/Reliefweb, 2022). Some communications about disaster response and recovery were unclear tracking the source(s) of the issues identified (Linyana, 2022). Drought is another disaster type that has plagued South Africa in recent years (Iheanetu and Tandlich, 2022). Other examples of recent disasters include the riots and widespread civil unrest, looting, blockages of highways and the destruction of economic assets across the Gauteng and the KwaZulu-Natal Provinces in July 2021 (Daily Maverick, 2021). The 2017 Knysna fire destroyed extensive parts of the Southern Cape and the DRM data were collected, e.g. the smoke extent over the impacted area via aerial photography to assess the size of burnt assets and forests (VWFM, 2017-present, page 7). Widespread inefficiencies in the delivery of stable electricity supply by the national electricity company of South Africa has also created conditions that precipitate or amplify disaster hazards, e.g. interruption of potable water supply and economic damage to mining and manufacturing (Winter, 2011; City of Johannesburg, 2018). In South Africa, lack of safe and sustainable potable water supply can be the result of a complicated socio-economic, political, and technical/infrastructure challenges (Calverley and Walther, 2022). The above-mentioned is just a snapshot of the South African disaster profile, and not an exhaustive list. It does, however, illustrate complex nature of the DRM landscape in the country and the type of quantitative/qualitative data that need to be collected and analysed by the DRM system in South Africa. As outlined by Madondo et al. (2023), data used in such evaluations are a combination of peer-reviewed and non-peer-reviewed types.

Data on disaster impacts are collected in various ways, in various databases and by various institutions (Jones et al., 2022). The collected data reflect the historical and current factors, contribute to the DRM landscape complexity, e.g. the well-documented and commonly known unequal distribution and access to resources in South Africa during apartheid and the resulting vulnerability in informal settlements (Mntambo and Adebayo, 2022). The National Disaster Management Centre, the central organ of state responsible for the coordination of the DRM system in South Africa, runs the historical database for declared disasters (NDMC, 2006-2023). The same institution also allows for the ongoing collection of data, e.g. on the municipal disaster management centres, hazards, and early warning (NDMC, 2023). At the same time, data are collected and released by other institutions, such as the South African Weather Service on drought (SAWS, 2022). At the same time, there has been tracking of the COVID19 pandemic information by various international stakeholders that South Africa collaborates with, e.g. the World Health Organisation (WHO, 2019-2023). South Africa's population at risk also carries a trauma and 'qualitative record of apartheid atrocities', a struggle for an inclusive society, the record of the manmade disaster. This is a legacy disaster and apartheid atrocities have made South African population under constant disaster and significant decrease in human wellbeing for a large part of the country's population (Mothhoki, 2017).

Historical and current human actions are dual in anthropogenic duality impact. This is because cumulative impact of human actions on the biosphere and environment might have short-term benefits to humanity, but they do negatively influence the human wellbeing in the long run (Iheanetu et al., 2023). This is long run across space, place and time...creating the necessary perspective that space/place/time will have ethical, qualitative, and quantitative dimensions in the DRM context (Leinfelder, 2020). The historical, cumulative, and current actions will also impact resilience, vulnerability, and the temporality of the transformation of population at risk into a population under disaster (Iheanetu et al., 2023). Human wellbeing is negatively impacted by those factors and actions, as these lead to hazard enhancement for a given population at risk, e.g. the population of South Africa. Current factors, which influence the DRM landscape and impacts on a population at risk or population under disaster, can be studied at various levels of complexity (Leinfelder, 2020; Madondo et al., 2023). Those levels can include the individual level, the level of a community...e.g. a town, city or village, a country or at the global level. It is possible to make the argument that whichever level one chooses, a human being, a population at risk, or under disaster can be considered part of a geographical system, e.g. an open system (Chick and Dow, 2005). South African population will be exposed to elimination of access to information, access to resources, transport in and out of an area at hazard, and to work during a disaster (Madondo et al., 2023). Thus, transformation of the population at risk in South Africa to a

population under disaster will be linked to closing off or shrinking of the open system. This is the system that an individual, a community, or the country's population was part of prior to the disaster onset. Disasters can thus be seen as a human-driven and impacts/unfolding of disaster takes place in open geographical systems. Therefore, the geographical space, place and time will be transformed as well, and this will in turn change the DRM landscape in the disaster-impacted area of South Africa (Madondo et al., 2023). In the next section, the DRR/DRM and its relationship to various types of geographical systems are described.

1.2. Context of the current paper

Disasters in South Africa, e.g. the 2022 floods, occurred and unfold in a discontinuous set of 'life space' objects which are in turn governed by factors which have been developing over time (Madondo et al., 2023). Floods occur in South Africa annually and the country is also prone to drought (see below). Both types of disasters have been increasing in frequency in last several years, due to climate change and their impacts are also increased due to the location of impacted settlements. Balance of current and historical factors which have played a role in shaping the relevant 'life space' as a concurrent DRM space in South Africa, are not simple but rather the cumulative result of the historically-driven shaping of the space and place at the time of life for and by the population at risk in South Africa (Iheanetu et al., 2023; Lawton, 1983; Stanford Encyclopedia of Philosophy, 2009-2022). In addition, the disaster for a given South African community will unfold at a place of their existence and against the history of the objects' organisation in that space and place of existence. Interactions of these factors will then precipitate a particular disaster, occurring at a given point in time and impacting a given South African community. Localisation of data from that community will play a critical role in the DRM of the disaster in question. Historical factors will overlap with the parameters of the current situation/current human actions in the disaster niche and the population at risk will transform into the particular population under disaster (Iheanetu et al., 2023). Indicators of disaster impacts, that are lagging and quantitative, provide a depersonalised perspective about the particular disaster impacts. Stripping away the information about, who individually is at risk or under disaster... who is the 'source of the data', allows the DRM practitioners to evaluate the general trends in data at the community level. This is then the foundation for dealing with the impacts of a particular disaster or hazard on a particular population at risk or under disaster. Correlation of such data, with other variables to establish DRM causality in the general sense (Madondo et al., 2023), will mainly be effective in the preparedness and mitigation phases of the disaster management cycle. Quantitative and real-time/near-real-time data will allow for tracking of the interest of the public in DRM information campaigns, to conduct triage of patients and resources in the disaster-impacted zone. This type of quantitative data is partially overlapping with qualitative data, e.g. medical history of a patient will be important to establish how a patient might have been injured and then diagnosis can provide an indication about the severity/frequency of impact of disaster on the population or individual under it. Personal identifiers are attached to data, which are related to a particular person, i.e. a human being under disaster with a name or biometric identification (IASC, 2021). It is necessary to assist the patients with the targeted medical care and other assistance in line with unit operations in the response and recovery phase of the disaster management cycle. The real-time or near-real-time qualitative data can be social media posts (Madondo et al., 2023). These are personal information-linked, e.g. the Twitter handle can be known for the message originator. Personal stories of the victims of human trafficking or refugees can be known but identifying marks can also be stripped away. Balancing the use of quantitative and qualitative data, which can be anonymised and personalised, provide a complete picture of the transformation of a population at risk into a population under disaster (IASC, 2021). It allows the DRM practitioners to gain understanding about the equality of presence and inequality of path for the members of the population under disaster from the space/place/time perspective.

The equality of presence means that all people impacted by a disaster are present in the disaster-impacted zone during the response and recovery phases of the disaster management cycle. All of such humans are equal and must be provided with assistance according to the principles of humanitarian

ethics (NRC, 2023). On the other hand, quantitative and qualitative data provide the basis for understanding the pathway of the population at risk into an unsteady state of the population under disaster. Highly personalised or de-personalised data provide a description of that path from a steady state of existence, from the multi-loci and discontinuous place of normalcy, towards the time of disaster (Madondo et al., 2023). Understanding of equality of presence is matched by data to investigate the inequality of path. Data collection should reflect this by keeping information flowing openly between the population at risk and the DRM practitioners. Analogical open system and human geography should apply in the conditions under disaster. Openness of the data and transparency of its evaluation/modelling is a necessity as the path from 'at risk' to 'under disaster' is linked to the DRM system. This will practically mean that data must be collected, about the changes to human life space at risk and under disaster. Such data must be evaluated and used continuously to test/evaluate, update, and improve the DRM system in a country. Results of that process are then applied as a foundation for protecting the wellbeing of the population at risk and under disaster. Data in DRM are thus part of an open system, and it depicts a geography of human wellbeing from a space/place/time perspective (Madondo et al., 2023). In this way, data about human impacts of a disaster can be seen as an embodiment of the civil protection in the DRM. Therefore data are part of a system aimed at decreasing human injuries and fatalities, so the data will be linked to the DRM policies and the whole DRM system in a country, e.g. South Africa.

Quantitative data and qualitative data being available, the South African DRM system does conduct unit operations in the individual phases in the disaster management cycle which are informed by data (based on the above). However, the extent varies greatly between the national, provincial, and local government. In an ideal situation, the multi-stakeholder platforms are involved in the use and analysis of data and making decisions based on them and to It is very redundant; reformulation needed increase resilience of systems (Ngqwala et al., 2017; Dormady et al., 2021). Ongoing evaluation of data on risk, hazards, and vulnerability analysis is part of continuous minimisation or likelihood reduction of the impacts of disasters on human wellbeing. Therefore DRM in the country is a combination of observations, data collection and evaluation; and targeted minimisation of disaster risk through specifically-tailored interventions to local conditions. This points to the fact that DRM has features of a natural experiment (Messer, 2016) and/or a quasi-experiment (Béné et al., 2020). A disaster will be classified by a type, e.g., a tornado, cyclone, flood or drought. Using the natural experiment/quasi-experiment analogy, the disaster onset can be seen as an intervention which targets a population at risk and its members are affected by disaster impacts. Based on the combination of the historical and current human actions influencing the life space of the population at risk, that population is not randomly split into sub-groups that are impacted by the disaster type to varying extents. However, human actions, at least in part, drive the disaster type as an intervention that transforms the population at risk into one under disaster. So the group selection for the degree and severity of the disaster impact does not take place intentionally, but disaster can be studied as being partly human-driven and intervention-like human actions lead to data production. The produced data are then evaluated to study the disaster impacts in order to speed up the return of population under disaster to the population at risk. In addition, evaluation of the natural experiment-like situation of disaster allows the DRM system to mitigate future transformation of the population at risk to a population under a type of disaster. Thus disaster can be looked as having properties of natural experiments through considering their utility (Crane et al., 2020, Box 1).

Interventions in natural experiments are targeted to impact everyday activities, e.g. changes to labelling of foodstuffs to fight obesity (Crane et al., 2020). Disasters are similar in the sense that they disrupt and change the everyday activities in the discontinuous and multi-loci life space of a single human or population at risk. Those impacts affect a particular population at risk, a population who are located in a specific life space(s). The onset of a disaster is followed by interventions, and wellbeing of the population at risk/under disaster can be protected or improved. The data collected at specific GPS coordinates and actions taken from them are based on and take into account the equality of presence and the inequality of path to the particular situation by the population under disaster. Mitigation and preparedness phases of DRM contain dedicated/intentional activities along the lines

of natural/quasi-experiments to minimise disaster risk impacts on human wellbeing based on data (Béné et al., 2020). Such a feedback loops into improvements of the DRM system from the space/place/time perspective (Lawton, 1983). Risk assessment and DRM are localised in nature, and they often target systemic issues and impacts of disaster in a highly localised settings of space/place and at a given time. In addition, this is the cyclic process of risk assessment (risk identification, risk analysis, risk evaluation) and risk treatment (ISO, 2018). This view of DRM places humans at the centre of the impacts and also at the need for conscious activities to decrease the disaster risk and disaster impacts on wellbeing of *Homo sapiens*. The current article builds on the theoretical perspective of Madondo et al. (2023) and it uses the disaster settings in a municipality in the Eastern Cape Province of South Africa to demonstrate the localisation of data for drought and fires, their evaluation and DRM implications.

1.3. Study settings and the working hypothesis

Localisation of the data will be examined in this paper for parts of the Sarah Baartman District Municipality (SBDMuni), where the profile of disaster risk management and relevant policies have been studied and analysed by Madikizela et al. (2019). Drought and its impact on the agricultural production were specifically seen as affected (Madikizela et al., 2019). The development costs and their investment mitigate possible disaster impacts in the future (Oosthuizen, 2018). Population of the SBDMuni has been impacted heavily by ongoing drought in the Eastern Cape Province of South Africa (Iheanetu and Tandlich, 2022).

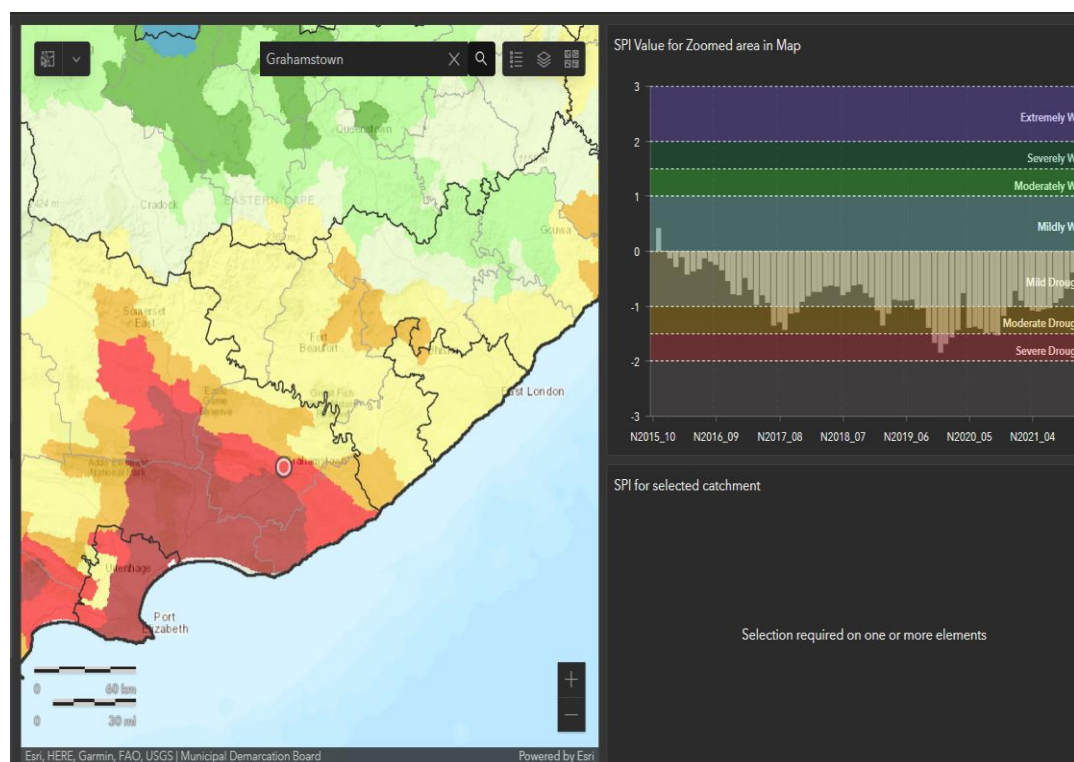


Fig. 1. The GIS presentation of the SPI index in Grahamstown/Makhanda, South Africa (NDMC, 2022).

South Africa is a water scarce country, and many citizens still lack access to sufficient quantities and quality of drinking water, e.g., in Makana Local Municipality, the Eastern Cape Province of South Africa (Iheanetu and Tandlich, 2022). Consequently, consumption of contaminated water has

potential health risks, and this requires regular water quality monitoring. Since 2015, Makana Local Municipality and the Sarah Baartman District have been in a state of drought disaster (NDMC, 2022). Drought is evaluated and classified using the SPI index, which is calculated using precipitation data in a given area (Karabulut, 2015).

As it can be seen from **figure 1**, the SPI values for the Makhanda/Grahamstown area have been equal to 0 or it has had negative values down to -2 since 2015 until present (NDMC, 2022). As a result, the area has experienced mild to severe drought in that time period (see below). This has led to cascading effects on the provision of drinking water to the population in Makana Local Municipality, part of the SBDMuni (Malema et al., 2019; Iheanetu and Tandlich, 2022). The decreased drinking water supply is further compounded by the fact that Makhanda/Grahamstown has long suffered from infrastructure problems and supply interruptions/water quality issues (Makana Local Municipality, 2020-2021). Drought and problems with the water reticulation infrastructure can contribute to the increased risk of fires and compromised firefighting if a fire had broken out.

Under conditions like these, it might be challenging to get the sufficient volumes of water to operate the fire hydrants to fight any ensuing fires (Martin, 2016). The situation in the SBDMuni is also complicated by loadshedding or controlled power cuts in South Africa, which can compromise water pumping and water availability (Winter, 2011). The DRM system in the SBDMuni and the Eastern Cape Disaster Management Centre put in place prohibition of open fires, with threat of prosecution for violators in 2020 and 2021 (SBDMuni, 2022). Exceptions had only been allowed under strict conditions, e.g. with the approval of the Chief Fire Officer for Makana Local Municipality (SBDMuni, 2022). The municipal website contained information about the details of the fire disaster management, but that might be outdated as no updates appear to have been done in the past 10 years (Makana, 2013). However, the DRM system worked in conjunction with the community, e.g. as documented with the coordinated efforts between the fire fighter and the community (Grocott's Mail, 2018). Business and government from SBDMuni have collaborated on boosting the capabilities of the Makana fire services, e.g. Santam donated personal protective equipment, foam cans and other materials to the worth of 220000 ZAR in 2016 (1 USD equal approximately to 16.0-17.5 ZAR; Creamer Media – Engineering News, 2016).

There are thus grey-literature sources and newspaper articles that indicate fire disaster management is actively pursued in Makana and SBDMuni. However, there has been no systematic and academic assessment of the fire disaster management in Makana Local Municipality as a model part of SBDMuni. This should urgently be addressed based on the policy dimension, conditions of drought and the resulting compounding factors for fire disaster management in the municipality. Therefore, the current paper is aimed at investigating some quantitative and some qualitative data, as well as their implications for the space/place/time perspective in Makana Local Municipality and SBDMuni, in terms of fire disaster management. The working hypothesis of the current article is that firefighting under drought conditions will pose challenges on the DRM system in SBDMuni and Makana Local Municipality. These challenges will be practical, ethical and adaptation will be required from the DRM system of the municipality. Understanding stakeholder involvement and gaps in the unit operations in the disaster management cycle can be identified using these tools and improvements can be proposed.

2. METHODOLOGY

2.1. Public interest as an open-system and quantitative data example for South Africa fires

An open system will require the free exchange of information between the SBDMuni/Makana population, the South African population and the global information/DRM landscape. Information about fires will be sought by the population on a continuous basis and thus there should be data sources to evaluate this interest. Some commonly known tools are questionnaires (Bird, 2009) and focus group discussions (Rivera, 2019). Excellent qualitative and quantitative data for DRM can be obtained through them if they are run or administered through openness of interaction and by following research ethics principles (Francioli, 2020). Results from the use of these tools can be

valuable for the DRM planning in the preparedness and mitigation phase of the disaster management cycle. This is mostly the case, as questionnaires and focus groups provide mostly lagging indicator data. In real time or near-real time, a different set of tools is necessary. One that allows for the evaluation of the public interest in a particular disaster type, i.e. fires in South Africa, over extended periods of time but without the delay of lagging indicators. Such a tool should be providing data within days or hours of the data being produced. Madikizela et al. (2022) tested the use of the Keywordseverywhere.com plugin to retrieve the WASH monthly search volumes from Google for the 2004-present time period. In the next article, Tandlich et al. (2023), who used a similar methodology to test the reliability of the plugin for real-time application in emergency management. Analogical methodology was used here with the focus on fires in South Africa. Therefore analysing these data can lead to the examination of the fluctuation and temporal variability in the public interest in disaster information, e.g. the fire-related search terms.

In the current article, the plugin was downloaded and installed on their PC by the authors and the online search credits were procured from the plugin developer (as shown on <https://keywordseverywhere.com/credits.html>; website accessed on 23rd January 2023), a four-prong strategy for public interest assessment and the data accuracy/validity provided by Keywordseverywhere. Firstly, the monthly search volumes for fire on Google in South Africa were obtained from the first month of 2004 until the sixth month of 2022. The monthly search volumes were extracted from Google (Y_i) on three separate occasions between June and November 2022. The extracted data for fire were averaged for the given month, and the standard deviation of the month search volumes from three data extractions was calculated using the Microsoft Excel 2022 software (Microsoft Inc., Johannesburg, South Africa). Any trends in those volumes were assessed for increase or decrease with time using the Mann-Kendall test at 5 % level of significance (Past 3.0, Hammer et al., 2001). Secondly, the Y_i values in each year were summed up to obtain the yearly volumes of fire searches in South Africa between 2004 and 2017. As shown in Equation (1), *TFSSA* is the yearly volume of the Google searches for fire in South Africa in a given year between 2004 and 2017.

$$TFSSA = \sum_1^{12} Y_i \tag{1}$$

Those yearly volumes were investigated for statistically significant correlation with the total number of fire callouts/fires in South Africa between 2004 and 2017 (as summarised by Madondo et al., 2022 and designated as *TFBC* in further text of the article). At the same time, the total financial losses from fires were correlated with the total yearly searches for fire in South Africa (see **Table 1** for value details and the summary by Madondo et al., 2022). That was done using the Spearman coefficient at 5 % level of significance (see <https://www.socscistatistics.com/tests/spearman/default2.aspx> for details; website accessed on 23rd January 2023). If the public interest followed the significance of fires as disasters in South Africa, then the number of yearly searches for fires on Google should correlate positively with the number of fires as disasters in South Africa. Fires in South Africa can be considered disasters, in terms of the fire brigade call outs, as the largest portion of the fire brigade call outs were to the domestic fires between 2004 and 2017. Such fires would have devastating consequences on the human wellbeing of the South African population, given unequal to distribution of income and other resources (IMF, 2020). Therefore, they are disasters from the viewpoint of civil protection and DRM.

Thirdly, a search was conducted for veld fire or veldfire, i.e. a term from South Africa which is not widely used outside of the country. Searches for this term were run for South Africa and for the global Google data. Veld fire/veldfire was chosen as a test term to assess the accuracy of the search results from the Keywordseverywhere.com plugin. If the plugin extracts reliable data from Google, then the search volumes for veld fire/veldfire from South Africa should accounts for the majority of the search volumes in the world. In other words, the monthly/yearly search volumes for veld fire/veldfire from South Africa should account for 100 % or close to 100 % of all global searches for the term. In the current study, veld fire/veldfire will be considered as a synonym of the wildfire.

Finally, the accuracy of the plugin will be Boksburg truck explosion/fire of December 2022. On Christmas Day 2022, a truck carrying liquefied natural gas got stuck under a bridge in the City of Ekurhuleni in the Gauteng Province (Pijoos, 2022). After about 60 minutes, there was a massive explosion and fire, which caused 37 immediate deaths and damage to a major regional hospital (Pijoos, 2022). The truck explosion and the ensuing fire was a major event which got national and international coverage (Banda and O'Reagan, 2022). It should therefore lead to the highest daily search volumes on Google Boksburg fire/explosion in the days right after the explosion and decline thereafter, i.e. about the end of next month.

The daily volumes were extracted for the time period from 26th October 2022 until 22nd January 2023. The term Boksburg explosion was chosen as a fire ensued after the truck exploded, and also because the reporting on the disasters was run under titles that contained the phrases Boksburg explosion. There was a concurrent fire and destruction due to the blast and fire, i.e. the term Boksburg explosion was deemed suitable in the context of the current article. There should be zero searches for Boksburg explosion from 26th October 2022 until 23rd December 2022. This should then be followed by sudden spikes in the search volumes and a maximum should be reached on 24th December 2022. After that, the search volumes should decrease from 25th December 2022 until 22nd January 2023.

The need to confirm data for the same time period, which had been extracted using the plugin on different occasions, are necessary as the indexing issues have been raised in relation to some Google data and the sliding time scale can cause shifts in the monthly volumes (Kovalenko et al., 2021; Madikizela et al., 2022; Tandlich et al., 2023). If the proposed pattern in the daily search volumes for the Boksburg explosion is observed, it would indicate that the Keywordseverywhere.com plugin extracts reliable search volume estimates from Google. Qualitative drivers of the South Africans' interest in fire were also analysed from the Keywordseverywhere.com plugin, to see and confirm that the disaster implications of fire drove the level of public interest in them.

2.2. Makana public interest and the DRM planning for fires at the local municipality level

Results from the previous section will indicate the level of public interest in fires and whether an online-Google linked tool can provide useful data tools for assessing the public interest in DRM. That section also states a bigger picture for the open system of South African DRM geography. It is important to use data available to assess the public interest in fires at the smaller geographical scales. Madondo et al. (2022) summarised the Makana fire callout numbers from 2004 until 2017. The data on fire brigade call outs in Makana can be used to estimate the probability of a fire on any day in a given calendar year in the municipality. That parameter was designated as *PFMM* in further text of the article and was calculated using Equation (2).

$$PFMM = 100 \times \frac{NFCM}{365.29} \quad (2)$$

In Equation (2), the number 100 allows for the reporting of probability as percentages. The numerator represents the number of the fire brigade callouts in Makana in a given calendar year, i.e. *NFCM*. The denominator represents the average days in a calendar year, namely 365.29 days, between 2004 and 2017. The calculated *PFMM* values indicate that fire hazard in Makana Local Municipality is significantly high to influence everyday lives of the population at risk there. The probability levels could be one of the drivers for the public's interest in fires. This interest was compared with other geographical scales in South Africa, as shown below.

To investigate how fires are addressed in the planning at the local government level in Makana Local Municipality, the integrated development plans from Makana Local Municipality were downloaded from the respective website for 2014 until present (Makana, 2013-present, a). Then the documents were searched for the word frequency of disaster and fire, using the Adobe Reader search function (Adobe Inc., USA) or Microsoft Word (Microsoft Inc., Johannesburg, South Africa). Then the words, notions or sentences that were associated with both terms were also analysed in each document (Fries, 2019). The ability to deal with fires the Makana DRM system was assessed by

extracting the description and/or quantity of capacity available, the resource allocation and the availability of quantitative and qualitative data on the fire disaster management, or the unit operations conducted in phases of the disaster management cycle.

The Keywordseverywhere.com plugin does not allow one to obtain a breakdown of the search volumes to smaller geographical resolution than the country level. Therefore, Google trends were used to investigate the differences in the open geographical system and the level of public interest in the fires as disasters. The monthly Google trends scores were extracted on one occasion for the 2004-2017 periods for South Africa and the Eastern Cape. The Google trends indicate the relative significance of the interest in fires in the specified geographical area, when compared to the other search term interest on Google by users in that area (see <https://support.google.com/trends/answer/4365533?hl=en> for details; website accessed on 29th January 2023). Any statistically significant difference between the two sets of scores would indicate whether there is a statistically significant difference in the relative interest of the public in fires in South Africa and the Eastern Cape population (tested using the Mann-Whitney test at 5% level of significance; Past 3.0; Hammer et al., 2001). For some towns in SBDMuni it was also possible to extract single scores, i.e. those were made part of the semi-qualitative evaluation of the fire interest in the district.

2.3. Financial estimates of the fire DRM burden on Makana population and system

Selected pieces of relevant South African legislation which governs firefighting at municipal level were assessed. One such element of legislation gives municipalities the possibility to charge tariffs for firefighting. Makana Local Municipality charges these based on an annual list of municipal charges and those were analysed in the context of the potential vulnerability implications of the Makana population (see Results and Discussion for details of relevant legislation). The costs structure of the fire tariffs will be changed on an annual basis and will likely be guided by two specific ethical considerations. Firstly, the emergency and humanitarian aspects of the fire DRM roles played by the fire departments must be taken into account. In other words, there will be activities that a fire brigade will conduct to protect and save human lives in the context of fires, in line with the principles of humanitarian ethics (NRC, 2023). Such call outs will likely not attract any charges, as the right to life is being protected (South African Constitution, 1996-present). Then there will be fires that require the protection of the assets, such as houses or infrastructure, which are like to attract some cost recovery by the municipal fire services.

The circumstances of such call outs will likely require case-by-case approach in the cost recovery, or tariff invoicing for firefighting. Equality of presence will play a significant role here. The second invoicing consideration will be the financial status of the recipient of fire brigade call outs, or activities. If a person is destitute by the impact of the fires and/or indigent prior to it (DPLG, 2009), then the person will not be in a financial position to pay for the fire brigade call outs. In such a case, the cost recovery would be unethical on the part of municipality as the controlling authority (see Results and Discussion section for details below). Inequality of path will be a key consideration in the invoicing here. A means test must be in place to decide on whether to invoice or not to invoice for the fire brigade call outs to particular Makana residents. The use of residents' information, that is available to the local municipality, will likely play a critical role in that context...as quantitative and qualitative data perspective of fire vulnerability and resilience of the Makana population at risk and under disaster.

In relation to invoicing for firefighting, there is another consideration that must be addressed. This third consideration is the estimation about the charges that a Makana household can expect to incur for a likely fire brigade-call-out scenario. For the third cost consideration, the Makana fire tariffs were extracted from the available online and open sources. To the best of the authors' knowledge, only fire tariffs for following financial years are available in the public domain for Makana Local Municipality: 2015/2016 and 2016/2017 (Makana, 2015-2017) and 2019/2020 (Makana, 2019-2020). Given the findings of Madondo et al. (2022), majority of the fire brigade call outs are related in South Africa to fires dwellings, at household level. Therefore, a model fire case, and the related tariffs likely

to be charged for it to residence in Makana Local Municipality, was run as follows. A fire response would require the mobilisation of one major appliance, one medium appliance and one auxiliary appliance. The service vehicle would also have to be deployed to fight a fire in the high-income household in Makana. For the informal dwelling, a flat rate would be charged (see Results and Discussion for details). Regression analyses were done for each appliance and fire tariff, and the r values were compared with the inflation rate in South Africa at the time. The water volume and flows were estimated from the information by Fire Protection Association of Southern Africa (FPASA, 2021) and the pricing of water used was estimated from the monthly water statement at the last author's house. The total cost of the hypothetical model case was estimated for the 2019/2020 financial year and calculated as shown in Equation (3).

$$FTMC = \sum(FTMA + FTMEA + FTAA + FTST + WC) \quad (3)$$

In Equation (3), $FTMC$ is the fire tariff charged for the use of major appliance. $FTMEA$ stands for the fire tariff charged for the use of medium appliance and $FTAA$ is the fire tariff charged for the use of auxiliary appliance. Finally, $FTST$ is the fire tariff charged for the use of service truck and WC stands for the cost of the water used. The costs were also compared to the income of a Makana household, namely 2016.96 and 3653.76 ZAR per month (1 USD = 16-17.5 ZAR; Iheanetu and Tandlich, 2022).

2.4. Compounding factors of fire disaster management in Makana

Drought in SBDMuni will lead to a decrease in the volume of available water in the district and in Makana Local Municipality. There are infrastructure problems in Makana Local Municipality that are linked to provision of public goods and service delivery. One of these challenges is the process of loadshedding, when a controlled shut down of part of the electricity grid in a geographical area/South Africa is done (Western Cape Government, 2019, page 2). Loadshedding is necessary as the generation capacity of the electricity system is not able to meet the demand for electricity (Western Cape Government, 2019, page 2). Such infrastructure problems will increase the problem in water delivery to fire sites and the electricity to pump the water to the necessary parts of the reticulation system. In South Africa and in Makana, loadshedding has been in place since 2007-2008, but the extent has been deepening since 2015 (CSIR, 2022). Loadshedding is spread geographical across the territory of South Africa and the electricity supply is cut to a particular area in 2.5-hour increments at a time (Eskom, undated). At the time of writing of the current article, there were 8 possible stages of loadshedding that Eskom, the national electricity company and the almost-monopoly of power supply in the country, had in place to deal with shortage of generation and the high demand for electricity in South Africa (Eskom, undated). The breakdown in the electricity delivery will have several implications for the fire disaster management in South Africa. Firstly, the loss of electricity can lead to the use of alternative fuel, e.g. wood and charcoal or gas, to heat residences of the Makana households (similar to the findings of Francioli, 2020). In addition, the ability to contact the fire department could be compromised. Therefore, the daily probability of loadshedding for Makana ($PLDY$) was calculated as shown below.

The power cuts in Makana Local Municipality are done by splitting the area in two sections, namely Grahamstown 1 and Grahamstown 2 (Loadshedding Schedule, 2022). For both sections of the Makhanda area, the number of hours of loadshedding at stages 1-6, which had been observed in South Africa between 2015 and 2021, were averaged out over a three-week period (see Results and Discussion for details). Raw data from the CSIR (2022) was extracted and can be found in Appendix I. In addition, the total hours of loadshedding in a given year were extracted for the 2015-2021 period (THL) were as follows: 852 hours in 2015, 0 hours in 2016 and 2017, 127 hours in 2018, 530 hours in 2019, 859 hours in 2020 and 1136 hours in 2021. The $PLDY$ value was calculated in Equation (4):

$$PLDY = 100 \times \frac{THL}{365.33 \times \sum_1^6 X \times MRSPC} \quad (4)$$

In Equation (4), X and $MRSPC$ definitions are found in Appendix I. The number 365.33 is the average number of days in a year between 2015 and 2021.

Municipal reticulation infrastructure will play a critical, namely conveyancing, role in delivering the drinking water to the consumer or residents Makana Local Municipality. It will also be used to deliver water to fire hydrants (Świętochowska and Bartkowska, 2022). That infrastructure in the Makhanda/Grahamstown area of Makana has long suffered from the pipe breaks and the results in the drinking water supply outages. This can be demonstrated by data which had been collected in the last author's house. There have been about 18 visible pipe breaks a year that have occurred over the pipe length of 1000 feet or 304.5 metres of road/pipe surface (designated as N in further text of the article) between 2015 and early 2022. The pipe break rate was accounted for until the time period of 2015-2022 and is based on visual observations by the authors in the area of the current study site. In early 2022, the asbestos/cement pipes were exchanged for the PVC pipes. The inner diameter of both types of pipes was equal to 148 mm and the outer diameter was equal to 200 mm. The pipe break rate can be used to estimate the age of the municipal pipes in the study area. Based on the data available to the author, the model of Shamir and Howard (Dehghan, 2009, page 37) is used and shown in Equation (5):

$$N(t) = N(t_0) \times e^{A \times (t-g)} \tag{5}$$

In Equation (5), $N(t)$ is the number of pipe breaks in the given year and $N(0)$ represents the same term in year 0 of pipe age. The number of pipe breaks is counted per 1000 feet or 304.5 metres. A is a constant and $(t-g)$ represents the age of the pipe. It might also be an indication about the problems with water delivery during firefighting, as the age of the pipe might be indicated by the number of pipe breaks.

3. RESULTS AND DISCUSSION

3.1. Public interest as an open-system and quantitative data example

The monthly and yearly search volumes for fire in South Africa are shown in **figure 2**, as a function of the number of month in the search history (a) and the fire brigade callouts/fires reported in the country between 2004 and 2017 (b). The search history was counted as 1 in January 2004 and 222 in June 2022.

There was an increasing trend in number of searches for fire by the South African public in Google between January 2004 and June 2022, and that trend was statistically significant at 5 % of level of significance (Mann-Kendall test with p -value = 2.5×10^{-7}). The South African public's interest in fire was directly proportional to the number of fires in the country, as the Spearman correlation coefficient was equal to 0.6429. That correlation was statistically significant at 5 % level of significant p -value = 0.0178. At the same time, the Spearman correlation coefficient between the $TFSSA$ and $TLFR$ was equal to 0.4780, but the correlation was not statistically significant at 5 % level of significance (p -value = 0.0985). Madondo et al. (2022) derived Equation (3) to predict the total number of fires outside of the 2004-2017 time period for which the fire brigade calls out statistics were available from the Fire Protection association of Southern Africa. Some of the data from that study are reused here, namely the total number of the Google searches for fire in South Africa between 2004 and 2017. However, the data here are based on three data extraction occasions and reported as averages, which are slightly different than the previously reported data by Madondo et al. (2022). That difference is minimal but is the results of the time sliding scale of the reverse data production by Keywordseverywhere.com plugin (Kovalenko et al., 2021). The average percentage of variation of the monthly and yearly search volumes for fires on Google, by the South African population was equal to 6.6 ± 1.2 %.

To gain more understanding in the causality of the public interest in fires in South Africa, the $TFSSA$ were correlated with the access to the internet by the population, i.e. the percentage of South African population to the internet between 2004 and 2017 (WB, 2022 and see also **Table 1** for details).

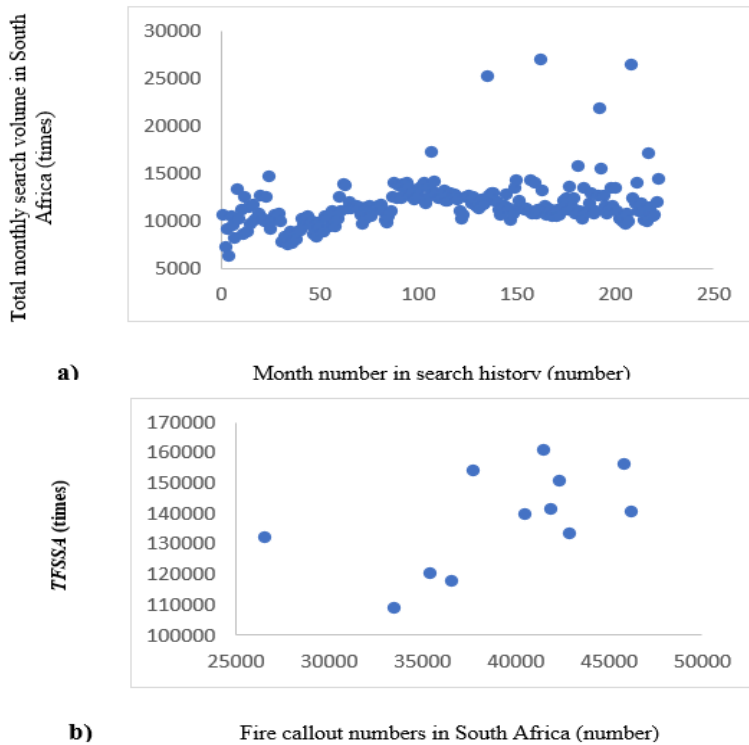


Fig. 2. The monthly search volumes for fire in South Africa from January 2004 until June 2022, as a function of the search history or month number (a), and the correlation between the total number of the fire brigade callout in South Africa from 2004 until 2017, as a function of the respective yearly search volumes on Google in the country (b). Terms are defined in the text of the article, e.g. Equation (1).

The Spearman correlation coefficient was equal to 0.7565 and correlation was statistically significant at 5 % level of significance as the p -value was equal to 0.0028. Therefore, the South African public's interest in fires will be driven by the number of fires in the country and the access to the internet. The Google searches are the result of the South Africans accessing the information in the open system of the internet. Setting the searches geographical scope to South Africa, the qualitative drivers of the interest in fires can be established by examining the related keywords, the keywords people also searched for, the long-tail keywords and additional information from the plugin of Keywordseverywhere.com. Out of the 431 words extracted, the top qualitative drivers of public interest were 'fire extinguisher, fire fighter learnership, fire fighter course, fire brigade and fire hydrant'. The number of monthly searches ranged from 2400 to 9900. However, large portion were terms related to entertain 'chicago fire' which might refer to the respective television series, with 18100.

The relative importance of the searches for fire in South Africa and in the Eastern Cape was compared and the data had following characteristics. For South Africa as a whole, the average g score was equal to 47 ± 10 , the median for g was equal to 46 and the mode g score was equal to 47. On the other hand, the Eastern Cape average g score was equal to 6 ± 10 and the median and mode value for g were both determined to stand at 5. The values of the relative interest in fire were higher for the whole of South Africa compared to the Eastern Cape. That conclusion was based on the results of the Mann-Whitney test at 5 % level of significance (p -value = 0.0001). Based on the additional information, South African with access to Google search for fire in terms of interest in disasters and their impacts, but also based on the popular culture links of the term 'fire'.

Table 1.
The total number of fire brigade call outs and estimation of the total public interest in fires in South Africa.

Calendar year	TFBC ^a (times)	TFBCM ^b (times)	TFSSA ^c (number of searches)	TLFR ^d (ZAR)	PSPA ^e (%)
2004	36591	159	118082	492120909	8.43
2005	42863	194	133400	350056296	7.49
2006	33499	135	109224	2023916105	7.61
2008	35434	218	120413	504966938	8.43
2009	40481	144	139960	667102742	10.00
2010	26574	145	132134	613802753	24.00
2011	37721	172	154112	728144691	33.97
2012	41481	152	161039	744278394	41.00
2013	42343	146	150982	1008867283	46.50
2014	46187	144	140693	680486831	49.00
2015	45784	99	156477	1186434833	51.92
2016	41873	280	141392	1843930163	54.00
2017	49567	136	156377	2773495906	56.17

^a Fire brigade callout in a given calendar year in South Africa as summarised for the 2004-2017 by Madondo et al. (2022) and as extracted from the *fpsa.co.za* database.

^a Fire brigade callout in a given calendar year in Makana Local Municipality as summarised for the 2004-2017 by Madondo et al. (2022) and as extracted from the *fpsa.co.za* database.

^c The total searches for fires in South Africa between 2004 and 2017, as extracted from Google by using the Keywordseverywher.com plugin

^d Financial losses from fires in a given calendar year in South Africa as summarised for the 2004-2017 by Madondo et al. (2022) and as extracted from the *fpsa.co.za* database.

^e Population percentage with access to the internet in South Africa as extracted from the World Bank database (WB, 2022).

The assessment of accuracy of the Keywordseverywhere.com plugin in extracting correct Google search volumes, the veld fire and veldfire monthly searches from South Africa vs. global landscape were assessed. The average percentage of the searches from South Africa as a portion of the global searches was equal to $50 \pm 39\%$. This is very different from 90-100% as was expected and not achieved. Between February 2004 and July 2007, the search volumes from South Africa were higher than the total search volumes for the global landscape (see **Fig. 3** below).

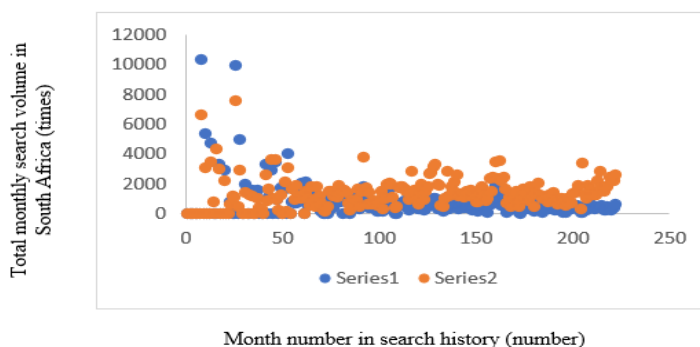


Fig. 3. The monthly search volumes for veld fire and veldfire in South Africa (series 1) and globally (series 2). Data was extracted from |the Keywordseverywhere.com plugin.

The data from the test indicate that some issues, with extracting accurate search volumes from Google by Keywordseverywhere.com, do exist. There was large number of the months in which the search volumes for veld fire/veldfire in South Africa, and globally, were equal to 0. The statistical characteristics of central tendency and variability were equal to the following number for South Africa: 741 ± 1221 for the average and standard deviation, 448 for median and 0 for mode. For the global landscape 1355 ± 1039 for the average and standard deviation, 1200 for the median and 0 for mode.

The Boksburg explosion was used to test whether the Keywordseverywhere.com plugin can provide search volumes on a short time scale, i.e. if there is a correct and sudden spike in interest of the South African public in particular disasters right after their onset. This would be especially true in terms of disaster which have local significance, e.g. to the territory of South Africa. The daily search volumes for the 'Boksburg explosion' are shown in **figure 4** below. The individual values ranged from 0 on all days from 26th October 2022 until 23rd December 2022, with one exception on 17th December 2022. On that day, the search volume was equal to 4600 and it could be considered at indexing issue, or the result of recalculation of the search volumes on a sliding scale by the plugin. However, the daily search volumes spiked to a maximum of 458300 searches on 24th December 2022 and then they declined steadily until 22nd January 2023.

The final search volumes on that day ranged from 600 to 1200 daily searches. Therefore, the temporal trend in Boksburg explosion has the shape expected by the authors, and it indicates that the Keywordseverywhere.com plugin provides reliable daily volumes on Google searches. Results of the study so far indicate that there has been a constant and increasing trend in the South African public's interest in fires. That trend is driven by interest in firefighting equipment and possible also by the interest of the South African population in firefighting as a career. On causality front, the interest in fires is quantitatively driven by the number of fires in South Africa between 2004 and 2017, as well as access to the internet by the South African population. The plugin used in this article provides data from Google which have various levels of accuracy and thus there must be some caution in the application of the plugin, i.e. results should be interpreted on a specific basis for each keyword studied or used.

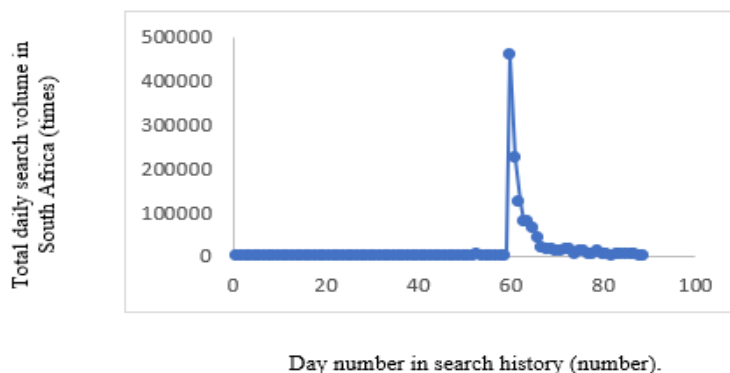


Fig. 4. The daily search volumes for Boksburg explosion from 26th October 2022 until 22nd January 2023, as extracted from Google using the Keywordseverywhere.com plugin. Day number in the search history is counted as follows: number 1 is 26th October 2022 and then the number increase by one per day until 89 on 22nd January 2023.

The plugin data is also an example of a low-cost and/or (near) real-time tool to evaluate the public interest in fires and related topics in South Africa. The plugin, along with Google trends, produces quantitative data which describe the space/place/time perspective of fires in South Africa. Extraction of this data provides for the DRM practitioner in South Africa with information and can be seen as an expression of the open geographical system and flow of information between the community of South Africa, a population at risk from fire, and the DRM practitioner to stop that.

3.2. Makana public interest and the DRM planning for fires at the local municipality level

Only single *g* scores could be extracted for the towns in the SBDMuni and those ranged from 41 to 54. For the Grahamstown/Makhandha area of Makana Local Municipality, the single *g* value was 41 or zero on two separate data-extraction occasions. Therefore, the relative interest in fires in South Africa was higher than in the Eastern Cape, but it was comparable to national values in urban centres of the SBDMuni. Based on this data, the interest in fires is high enough to ensure the penetration of awareness campaigns in towns and cities in SBDMuni. However, some door-to-door awareness campaigns might be needed in the rural parts of the district and Makana...places where internet access might be lower than provincial and national coverage. The yearly probability of fire in Makana Local Municipality ranged from 27.1 to 76.7 % between 2004 and 2017. From the data source by Madondo et al. (2022), it was not possible to estimate the number of false call outs for the fire brigade in Makana Local Municipality. However, as shown below, the Fire Department in the Makana often received all the complaints from the residents and so not all fires/emergencies were likely responded to. This uncertainty needs to be addressed in the future research. Therefore, it seems that the fire is always a possible hazard in the Makana territory and should thus be seen as a priority for planning at the local government level. The Integrated Development Plans (IDP) for Makana Local Municipality should take this into account. Only the annual IDP documents were analysed over time and evaluated for consistency. The word frequency and related analysis results are shown in **table 2** below. The word frequency ranged from 34 to 69 for disaster and from 29 to 61 for fire. The frequency was not dependent on financial year for disaster, but it seemed to increase for fire.

In the 2014-2015 financial year, firearms remained a concern and are mentioned extensively throughout the IDP, but no directly related to fires. Local government plans for the disasters and fires are in place in Makana Local Municipality. However, logistical and capacity challenges remain to be addressed. Compounding factors in firefighting include water provision. The 2015-2016 IDP document analysis indicated the following. Monitoring and evaluation of the influence of the geomorphological features of the Makana topography are still in focus. There was mentioning of the funding being sought to deal with damages from the 2008 disaster, i.e. a tornado which had hit Makana Local Municipality. Funding for fire services and the over-burdening of the fire services, as the designated complaints centre for Makana, were a challenge. SBDMuni and its DRM structures were asked for assistance. Topology and other geomorphological features of Makana geo-surface remain a target for DRM monitoring, as in the 2014-2015 financial year.

In the following financial year of 2016-2017, the drought is showing as having an impact on the firefighting capabilities in Makana Local Municipality, reconstructions from 2008 tornado and 2013 floods still not completed. Fire services are available 24 hours a day but remain underfunded and working with the district municipality is again seen as a way to mitigate the impact on fire DRM in Makana. First time a figure of financial resources available for firefighting is available. Establishment of fire outposts in outlying areas of Makana remains a major hazard in fire DRM.

That trend and focus on awareness campaigns remain constant and appeared again the 2018-2019 IDP document. There was an account given of the reconstruction efforts, and financial expenditure related to that, given and the hiring of new fire-fighter seemed to be a new challenge identified in the IDP. In the 2019-2020 financial year protection of Makana municipal records from fire and motivating for filling firefighting and DRM vacancies was made a priority, along with drought impacts in the municipality. More financial information than ever provided in the 2021-2022 IDP document. Analysis of the IDP documents indicates that drought does have some impacts on the firefighting in Makana Local Municipality, but the extent is not well documented. The personnel situation and requiring the fire-fighters to undertake other work outside of their mandate, e.g. the receipt of Makana complaints about municipal services, poses a problem. Settlements which are geographically isolated, such as Riebeeck East and Alicedale, are in trouble during a fire, as fire stations are not available there. Makana places a strong focus on awareness campaigns as a mitigation measure, and this is to be commended due to financial constraints and the need for ongoing DRM assistance from the SBDMuni authorities. Therefore, challenges do exist in firefighting and fire DRM in Makana Local Municipality, but mitigation measures are in place...at least on paper.

Table 2.

Coverage of fire disaster management in the IDP documents for Makana Local Municipality.

Financial year	WFD^a (times)	WFF^b (times)	Keywords associated with disaster	Keywords associated with fire
2014-2015	34	29	Management, topography, soil, slope, hydrology, act framework, plan, emergency response, incident centre, IT recovery planning, housing, manpower challenges, review, conducting risk assessment	Increased risk, firearms, firefighting, fire prevention, Chief Fire Officer, fire office Grahamstown, fire brigade services by-law, fire and rescue services, water delivery and logistical challenges, satellite fire stations to be built, fire proof storage a challenge, fire station upgrades are needed
2015-2016	61	37	Management, topography, soil, slope, hydrology, act framework, plan, emergency response, incident centre, Makana 2008 – 20 million ZAR investments in assisting 161 housing claimants (problems with contractors), planning for reconstruction of housing in Wards 9, 10, 14, Road reconstruction from 2013 disaster, Fire awareness programmes, inspections, update disaster management disaster management plan is in place and contingency for fires exists	Increased risk, firearms, firefighting, fire belongs under public safety and community services, 24 hour fire service in place, Chief Fire Officer appointed, veld and forest fires identified as a risk, underfunding of the firefighting at local level and SBDMuni contacted to resolve, complaints at the municipal level not handled properly, contingency plan for fires exists.
2016-2017	55	33	Water shortages necessitate updates to the DRM plan, disaster management falls under public safety, risk assessments for fires and other disasters, 2008 tornado still being dealt with, 2013 floods recovery steering committee in place in cooperation with the province, target for housing reconstruction the same as previous year, review of the disaster management plan seemed to be underway and comprehensive risk management to be adopted, new DRM plan passed onto the SBDMuni structures, contingency plans in place	Topology and related topics to be mapped remains as a task to complete, water shortage and increased fire risk remain, firefighting is related to air pollution, some fire fighter positions were allocated funding but not filled, fire and rescue services had a manager in place, 24 hour firefighting service and a Chief Fire officer in place, the DRM plan accounts for veld and forest fire risk, funding of some firefighting needs the support from SBDMuni (funding allocated at 233010 ZAR, Alicedale and Riebeeck East do not have fire stations, DRM and Fire/Rescue plan to be reviewed, fire contingency plans in place
2018-2019	64	43	Topology and related topics as before, moratorium placed on hiring a disaster officer, disaster impacts in ward 1 require fixing of 20 housing units, ward 7 to have some disaster-stricken houses demolished and wards 9/14 reconstruction to be done or underway, ward 10 completed reconstruction, Vukani house reconstruction continues, 2008 disaster funds not possible to give percentage spent, the 2012 floods damage to electricity and pumps repaired partially by national government funds from 0.3 to 2.4 million ZAR, changes to the steering committee targets necessary, review of fire and DRM plans, awareness campaigns to be run, contingency plan and interactions with district remain unchanged	Fire DRM remains largely the same as in prior years, 1 fire-fighter interviewed for 3 positions, but hiring not happened due to moratorium, building of outlying satellite fire stations to be made a priority, fire manager in place and it is the same person as before, access control and fire suppression system installed in Makana buildings, access to firefighting services and types of fires unchanged from previous year, awareness campaigns to be run on fire disaster management and DRM in general
2019-2020	58	38	Makana was declared a local disaster area due to poor service delivery, which was approved by SBDMuni, disaster officer motivated to be hired, lack of business continuity for Makana records identified, housing reconstruction from previous disaster still not completed, SBDMuni infrastructure and economic development planning to assist Makana in mitigating drought, recovery plans to be strengthened.	Senior fire-fighter and three rank-and-file fire-fighters motivated to be hired, some fire plans claimed to be in place not in all parts of Makana is this the case, the fire-proof storage of records to be made a priority with fire sensor and suppression systems were installed in ICT, plan review and awareness campaigns to be run
2021-2022	69	61	Up to 3.184 billion ZAR in COVID19 relief assistance was provided, Makana allocated 14.96 million from disaster management reports done but not implemented into the IDP, disaster officer post still vacant, outstanding RDP house construction in wards 10 and 13, 18.85 million ZAR for disaster management in coastal areas and in cleaning them up	DRM plans for all local municipalities in SBDMuni underway to deal more effectively with fires, fire DRM plans still inadequately done, fire department functions impaired by not hired staff, but focus on developing new fire-fighters

^a Word frequency for disaster in the given IDP document.

^b Word frequency for fire in the given IDP document.

The qualitative data from the IDP documents seems to indicate that awareness campaigns about fires are a priority and this seems to match the medium level of interest in fires in the Makana Local Municipality, as indicated by the Google trends data. The qualitative data seems to indicate that the local government in Makana requires outside assistance to deal with budgetary consideration in DRM. Capabilities in outlying areas of Makana are limited and places the populations there at heightened level of risk. Financial resources required by Makana government to hire fire-fighters and to make further arrangements in fire DRM are quantitative data. They point to the need for Makana to function as an open system in term of geography of fire DRM. This is especially the case for people in the space and place of residence in the outlying settlements of Alicedale and Riebeeck East since the 2016-2017 financial year. Interpretation of the qualitative data from the Makana IDP in this paper, in combination with the other data from this article, makes then creata by the authors who reside in the Eastern Cape and Makana Local Municipality. The financial implications of fire DRM in Makana are critical to the delivery of effective unit operations throughout the entire disaster management cycle. The financial implications are further examined in the next section of this article.

3.3. Financial estimates of the fire DRM burden on Makana population and system

In South Africa, parts of the fire DRM are governed in part by the Fire Brigade Services Act no. 99 of 1987 as amended (designated as Act in further text of the article; SAG, 1987-2000). Section 1 of the Act contains the definition of the controlling authority, namely

“controlling authority” means a local authority in control of a service or the person in control of a designated service; [Definition of “controlling authority” substituted by s. 18 (a) of Act No. 134 of 1992.]”.

Local government, i.e. the Makana Local Municipality here, is generally in charge of operating a fire brigade/firefighting service in South Africa (as proven above for Makana). In the same section of the Act, the definition of the Administrator is listed, as

“Administrator”, means the competent authority within the government of a province to whom the administration in that province of this Act was assigned under section 235 (8) of the Constitution of the Republic of South Africa, 1993 (Act No. 200 of 1993);”.

Therefore, there is a government official in each province, who is responsible for the administration of the Act in that province and who is de facto in charge of the fire DRM in it. Section 11(2) of the Act includes the provision that the Administrator may provide a so-called “grant-in-aid” to the controlling authority. In addition, SBDMuni will be involved based on the disaster management mandate of it as a district municipality and the Disaster Management Act no. 57 of 2002. In other words, the local municipality which operates a fire service can be awarded state funds to support running such a service. However, the controlling authority can also charge the residents of the local municipality fees for the firefighting call outs, as stipulated in section 10(1) of the Act. More specifically, the following text is written there

“Fees. - (1) A controlling authority may, subject to any condition contemplated in section 11 (2) (a), determine the fees payable by a person on whose behalf the service of the controlling authority is applied— (a) for the attendance of the service; (b) for the use of the service and equipment; (c) or for any material consumed.”

Section 10(2) further states that conditions under which the chief fire officer issues a payment notice, namely

“A person on whose behalf, in the opinion of the chief fire officer concerned, a service of a controlling authority has been employed, may in writing be assessed by that chief fire officer for the payment of the fees referred to in subsection (1) or any portion thereof.”

Based on the text in sections 10(1) and 10(2), it is possible for the residents of a municipality to might have to pay for fire brigade call outs if they require assistance with a fire in a residential or other setting. Such charges can pose financial burden on the residents, and it is necessary estimate the

burden such residents might be exposed to. The standard way of stipulating these charges is for the local municipality to issue a by-law and a yearly announcement of the fire brigade tariffs, as part of the annual budget. According to the Makana Tariff Policy, firefighting is considered a subsidised service provided by the municipality (Makana, 2014-present, section 9.3 on page 19). At the same time, the abstraction of water drawn at the fire station is to be charged a fixed water rate (Makana, 2014-present, section 15.4 n) on page 37). Subsidised services are defined in section 2.3 of the South Africa National Framework for municipal indigent policies (DPLG, 2009):

“Local government plays a role as part of the whole system of three spheres of government in addressing poverty through directly providing free or subsidised services to poor households.”

As a result of the above definition, firefighting or fire brigade call outs will not be paid for if a person is deemed indigent, i.e. the person is deemed not to be financially able to pay for municipal services and other public goods. A guideline for the definition of an indigent resident of South Africa is provided in section 3 on page 13 of the

“The term ‘indigent’ means ‘lacking the necessities of life’⁴. In interpreting this for the purpose of this policy a position has to be taken on the ‘necessities of life’ in a South African context”.

In more detail, the term indigent would include the social/essential household service package, namely the provision of water, sanitation, refuse removal and assistance with housing (see section 3.1 on page 15 in DPLG, 2009). The subsidised service should be provided to those who cannot afford to pay (see section 5.1 on page 19 in DPLG, 2009). At the same time, the three pillars of an indigent local municipality policy should be “targeting the poor, gaining and maintain access” to services. This implies services should be provided to indigent residents in local municipalities such as Makana. By extension, firefighting should be part of the expanded social/essential services package provided to indigent residents in Makana Local Municipality (based on the authors’ interpretation of section 3.1 on page 15 in DPLG, 2009).

For the 2004-2017 study period, the 2008 Assistance to the Poor/Indigent by-law for Makana Local Municipality contained various sections that are applicable to the general process of registration and service delivery to indigent household. In Section 1 (i), the 2008 by-law contained a definition that indigent residents are entitled to (Makana, 2008-2013, page 4):

“An access to at least minimum level of basic municipal services, such as water/sanitation/electricity/security in a safe and healthy environment”.

Firefighting services are not explicitly mentioned, but it can be argued that the provision of fire brigade call outs should be free of charge to residents of low-income parts of the Makana population...to ensure minimum basic level of security in a safe and healthy environment. Section 3 of the 2008 Makana by-law states provides more detail about the components of the social/essential services packages, e.g. solid waste removal (Makana, 2008-2013, page 4). Section 4 of the 2008 Makana by-law stated that the indigent status is awarded by the Chief Financial Officer of Makana Local Municipality to a household and must be renewed annually. At the same time, the principle is that the household should receive the service, i.e. the gaining and maintenance of the social/essential service package must be provided to all citizens/residents of the municipality (Makana, 2008-2013, pages 5-6). This is in line with the national framework for indigent policies (DPLG, 2009 and see above). Section 5 and 6 of the 2008 Makana by-law are aimed at stating that an account be issued to the resident, councilor (local elected representative in the Makana municipal council) and the municipal official work together to get the service provided indigent consumers. Practically, this is executed by subsidy being reflected monthly in the municipal account of the registered indigent household (Makana, 2008-2013, pages 6 and 7). The problem which would have arisen in part of the study period, is that many Makana residents inhabit informal settlements. That would have meant that their dwellings might have been tied to a title deed, might have been built on illegally-occupied land, or were built municipal land...they would not have a formal address to allocate a household to. As a result, those residents might have been ineligible for the indigent status and subsidised services, or any municipal services for that matter. Section 12 of the 2008 by-law states that the communication by all levels of political leadership of Makana Local Municipality, as well as the municipal staff and

the Makana community at large are key stakeholders in the communication and registration of the eligible citizens for indigent status (Makana, 2008-2013, page 8). Similar sentiment and strategy is outlined in the draft of the 2013. Assistance to the poor and indigent policy for Makana Local Municipality (Makana, 2013-present, b).

As a result, the indigent population of Makana must be provided with firefighting services free of charge. It would be possible to classify this under the category of no charge for the rescue involving public safety of humanitarian nature. This would not apply to all fire DRM situations, but as fires can spread the definitions should be applied as broadly as possible. In the 2021-2022 financial year, there were 6083 indigent households in Makana Local Municipality and register of them was a priority. Therefore, assisting these indigent households will be in the public safety interest and so that financial charges for firefighting here should not apply. Indigent households generally receive basic services for free by a financial transfer from the National Government of South Africa to Makana Local Municipality, based on the verifiable details and register of indigent household. In case of firefighting services, the amount for callouts which are to be classified as emergencies of humanitarian origin, it would be possible and necessary to collect the information about the indigent Makana residents impacted by the fire. This information is routine from the perspective of post-disaster response and recovery assistance provision. However, the recovery of these costs would have to be covered from the budgets of Makana Local Municipality or the transfers from the National Government post-hoc. Depending on the amounts, such funds could pose a budgetary risk for the annual and overall Makana budget. Mitigating budgetary mechanisms must be put in place, e.g. based on the updated disaster risk management plan by the SBDMuni.

On the other hand, the IDP analysis from the previous section of the article indicates that Makana government is lacking financial and other resources to deal with fire DRM. The Provincial government of the Eastern Cape should therefore provide assistance to Makana, as per the Section 11(2) Fire Brigade Services Act no. 99 of 1987. Low-income households, or households who reside in traditional dwellings, would be charged a flat rate per fire and this ranged from 121.40 to 161.50 ZAR between 2015 and 2020 (Makana, 2015-2017; Makana, 2019-2020). Financial burden and its increases in Makana were assessed for the major appliance, the medium appliance, an auxiliary appliance, and service vehicle. The duration of the model fire was 1 hour and the average charges would be (in ZAR): 1061.86 for a major appliance, 744.90 for a medium appliance, 602.26 for an auxiliary appliance and 285.27 for a service vehicle.

The one-hour long fire is supposed to happen in the urban area of Makana and houses there are to be 10.1 to 30 metres apart, i.e. the fire will be doused with 1200 litres per minutes of water or 72000 litres per hour. Charge for this volume of water is 16 ZAR per 10000 litres. Therefore, this fire would allow the Makana fire brigade to charge the household owner, where the fire took place, 115.20 ZAR for water to fight the fire and the total charge would be 2809.49 ZAR. This accounts for 71.8-76.9 % of the average Makana household income of 2016.96 and 3653.76 ZAR (see Methodology section for details). If each fire in Makana was equal in duration and this duration is assumed to be 1 hour, then the 2017 fire number for Makana, i.e. 136, would allow the fire brigade to collect or charge 382090.64 ZAR. This amount should be sought from SBDMuni or the Eastern Cape Provincial government. It should be budgeted for by the district or the province, and it should be sought as a matter of urgency, as Makana Local Municipality has struggled to meet its fire DRM financial needs. This is in line with Section 11(2) of the Fire Brigade Services Act no. 99 of 1987. Ethically, the household impacted by fire becomes a closed system which needs to be opened up and the price that household pays is the loss of their objects of space/place/time perspective and it is opened up by fire brigade assistance. Fire fighters in Makana must in turn be reimbursed for the equipment use and for the consumables/wear-and-tear must be compensated for, so that the fire protection and DRM can be provided on a continuous basis. At the same time, Makana Local Municipality needs the SBDMuni and the province of the Eastern Cape to help keep the fire DRM open in the municipality. Awareness and mitigation measures for fire must be a top priority as the use of water during drought in firefighting is a challenge in Makana Local Municipality.

3.4. Compounding factors of fire disaster management in Makana

The loadshedding parameters are shown in tables 3 and 4.

Table 3.
Loadshedding parameters for Grahamstown 1 section of Makana Local Municipality for the time period from 2015 to 2021.

LS ^a	RSPC ^b	ARSPC ^c	MRSPC ^d	X(2015) ^e	X(2016) ^f	X(2017) ^g	X(2018) ^h	X(2019) ⁱ	X(2020) ^j	X(2021) ^k
1	10-15	13.2 ± 2.4	1.89	406/1325	0	0	62/192	43/1352	133/1798	79/2455
2	22.5-27.5	26.3 ± 2.5	3.76	874/1325	0	0	130/192	618/1352	1192/1798	1782/2455
3	37.5-40	39.4 ± 1.2	5.63	45/1325	0	0	0	93/1352	141/1798	210/2455
4	52.5	52.5	7.50	0	0	0	0	568/1352	332/1798	384/2455
5	52.5	52.5	7.50	0	0	0	0	0	0	0
6	52.5	52.5	7.50	0	0	0	0	30/1352	0	0

^a Loadshedding stage.

^b Range of duration of power outages in Grahamstown 1 per loadshedding stage per week (h).

^c Average duration of power outages in Grahamstown 1 per loadshedding stage per week (h).

^d Mean duration of a power outages in Grahamstown 1 per loadshedding stage per day (h).

^e The average 2015 number of GWh loadshed per stage in a given year.

^f The average 2016 number of GWh loadshed per stage in a given year.

^g The average 2017 number of GWh loadshed per stage in a given year.

^h The average 2018 number of GWh loadshed per stage in a given year.

ⁱ The average 2019 number of GWh loadshed per stage in a given year.

^j The average 2020 number of GWh loadshed per stage in a given year.

^k The average 2015 number of GWh loadshed per stage in a given year.

Table 4.
Loadshedding parameters for Grahamstown 2 section of Makana Local Municipality for the time period from 2015 to 2021.

LS ^a	RSPC ^b	ARSPC ^c	MRSPC ^d	X(2015) ^e	X(2016) ^f	X(2017) ^g	X(2018) ^h	X(2019) ⁱ	X(2020) ^j	X(2021) ^k
1	12.5-15	13.1 ± 1.2	1.87	406/1325	0	0	62/192	43/1352	133/1798	79/2455
2	25-30	26.3 ± 2.5	3.76	874/1325	0	0	130/192	618/1352	1192/1798	1782/2455
3	37.5-40	39.4 ± 1.2	5.63	45/1325	0	0	0	93/1352	141/1798	210/2455
4	52.5	52.5	7.50	0	0	0	0	568/1352	332/1798	384/2455
5	52.5	52.5	7.50	0	0	0	0	30/1352	0	0
6	52.5	52.5	7.50	0	0	0	0	0	0	0

^a Loadshedding stage.

^b Range of duration of power outages in Grahamstown 2 per loadshedding stage per week (h).

^c Average duration of power outages in Grahamstown 2 per loadshedding stage per week (h).

^d Mean duration of a power outages in Grahamstown 2 per loadshedding stage per day (h).

^e The average 2015 number of GWh loadshed per stage in a given year.

^f The average 2016 number of GWh loadshed per stage in a given year.

^g The average 2017 number of GWh loadshed per stage in a given year.

^h The average 2018 number of GWh loadshed per stage in a given year.

ⁱ The average 2019 number of GWh loadshed per stage in a given year.

^j The average 2020 number of GWh loadshed per stage in a given year.

^k The average 2015 number of GWh loadshed per stage in a given year.

The total duration of the of loadshedding in hours was equal to 121 in 2015, 127 in 2018, 530 in 2019, 859 and 1136 in 2021 (CSIR, 2022). In the Grahamstown 1 area and Grahamstown 2, the probability of loadshedding increased from 10 % in 2015, 12 % in 2018, 26 % in 2019, 52 % in 2020 and 70 % in 2021. Therefore, the population in both sides of Makana main urban area would be likely resorting to energy stacking, which could increase the possibility of the fire breaking out in that area. Finally, the age of the pipes was calculated to be equal to 60 years, i.e. the pipe breakages could pose problem in reticulation of water to the fire hydrants. Large part of this problem was addressed by sinking in PVC pipes into the ground in a large part of Makana. However, it remains uncertain whether the entire Makana reticulation has been upgraded.

4. CONCLUSIONS

The financial challenges and the personnel shortages, as well as compounded effect of drought and the loadshedding, can be seen as complicating the fire DRM in Makana Local Municipality. Open system between the local municipality and the outside stakeholders such as SBDMuni are needed to address the financial challenges and to maintain ethical delivery of the fire DRM to the Makana population.

ACKNOWLEDGMENTS

The authors extend their gratitude to the Rhodes University Research Committee and the Rhodes University Sandisa Imbewu fund and the South African Chapter of the International Emergency Management Society for supporting the first author in their Master's studies. The North-West Umbrella Fire Protection Association and the National University of Public Service are acknowledged for providing the inputs on the practical implications in the DRR/DRM context of quantitative and qualitative data, and the ethical implications. No institutions, which are mentioned in this acknowledgement section, or any of their representatives have reviewed any drafts of the current article. Therefore, no formal or informal endorsement of any part of the current article by any nor all of the institutions, mentioned here, should be implied by the readers.

REFERENCES

- Banda, M., O'Reagan, V. (2022). Families and friends of victims of Boksburg gas tanker explosion share their heartache and trauma. Available at: <https://www.dailymaverick.co.za/article/2022-12-29-families-and-friends-of-victims-of-boksburg-gas-tanker-explosion-share-their-heartache-and-trauma/> (website accessed on 26th January 2023).
- Béné, C., Riba, A., Wilson, D. (2020). Impacts of resilience interventions – Evidence from a quasi-experimental assessment in Niger. *International Journal of Disaster Risk Reduction* 43: Article number 101390. <https://doi.org/10.1016/j.ijdr.2019.101390>.
- Bird, D. K. (2009). The use of questionnaires for acquiring information on public perception of natural hazards and risk mitigation – a review of current knowledge and practice. *Natural Hazards and Earth System Sciences* 9(4): 1307-1325. doi: 10.5194/nhess-9-1307-2009.
- Calverley, C. M., Walther, S. C. (2022). Drought, water management, and social equity: Analyzing Cape Town, South Africa's water crisis. *Frontiers in Water* 4: Article number 910149. <https://doi.org/10.3389/frwa.2022.910149>.
- Chick, V., Dow, S. (2005). The meaning of open systems. *Journal of Economic Methodology* 12(3): 363-381. <https://doi.org/10.1080/13501780500223585>.
- Chmutina, K., von Meding, J., Gaillard, J. C., Boshier, L. (2017). Why "natural" disasters aren't all that natural. Available at: <https://www.preventionweb.net/news/why-natural-disasters-arent-all-natural> (website accessed on 6th January 2023).
- City of Johannesburg (2018). Load shedding affects water supply. Available at: <https://www.joburg.org.za/media/Pages/Media/Media%20Statements/2020%20Media%20Statements/September%202020/Load-shedding-affects-water-supply.aspx> (website accessed on 6th January 2023).

- Council for Scientific and Industrial Research (CSIR, 2022). Load shedding statistics. Available at: <https://www.csir.co.za/load-shedding-statistics> (website accessed on 26th April 2022).
- Crane, M., Bohn-Goldbaum, E., Grunseit, A., Bauman, A. (2020). Using natural experiments to improve public health evidence: a review of context and utility for obesity prevention. *Health Research Policy and Systems* 18: Article number 48. <https://doi.org/10.1186/s12961-020-00564-2>.
- Creamer Media – Engineering News (2016). Santam hands over firefighting equipment to Makana local municipality in Grahamstown. Available at: <https://www.engineeringnews.co.za/article/santam-hands-over-firefighting-equipment-to-makana-local-municipality-in-grahamstown-2016-07-07> (website accessed on 24th January 2023).
- Daily Maverick (2022). South Africa’s deadly July 2021 riots may recur if there’s no change. Available at: <https://theconversation.com/south-africas-deadly-july-2021-riots-may-recur-if-theres-no-change-186397> (website accessed on 6th January 2023).
- Daly, P., Mahdi, S., McCaughey, J., Mundzir, I., Halim, A., Nizamuddin, Ardiansyah, Srimulyani, E. (2020). Rethinking relief, reconstruction and development: Evaluating the effectiveness and sustainability of post-disaster livelihood aid. *International Journal of Disaster Risk Reduction* 49: Article number 101650. <https://doi.org/10.1016/j.ijdr.2020.101650>.
- Dehghan, A. (2009). Chapter 2.5: Current model developed for pipe failure analysis and prediction. Failure prediction for water pipes. *PhD dissertation*, Swinburne University of Technology Faculty of Engineering and Industrial Sciences, Victoria, Australia, pp. 31-66.
- Dormady, N. C., Greenbaum, R. T., Young, K. A. (2021). An experimental investigation of resilience decision making in repeated disasters. *Environment Systems and Decisions* 41(4): 556-576. <https://doi.org/10.1007/s10669-021-09818-y>.
- Fire Protection Association of Southern Africa (FPASA, 2021). Hydrants (water infrastructure). Available at: <https://www.fpsa.co.za/blog/297-hydrants-water-infrastructure> (website accessed 5th February 2023).
- Francioli, A. P. M. (2020). Energy use strategies and implications for fire risk amongst low-income households. *Jàmbá: Journal of Disaster Risk Studies* 12(1): Article number a890. <https://doi.org/10.4102/jamba.v12i1.890>.
- Fries, M.-H. (2019). Explicit and implicit ethical issues in the reports of the Intergovernmental Panel on Climate Change: the example of the “tipping points” metaphor. *Asp* 76: 9-27. <https://doi.org/10.4000/asp.5945>.
- Gong, L., Jin, M., Liu, Q., Gong, Y., Liu, Y. (2020). Identifying Urban Residents’ Activity Space at Multiple Geographic Scales Using Mobile Phone Data. *ISPRS International Journal of Geo-Information* 9(4): Article number 241. <https://doi.org/10.3390/ijgi9040241>.
- Grocott’s Mail (2018). City unites to avert fire disaster. Available at: <https://grocotts.ru.ac.za/2018/07/13/city-unites-to-avert-fire-disaster/> (website accessed on 24th January 2023).
- Hammer, O., Harper, D. A.T., Ryan, P. D. (2001). PAST: Paleontological Statistics Software Package for Education and Data Analysis. *Palaeontologia Electronica* 4(1):1-9. Available at: https://www.researchgate.net/publication/259640226_PAST_Paleontological_Statistics_Software_Package_for_Education_and_Data_Analysis (website accessed on 18th July 2022).
- Inter-Agency Standing Committee (IASC, 2021). Available at: <https://interagencystandingcommittee.org/system/files/2021-02/IASC%20Operational%20Guidance%20on%20Data%20Responsibility%20in%20Humanitarian%20Action-%20February%202021.pdf> (website accessed on 13th January 2023).
- Iheanetu, C. U., Maguire, K. A., Moricová, V., Tandlich, R., Alloggio, S. (2023). Utilitarian Qubit, Human Geography, and Pandemic Preparedness in the 21st Century. *Sustainability* 15(1): Article number 321. <https://doi.org/10.3390/su15010321>.
- Iheanetu, C., Tandlich, R. (2022). Water provision under the COVID-19 lockdown conditions: Snapshot of microbial quality of alternative sources, the associated costs and carbon footprints. *Vedelem Tudomány (Protection Science)* VII(1): 162-190.
- International Monetary Fund (IMF, 2020). IMF COUNTRY FOCUS: Six Charts Explain South Africa's Inequality Available at: <https://www.imf.org/en/News/Articles/2020/01/29/na012820six-charts-on-south-africas-persistent-and-multi-faceted-inequality> (website accessed on 29th January 2023).
- International Standardisation Organisation (ISO, 2018). ISO 31000: Risk management – guidelines. Available at: <https://www.iso.org/obp/ui/#iso:std:iso:31000:ed-2:v:1:en> (website accessed on 29th January 2023).
- Jones, R. L., Guha-Sapir, D., Tubeuf, S. (2022). Human and economic impacts of natural disasters: can we trust the global data?. *Science Data* 9: Article number 572 <https://doi.org/10.1038/s41597-022-01667-x>.

- Karabulut, M. (2015). Drought analysis in Antakya-Kahramanmaraş Graben, Turkey. *Journal of Arid Land* 7: 741-754. <https://doi.org/10.1007/s40333-015-0011-6>.
- Kovalenko, K. E., Pelicice, F. M., Kats, L. B., Kotta, J., Thomaz, S. M. (2021) Aquatic invasive species: introduction to the Special Issue and dynamics of public interest. *Hydrobiologia* 848: 1939-1953. <https://doi.org/10.1007/s10750-021-04585-y>.
- Lawton, R. (1983). Space, Place and Time. *Geography* 68(3): 193-207. Available at: <https://www.jstor.org/stable/40570691> (website accessed on 2nd January 2023).
- Lee, A. C., Booth, A., Challen, K., Gardois, P., Goodacre, S. (2014). Disaster management in low- and middle-income countries: scoping review of the evidence base. *Emergency Medicine Journal* 31(e1): e78-83. doi: 10.1136/emered-2013-203298.
- Leinfelder, R. (2020). The Anthropocene - the Earth in Our Hands. *Refubium*, 1-13. <https://doi.org/10.17169/refubium-26459>. Available online: <https://refubium.fu-berlin.de/handle/fub188/26702> (website accessed on 23rd December 2022).
- Linyana, (2022). The quest for clarity on our water woes. Available at: <https://grocotts.ru.ac.za/2022/10/11/the-quest-for-clarity-on-our-water-woes/> (website accessed on 28th December 2022).
- Loadshedding Schedule (2022). Suburb finder. Available at: loadshedding.eskom.co.za (website accessed on 27th April 2022).
- Madikizela, P., Limson, J., Fogel, R., Ristvej, J., Tandlich, R. (2022). Evaluation of a desktop tool to measure public interest in water, sanitation, and hygiene in South Africa on a short-term and long-term time scale: links to disaster preparedness during coronavirus and beyond. *JAMBA-Journal of Disaster Risk Studies* (submitted on 28th October 2022).
- Madikizela, P., Madondo, R., Odume, N., Laubscher, R., Tandlich, R. (2019). Disaster management and land use policy in Sarah Baartman District Municipality. Published in the peer-reviewed proceedings from the 2019 CRISON – Crisis Management and the solutions for Crisis Situations, University of Tomáša Bařu, Uherské Hradiřte, Czech Republic from 12th until 13th September 2019, pp. 210-221 (ISBN: 978-80-7454-875-8).
- Madondo, R., Tandlich, R., Stoch, E. T., Restás, Á., Shwababa, S. (2023). A theoretical perspective on space-time of disaster risk reduction and management: role of data and its interpretation. *Journal of Emergency Management* (submitted on 23th February 2023; manuscript number JEM-D-23-00022).
- Madondo, R., Mutingwende, N., Shwababa, S., Bayne, R. J., Restás, Á., Tandlich, R. (2022). Analyses of trends in the fire losses and the fire-brigade call-outs in South Africa between 2004 and 2017. *Geographia Technica* 17(2): 54-68. doi: 10.21163/GT_2022.172.06.
- Makana Local Municipality (2020-2021). Water Crisis - Water resources, updates and information. Available at: <http://www.makana.gov.za/water-crisis/> (website accessed on 28th December 2022).
- Makana Local Municipality (Makana, 2019-2020). EC104 - DRAFT FIRE DEPARTMENT TARIFFS 2019-2020. Available at: <http://www.makana.gov.za/wp-content/uploads/2019/05/07-2019-20-DRAFT-FIRE-DEPARTMENT-TARIFFS1.pdf> (website accessed on 18th May 2022).
- Makana Local Municipality (Makana, 2015-2017). FIRE DEPARTMENT TARIFFS 2015-2017. Available at: <http://www.makana.gov.za/wp-content/uploads/2017/02/Fire-Dept-Tariffs-2016-2017.pdf> (website accessed on 18th May 2022).
- Makana Local Municipality (Makana, 2014-present). Tariff Policy. Available at: <http://www.makana.gov.za/wp-content/uploads/2014/09/Tariff-Policy-2014FINAL.pdf> (website accessed on 18th May 2022).
- Makana Local Municipality (Makana, 2013-present, a). Available at: <http://www.makana.gov.za/statutory-documents/idp-municipal-statistics/> (website accessed on 29th January 2023).
- Makana Local Municipality (Makana, 2013-present, b). Assistance to the poor and indigent policy (draft). Available at: <http://www.makana.gov.za/wp-content/uploads/2013/06/assistance-to-the-poor-and-indigent-policy-2013.pdf> (website accessed on 18th May 2022).
- Makana Local Municipality (Makana, 2013). Fire and Rescue Services. Available at: <http://www.makana.gov.za/fire-and-rescue-services/> (website accessed on 24th January 2023).
- Makana Local Municipality (Makana, 2008-2013). Assistance to the poor and indigent by-law. Available at: <http://www.makana.gov.za/wp-content/uploads/2013/06/Assistance-to-the-poor-indigent-By-Law-Makana-Municipality.pdf> (website accessed on 18th May 2022).
- Malema, M. S., Mwenge Kahinda, J.-M., Abia, A. L. K., Tandlich, R., Zuma, B. M., Ubomba-Jaswa, E. (2019). The efficiency of a low-cost hydrogen sulphide (H₂S) kit as an early warning test for assessing microbial

- rainwater quality and its correlation with standard indicators microorganisms. *Nova Biotechnologica et Chimica* 18(2): 133-143.
- Martin, D. A. (2016). At the nexus of fire, water and society. *Philosophical Transactions of the Royal Society B – Biological Sciences*. 371(1696): Article number 20150172. <https://doi.org/10.1098/rstb.2015.0172>.
- Meriläinen, E., Koro, M. (2021). Data, disasters, and space-time entanglements. *International Journal of Disaster Risk Science* 12: 157-168. <https://doi.org/10.1007/s13753-021-00333-x>.
- Messer, L. C. (2016). Natural experiment. *Encyclopedia Britannica*. Available at: <https://www.britannica.com/science/natural-experiment> (website accessed on 21st January 2023).
- Mizutori, M. (2020). Time to say goodbye to “natural” disasters. Available at: <https://www.preventionweb.net/blog/time-say-goodbye-natural-disasters> (website accessed on 6th January 2023).
- Mntambo, S., Adebayo, P. (2022). Disaster Management in South Africa’s Informal Settlements: Policy, Practice and COVID-19 Implications. *Journal of Inclusive Cities and Built Environment* 2(3): 87-100. <https://doi.org/10.54030/2788-564X/2022/v2s3a7%20%20e-ISSN%202788-564X>.
- Motlhoki, S. (2017). The effectiveness of the South African Truth and Reconciliation Commission in the context of the five pillars of transitional justice. *PhD thesis*, University of South Africa, Pretoria, South Africa.
- National Disaster Management Centre (NDMC, 2006-2023). Disaster Atlas application: Historical databases of disasters declared in South Africa 2006-2017. Available at: <https://gislive21.ndmc.gov.za/portal/apps/webappviewer/index.html?id=23357e584f7d4f94b5c36b6d65be9c44> (website accessed on 21st January 2023).
- National Disaster Management Centre (NDMC, 2023). Data Sourcing Tools. Available at: http://gismap.ndmc.gov.za/Data_Sources.aspx (website accessed on 21st January 2023).
- National Disaster Management Centre, South Africa (NDMC, 2022). DAILY FIRE INDEX EARLY WARNING SYSTEM – Grahamstown/Makhanda, Sarah Baartman District Municipality, the Eastern Cape Province, South Africa. Available at: <https://ndmcgis.maps.arcgis.com/apps/dashboards/42de70656a4545edbd627e157d515c17> (website accessed on 28th December 2022).
- Ngqwala, N. P., Srinivas, C. S., Tandlich, R., Pyle, D. M., Oosthuizen, R. (2017). Participatory multi-stakeholder platforms for effective disaster management in South Africa. *Journal of Disaster Research* 12(6): 1192-1203. doi: 10.20965/jdr.2017.p1192.
- Norwegian Refugee Council (NRC, 2023). Humanitarian principles. Available at: <https://www.nrc.no/what-we-do/speaking-up-for-rights/humanitarian-access/> (website accessed on 21st January 2023).
- Oosthuizen, R. C. (2018). A critical analysis of disaster risk management in local governance with reference to Sarah Baartman District Municipality. *PhD thesis*, Nelson Mandela Metropolitan University, Port Elizabeth/Gqeberha, South Africa. Available at: http://vital.seals.ac.za:8080/vital/access/manager/Repository/vital:33385?site_name=GlobalView&exact=sm_creator%3A%22Oosthuizen%2C+Rene+Cheryl%22&sort=sort_ss_title%2F (website accessed on 21st January 2023).
- Padli, J., Habibullah, S. M., Baharom, A. H. (2018). The impact of human development on natural disaster fatalities and damage: panel data evidence. *Economic Research-Ekonomska Istraživanja* 31(1): 1557-1573. <https://doi.org/10.1080/1331677X.2018.1504689>.
- Pijoo, I. (2022). Boksburg explosion: Driver warned people to stay away from truck fire before blast killed 15 people. Available at: <https://www.news24.com/news24/southafrica/news/boksburg-explosion-driver-warned-people-to-stay-away-from-truck-fire-before-blast-killed-15-people-20221225> (website accessed on 26th January 2023).
- Rivera, J. D. (2019). Focus Group Administration in Disaster Research: Methodological Transparency when Dealing with Challenges. *International Journal of Mass Emergencies & Disasters* 37(3): 241-263. <https://doi.org/10.1177/028072701903700301>.
- Sarah Baartman District Municipality (SBDMuni, 2022). FIRE PROHIBITION PERIOD 2020/2021 (press release – news). Available at: https://www.sarahbaartman.co.za/index.php?option=com_zoo&task=item&item_id=52&category_id=72&Itemid=1985&lang=en (website accessed on 21st January 2023).
- Sgqolana, T. (2021). Daily Maverick: The burning season: Wildfires sweeping across South Africa and Namibia have left devastation in their wake. Available at: <https://www.dailymaverick.co.za/article/2021-10-04-the-burning-season-wildfires-sweeping-across-south-africa-and-namibia-have-left-devastation-in-their-wake>

- [burning-season-wildfires-sweeping-across-south-africa-and-namibia-have-left-devastation-in-their-wake/](#) (website accessed on 10th May 2022).
- South African Constitution (1996-present). Chapter 2: Bill of Rights – section 11 – right to life. Available at: <https://www.justice.gov.za/legislation/constitution/saconstitution-web-eng.pdf> (website accessed on 29th January 2023).
- South African Government (SAG, 1987-2000). Fire Brigade Services Act no. 99 OF 1987 as amended. Available at: [https://www.ndmc.gov.za/Acts/Fire%20Brigade%20Services%20Act%20%20\(99%20of%201987\).pdf](https://www.ndmc.gov.za/Acts/Fire%20Brigade%20Services%20Act%20%20(99%20of%201987).pdf) (website accessed on 17th May 2022).
- South African National Department of Provincial and Local Government (DPLG, 2009). national framework for municipal indigent policies. Available at: https://www.westerncape.gov.za/text/2012/11/national_framework_for_municipal_indigent_policies.pdf (website accessed on 18th May 2022).
- South African Revenue Service (SARS, 2003-present). Exchange rate USD/ZAR – Table A: Average exchange rates for a year of assessment. Available at: <https://www.sars.gov.za/wp-content/uploads/Legal/Rates/LAPD-Pub-AER-2012-02-Average-Exchange-Rates-Table-A.pdf> (website accessed on 12th May 2022).
- South African Weather Service (SAWS, 2022). Monthly drought bulletin. Available at: https://www.weathersa.co.za/Documents/Climate/nr_drought.pdf (website accessed on 21st January 2023).
- Stanford Encyclopedia of Philosophy (2009-2022). Kant's views on space and time. Available at: <https://plato.stanford.edu/entries/kant-spacetime/> (website accessed on 2nd January 2023).
- Świętochowska, M., Bartkowska, I. (2022). Optimization of Energy Consumption in the Pumping Station Supplying Two Zones of the Water Supply System. *Energies* 15: Article number 310. <https://doi.org/10.3390/en15010310>.
- Tandlich, R., Msimang, A., Tamášová, V. (2023). Letter to the editor: use of low-cost online tools to estimate the public's interest in the changing conditions of their existence under the conditions during the COVID19, as a model for the emergency information assessment. *Journal of Emergency Management (submitted on 17th January 2023; manuscript number JEM-D-23-00004)*.
- The United Nations Office for the Coordination of Humanitarian Affairs (OCHA/Reliefweb, 2022). South Africa: Floods and Landslides - Apr 2022. Available at: <https://reliefweb.int/disaster/fl-2022-000201-zaf> (website accessed on 28th December 2022).
- Vhiriri, E. P., Msimang, A., Laubscher, R. K., Irwin, Y., Chiwanza, F., Tandlich, R. (2021). Natural Disasters and the Role of Pharmacists: A Focus on Policy and Protocols in South Africa. In: Nhamo G., Dube K. (eds) *Cyclones in Southern Africa. Sustainable Development Goals Series*. Springer, Cham., pp. 153-167. https://doi.org/10.1007/978-3-030-74262-1_10.
- Vulcan Wildfire Management (VWFM, 2017-present). Situational analysis of the 2017 Knysna fires (Executive summary). Available at: https://www.dropbox.com/sh/raxs0kwgmt9xd7/AAA4TL0_sBNivTVRwkYYSy9Wa?dl=0&preview=Knysna+Fires+Situational+Analysis+FULL+Report.pdf (website accessed on 21st January 2023).
- Western Cape Government (2019). Load shedding fact sheet. Available at: https://www.westerncape.gov.za/110green/files/atoms/files/Load%20Shedding%20FAQ%202019_FINAL.pdf (website accessed on 27th April 2022).
- Winter, D. (2011). Power outages and their impact on South Africa's water and wastewater sectors. *Report to the Water Research Commission by Frost & Sullivan and the South African Local Government Association*. WRC Report No. KV 267/11, Water Research Commission of South Africa, Pretoria, South Africa (ISBN 978-1-4312-0101-3).
- World Bank (2022e). Individuals using the Internet (% of population). Available at: <https://data.worldbank.org/indicator/IT.NET.USER.ZS> (website accessed on 18th July 2022).
- World Health Organisation (WHO, 2019-2023). WHO Coronavirus (COVID-19) Dashboard. Available at: <https://covid19.who.int/> (website accessed on 21st January 2023).

PRODUCTION OF HIGH GEOMETRIC RESOLUTION ORTHOPHOTOS BY PHOTOGRAMMETRIC APPROACH FOR THE ROYAL RACCONIGI CASTEL PARK DOCUMENTATION

Vincenzo Saverio ALFIO¹, Domenica COSTANTINO¹, Massimiliano PEPE²,
Gabriele ROSSI³, Massimo LESERRI¹

DOI: 10.21163/GT_2023.182.03

ABSTRACT:

The aim of this work concerns the development of a simple and rigorous procedure for the construction of metric orthophotos in high geometric resolution and rich in detail through the use of terrestrial and UAV photogrammetry techniques. This approach has been tested on various datasets relating to the Racconigi Castle (Italy) and has allowed the state of the sites to be documented. All the orthophotos produced made it possible to identify the critical areas from a conservation point of view and, at the same time, to create a support tool that makes it possible to identify, with high precision, the damaged areas in a short time thanks to the georeferencing of the processed models.

Key-words: *Photogrammetry, Orthophoto, UAV, Cultural Heritage.*

1. INTRODUCTION

The documentation of Cultural Heritage (CH) with appropriate surveying and modelling techniques allows to faithfully reconstruct a 3D object (in terms of position, shape and geometry). In addition, from 3D model, it is possible to extract profiles and facades in an accurate, fast and detailed way (Costantino et al., 2022).

The 3D survey can be performed using image-based 3D modelling (IBM) or range-based modelling (RBM). IBM methods use 2D images measurements in order to obtain 3D models. In particular, Structure from Motion (SfM) approach has become quite popular in Close Range Photogrammetry (CRP) thanks to ability to determine the parameters of external orientation without any a priori knowledge of the approximate positions for cameras and 3D points. SfM technique requires, in order realizing 3D models, a block of images with a high degree of overlap that capture the complete 3D structure of the scene viewed from several positions (Costantino et al., 2015; Alfio et al., 2022). In addition, using Multi-View-Stereo (MVS) algorithm, it is possible increasing the density of the point cloud generated in SfM process. In this way, a dense and very detailed point cloud can be generated. Furthermore, the passive sensors used in the IBM method may be used even on mobile platforms (such as cranes, unmanned aerial vehicles - UAVs, hot-air balloons, etc.). In this way, it is possible to acquire data even in big, complex, and inaccessible structures, such as upper parts of buildings, aqueducts, bridges etc. (Adami et al., 2019; Pepe et al., 2019; Baiocchi et al., 2021). Range-based modelling, instead, is based on active sensors, which provide a highly detailed and accurate representation of a 3D object or structure; an example of active sensor is the terrestrial laser scanner-TLS (Costantino et. al, 2021).

¹Polytechnic University of Bari - Department of Civil, Environmental, Land, Building Engineering and Chemistry (DICATECh), 70125, Bari, Italy, (vincenzosaverio.alfio@poliba.it, domenica.costantino@poliba.it, massimo.leserri@poliba.it)

²University of Chieti-Pescara "G. d'Annunzio", Department of Engineering and Geology (InGeo), 65127, Pescara, Italy, massimiliano.pepe@unich.it

³Polytechnic University of Bari - Department of Architecture, Construction and Design (ArCoD), 70125, Bari, Italy, gabriele.rossi@poliba.it

Some studies and researches in the field of cultural heritage digitisation, use graphic representation in order to extract information from orthophotos and/or graphic restitution of the key elements of the examined structure; in this way, it is possible to build parametric and semantic models with BIM (Vach et al., 2018; Bernardello et al., 2020; Solla et al., 2020) or 3D GIS (Jedlička, 2018; Pepe et al., 2021) systems. However, the survey for 2D representation through orthophotos and Computer Aided Design-CAD continues to be a method of analysis and research in digital heritage projects (Đurić et al., 2021). Two-dimensional (2D) shape analysis techniques can be used to numerically describe the stylistic features contained in surveyed structures derived from photogrammetric models. For example, in the case of facade restoration, the experts have to map the damage and plan the corresponding measures before the actual restoration can take place; therefore, two-dimensional CAD drawings depicting each individual stone serve as a basis (Cefalu et al., 2013). Similar experiences to the one just described can be found in the field of cultural heritage. Indeed, Kan et al., 2017 wrote about of Zırmıklı Vehbi Bey Mansion building situated near to the Castle, in Turkey, showing the CAD drawings of this structure which has significantly lost its spatial integrity; the survey of this structure was performed by 3D TLS. Kouimtzoğlu et al., 2017 analyse in a CAD environment the evolution of the Plaka Bridge, Greece, combining field survey data over time (1984, 2005 and 2015); the last survey campaign was carried out using SfM/MVS techniques and high quality orthorectified images of both facades of the remains of the bridge were produced. These data were in turn prepared for use in a similar way as in the ones referring to the before the collapse state in order to produce accurate 2D vector architectural drawings of the monument. Attenni et al., 2018 wrote about the important contribution given by the combination of topography and photogrammetry operations; in fact, thanks to the use of SfM/MVS software it has allowed the construction of a 2D model (orthophotos and CAD) that is metrically reliable and detailed in order to clearly distinguish the different materials and state of conservation of the structure under investigation. Donato et al., 2019 wrote about the combined methodologies for the survey and documentation of the Castle of Scalea (Italy); in order to represent the results of stratigraphic analysis, orthophoto 2D and orthoimage-based drawing was carried out. Using smartphone-based photogrammetry, Asadpour (2021) was able to reconstruct the 3D model of Historic tileworks in Hāfez tomb, Shiraz (Iran) and, subsequently, to generate an orthophoto useful for 2D representation.

The aim of this paper is to describe actual survey methodologies, based on the use of Image based models, and to identify a line of work able to produce 3D models, orthophotos with high geometric resolution and CAD representations useful for restoration activities. This approach allows a rapid identification of the areas of intervention; furthermore, the production in sheets has the notable advantage of being easily consulted in the various phases of work, that is, from the design and planning phase to the construction phase.

2. STUDY AREA

The case study concerns one of the Royal Castle of Racconigi, a UNESCO World Heritage Site since 1997, which is perhaps the one that best captures the life of the court and at the same time manifests the power of the Savoy family. The Royal Castle of Racconigi is a palace and landscape park in Racconigi, province of Cuneo, Italy (**Fig. 1a, b**). Founded around the 11th century as a stronghold in the March of Turin, Racconigi Castle later passed to the Marquises of Saluzzo and then to the Savoy family. Over the course of its almost thousand-year history, it has seen numerous alterations and became the property of the Savoy family from the second half of the 14th century.

The wall composed of brick elements, almost 7 km long and perimeter of a park of approximately 200 hectares - shows various forms of degradation and numerous additions made with the use of inconsistent material.

For this reason, it is necessary to produce adequate documentation to identify critical issues in the facilities and identify appropriate measures for their preservation and protection.

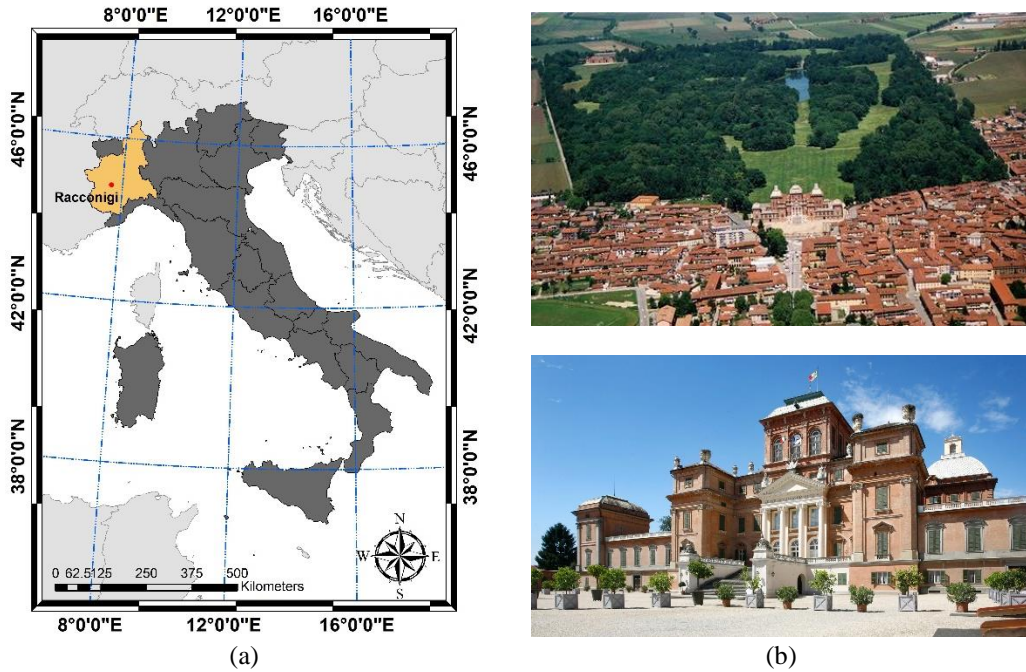


Fig. 1. Study area: geographical overview (a); panoramic view of the park and castle of Racconigi (b).

3. DATA AND METHODS

3.1. Survey techniques and methods

The methodological aspects addressed and described in the paper concern the terrestrial and UAV photogrammetry experiences conducted in the park of Racconigi for the realization of digital documentation of following structure:

- the park; and
- the perimeter walls.

The survey of the park was carried out using UAV photogrammetry while the perimeter walls was surveyed using terrestrial and UAV photogrammetry. In this latter case, the images acquired from the ground were integrated with oblique images acquired from a UAV platform; in this way, it was also possible to cover the parts not visible from the ground.

The photogrammetric process adopted in the 3D survey is based on the use of SfM/MVS algorithms. Since geometric distortions (distortion and tangential) are generated from the ideal to the real model in the formation of the image, additional parameters (APs) must be added to the collinearity equations. In general, the Brown's model is used in order to establish a mathematically rigorous relationship between image and object; this model taken into consideration 10 APs related to internal camera orientation (Δx_p , Δy_p , Δc), uncertainty about the shape of the pixel (Skew factor S_x), non-orthogonality of the reference system (shear factor Λ), radial symmetric distortion of the lenses (k_1 , k_2 , k_3) and tangential distortion of the lenses (p_1 , p_2). In this way, it is possible to write the collinearity equation as (Abdel-Aziz and H Karara, 1971):

$$\begin{aligned}
 x_i - x_o + \Delta x &= c \frac{m_{11}(X_j - X_o) + m_{12}(Y_j - Y_o) + m_{13}(Z_j - Z_o)}{m_{31}(X_j - X_o) + m_{32}(Y_j - Y_o) + m_{33}(Z_j - Z_o)} \\
 y_i - y_o + \Delta y &= c \frac{m_{21}(X_j - X_o) + m_{22}(Y_j - Y_o) + m_{23}(Z_j - Z_o)}{m_{31}(X_j - X_o) + m_{32}(Y_j - Y_o) + m_{33}(Z_j - Z_o)}
 \end{aligned} \tag{1}$$

where:

- x_i, y_i -measured image coordinates;
- X_j, Y_j, Z_j -object space coordinates of the measured points;
- X_o, Y_o, Z_o -object space coordinates of the perspective centre of the camera;
- c -focal length of lens;
- x_o, y_o -principal points of coordinates;
- $\Delta x, \Delta y$ -lens distortion parameters;

$m_{11}, m_{12}, m_{13}, m_{21}, m_{22}, m_{23}, m_{31}, m_{32}, m_{33}$ - individual elements of the orthogonal rotation matrix representing the three-angle omega, phi and kappa;

At present, several software packages are available on the market that are able to reconstruct the geometry of the scene being analysed on the base of SfM algorithms. In this paper, the processing of the image dataset was carried out by Agisoft Metashape since allows to process large datasets, connect them together and perform advanced editing operations on the images. In this latter software, it is possible to build 3D models or orthophotos through a few steps: (i) alignment of the images; (ii) building a dense point cloud (PC); (iii) building mesh and (iv) building an orthomosaic. In general, before to build the dense cloud, an evaluation of the metric quality of the 3d model is performed. This task is realized taking into account GCPs and calculating the root mean square error (RMSE). GCPs are reference points easily recognizable on the images, such as intersections, manholes, antennas, marks made by tracing an X shape on the ground with spray paint, panels made of waterproof, high-contrast material (black and white or yellow and black), with a matt finish to reduce reflections and improve visibility, and coded targets (Pepe et al., 2022). In addition, target sizes are variable depending on the design GSD. The coordinate of the GCPs can be obtained by Total Station o GNSS technology. Once the GCPs have been recognised in the software and their coordinates assigned, the RMSE for x, y, z coordinates can be calculated by following formula:

$$RMSE = \sqrt{\sum_{i=1}^n \frac{(x_{i,est} - x_i)^2 + (y_{i,est} - y_i)^2 + (z_{i,est} - z_i)^2}{n}} \quad (2)$$

where x_i is the input value for x coordinate, y_i the input value for y and z_i the input value for z coordinate for the i-th camera position, while $(x_{i,est}, y_{i,est}, z_{i,est})$ corresponds to its estimated position.

3.2. Application of the UAV photogrammetry to the park

UAV photogrammetry allows orthophotos of complex surfaces to be obtained with high geometric resolution. The steps leading to the construction of the photogrammetric model and subsequent orthophoto of the park were:

1. Flight planning;
2. Acquisition of the images;
3. Photogrammetric processing of the images;
4. Georeferencing of the model;
5. Building orthophoto and editing.

Flight planning was performed on Pix4D Capture software in order to achieve a pixel size of 2.4 cm. The UAS (Unmanned Aircraft Systems) used in the survey of the Area of Interest (AOI) was DJI Mavic 2 Pro, developed by DJI Company, Shenzhen. DJI Mavic 2 Pro is a quadcopter equipped with a high-resolution colour camera. Indeed, DJI Mavic 2 Pro, featuring the collaboratively developed Hasselblad L1D-20c, brings innovative experiences to the field with advancements in drone photography and UAV photogrammetry. The Hasselblad L1D-20c allows the user to obtain a higher standard for aerial image quality. A fully stabilized 3-axis gimbal with its powerful 20MP 1” sensor, it offers improved lowlight shooting capabilities in comparison to other drone cameras.

To cover the AOI, the relative altitude (Above Ground level – AGL) was 100m. The longitudinal and transversal overlap (overlap and side lap) of the photogrammetric block was 80%. However, to cover the AOI, five flight plans were planned (**Fig. 2a**). Once the UAV photogrammetric flight was planned, it was checked with the ENAC (Italian Civil Aviation Authority) regulations (**Fig. 2b**).

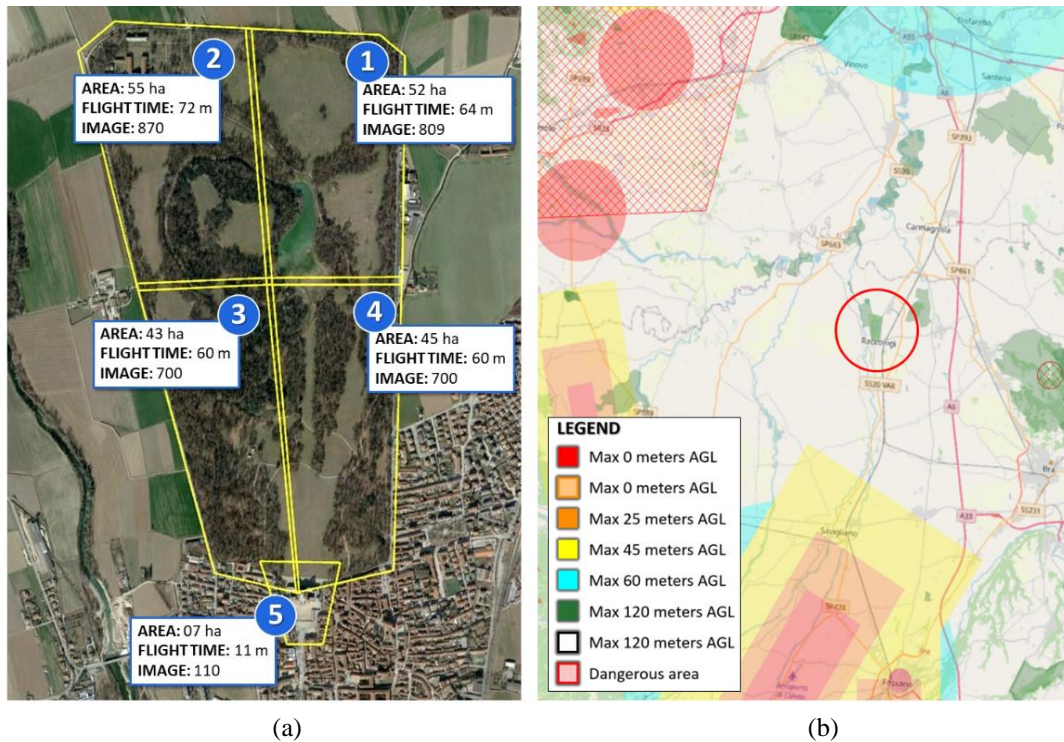


Fig. 2. Flight plan scheme: flight plan blocks (a) and flight plan verification on aeronautical chart (b).

A total amount of 3189 images were acquired in 14 sessions in order to take into account the battery endurance of the UAV and ensure safety. The post-processing of the images of the individual blocks was carried out in the Agisoft Metashape environment. In order to georeference the orthophoto, 25 targets (dimensions 100x100 mm) were located and surveyed by GNSS instrumentation in Network Real Time Kinematic (NRTK). In addition to the targets, 5 natural points were measured that were easily recognisable on the ground and unequivocally identifiable on the digital images.

The coordinates of the acquired points were referred to the UTM32-ETRF2000 cartographic system; the ellipsoidal heights were subsequently transformed into orthometric height by means of the Italian Military Geographic Institute (IGMI) grid (*.gk2). IGMI is the geographical support office of the Army and represents the Italian National Cartographic Authority. The values reported in this grid are based on the ITALGEO2005 model, which is given an absolute accuracy of about 4 cm. ITALGEO is the local geoid model for Italy that defines the relevant geoid undulation values; the most recently released and updated version of which is called ITALGEO2005. The interpolation of the ground control points surveyed by GNSS was carried out by the use of Verto 2.0 software. The different georeferenced models were merged and the orthophoto with a spatial resolution of 5cm was generated. Lastly, the orthophoto was edited in order to avoid perspective or unclear images. Regarding the cartographic aspect, it was possible also to build a detailed DEM (Digital Elevation Model) from the 3D model (dense point cloud). This DEM, appropriately filtered, i.e. distinguishing terrain from non-terrain (trees, buildings, etc.), allowed the creation, within the ArcMap software (produced and distributed by ESRI), of contour lines with an equidistance of 1m. Moreover, starting from the DEM and identifying appropriate sections, it was possible to extract the profiles.

The orthophoto with a geometric resolution of 0.05 m is reported in the **Appendix 1**.

3.3. Terrestrial and UAV photogrammetry applied to boundary wall

The 3D model of the wall (external part) was carried out through the use of terrestrial and UAV photogrammetry. In particular, the terrestrial survey was carried out using a dSLR Nikon D750 camera with a 20mm fixed focal length. This made it possible to fully exploit the advantages of an image sensor measuring 24 × 36 mm, which makes it possible to render a multitude of details and details that are lost with smaller sensors. The fixed focal length lens offers a high depth of field while achieving high sharpness at all distances. Furthermore, from a photogrammetric point of view, working with a focal length means improving the quality of the image alignment process. In fact, some software such as Agisoft Metashape recommends the use of images acquired with the same focal length, at least within the dataset to be processed to produce the photogrammetric model.

In order to survey the upper part of the wall, images were acquired with UAS. The UAV photogrammetry was carried out using a Parrot Anafi, a UAS quadcopter equipped with a Sony Sensor® 1/2.4" 21MP (5344 × 4016) CMOS (complementary metal-oxide semiconductor), which allows obtaining, thanks also to a 3-axis stabilizer, clear and detailed images. However, it was not possible to build the entire 3D model of the wall (i.e. the inner part of the wall facing the inside of the park) as there were tall trees and dense vegetation behind the wall.

The UAS flight was planned with accuracy in order to obtain a correct GSD. In addition, during the flight more attention was paid to the high vegetation present around the wall; in this task, a great contribute was provided by the sensors mounted on the UAV which signalled the possible presence of a very close obstacle. To cover all the walls, a total amount of 8701 pictures were acquired. In particular, taking into account the shape of the wall and the number of images that can be processed in SFM/MVS software, the datasets were divided in 4 blocks, as reported in following **Table 1**.

Table 1.

Terrestrial and UAV photogrammetric datasets.

Dataset		Images		
		Terrestrial	UAV	Total
I	North	1413	867	2280
II	East	1810	1152	2962
III	South-West	938	400	1338
IV	West	1327	794	2121

Calibrating the camera optics is necessary if the dimensions of the wall are not proportional, i.e. the ratio of length to height is very high. In this specific case, the wall was several kilometres long and several metres high. In other words, incorrect values of the calibration parameters affect the entire length of the structure. Therefore, a calibration procedure in the laboratory was performed using Agisoft Lens software. A TV with a 36" screen was used as a chessboard; the images acquired on this scene were processed within the software which generated a report not only with a plot of the radial and tangential distortion values but also of the internal parameters and additional parameters (APs).

The internal orientation parameters were introduced into Agisoft Metashape. In addition, in order to minimise the influence of the quality of the photogrammetric model, sub-blocks of a length of approximately 200 metres were constructed on each side of the park. Finally, in order to increase the probability of success in the construction of the 3D model, in addition to acquiring the images orthogonally, i.e. perpendicular to the direction of development of the wall, convergent and oblique images were taken.

The post processing of the images was carried out using Agisoft Metashape software. From the point of view of data organisation, 2 chunks were constructed, one for the terrestrial dataset and another for the UAV dataset. The merge of the datasets was performed through the choice of common points; to facilitate this operation of recognition of the common points, black and white targets of reduced dimensions (to cover as little as possible the wall texture) were positioned along the wall. After the alignment of each dataset, the point cloud was generated. Subsequently, after an operation of elimination of points not useful for the construction of the 3D model (outliers), the mesh was generated. In order to georeference and scale the 3D model obtained by terrestrial and UAV

photogrammetry, 250 targets (red cross) were located and surveyed by GNSS instrumentation with kinematic methodology in post-processing (stop and go). In addition to the targets, 50 natural points were taken into consideration on the walls and measured by means of integrated topographic instrumentation (Total Station and GNSS). In order to perform the elaborations of the acquired GNSS data, a post-processing was carried out using as known vertices those belonging to the Italpos permanent station network (HxGN SmartNet). The processing was carried out using LeicaGeoOffice (LGO) software and the ellipsoidal height were subsequently transformed into orthometric using specific grid on the study area and Verto 2.0 software.

Subsequently, a top-down orthophoto of the wall was generated; in this way, it was possible to identify the various directions of the wall. This is essential in order to identify the projection planes of the orthophotos of the wall. Therefore, for each direction of the wall, it was necessary to perform a roto-translation of the GCPs. In order to speed up this operation, an algorithm in lisp was used in the Autocad Autodesk environment (Costantino et al., 2020). In this way, the model was georeferenced in a local reference system and according to the direction of development of the wall and for each of them the orthophotos were constructed with a GSD suitable for a scale of 1:50 graphic representation. In particular, 20 facades were identified, and in the case of multi-long walls, the single facade was divided into parts of 100 m. The orthophotos with a spatial resolution of 5mm were imported into the CAD environment and were positioned spatially within the graphic drawings.

Lastly, in order to improve the graphic quality of the orthophotos, a subsequent editing in Adobe Photoshop was performed. According to Costantino et al., 2022, the pipeline of the several task can be summarized as follow (Fig. 3):

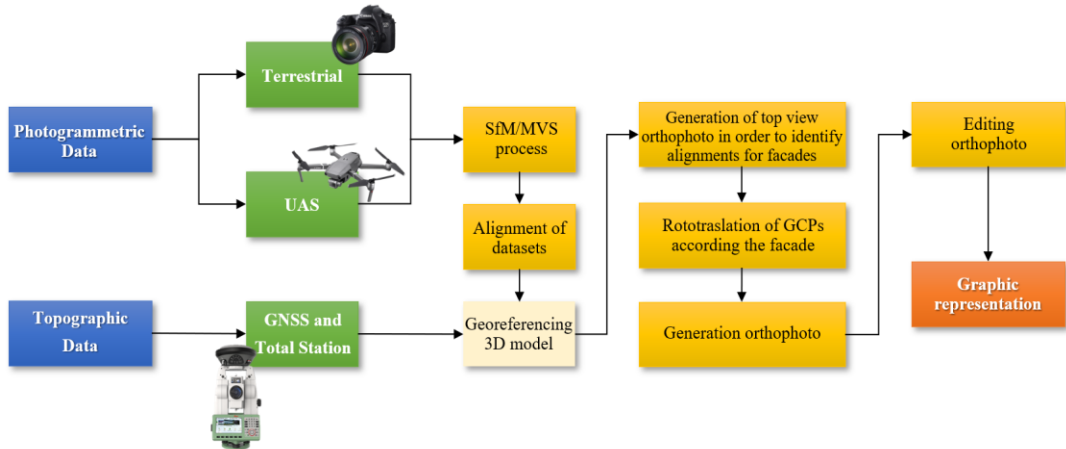


Fig.3. Pipeline of the developed method to produce a 2D graphic representation of the wall by IBM techniques.

In addition, thin elements such as gates and iron receptions were represented with polylines; in this way, it was possible to obtain not only a clear and orderly representation but also a precise and detailed representation of the thinner elements. Examples of graphic representation (orthophoto) of the walls around the south-west part of the park is shown in **Appendix 2**.

4. RESULTS AND DISCUSSIONS

The photogrammetric method described allowed to produce accurate and detailed orthophotos. In particular, the orthophoto of the park was realised with a geometric resolution of 0.03 m, while a geometric resolution of 0.005 m was obtained for the fence walls. In the latter case, characteristic elements such as the main entrance gate or those of the side entrances were represented by means of CAD reproduction, which allowed for a better interpretation of the state of the site.

The orthophotos in high resolution of the site allowed the framing of the structures surveyed by photogrammetric technique. In addition, the creation of an updated orthophoto has made it possible to identify all the natural and anthropic elements present in the park in order to define all future

maintenance and management activities. The survey and representation of the perimeter wall, which is about 7 km long, will provide an overview of the state of the damaged and compromised portions and allow maintenance and restoration work to be planned on this basis. In the graphic restitution of the wall, it was possible to identify the progressive coordinates (framed in a cartographic reference system, for example UTM-ETRF2000) in such a way as to manage all maintenance activities using the georeferenced positions subject to the intervention. Once the orthophoto was built, it is possible to quickly analyse the state of degradation of the structures which is a fundamental step in the restoration project (Randazzo et al., 2021). The analysis of the pathologies of degradation is necessary to choose the most suitable to the most suitable type of intervention. Therefore, the first step concerns the analysis of the state of the sites; furthermore, the possibility of easily identifying the area on which to intervene in a rapid and precise manner, not only must be the subject of study but could also be the subject of further investigations with additional sensors in specific points, such as the use of thermal cameras. For example, from the analysis of the structures, the most common surface degradation concerns the fracturing and cracking of the masonry, i.e. the phenomenon manifested by the formation of continuity solutions in the material and involving the mutual displacement of parts. The most common causes of this phenomenon are freeze-thaw cycles or failure of the supporting masonry. The contribution of geomatics in the identification of these phenomena assumes a key role. As shown in the following images (see Fig. 4), through a simple geo-referencing of structures and buildings it was very easy to analyse them from different aspects.

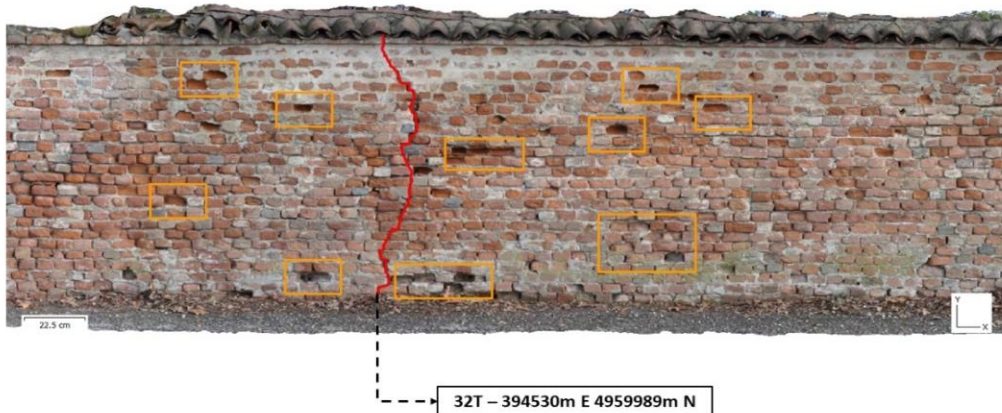


Fig. 4. Analysis of the state of deterioration of the wall on orthophoto.

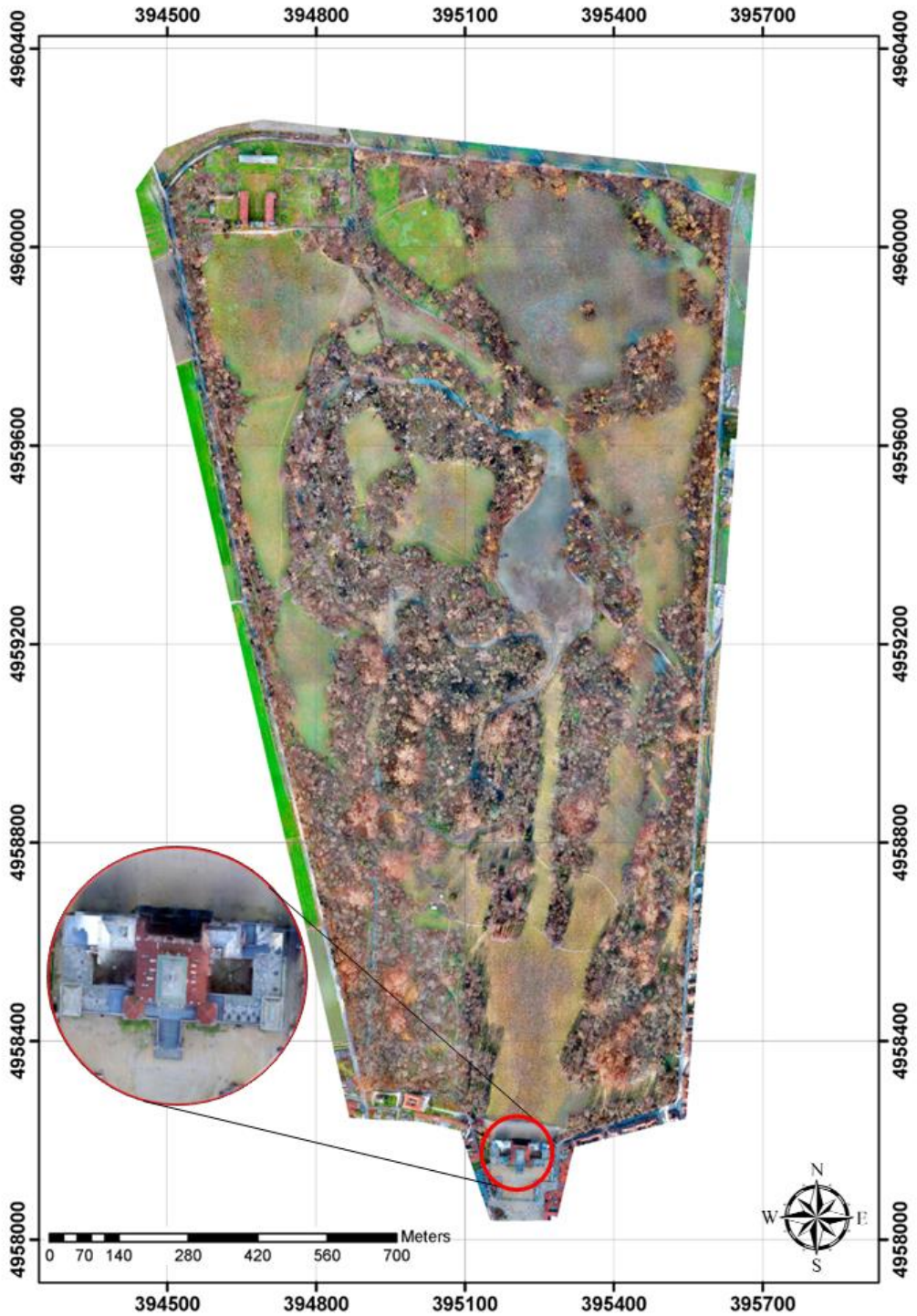
6. CONCLUSIONS

The paper showed the enormous potential offered by photogrammetric techniques for the documentation and representation of places; this approach is particularly useful in the digitisation of cultural heritage environment. Indeed, the representation in high resolution of the park by orthophoto and the detailed and precise drawings of the structure by orthophoto allowed to obtain an important documentation with elevated details. In addition, the geolocation of structures in a UTM32-ETRF2000 reference system allows maintenance and restoration workers to identify and intervene quickly and accurately in an area undergoing intervention.

The proposed method for digitising the entire Racconigi park complex can be applied in different territorial and structural contexts related to cultural heritage. In contexts where it is not possible to acquire information by terrestrial means, UAV photogrammetry makes it possible to overcome these limitations and integrate the datasets with additional information to reconstruct a complete 3D model.

The approach described in the paper aims to ensure that future generations can admire and use it, perpetuating its historical values without distorting or compromising its original meanings. Lastly, the study could be perfected by surveying the green and water system components and drawing up a complete documentation to support the recovery and enhancement of a World Heritage Site.

APPENDIX 1



Appendix 1. Orthophoto of the parks.

APPENDIX 2



Appendix 2.a Est side orthophoto extract.



Appendix 2.b Sud side orthophoto extract.



Appendix 2.c West side orthophoto extract.

REFERENCES

- Abdel-Aziz and H. Y. I., Karara, M. Direct linear transformation into object space coordinates in close-range photogrammetry. In *Proceedings of the Symposium Close-Range Photogrammetry* (pp. 1-18).
- Adami, A., Fregonese, L., Gallo, M., Helder, J., Pepe, M., Treccani, D. (2019). Ultra-light UAV systems for the metrical documentation of cultural heritage: Applications for architecture and archaeology. In *6th International Workshop LowCost 3D-Sensors, Algorithms, Applications* (Vol. 42, pp. 15-21).
- Alfio, V. S., Costantino, D., Pepe, M., Restuccia Garofalo, A. (2022). A Geomatics Approach in Scan to FEM Process Applied to Cultural Heritage Structure: The Case Study of the “Colossus of Barletta”. *Remote Sensing*, 14(3), 664.
- Asadpour, A. (2021). Documenting historic tileworks using smartphone-based photogrammetry. *Mersin Photogrammetry Journal*, 3(1), 15-20.
- Attenni, M., Bartolomei, C., Inglese, C., Ippolito, A., Morganti, C., Predari, G. (2018). Low-cost survey and heritage value. *SCIRES-IT-SCientific REsearch and Information Technology*, 7(2), 115-132.
- Baiocchi, V., Onori, M., Scuti, M. (2021). Integrated geomatic techniques for the localization and georeferencing of ancient hermitages. *ISPRS*, 46, 31-37.
- Bernardello, R. A., Borin, P., Panarotto, F., Giordano, A., Valluzzi, M. R. (2020). BIM representation and classification of masonry pathologies using semi-automatic procedure. In *Brick and Block Masonry-From Historical to Sustainable Masonry* (pp. 771-778). CRC Press.
- Cefalu, A., Abdel-Wahab, M., Peter, M., Wenzel, K., Fritsch, D. (2013, July). Image based 3D Reconstruction in Cultural Heritage Preservation. In *ICINCO* (1) (pp. 201-205).
- Costantino, D., Angelini, M. G. (2015). Three-dimensional integrated survey for building investigations. *Journal of forensic sciences*, 60(6), 1625-1632.
- Costantino, D., Pepe, M., Dardanelli, G., Baiocchi, V. (2020). Using optical Satellite and aerial imagery for automatic coastline mapping. *Geographia Technica*, 15(2), 171-190.
- Costantino, D., Pepe, M., Angelini, M. G. (2021). Evaluation of reflectance for building materials classification with terrestrial laser scanner radiation. *Acta Polytechnica*, 61(1), 174-198.
- Costantino, D., Rossi, G., Pepe, M., Leserri, M. (2022). Experiences of TLS, terrestrial and UAV photogrammetry in Cultural Heritage environment for restoration and maintenance purposes of Royal Racconigi castle, Italy.
- Donato, E., Giuffrida, D. (2019). Combined Methodologies for the Survey and Documentation of Historical Buildings: The Castle of Scalea (CS, Italy). *Heritage*, 2(3), 2384-2397.
- Đurić, I., Obradović, R., Vasiljević, I., Ralević, N., Stojaković, V. (2021). Two-Dimensional Shape Analysis of Complex Geometry Based on Photogrammetric Models of Iconostases. *Applied Sciences*, 11(15), 7042.
- Jedlička, K. (2018). A comprehensive overview of a core of 3D GIS. In *7th International Conference on Cartography and GIS Proceedings*. Sozopol. ISSN (pp. 1314-0604).
- Kan, T., Buyuksalih, G., Kaya, Y., Baskaraca, A. P. (2017). The importance of digital methods in preservation of cultural heritage the example of Zirnikli Mansion. *ISPRS*, 42.
- Kouimtzoğlu, T., Stathopoulou, E. K., Georgopoulos, A. (2017). Image-based 3D reconstruction data as an analysis and documentation tool for architects: the case of Plaka Bridge in Greece.
- Pepe, M., Costantino, D., Crocetto, N., Restuccia Garofalo, A. (2019). 3D modeling of roman bridge by the integration of terrestrial and UAV photogrammetric survey for structural analysis purpose. *ISPRS*, 42(2), W17.
- Pepe, M., Alfio, V. S., Costantino, D. (2022). UAV Platforms and the SfM-MVS Approach in the 3D Surveys and Modelling: A Review in the Cultural Heritage Field. *Applied Sciences*, 12(24), 12886.
- Pepe, M., Costantino, D., Alfio, V. S., Restuccia, A. G., Papalino, N. M. (2021). Scan to BIM for the digital management and representation in 3D GIS environment of cultural heritage site. *JCH*.
- Randazzo, L., Collina, M., Ricca, M., Barbieri, L., Bruno, F., Arcudi, A., La Russa, M. F. (2020). Damage indices and photogrammetry for decay assessment of stone-built cultural heritage: The case study of the San Domenico church main entrance portal (South Calabria, Italy). *Sustainability*, 12(12), 5198.
- Solla, M., Gonçalves, L., Gonçalves, G., Francisco, C., Puente, I., Providência, P., ... Rodrigues, H. (2020). A building information modeling approach to integrate geomatic data for the documentation and preservation of cultural heritage. *Remote Sensing*, 12(24), 4028.
- Vach, K., Holubec, P., Dleske, A. (2018). New trends in GIS and BIM for facility management in the Czech Republic. *ISPRS*, 42, 5.

TSUNAMI HAZARD MAPPING BASED ON COASTAL SYSTEM ANALYSIS USING HIGH-RESOLUTION UNMANNED AERIAL VEHICLE (UAV) IMAGERY (Case Study in Kukup Coastal Area, Gunungkidul Regency, Indonesia)

DANARDONO¹ , Afif Ari WIBOWO¹, Dewi Novita SARI² , Kuswaji Dwi PRIYONO¹ ,
Ecky Safira Maharani DEWI²

DOI: 10.21163/GT_2023.182.04

ABSTRACT:

The Kukup Coastal Area is located in the southern part of Java's coastal area, which has an active megathrust subduction zone. The dynamics of tectonic activities in this zone trigger earthquakes with various intensities. Some of these earthquakes can trigger a tsunami threatening human activities in this area. Therefore, a detailed study of tsunami hazards by integrating physical and socio-economic aspects needs to be done to estimate disaster risk and determine spatial planning in coastal areas. The objectives of this study are (1) to identify the coastal system and (2) to create a tsunami hazard map in the Kukup Coastal Area. Coastal systems can be identified by analyzing the physical and socio-economic conditions. Physical conditions such as morphological and coastal typology can be extracted from Digital Elevation Model (DEM) from aerial photo processing. Socio-economic conditions such as land use analysis and tourism activities can be extracted from orthophoto, which is extracted from aerial photo processing using drones. The tsunami hazard can be analyzed using three modelling stages: earthquake source modelling, tsunami wave propagation modelling, and tsunami inundation modelling using Geographic Information System (GIS). The results show that the morphological conditions in the study area were dominated by the formation of conical hills with a firm lineament pattern causing the formation of elongated basins such as labyrinths. This basin is a place for developing socio-economic activities, especially tourism, which can be seen from a large amount of built-up land area. The presence of these basins causes the tsunami inundation pattern to extend perpendicular to the shoreline, causing the tsunami inundation in the study area to extend as far as 2 km from the shoreline.

Key-words: *Tsunami, GIS Modelling, Coastal System, Coastal Typology, Remote Sensing.*

1. INTRODUCTION

The coastal area is a transition zone from land and sea, which has a unique natural and social process. The interaction between land and sea makes the physical and social environmental conditions in coastal areas dynamic and interrelated. The dynamics of the physical environment will affect changes in the social environment and vice versa. Therefore, a study on the development of coastal areas needs to be carried out comprehensively by taking into all aspects of the environment, both physical and social, often known as coastal system analysis.

Coastal system analysis can be studied from three aspects: natural processes, population development, and socio-economic activities in coastal areas (Supriharyono, 2000). Natural processes can be studied regarding the potential of natural resources and the threat of natural disasters. The potential of natural resources in the coastal areas causes the increasing population and the socio-economic development activities. This condition occurs in coastal areas in Gunungkidul Regency, one of which is the Kukup Coastal Area. The Kukup Coastal area has a natural beauty with white sandy beaches between the karst conical hills, which are used for mass tourism activities. Tourism activities in the Kukup coastal area trigger an increase in socio-economic activities.

¹Land Resources Laboratory, Faculty of Geography, Universitas Muhammadiyah Surakarta, Indonesia, danardono@ums.ac.id, aaw346@ums.ac.id, kdp130@ums.ac.id

²Geospatial Laboratory, Faculty of Geography, Universitas Muhammadiyah Surakarta, Indonesia, dns104@ums.ac.id, e100180088@student.ums.ac.id

It can be seen from the increasing number of tourist visits in Tanjungsari District, Gunungkidul Regency from 2011 to 2019 (see **Fig. 1**). The decline occurred in the 2019 to 2020 due to the policy of restricting public mobility due to the Coronavirus Disease 2019 pandemic (COVID-19).

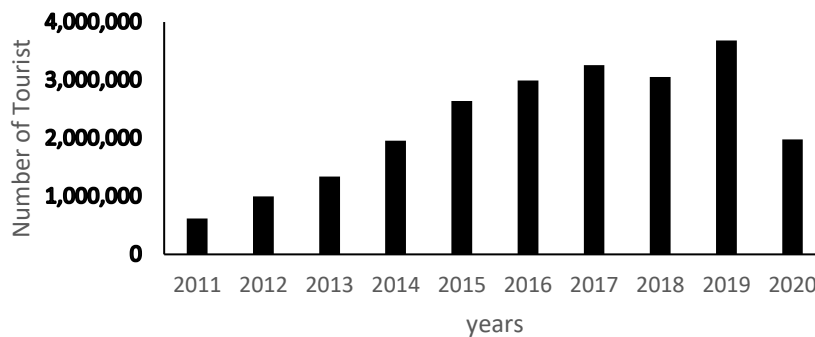


Fig. 1. The Number of Tourist in Gunungkidul Regency from 2011 to 2020
Source : Badan Pusat Statistik, 2021.

On the other hand, natural disasters can be a limiting factor in developing potential in coastal areas. Natural disasters often occur in coastal areas, such as land subsidence, abrasion, and tsunamis can be an inhibiting factor if they are not integrated into coastal area development planning. The occurrence of natural disasters not only changes the physical environment but also changes the pattern of socio-economic interaction (Rosselló, Becken, & Santana-Gallego, 2020) in coastal areas. Therefore, it is necessary to study the potential hazards of natural disasters by paying attention to the interaction of the physical and social environment (coastal system).

One natural disaster that potentially damages the Kukup Coastal Area is the tsunami. The Kukup Coastal Area is located in the southern coastal area of Java Island, which is close to the active megathrust subduction zone between the Eurasian Continental Plate and the Indo-Australian Ocean Plate in the Indian Ocean. Earthquakes still often occur in this subduction zone with varying intensities. Tectonic earthquakes with great intensity have caused tsunamis on the southern coast of Java Island in Banyuwangi in 1994 and Pangandaran in 2006 (Chaeroni, Hendriyono, & Kongko, 2013). The Pangandaran tsunami, with a height of 5-7 meters, surged along the southern coast of Java and was caused by an earthquake with a strength of > 7 Mw (moment magnitude) (Faiqoh, Gaol, & Ling, 2013; Widiyantoro et al., 2020). As a consequence of this incident, 664 people died, 498 people were injured, 1,623 houses were damaged, and economic loss reached 55 million US dollars (Anjar, Laksono, Widagdo, Aditama, & Fauzan, 2022). The southern coastal area of Java is the most at risk for tsunamis due to its dense population and proximity to an active subduction zone (Hall et al., 2017; Lavigne et al., 2007; Okamoto & Takenaka, 2009). Therefore, a study on the tsunami hazard is important to protect the socio-economic activities that develop in the Kukup Coastal Area and it also related to the opportunity to reduce the risk from tsunami.

The study of tsunami hazard has been widely studied, mainly in coastal areas in Indonesia with various approach methods such as in Cilacap Coast, Java, Indonesia (Anjar et al., 2022), Pangandaran Coast, Java, Indonesia (Faiqoh et al., 2013), Southern West Java Coast, Indonesia (Windupranata, Hanifa, Nusantara, Aristawati, & Arifianto, 2020), and Padang Coastal Area, Sumatra, Indonesia (Ashar, Amaratunga, & Haigh, 2018; Di Mauro, Megawati, Cedillos, & Tucker, 2013). Other research related to Tsunami risk and potential in this research such as from Mardiatno, Malawani, & Nisaa', (2020) The future tsunami risk potential as a consequence of building development in Pangandaran Region, West Java, Indonesia and Nisaa', Sartohadi, & Mardiatno, (2021) Participatory GIS Approach to Assessing Building Vulnerability to Tsunamis in Pangandaran Regency. The National Agency for Disaster Countermeasure, abbreviated (BNPB), as the state agency of disaster mitigation, has also produced a tsunami hazard map in the Southern Java coastal areas. However, most of the

previous studies that have been carried out still utilize data with a medium to the small scale of detail. The inundation model provided by the government is based on national topographic maps/ *peta rupabumi indonesia* (RBI) with 12.5 meters contour interval and 1: 25,000 scale for land use identification, resulting inaccurate models (Marfai, Khakim, Fatchurohman, & Salma, 2021). Consequently, it will cause errors in tsunami inundation modelling in coastal areas with various topographical conditions. Some areas that should have been inundated were not flooded because of generalizations. This condition often occurs, especially in the karst coastal areas where small hills are located close to each other, such as in the Kukup Coastal Area.

This research uses high-resolution imagery from the unmanned aerial vehicle to model tsunami hazards in the Kukup Coastal Area. High-resolution aerial photography makes it possible to identify structural mitigation in coastal areas. The existence of a wave-retaining embankment on the shore will be well-modelled by utilizing An unmanned aerial vehicle (UAV) technology. UAV technology is expected to produce tsunami hazard modelling with detailed accuracy and pays attention to structural mitigation efforts carried out by communities in coastal areas. Based on the background of the problem described, this study aims (1) to identify the coastal system in the Kukup Coastal Area and (2) to create a tsunami hazard map in the Kukup Coastal Area.

2. STUDY AREA

The Kukup Coastal Area is one of the coastal in the southern region of Java Island, which is administratively located in Tanjungsari District, Gunungkidul Regency, D.I. Yogyakarta Province (see Fig. 2.). The Kukup Coastal Area is located near Baron Beach which is a favourite destination for tourists visiting. This beach can be accessed from the capital of Gunungkidul Regency, namely Wonosari, as far as 23 kilometres which can be reached in approximately 1 hour.

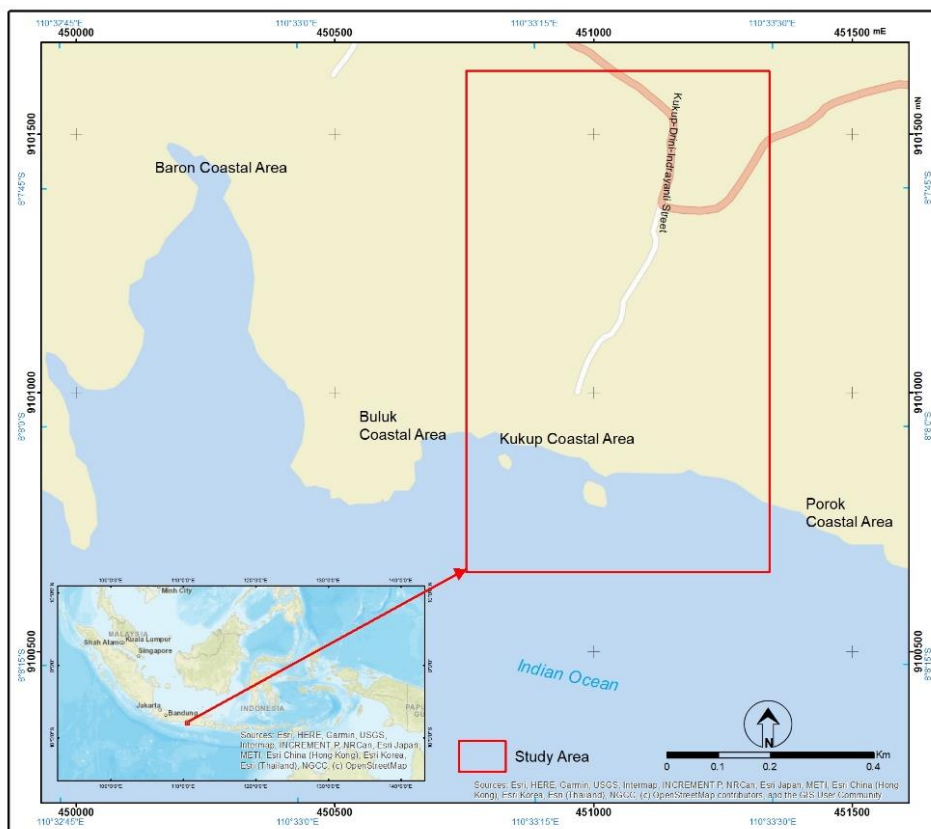


Fig. 2. Location of Kukup Coastal Area

The Kukup Coastal Area area has unique physical conditions in geology, geomorphology, and hydrology. Geologically, this coastal area is predominantly composed of reef limestone, characterized by the appearance of limestone with holes resembling coral reefs. Based on the geological map, this area is included in the Wonosari formation area, composed of reef limestone, calcarenite, and tuffaceous calcarenite. Calcarenite is a sandstone composed of carbonate minerals in it. The presence of reef limestones in the Kukup Coastal Area is in line with previous research, which states that the characteristics of the limestones in the Wonosari Formation are increasingly turning into hard reef limestones in the form of rudstone, framestone, and floatstone in the southern area (Bothe, 1929).

Geomorphologically, the Kukup Coastal Area area is controlled by two main processes, namely marine and structural processes. The structural process is seen by high cliffs directly adjacent to the sea around the Kukup Coastal Area, known as a cliff. The marine process is seen by the abrasion process caused by sea waves on the cliff. This process can be seen from the holes used by erosion from sea waves on high cliffs. In addition, the presence of beach sand with white sand material is a characteristic of deposition by sea waves resulting from erosion on limestone cliffs.

3. DATA AND METHODS

3.1. Coastal System Identification Using UAV Technology

UAV technology for aerial photo data acquisition has several advantages, including producing high-resolution aerial photos with relatively affordable costs or low costs. UAV technology for aerial photo data acquisition is suitable for detailed studies with a narrow area. This research has a narrow study area, namely the Kukup Coastal Area, which makes it easier for researchers to get detailed data. This study prioritizes detailed data to get a high accuracy of results. The utilization of UAV technology was chosen to obtain data with high accuracy. Utilization of GNSS technology with the Geodetic Global Positioning System (GPS) tool is also needed to improve the accuracy of the UAV result data. Geodetic GPS was used to obtain Ground Control Point (GCP).

Data that were obtained from UAV technology include orthophoto and Digital Elevation Model (DEM) data. The orthophoto data were used to interpret land use data and to analyze socio-economic data, especially the existence of built-up land. DEM data from UAVs were reprocessed into The Digital Terrain Model (DTM) data to obtain morphological and coastal typology data. Obtaining orthophoto and DTM data generally goes through two stages: field and post-field. Field observations, aerial photo data acquisition, and GCP acquisition were conducted during the field stage. After the field stage is complete, it proceeds to the aerial photo data processing stage. Aerial photo data was processed using the Agisoft PhotoScan Professional application.

There were several stages in processing aerial photo data using the Agisoft PhotoScan Professional application, including Align Photos, Inputting GCP coordinate to aerial photo, Build Dense Cloud, Build Mesh, Build Orthomosaic, and Build DEM. Align Photos is the process of identifying the points on each photo, and then a matching process is carried out between the same points. The following process is to build Dense Point Clouds. Dense Point Clouds are a collection of high points in thousands to millions resulting from photogrammetric processing of aerial photographs. This processing principle used structure from motion (SFM) which generated point cloud data from the reconstruction of patches between photos (Pranata & Cahyono, 2016). Point cloud data has 3D coordinate information (x, y, and z). Mesh, also called a 3D model, was the main processing output at Agisoft. The mesh data were used to generate DEM and Orthophoto data.

Output DEM data from UAV is Digital Surface Model (DSM). DSM data must be processed into Digital Terrain Model (DTM) data to obtain coastal morphology data. DTM is digital elevation data that eliminates the appearance of objects on the earth's surface, such as vegetation and buildings, so the surface relief is the actual condition of the relief above the earth's surface. The processing of DSM into DTM in this study was carried out in all study area both flat and hilly areas. DSM data processing into DTM data has been carried out using the PCI Geomatics application with the Terrain Filter (Flat) method.

Beside the DEM data, bathymetry data is also needed to create tsunami hazard modeling. There are two kinds of bathymetry data used in this research, namely GEBCO bathymetry data and BATNAS bathymetry data. GEBCO bathymetry data has a resolution of 30 arc seconds or around 1 km. BATNAS bathymetry data has a resolution of around 185 m. The BATNAS bathymetry data is used for modelling in the Indian Ocean region to the coastal areas. Meanwhile, GEBCO bathymetry data is used for modelling in the Indian Ocean region which is not covered by BATNAS bathymetry data.

3.2. Tsunami Hazard Modelling

One of the reasons that caused tsunami disasters in Southern Java Island is seabed dislocations that produce earthquakes (Wibowo, Marfai, Kongko, Mardiatno, & Nurwijayanti, 2019). The numerical modelling of tsunami wave processing was divided into three stages: earthquake source modelling, tsunami wave propagation modelling, and tsunami inundation modelling (Hasan, Rahman, & Mahamud, 2015). Massive earthquakes can occur because of the subduction zone of the Indo-Australian oceanic plate under the Eurasian continental plate in the south of Java Island. According to the 2017 Indonesia Earthquake Source and Hazard Map, the highest potential earthquake in the southern fault zone of Gunungkidul is 8.9 MW. This data is used by researchers to model the potential for a tsunami in the Coastal Area around Kukup Beach, Gunungkidul.

The following process was reconstructing the fault or vertical deformation, which could produce an 8.9 MW earthquake. Tsunami source construction was carried out by identifying earthquake parameters due to vertical deformation on the seabed surface. The dimensions and characteristics of deformation in this study were modelled based on the scaling law. Scaling law is a comparison of earthquake-triggering parameters used to estimate fault geometry. These parameters are magnitude, epicentre, depth, strike, dip, slip, L (length of the fault area), W (width of the fault area), and dislocations.

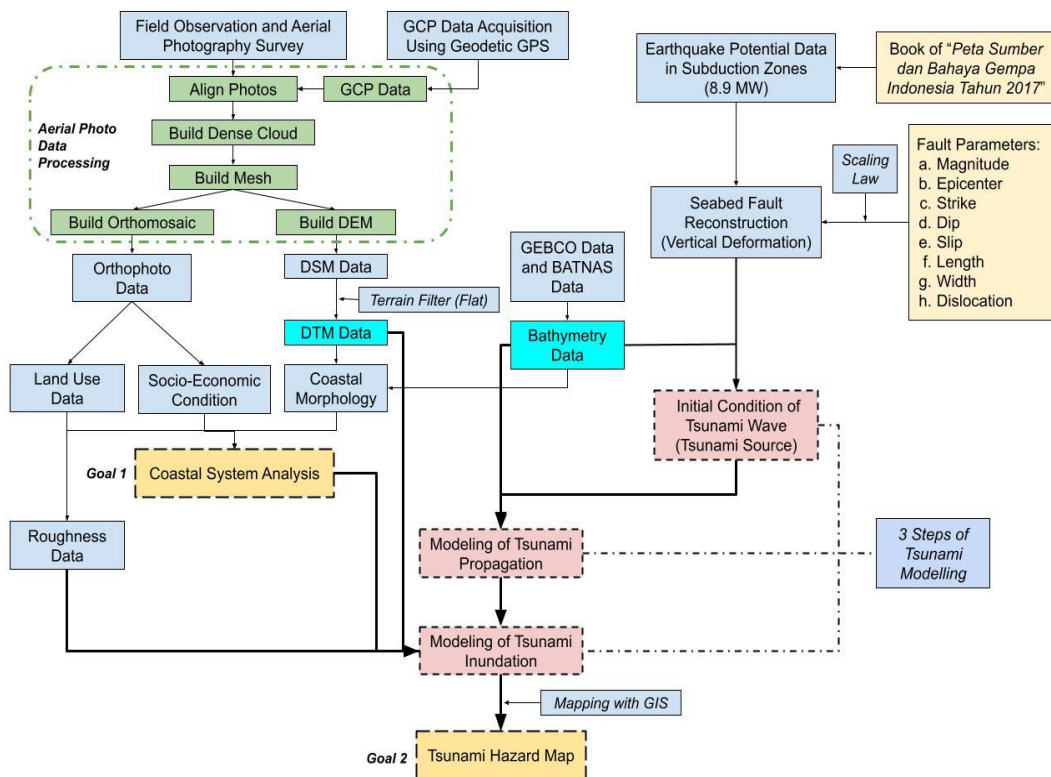


Fig. 3. Flowchart of Research Methodology.

After determining the earthquake source parameters, a tsunami source model was created to create a tsunami propagation and inundation model. The modelling of tsunami propagation and tsunami inundation was carried out using TUNAMI N3 software. Tsunami inundation modeling used a two data from UAV photo processing, namely DTM data and surface roughness from landuse interpretation and processing data. The modelling results were in the form of a tsunami inundation map of the potential of the highest waves. Next, the tsunami inundation map was classified to produce a tsunami hazard map based on the classification in the Head of BNPB Regulation No. 2 of 2012 (Perka BNPB No. 2 Tahun 2012). Overall, the research process is presented in **Fig. 3**.

4. RESULTS

4.1. Coastal System in Kukup Coastal Area

Coastal system analysis is important to study the dynamics that occur in coastal areas, especially for tsunami disaster identification. Identification of the coastal system can be made by utilizing remote sensing technology such as aerial photography imagery using drones. The results of aerial photography with drones can produce orthophoto and digital elevation model (DEM) data. The orthophoto was used to identify coastal areas' land cover and socio-economic activities. DEM can be used to describe the morphological conditions and physical environment characteristics in coastal areas.

4.1.1. Morphology and Physical Characteristics in Kukup Coastal Area

The results of processing aerial photos can produce Digital Surface Model (DSM) data using Agisoft Photoscan software. DSM is digital height data in the form of the height of objects that cover the earth's surface, so the presence of vegetation and building objects is identified as the height of the earth's surface. The results of DSM from aerial photo processing can be seen in **Fig. 4**. Furthermore, the DSM data can be modelled to produce a digital terrain model (DTM).

The comparison of DSM and DTM conditions in the Kukup Coastal Area can be seen in **Fig. 5**. Based on **Fig. 5**, the roughness of the surface relief of the plains in the DSM looks rougher, while the DTM data, the surface relief looks smoother.

Based on DTM, it can be seen that the Kukup Coastal Area has a morphology with various conical hills resembling a dome with closed basins, namely a cockpit. It is a characteristic of the karst landscape area in the southern part of Gunungsewu, namely the conical karst landscape. Some hills are also directly adjacent to the sea, so there are abrasion marks by sea waves known as cliff landforms. In addition, it can be seen that there is a straightness pattern on the karst hills in the coastal area of Kukup Beach with a northwest-southeast direction (see **Fig. 4**). The existence of straightness causes the conical hills to become interconnected so that the closed basin pattern forms labyrinths. It is also a characteristic of the karst formation on the south side of Gunungsewu, namely the labyrinthic karst type. The labyrinth extending north-south becomes the centre of tourist activities and is the only access to the Kukup Coastal Area. It needs to be a concern because this labyrinth can be the location of a water passage when a tsunami occurs. In addition to tsunami hazard processing, DTM can be used to classify the typology of the Kukup Coastal Area. The coastal typology is influenced by several factors, namely genesis, coastal dynamics, and the current dominant geomorphological process. The coastal typology classification in this study was determined based on the tidal range, the main material, the genesis process, the slope, and the shape of the beach (Khakim, Soedharma, Mardiasuti, Siregar, & Boer, 2008; Malawani & Mardiatno, 2015; Shepard, 1973).

Tidal range data was obtained from previous research according Wibowo (2019) which "*Data from Tidal Model Driver (TMD) was taken around the area of interest, namely between the Baron and Sepanjang Coastal Area. One of the results of data extraction from TMD was tidal constant data. Tidal constant data was used to calculate the value of each vertical datum. Datum Highest Astronomical Tide (HAT) is the highest tide condition in about 20 years. On the other hand, the Lowest Astronomical Tide (LAT) datum is the lowest condition during that period. The Tidal Range value shows the difference between the mean high-water level (MHWL) and the mean low water level (MLWL), which is 1.719 meters located in Kukup Coastal Area.*" (2019, pp 73-74).

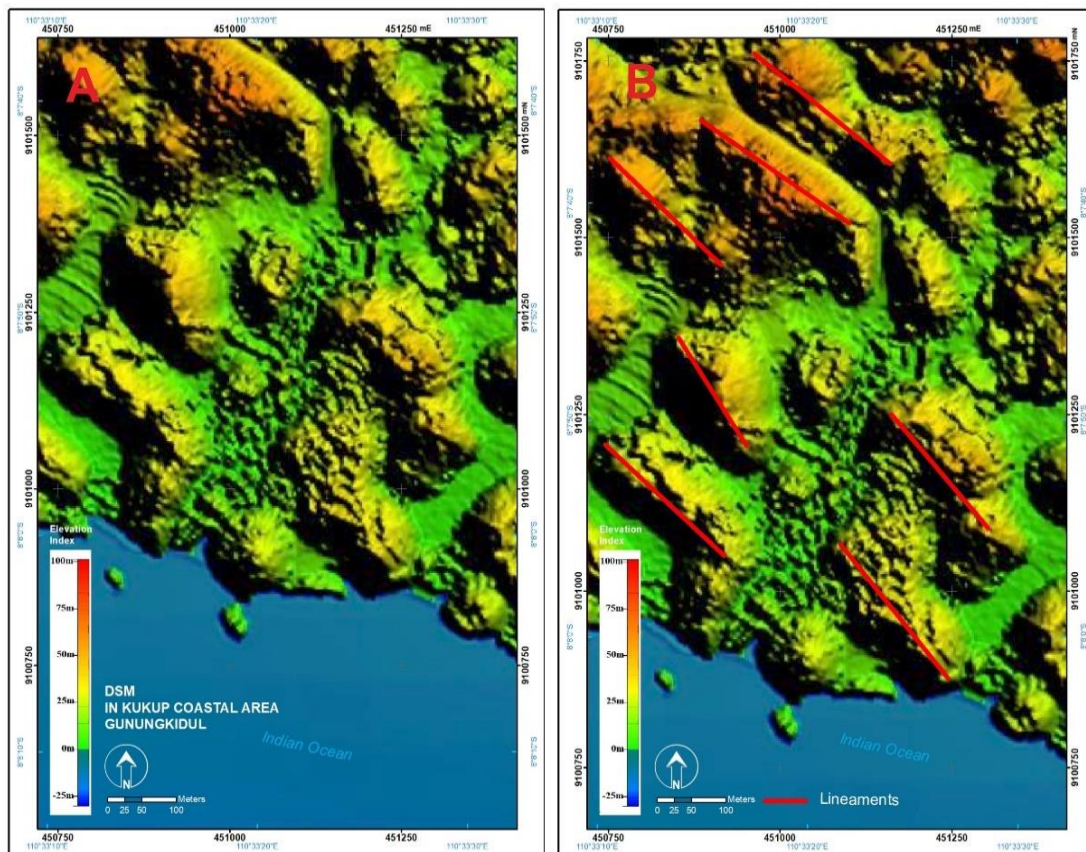


Fig. 4. DSM from UAV Foto Analysis (A) and Lineaments Identification Based on DSM Data in Kukup Coastal Area (B)

Tidal data range around Kukup Coastal Area was 1,719 meters (Wibowo, 2019). This value is similar to previous research (Khakim et al., 2008), which states that the tidal range on one of the beaches in Gunungkidul (Ngungap Beach) is less than 2 meters. The value of the tidal range of fewer than 2 meters indicates that the typology of the southern coast of Gunungkidul Regency, especially Kukup Beach, is dominated by the influence of waves (wave erosion coast).

Other parameters besides the tidal range are slope, constituent material, genesis, and beach shape. The Kukup Coastal Area is dominated by flat and steep slopes. In the flat area, the material is white sand with the primary dominant process, namely the deposition of marine deposits carried by longshore currents due to erosion on limestone cliffs. In the steep area, the material is hard reef limestone with the dominant processes in the form of structural and solutional. When viewed from the beach shape, all of the Kukup Coastal Areas have a concave shape. Based on these conditions, it can be concluded that there are two coastal typologies in the Kukup Coastal Area according to Shepard, (1973) classification, namely the Marine Deposition Coast on the flat area and the Wave Erosion Coast on the steep slope area (see **Table 1**).

Meanwhile, according to the local scale (1:15,000), the Kukup Coastal Area has two typologies: the Sandy Coast in the flat area and the Rocky Erosion Coast in the steep slopes area. Based on previous research, the coastal typology of karst areas begins with a structurally shaped coast typology, becomes a wave erosion coast, and ends as a marine deposition coast (Marfai, Cahyadi, & Anggraini, 2013). It implies that the coastal typology at Kukup Coastal Area in the steep slope area will eventually turn into a coastal typology as in the flat area in the future.

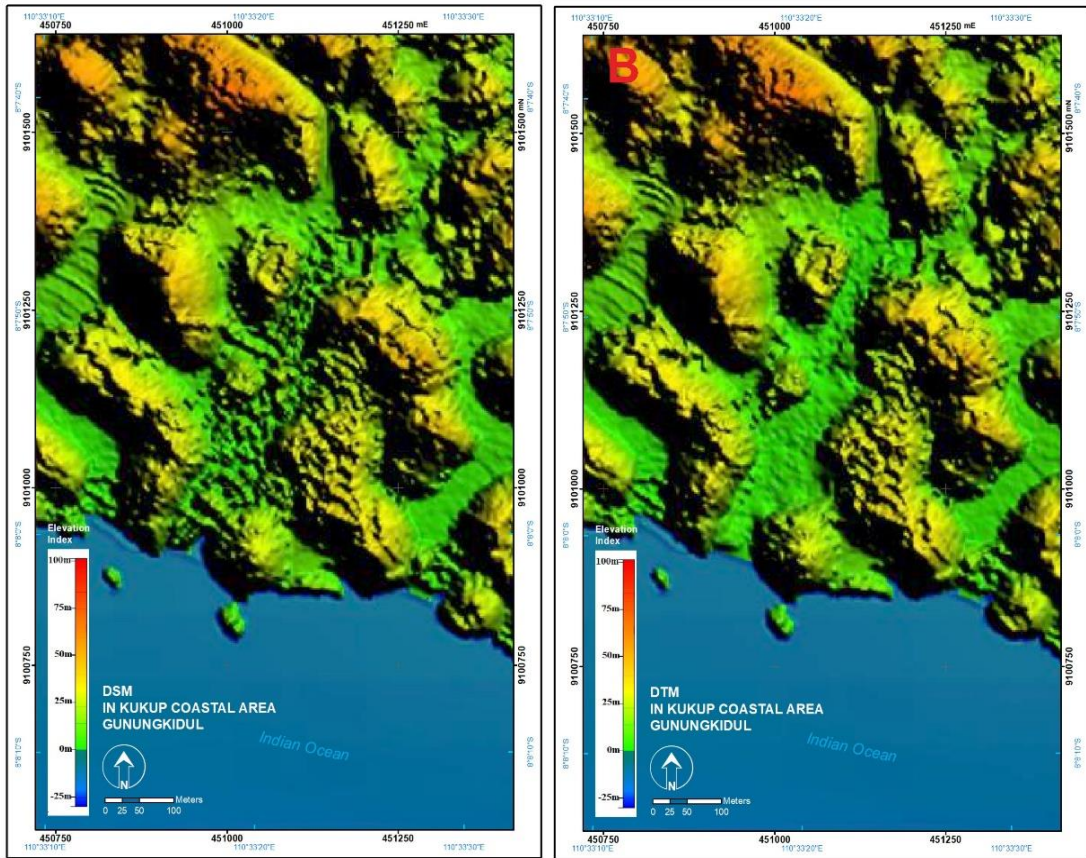


Fig. 5. Comparison of DSM and DTM Results Modelling.

Table 1.

Coastal Typology Classification in Kukup Coastal Area.

Coastal Area	Slope	Identification Parameters			Typology Classification		
		Parent Material	Genesis	Coastal Shape	Shepard (1973)	Local Scale (1:15,000)	
Kukup	Flat-Undulating	Sand	Deposition	Concave	Marine Deposition Coast	Sandy Coast	
	Steep	Calcareous Limestone	Erosion & Solutional	Concave	Wave Erosion Coast	Rocky Erosion Coast	

4.1.2. Land Cover and Social-Economic Activities in Kukup Coastal Area

Land cover data can be extracted from orthophoto (see Fig. 6.) through manual digitization on screen. Visual interpretation was used to extract land cover data because it is more appropriate for narrow areas with higher accuracy, better data completeness, and accuracy of area calculation (Sari, Weston, Newnham, & Volkova, 2021; Zanella, Sousa, Souza, Carvalho, & Borem, 2012). Visual interpretation is an approach based on the recognition of spatial characteristics of objects such as hue/color, size, shape, texture, pattern, height, shadow, location, association, and convergence of evidence (Sutanto, 1994). The interpretation results show that there are 11 types of land cover: road networks with pavement, house yards, mixed gardens, built-up land, buried land, sandy land, grass, shrubs, dry land, agricultural land, and ponds. The land cover map in the Kukup Coastal Area can be seen in Fig. 6. Mixed gardens and dry fields are the dominant land cover in the Kukup Coastal Area, with an area of more than 50% of the total study area.

Mixed gardens are primarily found in areas with steep slopes on the hills, while dry fields are mostly found in plains or basins between karst hills. Sandy land or buried land is found only in areas near the shoreline known as sandy beaches. Built-up land and roads are found in an elongated pattern along the valley in the middle of the hill, with the main dominance of buildings for trade, lodging, public facilities, and buildings to support other tourism activities. The dominance of built-up land indicates that socio-economic activities in the Kukup coastal area have developed. The main socio-economic activities in the study area are tourism activities. The land use data results were used to classify the roughness class.

The surface roughness condition was interpreted as the fundamental friction value possessed by each land cover. Surface roughness values in tsunami hazard studies were used to minimize the tsunami inundation area and its maximum range (Kongko & Schlurmann, 2011). Surface roughness values can be classified by various approaches. The classification approach used in this study is the Chow classification (Chow, 1959). Surface roughness is divided into 13 classes based on land cover: house yards, road, mixed garden, ponds/ water bodies, buried land, built-up land, dry land, sandy land, grass, agricultural land, and shrubs. The surface roughness value in the Kukup Coastal Area was derived from land cover data previously processed using orthophoto data from aerial photo processing. Based on the classification results, it was found that there are seven classes of classification of surface roughness values in the Kukup Coastal Area. The lowest value, 0.007, is in the waterbody in the form of a pond. Meanwhile, the highest value, 0.05, is on the built-up land area for settlements. The distribution of surface roughness values follows the pattern formed by the land cover, which can be seen in **Fig. 6**.

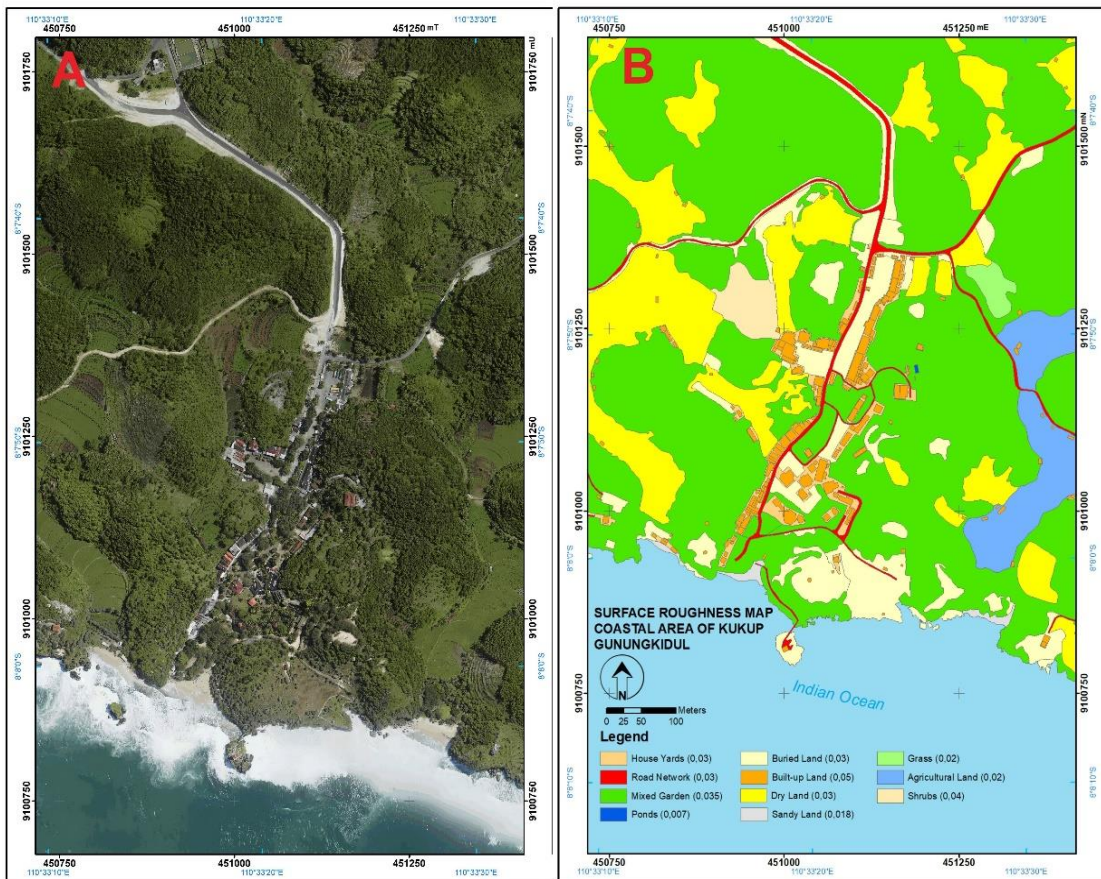


Fig. 6. Orthophoto (A) and Surface Roughness Based on Landuse Classification (B) in Kukup Coastal Area.

4.2. Tsunami Hazard in Kukup Coastal Area

The tsunami model created in this study uses earthquake data with a magnitude of 8.9 Mw. This magnitude was chosen based on the maximum earthquake potential in the southern megathrust segment of eastern Java (Tim Pusat Studi Gempa Nasional, 2017). This model also considers the suitability of the tsunami propagation into the mainland (run-up). Parameters that influence the suitability of tsunami run-up are DTM data and surface roughness. The DTM data has been processed based on aerial photography data, so it has a high spatial resolution. Meanwhile, the surface roughness data used in the modelling is non-uniform roughness based on the actual land cover conditions in the Kukup Coastal Area.

Based on the modelling results, there was an initial rise in sea level due to an earthquake with a magnitude of 8.9 Mw, as high as 6.7 meters, with a maximum decrease of 3.0 meters. Furthermore, a tsunami propagation model can be developed. Tsunami propagation modelling describes the process of tsunami propagation from the initial sea level condition after the earthquake and its distribution in all directions. This propagation is described as the relationship between tsunami height and time. Based on the modelling results, it was found that the tsunami reached the Kukup Coastal Area with a height of 5 cm in about 1,400 seconds (23 minutes). Next, the tsunami event was modelled for 90 minutes to determine the dynamics of the tsunami height for 90 minutes. Based on the modelling results, three high waves hit the Kukup Coastal Area. The first high waves came with a height of 10-12 meters at 23–25-minute intervals lasting 15 minutes. The second high wave came at 53-55 minutes intervals with a height of 12-14 meters for 5 minutes. The third wave is the highest compared to the two previous waves. The height of the third wave is 14.7 meters which occurred at 78-79 minutes.

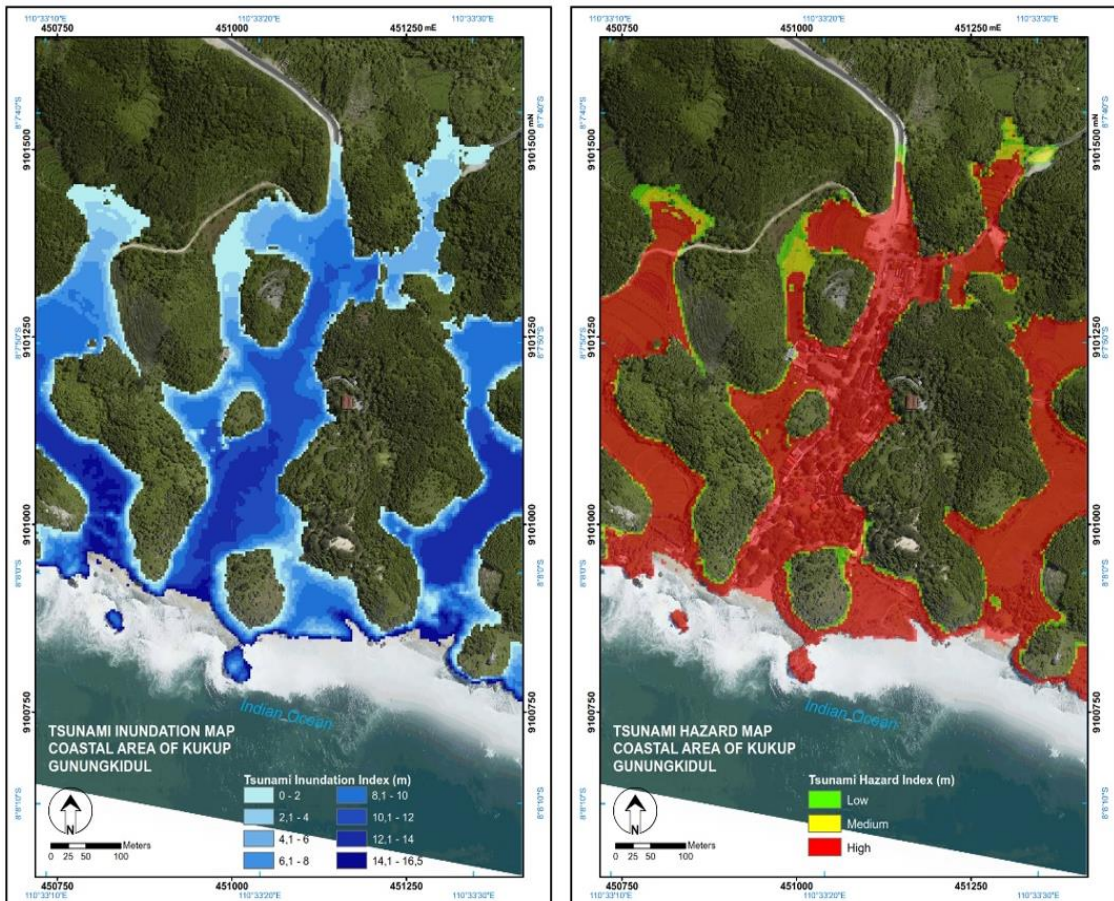


Fig. 7. Inundation (A) and Tsunami Hazard Maps (B) in Kukup Coastal Area.

Based on the tsunami source and propagation model, a tsunami inundation map can be made in the Kukup Coastal Area. This tsunami inundation map shows the inundation area due to the tsunami with an earthquake-triggering scenario of 8.9 Mw. The results show that the inundated area in the Kukup Coastal Area due to the tsunami was 23.53 hectares. The maximum height of tsunami inundation is 16.5 meters. The tsunami-formed inundation pattern shows a longitudinal pattern in the elongated basin between conical hills. This condition happens because the tsunami waves are concentrated at one point so that the run-up of the tsunami becomes elongated. Therefore, it can be concluded that the morphology in the coastal area also affects the propagation of tsunami inundation to the mainland. Understanding tsunami generation and subsequent inundation are needed in addition to the tsunami propagation model (Dias, Dutykh, O'Brien, Renzi, & Stefanakis, 2014). The tsunami inundation map in Kukup Coastal Area can be seen in **Fig. 7**.

The tsunami hazard map was made based on the tsunami inundation modelling in the Kukup Coastal Area. The assumptions used to create a tsunami hazard map follow BNPB regulations through the Head of BNPB Regulation No. 2 of 2012. This regulation has provided a standard for compiling disaster vulnerability classes, especially tsunami disasters, based on inundation heights. A tsunami inundation height of 0 - 1 meter is included in the low hazard index class, 1 - 3 meters is included in the medium hazard index class, and more than 3 meters is included in the high hazard index class.

Based on the results, it was found that the Kukup Coastal Area has a high tsunami hazard index, even far inland (see **Fig. 7**). The low and moderate tsunami hazard index values are only found in a few areas adjacent to the hill or already on the hill ridge. This condition happens because the value of the tsunami run-up height in the shoreline is 15 - 20 meters, so the tsunami inundation still has a height of more than 3 meters when it reaches the mainland.

5. DISCUSSION

The tsunami hazard pattern formed in the Kukup Coastal Area extends south-north in the elongated basin between the karst hills. This condition should be a concern, mainly when a tsunami occurs; all forms of tourist and human activities in the elongated basin can become elements at risk of being affected by a tsunami. Therefore, it is necessary to develop a good tsunami disaster mitigation strategy to reduce the risk of a tsunami disaster in the Kukup Coastal Area. In addition, it is also necessary to determine the appropriate evacuation points and routes, considering that there is only one access road to Kukup Beach through the elongated basin.

The results of the tsunami inundation model in the Kukup Coastal Area show a unique pattern. The maximum tsunami height generated by the 8.9 Mw earthquake scenario is 16.5 meters on the Kukup Shoreline. The results of the tsunami inundation model in the coastal area are similar to previous studies conducted in the southern coastal areas of Java Island as high as 12-16 meters (Horspool et al., 2014); Cilacap, Central Java as high as 10-15 meters (Gayer, Leschka, Nöhren, Larsen, & Günther, 2010); Pandeglang, West Java as high as 15 meters (Lestari, Fitriyani, Ahmad, Rais, & Azhari, 2021); Blitar and Malang, East Java as high as 17.5 meters (Armono, Putra, & Wahyudi, 2021).

The height of the tsunami inundation in the Kukup Coastal Area decreased in areas far from the coastline. The decrease in tsunami inundation occurred due to differences in slope conditions at locations near the shoreline, which were relatively flat. In contrast, it was relatively wavy or wavy in areas far from the shoreline. Previous studies on tsunamis have also shown this condition based on tsunami inundation modelling (Hebert et al., 2012; Smart, Crowley, & Lane, 2015). The inundation pattern in the Kukup Coastal Area extends perpendicular to the shoreline, with a range of about 2 km from the shoreline. It is very different from the pattern of tsunami inundation that was modelled in the Pelabuhan Ratu Coastal Area, West Java (Setiyono, Gusman, Satake, & Fujii, 2017); Kuta, Bali; Padang, Sumatra (Gayer et al., 2010); Wediombo, Gunungkidul, Central Java (H Fatchurohman & Handayani, 2022); Palu, Central Sulawesi (Mikami et al., 2019); Banda Aceh, Sumatra (Prasetya, Borrero, de Lange, Black, & Healy, 2011) which extend parallel to the shoreline. Differences in tsunami inundation patterns occur due to coastal typology and morphological conditions (Hendy Fatchurohman, Cahyadi, & Purwanto, 2022; Takabatake, Chenxi, Esteban, & Shibayama, 2022).

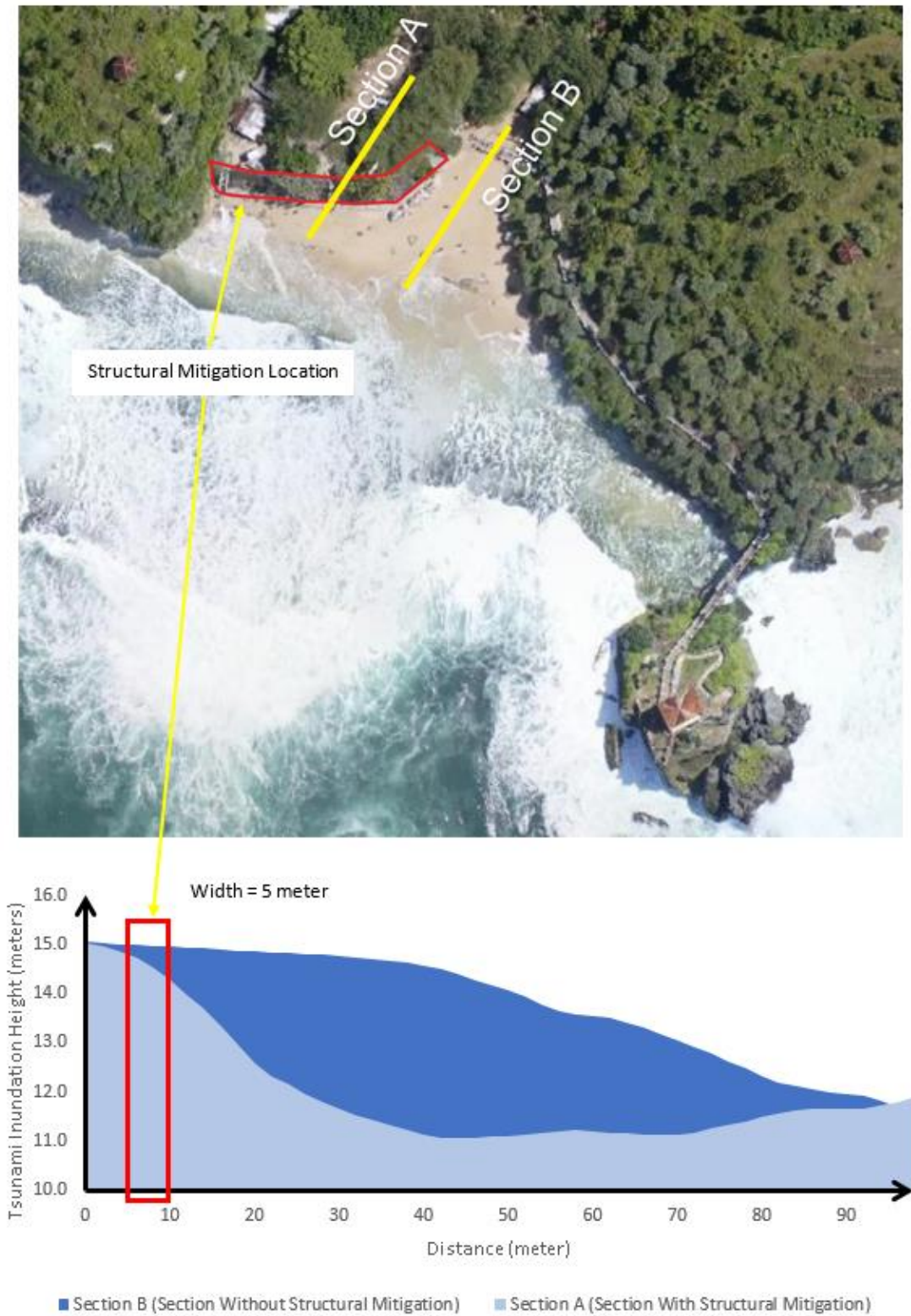


Fig. 8. Tsunami Inundation Slope Pattern in Segments with Barrier and Without Barrier.

The coastal typology of the Kukup Coastal Area, which is dominated by wave erosion, causes tsunami inundation concentrated in flat areas with a marine deposition coast typology. In addition, the morphological condition of the Kukup Coastal land, which is dominated by the appearance of conical hills with a firm lineament pattern, causes tsunami inundations concentrated lengthwise in the basins between these hills. It shows that the pattern of tsunami inundation is strongly controlled by physical conditions in the coastal area, mainly related to morphological conditions.

The accumulation of tsunami inundation concentrated and elongated in the inter-hill basin makes the risk in the Kukup Coastal Area relatively higher than other coastal areas because the nodal of human activity is in this elongated basin. The built-up land area has an elongated pattern in this basin which is also a place for the accumulation of tsunami inundation. This condition indicates that all human activities in the Kukup Coastal Area will be directly affected when a tsunami occurs. Therefore, it is necessary to carry out mitigation efforts to reduce the risk caused by a tsunami in this area.

One disaster mitigation that has been carried out in this coastal area is by making a long embankment near the shoreline. This embankment is made extending along the shoreline of the Kukup Coastal Area, which has the function of preventing coastal abrasion and preventing the big waves that will hit Kukup Beach. This building turned out to be quite effective in withstanding tsunami waves, as evidenced by the results of the inundation modelling. On the shore where there are embankments, the deflation of the tsunami inundation tends to be relatively fast compared to the tsunami inundation deflation on the shore without the embankment (see **Fig. 8**).

The role of tsunami barrier buildings in disaster risk reduction could be identified in detailed tsunami modelling using drones using high-resolution aerial photo data. Drone photography data could produce elevation data that can describe the details of the wave-retaining embankment in the study area. It is one of the advantages of using aerial photography data by using a drone in tsunami modelling, which could describe the effectiveness of tsunami mitigation buildings to withstand big waves in coastal areas. The role of tsunami mitigation buildings will not be modelled if the tsunami modelling is carried out using medium or small-scale DEM data (Takabatake et al., 2022; Yamanaka & Shimoazono, 2022). Therefore, it is crucial to use aerial photography data using a drone in tsunami studies, significantly to develop detailed mitigation planning in coastal areas, such as spatial planning for coastal areas, planning for evacuation points and routes, constructing wave retaining structures (Strusińska-Correia, 2017), and the use of wave-retaining vegetation (Wanger et al., 2020).

The results of this study indicate that structural mitigation by constructing a structural embankment is effective to reduce tsunami inundation in the Kukup Coastal Area. However, the construction of a structural mitigation for tsunami disaster mitigation has several weaknesses. First, the cost to build structural mitigation such as structural embankment is expensive. Second, the existence of additional buildings in coastal areas can change the dynamics of the abiotic and biotic environment such as changes in ecosystem conditions, especially natural vegetation and changes in patterns of physical distribution of sand in coastal areas. There is another alternative for mitigating tsunami, namely by utilizing natural embankments in the form of natural ecosystems such as mangroves, sand dunes, greenbelt, or other natural vegetation which can lives in coastal area. Utilization of natural embankments is also effective to reduce the risk of a tsunami without changing the dynamics of the abiotic and biotic environment in coastal areas (Harada1 & Imamura, 2005). However, natural embankment has several disadvantages. First, The effectiveness of vegetation also changes with the age and structure of the forest (Tanaka & Sasaki, 2007). Second, the nature embankment is fragile due to antropological activities such as land conversion and ecosystem exploitation (Tanaka, 2009). Apart from that, establishing evacuation points and routes as well as socializing the tsunami disaster to the public and tourists is also important to reduce the risk of tsunami by increasing community capacity in dealing with tsunami disasters (Agussaini, Sirojuzilam, Rujiman, & Purwoko, 2022; Baeda, Suriamihardja, Umar, & Rachman, 2015).

6. CONCLUSIONS

The Kukup Coastal Area has very complex and interrelated physical and socio-economic conditions. The physical environment, dominated by conical hills with a firm lineament pattern, causes the formation of elongated basins between the conical hills. This elongated basin is a place for human activities, as indicated by the density of built-up land area for trading and supporting coastal tourism activities. In addition, this elongated basin also became a passageway for waves when the tsunami hit this area. The existence of longitudinal basins between the conical hills causes the tsunami inundation pattern to extend perpendicular to the shoreline, causing the tsunami inundation to extend as far as 2 km from the shoreline. The existence of community activities that are also concentrated in this basin causes an increased risk of a tsunami disaster in the Kukup Coastal Area.

The tsunami inundation in the Kukup Coastal Area has a unique pattern caused by a morphological condition in this coastal area. Based on the tsunami inundation model, it shows that all of the plain areas in the Kukup Coastal Area were inundated with heights between 2 – 16 meters. In fact, most of the plain area in the Kukup Coastal Area were inundated with a height of more than 8 meters. Therefore, most of the plain area in the Kukup Coastal Area have a high tsunami hazard. Meanwhile, moderate and low tsunami hazard areas are only found on the lower slopes of the hills in the Kukup Coastal Area with an inundation of 0 – 6 meters. Conditions of plain areas with a high tsunami hazard that are widely used for tourism and economic activities make it necessary to plan a tsunami hazard mitigation to reduce the risk of a tsunami in the Kukup Coastal Area. However, the determination of tsunami hazard mitigation efforts needs to be based on several tsunami hazard scenarios with various magnitudes of earthquake as a source values. This is the limitation of this research. This research was modelled tsunami hazard only with one magnitude of earthquake source, so it needs to create a tsunami hazard model by using other scenario to produce more effective and efficient mitigation efforts.

This study also found that using aerial photographic data with drones was very helpful in making detailed studies on tsunami hazards and inundation modelling. The existence of structural mitigation can be modelled with drone aerial photography so that the role of structural mitigation in tsunami hazards can be known directly. The presence of a wave retaining structure can speed up the tsunami inundation sloping process so the height of the tsunami inundation can be minimized. Therefore, it is crucial to use drone aerial photo data for tsunami inundation modelling to develop detailed mitigation directions for various coastal typologies.

REFERENCES

- Agussaini, H., Sirojuzilam, Rujiman, & Purwoko, A. (2022). A New Approach of the Tsunami Mitigation Strategies for the City of Banda Aceh, Indonesia. *Indonesian Journal of Geography*, 54(1), 62–69. <https://doi.org/10.22146/ijg.66500>
- Anjar, F., Laksono, T., Widagdo, A., Aditama, M. R., & Fauzan, M. R. (2022). Tsunami Hazard Zone and Multiple Scenarios of Tsunami Evacuation Route at Jetis Beach , Cilacap Regency , Indonesia. *Sustainability*, 14(2726), 1–19. <https://doi.org/https://doi.org/10.3390/su14052726>
- Armono, H. D., Putra, A. R., & Wahyudi. (2021). Analysis of Tsunami Wave Height, Run-up, and Inundation in The Coastal of Blitar and Malang Regency. *IOP Conference Series: Earth and Environmental Science*, 936(1), 12013. <https://doi.org/10.1088/1755-1315/936/1/012013>
- Ashar, F., Amaratunga, D., & Haigh, R. (2018). Tsunami Evacuation Routes Using Network Analysis: A case study in Padang. *Procedia Engineering*, 212, 109–116. <https://doi.org/https://doi.org/10.1016/j.proeng.2018.01.015>
- Badan Pusat Statistik. (2021). *Statistik Gunungkidul dalam Angka 2012 - 2021 (Gunungkidul Statistics Data 2012 - 2021)*. Jakarta: Badan Pusat Statistik.
- Baeda, A. Y., Suriamihardja, D. A., Umar, H., & Rachman, T. (2015). Tsunami Mitigation Plan for Manakarra Beach of West Sulawesi Province, Indonesia. *Procedia Engineering*, 116, 134–140. <https://doi.org/https://doi.org/10.1016/j.proeng.2015.08.274>

- Bothe, A. C. D. (1929). Djiwo Hills and Southern Range. *Fourth Pacific Science Congress Excursion Guide*, 14h.
- Chaeroni, Hendriyono, W., & Kongko, W. (2013). Pemodelan Tsunami dan Pembuatan Peta Rendaman untuk Keperluan Mitigasi di Teluk Teleng, Pacitan (Tsunami Modeling and Making Inundation Maps for Mitigation Purposes in Teluk Teleng, Pacitan). *Jurnal Dialog Penanggulangan Bencana*, 4(2), 87–97.
- Chow, V. T. (1959). *Open Channel Hydraulics*. New York: McGraw-Hill.
- Di Mauro, M., Megawati, K., Cedillos, V., & Tucker, B. (2013). Tsunami risk reduction for densely populated Southeast Asian cities: analysis of vehicular and pedestrian evacuation for the city of Padang, Indonesia, and assessment of interventions. *Natural Hazards*, 68(2), 373–404. <https://doi.org/10.1007/s11069-013-0632-z>
- Dias, F., Dutykh, D., O'Brien, L., Renzi, E., & Stefanakis, T. (2014). On the Modelling of Tsunami Generation and Tsunami Inundation. *Procedia IUTAM*, 10(2014), 338–355. <https://doi.org/https://doi.org/10.1016/j.piutam.2014.01.029>
- Faiqoh, I., Gaol, J. L., & Ling, M. M. (2013). Vulnerability Level Map Of Tsunami Disaster in Pangandaran Beach, West Java. *International Journal of Remote Sensing and Earth Sciences*, 10(2), 90–103. <https://doi.org/http://dx.doi.org/10.30536/j.ijreses.2013.v10.a1848>
- Fatchurohman, H., & Handayani, W. (2022). Coastal hazards mapping using high-resolution UAV image and DEM. A Case study in Siung Beach, Gunungkidul, Indonesia. *IOP Conference Series: Earth and Environmental Science*, 1039(1), 12026. <https://doi.org/10.1088/1755-1315/1039/1/012026>
- Fatchurohman, Hendy, Cahyadi, A., & Purwanto, T. H. (2022). Worst-Case tsunami inundation modeling using high-resolution UAV-DEM in various coastal typologies, case study Gunungkidul coastal area. *IOP Conference Series: Earth and Environmental Science*, 986(1), 12027. <https://doi.org/10.1088/1755-1315/986/1/012027>
- Gayer, G., Leschka, S., Nöhren, I., Larsen, O., & Günther, H. (2010). Tsunami inundation modelling based on detailed roughness maps of densely populated areas. *Natural Hazards and Earth System Sciences*, 10(8), 1679–1687. <https://doi.org/10.5194/nhess-10-1679-2010>
- Hall, S., Pettersson, J., Meservy, W., Harris, R., Agustinawati, D., & Olson, J. (2017). Awareness of tsunami natural warning signs and intended evacuation behaviors in Java, Indonesia. *Natural Hazards*, 89(1), 473–496. <https://doi.org/10.1007/s11069-017-2975-3>
- Harada1, K., & Imamura, F. (2005). *Effects of Coastal Forest on Tsunami Hazard Mitigation — A Preliminary Investigation BT - Tsunamis: Case Studies and Recent Developments* (K. Satake, Ed.). https://doi.org/10.1007/1-4020-3331-1_17
- Hasan, M. M., Rahman, S. M., & Mahamud, U. (2015). Numerical Modeling for the Propagation of Tsunami Wave and Corresponding Inundation. *IOSR Journal of Mechanical and Civil Engineering*, 12(2), 55–62. <https://doi.org/DOI: 10.9790/1684-12245562>
- Hebert, H., Burg, P., Binet, R., Lavigne, F., Allgeyer, S., & Schindel, F. (2012). The 2006 July 17 Java (Indonesia) tsunami from satellite imagery and numerical modelling: a single or complex source? *Geophysical Journal International*, 191(2012), 1255–1271. <https://doi.org/10.1111/j.1365-246X.2012.05666.x>
- Horspool, N., Pranantyo, I., Griffin, J., Latief, H., Natawidjaja, D. H., Kongko, W., ... Thio, H. K. (2014). A probabilistic tsunami hazard assessment for Indonesia. *Natural Hazards and Earth System Sciences*, 14(11), 3105–3122. <https://doi.org/10.5194/nhess-14-3105-2014>
- Khakim, N., Soedharma, D., Mardiatuti, A., Siregar, V. P., & Boer, M. (2008). Analisis Preferensi Visual Lanskap Pesisir Daerah Istimewa Yogyakarta untuk Pengembangan Pariwisata Pesisir Menuju pada Pengelolaan Wilayah Pesisir Berkelanjutan. *Forum Geografi*, 22(1), 44–59. <https://doi.org/10.23917/forgeo.v22i1.4925>
- Kongko, W., & Schlurmann, T. (2011). THE JAVA TSUNAMI MODEL: USING HIGHLY-RESOLVED DATA TO MODEL THE PAST EVENT AND TO ESTIMATE THE FUTURE HAZARD. *Coastal Engineering Proceedings*, 1(32 SE-Coastal Management, Environment, and Risk), management.25. <https://doi.org/10.9753/icce.v32.management.25>
- Lavigne, F., Gomez, C., Giffò, M., Wassmer, P., Hoebreck, C., Mardiatno, D., ... Paris, R. (2007). Field observations of the 17 July 2006 Tsunami in Java. *Natural Hazards and Earth System Sciences*, 7(2007), 177–183. <https://doi.org/https://doi.org/10.5194/nhess-7-177-2007>

- Lestari, D. A., Fitriyanti, N. S., Ahmad, T. E., Rais, A., & Azhari, D. R. (2021). Spatial Analysis on Tsunami Predictions in Pandeglang Regency. *Forum Geografi*, 35(July), 103–115. <https://doi.org/10.23917/forgeo.v35i1.12367>
- Malawani, M. N., & Mardiatno, D. (2015). Rencana Aksi Mitigasi Bencana Tsunami melalui Pendekatan Tipologi Pesisir dan Permukiman Kasus: Pesisir Jayapura. *Prosiding Simposium Nasional Mitigasi Bencana Tsunami 2015*, 14–23.
- Mardiatno, D., Malawani, M. N., & Nisaa', R. M. (2020). The future tsunami risk potential as a consequence of building development in Pangandaran Region, West Java, Indonesia. *International Journal of Disaster Risk Reduction*, 46, 101523. <https://doi.org/https://doi.org/10.1016/j.ijdr.2020.101523>
- Marfai, M. A., Cahyadi, A., & Anggraini, D. F. (2013). Typology, Dynamics, and Potential Disaster in The Coastal Area District Karst Gunungkidul. *Forum Geografi*, 27(2), 147–158. <https://doi.org/10.23917/forgeo.v27i2.2373>
- Marfai, M. A., Khakim, N., Fatchurohman, H., & Salma, A. D. (2021). Planning tsunami vertical evacuation routes using high-resolution UAV digital elevation model: case study in Drini Coastal Area, Java, Indonesia. *Arabian Journal of Geosciences*, 14(19), 2028. <https://doi.org/10.1007/s12517-021-08357-9>
- Mikami, T., Shibayama, T., Esteban, M., Takabatake, T., Nakamura, R., Nishida, Y., ... Ohira, K. (2019). Field Survey of the 2018 Sulawesi Tsunami: Inundation and Run-up Heights and Damage to Coastal Communities. *Pure and Applied Geophysics*, 176(8), 3291 – 3304. <https://doi.org/10.1007/s00024-019-02258-5>
- Nisaa', R. M., Sartohadi, J., & Mardiatno, D. (2021). Participatory GIS Approach to Assessing Building Vulnerability to Tsunamis in Pangandaran Regency. *Forum Geografi*, 35(2), 130–141. <https://doi.org/10.23917/forgeo.v35i2.14003>
- Okamoto, T., & Takenaka, H. (2009). Waveform inversion for slip distribution of the 2006 Java tsunami earthquake by using 2 . 5D finite-difference Green ' s function. *Earth, Planets and Space*, 61(2009), 17–20. <https://doi.org/https://doi.org/10.1186/BF03352919>
- Pranata, Y. N., & Cahyono, A. B. (2016). Evaluasi Metode Aerial Videogrametri untuk Rekonstruksi 3D Bangunan (Studi Kasus: Candi Singasari, Jawa Timur) (Evaluation of Aerial Videogrammetry Methods for 3D Building Reconstruction (Case Study: Singasari Temple, East Java). *Jurnal Teknik ITS*, 5(2), 260–265. <https://doi.org/10.12962/j23373539.v5i2.17375>
- Prasetya, G., Borrero, J., de Lange, W., Black, K., & Healy, T. (2011). Modeling of inundation dynamics on Banda Aceh, Indonesia during the great Sumatra tsunamis December 26, 2004. *Natural Hazards*, 58(3), 1029–1055. <https://doi.org/10.1007/s11069-010-9710-7>
- Rosselló, J., Becken, S., & Santana-Gallego, M. (2020). The effects of natural disasters on international tourism: A global analysis. *Tourism Management*, 79, 104080. <https://doi.org/https://doi.org/10.1016/j.tourman.2020.104080>
- Sari, I. L., Weston, C. J., Newnham, G. J., & Volkova, L. (2021). Assessing Accuracy of Land Cover Change Maps Derived from Automated Digital Processing and Visual Interpretation in Tropical Forests in Indonesia. *Remote Sensing*, Vol. 13. <https://doi.org/10.3390/rs13081446>
- Setiyono, U., Gusman, A. R., Satake, K., & Fujii, Y. (2017). Pre-computed tsunami inundation database and forecast simulation in Pelabuhan Ratu, Indonesia. *Pure and Applied Geophysics*, 174, 3219–3235.
- Shepard, F. P. (1973). *Submarine Geology*. New York: Harper and Row.
- Smart, G., Crowley, K., & Lane, E. M. (2015). Estimating tsunami run-up. *Natural Hazards*, 80, 1933–1947.
- Strusińska-Correia, A. (2017). Tsunami mitigation in Japan after the 2011 Tōhoku Tsunami. *International Journal of Disaster Risk Reduction*, 22, 397–411. <https://doi.org/https://doi.org/10.1016/j.ijdr.2017.02.001>
- Supriharyono. (2000). *Pelestarian dan Pengelolaan Sumber Daya Alam di Wilayah Pesisir Tropis (Conservation and management of natural resources in tropical coastal areas)*. Jakarta: Gramedia Pustaka Utama.
- Sutanto. (1994). *Penginderaan Jauh Jilid 1 (Remote Sensing Part 1)*. Yogyakarta: Gadjah Mada University Press.
- Takabatake, T., Chenxi, D. H., Esteban, M., & Shibayama, T. (2022). Influence of road blockage on tsunami evacuation: A comparative study of three different coastal cities in Japan. *International Journal of Disaster Risk Reduction*, 68, 102684. <https://doi.org/https://doi.org/10.1016/j.ijdr.2021.102684>

- Tanaka, N. (2009). Vegetation bioshields for tsunami mitigation: review of effectiveness, limitations, construction, and sustainable management. *Landscape and Ecological Engineering*, 5(1), 71–79. <https://doi.org/10.1007/s11355-008-0058-z>
- Tanaka, N., & Sasaki, Y. (2007). Limitations of Coastal Vegetation in the 2004 Indian Ocean Tsunami and 2006 Java Tsunami. *Proceedings of the 32nd IAHR World Congress*. Venice.
- Tim Pusat Studi Gempa Nasional. (2017). *Peta Sumber dan Bahaya Gempa Indonesia Tahun 2017*. Jakarta: Pusat Penelitian dan Pengembangan Perumahan dan Permukiman, Kementerian PUPR.
- Wanger, T. C., Ainun, N., Brook, B. W., Friess, D. A., Oh, R. R. Y., Rusdin, A., ... Tjoa, A. (2020). Ecosystem-Based Tsunami Mitigation for Tropical Biodiversity Hotspots. *Trends in Ecology & Evolution*, 35(2), 96–100. <https://doi.org/https://doi.org/10.1016/j.tree.2019.10.008>
- Wibowo, A. A. (2019). *Pemodelan Respon Tsunami terhadap Tipologi Pesisir di Sebagian Kabupaten Gunungkidul serta Upaya Pengelolaannya (Modeling of Tsunami Response to Coastal Typology in Parts of Gunungkidul Regency and its Management Efforts)*. Tesis-Magister Geografi, Universitas Gadjah Mada.
- Wibowo, A. A., Marfai, M. A., Kongko, W., Mardiatno, D., & Nurwijayanti, A. (2019). Pemanfaatan Data DEM dan Orthophoto Hasil UAV untuk Pemodelan Tsunami di Wilayah Kepesisiran Baron dan Sepanjang. *Prosiding Seminar Nasional PPDAS V*, 42–49. Yogyakarta: Faculty of Geography UGM.
- Widiyantoro, S., Gunawan, E., Muhari, A., Rawlinson, N., Mori, J., & Hanifa, N. R. (2020). Implications for megathrust earthquakes and tsunamis from seismic gaps south of Java Indonesia. *Scientific Reports*, 10(15274), 1–11. <https://doi.org/10.1038/s41598-020-72142-z>
- Windupranata, W., Hanifa, N. R., Nusantara, C. A. D. S., Aristawati, G., & Arifianto, M. R. (2020). Analysis of tsunami hazard in the Southern Coast of West Java Province - Indonesia. *IOP Conference Series: Earth and Environmental Science*, 618(1), 12026. <https://doi.org/10.1088/1755-1315/618/1/012026>
- Yamanaka, Y., & Shimozono, T. (2022). Tsunami inundation characteristics along the Japan Sea coastline: effect of dunes, breakwaters, and rivers. *Earth, Planets and Space*, 74(1), 19. <https://doi.org/10.1186/s40623-022-01579-5>
- Zanella, L., Sousa, C. H. R., Souza, C. G., Carvalho, L. M. T., & Borem, R. A. T. (2012). A COMPARISON OF VISUAL INTERPRETATION AND OBJECT BASED IMAGE ANALYSIS FOR DERIVING LANDSCAPE METRICS. *Proceedings of the 4th GEOBIA*, 509–514. Rio de Janeiro.

SPATIAL MODEL OF RUNOFF FLOWING INTO THE NEWLY FORMED LAKE AT SINABUNG VOLCANO

Sandy Budi WIBOWO¹, **Polin Mouna TOGATOROP^{2,3}**, **Tsamara HANINDHIYA⁴**,
Barandi Sapta WIDARTONO¹, **R. Ibnu ROSYADI¹**

DOI: 10.21163/GT_2023.182.05

ABSTRACT:

Volcanic dams are formed when eruptions occur near rivers, obstructing the natural flow of water and creating a dam. The infrequent nature of volcanic dams has resulted in limited research and literature on this topic. However, the Sinabung stratovolcano offers a valuable opportunity to address these knowledge gaps. Over a span of ten years of eruptions, abundant volcanic materials have accumulated in the Lau Borus River, leading to the growth of a dam and the formation of a lake behind it. This research aims to develop a GIS model that simulates the runoff flowing into the newly formed lake at Sinabung volcano. The methodology employed in this study involves the integration of an Agent-Based Model and Geographic Information System to create a dynamic model of runoff and spatio-temporal mapping. The results indicate that raindrops transform into runoff, flowing down the eastern volcanic flank towards the lake, covering a distance of 3.7 km from the crater in 696 seconds, with an average flow velocity of 5.32 m/s. The runoff accumulates in three drainage networks and exhibits two flow pulsations. By combining the Agent-Based Model and Geographic Information System, the research successfully identifies the process of runoff accumulation into the newly formed lake at Sinabung volcano. Further investigation into potential lake outburst scenarios would be crucial for developing comprehensive mitigation strategies for cascading volcanic disasters.

Key-words: *Sinabung volcano, runoff, Agent Based Model, GIS, lahars, disasters.*

1. INTRODUCTION

Sinabung volcano (2,460 m) had been classified as dormant volcano by Vulcanological Survey of Indonesia until it surprisingly erupted in 2010. The eruption still continues in 2021 and produces abundant pyroclastic materials at eastern and southern flank after 11 years. Tropical climate regime in Indonesia accelerates the initiation of rain-triggered lahars at Sinabung volcano. Since the year 2010, the Lau Borus River channel has experienced noteworthy transformations in its physical characteristics. These alterations can be attributed to the occurrence of multiple massive lahars, which have been responsible for transporting significant quantities of sands, gravels, and boulders along the river. As a result of these lahars, the morphology of the river channel has been reshaped, leading to the formation of a new lake. The process by which this new lake has emerged bears resemblance to the formation of landslide dams in mountainous regions. In both cases, natural forces cause the accumulation of materials, such as sediments and debris, which obstruct the normal flow of water. This obstruction ultimately results in the creation of a lake or reservoir. Similarly, in the context of the Lau Borus River channel, the lahars have contributed to the buildup of materials that have acted as a barrier, leading to the formation of the new lake. The formation of this lake signifies a significant change in the local landscape and hydrological dynamics. It highlights the impact of lahars on the natural environment and serves as an example of the complex interactions between geological processes and the formation of landforms.

¹Department of Geographic Information Science, Faculty of Geography, Universitas Gadjah Mada, Indonesia; sandy_budi_wibowo@ugm.ac.id; barandi@geo.ugm.ac.id; ibnurosyadi@gmail.com)

²Ministry of Agrarian Affairs and Spatial Planning / National Land Agency, Indonesia, polin.mtogatorop@atrbpn.go.id

³Master of Science in Remote Sensing Study Program, Faculty of Geography, Universitas Gadjah Mada, Indonesia, polinmouna@mail.ugm.ac.id

⁴Cartography and Remote Sensing Study Program, Faculty of Geography, Universitas Gadjah Mada, Indonesia, tsamarahanindhiya@mail.ugm.ac.id

The existence of this newly formed lake is challenging because like other landslide dams in the world, there is possibility of failure. It could produce voluminous volcanic debris flows causing fatal and devastating impacts at downstream area. The objective of this study is to develop spatial model of runoff flowing into new formed lake at Sinabung volcano. This would be important to estimate the evolution of water volume and to support disaster mitigation strategies due to dam failure at the outlet.

2. LITERATURE REVIEW

North Sumatra is very well known worldwide for the Toba caldera, which resulted from the eruption of a supervolcano (Chesner et al., 2020; Mukhopadhyay et al., 2022; Naen et al., 2023). A dormant stratovolcano volcano is located at ignimbrite plateau 34 km north from this caldera, named Sinabung (Fig. 1).

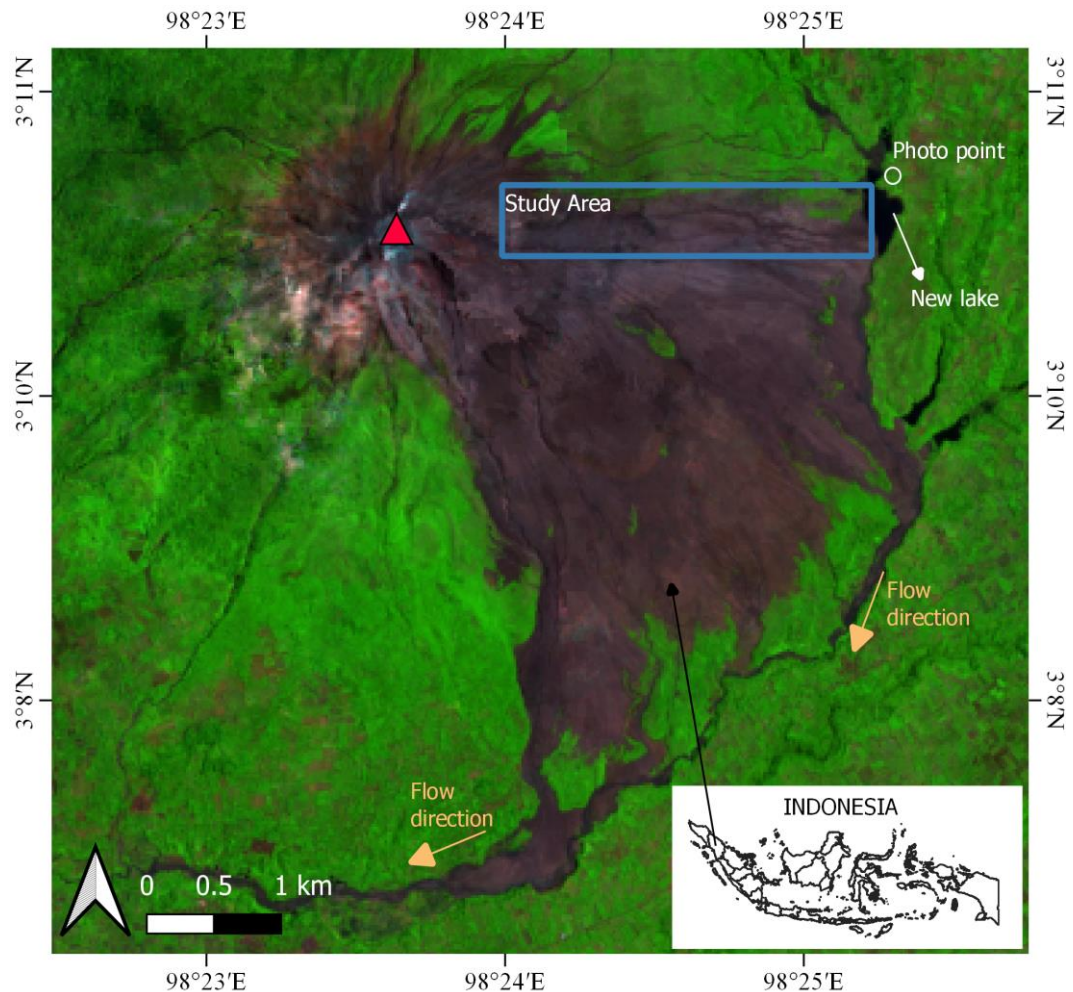


Fig. 1. Sentinel 2 satellite imagery (SWIR composite B12, B8A, B4) in 2020 showing the study area at the eastern flank of Sinabung volcano. New lake was formed due to excessive lahar deposition in Lau Borus River.

Unlike Toba caldera, Sinabung volcano was not famous at that time because there were no records on its volcanic activity since 1600. Then, its phreatic eruption in 2010 surprised Indonesian people, scientists, and volcanologists. The volcanic activity has undergone a transformation, shifting towards the formation and destruction of lava domes. This process has persisted for over ten years.

Consequently, the volcanoes have released an amount exceeding 0.16 km³ of pyroclastic materials (Nakada et al., 2019) over an area of approximately 25.5 km² (Kadavi et al., 2017). The last pre-historic eruption produced lava flows, deposit of Pyroclastic Density Currents (PDC) and lahars as well, without evidence of pumice-fall sedimentation. This indicates that this stratovolcano never had explosive/plinian eruption and it doesn't change until now. Most of the pyroclastic materials (basaltic andesite to andesite) are deposited 4.5 km from the summit. Some studies have been conducted at this volcano including photogrammetry (Carr et al., 2019), GPS observation (Hotta et al., 2019); tectonic activity (Kriswati et al., 2019), and tomography (Indrastuti et al., 2019).

Drainage pattern of this stratovolcano is classified as radial, where many tributaries radiate outward from summit (Supriyati and Tjahjono, 2018). At the downstream area, Lau Borus river channel connects these tributaries from north-eastern to south-western flank. It means that even if pyroclastic materials that transforms into lahars are eroded and transported through different tributaries and they still end up in the same main river channel (Lau Borus). Hence, this particular river has the capability to accumulate and transport significant amounts of materials (more than 0.16 km³ spread over 25.5 km²) through a single channel that ranges in width from 51.9 to 156.56 m (Adriani and Nurwihastuti, 2017). This leads to formation of a new temporary lake of 5 ha in 2017. The area of lake is increasing in 2021 (9.84 ha). **Fig. 2** shows the picture of this lake taken from photo point that is mentioned in **Fig. 1**.

The formation of this new lake is probably similar to the mechanism of landslide dam in mountainous regions (Zhong et al., 2021; Takayama et al., 2021; Sun et al., 2021). Earth materials coming from riverbank block the river and hold the water flow at the upstream part. The dimensions of landslide dams are predominantly determined by the topographical characteristics of the nearby hills and the morphometric attributes of the rivers. Serious consequences could happen in case of overtopping, breaching or dam failure (Zhong et al., 2020; Yang et al., 2020; Ruan et al., 2021; Tsai et al., 2021). Thus, detailed evaluation of these temporal dams is needed in order to support structural and non-structural mitigation strategies.

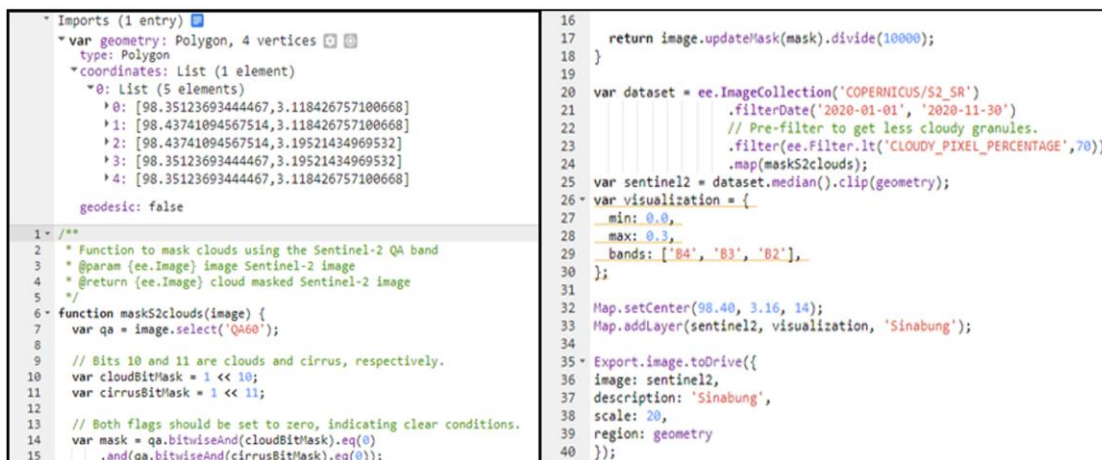


Fig. 2. Panoramic photo of a new lake formed in Lau Borus River channel.

Coupling between Agent Based Model (ABM) and Geographic Information System (GIS) allow to perform dynamic model. This is important to predict the quantity of runoff flowing into newly formed lake at Sinabung volcano. Agent Based Model focused on individual behavior in a complex environment (Abebe et al., 2019; Zhuo and Han, 2020; Aerts, 2020; Haer et al., 2020). In most of studies, agent is defined as human, vehicle, or animal who is facing a specific phenomenon. However, water, runoff or raindrop can also act as agent which respond the surrounding environment. GIS package is integrated in the ABM, so that any movement of agents still contains geographic coordinate.

3. DATA AND METHODS

This study was conducted at the eastern flank of Sinabung volcano (**Fig. 1**). The study area is located in Karo Regency, North Sumatra, Indonesia. The study area includes volcanic cone and new lake within Lau Borus River channel. Sentinel 2 satellite imagery in 2020 was used to map the area rapidly. However, clouds and cirrus had to be masked in order to get seamless imagery. The code to perform this procedure in Google Earth Engine is shown in **Fig. 3**.



```

Imports (1 entry)
var geometry: Polygon, 4 vertices
  type: Polygon
  coordinates: List (1 element)
    0: List (5 elements)
      0: [98.3512369344467, 3.118426757100668]
      1: [98.43741894567514, 3.118426757100668]
      2: [98.43741894567514, 3.19521434969532]
      3: [98.3512369344467, 3.19521434969532]
      4: [98.3512369344467, 3.118426757100668]
  geodesic: false

1 /**
2  * Function to mask clouds using the Sentinel-2 QA band
3  * @param (ee.Image) image Sentinel-2 image
4  * @return (ee.Image) cloud masked Sentinel-2 image
5  */
6 function maskS2clouds(image) {
7   var qa = image.select('QA60');
8
9   // Bits 10 and 11 are clouds and cirrus, respectively.
10  var cloudBitMask = 1 << 10;
11  var cirrusBitMask = 1 << 11;
12
13  // Both flags should be set to zero, indicating clear conditions.
14  var mask = qa.bitwiseAnd(cloudBitMask).eq(0)
15    .and(qa.bitwiseAnd(cirrusBitMask).eq(0));
16
17  return image.updateMask(mask).divide(10000);
18 }
19
20 var dataset = ee.ImageCollection('COPERNICUS/S2_SR')
21   .filterDate('2020-01-01', '2020-11-30')
22   // Pre-filter to get less cloudy granules.
23   .filter(ee.Filter.lt('CLOUDY_PIXEL_PERCENTAGE', 70))
24   .map(maskS2clouds);
25 var sentinel2 = dataset.median().clip(geometry);
26 var visualization = {
27   min: 0.0,
28   max: 0.3,
29   bands: ['B4', 'B3', 'B2'],
30 };
31
32 Map.setCenter(98.40, 3.16, 14);
33 Map.addLayer(sentinel2, visualization, 'Sinabung');
34
35 Export.image.toDrive({
36 image: sentinel2,
37 description: 'Sinabung',
38 scale: 20,
39 region: geometry
40 });

```

Fig. 3. Code for cloud masking of Sentinel 2 Imageries in Google Earth Engine.

This code was used to mask clouds in Sentinel-2 satellite images and display the resulting cloud-free composite image on a map. The code consists of two main parts: a function called `maskS2clouds` and the main script that uses this function. The `maskS2clouds` function takes an input Sentinel-2 image and applies a cloud mask to it. First of all, the function receives an input image as a parameter (`image`). It selects the Quality Assessment (QA) band from the input image using the `select` method and assigns it to the variable `qa`. The QA band contains information about different pixel attributes, including cloud and cirrus information. The cloud and cirrus bits are identified in the QA band. The variable `cloudBitMask` represents the bit for clouds, and `cirrusBitMask` represents the bit for cirrus. The `mask` variable is created by performing bitwise operations on the QA band. It checks if the cloud and cirrus bits are equal to zero, indicating clear conditions. The `bitwiseAnd` method is used to perform a bitwise AND operation between the QA band and the respective bit masks. The `eq` method is used to compare the result with zero, creating a binary mask. Finally, the function applies the mask to the input image using the `updateMask` method and divides the image by 10000 to scale the pixel values. The resulting masked image is returned.

After defining the `maskS2clouds` function, the main script was developed. An Image Collection from the COPERNICUS/S2_SR dataset is created using `ee.ImageCollection('COPERNICUS/S2_SR')`. The collection is filtered to include images within a specific date range using the `filterDate` method from January to November 2020. A pre-filter is applied to the collection to further filter out images with a cloudy pixel percentage greater than 60% using the `filter` method with the `ee.Filter.lt` function. The `maskS2clouds` function is mapped over the Image Collection using the `map` method. This applies the cloud mask to each image in the collection. A visualization parameter object named `visualization` is created, specifying the minimum and maximum values for visualization (`min` and `max`) and the bands to display (`bands`). The center of the map is set using the `Map.setCenter` method, providing the longitude, latitude, and zoom level of the study area. The resulting cloud-free composite image, computed and added to the map using the `Map.addLayer` method. The visualization parameter object (`visualization`) is provided to specify how the image should be displayed, and a name (`Sinabung`) is given to the layer.

The highest quality topography data available for remote area such as Sinabung volcano is DEMNAS. The Indonesia National Digital Elevation Model (DEMNAS) is constructed using several SAR imageries, such as IFSAR data with a resolution of 5m, TERRASAR-X data that has been resampled to 5m resolution from its original 5-10m resolution, and ALOS PALSAR data resampled to 5m resolution from its initial 11.25m resolution. The resampling process involves the widespread utilization of Mass Point data from the Indonesian Topography Map (Rupabumi Indonesia or RBI). DEMNAS has a spatial resolution of 0.27 arc-seconds and employs the EGM2008 vertical datum and Geotiff 32-bit float data format. For validation and accuracy of DEM, measurement of Ground Control Point (GCP) and the Geodetic Control Network (JKG) are applied (Ville et al., 2015; Wibowo and Nurani 2019; Wibowo et al., 2021; Gomez et al., 2023). The validation outcomes in Sumatra indicate that DEMNAS exhibits superior accuracy compared to high-resolution data models created using mass points, spot heights, and breaklines (referred to as DTM). The DEMNAS for the Sumatra region display Root Mean Square Errors (RMSE) of 2.79 m with bias errors of -0.13 m (Badan Informasi Geospasial, 2018).

This topography data is very important because it provides environment for agents. The code of Agent Based Model was written in NetLogo, a multi-agent programming language commonly used for simulating complex systems. It requires the NetLogo extension (GIS) and defines three global variables: `elevation`, `slope`, and `aspect`. These variables will be used to store data related to the elevation, slope, and aspect of the terrain. The `setup` procedure is responsible for initializing the simulation environment. First of all, the current state of the simulation should be cleared from any potential bugs using the function `clear-all`. The current directory should be set to load the DEM in ASCII format and assigned to the `elevation` variable. The world envelope is also set based on the envelope of the `elevation` dataset. Furthermore, the functions `set slope gis:create-raster` and `set aspect gis:create-raster` create two new raster datasets named consecutively `slope` and `aspect` with the same dimensions and envelope as the previous `elevation` dataset. A convolution operation on the `elevation` dataset is performed using a 3x3 kernel to produce the `gradient` variables. The purpose of applying the convolution operation is to compute the gradient of the elevation in both horizontal and vertical directions. Afterward, this simulation calculates the slope and aspect of the terrain based on the computed gradients. After finishing the `setup` procedure, the next step is the `go` procedure, which is the main code block that runs repeatedly to simulate the movement of agents (i.e., simulation loop) based on the gradient of the terrain. A tick counter is used to control the timing and sequencing of events. The simulation stops when there are no more agents remaining. This was used as fundamental of determination of the direction of agents during their downward movement.

Rainfall data was obtained from the Climate Hazards Group InfraRed Precipitation with Station data (CHIRPS) with a resolution of 0.05° (5.5 km). The annual precipitation in 2020 was 2737 mm/year, which is typical for a tropical climate (Wibowo, 2010). Lahars were generated when the precipitation exceeded 15 mm/day, indicating excessive runoff. For example, this occurred on 22 April, 22 August, 2 September, 8-9 September, and 3 November 2020. Spatial distribution of overland flow points was set as agent in this model. We performed more than 60,000 overland flow points which were randomly distributed at the very beginning of this simulation. The movement of these raindrops followed the slope and the aspect of the eastern flank of Sinabung volcano. The limitation of this study is that it is impossible to install field instrumentation (i.e., water level logger, load cell, automated video, geophone) to monitor runoff (Wibowo et al., 2015). Due to the highly volcanic activity producing hot pyroclastic flows toward the study area, it is strictly prohibited to conduct any activities within 5 km from the crater. The slope length along the eastern flank of this volcano, where this research was conducted, is only 3.7 km. To overcome this limitation, nine observation points were used in this simulation to replace field instrumentation. This approach allowed for the extraction of hydrographs and their comparison with the lahars hydrographs documented in the existing literature. The criteria for selecting observation points depend on the drainage network. For monitoring the main channel, observation points should be located upstream, in the middle stream, or downstream. To monitor tributaries, observation points should be placed at the confluence.

4. RESULTS AND DISCUSSIONS

Spatial model of runoff flowing into new formed lake at Sinabung volcano has been conducted in this study. DEM (9 m resolution) is employed as the environment in which each 63855 overland flow points are set up as agents. The number of agents correspond to the number of pixels, i.e. one agent per pixel. The time step unit is seconds (s). At the beginning, each agent starts to flow from their original pixel/position. However, the pattern of their movement is still unclear at time step 1 and 2. The agents begin to segregate at time step 3, even if their spatial distribution is unclear and still spread out randomly (Fig. 4).

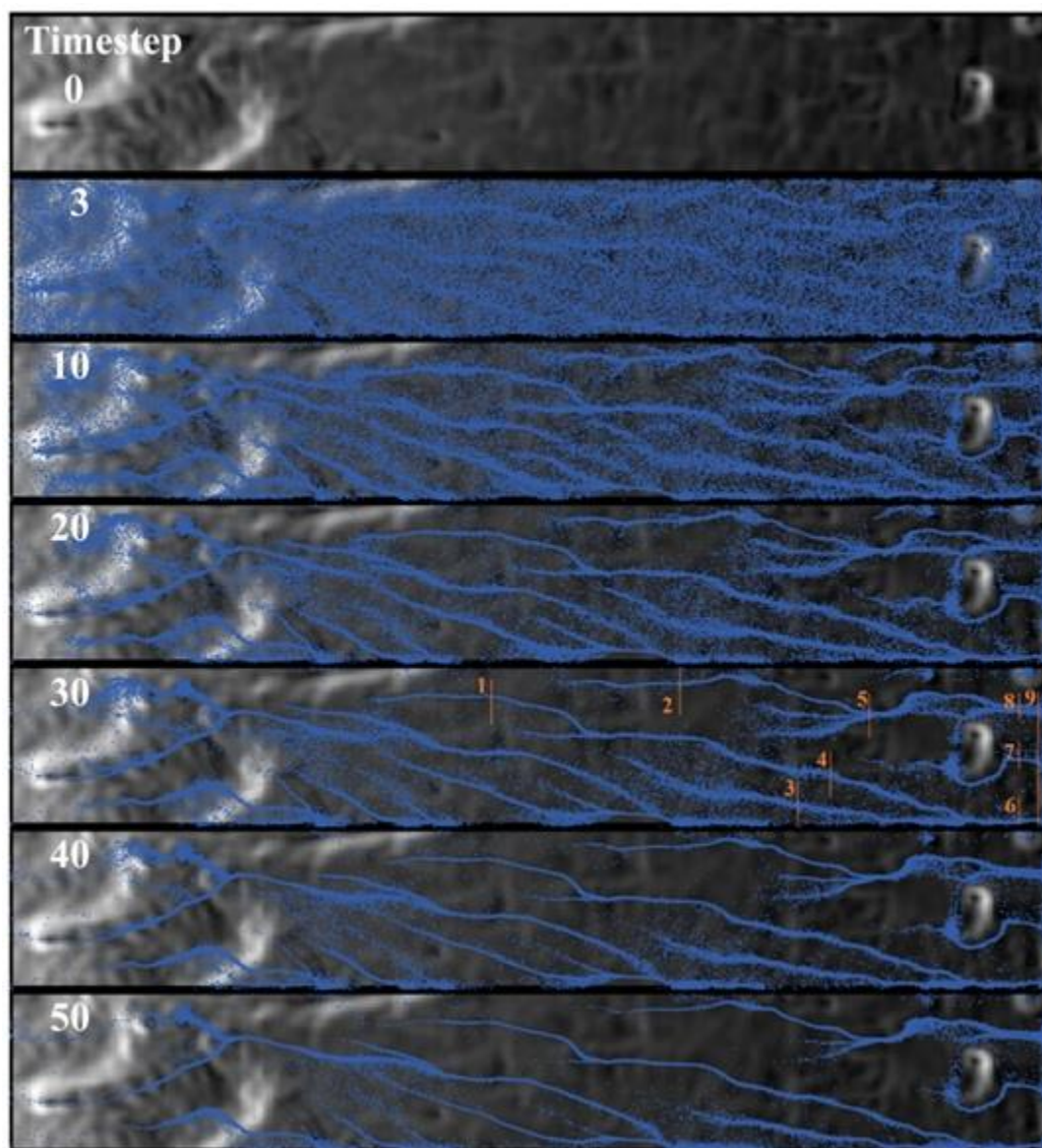


Fig. 4. Agent Based Modeling at timestep 0-50 draped over Digital Elevation Model. High and low altitude are shown by bright and dark color consecutively. The lowest altitude is the new formed lake. Hydrographs are measured at 9 observation sites.

At time step 10, the drainage pattern starts to influence the movement of agents. They are accumulated in the nearest valley. Some of agents are still on the ridge of hills, but they tend to move downward following the result of bilinear sampling between adjacent pixels of the DEM. In this Agent Based Model, the technique of bilinear sampling in GIS enables the adjustment and interpolation of pixel values between two raster grids. Its purpose is to align and harmonize the coordinates and resolutions of disparate raster datasets. The algorithm takes into account the four closest neighboring pixels to estimate the value of the desired pixel. These four pixels create a square, and their specific positions are determined by the coordinates of the target pixel. By calculating a weighted average of these neighboring pixel values, the bilinear sampling algorithm assigns a value to the target pixel. Furthermore, the pixel values within the source raster grid undergo linear changes as one moves between adjacent pixels.

At time step 20, the movement pattern of agents is clear. They follow the radial drainage pattern of the Sinabung volcanic cone. More agents are accumulated in the drainage network and they started to flow downward of the volcanic cone. At time step 30, we notice clearly the tributaries. Thus, it is easier to set up observation points in order to measure hydrograph. There are 9 observation points for each tributary which are directly connected to the lake (**Fig. 4** and **Fig. 5**). Other tributaries were not measured in detail because their estuary is located at after the lake outlet. It means that the agents do not flow to the lake direction due to the radial drainage pattern of the stratovolcano. Time step 40 is characterized by minimum number of agents that are still on the ridge. More agents are already in the tributaries compared to time step 30. While time step 50 shows total accumulation of agents within the tributaries, especially the bigger one. Smaller tributaries start losing agents since they flow downward. Time step 60 is characterized by disappearance of agents in smaller tributaries, on the contrary in bigger tributaries they accumulate and flow downstream like ordinary streamflow. Time step 70 has pretty much similar characteristic than time step 60, but the flow is steadier. This lasts until time step 100 where overland flow can only be found in bigger tributaries. After time step 100, the flow decreases gradually until time step 150. At this point, only 2 tributaries which are connected directly to the lake. The flow is still decreasing until time step 200. Time step 200 until 696 is characterized by gradual disappearance of agents at all tributaries.

Hydrogram calculated at nine observation points shows interesting pattern and also relation between upstream and downstream area. At observation point 1, there is only limited accumulation of agents from time step 0 to 50. Similar characteristics is found at observation point 2 as well. Observation point 3 which is located further downstream, has different signature. The overland flow is detected from time step 0 to 114. Overland flow at observation point 4 occurs from time step 0 to 250 with two pulsations because it is directly connected to observation 1 at upstream area. While observation point 5 which is located at the downstream part of observation 2 has an accumulation of overland flow from time step 0 to 170. The hydrograph contains two pulsations with maximum number of agents of 60. The observation point 6 is connected directly to observation 3 and 4. Its hydrogram shows an accumulation agent from time step 0 to 300 with two pulsations. Observation point 7 shares similar characteristic with observation point 1,2 and 3 since there is no other observation point at its upstream area. While observation point 8 has the same characteristic than observation point 6 since it is connected to other observation points at upstream area (2 and 5). Observation point 9 is the total accumulation of agents before they flow into the lake. Majority of the flow take place from time step 0 to 450 and it gradually diminish until time step 696.

Several lessons can be derived from the results of this study. The histogram from this model is similar and identical to that of lahars at Merapi volcano (Wibowo et al., 2015) where it involves several pulsations in it. In this study, the runoff doesn't flow more than 4 km, so that the histogram can only have 2 pulsations. At Merapi volcano, lahars can flow more than 15 km, thus it is normal to get 3-5 pulsations in a single lahar event due to its dynamic characteristics. This is caused by geological formations, topography, and drainage patterns. The topography of the Merapi stratovolcano is more complex due to the alternating formation of the old and new Merapi. It leads to meandering river channels due to the presence of Mount Kendil, located 2 km southeast of the Merapi Crater.

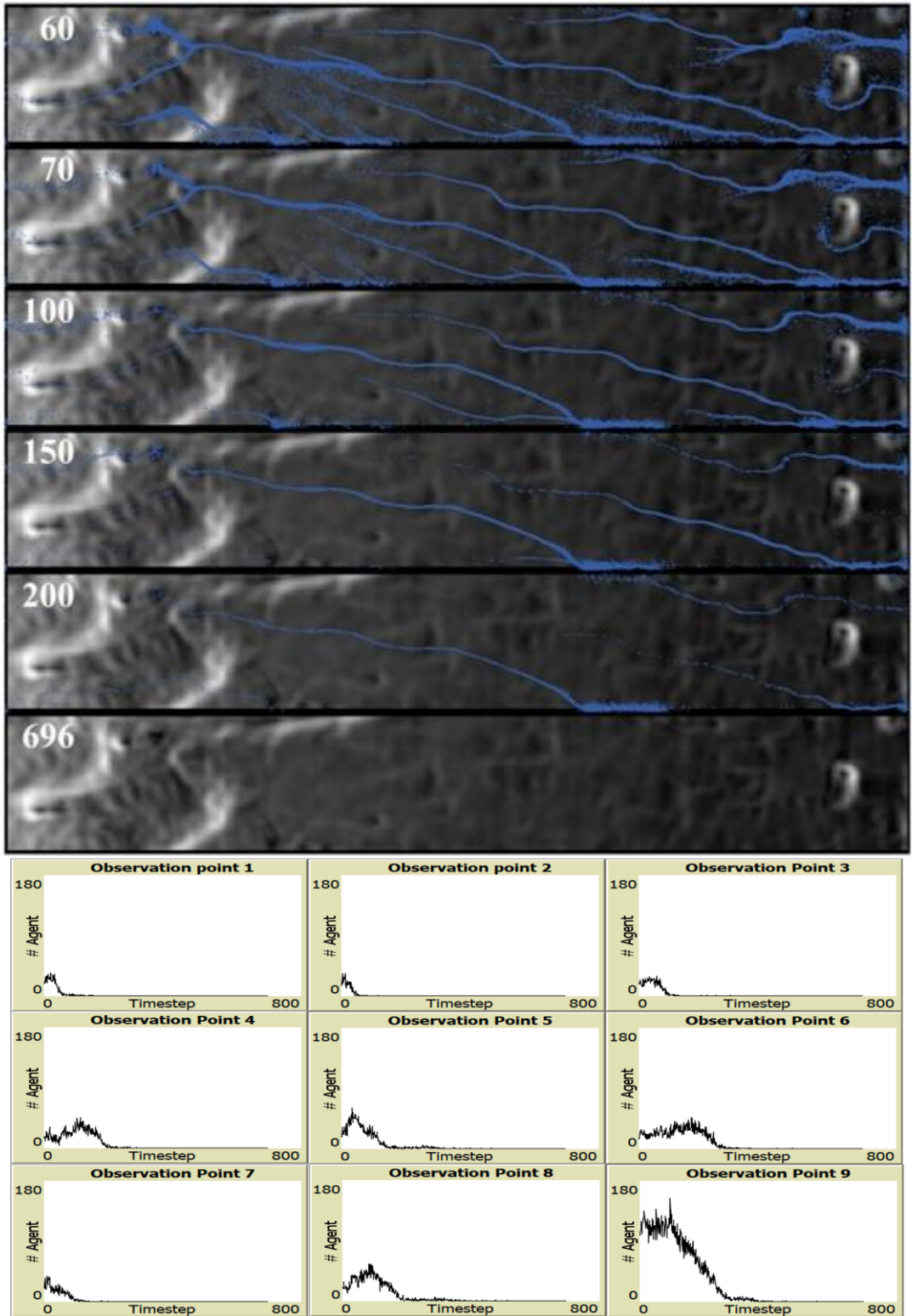


Fig. 5. Agent Based Modeling at timestep 60-696 (above) and Hydrograph at observation points (Below).

Meanwhile, the edifice of the Sinabung stratovolcano is formed only by one geological formation, producing a more perfect topography of the volcanic cone, which is efficient for a radial drainage pattern (i.e., shorter river channels with less meandering). As a consequence, the flow velocity is more rapid on the Sinabung volcano, with an average of 5.32 m/s compared to 4.12 m/s on the Merapi volcano. This faster flow velocity did not provide enough opportunity to form many pulsations.

In general, lahar histogram contains three main parts: lahar front, body and tail. These three main parts are also found in the model in this study through histogram (**Fig. 5**) and spatio-temporal distribution map of involved agents (**Fig. 4**). Each tributaries have flow front, body, and tail. Flow front is indicated by rapid augmentation of accumulated agent. Body is characterized by steady accumulation of agent, while tail is gradual diminution of the accumulated agent. Indeed, runoff at Sinabung volcano would erode pyroclastic materials that could trigger lahars (Nakada et al., 2019). The result of these lahars is abundant progressive aggradation that can be found along the Lau Borus River (Adriani and Nurwihastuti, 2017; Kadavi et al., 2017; Supriyati and Tjahjono, 2018).

Agent Based Model (ABM) used in this study is identic to Smoothed-Particle Hydrodynamics (SPH) which is defined as computational method to analyze two phase non-newtonian fluid (Albano et al., 2016; Hårdi et al., 2021). However, coupling between ABM and GIS allows us to retain geographic aspect within the model, such as DEM, slope, aspect, coordinates, and map algebra. This is important to help us bringing the real environment into the model where agents are set to react based on its behavior. The output of this model is adequate for flow analysis since it produced spatio-temporal map and also hydrogram.

5. CONCLUSIONS

This study emphasizes the development model of runoff flowing into the newly formed lake at Sinabung volcano. Its ongoing escalated volcanic activity and continuous eruption have been observed since 2010, although there has been no historical eruption of this volcano since 1600. Abundant pyroclastic materials from Sinabung volcano are eroded and deposited on the eastern and southern flanks, leading to the formation of a new lake at the Lau Borus River. A coupling between an Agent-Based Model and Geographic Information System is designed to conduct a dynamic model of runoff and spatio-temporal mapping.

Hydrographs from observation points allow for a comparison of flow dynamics between the two most active stratovolcanoes in the same tropical region (Sinabung and Merapi volcano). They share similar characteristics, such as runoff accumulation in the river channel that triggers lahars. However, they also exhibit two different characteristics regarding the quantity of flow pulsations due to their differences in the complexity of geological formations, topography, and drainage patterns. After identifying the accumulation process of runoff flowing into the newly formed lake at Sinabung volcano, further studies might be needed to anticipate the outburst of this new lake.

ACKNOWLEDGEMENT


This research was undertaken at the GIS Laboratory, Department of GIScience, Faculty of Geography, Universitas Gadjah Mada, as part of independent lecturer research. Badan Informasi Geospasial (BIG) and European Space Agency (ESA) were very helpful by granting easy access to DEM Data and Sentinel 2 imagery. We also express our gratitude to the anonymous reviewers and the editors for generously dedicating their time to offer constructive feedback.

REFERENCES

- Abebe, Y.A., Ghorbani, A., Nikolic, I., Vojinovic, Z., Sanchez, A. (2019) Flood risk management in Sint Maarten – A coupled agent-based and flood modelling method. *Journal of Environmental Management*, 248, 109317. <https://doi.org/10.1016/j.jenvman.2019.109317>
- Aerts, J.C.J.H. (2020) Integrating agent-based approaches with flood risk models: A review and perspective. *Water Security*, 11, 100076. <https://doi.org/10.1016/j.wasec.2020.100076>
- Albano, R., Sole, A., Mirauda D., Adamowski, J. (2016) Modelling large floating bodies in urban area flash-floods via a Smoothed Particle Hydrodynamics model. *Journal of Hydrology*, 541, Part A, 344-358. <https://doi.org/10.1016/j.jhydrol.2016.02.009>
- Aldriani, S., & Nurwihastuti D.W. (2017) Kajian Morfologi Sungai Lau Borus Di Kabupaten Karo Akibat Aliran Lahar Dingin Pasca Erupsi Gunungapi Sinabung Tahun 2016. *Tunas Geografi*. 6 (1), 74-87. <https://doi.org/10.24114/tgeo.v6i1.8351>
- Badan Informasi Geospasial, 2018. DEMNAS: Seamless Seamless Digital Elevation Model (DEM) dan Batimetri Nasional. Last access on 18 May 2023, <https://tanahair.indonesia.go.id/demnas/#/>.
- Carr, B.B., Clarke, A.B., Ramón Arrowsmith, J., Vanderkluisen, L., & Dhanu, B.E. (2019) The emplacement of the active lava flow at Sinabung Volcano, Sumatra, Indonesia, documented by structure-from-motion photogrammetry. *Journal of Volcanology and Geothermal Research*, 382, 164-172. <https://doi.org/10.1016/j.jvolgeores.2018.02.004>
- Chesner C.A., Barbee O.A., McIntosh W.C. (2020) The enigmatic origin and emplacement of the Samosir Island lava domes, Toba Caldera, Sumatra, Indonesia. *Bulletin of Volcanology*. 82, 26. <https://doi.org/10.1007/s00445-020-1359-9>
- Gomez C., Hotta H., Shinohara Y., Park J.-H., Tsunetaka H., Zhang M., Bradak B., Hadmoko D.S., Wibowo S.B., Daikai R., Yoshida M. (2023) Formation Processes of Gully-side Debris-Cones Determined from Ground-Penetrating Radar (Mt. Unzen, Japan). *Journal of Applied Geophysics*. 209, 104919. <https://doi.org/10.1016/j.jappgeo.2022.104919>
- Haer, T., Husby, T.G., Wouter Botzen, W.J., & Aerts, J.C.J.H. (2020) The safe development paradox: An agent-based model for flood risk under climate change in the European Union. *Global Environmental Change*, 60, 102009. <https://doi.org/10.1016/j.gloenvcha.2019.102009>
- Härdi, S., Schreiner, M., Janoske, U. (2021) On a new algorithm for incorporating the contact angle forces in a simulation using the shallow water equation and smoothed particle hydrodynamics. *Computers & Fluids*, 215, 104793. <https://doi.org/10.1016/j.compfluid.2020.104793>
- Hotta, K., Iguchi, M., Ohkura, T., Hendrasto, M., Gunawan, H., Rosadi, U., & Kriswati E. (2019) Magma intrusion and effusion at Sinabung volcano, Indonesia, from 2013 to 2016, as revealed by continuous GPS observation. *Journal of Volcanology and Geothermal Research*, 382, 173-183. <https://doi.org/10.1016/j.jvolgeores.2017.12.015>
- Indrastuti, N., Nugraha, A.D., McCausland, W.A., Hendrasto, M., Gunawan, H., Kusnandar, R., Kasbani, & Kristianto. (2019) 3-D Seismic Tomographic study of Sinabung Volcano, Northern Sumatra, Indonesia, during the inter-eruptive period October 2010–July 2013. *Journal of Volcanology and Geothermal Research*, 382, 197-209. <https://doi.org/10.1016/j.jvolgeores.2019.03.001>
- Kadavi, P., Lee, W.-J., & Lee, C.-W. (2017) Analysis of the Pyroclastic Flow Deposits of Mount Sinabung and Merapi Using Landsat Imagery and the Artificial Neural Networks Approach. *Applied Sciences*, 7(9), 935. doi:10.3390/app7090935
- Kriswati, E., Meilano, I., Iguchi, M., Abidin, H.Z., & Surono. (2019) An evaluation of the possibility of tectonic triggering of the Sinabung eruption. *Journal of Volcanology and Geothermal Research*, 382, 224-232. <https://doi.org/10.1016/j.jvolgeores.2018.04.031>
- Mukhopadhyay S., Roy B., Sangode S.J., Jaiswal M.K., Dutta S. (2022) Late Quaternary sediments from Barakar-Damodar Basin, Eastern India include the 74 ka Toba ash and a 17 ka microlith toolkit. *Journal of Asian Earth Sciences: X*. 9: 100135. <https://doi.org/10.1016/j.jaesx.2022.100135>
- Naen G.N.R.B., Toramaru A., Juhri S., Yonezu K., Wibowo H.E., Gunawan R.M.P.P., Disando T. (2023) Distinct pumice populations in the 74 ka Youngest Toba Tuff: Evidence for eruptions from multiple magma chambers. *Journal of Volcanology and Geothermal Research*. 437, 107804. <https://doi.org/10.1016/j.jvolgeores.2023.107804>

- Nakada, S., Zaennudin, A., Yoshimoto, M., Maeno, F., Suzuki, Y., Hokanishi, N., Sasaki, H., Iguchi, M., Ohkura, T., Gunawan, H., & Triastuty H. (2019) Growth process of the lava dome/flow complex at Sinabung Volcano during 2013–2016. *Journal of Volcanology and Geothermal Research*, 382, 120-136. <https://doi.org/10.1016/j.jvolgeores.2017.06.012>
- Ruan, H., Chen, H., Wang, T., Chen, J., & Li, H. (2021) Modeling Flood Peak Discharge Caused by Overtopping Failure of a Landslide Dam. *Water*, 13(7), 921. doi:10.3390/w13070921
- Sun, W., Zhang, Ga., Zhang, Z. (2021) Damage analysis of the cut-off wall in a landslide dam based on centrifuge and numerical modeling. *Computers and Geotechnics*, 130, 103936. <https://doi.org/10.1016/j.compgeo.2020.103936>
- Supriyati, & Tjahjono, B. (2018) Analisis Morfometri Bentanglahan Untuk Prediksi Bahaya Aliran Lahar Gunungapi Sinabung. *Seminar Nasional Geomatika 2018*. 1265-1272. <http://dx.doi.org/10.24895/SNG.2018.3-0.1052>
- Takayama, S., Fujimoto, M., Satofuka, Y. (2021) Amplification of flood discharge caused by the cascading failure of landslide dams. *International Journal of Sediment Research*, 36 (3), 430-438. <https://doi.org/10.1016/j.ijsrc.2020.10.007>
- Tsai, Y.-J., Syu, F.-T., Shieh, C.-L., Chung, C.-R., Lin, S.-S., & Yin, H.-Y. (2021) Framework of Emergency Response System for Potential Large-Scale Landslide in Taiwan. *Water*, 13(5), 712. doi:10.3390/w13050712
- Ville A., Lavigne F., Virmoux C., Brunstein D., De Bélizal E., Wibowo S. B., Hadmoko D. S. (2015) Geomorphological evolution of the Gendol valley following the October 2010 eruption of Mt Merapi (Java, Indonesia). *Geomorphology: relief, processus, environnement*, 21 (3), 235-250. <https://dx.doi.org/10.4000/geomorphologie.11073>
- Wibowo, S.B. (2010) Utilisation des classifications d'Oldeman et de Schmidt-Ferguson pour l'aptitude culturale des sols à Batu, Indonésie. In S. Khan, H.G.H Savenije, S. Demuth, P. Hubert (dir.). *Hydrocomplexity: new tools for solving wicked water problems*. IAHS publication, 338, 181-182
- Wibowo, S.B., Lavigne, F., Mourot, P., Métaixian, J.-P., Zeghdoudi, M., Virmoux, C., Sukatja, C.B, Hadmoko, D.S., Mutaqin, B.W. (2015) Coupling between Video and Seismic Data Analysis for the Study of Lahar Dynamics at Merapi Volcano, Indonesia. *Géomorphologie : relief, processus, environnement*. 21, 3, 251-266. doi: 10.4000/geomorphologie.11090
- Wibowo S.B., Nurani I.W. (2019) Improving geoinformation technology by incorporating local participation. *Proceedings of SPIE - The International Society for Optical Engineering*. 11311,113110C. <https://doi.org/10.1117/12.2550320>
- Wibowo S.B., Hadmoko D.S., Isnaeni Y., Farda N.M., Putri A.F.S., Nurani I.W., Supangkat S.H. (2021) Spatio Temporal Distribution of Ground Deformation Due to 2018 Lombok Earthquake Series. *Remote Sensing*. 13, 2222. <https://doi.org/10.3390/rs13112222>
- Yang, Q., Guan, M., Peng, Y., Chen, H. (2020) Numerical investigation of flash flood dynamics due to cascading failures of natural landslide dams. *Engineering Geology*, 276, 105765. <https://doi.org/10.1016/j.enggeo.2020.105765>
- Zhong, Q., Wang, L., Chen, S., Chen, Z., Shan Y., Zhang Q., Ren Q., Mei S., Jiang J., Hu, L., & Liu, J. (2021) Breaches of embankment and landslide dams - State of the art review. *Earth-Science Reviews*, 216, 103597. <https://doi.org/10.1016/j.earscirev.2021.103597>
- Zhong, Q., Chen, S., Shan, Y. (2020) Prediction of the overtopping-induced breach process of the landslide dam, *Engineering Geology*, 274, 105709. <https://doi.org/10.1016/j.enggeo.2020.105709>
- Zhuo, L., Han, D. (2020) Agent-based modelling and flood risk management: A compendious literature review. *Journal of Hydrology*, 591, 125600. <https://doi.org/10.1016/j.jhydrol.2020.125600>

COMPARISON OF TWO SEPARATION MULTIPATH TECHNIQUES IN GNSS REFLECTOMETRY FOR SEA LEVEL DETERMINATION IN INDONESIA

Lisa A. CAHYANINGTYAS¹, Dudy D. WIJAYA^{1*}, Nabila S.E. PUTRI²

DOI: 10.21163/GT_2023.182.06

ABSTRACT:

GNSS reflectometry (GNSS-R) is a method to derive sea level using Signal to Noise Ratio (SNR) from the Global Navigation Satellite Systems (GNSS). SNR data consist of the direct signal from the satellite (multipath) and of the signals reflected by the sea surface, and hence separating the multipath is necessary to extract the signal from the sea surface. The process of separating multipath may affect the number of data and may eventually affect the quality of the derived sea level values. There are two multipath separation techniques that are mostly used: polynomial fitting and wavelet decomposition. This study investigates the performance of both techniques by applying them to analyze three months of the L1 SNR data of Global Positioning System (GPS) and Globalnaya Navigatsionnaya Sputnikovaya Sistema (GLONASS) as observed from two stations, Barus (CBRS) at North Sumatera from January 1 to March 31, 2022, and Morotai (CMOR) at North Maluku, Indonesia using data from February 1 to May 1, 2022. Comparison with sea level from tide gauge observations shows a high correlation for both techniques, with correlation coefficients of approximately 0.90 and 0.97 for CBRS and CMOR, respectively. The Root Mean Square Error (RMSE) of polynomial fitting for CBRS and CMOR have the same value, 11.5 cm, whereas those of wavelet are 11.4 cm and 11.5 cm. Since polynomial fitting and wavelet decomposition show similar performance, we conclude that both techniques give comparable accuracy of multipath SNR data for GNSS-R in Indonesia with appropriate quality control parameters.

Keywords: GNSS reflectometry, multipath, polynomial fitting, wavelet analysis, sea level.

1. INTRODUCTION

Multipath or reflected signals are one of the major error sources in high accuracy Global Navigation Satellite System (GNSS) positioning and numerous studies have presented multiple ways to mitigate the effects (Georgiadou and Kleusberg, 1987; Bilich et al., 2008). In contrast, Martin-Neira (1993) introduced the use of reflected GNSS signals for environmental sensing. Since then, various research related to the so-called GNSS reflectometry (GNSS-R), have been carried out to measure sea level (Anderson, 1999; Lofgren et al., 2011), snow depth (Larson et al., 2009), soil moisture (Chew et al., 2014), and vegetation water content (Wan et al., 2015). In terms of measuring sea level, GNSS-R has the advantage of allowing sea level observations to refer to a geocentric frame (Peng et al., 2021); reaching a large area rather than a single point (Roussel et al., 2014; Wang et al., 2018a); and being installed at a safe height on land to avoid extreme conditions in coastal areas (Peng et al., 2019). Anderson (1999) introduced the signal-to-noise ratio (SNR) to investigate interference patterns of the reflected GNSS signals. The SNR data were then exploited by Bilich and Larson (2007) for mapping the GNSS multipath on the reflected surface. To take advantage of the SNR data, the multipath frequency is usually separated using polynomial fitting (Larson et al., 2013; Lofgren, 2014).

Low-order polynomials are applied to extract multipath frequencies from the SNR data by removing the direct signal trend (Larson et al., 2008). Another method for separating multipath frequency is wavelet analysis, which is used in some SNR research. Bilich and Larson (2007) used wavelet analysis to extract the time-varying amplitude and frequency content of each signal. Wavelet analysis was also used by Wang et al. (2018b) to extract instantaneous Global Positioning System

¹ Geodesy Research Group, Faculty of Earth Science and Technology, Bandung Institute of Technology, Jl. Ganesha 10, Bandung, Indonesia 40132, lisaayuc@gmail.com, *Corresponding author dudy.wijaya@itb.ac.id

² Surveying and Cadastre Research Group, Faculty of Earth Science and Technology, Bandung Institute of Technology, Jl. Ganesha 10, Bandung, Indonesia 40132, nabila.sofia@office.itb.ac.id

(GPS) L1 SNR data and it significantly improves the time resolution but introduce additional outliers and errors. Wang et al. (2019) applied wavelet analysis to reduce noise using coherent superposition in multifrequency GNSS signals and the considerable improvements in data utilization and RMSEs can be achieved. Other study shows that applying wavelet decomposition can improve retrieval accuracy (Chen et al., 2019; Wang et al., 2018). It has been found that wavelet analysis if the following conditions surrounding the GNSS station hold: a narrow reflecting sensing zone, a small sea azimuth range, and fewer satellites over the GNSS station (Wang et al., 2019).

In this paper, we briefly summarize the results from our assessments on the performance of polynomial fitting and wavelet decomposition techniques in separating the multipath signals and in deriving the sea level values at some GNSS stations in Indonesia. After briefly mentioning the data and method (Section 2) used in our study, we analyze and discuss all numerical results (Section 3). Some remarks and conclusions are presented in Section 4.

2. DATA AND METHODS

2.1 Data and site description

We used three months of the SNR data of GPS and GLONASS (Globalnaya Navigatsionnaya Sputnikovaya Sistema) satellites as observed from two stations: Barus (CBRS) at North Sumatera (January 1-March 31, 2022) and Morotai (CMOR) at North Maluku, Indonesia (February 1-May 1, 2022). The three months data were used to get the sea level variations during neap tide and spring tide. The observation data were sampled every 30 seconds using right-handed circularly polarized (RHCP) geodetic antenna TRM159900 and Trimble Alloy receiver at both stations. We extracted the L1 SNR data by analyzing the S1 variable written in the GNSS RINEX (Receiver Independent Exchange format) files. CMOR and CBRS stations are co-located with continuous tide gauges measurements, with one hour sampling rate. Satellite observation documents in RINEX format and detailed satellite orbit information were then processed using the FORTRAN90 program (developed by our group) to extract the SNR data. Broadcast ephemeris data were used to determine the reflected plane above the sea surface and the direction of the plane. MATLAB programs developed by Roesler & Larson (2018) were modified to analyze the SNR data and to visualize the results.

Fig. 1 shows the location of the two sites. CMOR is located in the southern part of Morotai Island, North Maluku ($2^{\circ}0'59.624''$ N, $128^{\circ}16'49.386''$ E) and CBRS is located in the southern part of North Sumatra Province, at $2^{\circ}0'18,053''$ N and $98^{\circ}23'52.445''$ E).

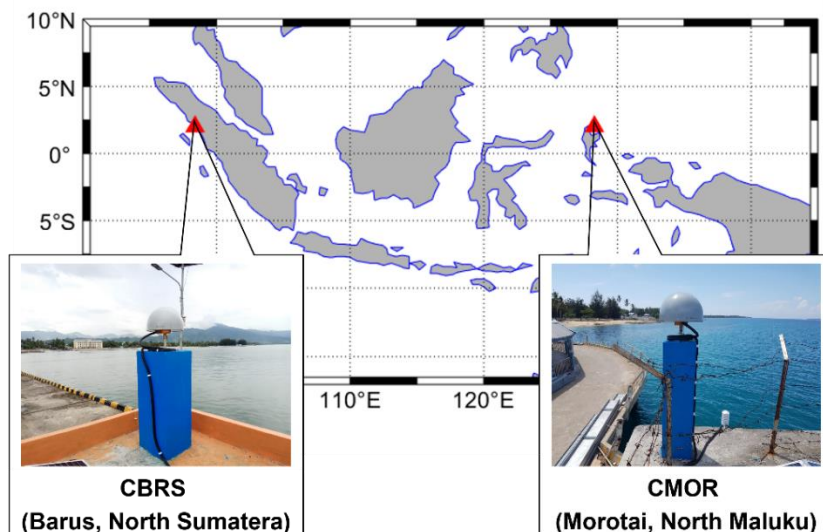


Fig. 1. Location of the two sites, CBRS and CMOR, and the view from the top of the tide station. Both stations are equipped with TRM159900 antenna and Trimble Alloy receiver.

2.2 SNR analysis method

As the satellite moves through space, the phase difference between the direct and multipath signals received by the receiver changes and then it creates an interference pattern. This interference pattern can be seen in the SNR data recorded by the receiver. Although the reflected signal will be suppressed by receiver gain on the geodetic antenna, data can still be obtained from satellites with low elevation angles (Larson et al., 2013; Lofgren, 2014; Wang et al., 2018b). Composite SNR due to the direct signal and reflected signal (multipath) can be defined using the law of cosine and geometric relations (Bilich et al., 2008; Larson and Nievinski, 2013; Lofgren, 2014; Wang et al., 2019):

$$SNR^2 = A_d^2 + A_m^2 + 2A_dA_m \cos \theta \quad (1)$$

the SNR in equation 1 is a function of the amplitude of the direct signal A_d , the amplitude of the multipath signal A_m , and the relative phase of the multipath θ .

The SNR data obtained from the measurement is the amplitude of the composite signal. By eliminating the contribution of signal errors, the SNR data for a single satellite and receiver observation can be modeled as follows (Larson et al., 2013; Lofgren and Haas, 2014; Roesler and Larson, 2018):

$$SNR(e) \approx A(e) \sin \left(\frac{4\pi H_R}{\lambda} \sin e + \phi \right) \quad (2)$$

where e is the elevation angle of the GNSS satellite relative to the horizon, $A(e)$ represents the amplitude of the SNR data, λ is the wavelength of the GNSS signal, ϕ is the phase difference, and H_R is the vertical distance between the antenna phase center and the surface of the horizontal reflecting plane (i.e. reflector height).

When the signal is received by the antenna, the receiver will record both the data from the direct signal and the reflected signal (i.e. the multipath). The geometry of the signal reflection will change as the satellite moves across the sky. This implies that the phase difference between the direct signal and the reflected signal changes, the SNR amplitude changes, and creates an interference pattern. By ignoring the phase effect of the antenna radiation pattern caused by the composition of the surface material and the plane of the planar reflection, the relative phase angle can be derived geometrically from the path delay δ of the reflected signal as (Larson and Nievinski, 2013; Lofgren, 2014; Wang et al., 2018a):

$$2\pi f = \frac{d\phi}{d \sin e} = 4\pi \frac{H_R}{\lambda} \quad (3)$$

where f and λ are the sinusoidal frequency and wavelength. This shows that under the condition of one ray reflection ϕ , the parameter has a linear relationship with $\sin(e)$.

Equation 2 shows that the SNR observations has a sinusoidal relationship with the relative phase ϕ . Therefore, the SNR can be approximated by a sinusoidal relationship at a certain frequency. Using Equations (2) and (3), the reflector height can then be obtained:

$$H_R = \frac{\lambda f}{2} \quad (4)$$

The estimated reflector height over time can be obtained from the amplitude spectra of the irregular SNR data sample (Larson et al., 2009, 2013). Here, we employed the Lomb Scargle Periodogram (LSP) to analyze the power spectra of the SNR data, (Lomb, 1976; Scargle, 1982). The spectral power analysis of the SNR data as a function of the $\sin(e)$ of the elevation angle enables the deriving of the multipath's dominant frequency (Lofgren and Haas, 2014).

2.2.1 Polynomial fitting

One of the most widely used multipath separation techniques in GNSS-R is polynomial fitting. Multipath separation using low-order polynomials (order 3–15) is suitable to analyze the SNR time series data (Bilich and Larson, 2007). Low-order polynomials were applied in the detrended SNR process to obtain multipath effects from the SNR data (Larson and Nievinski, 2013). The multipath effect of the SNR data will be used to obtain the reflector height. The SNR data units need to be converted into a linear scale from dB-Hz to volts/volts (Roesler and Larson, 2018; Geremia-Nievinski et al., 2020), using the equation 7:

$$SNR(dBHz) = 10 \log SNR \left(\frac{\text{volts}}{\text{volts}} \right)^2 \quad (5)$$

$$SNR(dBHz) = 20 \log SNR \left(\frac{\text{volts}}{\text{volts}} \right) \quad (6)$$

$$SNR \left(\frac{\text{volts}}{\text{volts}} \right) = 10^{\frac{SNR(dBHz)}{20}} \quad (7)$$

After being converted into linear units, the SNR data can be used in the detrending process to eliminate the trend of the direct signal. In this study, we accomplished some trials to find an optimal polynomial order used for the detrending process. We found that the fourth-order polynomial seems more appropriate than the second-order or third-order polynomial. For each satellite arc, these low-order polynomials are then used to remove the trend, creating a dSNR (detrended SNR or the composite SNR) arc. The dSNR represents the effect of the reflected signal on the SNR data, which consists of the multipath oscillations as written in Equation 8 (Zhou et al., 2019):

$$dSNR_{com} = SNR_{com} - \frac{P_d + P_r + P^l}{P_n} = A \cos \left(\frac{4\pi H_R \sin e}{\lambda} + \phi \right) \quad (8)$$

where A is the amplitude of the composite SNR. After extracting the direct SNR trend, it can get the multipath SNR by removing the direct SNR trend.

2.2.2 Wavelet analysis

Wavelet is used in the direct signal detrending process to obtain a multipath SNR with minimum noise (Wang et al., 2018a). The frequency component of the signal above sea level and the noise frequency can be separated using the wavelet decomposition. The accuracy of the GNSS-R sea level estimation data is improved by the wavelet decomposition (Chen et al., 2019). The wavelet decomposition is simply a technique that aids in splitting the original signal into its low-frequency and high-frequency components. It will also be possible to further separate the low-frequency part into its into lower-frequency and higher-frequency components.

The concept of wavelet was first introduced by Morlet in 1984. Under the guidance of Grossman, Morlet introduced the continuous wavelet transform (CWT), which is shown in equation 9 (Peng and Chu, 2004):

$$W_\psi f(m, n) = \langle f, \psi_{m,n} \rangle = m^{-1/2} \int_{-\infty}^{\infty} f(t) \bar{\psi} \left(\frac{t-n}{m} \right) dt \quad (9)$$

where m is the scale parameter, n is the time parameter, $\psi(t)$ is the wavelet analysis, and (\bullet) represents the complex conjugate of $\psi(\bullet)$. In the process of analyzing real data, the parameters must be made in discrete form (Chen et al., 2019). Daubechies and Mallat developed wavelet to analyze the continuous signals become discrete forms. To solve the discrete wavelet transform (DWT), Mallat (1989) proposed an approach that uses wavelet filters to decompose and reconstruct the signal. According to Mallat (1989), the decomposition algorithm is written as follows:

$$A_j[f(t)] = f(t) \quad (10)$$

$$A_x[f(t)] = \sum_y H(2t - k) A_{x-1}[f(t)] \quad (11)$$

$$D_x[f(t)] = \sum_y G(2t - k) A_{x-1}[f(t)] \quad (12)$$

where A_i is the amplitude of the decomposed signal, $t = 1, 2, \dots, N$ is a discrete serial time number, N denotes the signal length, represents the original signal, $m = 1, 2, \dots, M$ represents the decomposition level and M represents the maximum decomposition level, H and G are the low-frequency and high-frequency wavelets that pass through the decomposition filter, and are the wavelet coefficients of at the low and high frequencies of the M -level.

The SNR data, as previously explained, are composite signals of SNR data, which are the sum of the direct and multipath signal strengths. By subtracting the composite signal from the decomposed low-frequency signal, the multipath effect of wavelet decomposition is obtained. In this study, we used 8-level Daubechies 4 wavelet (db4) as a wavelet function to decompose and reconstruct the signal. Following the collection of multipath SNR data, an analysis process is carried out using LSP, as explained in the following section.

2.3 Validation

The accuracy and correlation between the GNSS-R and the tide gauges shall be used as the main indicators to assess the the quality of sea level values as derived by the GNSS-R. The root means square error (RMSE) value shows the accuracy, while the R-square value (R^2) represents the correlation between the two data sets. The RMSE value is calculated using equation 13:

$$RMSE = \sqrt{\frac{\sum_{i=1}^n (\hat{y}_i - y_i)^2}{n}} \quad (13)$$

where \hat{y}_i is the sea level from GNSS-R, y_i represents the sea level from tide gauges, and n is the amount of data. The correlation coefficient, or r (see equation 14), is the square root of the comparison between the square of the difference between the GNSS-R data and the model and the square of the difference between the data and the GNSS-R data average.

$$r = \sqrt{R^2} = \sqrt{1 - \frac{\sum (y_i - \hat{y}_i)^2}{\sum (y_i - \bar{y}_i)^2}} \quad (14)$$

where \hat{y}_i is the output of the GNSS-R data regression. When the resulting correlation coefficient value is close to 1, the correlation between the GNSS-R data results is strong. The correlation coefficient shows that the produced regression results may explain and show how close the data correlate to the obtained regression results.

In addition to examining the accuracy and correlation of the GNSS-R data with tide gauge, tidal constituents are calculated from the GNSS-R sea level height results at both stations. Because the GNSS-R sea level height data are not regularly sampled, the response method was used to obtain the tidal components (Munk and Cartwright, 1966). Tidal analysis using the response method was also applied to tide gauge data. The amplitude and phase values of the four main tidal constituents, S2, M2, K1, and O1, are compared in this study.

To compare the quality of GNSS-R and tide gauge sea level height measurements, the absolute error value is calculated. The absolute error value is calculated from the difference between GNSS-R and tide gauge amplitude and phase of the tidal components. Equation 17 were used to calculate the absolute error:

$$R_{amp} = \sqrt{A_1^2 + A_2^2 - 2A_1A_2 \cos(\Phi_1 - \Phi_2)} \quad (15)$$

$$R_{phase} = \arctan\left(\frac{A_2 \sin \Phi_2 - A_1 \sin \Phi_1}{A_2 \cos \Phi_2 - A_1 \cos \Phi_1}\right) \quad (16)$$

$$Error_{absolute} = R_{amp} \cdot \cos R_{phase} \quad (17)$$

where A_1 is the amplitude of tidal constituents from tide gauges, A_2 is the amplitude of tidal constituents calculated from GNSS-R data, Φ_1 is the phase of tidal constituents from tide gauges data, Φ_2 is the phase of tidal constituents from GNSS-R data, R_{amp} is the residual amplitude, R_{phase} is the residual phase. The absolute error was used to determine the total residuals from the tidal amplitude and phase values.

3. RESULTS AND DISCUSSIONS

3.1. GNSS signal reflection area

The GNSS satellite signals that reflect off the ocean's surface form an area rather than specular point. Assuming that the reflecting plane is planar, the reflected signal can be described by specifying the First Fresnel Zone (FFZ). The signal reflection area above sea level was determined using the FFZ data to investigate the study area (Roussel et al., 2014; Geremia-Nievenski et al., 2016). The coverage area of the reflected plane may be seen using the FFZ position mapping, which also aids in calculating the optimal elevation and azimuth angle for each study site. According to the FFZ data, the Fresnel zone becomes smaller as satellite height increases. As the satellite height rises, the multipath impact diminishes, which is exactly proportional to it.

The FFZ at CBRS and CMOR are generated by using 6 m reflected height, with respect to the sea surface. **Fig. 2** shows the reflected signal at CBRS and CMOR as a 2D ellipse shape of the FFZ. Yellow, dark blue, red, green, and cyan ellipses represent the reflected signal region from satellites with an elevation of 5°, 10°, 15°, 20°, and 25° elevation. In comparison to ellipses at other elevation angles, those at an elevation angle of 5° have the longest major axes. At elevation angle of more than 25°, the multipath no longer comes from the sea surface reflection plane. The mapping results of the FFZ are displayed in **Fig. 2**.

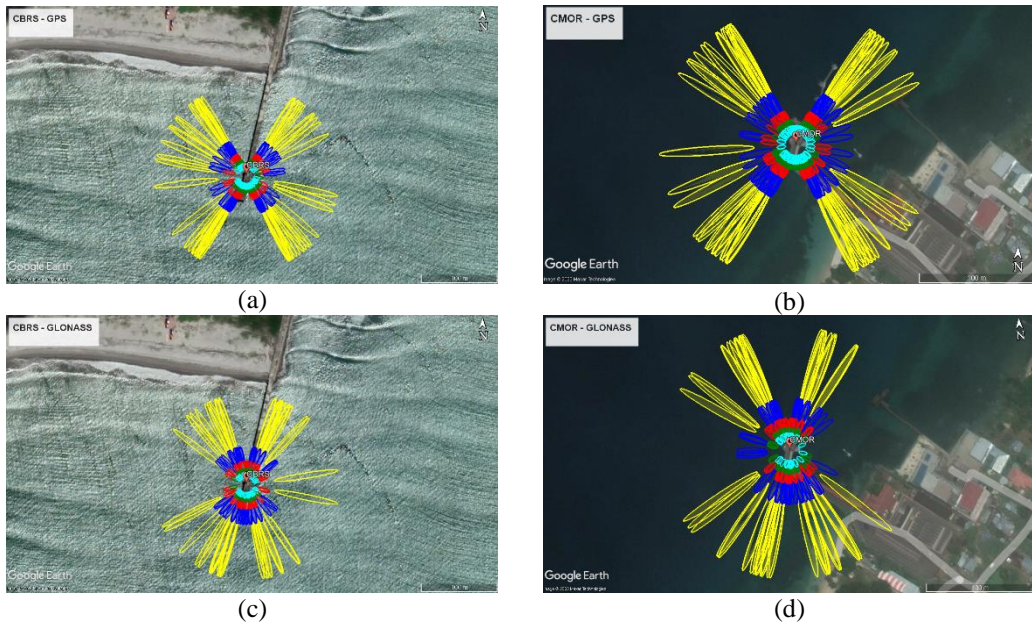


Fig. 2. The reflection areas were approximated by the FFZ at CBRS (a, c) and CMOR (b, d). The ellipses represent the reflected GPS L1 signals for elevation angles 5° (yellow), 10° (blue), 15° (red), 20° (green), and 25° (cyan). (Generated using <https://github.com/kristinemlarson/gnssrefl>).

All FFZ at CMOR are discovered to be above the sea surface reflection plane, as shown in **Fig. 2b and 2d** (right). Above the pier bridge, the reflected signal is visible as an ellipse at 25° elevation angle. This indicates that the reflected signal from the pier has been composited with the reflected signal at 25°. Based on Purnell et al. (2021), the reflector height measurements are generally less precise at elevation angles greater than 30°. The effect of random noise in SNR data leads to a greater uncertainty at larger elevation angles by using geodetic-standard antennas (Purnell et al., 2020). The reflected signal with an elevation angle above 25° is therefore not used in the following data processing.

According to the Fresnel zone mapping at CBRS, the multipath cannot be analyzed on the northern portions of the azimuths 350°-0° and 0°-30° since the Fresnel zone is on the pier bridge.

The Fresnel zone is also located above the pier bridge in the azimuth range of 160° to 208° in the southern section of the range, causing multipath from this region useless as well. Therefore, it is determined that CBRS uses reflected signals from the satellites with elevation angles of 5°-20° at azimuths of 30°-160° and 208°-350° based on the findings of FFZ visualization in **Fig. 2**. The area of the study based on the FFZ analysis can be seen in **Table 1**.

Table 1.
Area of the study including azimuth and elevation angle at CBRS and CMOR

Study area	CBRS	CMOR
Azimuth	30°-160° and 208°-350°	180°-360°
Elevation	5°-20°	5°-20°

3.2. Data analysis

As described in Section 2.2, multipath separation is accomplished by eliminating the direct signal. Detrending methods for signal processing, such as polynomial fitting or wavelet decomposition, can be used to determine the trends of direct signals. The detrended procedure is performed on each satellite arc, which is split into 30 epochs, meaning that every 15 minutes. The time span of satellite arc must be 15 minutes to compute frequencies up to the pseudo-Nyquist limit and get valid reflector height (Roesler & Larson, 2018). Detrending the polynomial fit is performed to obtain a trending direct signal. In addition, to get the multipath SNR value, the value of the combined SNR is lowered by the trend value of the direct signal derived from the detrending method.

Fig. 3 shows the results of multipath signal separation using polynomial fitting at CBRS and CMOR. The figure contains three components: the composite signal (green), the trend of the polynomial fitting (red), and the multipath (blue). A direct signal is indicated by the red line that shows the trend from polynomial fitting. **Fig. 3** shows that the direct signal increases as the elevation angle increases. The blue line depicting the multipath SNR is obtained by combining the SNR reduction with the trend value of the polynomial fitting, thus the results are unaffected by direct signal effects.

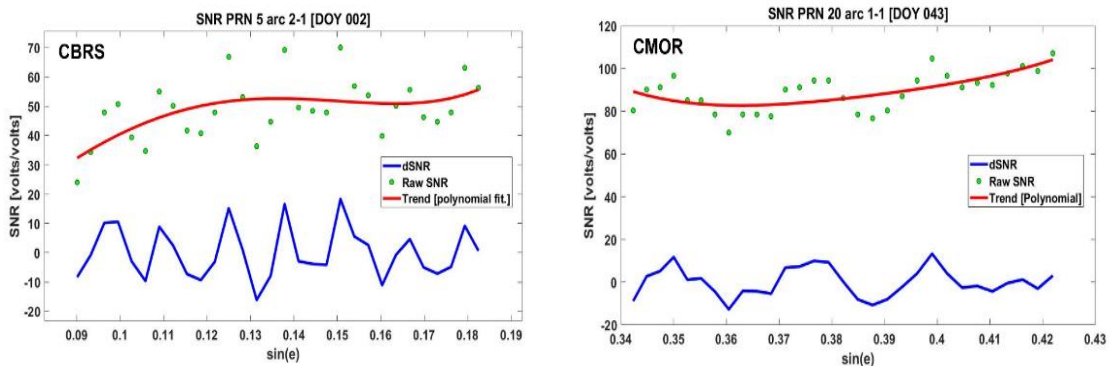


Fig. 3. Multipath separation using polynomial fitting. The green dots are the raw data of SNR from RINEX file. The red line is the trend of the SNR approached by 4th degree polynomial. The blue line is the detrended SNR.

In contrast to polynomial fitting, the signal detrending process in wavelet decomposition is performed to obtain the low-frequency trend of SNR data. By obtaining low frequencies (low wavelets) from the wavelet decomposition, multipath SNR values can be determined. The multipath SNR is determined by subtracting the composite and low-wavelet SNR. The low frequency of the wavelet decomposition results indicates a direct signal. Therefore, a reduction between the composite SNR and low-wavelet is performed to eliminate the direct signal effect, and a multipath SNR is obtained.

Fig. 4 depicts the detrended wavelet decomposition results from SNR data at CBRS and CMOR. Each image consists of three components: the composite signal, multipath, and low wavelet trend. Green dots represent the composite signal, which is also known as raw SNR. The blue line represents

the multipath result of wavelet decomposition, and the red line represents the trend of low wavelets. **Fig. 4** shows that the multipath SNR value of the decomposition results is approximately equal to the composite SNR, due to the signal scaling performed on the $\sin(e)$. The low wavelet trend from the two stations, CBRS and CMOR, appears to be increasing as the elevation angle increases.

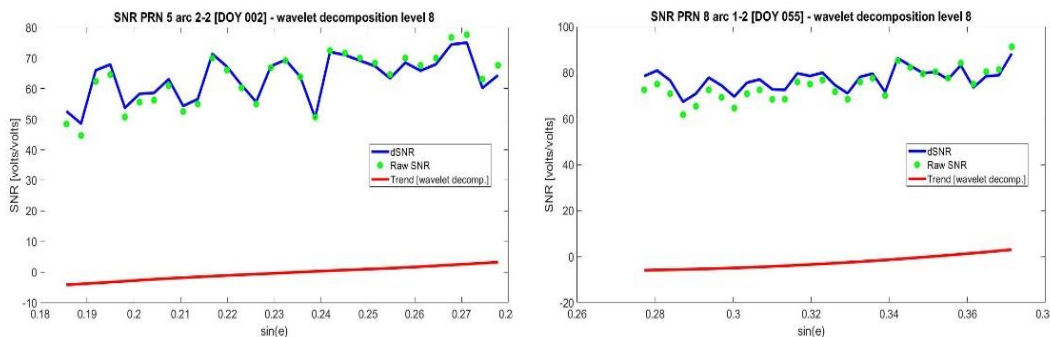


Fig. 4. Multipath separation using wavelet analysis. The green dots are the raw data of SNR from RINEX file. The red line is the trend of the SNR filtered using wavelet decomposition. The blue line is the detrended SNR.

The multipath SNR is processed with an LSP to obtain the reflector height. The LSP algorithm is used to generate the normalized spectral strength or periodogram from a set of SNR time series data for each predefined time range. To get an accurate reflector height, quality control is applied to the data from both stations during the LSP process by adjusting the peak-to-noise ratio (>2.4 for both stations), minimum amplitude (>4 for both stations), and reflector height (4-10 for both stations).

After the LSP analysis and quality control, sea level height was estimated from the separation results using polynomial fitting and wavelet analysis. The quality control is applied in the process, including the amplitude of the normalized spectrogram, peak-to-noise ratio, and range of the reflector height. **Fig. 5** show the sea level height from multipath separation technique using polynomial fitting (upper) and wavelet analysis (lower) at CBRS and CMOR. After applying the quality control, the number of observations obtained decreased.

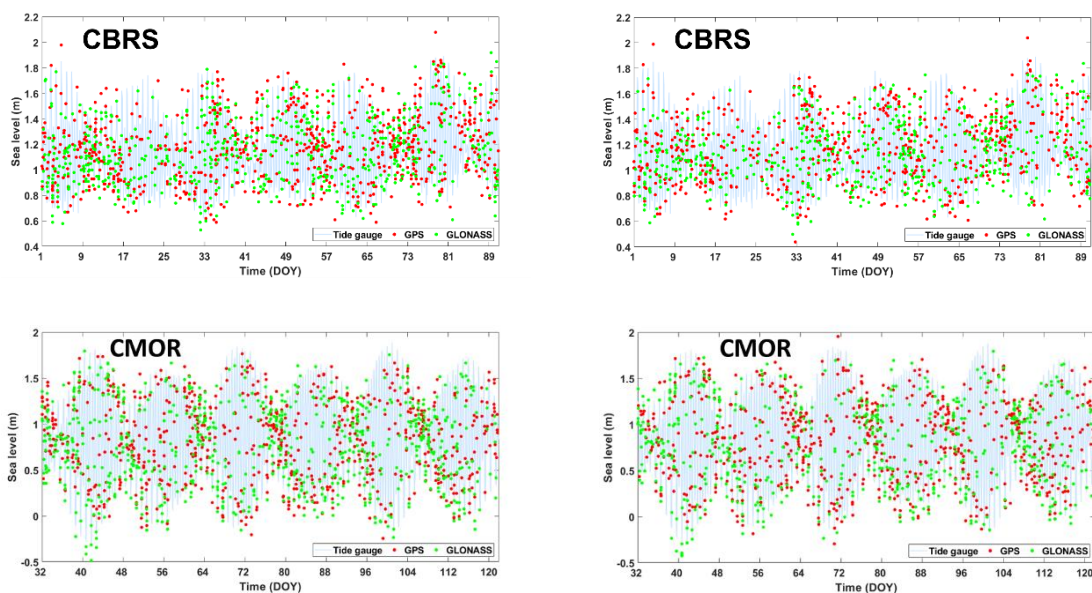


Fig. 5. The timeseries of sea level from GNSS-R (L1 GPS and GLONASS signals) using polynomial fitting (left) and wavelet analysis (right) for multipath separation at CBRS (upper) and CMOR (lower).

A significant amount of data is eliminated since it does not pass the specified threshold due to the usage of several parameters. The data collected at two stations from GNSS-R using all the methods of multipath separation are generally similar. However, by applying polynomial fitting at both stations, more data can be generated than by using wavelet analysis.

Initially, the reflector height obtained is that of the sea level relative to the antenna phase centre. The reflector height was corrected in this study by measuring the height difference between the zero tidal palm and the phase center antenna using precise levelling method. Therefore, GNSS-R and tide gauge data refer to the same reference sea level.

3.3. Comparison with co-located tide gauge

The results from the polynomial fitting and wavelet analysis on sea level height were then compared with tide gauge data. GNSS-R sea levels are irregularly sampled as it is displayed in Fig. 5 and more data are obtained on the day with low tidal ranges. The residuals were calculated from the difference between sea level from GNSS-R and tide gauge at the time-tag of GNSS-R. Therefore, the hourly tide gauge data were interpolated to the GNSS-R time-tag. From the sea level at the same time-tag, the correlation between sea level from tide gauges and GNSSR are also calculated (see Fig. 6). Table 2 summarizes the RMSE results and correlations at each station from the separation results using polynomial fitting (polyfit) and wavelet decomposition (waveldec) with tide gauge observations.

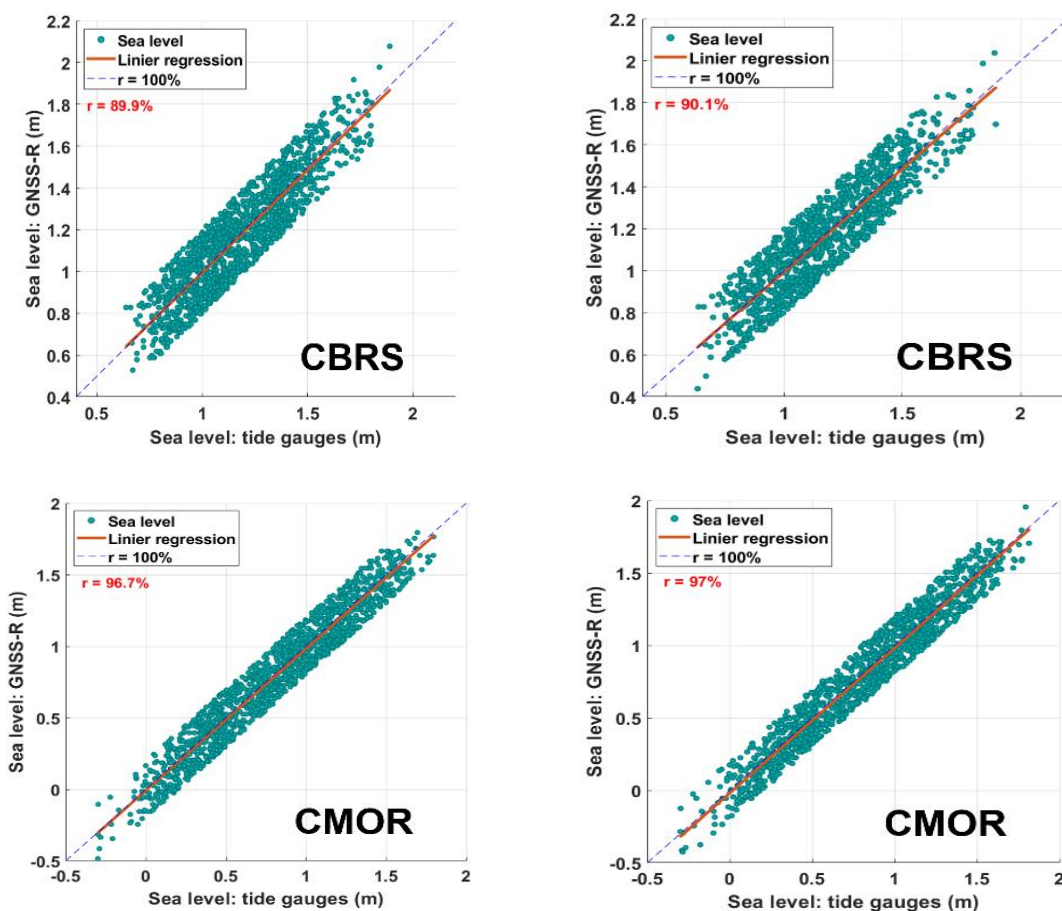


Fig. 6. The correlation between sea level from tide gauges and GNSSR using polynomial fitting (left) and wavelet analysis (right) for multipath separation at CBRS (upper) and CMOR (lower)

Table 2.
RMSE, correlation with tide gauge, and the number of observations from GNSSR using polynomial fitting and wavelet analysis at CBRS and CMOR

Station	RMSE (cm)		Correlation (%)		Number of Observations	
	Polyfit	Waveldec	Polyfit	Waveldec	Polyfit	Waveldec
CBRS	11.5	11.4	89.9	90.1	1470	1235
CMOR	11.5	11.3	96.7	97	1525	1322

Based on the correlation value obtained by comparing the GNSS-R results with a tide gauge, the GNSS-R results using wavelet decomposition for multipath separation show slightly better results at both stations and higher correlation value. However, both stations have shown that multipath separation using polynomial fitting gets more measurement data than wavelet analysis.

Table 3 shows the summarize the amplitude and phase values of GNSS-R from polynomial fitting and GNSS-R from wavelet analysis at the CBRS. The response method tidal analysis results show a difference in the amplitude values of the M2 constituents. Figure 3.15 depicts the amplitude and phase values of the CMOR data. The three data sets used produced similar results for all tidal constituents (S2, M2, K1, and O1).

Table 3.
Tidal constituents from GNSS-R using polynomial fitting and wavelet decomposition at CBRS and CMOR.

Sta	S2		M2		K1		O1	
	Polyfit	Waveldec	Polyfit	Waveldec	Polyfit	Waveldec	Polyfit	Waveldec
Amplitude (m)								
CBRS	0.1040	0.1078	0.1565	0.1698	0.0812	0.0863	0.0574	0.0556
CMOR	0.2571	0.2551	0.5176	0.5208	0.1730	0.1732	0.1199	0.1179
Phase (°)								
CBRS	358.39	359.04	322.56	319.17	25.53	32.83	189.89	197.35
CMOR	306.83	307.71	283.35	283.46	262.50	261.73	74.53	75.71

Fig. 7 depicts the absolute error values at CBRS and CMOR stations. The errors at CBRS are obviously larger than those at CMOR.

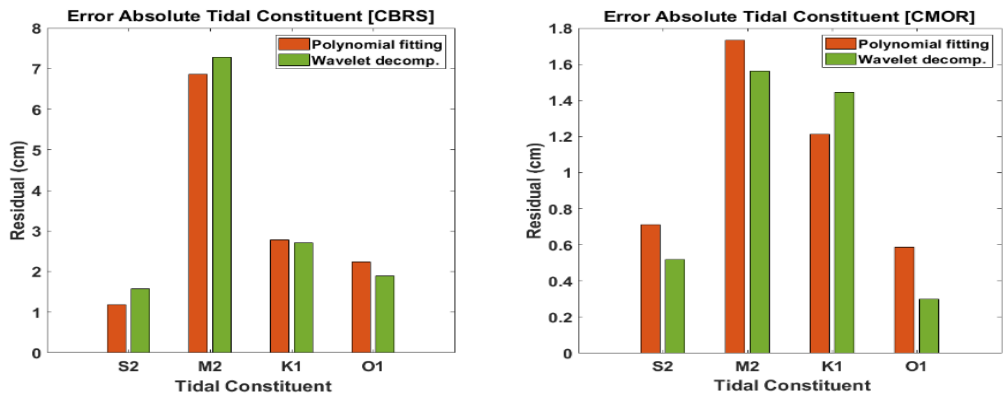


Fig. 7. Absolute error of tidal constituents at CBRS (left) and CMOR (right).

At CBRS station, the total value of the residual vector is almost the same for multipath separation using polynomial fitting and wavelet decomposition, namely between 1 cm to 7 cm. Both the GNSS-R polynomial fitting and the wavelet analysis show a significant difference of 7 cm in the M2. At CMOR station, the error of M2 is larger than that of another tidal constituent. This result suggests that the data from multipath separation using wavelet decomposition has a higher proximity value to tide gauge than the data from multipath separation using polynomial fitting.

The characteristics of the tides at the observation locations influence the difference in residual vector values from the two tidal stations in general. The number of observations obtained is also affected using quality control. The number of parameters used when processing with LSP yields a lot of unused data. On the other hand, the use of quality control parameters can result in data with high quality and reliability.

4. REMARKS AND CONCLUSION

In terms of determining sea level with GNSS-R, both multipath separation algorithms perform equally well. The sea level height results from the GNSS-R are in good agreement with those observed by the tidal gauges. The correlation value of the CBRS and CMOR using GNSS-R are respectively 90% and 96%, compared to the tidal gauges. These results indicate that the capability of the GNSS-R depends on the characteristics and environmental conditions nearby the station. During low tide range conditions, the two stations can produce more data. Despite a significant amount of data, the precision of the derived sea level height is not high; the RMSE for CBRS is 8.7 cm and 8.4–8.8 cm for CMOR. The station environment's wind speed is another aspect that affects the accuracy of the data obtained. Due to a lack of meteorological data near the observation site, the wind speed was not considered in this study. The roughness of the ocean is influenced by the velocity of the wind, which may violate the assumption of the planar sea surface.

The GNSS-R sea level results from the two multipath separation techniques are comparable. The implementation of the two techniques depends on the conditions at the observation area. By establishing a low order polynomial, the polynomial fitting technique is highly practical. On the other hand, to use wavelets, it is important to evaluate the proper wavelet family and order. The Wavelet decomposition is a technique for eliminating noise while preserving the frequency characteristics of the observed data. However, the wavelet decomposition is sensitive to noise. The process of multipath separation has a substantial effect on the quality of estimating sea level height from GNSS-R.

The quality of the sea level height results is also proven by the residual vector of the tidal constituents. The tidal characteristics at the observation locations impact the residual vector differences between the two tide stations. In addition, the total amount and density of the obtained data impact its accuracy. The implementation of quality control affects the amount of data obtained. The number of parameters applied during LSP processing causes a significant amount of unwanted data. However, using quality control settings can result in dependable and high-quality data.

GNSS-R sea level data derived from the two multipath separation techniques employed have RMSE values between 8-9 cm and a correlation of more than 90%. Based on these results, it is technically possible to apply polynomial fitting and wavelet as a multipath separating technique in GNSS-R. The quality of the data is influenced by quality control, the effect of rising and setting satellites, the tides at each station, the temporal resolution of the data obtained, and the characteristics and conditions of the study area.

The GNSS-R method for determining sea level height can be used to combine the existing tides data. In this study, the same quality control parameter values were applied throughout the process by using LSP to compare the sea level height from both methods. To achieve high-quality GNSS-R sea level estimates, LSP analysis for each multipath SNR data from polynomial fitting and wavelet decomposition is required. Observational data with high rate, multi frequencies and multi constellation satellites can be used to improve the temporal resolution of the data. The application of quality control to multipath SNRs resulting from the separation of polynomial fitting and wavelet decomposition can be identified because the resulting SNR series may be distinct.

ACKNOWLEDGEMENTS

We would like to thank the Lembaga Penelitian dan Pengabdian Masyarakat-Institut Teknologi Bandung (LPPM-ITB) for supporting this research under the ITB International Research Grant 2022 (Contract No. PAN-6-03-718 2022). We also thank Geospatial National Agency (BIG) for providing the GNSS and sea level observation data.

REFERENCES

- Anderson, K. D. (1999). Determination of Water Level and Tides Using Interferometric Observations of GPS Signals.
- Bilich, A., & Larson, K. M. (2007). Mapping the GPS multipath environment using the signal-to-noise ratio (SNR). *Radio Science*, 42(6). <https://doi.org/10.1029/2007RS003652>
- Bilich, A., Larson, K. M., & Axelrad, P. (2008). Modeling GPS phase multipath with SNR: Case study from the Salar de Uyuni, Boliva. *Journal of Geophysical Research: Solid Earth*, 113(4), 1–12. <https://doi.org/10.1029/2007JB005194>
- Chen, F., Liu, L., & Guo, F. (2019). Sea Surface Height Estimation with Multi-GNSS and Wavelet De-noising. *Scientific Reports*, 9(1). <https://doi.org/10.1038/s41598-019-51802-9>
- Chew, C. C., Small, E. E., Larson, K. M., & Zavorotny, V. U. (2014). Effects of near-surface soil moisture on GPS SNR data: Development of a retrieval algorithm for soil moisture. *IEEE Transactions on Geoscience and Remote Sensing*, 52(1), 537–543. <https://doi.org/10.1109/TGRS.2013.2242332>
- Daubechies, I. (1990). The Wavelet Transform, Time-Frequency Localization and Signal Analysis. *IEEE*, 36, 961–1005.
- Georgiadou, Y., & Kleusberg, A. (1987). On carrier signal multipath effects in relative gps positioning.pdf. *Manuscripta Geodaetica*, 13, 172–179.
- Geremia-Nievinski, F., Hobiger, T., Haas, R., Liu, W., Strandberg, J., Tabibi, S., Vey, S., Wickert, J., & Williams, S. (2020). SNR-based GNSS reflectometry for coastal sea-level altimetry: results from the first IAG inter-comparison campaign. *Journal of Geodesy*, 94(8). <https://doi.org/10.1007/s00190-020-01387-3>
- Geremia-Nievinski, F., Silva, M. F. E., Boniface, K., & Monico, J. F. G. (2016). GPS Diffractive Reflectometry: Footprint of a Coherent Radio Reflection Inferred from the Sensitivity Kernel of Multipath SNR. *IEEE Journal of Selected Topics in Applied Earth Observations and Remote Sensing*, 9(10), 4884–4891. <https://doi.org/10.1109/JSTARS.2016.2579599>
- Larson, K. M., Gutmann, E. D., Zavorotny, V. U., Braun, J. J., Williams, M. W., & Nievinski, F. G. (2009). Can we measure snow depth with GPS receivers? *Geophysical Research Letters*, 36(17), 1–5. <https://doi.org/10.1029/2009GL039430>
- Larson, K. M., Löfgren, J. S., & Haas, R. (2013). Coastal sea level measurements using a single geodetic GPS receiver. *Advances in Space Research*, 51(8), 1301–1310. <https://doi.org/10.1016/j.asr.2012.04.017>
- Larson, K. M., & Nievinski, F. G. (2013). GPS snow sensing: Results from the EarthScope Plate Boundary Observatory. *GPS Solutions*, 17(1), 41–52. <https://doi.org/10.1007/s10291-012-0259-7>

- Larson, K. M., Small, E. E., Gutmann, E. D., Bilich, A. L., Braun, J. J., & Zavorotny, V. U. (2008). Use of GPS receivers as a soil moisture network for water cycle studies. *Geophysical Research Letters*, 35(24), 1–5. <https://doi.org/10.1029/2008GL036013>
- Löfgren, J. S., & Haas, R. (2014). Sea level measurements using multi-frequency GPS and GLONASS observations. *Eurasip Journal on Advances in Signal Processing*, 2014(1). <https://doi.org/10.1186/1687-6180-2014-50>
- Löfgren, J. S., Haas, R., & Johansson, J. M. (2011). Monitoring coastal sea level using reflected GNSS signals. *Advances in Space Research*, 47(2), 213–220. <https://doi.org/10.1016/j.asr.2010.08.015>
- Löfgren, J. S., & Haas, R. (2014). Sea level observations using multi-system GNSS reflectometry. Chalmers University of Technology.
- Lomb, N. R. (1976). Least-squares frequency analysis of unequally spaced data. *Astrophysics and Space Science*, 39(2), 447–462. <https://doi.org/10.1007/BF00648343>
- Mallat, S. G. (1989). A Theory for Multiresolution Signal Decomposition: The Wavelet Representation. In *IEEE TRANSACTIONS ON PATTERN ANALYSIS AND MACHINE INTELLIGENCE: Vol. I (Issue 7)*.
- Martin-Neira, M., Colmenarejo, P., Ruffini, G., & Serra, C. (2002). Altimetry precision of 1 cm over a pond using the wide-lane carrier phase of GPS reflected signals. *Remote Sensing*, 28(3), 394–403.
- Munk, W.H., Cartwright, D.E., 1966. Tidal Spectroscopy and Prediction, in: *Mathematical and Physical Sciences*. volume 259, pp. 533–581.
- Peng, D., Feng, L., Larson, K. M., & Hill, E. M. (2021). Measuring coastal absolute sea-level changes using GNSS interferometric reflectometry. *Remote Sensing*, 13(21). <https://doi.org/10.3390/rs13214319>
- Peng, D., Hill, E. M., Li, L., Switzer, A. D., & Larson, K. M. (2019). Application of GNSS interferometric reflectometry for detecting storm surges. *GPS Solutions*, 23(2), 1–11. <https://doi.org/10.1007/s10291-019-0838-y>
- Peng, Z. K., & Chu, F. L. (2004). Application of the wavelet transform in machine condition monitoring and fault diagnostics: A review with bibliography. *Mechanical Systems and Signal Processing*, 18(2), 199–221. [https://doi.org/10.1016/S0888-3270\(03\)00075-X](https://doi.org/10.1016/S0888-3270(03)00075-X)
- Purnell, D. J., Gomez, N., Minarik, W., Porter, D., & Langston, G. (2021). Precise water level measurements using low-cost GNSS antenna arrays. *Earth Surface Dynamics*, 9(3), 673–685. <https://doi.org/10.5194/esurf-9-673-2021>
- Purnell, D., Gomez, N., Chan, N. H., Strandberg, J., Holland, D. M., & Hobiger, T. (2020). Quantifying the Uncertainty in Ground-Based GNSS-Reflectometry Sea Level Measurements. *IEEE Journal of Selected Topics in Applied Earth Observations and Remote Sensing*, 13, 4419–4428. <https://doi.org/10.1109/JSTARS.2020.3010413>
- Roesler, C., & Larson, K. M. (2018). Software tools for GNSS interferometric reflectometry (GNSS-IR). *GPS Solutions*, 22(3). <https://doi.org/10.1007/s10291-018-0744-8>
- Roussel, N., Frappart, F., Ramillien, G., Darrozes, J., Desjardins, C., Gegout, P., Pérosanz, F., & Biancale, R. (2014). Simulations of direct and reflected wave trajectories for ground-based GNSS-R experiments. *Geoscientific Model Development*, 7(5), 2261–2279. <https://doi.org/10.5194/gmd-7-2261-2014>
- Scargle, J. D. (1982). Statistical aspects of spectral analysis of unevenly spaced data. *Astrophysical Journal*, 263, 835–853.
- Wan, W., Larson, K. M., Small, E. E., Chew, C. C., & Braun, J. J. (2015). Using geodetic GPS receivers to measure vegetation water content. *GPS Solutions*, 19(2), 237–248. <https://doi.org/10.1007/s10291-014-0383-7>
- Wang, X., Zhang, Q., & Zhang, S. (2018a). Water levels measured with SNR using wavelet decomposition and Lomb–Scargle periodogram. *GPS Solutions*, 22(22). <https://doi.org/10.1007/s10291-017-0684-8>

- Wang, X., Zhang, Q., & Zhang, S. (2018b). Azimuth selection for sea level measurements using geodetic GPS receivers. *Advances in Space Research*, 61(6), 1546–1557. <https://doi.org/10.1016/j.asr.2018.01.002>
- Wang, X., Zhang, Q., & Zhang, S. (2019). Sea level estimation from SNR data of geodetic receivers using wavelet analysis. *GPS Solutions*, 23(6). <https://doi.org/10.1007/s10291-018-0798-7>

ASSESSMENT OF INUNDATION SUSCEPTIBILITY IN THE CONTEXT OF CLIMATE CHANGE, BASED ON MACHINE LEARNING AND REMOTE SENSING: CASE STUDY IN VINH PHUC PROVINCE OF VIETNAM

Phan Manh HUNG¹, Huu Duy NGUYEN^{2*} , Chien Pham VAN³

DOI: 10.21163/GT_2023.182.07

ABSTRACT:

Accurate prediction of streamflow plays an important role in water resource management and the continuous assessment of inundation susceptibility in the context of climate change plays a key role in facilitating the construction of appropriate strategies for sustainable development. So far, few studies into inundation susceptibility have explicitly incorporated the effects of climate change into their methodologies. This study aimed to assess inundation susceptibility for Vinh Phuc province in Vietnam, from 2000 to 2020, using machine learning and remote sensing. The algorithms used were support vector machine, catboost, and extratrees. A geo-spatial database of 206 inundation points and 11 conditioning factors (namely elevation, slope, curvature, aspect, distance to river, distance to road, NDVI, NDBI, rainfall, soil type, and TWI) from 2000 to 2020 was developed to be used as the input data. RMSE, MAE, AUC, and R² were used to assess the fit of the models. The results showed that all the proposed models were a good fit, with AUC values of 0.95 and over. In general, the total area marked as very low risk or low risk has increased, with the high risk and very high-risk areas having decreased over the period studied. This change was mainly concentrated in the city of Vinh Yen where there has been strong urban growth. The models proposed in this study are a promising toolkit to assess inundation susceptibility continuously and can support decision makers involved in sustainable development. Our results highlight the benefits and consequences of planned and unplanned development. Properly planned can reduce the flood risk, while unplanned development can increase the risk. Therefore, by applying the theoretical framework in this study, decision makers or planners can build the most appropriate strategies for flood control in the context of climate change. Our approach in this study represents a theoretical framework for future research not only on inundation management but also natural hazard management, in regions around the world.

Key-words: *inundation, support vector machine, Catboost, Extratree, machine learning, Vinh Phuc.*

1. INTRODUCTION

Climate change is considered one of the three key factors for "global changes". This process is the transformation of nature to human, important influence on the biological, the natural resource such as water, land and air resource, the weather system and the natural hazard such as forest fire, flood, and inundation (Petrişor et al. 2020, Nguyen et al. 2022a). Climate change can alter the frequency and intensity of precipitation and the hydrological regime of a region and therefore can influence the occurrence and frequency of inundation. Several studies have established that inundation is the result of climate change and is influenced by climatic determinants such as increased precipitation (Roy et al. 2020, Avand and Moradi 2021, Li et al. 2021, Rajkhowa and Sarma 2021). According to the Center for Research on the Epidemiology of Disasters (CRED), inundation is one of the most damaging natural hazards to human life and property. According to the World Bank, in the period 1995-2005, approximately 150,000 floods and inundation occurred worldwide, leading to some 157,000 deaths, representing 11% of all victims of natural disasters (Janizadeh et al. 2021a, Ghosh et al. 2022c, Ghosh et al. 2022b). Multiple studies have indicated that flood and inundation affect in the region of 200 million people each year and that these numbers are likely to increase significantly by 2050 due to climate change and urban growth (Pourghasemi et al. 2020, Janizadeh et al. 2021b).

¹Department of Agriculture and Rural Development, Vinh Phuc, Vietnam, hungccdd@gmail.com

²Faculty of Geography, National University, Hanoi, Vietnam, *Corresponding author nguyenduuy@hus.edu.vn

³Thuyloi University, Dong Da, Hanoi, Vietnam, Pchientvct_tv@tlu.edu.vn

41% of the deaths mentioned above were in Asia, and of all Asian countries, Vietnam is one of the countries most vulnerable to flood and inundation (Nguyen 2022a). For example, severe flood and inundation in the Central region of Vietnam in 1999 caused 547 deaths and damaged 630,000 homes. This is why predicting flood and inundation susceptibility has become a top priority for the scientific community and local authorities across the country.

Inundation susceptibility is the likelihood of the occurrence of high-water resources in a given region. Most studies in this area have focused on the assessment of inundation susceptibility at a specific time. However, the continuous assessment of inundation susceptibility is an effective framework to better support decision makers to understand the causes of increased inundation. Nguyen et al. (2022a) showed that constructing strategies that mitigate against inundation is more effective when susceptibility is continuously evaluated. Penning-Rowsell et al. (2013) also indicated that continuous inundation assessment plays an important role in building appropriate strategies to reduce inundation damage.

Previous studies have used different methodologies to assess inundation susceptibility. These can be divided into three main groups: hydrodynamic, remote sensing and GIS, and machine learning. The hydrodynamic approach - which features models such as Mike (Tansar et al. 2020, NGUYEN et al. 2023), HEC-RAS (Ongdas et al. 2020, Psomiadis et al. 2021), and SWAT (Jodar-Abellan et al. 2019, Liu et al. 2022) - uses mathematical equations to predict the flow of water in rivers, streams, and other waterways, and the relationship between river flows and precipitation. Although this approach has been used extensively in previous studies, the hydrodynamic model requires detailed topographical, meteorological, and other terrain data (Nguyen et al. 2021). Therefore, these models are limited to application in small areas or locations where there is plenty of data. The construction of hydrodynamic models also requires comprehensive knowledge of the relevant hydrological parameters. In recent years, with the development of remote sensing data and the data sharing policies of agencies such as NASA and NOAA, remote sensing and GIS have become a more viable option for assessing inundation susceptibility over a wide region. However, this approach is limited in its ability to identify the relationship between inundation and its causes (Wang and Xie 2018). It is clear, then, that these approaches will likely be superseded by more state-of-the-art methods.

A number of recent studies have used data-driver, integrated with remote sensing data, to continuously assess inundation susceptibility by analyzing the relationships between past inundation events and conditioning factors (Bui et al. 2020). Data-driver approach requires less input data than hydrodynamic models. This approach was separated by the statistical models and machine learning. Statistical models such as logistic regression (Al-Juaidi et al. 2018, Lim and Lee 2018), frequency ratio (Ghosh et al. 2022a), weight of evidence (Hong et al. 2018), fuzzy logic (Sahana and Patel 2019), and AHP (Swain et al. 2020) have shown promise, but in the context of climate change and urbanizations, inundation is becoming ever more complicated and non-linear; therefore, statistical models cannot achieve adequate levels of accuracy in their predictions. The machine learning approach has been receiving a great deal of attention within the scientific community. This approach includes models such as support vector machine (SVM) (Mohammady et al. 2019), random forest (Lee et al. 2017), bagging (Talukdar et al. 2020), adaboost (Tien Bui et al. 2016), artificial neural networks (Priscillia et al. 2021) and decision tree (Khosravi et al. 2018, Pham et al. 2021a). There is, however, no universal consensus as to which algorithm(s) - from the thousand available options - may best simulate inundation susceptibility in a given region.

In summary, there are two major gaps in the literature. First, most studies focus on the assessment of inundation susceptibility at a specific time, when assessment at different times has been shown to be important in the development of appropriate inundation prevention measures. Second, the selection of appropriate methods to predict the inundation susceptibility in a specific region continues to be a major challenge for the scientific community. In response to these two issues, this study has aimed to carry out (i) a continuous inundation susceptibility assessment for the period 2000-2020 and (ii) a comparison of models to select the best one for predicting inundation susceptibility. Although this study was carried out in a province in Vietnam and was focused on inundation, our findings may be applied in many other geographical regions and used to evaluate other natural hazards.

2. STUDY AREA AND DATA USE

2.1. Study area

Vinh Phuc province is located in the Red River Delta, in the Northern Midlands and Mountains region of Vietnam. It covers an area of approximately 1,236 km² (Fig. 1). The province descends from the northeast to the southwest, and its diverse topography can be divided into three categories: high mountains, middle lands, and plains. The high mountain region, with an elevation ranging from 200 to 1000 m, covers 65,500 ha of the province. The middle lands, with an elevation from 20 to 200 m, occupy 25,100 ha, and the plains, with an elevation of 0 to 20 m, occupy 33,500 ha. Vinh Phuc is located in the tropical monsoon climate region and has an average annual rainfall of 1400-1900 mm, mainly concentrated between May and October, accounting for 80% of the total rainfall. The dry season lasts from November to April and accounts for the remaining 20%. The river system in the study area is dense and the hydrological regime is mainly depending on the flow in two main river systems named the Red River and the Phan - Ca Lo River. According to statistics from the Forest Protection Department, the forested area of Vinh Phuc accounts for about 22% of the province. However, in recent years, under the pressure of a population explosion and accelerating urbanization, the forest area has been seriously reduced. This is thought to have been the main cause for the increasing severity of inundations and landslides in the province.

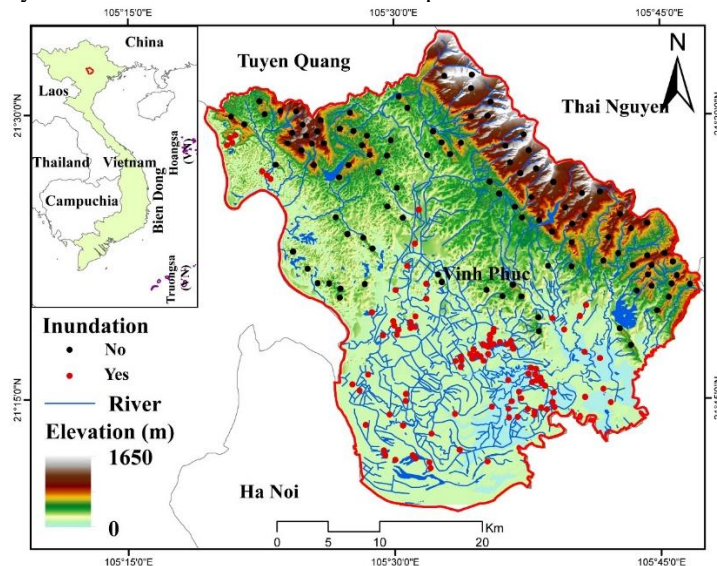


Fig. 1. The location of Vinh Phuc province.

2.2. Data use

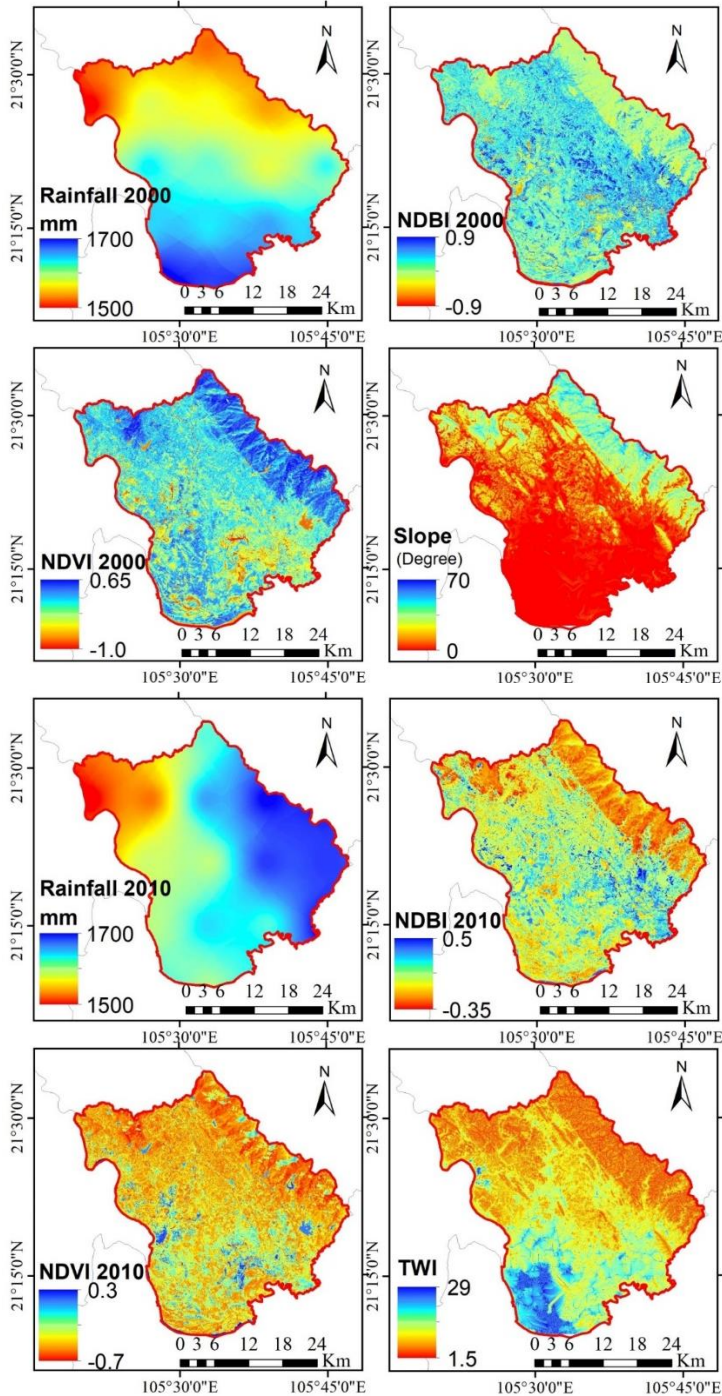
Inundation inventory

Inundation inventory preparation is essential in building an inundation susceptibility model and describes the relationships between past inundation events and conditioning factors (Nguyen et al. 2022b, Yaseen et al. 2022). In this study, 106 inundation points were collected from different sources such as the province's Department of Natural Resources and Environment, field missions in 2021 and 2022, and Sentinel 1A imagery. The construction of inundation susceptibility maps requires the binary classification of inundation inventory into two groups: inundation points and non-inundation points. Non-inundation points were taken from high-altitude locations that have never been affected by inundation. The inundation inventory was divided into two groups: 70% of the data for training and 30% for validation).

Conditioning factors

The construction of inundation susceptibility models is very complicated because it requires data regarding environmental, hydrological, climatic, and anthropic factors (Ghosh et al. 2022c, Nguyen

2022b). The selection of appropriate conditioning factors is critical and determines the accuracy of the inundation susceptibility model. After reviewing the existing literature, 11 conditioning factors were selected, namely altitude, slope, aspect, curvature, distance to river, distance to road, NDVI, NDBI, rainfall, soil type, and TWI. All conditioning factors were transformed to raster format at a resolution of 10 m (Fig. 2).



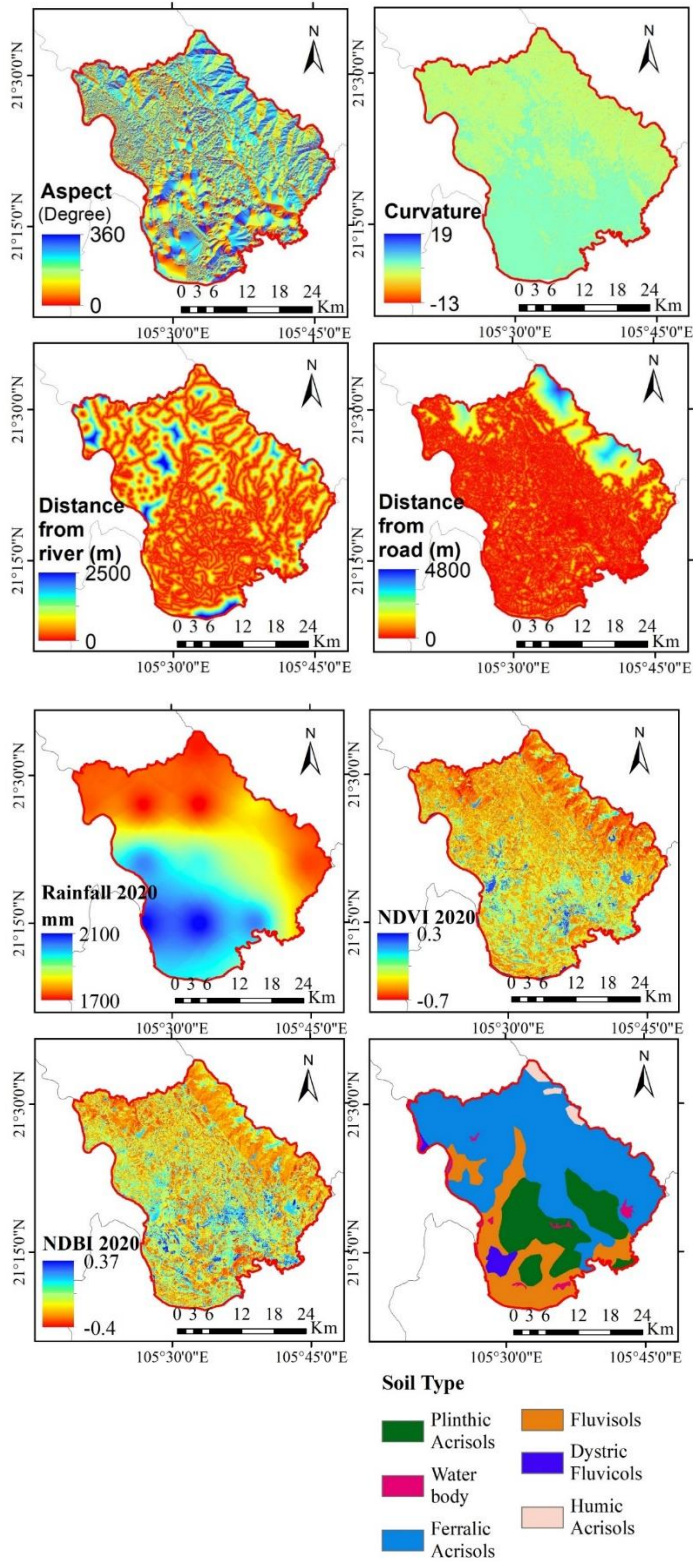


Fig. 2. Conditioning factor used for the flood susceptibility model.

Elevation, slope, aspect, curvature, and TWI were extracted from a DEM constructed by topographic map with the scale of 1:50,000 m. Note that the map was obtained from the Ministry of Natural Resources and Environment. Distance to river and distance to road were extracted from the topographic map. NDVI and NDBI in 2000, 2010, and 2020 were calculated from Landsat 7 and 8 images. Rainfall in 2000, 2010, and 2020 were downloaded from <https://chrsdata.eng.uci.edu/>. Soil type was collected from Ministry of Natural Resources and Environment.

Inundation likelihood is inversely proportional with altitude. The south of the area is characterized by flat and low land, so this region is often affected by inundation (Dahri et al. 2022). The altitude value in the province ranged from 0 to 1650 m. Slope directly influences the probability of inundation occurrence as it controls flow velocity. The probability of occurrence of inundation is inversely proportional with slope (Arabameri et al. 2022). In the study area, the slope value ranged from 0 to 70 degrees. Aspect is indirectly related to the occurrence of inundation because it influences the direction of flow and the maintenance of soil moisture (Nguyen 2022a). In the study area, the aspect value ranged from 0 to 360 degrees. Curvature plays an important role in assessing the likelihood of inundation occurrence. It is directly linked to the heterogeneity of each region. The curvature value is inversely proportional to the occurrence of inundation (Sachdeva and Kumar 2022). In the study area, the curvature value ranged from -13 to 19.

TWI is a measure of how likely a region is to experience inundation. The higher the value of TWI, the higher the probability of flood or inundation (Tehrany et al. 2014). In the study area, the TWI was found to range from 1.5 to 29. The type of soil in a region plays a significant role in the likelihood of inundation. This is because soil affects the rate of infiltration (water soaking into the ground) and the formation of runoff (water flowing on the surface) (Bui et al. 2019). In the study area, the soil types were classified into five groups: plinthic Acrisols, ferralic Acrisols, Fluvisols, Dystric Fluvisols, and humic Acrisols.

NDVI represents the density of vegetation in an area and directly influences the infiltration capacity and the speed of flow. Regions with low vegetation density are more vulnerable to inundation (Nachappa et al. 2020). In the study area, the range of NDVI values in 2000, 2010, and 2020 were -1-0.65, 0-0.5, and -0.7-0.3 respectively. NDBI represents the density of construction in a specific region, which influences the probability of inundation as concrete constructions do not allow water to seep into the ground (Saha et al. 2021, Nguyen 2022b). In this study, the value ranges of NDBI in 2000, 2010, and 2020 were -0.9-0.9, -0.35-0.5, and -0.4-0.37 respectively.

Rainfall was selected because precipitation of high intensity over a short time are closely linked with river flow and therefore inundation susceptibility (Band et al. 2020). In the study area, value ranges of rainfall 2000, 2010, and 2020 were 1500-1700 mm, 1500-1700 mm and 1700-2100 mm respectively. Distance to road directly influences the capacity of infiltration and evacuation of water (Linh et al. 2022).

In the study area, distance to road ranged from 0 to 4800 m. Because most inundation occurs along the rivers, the further the region is from a river, the less likely it is to inundation (Chowdhuri et al. 2020). In this study, the distance to river value ranged from 0 to 2500 m.

3. METHODOLOGY

We applied machine learning and remote sensing in our study. This process was divided into four main steps: (i) collection and pre-processing of input data, (ii) construction of inundation susceptibility models, (iii) assessment of the accuracy of the proposed models, and (iv) analysis of the effects of climate change on inundation susceptibility in the period 2000-2020 (**Fig. 3**).

(i) Collection and pre-processing of input data

The input data of the inundation susceptibility model constituted two groups: inundation inventory and conditioning factors. Inundation inventory comprises historical inundation - and non-inundation points, which were coded as 1 and 0, respectively. These points were collected from different sources: reports from the Department of Natural Resources and Environment, field missions, and Sentinel 1A imagery.

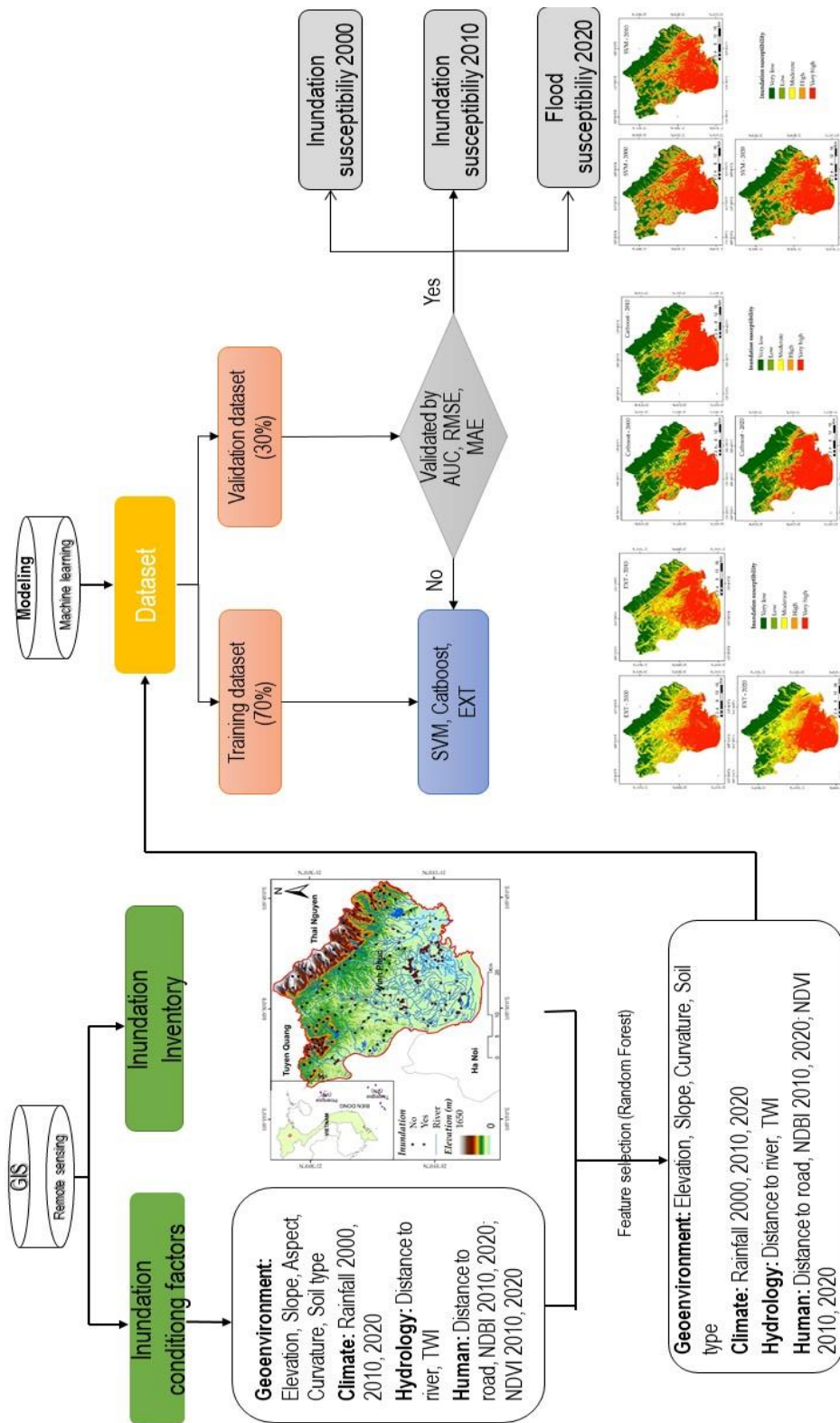


Fig. 3. The methodology used in this study.

While this study assesses inundation susceptibility continuously over the period 2000-2020, theoretically, the conditioning factors should be collected from 2000 to 2020 to use as input data to assess changes in inundation susceptibility over this period. However, due to difficulties in data collection, we hypothesize that the topographic features did not change over the period in question, and that the relevant changes were instead in hydro-meteorological conditions and anthropic activity. These factors were calculated from the 1/50,000 m topographic map and from remote sensing data.

(ii) Building the inundation susceptibility model

206 inundation points and 11 conditioning factors were used as input data for the inundation susceptibility model. This data was divided into two groups: 70% to train the models (the adjustment of hyper-parameters) and 30% to evaluate the accuracy of the models. Other rates (50/50, 60/40, and 80/20) were tested, but 70/30 performed better. Building inundation susceptibility models can be challenging when data is limited. In order to validate the model, a 10-fold cross-validation method was applied to the dataset. The results of this validation were used to evaluate the model's performance through various performance indices. To find the best model, Bayesian optimization was used to select the optimal hyper-parameter values. Additionally, different models such as SVM, catboost (CB), EXT, adaboost, random forest, and xgboost were tested, and ultimately SVM, CB, and EXT were chosen as the best performing models. The accuracy of the models is impacted by the process of tuning their hyper-parameters. RMSE was used as the objective function to find the hyper-parameters that resulted in the highest accuracy after the training process. The hyper-parameters for the models SVM, CB, and EXT were determined through trial and error and set to $C=0.1$, $\text{Gamma}=0.5$ for SVM; $\text{depth}=3$, $\text{learning_rate}=0.01$ for CB; and $\text{max_depth}=2$, $\text{min_samples_split}=2$ for EXT.

(iii) Evaluation of the accuracy of the proposed models

The statistical indices AUC, RMSE, R^2 , and MAE were applied to evaluate the inundation susceptibility models.

(iv) Analysis of the effects of climate change on the inundation susceptibility from 2000 to 2020

After validation of the inundation susceptibility models, the inundation susceptibility maps for 2000, 2010, and 2020 were generated using SVM, CB, and EXT. The maps were compared to assess changes and how they were connected with climate change.

3.1. Support vector machines (SVMs)

SVMs are supervised machine learning models that can solve mathematical discrimination and regression problems. They were conceptualized in the 1990s from a statistical learning theory proposed by (Cortes and Vapnik 1995). The models have the ability to work with high-dimensional data and achieve good results. Requiring only a small number of parameters, they are appreciated for their ease of use. The main operating principle of the SVM model is the search for a hyperplane (feature space) in which the data is separated into several classes whose boundary is as far as possible from the data points (or "maximum margin") (Tehrany et al. 2014). To achieve this, SVMs use kernels, i.e. mathematical functions to project and separate data in vector space, with "support vectors" being the data closest to the border. The furthest boundary of all the training points is optimal and therefore presents the best capacity for generalization (Choubin et al. 2019). The accuracy of the SVM model is characterized by two main hyper-parameters: gamma and C. The adjustment of the C parameter aims to eliminate outliers in the data. Increasing the value of C makes the SVM model able to choose the hyperplane to better separate the data points, while the gamma parameter determines the number of data points in the construction of the hyperplane. If the value of gamma is low, all data points far from the median will be used to calculate the median, and vice versa (Nguyen 2022a). In this study, using trial and error, the value of C and gamma were set at 0.1 and 0.5 respectively.

3.2. Catboost (CB)

HGS is a swarm-based optimizer algorithm, first introduced by Yang et al. (2021). This algorithm is inspired by the behavior of animals in a state of starvation. In order to find food and improve their survival, animals tend to cooperate with each other. Stronger animals have a greater heart capacity to obtain food than weak animals (Yang et al., 2021). In nature, animal behavior is

influenced by many different factors, a primary one being hunger. When the food source is limited, it leads to competition between animals - a “hunger game.” The HGS algorithm is divided into two stages: the first stage simulates the process of cooperation between animals to find a food source; the second step describes the animals’ activities in a state of starvation (AbuShanab et al., 2021; Yang et al., 2021). The HGS algorithm has proven effective in the technical assessment and analysis of natural hazards (Nguyen, 2022b).

3.3. Extratrees (EXT)

EXT is a powerful algorithm developed by an unknown creator. It is used to address both classification and regression problems by using decision trees (Sachdeva and Kumar 2022). The EXT algorithm builds multiple decision trees from the original training sample, and each node in the tree selects the best feature from a random set of K features to split the data based on mathematical indices. Like the random forest algorithm, the EXT algorithm generates several decision trees by randomly sampling the data, leading to unique patterns in each tree.

Predictions are made through majority voting from the multiple decision trees (Heddam et al. 2020, Heddam 2023). The precision of the EXT model is influenced by the hyper-parameters `max_depth` and `min_samples_split`. In this study, the hyper-parameters were determined through trial-and-error to be `max_depth=2` and `min_samples_split=2`.

3.4. Performance assessment

Assessing the fit of a model is a crucial step in model building. In this study, the ROC, AUC, RMSE, MAE, and R^2 indices were used to evaluate the fit of the model, which have been widely used in previous studies. The ROC curve illustrates the performance of a model by plotting the true positive rate on the Y-axis and false positive rate on the X-axis.

The AUC (area under the curve) ROC summarizes the overall performance of a classification model, with a value ranging from 0 to 1. A value of 1 indicates a perfect model, while 0.5 represents a non-informative model (Nachappa et al. 2020, Rehman et al. 2022).

RMSE and MAE give insight into the dispersion or variability of prediction accuracy by measuring the errors between the predicted and observed values (Chapi et al. 2017, Wang et al. 2019):

$$RMSE = \sqrt{\frac{1}{m} \sum_{i=1}^m (Y_{ipredicted} - Y_{iobserved})^2}$$

$$MAE = \frac{1}{m} \sum_{i=1}^m |Y_{ipredicted} - Y_{iobserved}|$$

where $Y_{iobserved}$ is the value of the i^{th} observation from the validation dataset and $Y_{ipredicted}$ is the predicted value for the i^{th} observation.

4. RESULTS AND DISCUSSIONS

4.1. Rainfall change between 2000 and 2020

Fig. 4 shows the annual precipitation in Vinh Phuc province between 2000 and 2020. The annual precipitation in 2000 ranged from 1542.38 to 1636.86mm, in 2010 from 1439.8 to 1647.18 mm, and in 2020 from 1748.64 to 2025.46 mm. During the period 2000-2010, precipitation increased in the northern mountainous region and decreased in the southern region. From 2010 to 2020, precipitation became stronger and was concentrated in the southern region.

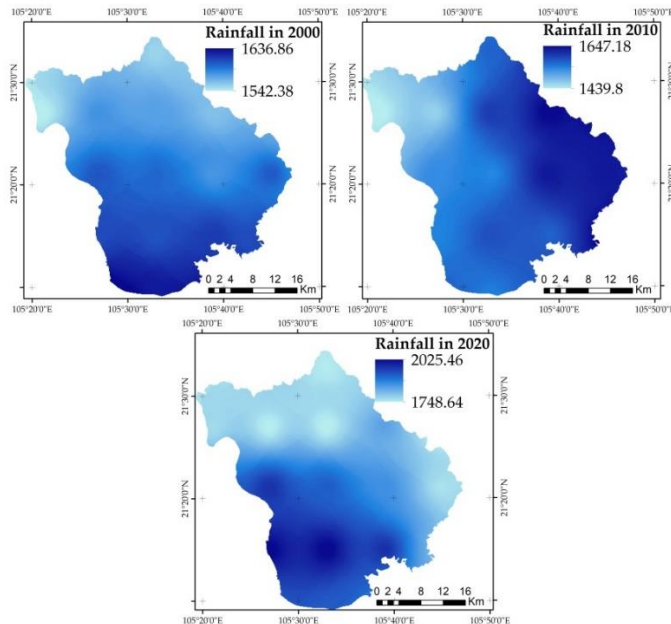


Fig. 4. Rainfall in Vinh Phuc province between 2000 and 2020.

4.2. Feature selection analysis

Assessing the importance of each conditioning factor is essential in the process of building a inundation susceptibility model. In this study the random forest technique was used to assess the importance of each factor. The results (Fig. 5) showed slope (0.3), altitude (0.265), TWI (0.15), and rainfall (0.11) to be the most important predictors of inundation occurrence, followed by NDVI (0.06), distance to river (0.05), curvature (0.025), soil type (0.02), distance to road (0.01), and NDBI (0.005). Aspect had no influence on the occurrence of inundation and so was eliminated from the inundation susceptibility model.

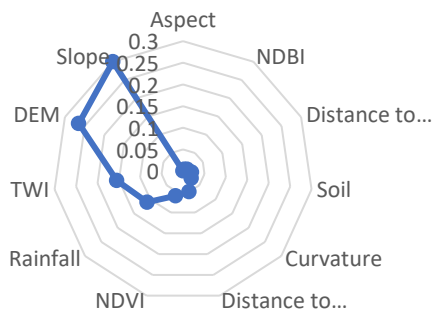


Fig. 5. Feature selection and ranking using random forest.

4.3. Model comparison

Ideally, a machine learning model should not be evaluated on the same dataset it uses for training, because the model will overfit the dataset and not perform better than the previous model. Therefore, for a model to be evaluated objectively, it must be evaluated on a test dataset that has not been used before. Fig. 6 shows the AUC-ROC results for the training dataset and validating dataset. According to the AUC results for the training dataset, the CB model (AUC=0.99) outperformed SVM (AUC=0.98) and EXT (AUC=0.98). Similarly, for the validating dataset the AUC value for the CB model was 0.99, beating SVM (AUC=0.97) and EXT (AUC=0.97). Although all the proposed models returned results with high accuracy, the CB model was the best performing in the study area.

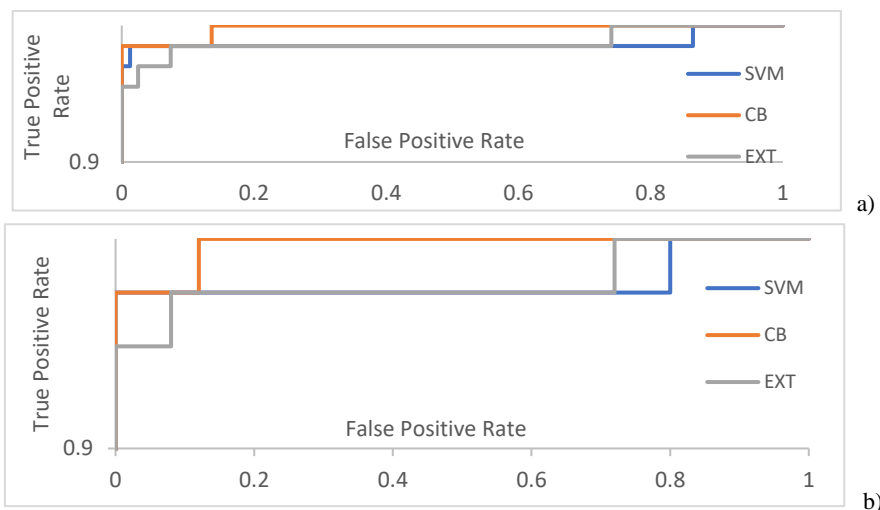


Fig. 6. The validation of three inundation susceptibility models using ROC based on training dataset (a) and validating dataset (b)

Table 1 presents the value of RMSE, MAE, and R^2 for the training dataset and validating dataset. For the CB model, the training dataset results for RMSE, MAE, and R^2 were 0.12, 0.05, and 0.95 respectively, outperforming SVM (RMSE=0.14, MAE=0.06, R^2 =0.91) and EXT (RMSE=0.24, MAE=0.21, R^2 =0.75). For the validating dataset, for the CB model, the value of RMSE (0.17), MAE (0.07), and R^2 (0.96) was better than the other models, followed by SVM (RMSE=0.18, MAE=0.08 and R^2 =0.96) and EXT (RMSE=0.26, MAE=0.22 and R^2 =0.72), respectively.

Table 1.

The accuracy assessment of three inundation susceptibility models for the training dataset and the validating dataset.

	Training dataset				Validating dataset			
	RMSE	MAE	AUC	R^2	RMSE	MAE	AUC	R^2
SVM	0.14	0.06	0.98	0.91	0.18	0.08	0.97	0.96
CB	0.12	0.05	0.99	0.95	0.17	0.07	0.99	0.96
EXT	0.24	0.21	0.98	0.75	0.26	0.22	0.97	0.72

4.4. Inundation susceptibility prediction

After validation, the models were used to evaluate inundation susceptibility in 2000, 2010, and 2020. The models were fed pixels from the study area and the 11 conditioning factors for each of 2000, 2010, and 2020. Although there were small differences between each of the models' predictions, inundation was forecast to occur mainly in the southern region where there is low elevation and slope. The area of very low inundation susceptibility increased from 2000 to 2020, while the high and very high risk areas decreased in size.

For the SVM model, the very low area increased from 264.736 km² in 2000 to 345.537 km² in 2010 and 369.0107 km² in 2020. The low area decreased from 124.6562 km² in 2000 to 121.4723 km² in 2010 and increases to 125.3921 km² in 2020. Similarly, the moderate risk area decreased from 127.5294 km² in 2000 to 121.6532 km² in 2010 and then grew to 123.8686 km² in 2020. The high risk area decreased from 188.7407 km² in 2000 to 183.5609 km² in 2010 and again to 170.7813 km² in 2020. The very high risk area shrank from 514,3594 km² in 2000 to 447,712 km² in 2010 and then further to 430,8828 km² in 2020.

For the CB model, the very low inundation susceptibility area decreased from 414.1629 km² in 2000 to 411.6574 km² in 2010; the 2020 figure stayed almost the same at 411.689 km². The low risk area grew from 101.0637 km² in 2000 to 115.8995 km² in 2010 and decreased slightly to 114.0801

km² in 2020. The area of moderate inundation susceptibility decreased from 115.532 km² in 2000 to 105.312 km² in 2010 and again to 104.2839 km² in 2020. The high risk area increased from 125.194 km² in 2000 to 128.2546 km² in 2010 and again to 131.2367 km² in 2020. The very high susceptibility area shrank slightly from 464.0691 km² in 2000 to 458.812 km² in 2010 and then to 458.6458 km² in 2020.

For the EXT model, the very low area decreased from 235.4863 km² in 2000 to 232.4067 km² in 2010 and then increased significantly to 271.7133 km² in 2020. The low area grew from 171.2381 km² in 2000 to 177.6635 km² in 2010 and shrank slightly to 174.3416 km² in 2020. The moderate areas diminished from 225.0975 km² in 2000 to 191.1555 km² in 2010 and grew again to 213.1152 km² in 2020. The high inundation susceptibility area increased from 252.6806 km² in 2000 to 265.4405 km² in 2010 and decreased to 236.7902 km² in 2020. The very high-risk area decreased from 335.5191 km² in 2000 to 265.4405 km² in 2010 and then increased to 323.9735 km² in 2020 (Table 2, Fig. 7 and 8).

Table 2.

The distribution of five classes of inundation susceptibility zones as generated by SVM, CB, and EXT.

		Very low (Km ²)	Low (Km ²)	Moderate (Km ²)	High (Km ²)	Very high (Km ²)
SVM	2000	264.736	124.6562	127.5294	188.7407	514.3594
	2010	345.537	121.4723	121.6532	183.5609	447.712
	2020	369.0107	125.3921	123.8686	170.7813	430.8828
CB	2000	414.1629	101.0637	115.532	125.194	464.0691
	2010	411.6574	115.8995	105.312	128.2546	458.812
	2020	411.689	114.0801	104.2839	131.2367	458.6458
EXT	2000	235.4863	171.2381	225.0975	252.6806	335.5191
	2010	232.4067	177.6635	191.1555	265.4405	265.4405
	2020	271.7133	174.3416	213.1152	236.7902	323.9735

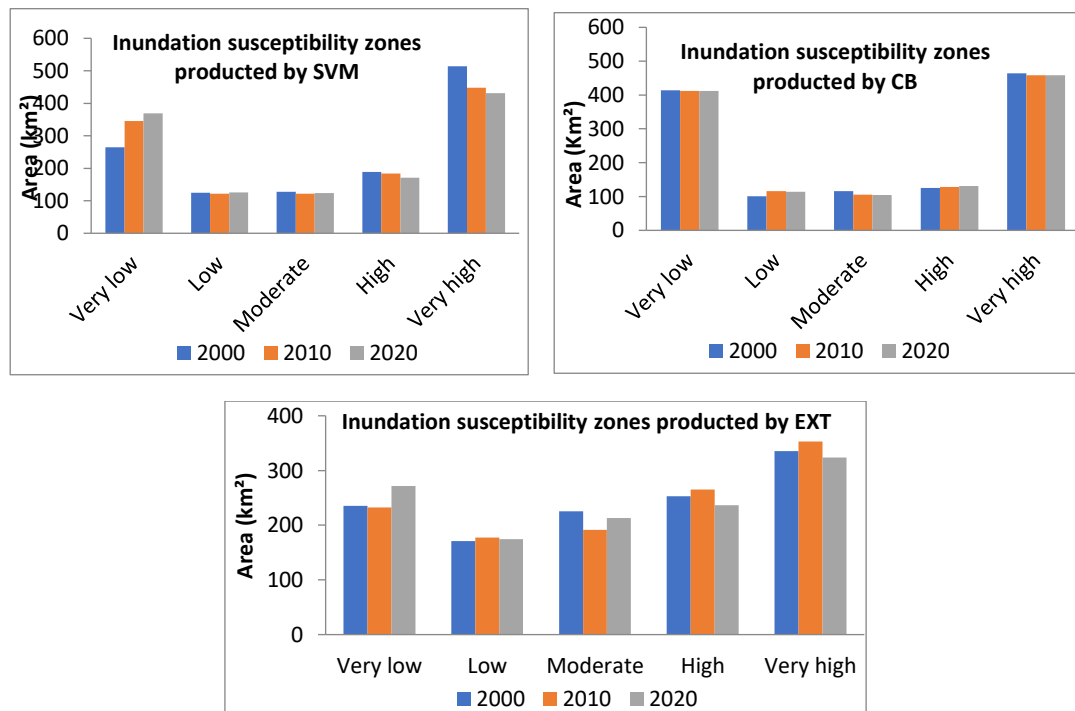
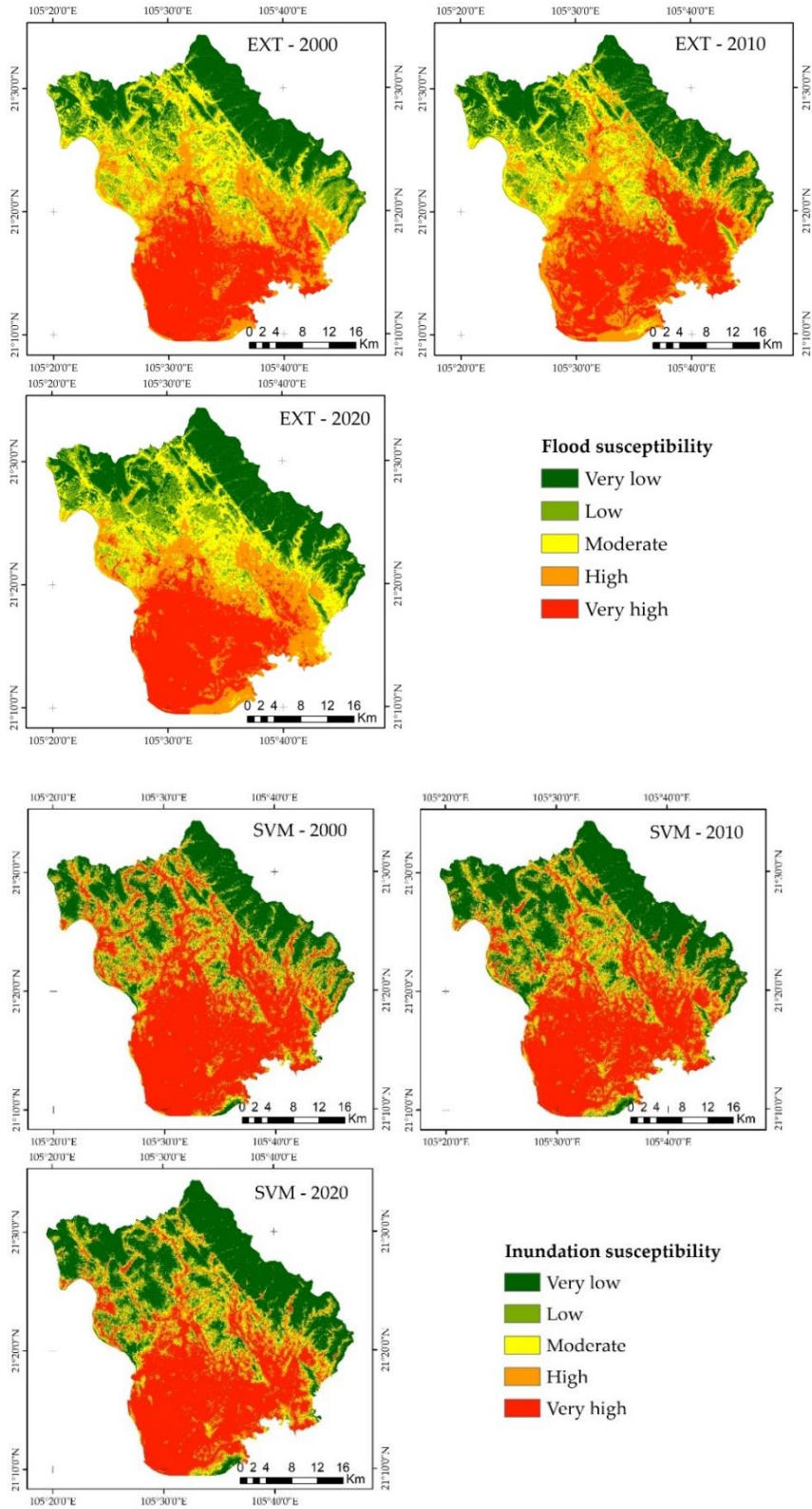


Fig.7. The inundation susceptibility zones under five classes produced by SVM, CB and EXT.



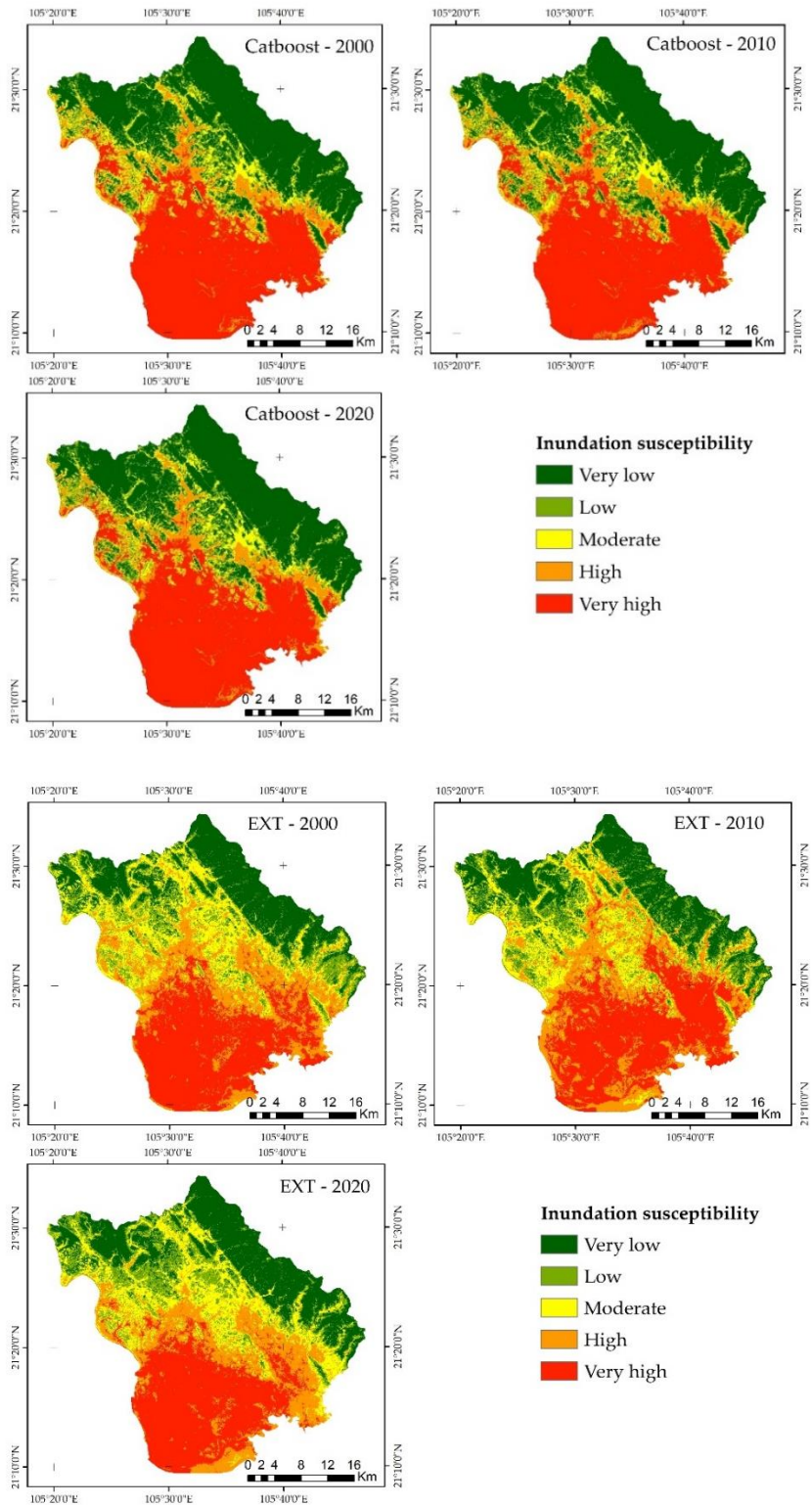


Fig. 8. Inundation susceptibility in 2000, 2010, and 2020 as generated by SVM, CB, and EXT.

5. DISCUSSION

5.1. The significance of results

The inundation is considered the most destructive natural hazard in the world, causing significant damage to human life and the economy of the country, especially in the coastal country. These damages are more and more serious in the last years due to climate change. So the understanding of effects of climate change on inundation susceptibility have received great attention from the global scientific community, particularly with a view to better support those tasked with designing appropriate strategies for inundation control in the context of climate change (Li et al. 2020, Nguyen et al. 2022a). This study develops a theoretical framework with which to assess the effects of climate change in general, and precipitation in particular, on inundation susceptibility in Vinh Phuc province, using machine learning and remote sensing. Although several previous studies have analyzed inundation susceptibility, most of these focused on the assessment of susceptibility for a specific time. Continuous inundation susceptibility assessment is necessary to consider more fully the effects of climate change on future flood or inundation. The results in our study indicate that the relationships between climate change and inundation play a key role in the strategy of flood risk management in the future, can be used by decision makers and local authorities in the construction of flood risk reduction strategies.

5.2. Inner validation of the results

The results support the first hypothesis in the introduction section that the inundation susceptibility exhibits strong relationships with natural and human factors as the slope, elevation, TWI and rainfall. For inundation susceptibility model development, studies have indicated that low quality of data has a negative effect on the quality of inundation susceptibility models and that, therefore, pre-processing of the data is critical (Du et al. 2023). In this study, random forest was used to assess the importance of each of 11 conditioning factors. It should be noted that the importance of conditioning factors depends on the natural and socio-economic condition of each region and the method used. Previous study, Islam et al. (2021) used information gain ratio to assess the importance of 10 conditioning factors.

The results highlighted that LULC, distance to road, and elevation were three most important factors in the construction of a model of inundation susceptibility for the Teesta sub-catchment of northern Bangladesh. Pham et al. (2021b) applied frequency ratio to rank 16 conditioning factors and the results showed that elevation, rainfall, and slope were most important for their model for the Vu Gia-Thu Bon watershed in Vietnam. Huu Duy Nguyen (2022) used the random forest technique to analyze the importance of 13 conditioning factors and reported that LULC, elevation, and slope were most important for his map in Vietnam's Ha Tinh province.

In this study, slope, elevation, TWI, and rainfall were the most important factors on the probability of inundation occurrence in Vinh Phuc province. Slope and elevation scored highest as they have critical effects on flow regime and flow velocity. TWI was ranked third as it describes the wetness of a given area and therefore the soil saturation capacity.

Rainfall was ranked fourth in importance. In Vietnam, there are three main types of inundation: fluvial, coastal, and pluvial. Coastal inundation does not exist in the study area because Vinh Phuc province is not influenced by the sea and the tide. Fluvial inundation is insignificant because the study area is not affected by major rivers. The province is often hit by heavy rainfall over a short period, which causes inundation. In recent years, inundations have also increased in intensity and number due to the reduction of surface vegetation, which influences the flow regime, and soil saturation capacity. This is why NDVI was ranked fifth of the factors featured.

Distance to river, curvature, soil type, distance to road, and NDBI were ranked from six to ten respectively, because the inundation in the study area mainly occurs in the low altitude area during the period of heavy rainfall. Heavy rainfall and low altitude are the main factors for the occurrence of inundation. Aspect did not influence the probability of inundation occurrence in the study area. It is worth noting that the models used in this study are driver-models, therefore, the importance of each

of the conditioning factors depends on the statistical relationship between past events and conditioning factors. In this way, inundation in the study area can be seen mainly to depend on four factors: elevation, slope, TWI, and rainfall.

This study also confirms that all machine learning models were successful in assessing the effects of climate change in inundation susceptibility in Vinh Phuc province. Previous studies have demonstrated that model accuracy depends on model structure and the data characteristics of each region (Bui et al. 2020). Therefore, the selection of models is one of the most important steps. In this study, the models SVM, CB, and EXT were selected. Of the three, CB performed best. CB is considered to be one of the most powerful and precise machine learning tools as, unlike other machine learning tools, it does not need to run multiple trials to get good results. It provides optimum models from the first round (Lu et al. 2022). The SVM model was the second best performing. It not only performs well with large datasets, but also with small datasets. Moreover, SVM has the advantage of reducing dataset noise and has high generalizability (Deka 2014). EXT was third best performing. Although it has advantages such as generalizability and bias reduction, it struggles with nonlinear problem solving (Geurts et al. 2006).

5.3. The external validation of results

The results of this study were unexpected, because the initial hypothesis was that inundation susceptibility in the study area had increased from 2010 to 2020 due to the change in precipitation in the context of climate change. This trend is typical of several regions in the world: Nguyen et al. (2022a) pointed out that inundation susceptibility in Nhat Le-Kien Giang had increased due to the change in precipitation in the context of climate change. Previous study, Chen et al. (2022) described an increase in inundation risk in Taiwan over the period 1979–2099. Javari (2022) found inundation risk in Iran to have grown due to the increase in precipitation between 1975 and 2017. However, in this study, although the increase in precipitation from 2010 to 2020, however, in this period, good planning can reduce the effects of inundation.

5.4. The importance of results

The results of this study contribute important aspects of flood risk management strategies. The construction of the models in this study represents a high quality tool to assess the effects of climate change on floods or inundations. The models proposed in this study showed a more reliable performance than the previously cited studies. We can conclude that this is the first time that these models are used to build a inundation susceptibility map and assess the effects of climate change on inundation susceptibility. In addition, our results are important in answering the first question which has not been addressed in previous studies. Good land planning plays an essential role in reducing the flood risk. However, the success of putting in place good planning depends on determining the areas prone to flood and the impact of climate change. This can be achieved by understanding inundation susceptibility in a complex way in the context of climate change, as well as limiting new construction in areas with high or very high inundation susceptibility.

5.5. Limitation and Future Research

This study presents the general limitation related to the use of the data. This study uses Landsat 08 with the resolution of 30m to extract the NDVI and NDBI in 2020. However, several studies have pointed out that the Sentinel 2A can present the information in more detail. In addition, non-flood or non-inundation points were selected in the never-flooded area. However, given the context of climate change and the non-linear nature of the flood or inundation phenomenon, this leads to uncertainties in the selection of these points. Ultimately, flood intensity is strongly influenced by climate change scenarios and land use. Therefore, it is necessary to evaluate the scenarios of this change on floods in future studies. These results may be important for policy makers and local authorities to promote sustainable land use planning in the future.

6. CONCLUSIONS

Every year, the flood causes major damage to human life and the country's economy in the world. With the geographical location, Vietnam is considered a country most affected by this natural hazard. Among the provinces, Vinh Phuc province is one of the provinces most damaged by inundation, especially in the context of climate change. This study assesses the impacts of climate change in general and rainfall change in particular on inundation susceptibility in Vinh Phuc province over the period 2000-2020, using machine learning (SVM, CB, and EXT) and remote sensing. The results of this study can help managers and planners understand the causes of changes in inundation susceptibility and thus develop appropriate strategies and policies to reduce future inundation damage.

All the models proposed in this study used good fit to assess the effects of climate change and rainfall on inundation susceptibility from 2000 to 2020. All three achieved AUC of over 0.95. Of the three, CB was most accurate (AUC=0.99). SVM and EXT both scored AUC=0.98. The models proposed in this study can be used to assess the effects of climate change on inundation susceptibility in other regions of the world, particularly in regions with limited data.

In general, the size of the areas of very low and low inundation susceptibility increased in from 2000 to 2020, while the high and very high risk areas decreased, due to changes in rainfall, vegetation, and infrastructure.

With the development of remote sensing data covering the entire planet, the approach used in this study can be easily applied to assess the effects of climate change on other natural hazard in different regions of the world. The models proposed in this study provide good results at large scales, which can help decision-makers and local authorities to determine the regions likely to be affected by climate change in large-scale.

The findings of this study may support managers and planners to implement appropriate measures in areas with high and very high inundation susceptibility, to reduce damage to human life and property. Moreover, the theoretical framework in this study highlights the effects of the change in rainfall on inundation susceptibility.

REFERENCES

- Al-Juaidi, A.E., Nassar, A.M. & Al-Juaidi, O.E., 2018. Evaluation of flood susceptibility mapping using logistic regression and gis conditioning factors. *Arabian Journal of Geosciences*, 11, 1-10.
- Arabameri, A., Seyed Danesh, A., Santosh, M., Cerda, A., Chandra Pal, S., Ghorbanzadeh, O., Roy, P. & Chowdhuri, I., 2022. Flood susceptibility mapping using meta-heuristic algorithms. *Geomatics, Natural Hazards and Risk*, 13 (1), 949-974.
- Avand, M. & Moradi, H., 2021. Using machine learning models, remote sensing, and gis to investigate the effects of changing climates and land uses on flood probability. *Journal of Hydrology*, 595, 125663.
- Band, S.S., Janizadeh, S., Chandra Pal, S., Saha, A., Chakraborty, R., Melesse, A.M. & Mosavi, A., 2020. Flash flood susceptibility modeling using new approaches of hybrid and ensemble tree-based machine learning algorithms. *Remote Sensing*, 12 (21), 3568.
- Bui, D.T., Ngo, P.-T.T., Pham, T.D., Jaafari, A., Minh, N.Q., Hoa, P.V. & Samui, P., 2019. A novel hybrid approach based on a swarm intelligence optimized extreme learning machine for flash flood susceptibility mapping. *Catena*, 179, 184-196.
- Bui, Q.-T., Nguyen, Q.-H., Nguyen, X.L., Pham, V.D., Nguyen, H.D. & Pham, V.-M., 2020. Verification of novel integrations of swarm intelligence algorithms into deep learning neural network for flood susceptibility mapping. *Journal of Hydrology*, 581, 124379.
- Chapi, K., Singh, V.P., Shirzadi, A., Shahabi, H., Bui, D.T., Pham, B.T. & Khosravi, K., 2017. A novel hybrid artificial intelligence approach for flood susceptibility assessment. *Environmental modelling & software*, 95, 229-245.
- Chen, Y.-J., Lin, H.-J., Liou, J.-J., Cheng, C.-T. & Chen, Y.-M., 2022. Assessment of flood risk map under climate change rcp8.5 scenarios in taiwan. *Water*, 14 (2), 207.
- Choubin, B., Moradi, E., Golshan, M., Adamowski, J., Sajedi-Hosseini, F. & Mosavi, A., 2019. An ensemble prediction of flood susceptibility using multivariate discriminant analysis, classification and regression trees, and support vector machines. *Science of the Total Environment*, 651, 2087-2096.

- Chowdhuri, I., Pal, S.C. & Chakraborty, R., 2020. Flood susceptibility mapping by ensemble evidential belief function and binomial logistic regression model on river basin of eastern india. *Advances in Space Research*, 65 (5), 1466-1489.
- Cortes, C. & Vapnik, V., 1995. Support vector machine. *Machine learning*, 20 (3), 273-297.
- Dahri, N., Yousfi, R., Bouamrane, A., Abida, H., Pham, Q.B. & Derdous, O., 2022. Comparison of analytic network process and artificial neural network models for flash flood susceptibility assessment. *Journal of African Earth Sciences*, 193, 104576.
- Deka, P.C., 2014. Support vector machine applications in the field of hydrology: A review. *Applied soft computing*, 19, 372-386.
- Dorogush, A.V., Ershov, V. & Gulin, A., 2018. Catboost: Gradient boosting with categorical features support. arXiv preprint arXiv:1810.11363.
- Du, Q.V.V., Nguyen, H.D., Pham, V.T., Nguyen, C.H., Nguyen, Q.-H., Bui, Q.-T., Doan, T.T., Tran, A.T. & Petrisor, A.-I., 2023. Deep learning to assess the effects of land use/land cover and climate change on landslide susceptibility in the tra khuc river bassin of vietnam. *Geocarto International*, (just-accepted), 1-40.
- Geurts, P., Ernst, D. & Wehenkel, L., 2006. Extremely randomized trees. *Machine learning*, 63, 3-42.
- Ghosh, A., Dey, P. & Ghosh, T., 2022a. Integration of rs-gis with frequency ratio, fuzzy logic, logistic regression and decision tree models for flood susceptibility prediction in lower gangetic plain: A study on malda district of west bengal, india. *Journal of the Indian Society of Remote Sensing*, 50 (9), 1725-1745.
- Ghosh, S., Saha, S. & Bera, B., 2022b. Flood susceptibility zonation using advanced ensemble machine learning models within himalayan foreland basin. *Natural Hazards Research*, 2 (4), 363-374 Available from: <https://www.sciencedirect.com/science/article/pii/S2666592122000245>.
- Ghosh, S., Saha, S. & Bera, B., 2022c. Flood susceptibility zonation using advanced ensemble machine learning models within himalayan foreland basin. *Natural Hazards Research*.
- Hai Ly, N., Nguyen, H.D., Loubiere, P., Van Tran, T., Şerban, G., Zelenakova, M., Breţcan, P. & Laffly, D., 2022. The composition of time-series images and using the technique smote enn for balancing datasets in land use/cover mapping. *Acta Montanistica Slovaca*, 27, 2.
- Heddam, S., 2023. Extremely randomized trees versus random forest, group method of data handling, and artificial neural network. *Handbook of hydroinformatics*. Elsevier, 291-304.
- Heddam, S., Ptak, M. & Zhu, S., 2020. Modelling of daily lake surface water temperature from air temperature: Extremely randomized trees (ert) versus air2water, mars, m5tree, rf and mlpnn. *Journal of Hydrology*, 588, 125130.
- Hong, H., Tsangaratos, P., Ilija, I., Liu, J., Zhu, A.-X. & Chen, W., 2018. Application of fuzzy weight of evidence and data mining techniques in construction of flood susceptibility map of poyang county, china. *Science of the total environment*, 625, 575-588.
- Islam, A.R.M.T., Talukdar, S., Mahato, S., Kundu, S., Eibek, K.U., Pham, Q.B., Kuriqi, A. & Linh, N.T.T., 2021. Flood susceptibility modelling using advanced ensemble machine learning models. *Geoscience Frontiers*, 12 (3), 101075.
- Janizadeh, S., Chandra Pal, S., Saha, A., Chowdhuri, I., Ahmadi, K., Mirzaei, S., Mosavi, A.H. & Tiefenbacher, J.P., 2021a. Mapping the spatial and temporal variability of flood hazard affected by climate and land-use changes in the future. *Journal of Environmental Management*, 298, 113551 Available from: <https://www.sciencedirect.com/science/article/pii/S0301479721016133>.
- Janizadeh, S., Pal, S.C., Saha, A., Chowdhuri, I., Ahmadi, K., Mirzaei, S., Mosavi, A.H. & Tiefenbacher, J.P., 2021b. Mapping the spatial and temporal variability of flood hazard affected by climate and land-use changes in the future. *Journal of Environmental Management*, 298, 113551.
- Javari, M., 2022. Rainfall random variability and its effects on flood risk management in iran. *Modeling Earth Systems and Environment*, 8 (1), 1109-1133.
- Jodar-Abellan, A., Valdes-Abellan, J., Pla, C. & Gomariz-Castillo, F., 2019. Impact of land use changes on flash flood prediction using a sub-daily swat model in five mediterranean ungauged watersheds (se spain). *Science of the Total Environment*, 657, 1578-1591.
- Khosravi, K., Pham, B.T., Chapi, K., Shirzadi, A., Shahabi, H., Revhaug, I., Prakash, I. & Bui, D.T., 2018. A comparative assessment of decision trees algorithms for flash flood susceptibility modeling at haraz watershed, northern iran. *Science of the Total Environment*, 627, 744-755.
- Lee, S., Kim, J.-C., Jung, H.-S., Lee, M.J. & Lee, S., 2017. Spatial prediction of flood susceptibility using random-forest and boosted-tree models in seoul metropolitan city, korea. *Geomatics, Natural Hazards and Risk*, 8 (2), 1185-1203.

- Li, S., Wang, Z., Lai, C. & Lin, G., 2020. Quantitative assessment of the relative impacts of climate change and human activity on flood susceptibility based on a cloud model. *Journal of hydrology*, 588, 125051.
- Li, Z., Song, K. & Peng, L., 2021. Flood risk assessment under land use and climate change in wuhan city of the yangtze river basin, china. *Land*, 10 (8), 878.
- Lim, J. & Lee, K.-S., 2018. Flood mapping using multi-source remotely sensed data and logistic regression in the heterogeneous mountainous regions in north korea. *Remote Sensing*, 10 (7), 1036.
- Linh, N.T.T., Pandey, M., Janizadeh, S., Bhunia, G.S., Norouzi, A., Ali, S., Pham, Q.B., Anh, D.T. & Ahmadi, K., 2022. Flood susceptibility modeling based on new hybrid intelligence model: Optimization of xgboost model using ga metaheuristic algorithm. *Advances in Space Research*, 69 (9), 3301-3318.
- Liu, Y., Xu, Y., Zhao, Y. & Long, Y., 2022. Using swat model to assess the impacts of land use and climate changes on flood in the upper weihe river, china. *Water*, 14 (13), 2098.
- Lu, C., Zhang, S., Xue, D., Xiao, F. & Liu, C., 2022. Improved estimation of coalbed methane content using the revised estimate of depth and catboost algorithm: A case study from southern sichuan basin, china. *Computers & Geosciences*, 158, 104973.
- Mohammady, M., Pourghasemi, H.R. & Amiri, M., 2019. Assessment of land subsidence susceptibility in semnan plain (iran): A comparison of support vector machine and weights of evidence data mining algorithms. *Natural Hazards*, 99, 951-971.
- Nachappa, T.G., Pirailiou, S.T., Gholamnia, K., Ghorbanzadeh, O., Rahmati, O. & Blaschke, T., 2020. Flood susceptibility mapping with machine learning, multi-criteria decision analysis and ensemble using Dempster Shafer theory. *Journal of hydrology*, 590, 125275.
- Nguyen, H.D., 2022a. Flood susceptibility assessment using hybrid machine learning and remote sensing in Quang Tri province, Vietnam. *Transactions in GIS*, 26 (7), 2776-2801.
- Nguyen, H.D., 2022b. GIS-based hybrid machine learning for flood susceptibility prediction in the Nhat Le-Kien Giang watershed, Vietnam. *Earth Science Informatics*, 1-18.
- Nguyen, H.D., Dang, D.K., Nguyen, Q.-H., Bui, Q.-T. & Petrisor, A.-I., 2022a. Evaluating the effects of climate and land use change on the future flood susceptibility in the central region of Vietnam by integrating land change modeler, machine learning methods. *Geocarto International*, 1-36.
- Nguyen, H.D., Nguyen, Q.-H., Du, Q.V.V., Nguyen, T.H.T., Nguyen, T.G. & Bui, Q.-T., 2021. A novel combination of deep neural network and manta ray foraging optimization for flood susceptibility mapping in Quang Ngai province, Vietnam. *Geocarto International*, 1-25.
- Nguyen, H.D., Quang-Thanh, B., Nguyen, Q.-H., Nguyen, T.G., Pham, L.T., Nguyen, X.L., Vu, P.L., Thanh Nguyen, T.H., Nguyen, A.T. & Petrisor, A.-I., 2022b. A novel hybrid approach to flood susceptibility assessment based on machine learning and land use change. Case study: A river watershed in Vietnam. *Hydrological Sciences Journal*, 67 (7), 1065-1083.
- Nguyen, H.D., Trinh, T.T.H. & Dang, D.K., 2023. Flood hazard and resilience in the watershed Nhat Le-Kien Giang in Vietnam. *Urbanism. Architecture. Constructions/Urbanism. Architectura. Constructii*, 14 (1).
- Ongdas, N., Akiyanova, F., Karakulov, Y., Muratbayeva, A. & Zinabdin, N., 2020. Application of Hec-RAS (2D) for flood hazard maps generation for Yesil (Ishim) river in Kazakhstan. *Water*, 12 (10), 2672.
- Penning-Rowsell, E., Yanyan, W., Watkinson, A., Jiang, J. & Thorne, C., 2013. Socioeconomic scenarios and flood damage assessment methodologies for the Taihu Basin, China. *Journal of Flood Risk Management*, 6 (1), 23-32.
- Petrisor, A.-I., Sirodoev, I. & Ianoş, I., 2020. Trends in the national and regional transitional dynamics of land cover and use changes in Romania. *Remote Sensing*, 12 (2), 230.
- Pham, B.T., Jaafari, A., Van Phong, T., Yen, H.P.H., Tuyen, T.T., Van Luong, V., Nguyen, H.D., Van Le, H. & Foong, L.K., 2021a. Improved flood susceptibility mapping using a best first decision tree integrated with ensemble learning techniques. *Geoscience Frontiers*, 12 (3), 101105.
- Pham, B.T., Luu, C., Van Phong, T., Trinh, P.T., Shirzadi, A., Renoud, S., Asadi, S., Van Le, H., Von Meding, J. & Clague, J.J., 2021b. Can deep learning algorithms outperform benchmark machine learning algorithms in flood susceptibility modeling? *Journal of hydrology*, 592, 125615.
- Pourghasemi, H.R., Kariminejad, N., Amiri, M., Edalat, M., Zarafshar, M., Blaschke, T. & Cerda, A., 2020. Assessing and mapping multi-hazard risk susceptibility using a machine learning technique. *Scientific Reports*, 10 (1), 3203.
- Priscillia, S., Schillaci, C. & Lipani, A., 2021. Flood susceptibility assessment using artificial neural networks in Indonesia. *Artificial Intelligence in Geosciences*, 2, 215-222.
- Psomiadis, E., Tomanis, L., Kavvadias, A., Soulis, K.X., Charizopoulos, N. & Michas, S., 2021. Potential dam breach analysis and flood wave risk assessment using Hec-RAS and remote sensing data: A multicriteria approach. *Water*, 13 (3), 364.

- Rajkhowa, S. & Sarma, J., 2021. Climate change and flood risk, global climate change. Global climate change. Elsevier, 321-339.
- Rehman, S., Hasan, M.S.U., Rai, A.K., Rahaman, M.H., Avtar, R. & Sajjad, H., 2022. Integrated approach for spatial flood susceptibility assessment in bhagirathi sub-basin, india using entropy information theory and geospatial technology. Risk Analysis.
- Roy, P., Pal, S.C., Chakraborty, R., Chowdhuri, I., Malik, S. & Das, B., 2020. Threats of climate and land use change on future flood susceptibility. Journal of Cleaner Production, 272, 122757.
- Saber, M., Boulmaiz, T., Guermoui, M., Abdrabo, K.I., Kantoush, S.A., Sumi, T., Boutaghane, H., Nohara, D. & Mabrouk, E., 2021. Examining lightgbm and catboost models for wadi flash flood susceptibility prediction. Geocarto International, 1-26.
- Sachdeva, S. & Kumar, B., 2022. Flood susceptibility mapping using extremely randomized trees for assam 2020 floods. Ecological Informatics, 67, 101498.
- Saha, T.K., Pal, S., Talukdar, S., Debanshi, S., Khatun, R., Singha, P. & Mandal, I., 2021. How far spatial resolution affects the ensemble machine learning based flood susceptibility prediction in data sparse region. Journal of Environmental Management, 297, 113344.
- Sahana, M. & Patel, P.P., 2019. A comparison of frequency ratio and fuzzy logic models for flood susceptibility assessment of the lower kosi river basin in india. Environmental Earth Sciences, 78, 1-27.
- Swain, K.C., Singha, C. & Nayak, L., 2020. Flood susceptibility mapping through the gis-ahp technique using the cloud. ISPRS International Journal of Geo-Information, 9 (12), 720.
- Talukdar, S., Ghose, B., Salam, R., Mahato, S., Pham, Q.B., Linh, N.T.T., Costache, R. & Avand, M., 2020. Flood susceptibility modeling in teesta river basin, bangladesh using novel ensembles of bagging algorithms. Stochastic Environmental Research and Risk Assessment, 34, 2277-2300.
- Tansar, H., Babur, M. & Karnchanapaiboon, S.L., 2020. Flood inundation modeling and hazard assessment in lower ping river basin using mike flood. Arabian Journal of Geosciences, 13, 1-16.
- Tehrany, M.S., Pradhan, B. & Jebur, M.N., 2014. Flood susceptibility mapping using a novel ensemble weights-of-evidence and support vector machine models in gis. Journal of hydrology, 512, 332-343.
- Tien Bui, D., Ho, T.-C., Pradhan, B., Pham, B.-T., Nhu, V.-H. & Revhaug, I., 2016. Gis-based modeling of rainfall-induced landslides using data mining-based functional trees classifier with adaboost, bagging, and multiboost ensemble frameworks. Environmental Earth Sciences, 75, 1-22.
- Wang, X. & Xie, H., 2018. A review on applications of remote sensing and geographic information systems (gis) in water resources and flood risk management. Water, 10 (5), 608.
- Wang, Y., Hong, H., Chen, W., Li, S., Panahi, M., Khosravi, K., Shirzadi, A., Shahabi, H., Panahi, S. & Costache, R., 2019. Flood susceptibility mapping in dingnan county (china) using adaptive neuro-fuzzy inference system with biogeography based optimization and imperialistic competitive algorithm. Journal of environmental management, 247, 712-729.
- Yaseen, A., Lu, J. & Chen, X., 2022. Flood susceptibility mapping in an arid region of pakistan through ensemble machine learning model. Stochastic Environmental Research and Risk Assessment, 36 (10), 3041-3061.

A MULTISCALE GEOMATIC APPROACH FOR THE SURVEY OF HISTORIC CENTRES MAIN STREETS: THE CASE STUDY OF CAPITIGNANO, ITALY

Giovanni MATALONI¹, Donato PALUMBO¹, Massimiliano PEPE¹ , Claudio VARAGNOLI¹ 

DOI: 10.21163/GT_2023.182.08

ABSTRACT:

The aim of this research is the identification of geomatics techniques and methods capable of representing historic centres in a rapid, detailed and accurate manner. Indeed, historic centres are a cultural heritage asset to be preserved, protected and conserved for future generations, taking into account the history of a community. The paper describes a geomatics methodology applied to the case study of Capitignano (Italy), one of the municipalities that was affected by the 2009 earthquake that involved numerous historic centres causing extensive damage, not only in terms of human lives but also to the cultural heritage. The integration of geomatics techniques made it possible to obtain a georeferenced point cloud that is particularly useful for the description of buildings in historic centres, both at the urban scale and at the scale of individual artefacts. In addition, it was also possible to produce orthophotos with a high geometric resolution that made it possible to identify lesions in structures quickly and accurately.

Key-words: 3D survey, TLS, Geomatics, Historical center, Conservation, 3D model

1. INTRODUCTION

Multiscale territorial knowledge is an important tool for the protection and conservation of historic centres (Pepe et al., 2020; Fiorini et al., 2022); digital survey and 3D representation are the first step for the implementation of cultural heritage protection and conservation activities (Costantino et al., 2016). Nowadays, new methods and techniques for geomatics surveying are emerging to digitally describe historic centres (Tenedório et al., 2016) and, more generally, cultural heritage (Bitelli et al., 2017; Pepe et al., 2022). Especially for historical centres characterised by multiple risk factors, such as the seismic one, a detailed survey of characteristic elements and spatial relations with other buildings play a fundamental role. In fact, Italy is characterised by insisting on a territory at seismic risk; from north to south, mainly following the Apennine ridge, earthquakes cyclically occur that strongly damage entire geographical areas, putting the lives of hundreds of people at risk (Bini and Bertocci, 2017). Therefore, the realisation of an accurate 3D survey makes it possible to analyse the criticalities present on structures and, consequently, to identify measures aimed at protecting and safeguarding historical centres.

3D models can be performed using image-based 3D modelling or range-based modelling (RBM) (Luhmann et al., 2019). In this paper, we will use an approach based on the use of RBM, which provide a highly detailed and accurate representation of a 3D object or structure. An example of an active sensor is the terrestrial laser scanner (TLS), which enables the rapid acquisition of 3D point clouds in an accurate and detailed manner (Elbshbeshi et al., 2023). For this reason, the TLS is commonly used in construction, architecture and engineering for precise measurements of buildings, as shown in Liu et al., 2023.

¹“G. d’Annunzio” University of Chieti-Pescara, Viale Pindaro, 42, 65127 Pescara, Italy.

giovanni.mataloni@unich.it, archi.palumbo@gmail.com, claudio.varagnoli@unich.it,

*Corresponding author massimiliano.pepe@unich.it

TLS offers many advantages with respect to other surveying techniques, acquisition speed, reliability of data, etc. and it allows to obtain point clouds even with high accuracy, even up to a few millimetres (Ebolese et al., 2019). Furthermore, 3D lasers are now available on the market with different features that can be easily adapted to each application (Costantino et al., 2022). The output of a scan is in general a point cloud of n observations consisting of 3D positions $(x_i, y_i, z_i)_{i = 1 \dots n}$ of each point in a Cartesian coordinate system with the origin in the lasers canner centre, as well as an uncalibrated intensity value of the reflected light.

The TLS uses these principles; time-of-flight (TOF) and phase-shift (PS). In the TOF, a short laser pulse is emitted towards the target and reflected from the surface; the scanner detector measures the difference of the sending and arrival time. In the PS measurement method, the distance is determined by the phase difference between the sent and received waveforms (Soudarissanane et al., 2021; Costantino et al., 2021).

The paper illustrates an urban survey experience aimed at the preparation of multi-scalar 3D digital models of the territory of Capitignano (Italy), one of the municipalities included in the crater of the 2009 L'Aquila earthquake, which not only caused painful events, but also took on the connotations of a destructive event for the historical and artistic identity of a territory (Varagnoli et al., 2009).

2. METHOD

Architectural and urban surveying in extensive post-earthquake areas, such as the urban centre of Capitignano, implies carrying out survey activities on a wide variety of inhomogeneous artefacts, with different problems, related for example to: the 'state of health' of the structures; the limited accessibility; the difference in survey scale, where it is not possible to proceed according to standardised operational and methodological schemes. The great diversification of scale is often found within the same site, implying the need to use more than one surveying instrument to survey and control them. The knowledge of the current state, conservation and valorisation, involve document-based interventions that can affect both the construction aspects of individual buildings and those related to the urban form.

The process that leads to the construction of the model can be summarised in the following steps: i) planning of survey activities; ii) geodetic framing and topographical survey at different scales; iii) laser scanner survey; iv) post-processing of geomatic data and identification of critical issues on structures.

3. CASE STUDY

The present study concerns the territory of the Municipality of Capitignano (Italy), which is composed of six hamlets: Aglioni, Colle noveri, Mopolino, Pag-Rovagnano, Paterno, Sivignano (**Fig.1**). In fact, the 2009 earthquake with epicentre in Amatrice (Italy) caused extensive damage to the public and private building heritage, both in the hamlets and in the historical centre, where there are important examples of historical buildings such as Palazzo Ricci, rebuilt between 1783 and 1839, and the adjacent Church of San Domenico built in 1579 (Varagnoli, 2015).

Moreover, the earthquake affected not only the heritage in its historical strongholds, but the entire housing fabric, rich in stratified layers from the various eras. Consequently, the identification of a methodology capable of representing the heritage of historic centres in a detailed, timely and precise manner assumes an important role.

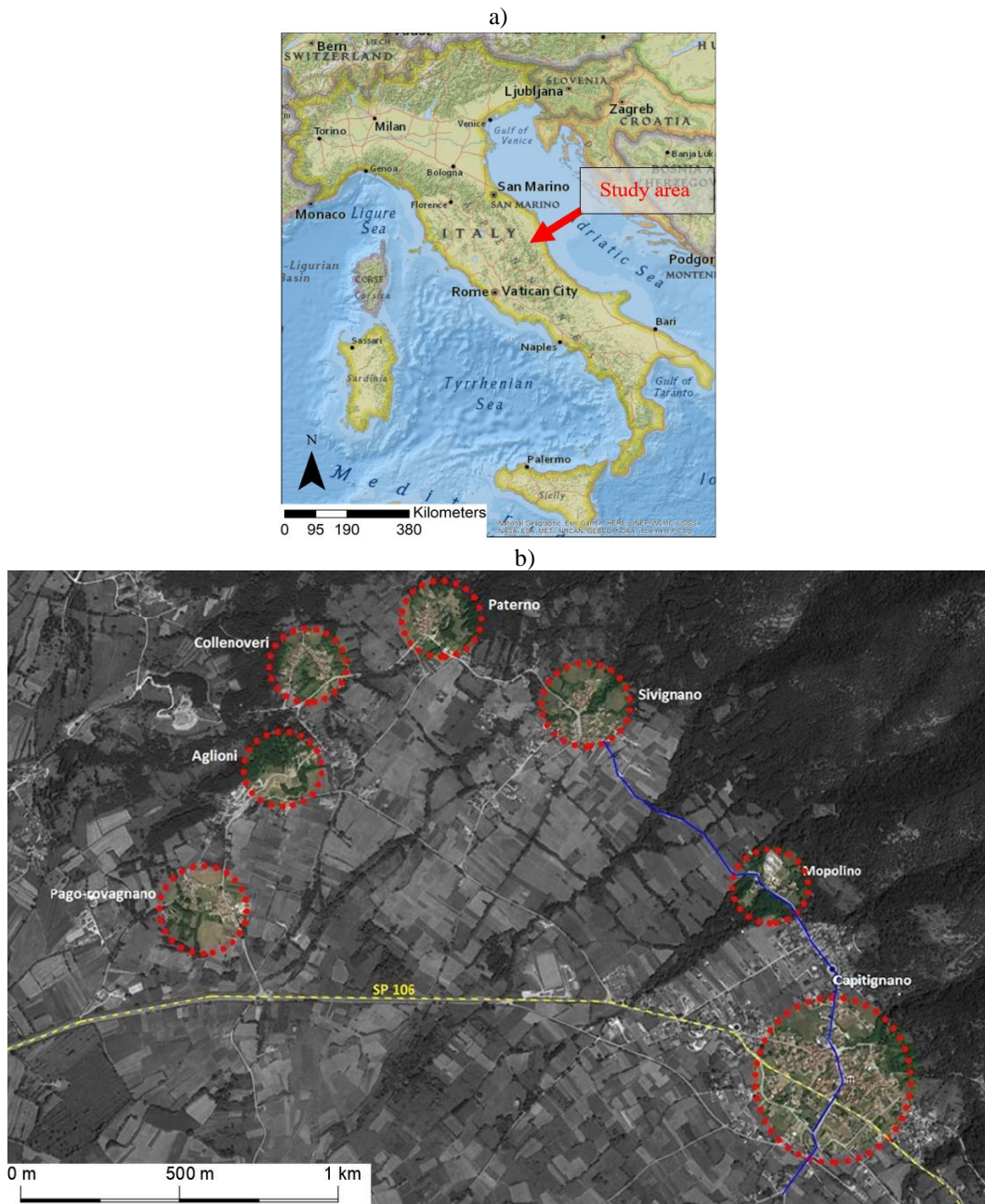


Fig.1 Cartographic outline (a) and identification of the six hamlets that make up the Municipality of Capitignano (b).

3.1. Planning of survey activities

Over the years, the study of architecture, historical centres, art and architectural artefacts has been characterised with multiple methodologies, both theoretical and technological. The intercommunication between the different surveying techniques provides indispensable elements of control and completion. In the light of the problems outlined above, it was considered that the

use of the TLS technique supported by the established topographic techniques was particularly suitable for obtaining an exhaustive documentation of the heritage in a very rapid and economical manner. In planning the survey, account was taken of the indications provided by the 'Struttura Tecnica di Missione-STM' in the draft special specifications which represent an excellent contribution for both technicians and administrations in supporting the municipalities affected by the earthquake of 6 April 2009. The survey of the municipality of Capitignano is more concerned with the main axis of the village that connects the municipality to the six hamlets, up to interior details of the church of San Domenico built in the highest part of Capitignano. In planning the survey, several difficulties were taken into account, including:

- The vastness and fragmentation of the areas to be surveyed;
- The framing of the six hamlets and the village in a single reference system;
- The need to survey different areas, both on an urban scale (building encumbrances) and on an architectural scale (decorative details);

The surveying operations were preceded by careful planning that included the identification of homogeneous zones, and the consequent choice of suitable instrumentation. In particular, an ordered series of methodologies and procedures distinguished in the following phases were planned and implemented (see Fig. 2):

- GNSS geodetic survey (Leica ATX1230);
- Total station survey (Leica TCR 705);
- TLS long range survey (Topcon GLS1000);
- TLS medium range survey (Faro focus x130);
- Post processing of geomatics data.

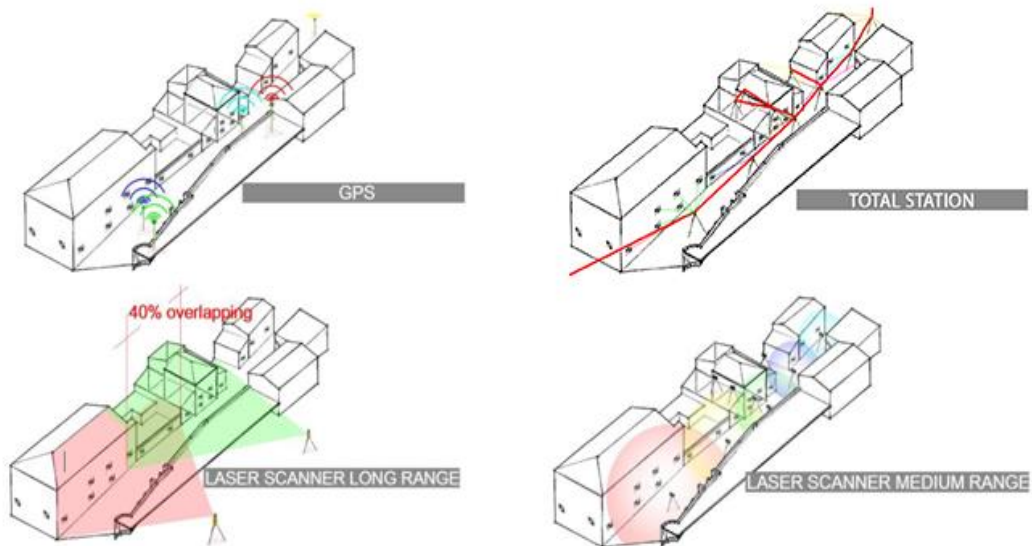


Fig. 2. Outline of the survey techniques used.

3.2. Geodetic survey and topographical survey

In order to unify the surveys of the various hamlets of the Municipality of Capitignano in a single reference system, it was decided to carry out a GNSS survey. The survey phase was preceded by a careful selection of the nearest points of the regional geodetic network; the points of the network thus identified will support the secondary network acquired with the GNSS. In particular, three points of the regional network were taken into consideration that frame all the areas to be surveyed. For the survey of the main street of Capitignano, a Leica ATX GNSS was used, taking care, after appropriate reconnaissance, to position the points of the secondary network so that they are clearly

visible from the satellites and without reception obstacles. The points thus chosen are of service to the subsequent survey phases, both with the total station and the laser scanner, thus providing a common reference system for the various survey techniques and the six hamlets of the municipality. The result obtained from this survey methodology is a network of georeferenced three-dimensional points, homogeneously distributed over the survey area. Additional control points were materialised through the use of targets appropriately registered with the total station. The correct distribution of the targets in view and within the range of the instrumentation, were used for the integration of the surveys performed with the total station, and the surveys performed with the laser sensors. Two types of targets were prepared, two-dimensional flat targets and three-dimensional spherical targets. The flat targets consist of appropriately sized chequered sheets imprinted on the surfaces, while the spherical three-dimensional targets consist of spheres with a calibrated diameter of 145 mm. Both spherical and flat targets are recognised semi-automatically by specific software, thus constituting a true dialogue and control tool for the various measurement techniques. The GNSS survey was followed by the topographic, urban and detailed survey phase. The topographic survey was carried out using a Leica TCR 705 total station (angular accuracy 5" -1.5 mgon and d Electrooptic Distance Meter - EDM measuring program: Standard measurement of 2 mm + 2 ppm while infrared Tape of 5 mm + 2 ppm). The first step was designing the topographic network and, of consequence, identify the closed traverse. In this phase, flat targets were surveyed for the orientation of the scans, detailed points for the definition of the infrastructure networks (manholes, light poles, etc.) and for the 3D wireframe plano volumetric model. Lastly, each station of the topographic network was georeferenced using the GNSS secondary network Ground Control Points (GCPs).

3.3. TLS Survey

Once obtained the coordinates of GCP and targets by GNSS, the next survey phase involves the use of TLS instrumentation. For such a diversified urban scale survey, the use of two different types of terrestrial laser scanners was planned, one of the medium range type and another of the long range type. The long-range type laser scanner used is a Topcon GLS 1000 with a range of approximately 300 metres; the main feature of this latter TLS is:

- 3000 precise points/second scan rate;
- 330m maximum range at 90% reflectivity;
- 150m maximum range at 18% reflectivity;
- 4mm accuracy from 1m to 150m;
- 6" horizontal and vertical angular accuracy.

This type of instrumentation lends itself well to surveys of large portions of the territory, while it is slow and not very versatile for architectural surveys and surveys of small environments, having as a disadvantage the reduced camera angle (70 degrees). In particular, it was decided to carry out the survey with this type of instrumentation (Topcon GLS 1000), positioning the laser scanner at the furthest points of the country, so as to obtain a georeferenced point cloud using the previous GNSS points. The medium-range laser scanner used is a Faro Focusx130, which is capable of measuring up to speeds of 976,000 points/sec and up to a range of 130 m; the system also includes an integrated colour camera, equipped with automatic parallax-free colour overlay of 70 megapixels. By the use of this latter TLS, it is possible to obtain a 3D coloured point cloud in easy and quick way. The individual scans were joined together using both flat targets whose coordinates are known, and spherical targets, whose centre of the sphere is taken into account. The scans were carried out by imposing fixed quality and resolution parameters in homogenous areas in order to achieve uniformity in the post-processing of the data.

Figure 3 shows the integration of the different geomatics techniques used for the surveys along the street of Capitignano.

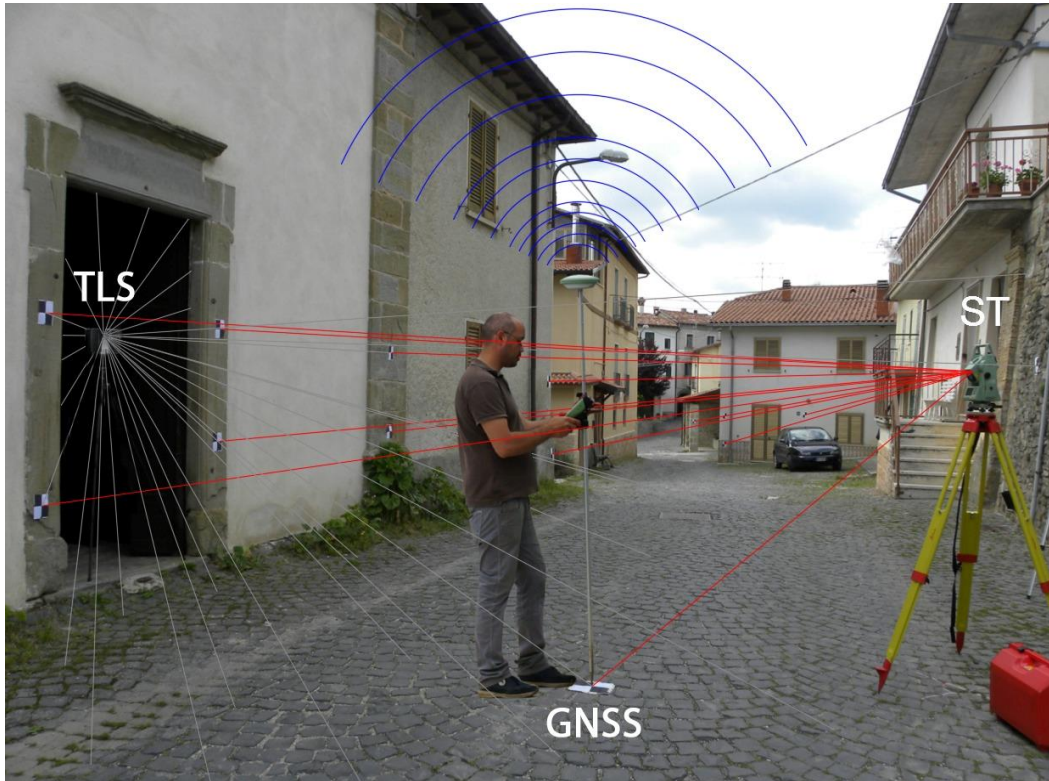


Fig. 3. Survey phases with GNSS, TLS and Total Station.

3.4. Post-processing of data

The post-processing of the data followed the same hierarchical line as the acquisition phases. Initially, the data obtained from the GNSS survey were processed to form a mathematical model, i.e. a table of data that was transformed into a geometric model by creating a general plano-altimetric table.

The processing of the data obtained from the total station survey involved the creation of two networks (primary and secondary) giving a higher hierarchical value to the primary network which was in turn linked to the GNSS survey. The result of this first processing phase is a three-dimensional and georeferenced planimetry, not only of the main village, but also of its hamlets. The plane coordinates thus extrapolated were used for the point cloud registration phase carried out with Topcon's Long range laser scanner.

Using the same methodology as for the topographical network, the wide-range scans were initially recorded using the coordinates of the targets and GNSS points whose coordinates were known, and then the scans made with the medium-range laser scanner were recorded using GNSS coordinates. The data obtained from this processing is of such a high consistency that, in addition to computers and software with great computing power, it is necessary to divide the work into several stages.

At the end of the process, it is possible to obtain a georeferenced point cloud:

4. RESULTS

The methodological approach described in the paper made it possible to obtain accurate and detailed models of the historic city centre examined. In particular, the output of the point cloud was generated in UTM33-ETRF2000 (EPSG:32633) cartographic system and in LAS format (a file format for the interchange of 3-dimensional point cloud data). The ellipsoidal heights were subsequently transformed into orthometric height by means by the Italian Military Geographic Institute (IGMI) grid *.gk2 based on ITALGEO geoid model (Barzaghi et al., 2007) and use of suitable software able to perform this task. **Figure 4** shows the high degree of detail of the urban-scale 3D models. The main road was divided into regular and morphology-related areas ensuring the same quality and resolution parameters in order to obtain homogeneous and easily manageable point clouds for the different users who can collaborate on the project. Furthermore, the several fractions were processed individually considering the number of scans.

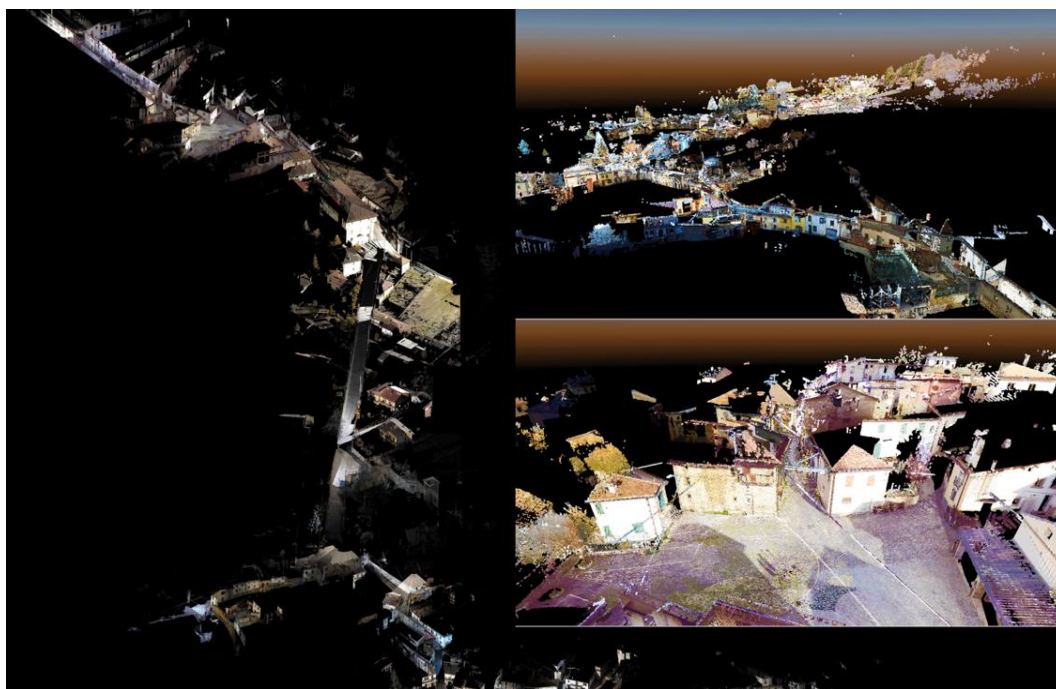


Fig. 4. 3D point cloud of the part of main street.

In addition, at the scale of the individual building, it was possible to obtain detailed models describing the geometry of the structure; indeed, thanks to the data acquisition with the internal camera present in the TLS, it was possible to obtain a coloured dense point cloud. One of the architectural emergencies in the area that has been noted is the Church of San Domenico in the hamlet of Mopolino. It was built in 1579 and suffered significant damage in the 1703 earthquake; in 1839, the building was restored to a design by Giuseppe Valadier, who worked at the Bishopric of Rieti (Varagnoli, 2021). A representation by point cloud of this church is showed in **figure 5a, 4b and 4c**. The further processing of the geomatics data makes it possible to extrapolate both horizontal and vertical sections of the entire urban complex, in order to be able to know, in addition to the geometries, any deformations due to the earthquake disruptions. Once the point cloud was obtained, it was possible to build a mesh model and, of consequence, to obtain a representation of a continuous surface consisting entirely of triangular facets (a triangle mesh). Subsequently, identifying a suitable plane of projection, it was possible to build the orthophoto of the area taken into consideration. On the orthophotos, it was possible to identify the areas with lesions by photointerpretation and analysis

of an expert in the field of facility monitoring. For example, in **figure 5d** are showed in red colour the areas with lesions on the vault of the church of San Domenico.

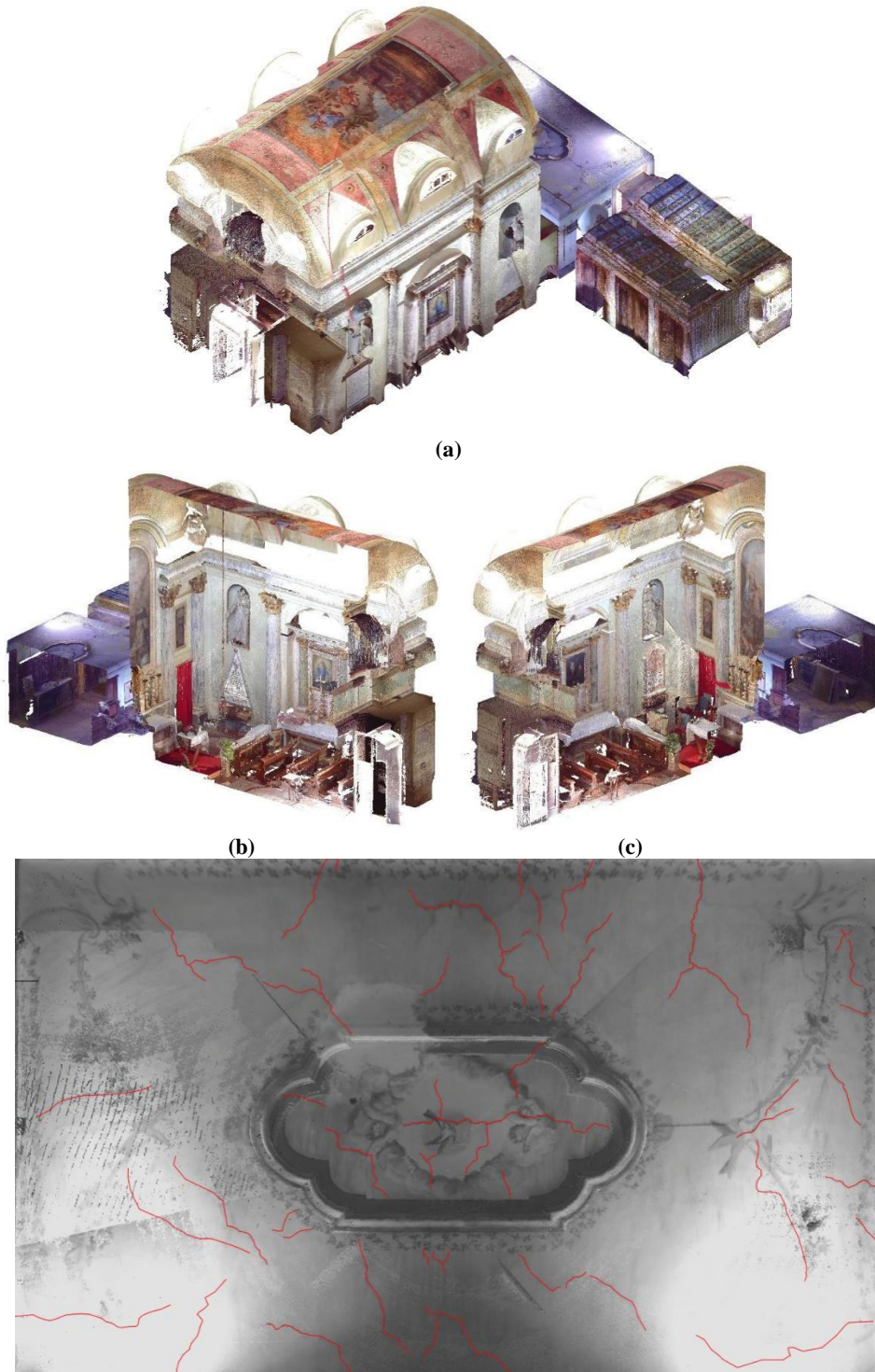


Fig. 5. 3D models of the Church of San Domenico: axonometric view of the point cloud (a, b, c) and orthophotos with indications of critical areas (d).

5. CONCLUSIONS

Over the years, the study of architecture, of historical centres, has been adorned with multiple methodologies, both theoretical and technological, which allow realistic 3D models to be obtained. The approach to the Capitignano case study, while addressing different urban scale survey problems, from a geomatics point of view, involved the use of techniques such as TLS, GNSS and total station. An interesting aspect discussed in the paper concerns the integration of the various geomatics techniques, which has allowed not only the integration of the various techniques, but also the unification in a single reference system of the hamlets located near the historic centre.

All the documentation produced thus represents an important support for future projects of restoration, maintenance, redevelopment and enhancement of the entire urban context and its individual constituent architectural entities. The creation of a database can therefore be used for an eventual cartographic update of the area subjected to the integrated survey.

REFERENCES

- Barzaghi, R., Borghi, A., Carrion, D., & Sona, G. (2007). Refining the estimate of the Italian quasi-geoid. *Bollettino di Geodesia e Scienze Affini*, 3, 145-160.
- Bini, M., & Bertocci, S. (2017). Il rilievo per il restauro dei tessuti storici, in contesti colpiti da eventi sismici. *DisegnareCON*, 10(18), 0-1.
- Costantino, D., Settembrini, F., Pepe, M., & Alfio, V. S. (2021). Develop of new tools for 4D monitoring: Case study of Cliff in Apulia Region (Italy). *Remote Sensing*, 13(9), 1857.
- Costantino, D., Angelini, M. G., & Baiocchi, V. (2016). Integrated surveying for the archaeological documentation of a neolithic site. *Geographia Technica*, 11(2).
- Costantino, D., Vozza, G., Pepe, M., & Alfio, V. S. (2022). Smartphone LiDAR Technologies for Surveying and Reality Modelling in Urban Scenarios: Evaluation Methods, Performance and Challenges. *Applied System Innovation*, 5(4), 63.
- Bitelli, G., Dellapasqua, M., Girelli, V. A., Sbaraglia, S., & Tinia, M. A. (2017). Historical photogrammetry and terrestrial laser scanning for the 3D virtual reconstruction of destroyed structures: a case study in Italy. *The international archives of the photogrammetry, remote sensing and spatial information sciences*, 42, 113-119.
- Ebolese, D., Lo Brutto, M., & Dardanelli, G. (2019). 3D reconstruction of the roman domus in the archaeological site of Ilyibaeum (marsala, italy). *International Archives of the Photogrammetry, Remote Sensing & Spatial Information Sciences*.
- Elbshbeshi, A., Gomaa, A., Mohamed, A., Othman, A., Ibraheem, I. M., & Ghazala, H. (2023). Applying geomatics techniques for documenting heritage buildings in Aswan region, Egypt: A Case study of the Temple of Abu Simbel. *Heritage*, 6(1), 742-761.
- Fiorini, G., Friso, I., & Balletti, C. (2022). A Geomatic Approach to the Preservation and 3D Communication of Urban Cultural Heritage for the History of the City: The Journey of Napoleon in Venice. *Remote Sensing*, 14(14), 3242.
- Liu, J., Azhar, S., Willkens, D., & Li, B. (2023, April). Static Terrestrial Laser Scanning (TLS) for Heritage Building Information Modeling (HBIM): A Systematic Review. In *Virtual Worlds* (Vol. 2, No. 2, pp. 90-114). MDPI.
- Luhmann, T., Robson, S., Kyle, S., & Boehm, J. (2019). Close-range photogrammetry and 3D imaging. In *Close-Range Photogrammetry and 3D Imaging*. de Gruyter.
- Pepe, M., Costantino, D., Alfio, V. S., Angelini, M. G., & Restuccia Garofalo, A. (2020). A CityGML multiscale approach for the conservation and management of cultural heritage: The case study of the old town of Taranto (Italy). *ISPRS International Journal of Geo-Information*, 9(7), 449.

- Pepe, M., Alfio, V. S., Costantino, D., & Herban, S. (2022). Rapid and Accurate Production of 3D Point Cloud via Latest-Generation Sensors in the Field of Cultural Heritage: A Comparison between SLAM and Spherical Videogrammetry. *Heritage*, 5(3), 1910-1928.
- Soudarissanane, S., Lindenbergh, R., Menenti, M., & Teunissen, P. (2011). Scanning geometry: Influencing factor on the quality of terrestrial laser scanning points. *ISPRS journal of photogrammetry and remote sensing*, 66(4), 389-399.
- Tenedório, J. A., Estanqueiro, R., Matos Lima, A., & Marques, J. (2016). Remote sensing from unmanned aerial vehicles for 3D urban modelling: case study of Loulé, Portugal. In *Back to the Sense of the City: International Monograph Book* (pp. 1118-1128). Centre de Política de Sòl i Valoracions.
- Varagnoli, C. (2009). Tecniche costruttive tradizionali e terremoto. *Ricerche di storia dell'arte*, 32(3), 65-0.
- Varagnoli, Claudio, Valadier tra i monti d'Abruzzo: la chiesa di San Domenico per la famiglia Ricci a Mopolino di Capitignano. 2022, In: *Palladio*, Nuova serie, anno 35, n. 68 (luglio-dicembre 2021), pp 57-76.
- Varagnoli, Claudio, Dal terremoto al restauro: il palazzo Ricci a Capitignano (2015) In: *Quaderni dell'Istituto di Storia dell'Architettura*, n.s., 63 (2014/2015), pp. 69-80.

THAI EASTERN ECONOMIC CORRIDOR DROUGHT MONITORING USING TERRA/MODIS SATELLITE-BASED DATA

Phaisarn JEEFOO¹ 

DOI: 10.21163/GT_2023.182.09

ABSTRACT:

One of the main natural disasters that has an impact on the environment and economy of nations throughout the world is drought. It has an impact on the local vegetation's state. The study's main goal was to look for years of severe drought by looking at Thailand's Eastern Economic Corridor (EEC). To determine the vegetation condition in the research area between 2017 and 2021, the Normalized Vegetation Index (NDVI) from Terra/MODIS data was employed. The area with the NDVI difference from the average value of NDVI during the same time period was examined using the Standardized Vegetation Index (SVI). Through the vegetation index, the drought can be reflected in this. According to the study, the highest drought area covered an area of 216.36 km² in 2017. This was followed by years 2019 and 2020, which each covered an area of 212.65 km², 211.23 km², 197.09 km², and 178.07 km². Additionally, a statistical analysis of the monthly correlation between the SVI (independent variable) and rainfall (dependent variable) over the course of the five years revealed that the coefficient of determination R² was 0.8018 in 2020, 0.6819 in 2021, 0.6262 in 2017, 0.5772 in 2018, and 0.5108 in 2019. The methodology can be obtained and used by other departments to assess and forecast drought in other regions of Thailand and other nations.

Key-words: Drought, Terra/MODIS, NDVI, SVI, Thai Eastern Economic Corridor.

1. INTRODUCTION

One of the worst weather-related catastrophes is drought. For drought management, accurate information about its length, spatial coverage, intensity, and impact is crucial. Especially in the agricultural sector, droughts frequently result in the loss of livelihoods along with various negative environmental effects (Willibroad & Sang-Il, 2019; Abbas et al., 2022). Identification of drought trends could be utilized as a strategy for monitoring and sustainable management because marshes and vegetation next to inland water bodies depend on the water supply within their ecosystem (Villarreal et al., 2016). A drought was a natural water shortage brought on by erratic and delayed rain. Devastated crops, starvation, conflicts, and wars are a few effects of drought (Su et al., 2017). When the demand for water exceeds the supply, a drought occurs. It is believed that among all dangers, natural disasters have the greatest effects on people (Qin et al., 2021). That had an impact on lifestyle and the global economic system, with emphasis on Thailand (Gomasathit et al., 2015). Therefore, it is crucial to consider rainfall while looking for relationships between it and the spectral index. Additionally, the correlation between rainfall and the spectral index is a key metric for identifying drought zones in order to analyze the length of rainfall that impacts vegetation (Rimkus et al., 2017). Rainfall was the primary source of the drought in Thailand, which had been an ongoing issue, particularly in the northern east and western south. Every year, there has been a lack of rain, especially from winter to summer (Thai Meteorological Department, 2021). Although drought is not a new problem, it recurs every year, particularly in the north and east of the country. Low precipitation levels, which frequently recur every cold season until hot season, are the main cause of drought. Water scarcity has an impact on vegetation phenology, which will then reveal the amount of drought severity (Laosuwan et al., 2016).

¹ Research Unit of Spatial Innovation Development (RUSID), Geographic Information Science, School of Information and Communication Technology, University of Phayao, Thailand, phaisarn.je@up.ac.th.

Modern and cutting-edge technology, remote sensing is particularly useful for predicting natural disasters including flooding, drought, sea level rise, changes in land use and cover, and so forth (Uttarak & Laosuwan, 2017a). Remote sensing-based indices frequently make use of observations from a variety of spectral bands, each of which offers a unique perspective on the surface's state at various periods. Standardized Vegetation Index (SVI) and Normalized Vegetation Index (NDVI) are two remote sensing-based indicators (Rotjanakusol, T. & Laosuwan, 2018; Buma & Sang-II, 2019). Data from satellites that have undergone image processing and mathematical calculations will clearly show the study's specifics. For instance, the NDVI is determined by the variations in red and near-infrared wavelengths (Kaspersen et al., 2015; Ganie & Nusrath, 2016). To determine the state of the vegetation in the research area, NDVI from MODIS data was employed. The area with the NDVI difference from the average value of NDVI over the same time period was also examined using SVI. Through the vegetation index, the drought can be reflected in this. The study has used an analysis technique to determine how a drought develops through time and space. Effectively identifying the origin and type of drought was possible thanks to several satellite photos collected from MODIS data. The preparation of the drought mitigation in the area for the concerned agencies will benefit from this.

In addition, the SVI, which is based on calculations from 16-day NDVI data, represents the possibility of vegetation condition deviation from normal. The goal of this work was to standardize, by time of year, the NDVI to enhance drought-monitoring techniques. For the three provinces or Eastern Economic Corridor (EEC) of Thailand, the study used series of MOD13Q1 MODIS satellite pictures over a 5-year period (2017, 2018, 2019, 2020, and 2021), (Fig. 1).

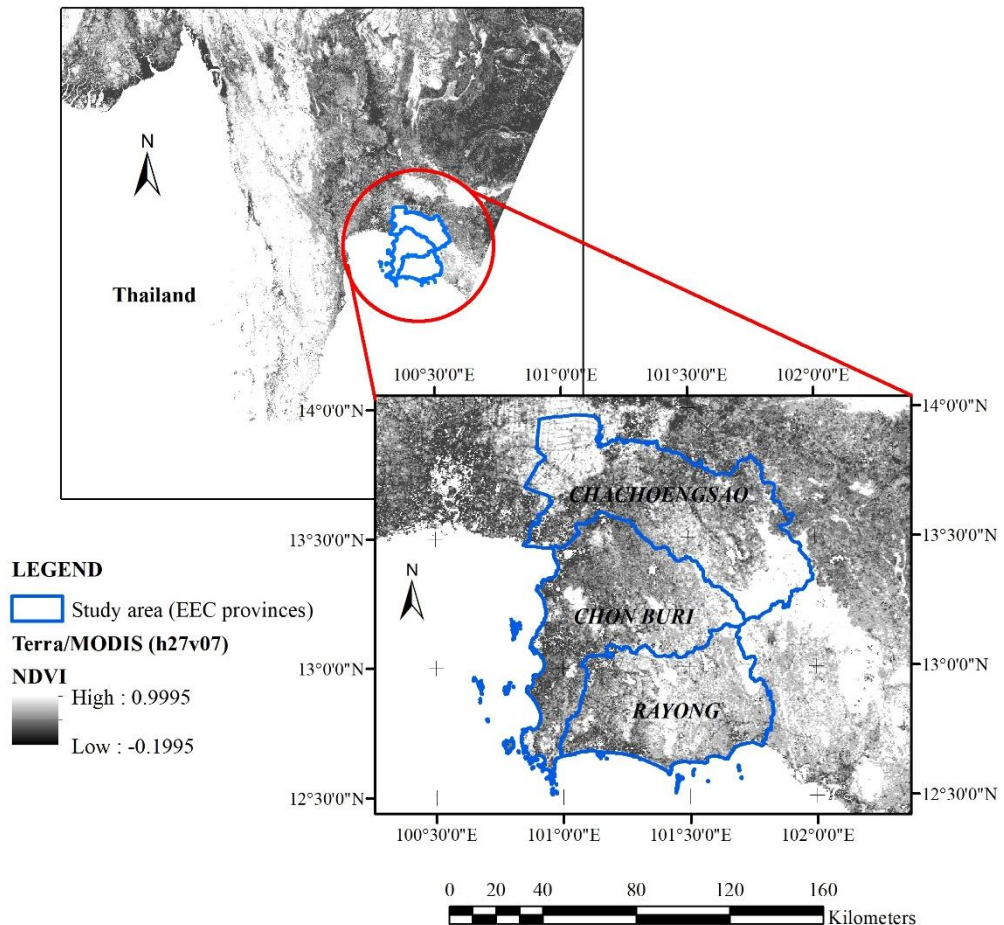


Fig. 1. The study area: Eastern Economic Corridor of Thailand (EEC).

2. STUDY AREA

The well-known Eastern Seaboard Development Program, which has supported Thailand as a driving force for industrial output in Thailand for more than 30 years, is being revitalized and enhanced as part of the Thailand 4.0 scheme's EEC development plan. The Eastern Economic Corridor Office of Thailand (the EECO) has been tasked with leading the nation's investment in advancing innovation and cutting-edge technology for the next generation under this program. Thailand's investment in the region's physical and social infrastructure will significantly advance and change under the direction of the EEC Development Plan. The first focus of the EEC project will be on three eastern provinces: Chachoengsao, Chonburi, and Rayong (**Fig. 1**). The EEC is 120 km east of Bangkok, and covers an area of 13,418 km² with geographical location between 12°30'0''N to 14°0'0''N and 100°30'0''E to 102°0'0''E. In terms of climate characteristics, the region experiences a tropical monsoon, with sea breezes blowing all year round. The temperature is moderately warm. Rainfall is heavy from May to October every year in the cool coastal regions during the rainy season. With an approximate elevation of 1,050 meters above mean sea level, it is primarily covered by mountainous terrain.

3. DATA AND METHODS

3.1. Data from Terra/MODIS satellite

Data on natural resources will be monitored and examined by the Terra/MODIS satellite. With a spatial resolution of 250 to 1,000 meters and 36 spectral bands, the sweep width is approximately 2,330 kilometers. Within two days, the Terra/MODIS satellite collects worldwide digital data. Terra/MODIS data (Buma & Sang-II, 2019) are therefore suitable for tracking spatial changes that are widespread. The MOD13Q1 product (h27v07), whose NDVI data sets covered the period from 2017 to 2021, was used in this study. Data collected in each month of the years 2017, 2018, 2019, 2020, and 2021 are used to create the MOD13Q1 data. WGS84-UTM zone 47N coordinates will be used for geometric adjustment. The closest neighbor method will be used to evaluate pixel locations, and a subset of satellite data will be created that solely includes the provinces of the EEC.

3.2. Data from rainfall and temperature

In order to establish the temporal association with the SVI mean, the average monthly rainfall data for the years 2017, 2018, 2019, 2020, and 2021 was used. For data collection, only Thai Meteorological Department (TMD) ground stations that monitor rainfall in the eastern region were utilized. Procedures of data analysis are determined in a logical order for analyzing drought in Rayong province (**Fig. 2**).

The vegetation condition in the study region has been determined using the NDVI acquired from the MODIS data. Additionally, the SVI was utilized to evaluate the region where the NDVI value differed from the NDVI average throughout the same time period. Through the vegetation index, the drought can be reflected in this. The study has used an analysis technique to determine how a drought develops through time and space. Effectively identifying the origin and type of drought was possible thanks to several satellite photos collected from MODIS data. The preparation of the drought mitigation in the area for the concerned agencies will benefit from this.

3.3. NDVI analysis

Equation 1 demonstrates that the electromagnetic reflection of RED wave and NIR wave were calculated differently.

$$NDVI = \frac{NIR-RED}{NIR+RED} \quad (1)$$

The NDVI readings ranged from -1 to +1. The NDVI displayed a negative result for the water area. The NDVI value for the land region with less vegetation was almost zero. A +1 was indicated for the green region. Because of these capabilities, NDVI was used as a tool to forecast and study changes in vegetation that were influenced by the environment (Laosuwan et al., 2016; Buma & Sang-II, 2019).

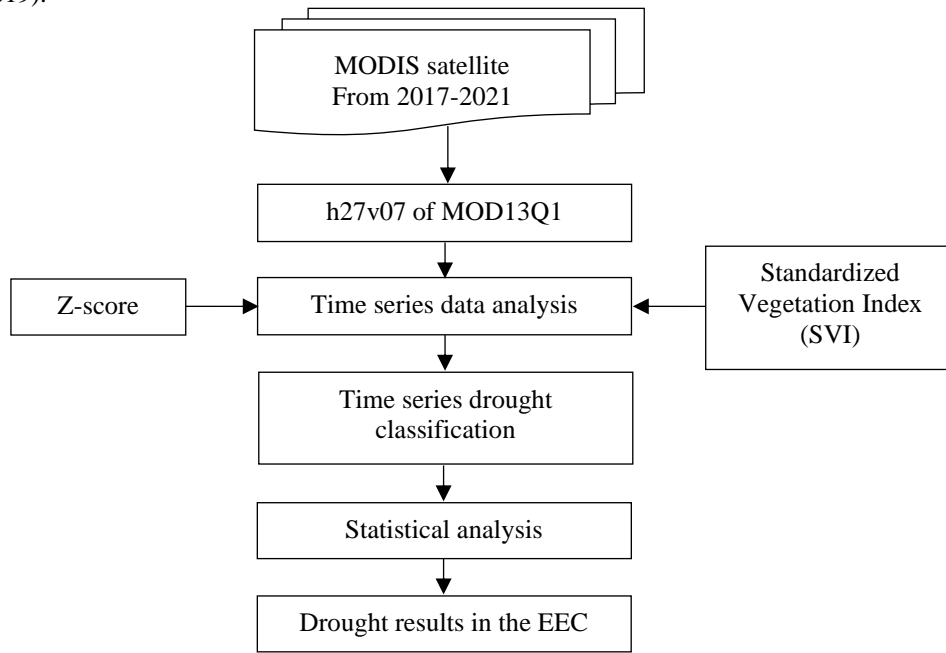


Fig. 2. Flowchart of methodology.

3.4. SVI analysis

The monthly MOD13Q1 (NDVI) data are utilized because the SVI value was derived from NDVI and because they can be a valuable indicator and are frequently used for monitoring and analyzing vegetation dynamics. The MOD13Q1 (NDVI) data's z-scores are used to calculate the SVI value for each pixel point. The standard score is generated using the NDVI of each pixel location for each season to determine the standard deviation from the mean in a unit of standard deviation. The three periods (seasons in Thailand) that make up this study's classification of the seasons are the summer (17 February to 16 May), the rainy season (17 May to 16 October), and the winter (17 October to 16 February). The specifics of the z-score analysis were shown in equation 2.

$$Z_{ijk} = \frac{NDVI_{ijk} - \overline{NDVI}_{ij}}{\sigma_{ij}} \quad (2)$$

where;

Z_{ijk} = the z-value for pixel i during week j for year k

$NDVI_{ijk}$ = the weekly NDVI value for pixel i during week j over year k

\overline{NDVI}_{ij} = the mean NDVI for pixel i during week j over n year and

σ_{ij} = the standard deviation of pixel i during week j over n years

From the equation 2, the Z_{ijk} value is a hypothesis value to be consistent with a standard normal distribution with the mean of 0 and standard deviation of 1 to examine hypothesis from pixel locations in each season of the year 2017, 2018, 2019, 2020 and 2021. The probability value of $SVI = P(Z_{ijk})$ of the standard score of NDVI to reflect the probability of plant conditions. The SVI analysis can be seen in the equation 3 (Uttaruk & Laosuwan, 2017a; Uttaruk & Laosuwan, 2019; Pachanaparn et al., 2022).

$$SVI = \frac{Z_{ijk} - Z_{ijMIN}}{Z_{ijMAX} - Z_{ijMIN}} \quad (3)$$

where;

Z_{ijk} = z-value for pixel i during week j for year k;

Z_{ijMAX} = maximum of z-value for pixel i during week j

Z_{ijMIN} = minimum of z-value for pixel i during week j

From the Equation 3, the probability of each pixel location will be shown in SVI value to recognize the greenness of plants in different seasons or different periods. The study will conduct over the 5 years periods (2017-2021) to indicate comparison of high level and low level of drought observed in the mentioned periods based on the seasons. It is an estimation of probability of current vegetation condition from previous vegetation condition. SVI value would lie above zero but lower than one ($0 < SVI < 1$) where 0 is the lowest standard score of NDVI value at a pixel location observed at a certain time of the 5 years period and 1 is the highest standard score of NDVI value at a pixel location observed at a certain time of the 5 years period.

3.5. Spatial analysis of drought

In each month of the years 2017, 2018, 2019, 2020, and 2021, the critical levels of vegetation were used to categorize the spatial study of drought intensity. There are 5 levels of SVI drought severity. **Table 1**, lists the five SVI drought levels, with the lowest level (0.00–0.05) denoting a very high drought and the highest level (0.9–1.00) denoting a very low drought.

Table 1.

SVI level, percentage of SVI and drought level.

Drought level of SVI	Percentage of SVI	Vegetation density
1.00 – 0.95	96.0% - 100%	Very high
0.95 – 0.75	76.0% - 95.0%	High
0.75 – 0.25	26.0% - 75.0%	Moderate
0.25 – 0.05	6.0% - 25.0%	Low
0.05 – 0.00	0% - 5.0%	Very low

3.6. Multi-temporal drought analysis

In this study, the average monthly rainfall data for the years 2017, 2018, 2019, 2020, and 2021 collected from TMD's rainfall measurement earth station, a total of 28 stations covering only the study area, will be analyzed with the SVI analysis results.

3.7. Statistic correlation analysis

The results of the SVI analysis and the rainfall data for the years 2017, 2018, 2019, 2020, and 2021 are shown to explain how the linear regression analysis technique was used to rectify the statistical errors. The SVI index was used to display the probabilities in the photos. Using the vegetation state from the pass, it was possible to estimate the likelihood of the current vegetation. The SVI values ranged from greater than zero to less than one ($0 < SVI < 1$). The lowest standard SVI score from photos taken in 2017 through 2021 was zero.

3.8. SVI Analysis for Drought Monitoring

The standard scores used for the SVI computation were derived using monthly SVI data for the years 2017, 2018, 2019, 2020, and 2021. The average and standard deviation for each image then needed to be determined. The standard scores for each month and year were needed for the SVI calculation, which was followed by an analysis for monthly likelihood in each image's point. By categorizing SVI values into levels, the monthly SVI maps for the years 2017, 2018, 2019, 2020, and 2021 were created.

4. RESULTS AND DISCUSSIONS

4.1. SVI analysis results

The SVI was used to track droughts by analyzing reflections of vegetation probabilities throughout a variety of time periods. Calculations were made of the SVI variations at each point and time period in each year. The findings showed that in 2017, the vegetation density ranged from 0 to 1, with the lowest, greatest, average, and standard deviation of SVI representing it.

In each season and time period, the average represented vegetation density and drought. The lowest average was 0.1252 in February, the previous winter season, and the highest average was 0.1484 in October (16/10/2017), the rainy season. In 2018, the winter season's highest average was 0.1467 while the early wet season's lowest average was 0.1140. The lowest average was 0.1262 in August during the rainy season, and the highest average in 2019 was 0.1429 in November (01/11/2019).

The winter season's highest average in 2020 was 0.2053 in December, while the winter season's lowest average was 0.1269 in February. In 2021, the early rainy season's May had the greatest average of 0.2101 and the winter season's January had the lowest average of 0.1231. The averages, SVI standard deviation, and the lowest and highest standard scores all played a role in determining the SVI variances for each season and time period. Therefore, the fifth year SVI averages could be concluded (**Fig. 3**).

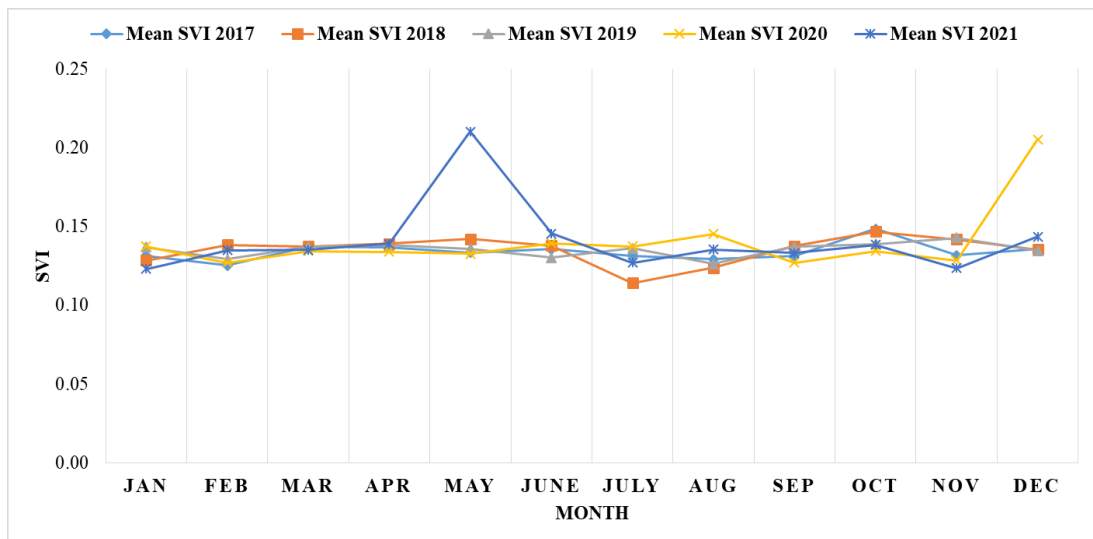


Fig. 3. Fifth year SVI averages.

The SVI variations in each period and season, which were influenced by vegetation density and rainfall, were depicted by the graphs. Results were poor from January through April during the heat. The lowest result was obtained in July 2018, and it rose to the highest level during the winter months of December 2020 and early rainy season in May 2021. Early in the winter, in October, it had begun to decline once more.

Additionally, this study's analysis of the yearly SVI included data from monthly data overlays, which allowed it to more accurately depict the spatial and temporal nature of droughts than monthly data alone. In **Fig. 4**, the year 2021 had the worst spatial drought, which was followed by the years 2018, 2020, 2019, and 2017 in that order.

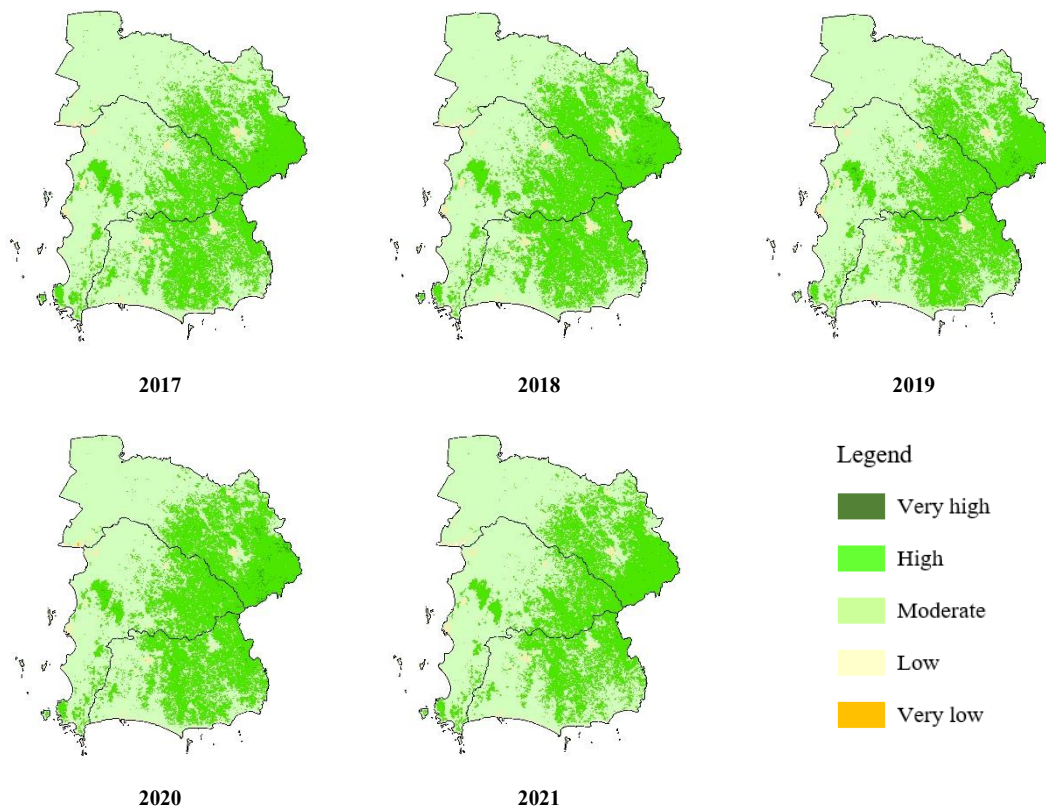


Fig. 4. SVI yearly analysis from 2017 - 2021.

4.2. Multi-Temporal analysis results

SVI monthly average and rainfall during a five-year period revealed that the SVI average's temporal variation matched the monthly rainfall; however, the change in SVI was slower than that of rainfall because vegetation only began to grow after receiving enough water for leaf formation or growth. The summary of the multitemporal drought analysis is shown in Fig 5

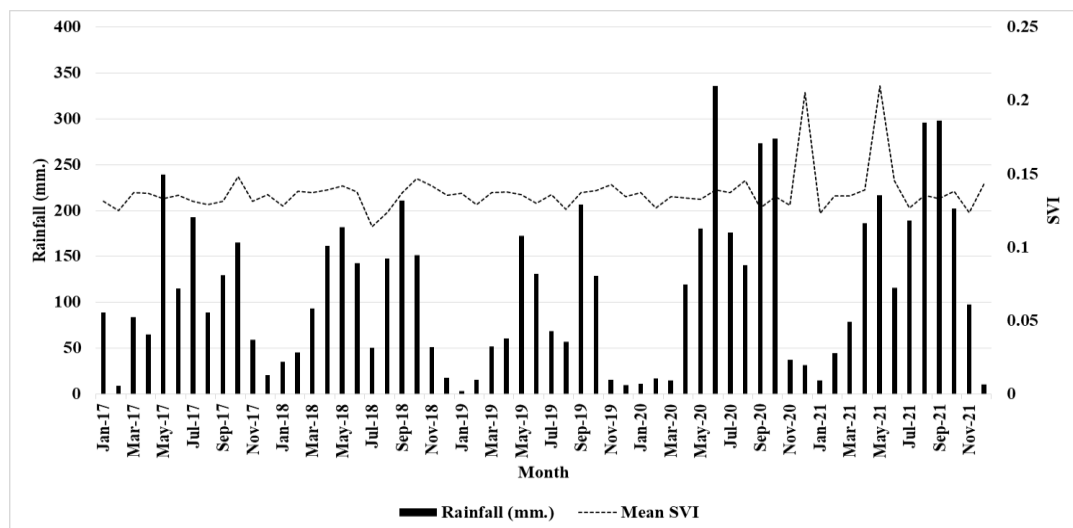


Fig. 5. Multi-temporal drought analysis.

In 2017, variations in rainfall were lowest from January to April, peaked in May, and then fell to their lowest level in October. In 2018 and 2019, variations in rainfall were lowest in January, climbed steadily, peaked in May, dropped to their lowest in July, peaked again in September, and finally decreased to their lowest in December. Rainfall variations in 2020 and 2021 were somewhat greater in January and then decreased until May, grew steadily and peaked in June, September, and October, and then steadily decreased and reached their lowest point in December.

4.3. Statistical correlation analysis results

The outcome of a statistical correlation analysis between SVI (the independent variable) and rainfall (the dependent variable) from 2017 to 2021 revealed a correlation between the two variables. The correlation equation for SVI and rainfall in 2020 is given by the statistical correlation analysis, and it is given by $y = 1623.1 \times -148.31$, with an R^2 coefficient of determination of 0.8018. The correlation equation for SVI and rainfall in 2021 was determined to be $y = 2107.5 \times -181.96$ and the coefficient of determination R^2 was found to be 0.6819. SVI and rainfall data from 2017 were statistically correlated, and the correlation equation was given as $y = 8745.2 \times -1096.6$ with an R^2 coefficient of determination of 0.6262. A correlation equation of $y = 6419.8 \times -758.51$ and a coefficient of determination of $R^2 = 0.5772$ were produced by the statistical correlation analysis results between SVI and rainfall in 2018. A correlation equation of $y = 12103 \times -1544.7$ and a coefficient of determination $R^2 = 0.5108$ were obtained by the most recent statistical investigation of the relationship between SVI and rainfall in 2019 (Table 2).

Table 2.
Statistical correlation analysis from 2017 – 2021.

Year	Correlation equation	R^2
2017	$y = 8745.2x - 1096.6$	0.6262
2018	$y = 6419.8x - 758.51$	0.5772
2019	$y = 12103x - 1544.7$	0.5108
2020	$y = 1623.1x - 148.31$	0.8018
2021	$y = 2107.5x - 181.96$	0.6819

5. CONCLUSIONS

The average SVI could be employed as a comparison operator in this study. Drought was implied by low SVI levels, and the closer to zero the value was, the worse the drought. High SVI, however, indicated abundance; the closer to 1, the greater the abundance and absence of drought. The study also discovered that the largest drought area was in 2017, covering an area of 216.36 km², followed by 2019 (212.65 km²), 2021 (211.23 km²), 2020 (197.09 km²), and 2018 (178.07 km²), respectively. Results of a multitemporal drought analysis between SVI and rainfall revealed that during the course of the five-year study period, the monthly averages of SVI and rainfall were consistent with one another, as depicted in the typical graph in Fig. 5. SVI increased in response to increasing rainfall, and declined in response to decreasing rainfall. However, because vegetation only began to grow once enough water was available for leaf formation or growth, the change in SVI was slower than the rise in rainfall. The coefficients of determination (R^2) for the correlation between SVI and rainfall over the 5 years (2017 to 2021) were found to be 0.8018, 0.6819, 0.6262, 0.5772, and 0.5108, respectively. The findings of this study align with those of similar research on drought analysis using satellite-based data and spectral indices, such as studies conducted in upper northeastern Thailand and Mahasarakham province (Laosuwan et al., 2016; Rotjanakusol, & Laosuwan, 2018), drought detection by application of remote sensing technology and vegetation phenology (Uttaruk & Laosuwan, 2017b). The SVI is a helpful instrument that can provide information about the onset, scope, intensity, and duration of vegetative stress in close to real-time (Sruthi & Mohammed Aslam, 2015; Vicente-Serrane et al., 2015; Pachanaparn et al., 2022). The findings of this study offer a standard for accurately identifying the drought region in the EEC provinces of Chachoengsao, Chonburi, and Rayong. Additionally, the appraisal of the drought area will be reliable and reasonably quick. The methodology can be obtained and used by other departments to assess and forecast drought in other regions of Thailand and other nations.

ARCKNOWLEDGEMENT

I wish to acknowledge funding from the United Nations Development Programme (UNDP), which supports a project through the Climate Change Modelling in coastal zones in the Gulf of Thailand. I acknowledge the School of Information and Communication Technology (ICT), University of Phayao Thailand for providing the available facilities to carry out this research.

REFERENCES

- Abbas, A., Huang, P., Hussain, S., Shen, F., Wang, H. & Du, D. (2022) Mild Evidence for Local Adaptation of *Solidago Canadensis* under Different Salinity, Drought, and Abscisic Acid Conditions. *Polish Journal of Environmental Studies*, 31(4), 2987-2995.
- Buma, W.G. & Sang-II, L. (2019) Multispectral Image-Based Estimation of Drought Patterns and Intensity around Lake Chad, Africa. *Remote Sensing*, 11(2534), 1-21.
- Ganie, M.A. & Nusrath, A. (2016) Determining the Vegetation Indices (NDVI) from Landsat 8 Satellite Data. *International Journal of Advanced Research*, 4(8), 1459-1463.
- Gomasathit, T., Laosuwan, T., Sangpradid, S. & Rotjanakusol, T. (2015) Assessment of Drought Risk Area in Thung Kula Rong Hai using Geographic Information System and Analytical Hierarchy Process. *International Journal of Geoinformatics*, 11(2), 21-27.
- Kaspersen, P.S., Fensholt, R. & Drews, A. (2015) Using landsat Vegetation Indices to Estimate Impervious Surface Fractions for European Cities. *Remote Sensing*, 7, 8224-8249.
- Laosuwan, T., Sangpradid, S., Gomasathit, T. & Rotjanakusol, T. (2016) Application of remote Sensing Technology for Drought Monitoring in Mahasarakham Province, Thailand. *International Journal of Geoinformatics*, 12(3), 17-25.
- Pachanaparn, C., Jeefoo, P. & Rojanavasuu, P. (2022) Application of Remote Sensing for Drought Monitoring with NDVI-based Standardized Vegetation Index in nan Province, Thailand. The 7th International Conference on Digital Arts, Media and Technology (DAMT) and 5th ECTI Northern Section Conference on Electrical, Electronics, Computer and Telecommunications Engineering (NCON), pp. 330-335, Chiang Rai, Thailand, 26-28 January 2022.
- Qin, Q. Wu, Z. Zhang, T. Sagan, V., Zhang, Z., Zhang, Y., Zhang, C., Ren, H., Sun, Y., Xu, W. & Zhao, C. (2021) Optical and Thermal Remote Sensing for Monitoring Agricultural Drought. *Remote Sensing*, 13(5092), 1-34.
- Rimkus, E., Stonevicius, E., Kipys, J., Maciulyte, V. & Valiukas, D. (2017) Drought Identification in the Eastern Baltic Region using NDVI. *Earth System Dynamics*, 8(3), 627-637.
- Rotjanakusol, T. & Laosuwan, T. (2018) Remote Sensing Based Drought Monitoring in the Middle-Part of Northeast Region of Thailand. *Studia University*, 28(1), 14-21.
- Sruthi, S. & Mohammed Aslam, M.A. (2015) Agriculture Drought Analysis Using the NDVI and Land Surface Temperature Data; a Case Study of Raichur District. *Aquatic Procedia*, 4, 1258-1264.
- Su, Z., He, Y., Dong, X. & Wang, L. (2017) Chapter 8: Drought Monitoring and Assessment using Remote Sensing. *Springer International Publishing Switzerland, V. Lakshmi (ed.), Remote Sensing of Hydrological Extremes, Springer Remote Sensing/Photogrammetry*, 151-172.
- Thai Meteorological Department, (2021) The Expectation of the Weather during the Rainy Season of 2013. Available online: <http://www.tmd.go.th> (accessed on 11 October 2021).
- Uttaruk, Y. & Laosuwan, T. (2017a) Carbon Sequestration Assessment of the Orchards using Satellite Data. *Journal of Ecological Engineering*, 18(1), 11-17.
- Uttaruk, Y. & Laosuwan, T. (2017b) Drought detection by application of Remote Sensing technology and vegetation phenology. *Journal of Ecology Engineering*, 18(6), 115-121.
- Uttaruk, Y. & Laosuwan, T. (2019) Drought analysis using satellite-based data and spectral index in upper northeastern Thailand. *Polish Journal of Environmental Studies*, 28(6), 4447-4454.
- Vicente-Serrane, S.M., Cabello, D., Tomas-Burguera, M., Martin-Hernandez, N., Beegueria, S., Azorin-Molina, C. & Kenawy, A.E. (2015) Drought Variability and Land Degradation in Semiarid Regions: Assessment Using Remote Sensing Data and Drought Indices (1982-2011). *Remote Sensing*, 7, 4391-4423.
- Villarreal, M.L., Norman, L.M., Buckley, S., Wallace, C.S.A. & Coe, M.A. (2016) Multi-index time series monitoring of drought and fire effects on desert grasslands. *Remote Sensing of Environment*, 183, 186-197.
- Willibroad, G.B. & Sang-II, L. (2019) Multispectral Image-Based Estimation of Drought Patterns and Intensity around Lake Chad, Africa. *Remote Sensing*, 11, 1-21.

TSUNAMI EVACUATION MODEL IN THE PANIMBANG SUBDISTRICT, BANTEN PROVINCE, INDONESIA: GIS- AND AGENT-BASED MODELING APPROACHES

Dini PURBAN¹, **Marza Ihsan MARZUK²**, **Budianto ONTOWIRJO³**, **Farhan Makarim ZEIN⁴**, **Didik Wahyu Hendro TJAHO⁵**, **Sri Endah PURNAMANINGTYAS⁶**, **Rudhy AKHWADY⁷**, **Amran Ronny SYAM⁸**, **Arip RAHMAN¹**, **Yayuk SUGIANT¹**, **Safar DODY⁵**, **Adriani Sri NASTITI¹**, **Andri WARSA¹**, **Lismining Pujiyani ASTUTI¹**, **YOSMANIAR⁶**, **Tutik KADARIN⁷**, **Tri Heru PRIHADI¹** and **Ulung Jantama WISHA^{5,8*}**

DOI: 10.21163/GT_2023.182.10

ABSTRACT:

This study examines the agent behavior during a complex tsunami process to reach designated shelters based on the agent-based modeling approach. A GIS-based tsunami inundation modeling is employed considering the land slope and surface roughness coefficient to estimate the tsunami height loss. This model becomes the basis for determining the service area within the study site. Five shelter candidates are assessed using agent-based modeling simulated in the NetLogo, implementing the 50 minutes ETA and 9 meters tsunami run-up propagation for four population age classifications. Overall, the Panimbang coastal area is categorized as a high vulnerability to tsunamis (14.68% of the total area), where the run-up propagation is extended due to the tsunami invading rivers, thereby increasing the risk toward local society. Of particular concern, two proposed shelters (SA1 and SA5) exceed the capacity by 12.43% and 59.44% of their maximum capacity, respectively. Of 9,640 agents (people) simulated, 77.7% are evacuated, and 22.3% fail to reach the shelters, with a majority of the adult category. A sufficiently high casualty number is due to a "bottleneck" in the overlapping service areas. However, reconsidering the overcapacity TES with some additional shelters in the surrounding area is recommended.

Key-words: *evacuation service area, NetLogo, volcanic tsunami, spatial analysis, bottleneck conditions*

1. INTRODUCTION

The strategic position of the Indonesian archipelago is always linked to the potency of geological hazards and disasters. One is the volcanic tsunami threat in the Sunda Strait. On 22 December 2018, a giant tsunami occurred, affected by a lateral collapse on the southwest flank of Anak Krakatau (AK) (Grilli et al., 2019; Muhari et al., 2019). According to BNPB (National Disaster Management Authority) in 2019, casualties resulted from that event 437 people were killed, more than 7200 injured,

¹Research Center for Conservation of Marine and Inland Water Resources, National Research and Innovation Agency (BRIN), Cibinong, Indonesia, dini017@brin.go.id, didi029@brin.go.id, srie005@brin.go.id, rudh002@brin.go.id, amra002@brin.go.id, arip004@brin.go.id, vayu003@brin.go.id, adri005@brin.go.id, andr055@brin.go.id, lism003@brin.go.id.

²Research Center for Artificial Intelligence and Cyber Security, National Research and Innovation Agency (BRIN), Bandung, Indonesia, marz002@brin.go.id.

³Civil Engineering Department, Faculty of Engineering and Computer Sciences, Bakrie University, Jakarta, Indonesia, budianto.ontowirjo@bakrie.ac.id

⁴Department of Geography, Faculty Mathematics and Natural Sciences, University of Indonesia, Depok, Indonesia, farhan.makarim@ui.ac.id

⁵Research Center for Oceanography, National Research and Innovation Agency (BRIN), Jakarta, Indonesia, safa001@brin.go.id, ulun002@brin.go.id *.

⁶Research Center for Marine and Land Bioindustry, National Research and Innovation Agency (BRIN), North Lombok, Indonesia, yosm003@brin.go.id.

⁷Fisheries Research Center, National Research and Innovation Agency (BRIN), Cibinong, Indonesia, tuti006@brin.go.id, trih016@brin.go.id.

⁸Department of Physics and Earth Sciences, Graduat School of Engineering and Science, University of the Ryukyus, Nishihara, Japan.

and 46,646 people lost their homes. The volcanic eruption-induced tsunami is generally evoked by an underwater explosion or airwave generated by the blast. These pyroclastic flows entered the sea, causing the collapse of an underwater caldera, subaerial and submarine failure (Paris et al., 2014).

In the Sunda Strait, a Megathrust subduction zone has previously been observed (Kurniawan et al., 2021). On the other hand, the AK Volcano makes this area more prone to tsunamis, both caused by earthquakes and volcanic eruptions. From year 416 to 2018, the immense strength of a tectonic earthquake was reported on 24 August 1757 in the Java Sea (northeast of the Sunda Strait) with a magnitude of 7.5 and 16 December 1963 in Banten with a magnitude of 6.5 (Triyono et al., 2019).

Since several extraordinary earthquake and tsunami events had occurred in western Sumatra and the south of Java, these regions have become more vulnerable. On the other hand, due to the prone area, the Agency for Assessment and Application of Technology (BPPT) has designed and created a system for the Tsunami Early Warning System (TEWS), which has been deployed in places with high potency of tsunami events (Priohutomo et al., 2022). Locations with frequent occurrences of the tsunami are southern Sumatra, southern Java, and the waters of Maluku and Halmahera. Several systems have been initiated based on sudden sea-level changes in the West Sumatra, Aceh, Pangandaran, and Sunda Straits, such as the Inexpensive Device for Sea Level (IDSL) monitoring (Husrin et al., 2021). In addition to disaster mitigation, evacuation routes in the prone areas do not exist, and in some cases, it does not show the proper and safe evacuation routes. These issues can be found in several prone areas in the surrounding Sunda Strait.

Tsunami preparedness strategies in vulnerable areas are crucial to initiate where information about evacuation routes is not entirely established. One is the Panimbang Subdistrict, located at the westernmost tip of Pandeglang Regency, Banten Province, directly facing the Sunda Strait (Sari & Soesilo, 2020). Panimbang Subdistrict has become an area of significance because of an exclusive tourism development where Tanjung Lesung has become the point of the developing economy (Mulyadi & Nur, 2018). Furthermore, even though a natural green belt (mangrove conservation area) is situated in Panimbang Subdistrict, the other land uses of the coastal zone for settlement and tourism could increase the risk of tsunami or other disasters. Therefore, information regarding this area's hazardous seismic events and evacuation routes is crucial and could be a basis for future developments.

Concerning the evacuation routes, since, to date, there are no evacuation shelters and signs established in the Panimbang Subdistrict, an evaluation of the transportation lane network and agent-based modeling (ABM) is essential to be conducted in this region. This approach was previously introduced by Mas et al. (2012), where every individual (agent) is a part of a system modeled as an entity of autonomous decision-makers, and every agent obeys specific rules as their roles within the system (Pizarro et al., 2022). This method is often used and simulated in tsunami-impacted areas to determine any possibilities when a tsunami occurs (Jacob et al., 2014; Kim et al., 2022; Mas et al., 2012; Mostafizi et al., 2017; Usman et al., 2017; Wafda et al., 2013; Wang & Jia, 2021, 2022). Since agent-based modeling is well-known among scholars and could concisely simulate the evacuation routes of any conditions during tsunami run-up, we used this method for a case study in Panimbang Subdistrict with some modifications based on local environmental states.

We report herein the result of ABM combined with several GIS-based techniques to map the evacuation routes, shelter capacity, and any possibility of agent behavior during tsunami events applied in the Panimbang Subdistrict, considering the social and population data. A few studies have reported tsunami inundation and ABM modeling in the study area. Farahdita & Siagian (2020) assessed the tsunami inundation and the land use change due to the tsunami in the coastal area of Panimbang Subdistrict using Sentinel-2 images, DEM, and unsupervised classification methods.

On the other hand, Lee et al. (2022), modeled the tsunami hazard in the Panimbang Subdistrict using the ABM approach, where they considered several transportation modes and existing physical buildings as shelters. Spatial-based estimation of the tsunami inundation area with several scenarios of tsunami height has never been done to date. Moreover, since the number of transportation modes in the Panimbang could not be precisely determined, the ABM simulation considering travel time on foot as the worst-case during a tsunami event is also essential to examine. As such, these aspects

should be investigated. Therefore, this study aimed to evaluate horizontal evacuation zones based on the pattern of agent's mobility during a scenario of tsunami event in the Panimbang Subdistrict. This study is also expected to be a basis for future decision-making and development of the Pandeglang Regency, especially for early mitigation and preparing the proper evacuation routes and tsunami shelters.

2. STUDY AREA

As previously introduced, the study area is situated in the Panimbang Subdistrict, Pandeglang Regency, Banten Province, Indonesia. Based on overlaid DEM (Digital Elevation Model) and SRTM (Shuttle Radar Topography Mission) data, the coastal morphology of the Panimbang Subdistrict is a flat beach with a slope ranging from <2.5 to 5 m above sea level (**Fig. 1**). The total area of the Panimbang Subdistrict is approximately 97.75 km² (3.56% of the total area of the Pandeglang Regency). It is bordered by Sukaresmi Subdistrict in the north, Angsana Subdistrict in the east, Cigeulis and Sobang Subdistricts in the south, and the Sunda Strait in the west. In particular, the total area of Citeureup and Mekarsari, the area of interest in this study, is approximately 17.1 and 23.1 km², respectively (about 17.4 and 23.6% out of the Panimbang Subdistrict). Concerning the total population, the number of villagers in Citeureup and Mekarsari is about 9,174 and 11,189, respectively.

The tsunami event in 2018 induced by the Krakatoa volcano significantly impacted the environment in the locality, specifically resulting in a change in land use, whereby the prone area is situated between 50-300 meters from the coastline (Farahdita & Siagian, 2020). The green belt declined by 205.714 ha, and the settlement area decreased by 25.17 ha. The farming area and the shoreline pattern of rivers and estuaries have also been altered. Many empty and open land areas show how powerful the volcanic tsunami event was in the past (Pradjoko et al., 2015).

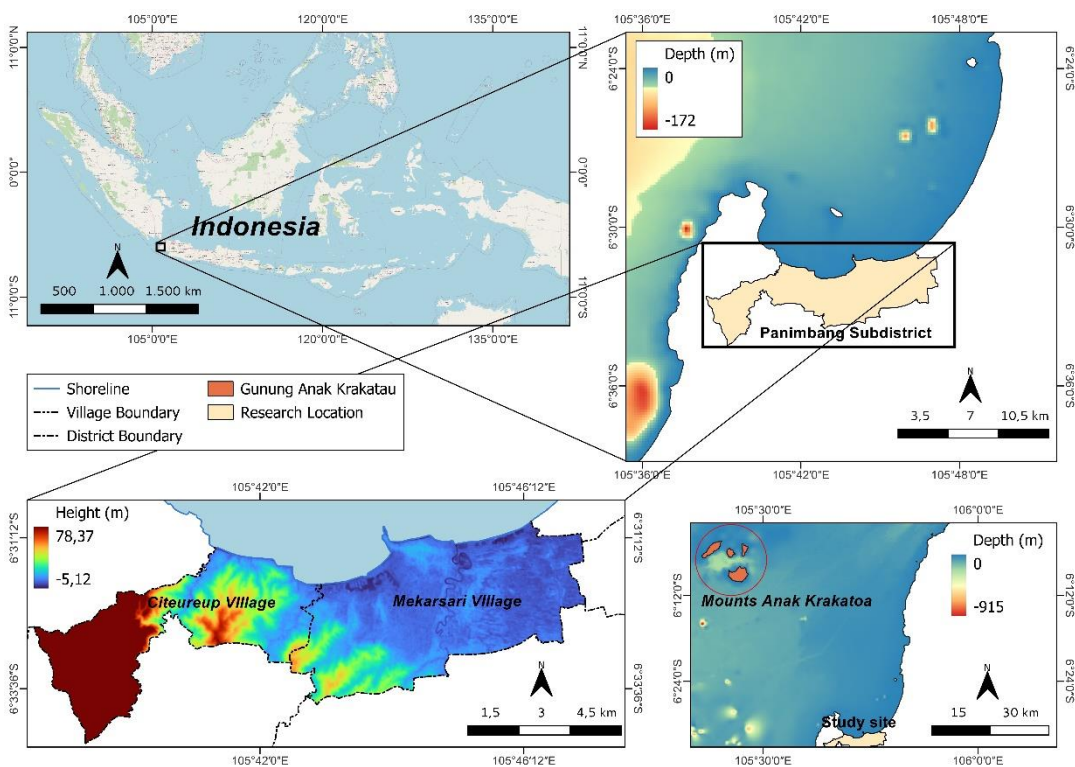


Fig. 1. The assessed area covering Citeureup and Mekarsari Villages in the Panimbang Subdistrict.

3. DATA AND METHODS

3.1. Spatial-based tsunami inundation modeling

Berryman (Berryman, 2006) previously established a numerical modeling approach, which was used in this study. This method calculates the tsunami height loss for every one meter of inundation distance, considering the slope and surface roughness as follows:

$$H_l = \left(\frac{167sr^2}{H_0^{1/3}} \right) + 5 \sin S \tag{1}$$

where:

H_l = the loss in wave height per meter of inundation slope (m)

sr = surface roughness coefficient

H_0 = initial wave height in the coastline (m)

S = land surface slope (degree)

The data used to simulate tsunami inundation model consist of Panimbang’s administration data, DEM, and Sentinel-2 imagery (**Table 1**). The DEM data were resampled to equalize the spatial resolution between DEM and Sentinel-2 imagery (Danardono et al., 2023). The resampled data were then processed using the slope generation technique to produce the land surface slope of the study area (Marzuki et al., 2021). The Sentinel-2 image used in this study was acquired on August 12th, 2021, with the tile of T48MWT. Sentinel-2 has 13 spectral bands: four bands with a 10-meter resolution, six bands with a 20-meter resolution, and three bands with a 60-meter resolution (Phiri et al., 2020). This image's orbital coverage area is approximately 290 km. In this simulation, we only used four bands: band 2 (blue), 3 (green), 4 (red), and 8 (Near-Infrared/NIR). These four bands were classified by applying Spectral Angle Mapping with 94% accuracy, in which the classification used consisted of developed areas, rice fields, forests, and water bodies (Pesaresi et al., 2016).

Table 1.

The primary data used in the tsunami inundation modeling.

Data	Type	Resolution	Source
Administration data	Polygon	-	GADM (Global Administrative Areas)
DEM (1109-24, 1109-23, 1109-52, 1109-51)	Raster	8.5 m	DEMNAS (National Digital Elevation Model for Coastal Application)
Sentinel-2 Imagery	Raster	10 m	ESA (European Space Agency)

The classification results were then reclassified based on the concept of empirical multidimensional histogram to produce the surface roughness coefficient (Pesaresi et al., 2016) (**Table 2**). The value of surface roughness was considered to estimate the wave height attenuation. According to Borrero et al. (2020), the expected tsunami run-up in the northern tip of Tanjung Lesung Peninsula approximately ranges from 7 to 13.5 meters. However, this study simulated the 9-meter run-up height of a volcanic-induced tsunami in the Panimbang Subdistrict. Moreover, simulations with variations in tsunami run-up heights (7 and 13.5 meters) were also performed for different tsunami run-ups in the Panimbang coastal zone. The tsunami run-up combined with water channels flowing in the rough topography regimes, such as dunes, coastal vegetation, buildings, erratic topography profile, rivers, and other land covers on the surface, is the most significant parameter to estimate the inundated area (Berryman, 2006).

After gaining the tsunami height loss, a cost distance analysis was employed to estimate the cost distance of a one-meter tsunami height loss, where the height loss was used to monitor the maximum inundated area. The result of cost distance was then used for processing fuzzy membership and index for creating classification levels within a category or class (Berryman, 2006; Zaman et al., 2014). In this case, the impacted region was classified into highly vulnerable (3), moderately vulnerable (2), and lowly vulnerable (1).

Table 2.
The value of surface roughness for every land cover type,
modified from (Berryman, 2006).

Land cover	Surface roughness coefficient
Water body	0.007
Swamp	0.015
Pond	0.007
Embankment	0.010
Sands/dunes	0.018
Bushes	0.040
Meadow	0.020
Forest	0.070
Plantation	0.035
Moore/Field	0.030
Rice field	0.020
Agriculture area	0.025
Settlement/developed area	0.050
Mangrove forest	0.060

3.2. Deciding TES in the Panimbang Subdistrict

A genuine horizontal temporary evacuation shelter (TES) was assessed in this study. A horizontal shelter is a public area that area-wise could accommodate evacuees (Mück & Post, 2008). Several parameters were considered to decide the shelter criteria relying on the local administrative data, such as road networks, building existence, demography, overlaid using tsunami vulnerability map. The proposed horizontal TES should be situated at a higher elevation (above the tsunami-inundated area), on a less than 20° slope and flat terrain, with easy access to the main road (secondary road), in the surrounding dense area (settlement), in the area more than 10,000 m², located in an open area 200 meters off the coastline (Lakshay et al., 2016; Mück & Post, 2008; Taubenböck et al., 2013).

The road network, width, and conditions in the study area were surveyed using OpenStreetMap application and validated using a high-resolution Google Earth image. The open area was determined by applying Google Street View with a 360° angle to analyze the land use of each proposed shelter (Li et al., 2017). These data are fairly accurate since it is recorded within on average 6 meters distance from the object, with approximately 80% overlap of moving objects between two datasets (Brovelli and Zambogini, 2018).

3.3. Shelter assessment based on Agent-Based Modeling

The proposed TES was assessed using an agent-based model (ABM). This modeling technique is based on agents and simulates evacuation of a natural hazard (Pizarro et al., 2022). The model processing is based on the agent behavior where the evacuee (agent) is the entity to decide whether to evacuate or not during a disaster event. The evacuation modeling is built using a NetLogo application, multi-agent programming language, and environmental modeling for a complex phenomenon (Mas et al., 2012).

Agents will move toward the closest proposed shelters via the most accessible way. Therefore, the maximum population capacity that each shelter could service was estimated using a service area analysis. This analysis is based on a network analysis method, considering the road facility, dense settlement area, travel speed and time, and travel distance (Kuller et al., 2019). The slowest speed belongs to the elders' cohort, with 0.93 m/s (Mas et al., 2012). The time travel of tsunami wave inundation was 40 minutes, estimated by the last report of volcanic-based tsunami modeling in the Sunda Strait (Dogan et al., 2021).

After gaining each shelter's service area, the building amount and road networks in the surrounding location was calculated and extracted from OpenStreetMap data. Concerning four people in a building, every building was multiplied by four to obtain the maximum population capacity that

shelters could service. This consideration was based on the Central Agency of Statistics data in 2019, whereby the average amount of family members in one house/building in the study area was $3.9 \approx 4$. However, the actual field data could be more than that. On the other hand, the population was classified into four classes: kids (0–9 years old), teens (10–19 years old), adults (20–64 years old), and elders (>64 years old). In addition to the number of agents, we considered the maximum population capacity that could be serviced by all shelters as follows:

$$Ta = 4 \times Tb \times Cp \tag{2}$$

where:

Ta = The total of agent

Tb = The total of calculated buildings

Cp = The age class percentage

The amount of agent was used for further processing in the NetLogo application applying a modified code previously established by Mas et al. (2015). The considered parameters were ETA (estimated time of arrival, about 50 minutes) and the number of agents according to the age classification. The workflow of this study is shown in Fig. 2.

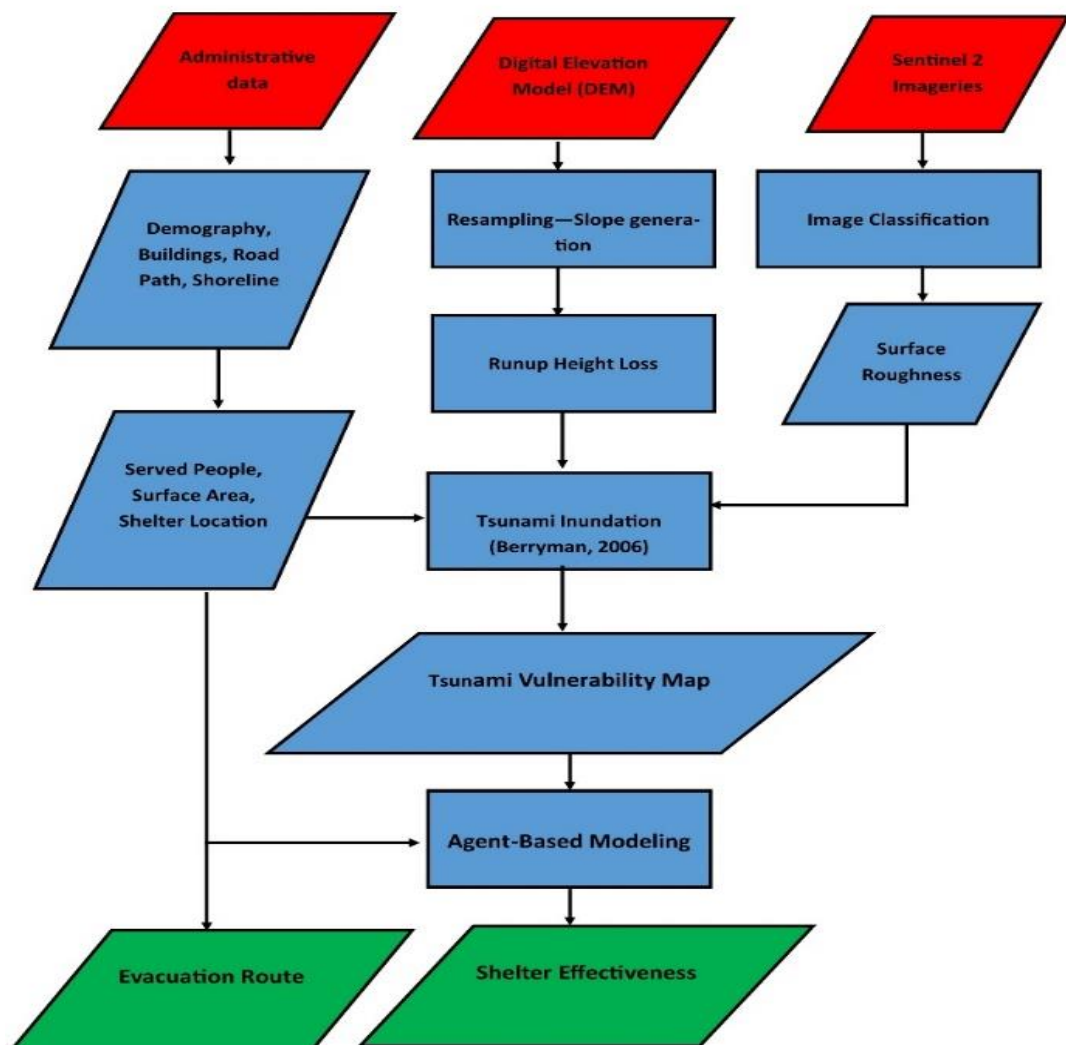


Fig. 2. The workflow of this study.

4. RESULTS AND DISCUSSIONS

4.1. The vulnerability map of tsunami in the Panimbang Subdistrict

Panimbang Subdistrict consists of two villages, Citeureup and Mekarsari, situated on the coastline of Sunda Strait. **Fig. 3A** shows the vulnerable areas prone to tsunamis based on inundation modeling. Overall, the vulnerable coastal area is only 14.68% of the total area of the Panimbang Subdistrict. The most impacted area by the tsunami is observed in the Mekarsari Village, with 7.89% highly vulnerable area. The remnant classifications are moderately vulnerable (2.59%) and lowly vulnerable (1.86%) (**Fig. 3D**). By contrast, in the Citeureup Village, the area categorized as high vulnerability only covers 2.06%, with a small portion of moderate-low categories (less than 1%) (**Fig. 3C**). Since tsunami inundation modeling relies on land topography and elevation, the more declivous the slope, the more vulnerable to tsunami (Berryman, 2006). In this case, Mekarsari Village is situated on the more declivous slope ranging between 15 to 25°, while the Citeureup is situated in a higher elevation with a slope reaching 30°.

The vulnerable area to the tsunami in the Panimbang Subdistrict encompasses many types of land use (**Fig. 3B**). Based on GIS-based analysis, the volcanic-induced tsunami inundates approximately 190.384 ha (49.57%) of agricultural areas. Moreover, the other impacted areas are settlements (built areas) with a coverage of 87.23 ha (21.93%), 71.37 ha (18.84%) of forest, and 37.04 ha (9.65%) of water bodies. Concerning the built area, the number of impacted buildings is approximately 519 in Citeureup and 753 in Mekarsari, respectively, which are mainly located in the highly vulnerable area (26% out of 36.64% of impacted buildings). Even though the inundated area is more extensive in Mekarsari than in Citeureup, the number of impacted buildings is higher in Citeureup.

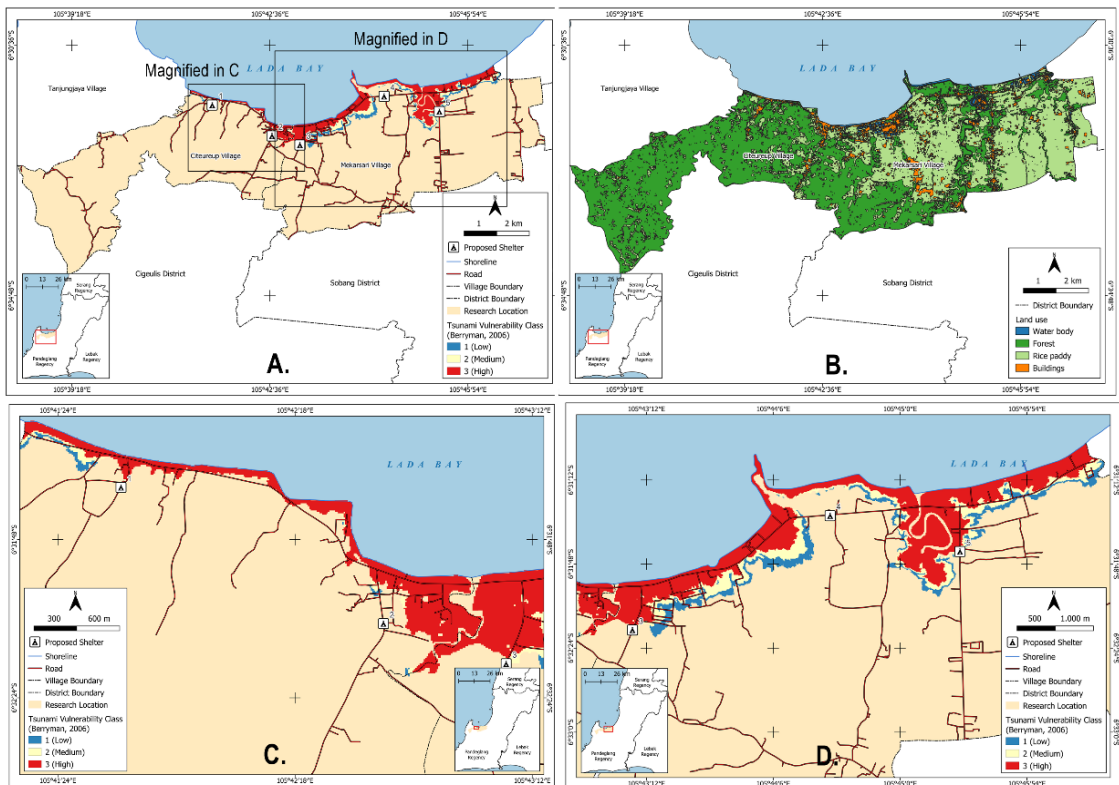


Fig. 3. The vulnerable coastal area based on tsunami inundation modeling with 9-m tsunami run-up height (A), the land use of Panimbang Subdistrict (B), the magnified inundated area in the Citeureup Village (C), and the magnified inundated area in the Mekarsari Village (D).

The most extensive inundation zone is observed in the surrounding estuaries and rivers (**Fig. 3**). However, the area with a higher surface roughness coefficient could significantly reduce tsunami propagation. According to Yamanaka & Shimozono (2022) and Yeh et al. (2012), a tsunami invading a river channel could cause it to overflow. By contrast, the built-up areas could significantly decrease the total amount of tsunami inundation for the sites behind them, even though at some points, the building and coastal structures may increase the tsunami height immediately in other areas nearby (Bricker et al., 2015). Concerning the land use of Panimbang Regency, the dense population and buildings are situated in the coastal zone and rivers (highly vulnerable to tsunamis). Therefore, mitigation efforts to minimize the impact of tsunami hazards are crucial to be initiated by local and central government since there is no protection, shelter, or proper evacuation route in the Panimbang Regency.

The coastal vulnerability maps based on scenarios of 7-meter and 13.5-meter run-up heights are shown in **Fig. 4**.

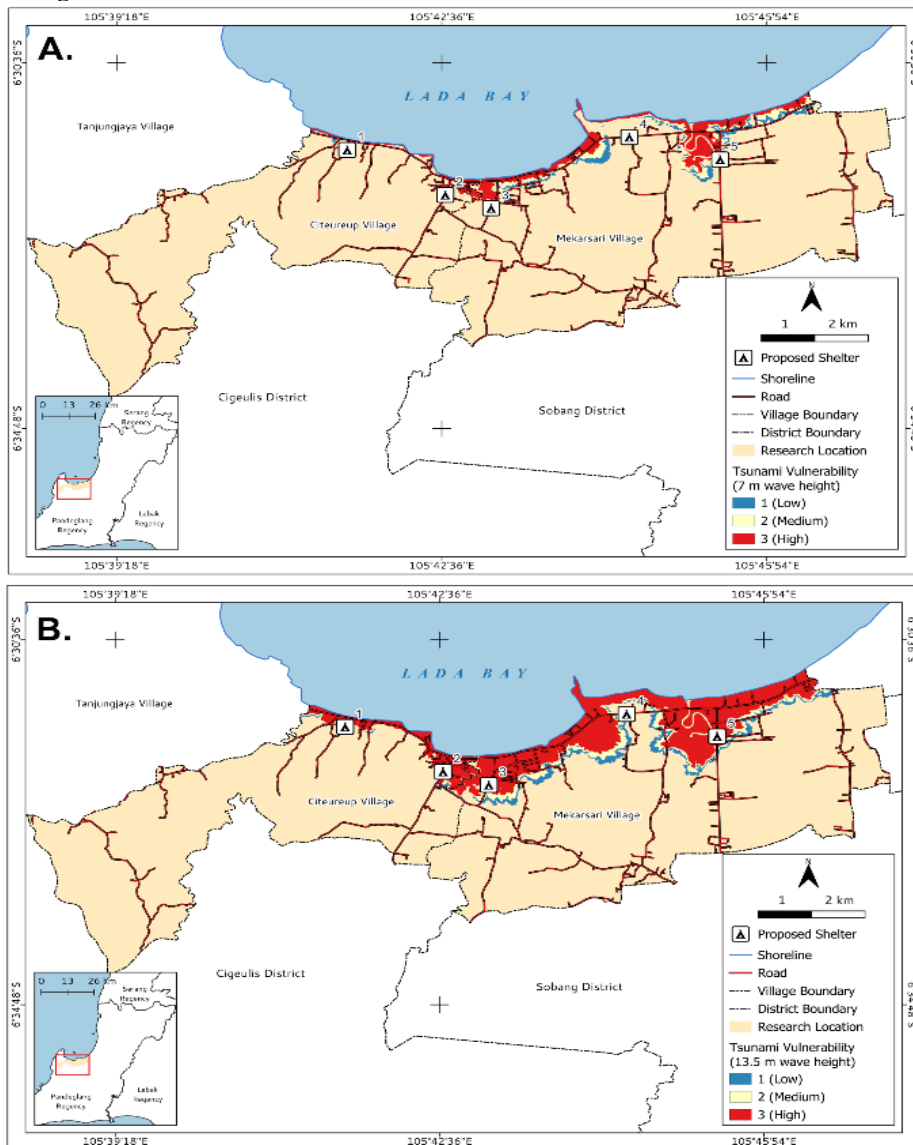


Fig. 4. The vulnerable coastal area based on tsunami inundation modeling with run-up height of 7 meters (A) and 13.5 meters (B).

Overall, compared to the result of the 9-meter tsunami run-up height, the lower run-up decreases the amount of the impacted areas over the Panimbang Subdistrict by less than 50%. On the other hand, the higher run-up height (13.5 m in maximum) will significantly increase the inundated area by more than 50%.

By reducing the run-up height set up by about 2 meters, the low vulnerability area decreases by about 42,800 m² (8.03%), the moderate vulnerability area decreases by about 79,300 m² (10.61%), and the highly vulnerable area reduces by approximately 43.34% (**Fig. 4A**). On the other hand, compared to the total area of the Panimbang Subdistrict, the low, moderate, and high vulnerability areas cover about 1.13%, 1.59%, and 5.48%, respectively.

Another simulation with a 13.5-m run-up height is shown in **Fig. 4B**. Based on the spatial calculation, with the increase of run-up height of about 4.5 meters, the inundated area categorized as highly vulnerable covers 11.03% of the total area of Panimbang. On the other hand, the regions with moderate and low vulnerability only expand by less than 2%. Compared to the inundation area in the 9-meter run-up height simulation, the coverage area increases by 29.12%, 14.23%, and 50.35% for low, moderate, and high vulnerability categories, respectively.

4.2. Proposed horizontal TES in the Panimbang Subdistrict

Based on the tsunami inundation area, five prospective horizontal shelters throughout the Panimbang Subdistrict were proposed in this study. Overall, the proposed shelters meet the requirement for an evacuation area, consisting of one shelter in Citeureup, three shelters in Mekarsari, and another in between. Except for shelters SA2 and SA3, the other shelters could be accessed using vehicles due to more extensive access (around 10 meters in width). Furthermore, all shelters were positioned in the declivous area with a slope ranging from 0–10° and land elevation of around 10–15 meters (**Table 3**).

Table 3.

The information of tsunami shelters in the Panimbang Subdistrict.

Shelter Code	Longitude (°East)	Latitude (°South)	Location	The road width (m)	Materials	Elevation (m)	Slope (°)	The number of buildings	Capacity (people)	The area of shelter (ha)
SA1	105.6939	6.5433	Citeureup Village	10	Paving blocks	14.39	10.11	137	548	308.7
SA2	105.7106	6.5353	(Citeureup-Mekarsari)	7	Asphalt	12.12	4.25	753	3012	748.33
SA3	105.7184	6.5378	Mekarsari Village	1.5	Concrete	9.58	4.10	764	3056	597.29
SA4	105.7417	6.5242	Mekarsari Village	2.5	Soil and rocks	11.39	2.48	396	1584	455.47
SA5	105.7571	6.5285	Mekarsari Village	10	Concrete	9.34	0.89	360	1440	552.58

Shelter 1 (SA1) is positioned approximately 230 meters from the coastline, 60 meters from the low vulnerability area, and about 2.3 km from shelter 2 (SA2) (**Fig. 5A**). This shelter is situated in a resort with a 10 meters road width and paving block materials. Land use-wise, this area is categorized as an open space with a total area of about 308.7 ha. This area is smaller than the other shelters that could only service 548 people with a density of one person per hectare.

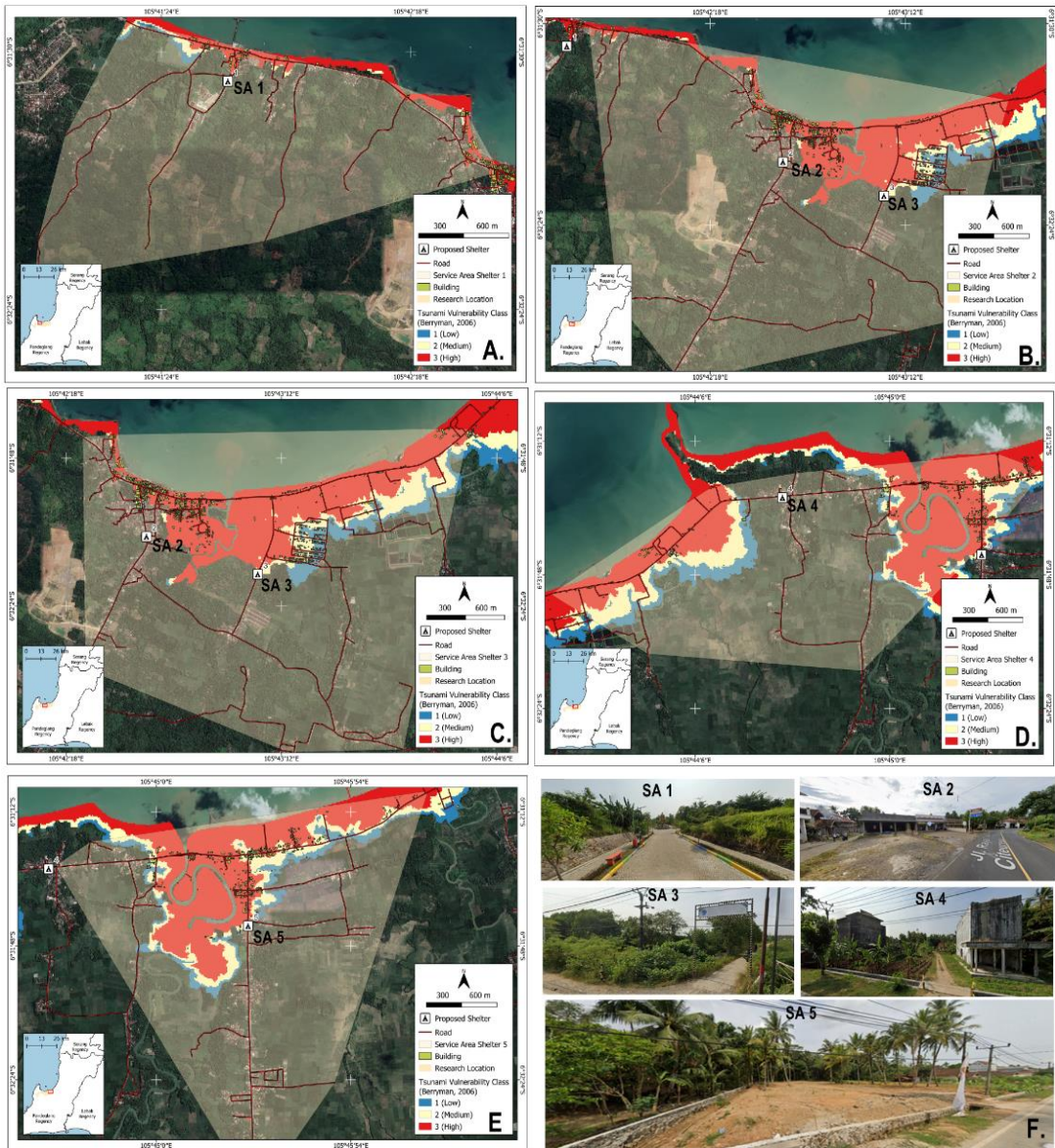


Fig. 5. The service area, proposed as tsunami shelters in the Panimbang Subdistrict; service area 1 (A); service area 2 (B); service area 3 (C); service area 4 (D); service area 5 (E); and the documentation of each shelter (F).

The dense population is observed in the surrounding shelters 2 and 3 (SA2 and SA3), where approximately 6,000 people live. It is situated more than 400 meters from the coastline and on a declivous slope of 4° (Table 3). Even though these shelters are sufficiently close to the tsunami inundation zone, they are situated in a higher elevation area (more than 10 meters) (Figs. 5B and 5C). Concerning the service area, these shelters provide the most prominent place amongst the other proposed horizontal TES, with 748.33 and 597.00 ha, respectively.

Shelter 4 (SA4), located in Mekarsari Village, is approximately 400 meters from the coastline with an elevation of 11.93 meters and a slope of 2.48° . This shelter is the closest one to the main road of Panimbang Subdistrict, outside the tsunami inundation zone (Fig. 5D). The capacity in this shelter is about 1,584 people, and the service area is 455.47 ha. Therefore, the population density is around

three people per hectare. Unfortunately, compared to the other shelters, this area is the narrowest, with an access width of 2.5 meters and a little offroad. However, land use-wise, the shelter is categorized as an open space (Table 3).

The last shelter is SA5, located within Mekarsari Village. It is situated 830 meters from the coastline, with a 9.34 meters elevation and a 0.89° slope (Fig. 5E and Table 3). This shelter is positioned around 10 meters from the tsunami inundation zone with relatively concrete road materials. It is on the secondary road connecting the Panimbang to Cigeulis Subdistrict, categorized as an open space area. The capacity that could be serviced is approximately 1,440 people within an area of 552.58 ha. Therefore, the population density is two persons per hectare. In addition to the shelter's actual condition, the documentation of every shelter proposed in this study is shown in Fig. 5F, where it is generally categorized as an open space area that meets the required criteria for a horizontal tsunami evacuation shelter.

The five proposed horizontal shelters are considered based on the topographical state, accessibility, settlement area's location, open space, and about 200 meters from the coastline. Moreover, these locations were chosen as the safe area based on a 9-meter tsunami simulation. However, different shelter location candidates are possible considering the miscellaneous tsunami properties since there will be a tsunami ranging from 7 to 13.5 meters induced by the Krakatoa eruption in the Sunda Strait, and even a megathrust tsunami may produce a higher run-up propagation (Borrero et al., 2020; Helmi et al., 2020; Ponangsera et al., 2021).

Regarding the service area of shelters, the various shelter area and capacity results in different adaptation for the simulated agents. Several agents are found to evacuate in the other service areas outside their provenance. This decision may also happen during an actual tsunami event. In the ABM simulation, some service areas are overlapping, such as shelters SA2 and SA3, aiming to create a condition where all agents could be accommodated throughout the study area. However, this creates a possibility for agents in these regions to evacuate to nearby shelters where the user has no control over the agent behavior simulated in the model (Almeida et al., 2012; Mas et al., 2012). Since the model considers a coastal topography extracted from DEM data, the inundation pattern seems almost the same with a 9-meter run-up simulation. In this case, the designated shelters are safe from inundation, so the proposed shelters are suitable for mitigating the tsunami impacts when the run-up height is less than 9 meters. More interestingly, a sufficiently high effect is observed in the surrounding estuaries, where estuarine existence and formation could amplify the tsunami run-up in the coastal area (Yeh et al., 2012).

4.3. Results of ABM simulation and estimated casualties

Based on the scenario of five proposed shelters, the ABM was simulated using a NetLogo application to estimate how effective shelter placement is during a tsunami. In this simulation, all evacuees are set to access the shelters on foot at various speeds based on their ages, with a 9-meter tsunami run-up height applied in this scenario. It should be noted that this modeling technique has been tested and used many times by the developer, with, on average, three trials in every single stage (Mas et al., 2015). On the other hand, it is impossible to examine the error of the simulated model when the user cannot look at a piece of code and state that the model has errors (or otherwise) if the programmer's intention is not clearly fathomed and the field data is unavailable (Galán et al., 2009). However, the model certainty was set for a 95% confidence level in this study. Overall, not all evacuees (agents) could be well-evacuated due to several bottleneck blockages (traffic jams) toward the shelter location, resulting in a longer evacuation process.

The ABM was simulated for 50 minutes, whereby the records of agent behavior in every ten minutes are shown in Fig. 6, representing the initial collapse due to volcanic-induced tsunami and the ending of the evacuation process done by the simulated agents. The initial condition shown in Fig. 6A represents the actual residents' initial location. In this stage, the tsunami commences invading the coastline. After 10 minutes of the simulation, a plethora of agent's movements are observed moving toward the closest proposed shelters. The most observable movements are in the surrounding Ciseukeut estuary (closer to shelter SA5) and shelters 2 and 3 (SA2 and SA3) (Fig. 6B).

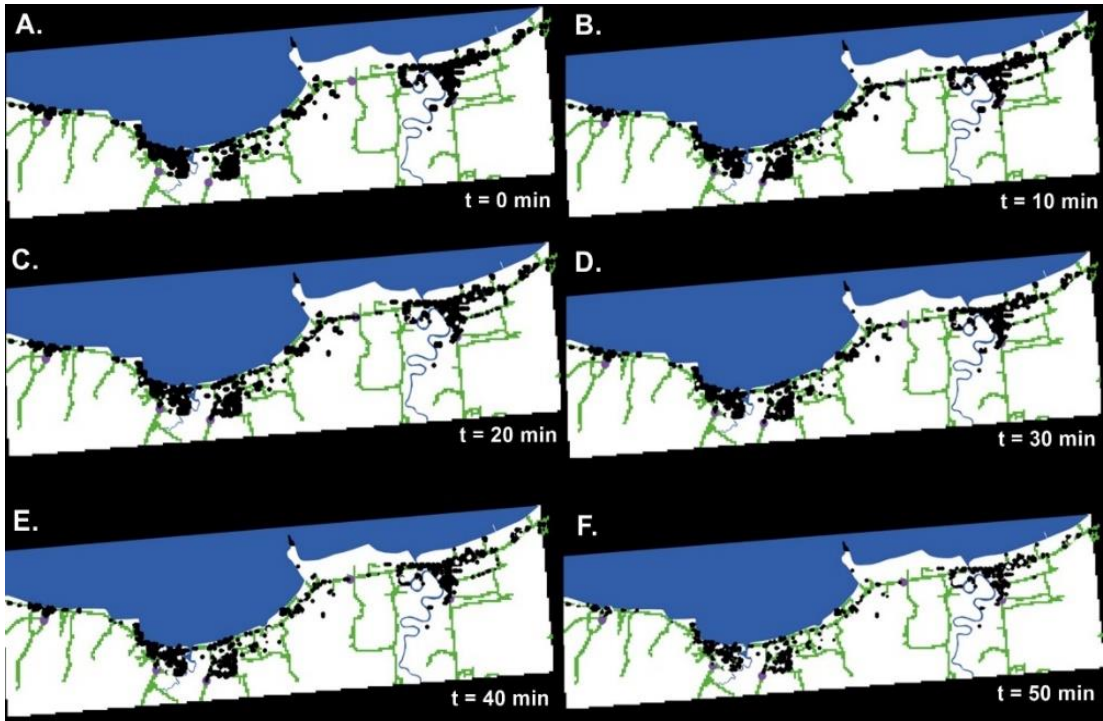


Fig. 6. Agent behavior overview in the study area at different simulation times, $t = 0$ (A), $t = 10$ (B), $t = 20$ (C), $t = 30$ (D), $t = 40$ (E), and $t = 50$ (F) minutes. Black circles denote the simulated agents and purple circles denote the designated shelters.

The number of agents gradually decreases since many of them are evacuated to the nearest proposed shelters. In the time span between 20–30 minutes (**Figs. 6C and D**) when the wave height toward the shelters is about 5–6 meters, casualties probably commence to occur where several agents are trapped due to the overcapacity of the primary road towards the shelters. At the 40-minute of the simulation, the total casualties increase, and the inundation level reaches less than three meters towards the shelters (see in **Fig. 6E**).

Generally, the agents will preferably choose the primary roads where several bottleneck blockades are observed in several proposed shelters. At the end of simulation ($t = 50$ minutes) (**Fig. 6F**), it shows the remnant of agents that fail to evacuate, wherein at some points, there are several agents that do not move anywhere, particularly in the unimpacted areas. More interestingly, due to the crowd passing the primary road toward shelters SA2, SA3, and SA5, the number of casualties is sufficiently high on these shelters.

Of a total of 9,640 agents (people) simulated in the NetLogo, 77.7% are evacuated into the five shelters, and the remnant 22.3% fail to reach the shelters. The highest evacuated agents are observed at shelters SA2 and SA5 (more than 2,000 agents). In contrast, at shelters SA1 and SA4, evacuated agents are under 900. Furthermore, at SA3, around one-third of the total evacuated agent is observed (**Fig. 7**). Concerning the capacity of each shelter, we found that overcapacity shelters are observed at shelters SA1 and SA5, with 12.23% and 59.44%, respectively. By contrast, the other shelters are under the maximum capacity of approximately 40% (**Fig. 7**).

The overcapacity observed at shelters SA1 and SA5 (**Fig. 7**) is unpredictable because it was only considered the denser area with plenty of buildings and settlements as shelters. However, there is no control over agents' fate and response during a tsunami event; this is the limitation of the ABM simulation in this study. This state indicates that shelters SA1 and SA5 cannot accommodate too many evacuees if the tsunami occurs.

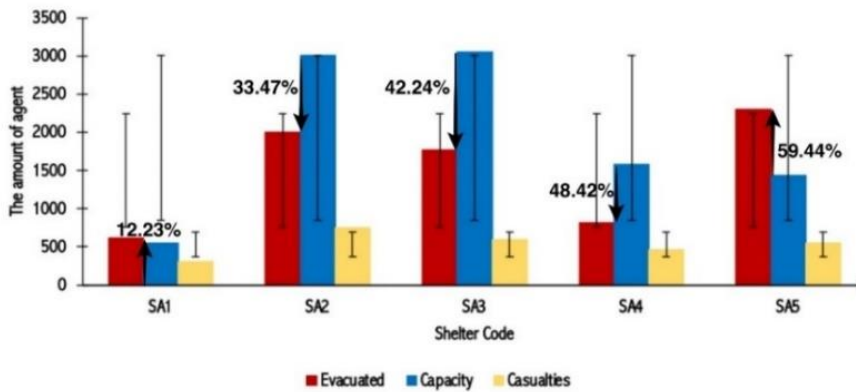


Fig. 7. The estimated amount of evacuated people in every shelter resulted from the ABM modeling. The upward arrows show the shelter's overcapacity condition, and the downward arrows show the shelter's undercapacity condition. Black lines denote the standard deviation of each data.

Regarding the unexpected agent's behavior, they might confuse about where to evacuate during a tsunami invasion, resulting in overcapacity in several shelters (Pamukcu et al., 2020). According to Mas et al. (2012), the ABM simulation could study individual behavior in a complex process of a tsunami. The overcapacity risk condition may occur at shelters SA1 and SA5 if applied in the actual tsunami situation. Therefore, reconsidering these two areas for horizontal evacuation shelters is recommended for further studies whereby the additional shelters in the surrounding areas, perhaps, can avoid the overcapacity conditions.

Regarding the casualties in this simulation, 2,622 agents could not reach the proposed shelters. The highest losses are observed at shelter SA2, with 28% of the total unsafe agents. By contrast, the lowest value is found in the surrounding shelter SA1, with 11% of the total casualties. The other shelters show an almost similar trend, with the losses of approximately 500 agents (**Fig. 7**).

Based on the age classification, the adult category is the most evacuated group, with 3,771 agents compared to the other cohorts (kids, teens, and elders), that only cover around one-third of the highest amount (**Fig. 8**). The exact number of casualties is also observed based on ages ranging from 289 to 1,051 agents. Therefore, most of the residents of Panimbang Subdistrict are categorized as adults (20–64 years old) that can reach the shelter on time. By contrast, the other categories are slower to reach shelters during a tsunami situation.

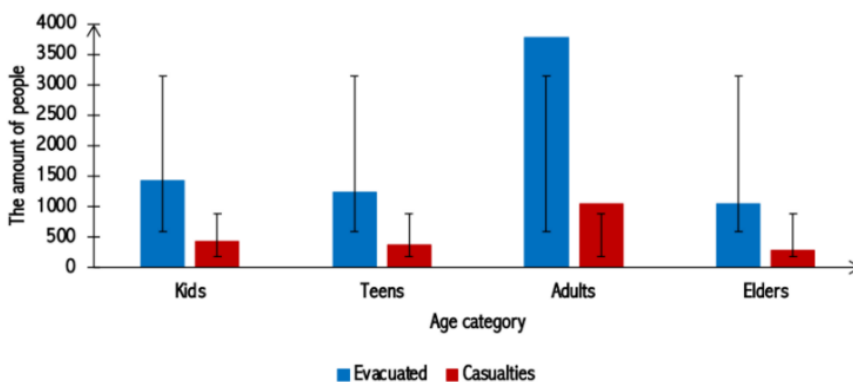


Fig. 8. The estimated amount of evacuated agent and casualties according to the age category. Black lines denote the standard deviation of each data.

In addition to the road accessibility, a "bottleneck" situation is observed, where in the densely populated area, the blocked and collided agents caused by the narrowed road/access are possible (such as at shelters SA2, SA3, and SA4), even though the shelter area and capacity are adequate (Ogawa et al., 2019). That is why the number of casualties simulated via ABM is sufficiently high in these shelters, commonly predominated by the adult category (**Figs. 7 and 8**). However, the study area's demography, the evacuation time, and the evacuee's walking speed also play a significant role in determining the casualties (Ito et al., 2021; Mas et al., 2012). The high value of casualties in this simulation is due to road accessibility, where there is only one main road and some secondary offroad tracks to access the shelters. On the other hand, the model limitation that did not consider the queue toward the proposed shelters and the inability of the agent to reach the shelters also triggers the high number of casualties. This condition may occur during the actual tsunami because of the stressful environment and the effort to survive the tsunami invading the coastal areas (Bakar et al., 2016).

6. CONCLUSIONS

The coastal area of the Panimbang Subdistrict is predominated by highly vulnerable classification based on a 9-meter tsunami inundation modeling. The higher impacted area is observed in the Mekarsari Village than in Citeureup. The highly vulnerable zone to tsunamis is commonly covered by buildings, settlements, and agricultural areas with a declivous slope and low elevation. The extensive tsunami run-up propagation is observed in the riverine and estuarine systems where the dense population does exist, thereby increasing the risk of tsunami-invading rivers.

The five proposed service areas in the Panimbang Subdistrict have met the required criteria for a horizontal evacuation shelter. However, two shelters are reported exceeding the capacity due to the overlapping service area and the limitation of the agent-based modeling used in this study. Moreover, the individual behavior during a complex tsunami process could be studied. Reconsidering the overcapacity shelters by adding several other shelters in the surrounding areas nearby is possible for future studies.

Most evacuees and casualties are of adult age, representing the dominant population of the Panimbang Subdistrict. However, the exact demographic data are essential to estimate the number of evacuees and casualties in the ABM simulation. On the other hand, the sufficiently high casualties are due to the accessibility-induced bottleneck situation whereby the narrowed settlement-shelter connecting road could not accommodate the agents. Furthermore, the simulation did not consider the queue and the inability of agents to reach the designated shelters.

AUTHOR CONTRIBUTIONS

Dini PURBANI, Marza Ihsan MARZUKI, Budianto ONTOWIRJO, Farhan Makarim ZEIN, Didik Wahyu Hendro TJAHO, Sri Endah PURNAMANINGTYAS, Rudhy AKHWADY, and Ulung Jantama WISHA are considered as the main contributors of this article. All authors have read and agreed to the published version of the manuscript.

ACKNOWLEDGMENT

We would like to thank the head of the Research Center for Conservation of Marine and Inland Water Resources, National Research and Innovation Agency (BRIN), Arif Wibowo. Gratitude is also given to those who have helped with the completion of this article.





REFERENCES

- Ai, F., Comfort, L. K., Dong, Y., & Znati, T. (2016) A dynamic decision support system based on geographical information and mobile social networks: A model for tsunami risk mitigation in Padang, Indonesia. *Safety Science*, 90. <https://doi.org/10.1016/j.ssci.2015.09.022>
- Almeida, J. E., Kokkinogenis, Z., & Rossetti, R. J. F. (2012) NetLogo implementation of an evacuation scenario. Iberian Conference on Information Systems and Technologies, CISTI.
- Bakar, J. A. A., Mat, R. C., Aziz, A. A., Jasri, N. A. N., & Yusoff, M. F. (2016) Designing agent-based modeling in dynamic crowd simulation for stressful environment. *Journal of Telecommunication, Electronic and Computer Engineering*, 8(10).
- Berryman, K. (2006) Review of Tsunami Hazard and Risk in New Zealand. In Institute of Geological and Nuclear Sciences (Issue September).
- Borrero, J. C., Solihuddin, T., Fritz, H. M., Lynett, P. J., Prasetya, G. S., Skanavis, V., Husrin, S., Kushendratno, Kongko, W., Istiyanto, D. C., Daulat, A., Purbani, D., Salim, H. L., Hidayat, R., Asvaliantina, V., Usman, M., Kodijat, A., Son, S., & Synolakis, C. E. (2020) Field Survey and Numerical Modelling of the December 22, 2018 Anak Krakatau Tsunami. *Pure and Applied Geophysics*, 177(6), 2457-2475. <https://doi.org/10.1007/s00024-020-02515-y>
- Bricker, J. D., Gibson, S., Takagi, H., & Imamura, F. (2015) On the need for larger Manning' s roughness coefficients in depth-integrated tsunami inundation models. *Coastal Engineering Journal*, 57(2). <https://doi.org/10.1142/S0578563415500059>
- Brovelli, M. A., & Zamboni, G. (2018) A new method for the assessment of spatial accuracy and completeness of OpenStreetMap building footprints. *ISPRS International Journal of Geo-Information*, 7(8), 289. <https://doi.org/10.3390/ijgi7080289>
- Danardono, D., Wibowo, A. A., Sari, D. N., Priyono, K. D., & Dewi, E. S. M. (2023) Tsunami Hazard Mapping Based on Coastal System Analysis Using High-Resolution Unmanned Aerial Vehicle (UAV) Imagery (Case Study in Kukup Coastal Area, Gunungkidul Regency, Indonesia). *Geographia Technica*, 18(2), 51-67. http://dx.doi.org/10.21163/GT_2023.182.04
- Dogan, G. G., Annunziato, A., Hidayat, R., Husrin, S., Prasetya, G., Kongko, W., Zaytsev, A., Pelinovsky, E., Imamura, F., & Yalciner, A. C. (2021) Numerical Simulations of December 22, 2018 Anak Krakatau Tsunami and Examination of Possible Submarine Landslide Scenarios. *Pure and Applied Geophysics*, 178(1), 1-20. <https://doi.org/10.1007/s00024-020-02641-7>
- Farahdita, W. L., & Siagian, H. S. R. (2020) Analysis of the area affected by the tsunami in Pandeglang, Banten: A case study of the Sunda Strait Tsunami, in proceedings of IOP Conference Series: Earth and Environmental Science, 429(1). <https://doi.org/10.1088/1755-1315/429/1/012052>
- Galán, J. M., Izquierdo, L. R., Izquierdo, S. S., Santos, J. I., Del Olmo, R., López-Paredes, A., & Edmonds, B. M. (2009) Errors and artefacts in agent-based modelling. *Journal of Artificial Societies and Social Simulation*, 12(1), 1-1.
- Grilli, S. T., Tappin, D. R., Carey, S., Watt, S. F. L., Ward, S. N., Grilli, A. R., Engwell, S. L., Zhang, C., Kirby, J. T., Schambach, L., & Muin, M. (2019) Modelling of the tsunami from the December 22, 2018 lateral collapse of Anak Krakatau volcano in the Sunda Straits, Indonesia. *Scientific Reports*, 9(1). <https://doi.org/10.1038/s41598-019-48327-6>
- Helmi, M., Pholandani, Y. H., Setiyono, H., Wirasatriya, A., Atmodjo, W., Widyaratih, R., & Suryoputro, A. A. D. (2020) Intergrated approach of tsunami vulnerability assessment at coastal area of kalianda sub district, south lampung district, lampung Province, Indonesia. *International Journal of Scientific and Technology Research*, 9(3), 1803-1808.
- Husrin, S., Novianto, D., Bramawanto, R., Setiawan, A., Nugroho, D., Permana, S. M., Sufyan, A., Sarnanda, S., Sianturi, D. S. A., Mulyadi, U., Daniel, D., Suhelmi, I. R., & Purnama, M. S. B. (2021). Analisa Kinerja IDSL/PUMMA untuk Peringatan Dini Tsunami di Pangandaran. *Jurnal Kelautan Nasional*, 16(2). <https://doi.org/10.15578/jkn.v16i2.9846>
- Ito, E., Kosaka, T., Hatayama, M., Urra, L., Mas, E., & Koshimura, S. (2021) Method to extract difficult-to-evacuate areas by using tsunami evacuation simulation and numerical analysis. *International Journal of Disaster Risk Reduction*, 64(102486). <https://doi.org/10.1016/j.ijdr.2021.102486>
- Jacob, S., Aguilar, L., Wijerathne, L., Hori, M., Ichimura, T., & Tanaka, S. (2014) Agent Based Modeling and Simulation of Tsunami Triggered Mass Evacuation Considering Changes of Environment Due to

- Earthquake and Inundation. *Journal of Japan Society of Civil Engineers, Ser. A2 (Applied Mechanics (AM))*, 70(2), 671-680. https://doi.org/10.2208/jscejam.70.i_671
- Kim, K., Kaviari, F., Pant, P., & Yamashita, E. (2022) An agent-based model of short-notice tsunami evacuation in Waikiki, Hawaii. *Transportation Research Part D: Transport and Environment*, 105. <https://doi.org/10.1016/j.trd.2022.103239>
- Kuller, M., Bach, P. M., Roberts, S., Browne, D., & Deletic, A. (2019) A planning-support tool for spatial suitability assessment of green urban stormwater infrastructure. *Science of the Total Environment*, 686, 856-868. <https://doi.org/10.1016/j.scitotenv.2019.06.051>
- Kurniawan, W., Daryono, Kerta, I., Pranata, B., & Winugroho, T. (2021) Monitoring and analysis of seismic data during the 2018 sunda strait tsunami, in proceedings of E3S Web of Conferences, 331. <https://doi.org/10.1051/e3sconf/202133107006>
- Lakshay, -, Agarwal, A., & Bolia, N. B. (2016) Route Guidance Map for Emergency Evacuation. *Journal of Risk Analysis and Crisis Response*, 6(3), 135-144. <https://doi.org/10.2991/jrarc.2016.6.3.3>
- Lee, H. S., Sambuaga, R. D., & Flores, C. (2022) Effects of Tsunami Shelters in Pandeglang, Banten, Indonesia, Based on Agent-Based Modelling: A Case Study of the 2018 Anak Krakatoa Volcanic Tsunami. *Journal of Marine Science and Engineering*, 10(8), 1055. <https://doi.org/10.3390/jmse10081055>
- Li, X., Zhang, C., & Li, W. (2017) Building block level urban land-use information retrieval based on Google Street View images. *GIScience and Remote Sensing*, 54(6), 819-835. <https://doi.org/10.1080/15481603.2017.1338389>
- Marzuki, M. I., Rahmania, R., Kusumaningrum, P. D., Akhwady, R., Sianturi, D. S. A., Firdaus, Y., Sufyan, A., Hatori, C.A. & Chandra, H. (2021) Fishing boat detection using Sentinel-1 validated with VIIRS Data, in Proceedings of IOP Conference Series: Earth and Environmental Science (Vol. 925, No. 1, p. 012058). IOP Publishing.
- Mas, E., Koshimura, S., Imamura, F., Suppasri, A., Muhari, A., & Adriano, B. (2015) Recent Advances in Agent-Based Tsunami Evacuation Simulations: Case Studies in Indonesia, Thailand, Japan and Peru. *Pure and Applied Geophysics*, 172(12), 3409-3424. <https://doi.org/10.1007/s00024-015-1105-y>
- Mas, E., Suppasri, A., Imamura, F., & Koshimura, S. (2012) Agent-based Simulation of the 2011 Great East Japan Earthquake/Tsunami Evacuation: An Integrated Model of Tsunami Inundation and Evacuation. *Journal of Natural Disaster Science*, 34(1), 41-57. <https://doi.org/10.2328/jnds.34.41>
- Mostafizi, A., Wang, H., Cox, D., Cramer, L. A., & Dong, S. (2017) Agent-based tsunami evacuation modeling of unplanned network disruptions for evidence-driven resource allocation and retrofitting strategies. *Natural Hazards*, 88(3), 1347-1372. <https://doi.org/10.1007/s11069-017-2927-y>
- Mück, M., & Post, D. J. (2008). Mück, M., & Post, D. J. (2008) Tsunami Evacuation Modelling. Development and application of a spatial information system supporting tsunami evacuation planning in South-West Bali (Vol. 131). Institut für Geographie Universität Regensburg.
- Muhari, A., Heidarzadeh, M., Susmoro, H., Nugroho, H. D., Kriswati, E., Supartoyo, Wijanarto, A. B., Imamura, F., & Arikawa, T. (2019) The December 2018 Anak Krakatau Volcano Tsunami as Inferred from Post-Tsunami Field Surveys and Spectral Analysis. *Pure and Applied Geophysics*, 176(12), 5219-5233. <https://doi.org/10.1007/s00024-019-02358-2>
- Mulyadi, D., & Nur, W. H. (2018) The Analytic Hierarchy Process Application for EarthQuacke Hazard in Tanjung Lesung-Panimbang Pandeglang. *RISSET Geologi Dan Pertambangan*, 28(1), 37-48. <https://doi.org/10.14203/risetgeotam2018.v28.387>
- Naser, M., & Birst, S. C. (2010) Mesoscopic evacuation modeling for small to medium size metropolitan areas.
- OGAWA, Y., AKIYAMA, Y., YOKOMATSU, M., SEKIMOTO, Y., & SHIBASAKI, R. (2019). Estimation of supply chain network disruption of companies across the country affected by the Nankai trough earthquake Tsunami in Kochi city. *Journal of Disaster Research*, 14(3), 508-520. <https://doi.org/10.20965/jdr.2019.p0508>
- Pamukcu, D., Zobel, C. W., & Arnette, A. (2020) Characterizing social community structures in emergency shelter planning, In Proceedings of the International ISCRAM Conference, 2020-May.
- Paris, R., Switzer, A. D., Belousova, M., Belousov, A., Ontowirjo, B., Whelley, P. L., & Ulvrova, M. (2014) Volcanic tsunami: A review of source mechanisms, past events and hazards in Southeast Asia (Indonesia, Philippines, Papua New Guinea). *Natural Hazards*, 70(1), 447-470. <https://doi.org/10.1007/s11069-013-0822-8>

- Pesaresi, M., Corbane, C., Julea, A., Florczyk, A. J., Syrris, V., & Soille, P. (2016) Assessment of the added-value of Sentinel-2 for detecting built-up areas. *Remote Sensing*, 8(4), 299. <https://doi.org/10.3390/rs8040299>
- Phiri, D., Simwanda, M., Salekin, S., Nyirenda, V. R., Murayama, Y., & Ranagalage, M. (2020) Sentinel-2 data for land cover/use mapping: A review. *Remote Sensing*, 12, (14). <https://doi.org/10.3390/rs12142291>
- Pizarro, V., Leger, P., Hidalgo-Alcázar, C., & Figueroa, I. (2022) ABM RoutePlanner: An agent-based model simulation for suggesting preference-based routes in Spain. *Journal of Simulation*. <https://doi.org/10.1080/17477778.2022.2027826>
- Ponangsera, I. S., Kurniadi, A., Ayu Puspitosari, D., & Hartono, D. (2021) Determination of tsunami run-up and golden time in the megathrust subduction zone of the sunda strait segment, in proceedings of E3S Web of Conferences, 331. <https://doi.org/10.1051/e3sconf/202133107007>
- Pradjoko, E., Kusuma, T., Setyandito, O., Suroso, A., & Harianto, B. (2015) The Tsunami Run-up Assesment of 1977 Sumba Earthquake in Kuta, Center of Lombok, Indonesia. *Procedia Earth and Planetary Science*, 14, 9-16. <https://doi.org/10.1016/j.proeps.2015.07.079>
- Priohutomo, K., Nugroho, W. H., Arianti, E., & Priatno, D. H. (2022) Fatigue Life Prediction of Mooring Line on Indonesian Tsunami Early Warning Systems (Ina-TEWS) Buoy, in proceedings of IOP Conference Series: Earth and Environmental Science, 972(1). <https://doi.org/10.1088/1755-1315/972/1/012011>
- Sahal, A., Leone, F., & Péroche, M. (2013) Complementary methods to plan pedestrian evacuation of the French Riviera' s beaches in case of tsunami threat: Graph-and multi-agent-based modelling. *Natural Hazards and Earth System Sciences*, 13(7). <https://doi.org/10.5194/nhess-13-1735-2013>
- Sari, D. A. P., & Soesilo, T. E. B. (2020) Measuring Community Resilience to the Tsunami Disaster (Study of Sukarame Village, Carita District, Pandeglang Regency). In proceedings of IOP Conference Series: Earth and Environmental Science, 448(1). <https://doi.org/10.1088/1755-1315/448/1/012092>
- Taubenböck, H., Goseberg, N., Lämmel, G., Setiadi, N., Schlurmann, T., Nagel, K., Siegert, F., Birkmann, J., Traub, K.-P., Dech, S., Keuck, V., Lehmann, F., Strunz, G., & Klüpfel, H. (2013) Risk reduction at the “ Last-Mile” : an attempt to turn science into action by the example of Padang, Indonesia. *Natural Hazards*, 65(1), 915-945. <https://doi.org/10.1007/s11069-012-0377-0>
- Triyono, R., Prasetya, T., Daryono, D., Anugrah, S. D., Sudrajat, A., Setiyono, U., Gunawan, I., Priyobudi, P., Yatimantoro, T., Hidayanti, H., Anggraini, S., Rahayu, R. H., Yogaswara, D. S., Hawati, P., Apriani, M., Julius, A. M., Harvan, M., Simangunsong, G., & Kriswinarso, T. (2019) Katalog Tsunami Indonesia Tahun 416-2018 (M. Sadly (ed.); 1st ed.). Badan Meteorologi dan Geofisika (BMKG). (In Indonesian).
- Usman, F., Murakami, K., Dwi Wicaksono, A., & Setiawan, E. (2017) Application of Agent-Based Model Simulation for Tsunami Evacuation in Pacitan, Indonesia, in proceedings of MATEC Web of Conferences, 97. <https://doi.org/10.1051/mateconf/20179701064>
- Vargas-Munoz, J. E., Srivastava, S., Tuia, D., & Falcao, A. X. (2021) OpenStreetMap: Challenges and Opportunities in Machine Learning and Remote Sensing. *IEEE Geoscience and Remote Sensing Magazine*, 9(1). <https://doi.org/10.1109/MGRS.2020.2994107>
- Wafda, F., Saputra, R. W., Nurdin, Y., Nasaruddin, & Munadi, K. (2013) Agent-based tsunami evacuation simulation for disaster education, in proceedings of International Conference on ICT for Smart Society 2013: “Think Ecosystem Act Convergence” , ICISS 2013. <https://doi.org/10.1109/ICTSS.2013.6588087>
- Wang, Z., & Jia, G. (2021) A novel agent-based model for tsunami evacuation simulation and risk assessment. *Natural Hazards*, 105(2), 2045-2071. <https://doi.org/10.1007/s11069-020-04389-8>
- Wang, Z., & Jia, G. (2022) Simulation-Based and Risk-Informed Assessment of the Effectiveness of Tsunami Evacuation Routes Using Agent-Based Modeling: A Case Study of Seaside, Oregon. *International Journal of Disaster Risk Science*, 13(1). <https://doi.org/10.1007/s13753-021-00387-x>
- Yamanaka, Y., & Shimoazono, T. (2022) Tsunami inundation characteristics along the Japan Sea coastline: effect of dunes, breakwaters, and rivers. *Earth, Planets and Space*, 74(1). <https://doi.org/10.1186/s40623-022-01579-5>
- Yeh, H., Tolkova, E., Jay, D., Talke, S., & Fritz, H. (2012) Tsunami hydrodynamics in the Columbia River. *Journal of Disaster Research*, 7(5), 604-608. <https://doi.org/10.20965/jdr.2012.p0604>
- Zaman, M. B., Kobayashi, E., Wakabayashi, N., Khanfir, S., Pitana, T., & Maimun, A. (2014) Fuzzy FMEA model for risk evaluation of ship collisions in the Malacca Strait: Based on AIS data. *Journal of Simulation*, 8(1). <https://doi.org/10.1057/jos.2013.9>

CONTRIBUTION OF SPACE REMOTE SENSING AND NEW GIS TOOLS FOR MAPPING GEOLOGICAL STRUCTURES IN THE MEKKAM REGION OF NORTHEAST MOROCCO

Abdelali GOUISS ^{1*}, Youness TAYBI ², Youssef GHARMANE ³, Souad M'RABET ¹

DOI : 10.21163/GT_2023.182.11

ABSTRACT:

The Paleozoic buttonhole of Mekkam is located in the SE of the town of Taourirt, North Eastern Morocco. The geological framework of this buttonhole is characterized by the presence of terrains of different ages and lithologies. The oldest terrain forms a monotonous schistose bedrock with a flyshoid character of Devonian age unconformably underlain by volcanic and sedimentary formations of probable Upper Visean age, which have not been the subject of detailed structural studies. The objective of this work is to create a structural map based on satellite image processing techniques from space remote sensing. Our methodology uses remote sensing data composed of LANDSAT 8 Oli satellite imagery, taken under favorable weather conditions. Principal Component Analysis (PCA) and directional filtering were applied specifically. Thus, a map was produced using ArcGIS and Rockworks16 software. The application of these techniques allowed us to highlight the presence of lineaments with four main directions: N-S, NE-SW, E-W and NW-SE with a dominance of NW-SE and E-W directions. The interpretation of the obtained map was verified by field missions (measurements of faults, veins, and dykes). The NW-SE and E-W directions correspond in the field to mineralized quartz dykes and veins. The highlighted lineaments are concentrated in the Devonian-aged terrains where the geological material is represented by schists and volcanic rocks. The terrain is characterized by steep and rugged relief, sometimes difficult to access, such as the Sidi Lahcen massifs, the present study will initially help guide mining exploration by determining the geological lineaments in the region. Thus, it confirms that remote sensing is an effective and less costly means of structural mapping in arid and semi-arid areas.

Key-words: Remote Sensing, GIS, Rockworks16, Mapping, Lineaments, Mineralization, Mekkam, Morocco

1. INTRODUCTION

In remote sensing, lineaments are any straight or curvilinear structure, some of which may have geological significance (fault, dyke, etc.) (Hobbs, 1904; O'Leary et al. 1976). Their study is of crucial importance for the analysis and understanding of the regional structural context. Today, their extraction has become possible thanks to digital processing of satellite images. As their tensor translates into a binary black and white representation on the satellite image, it is easy to extract the lineaments by noise removal. (Han et al. 2018).

In the present study, the Landsat 8 OLI satellite image of the Mekkam buttonhole was used. The extraction of lineaments was carried out using the automated extraction method guided by PCI Geomatica software, aiming to create an initial map of the different lineaments of the buttonhole.

¹ Geosciences Laboratory, Faculty of Sciences, Ibn Tofaïl University, Kénitra, *Corresponding author abdelali.gouiss@uit.ac.ma, mrabet.souad@uit.ac.ma

² Laboratory of Molecular Chemistry, Materials and Environment (CM2E), Multidisciplinary Faculty of Nador, y.taybi@ump.ac.ma

³ Laboratory of Intelligent Systems, Department of Geology, Faculty of Sciences and Techniques, Sidi Mohamed Ben Abdellah University, Fez, Morocco, gharmaneyoussef@gmail.com

2. STUDY AREA

The study area is a Paleozoic boutonhole attributed to the Eastern Meseta, located 50 km SE of the town of Taourirt. Access to this boutonhole is provided by road P6052 between Taourirt and Berguent. The dominant climate in the region is arid, with a succession of two seasons: one cold in winter and one hot in summer. Previous works (Médioni, 1980; Marhouni et al. 1983; Chegham, 1985 et Hoepffner, 1987) have described the geological context of this massif, noting a monotonous schistose bedrock with a flyshoid character of Devonian age unconformably underlain by volcanic and sedimentary formations of probable Upper Viséan age. The volcano-sedimentary complex known as Ez-Ziroug is in abnormal contact with the granitoids of Soulouina-Hassiane-Diab. These Paleozoic terrains are overlain by Triassic and Quaternary formations (**Fig. 1**).

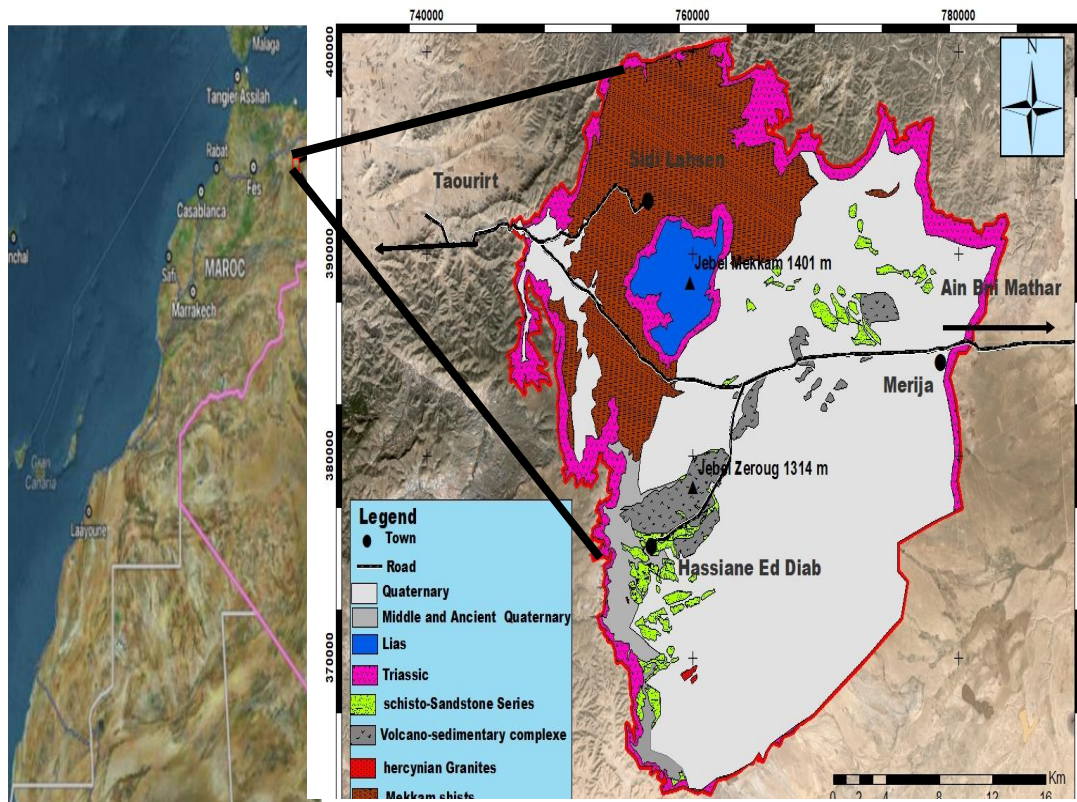


Fig 1. Location and geological map of the Mekkam boutonhole.

3. DATA AND METHODS

The Landsat 8 OLI image was chosen due to its relevance in extracting lineaments (Abdelouhed et al. 2021). The image covers the entire study area, and its acquisition date of 11/08/2019 was chosen to avoid clouds that could obstruct the area. The Landsat images are available on the website « arthexplorer.usgs.gov ». The Mekkam boutonhole, which constitutes our study area, has been delineated on four topographic maps (Taourirt, Ain Bnimathar, Hassiane Ed Diab, and Oued Charfe sheets, at a scale of 1:100000). Consequently, the study area was extracted from the satellite image.

Then, based on digital image processing techniques, an atmospheric and radiometric correction was applied using the INVI 5.3 software. Subsequently, the extraction of lineaments was carried out following four main steps, which are: (1) Principal Component Analysis using INVI 5.3; (2) Filtering using INVI 5.3; (3) Automatic lineament extraction using PCI Geomatica; and (4) Verification and validation of results in the field and using ArcGIS and Rock Works.

3.1. Principal Component Analysis (PCA)

Principal Component Analysis (PCA) is a technique for image transformation based on complex digital processing of statistical characteristics of multi-band data to reduce data redundancy and establish the correlation between frequency bands (Pandey et Sharma, 2019). This technique is widely used by geologists in digital mapping, it reduces the information contained in multiple, sometimes highly correlated bands, into a smaller number of components. These components typically represent around 97% of the total variation in the original data set (Deslandes, 1986). With this analysis, the information presented in 5 or 6 bands is compressed into two or three principal components. Previous work (Hammed et al. 2020; Ba et al. 2020; Tözün et Özyavaş, 2022) have shown that the first three principal components contain over 90% of the spectral information. In our case, the first components CP1, CP2, and CP3 were chosen for the extraction of lineaments. High-quality information was acquired during the applied tests. The new images obtained from the original data provide the opportunity to create color compositions that enable a better visual interpretation. PCA was carried out using INVI 5.3 software, and the results obtained were subsequently used in the sequence followed to locate the lineaments.

3.2. Directional filtering

Directional filtering is crucial for lineament extraction. It helps improve the visualization of the image by eliminating noise present in the image data, making interpretation easier (Amrani, 2007; Abdelouafi, 2007; Ezzine et al. 2011). Its principle is manifested by a rectangular window (3x3, 5x5, 7x7...) that moves line by line and column by column to calculate the new value of the central pixel (Amrani, 2007). In geology, we are interested in irregularities or interruptions in imaging textures, which can reveal the presence of faults, dykes or veins. (Ezzine et al. 2011). Sobel directional filtering is based on convolving the image with a small kernel in both vertical and horizontal directions. It calculates the gradient of the image intensity at each point and gives the direction of the possible increase from light to dark (Al-Djazouli et al. 2019). In our case, this filtering is applied to the different main directions, which are: N-S, NE-SW, NW-SE et E-W, by adopting the different windows (3x3, 5x5, 7x7, 9x9...). The 5x5 window proved to be the most favorable for the Landsat 8 image with a spatial resolution of 30 m x 30 m that we adopted. The results obtained from the filtering are presented in **Figure 2**.

3.3. Automatic lineament extraction

The lineaments were automatically extracted from the images obtained through directional filtering using the "line" option in PCI Geomatica software. The reliability of this method has been confirmed in comparison to manual lineament extraction, as assessed through a comparison conducted by Hung et al. 2005. This technique is faster and simpler, relying solely on the quality of the image used. A higher number of lineaments is revealed, as well as smaller structures. The principle of this method is based on an algorithm designed to work with the « PCI Geomatica » software. to obtain a final map in vector format by following three essential steps: (1) edge recognition, (2) thresholding and (3) curve extraction (Kiran et Ahmed, 2014 ; Pandey et Sharma, 2019).

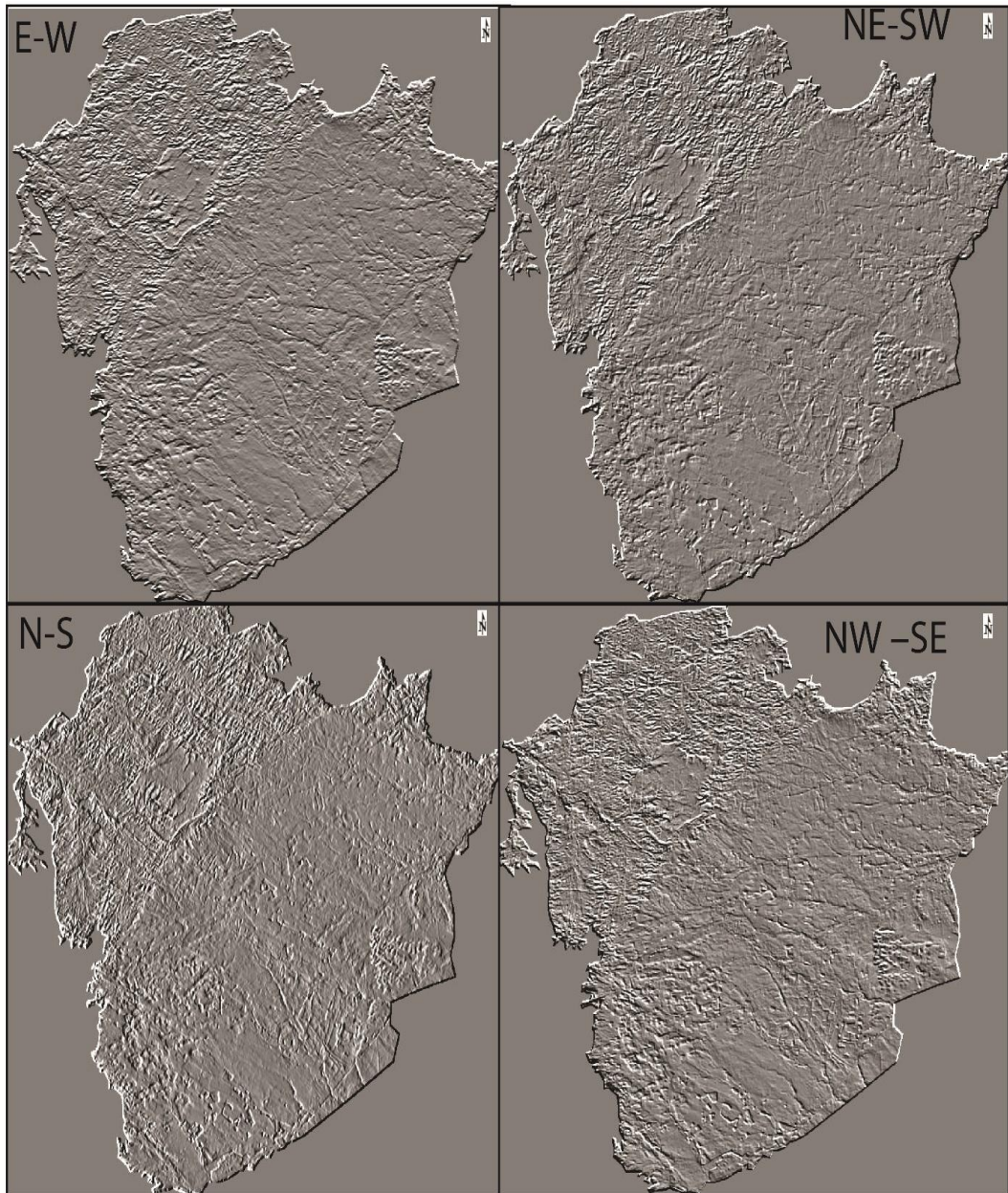


Fig. 2. Directional filtering.

3.4. Verification and validation of results

These steps were applied in our case to the four images obtained through filtering. The Arc GIS software allowed for the combination of the four images to create a synthetic map without distinguishing between lineaments of geological significance (faults, veins, dykes, and lithological contacts) and man-made lineaments (roads, tracks, and high-voltage lines). Field verification was conducted to distinguish between different types of lineaments. Then, a statistical study was conducted to quantify the lineaments and establish the directional rose diagram of the dominant directions using the "Rock Works" software.

4. RESULTS

The lineament map produced is shown in **Figure 3**. Anthropogenic lineaments have been subtracted. Overall, the results obtained from digital processing of satellite images are in line with existing data. New geological structures are revealed in comparison with previous work of Chegham, 1981 and d'Hoepffner, 1987. A second confirmation of the numerical results was provided by four field missions. During which we recorded the measurements of the various directional families of the structures observed, as well as their locations. The nature of the lineaments is varied, it corresponds to either faults, dykes or mineralized quartz veins, the number of faults is predominant.

The interpretation of the results allowed us to highlight the following observations: (1) The structural complexity of the Mekkam sector, where we can distinguish the existence of four main directions. N-S, NE-SW, E-W, NW-SE (**Fig. 4**) with the dominance of the E-W direction and the NW-SE direction; (2) The frequency of lineaments shows that the Sidi Lahsen schistose terrain in the north is affected by more faults and dykes than the terrain of the Hassiane Diab volcano-sedimentary complex in the south; (3) The existence of several directions in the same sector most probably shows that the study area underwent successive phases of orogenic deformation.

Field missions confirm the presence of eruptive rock dykes (**Fig. 5**). With directions that are generally E-W, quartz veins running NW-SE (Hassiane-Diab) and E-W (Sidi Lahcen) These are consistently associated with different types of mineralization, including Pb-Zn-Ag and W, Ba, some of them have been exploited or are currently under exploitation. Our field work has led to the discovery of new mineralized veins not reported in the literature, which can be used to delineate and estimate their mineral resources.

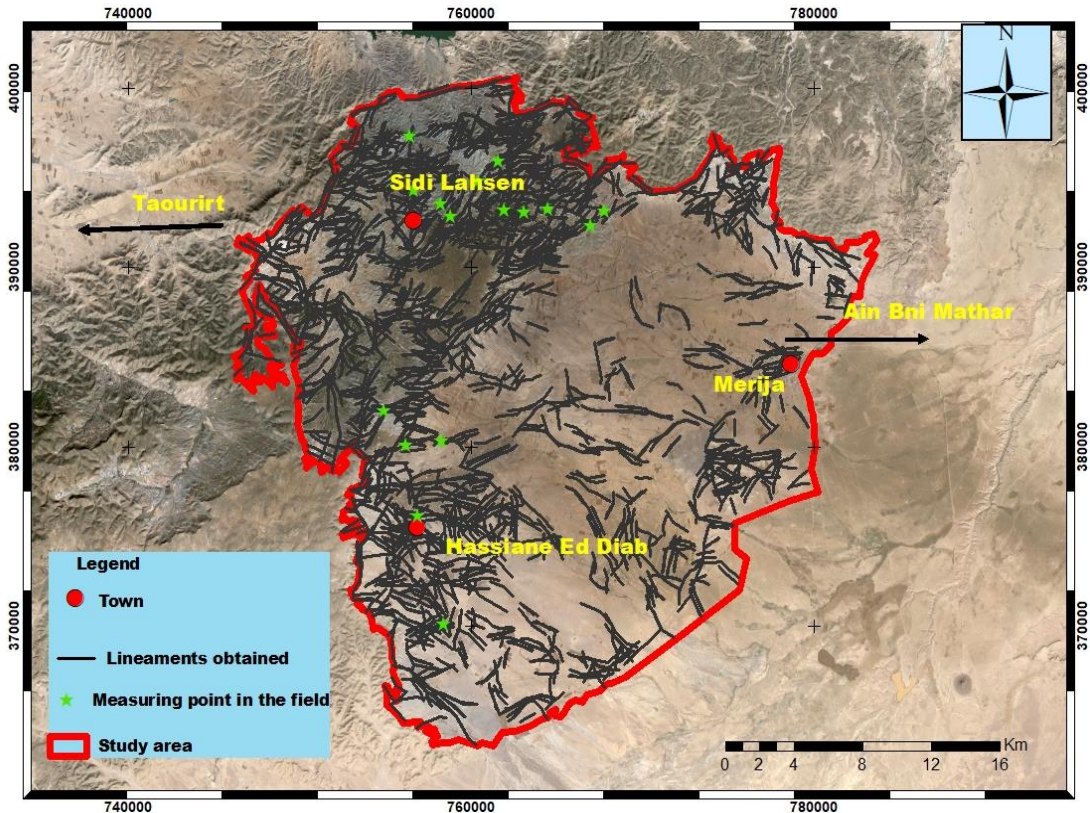


Fig. 3. Map of lineaments obtained.

To understand the distribution of lineaments and define their characteristics, a statistical analysis was carried out using "Arc Map & Rock works" software. The first is used to calculate the length of each lineament and the second to create the directional Rose. These two software programs were used to calculate the number of lineaments and to determine their direction over the total area of the Mekkam buttonhole, i.e., 855,21 km². 1624 lineaments were identified in all directions. Lineament lengths vary from 0.9 km to 7 km. We distinguish 4 classes:

- class 1, NW-SE direction, represents 28% of total lineaments.
- class 2, direction E-W, represents 26% of total lineaments.
- class 3, running N-S, accounts for 23% of all lineaments.
- class 4, direction NE-SW, also represents 23% of total lineaments.

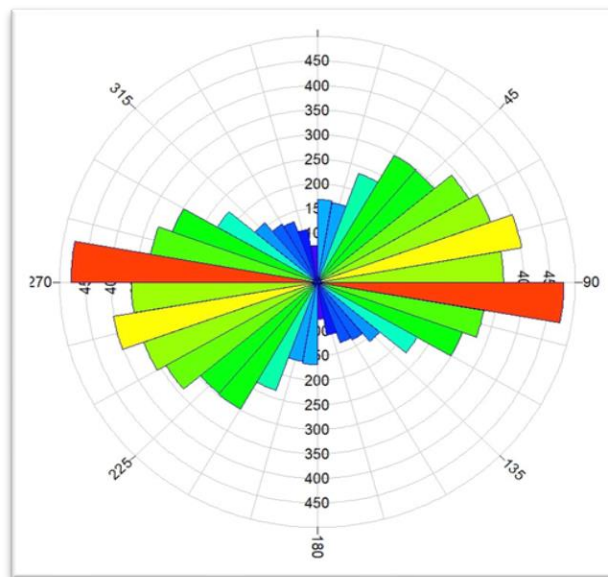


Fig. 4. Rose Diagram.

5. DISCUSSION

On a regional scale, the structural complexity and number of faults and dykes in the Debdou-Mekkam zone is linked, as pointed out by Chegham (1985) to character polyphase of the deformation. According to this author, shists of the Devonian age have undergone at least three phases of deformation that have generated various types of folds and anchizone metamorphism. Hoepffner's (1987) tectonic analysis revealed two episodes of deformation, D1 and D2, attributable to the Eovaric (Breton) phase. D1 corresponds to the initial structuring of the Debdou-Mekkam schists, where the folds have a homogeneous NW-SE direction. D2 is attributed to a deformation episode that probably occurred during the Eovaristic phase (Breton), anterior to the Upper Viséen deposits and characterized by folds running N 120 to N 150. The post-Westphalian D3 phase is superimposed on the two preceding episodes. The multitude of geological lineaments that we have extracted and presented on the map is the signature of this tectonics and the rheological response of the terrain to deformation.

Our results provide new information that confirms the polyphase nature of the structural history in the area studied. On the map obtained, the accidents are located in the Paleozoic terrain of the Mekkam buttonhole. In Mesozoic and Cenozoic terrains, lineaments are less frequent or even absent, recent cover masks the deeper Paleozoic fault and dyke network.

On a large scale, according to Lagarde (1989), the overall deformation of the Moroccan Meseta was followed by the emplacement of late-Hercynian syntectonic granitoids. In our study area, we note the presence of a multitude of mainly microdiorite dykes and mineralized veins attributed to this tectonic phase. All the lineaments extracted by satellite image processing are in overall agreement with the geological data observed in the field.

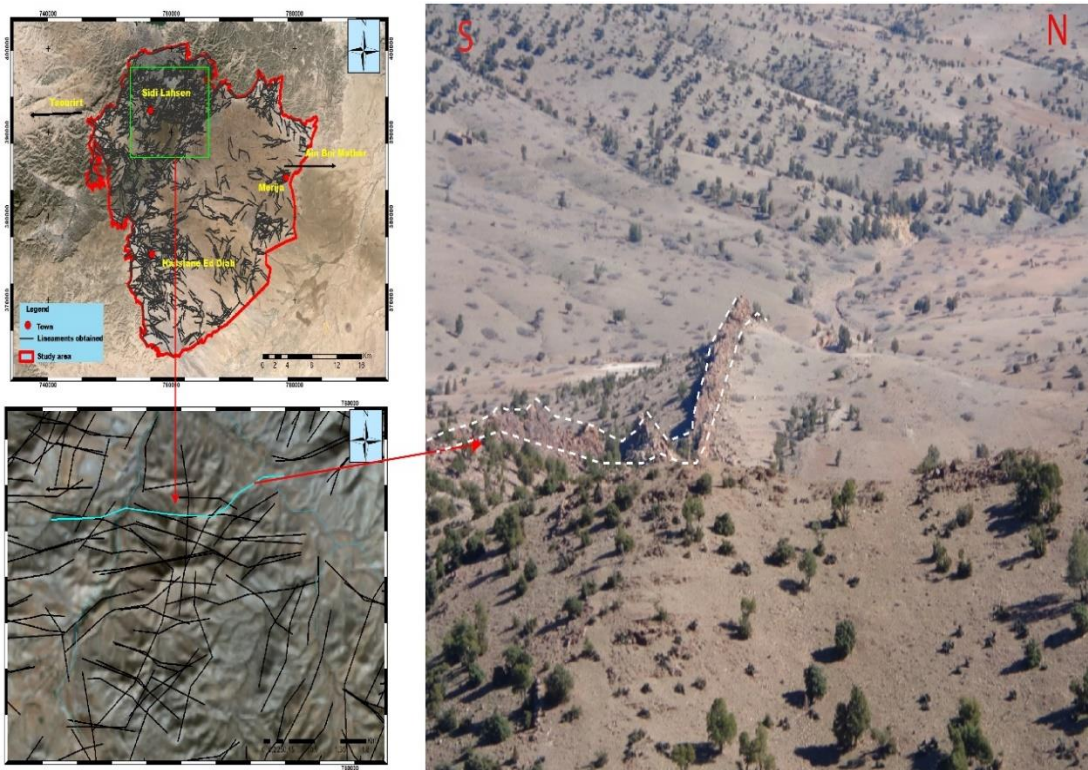


Fig. 5. E-W Dyke at Sidi Lahcen.

6. CONCLUSIONS

Our approach, based on remote sensing image processing and geological field surveys, has enabled us to map geological lineaments in a difficult-to-access area.

Four preferential directions, N-S, NE-SW, E-W and NW-SE, have been identified, corresponding in the field to mineralized dykes and veins, or even faults.

A database of all lineaments has been established that can be used for mineral exploration in the region.

Spatial remote sensing data combined with field work offer an encouraging approach to structural studies. These tools make the task easier and contribute to a better understanding of structural contexts.

REFERENCES

- Abdelouafi A. (2007). Approche multi-sources pour l'élaboration d'un outil d'aide à la décision dans le cadre du développement durable du Maroc oriental : (Géologie, Télédétection, Géophysique, Hydrogéologie, Couvert végétal, Substances utiles). Thèse de Doctorat, Faculté des Sciences Agdal de Rabat, (296 p).
- Abdelouhed F., Ahmed A., Abdellah A., Mohammed I. (2021) Lineament mapping in the Ikniouen area (eastern anti-atlas, Morocco) using Landsat-8 Oli and SRTM data. In: Remote sensing applications: society and environment, vol. **23**, 100606. <https://doi.org/10.1016/j.rsase.2021.100606>
- Al-Djazouli, M.O., Elmorabiti, K., Zoheir, B. et al. (2019). Use of Landsat-8 Oli data for delineating fracture systems in subsoil regions: implications for groundwater prospection in the Waddai area, eastern Chad. Arab J Geosci 12, 241. <https://doi.org/10.1007/s12517-019-4354-8>
- Amrani, A. (2007). Apport des données couplées d'imagerie satellitaire Etm+ de landsat 7 et modèle numérique de terrain appliquées à l'étude morphogénétique de la haute et moyenne Moulouya (Maroc). Thèse de Doctorat, Faculté des Sciences Agdal de Rabat, (217 p).
- Ba M.H., Ibouh H., Lo K. et al. (2020). Spatial and temporal distribution patterns of Precambrian mafic dyke swarms in northern Mauritania (West African craton): analysis and results from remote-sensing interpretation, geographical information systems (GIS), Google Earth™ images, and regional geology. Arab J Geosci 13, 209. <https://doi.org/10.1007/s12517-020-5194-2>
- Chegham A. (1985). Etude minéralogique et géologique des filons Pb-Zn-Ag (Fe, Cu, Ba) de Sidi Lahcen (boutonnière de Mekkam, Maroc oriental) (Doctoral dissertation).
- Deslandes S. (1986). Évaluation des images Spot et Seasat pour la cartographie des linéaments du secteur des Monts Stoke, au Québec, une comparaison basée sur l'analyse du spectre de Foumer. Mémoire de maîtrise, Département de géographie, Université de Sherbrooke, 62 p.
- Ezzine I., Zargouni F., Ghanmi M., (2011). Analyse linéamentaire des images landsat-tm et spot de l'atlas centro-septentrional: cartographie du prolongement SW de la cicatrice de Zaghouan Teledetection, **10**(4), pp.199-211 hal-01948894
- Hammed M. S., Shallaly N. A., Abdelghani I. M., Badr Y. S., & Sayed S. A. (2020). Application of remotely sensing data in the geologic and radioactive mapping of Wadi Fatirah Precambrian rocks, north Eastern Desert, Egypt. Nuclear Sciences Scientific Journal, **9**(1), 227-253.
- Han, L., Liu, Z., Ning, Y., Zhao, Z., (2018). Extraction and analysis of geological lineaments combining a DEM and remote sensing images from the northern Baoji loess area. Adv. Space Res. 62, 2480–2493. <https://doi.org/10.1016/j.asr.2018.07.030>
- Hobbs W. H. (1904). Lineaments of the Atlantic border region. Bulletin of the Geological Society of America, **15**(1), 483-506.
- Hoepffner C. (1987). La tectonique hercynienne dans l'est du Maroc. Thèse Docteur ès sciences Naturelles, Strasbourg, 257 p.
- Hung, L. Q., Batelaan, O., & De Smedt, F. (2005). Lineament extraction and analysis, comparison of Landsat ETM and Aster imagery. Case study: Suoimuoi tropical karst catchment, Vietnam. In Remote sensing for environmental monitoring, GIS applications, and geology V (Vol. 5983OT, pp. 182-193). Event: SPIE Remote Sensing, <https://doi.org/10.1117/12.627699>
- Kiran Raj S. & Ahmed A. S. (2014). Lineament Extraction from Southern Chitradurga Schist Belt using Landsat TM, ASTERGDEM and Geomatics Techniques. Int. J. Comput. Appl. 93, 12–20. <https://doi.org/10.5120/16266-5993>
- Lagarde J-L., (1989) : Granites tardi-carbonifères et déformation crustale : l'exemple de la Meseta Marocaine. Mém. Doc. Centre Armor. Etudes. Socles, n°26, 342 p.

- Marhoumi M.R., Hoepffner C., Doubinger J. et Rausher R. (1983). Données nouvelles sur l'histoire hercynienne de la méséta orientale du Maroc. L'âge Dev. Des schistes de Debdou et du Mekam. C.R. Acad. Sc., Paris, T. 297.
- Médioni R. (1980). Mise au point stratigraphique sur les terrains carbonifères de la bordure septentrionale des hauts plateaux marocains (Masif de Debdou, boutonnière de Lalla Mimouna et du Mekam). Notes, Serv. geol., Maroc, T. 41, n° 285, p. 25-37.
- O'leary, D. W., Friedman, J. D., & Pohn, H. A. (1976). Lineament, linear, lineation: some proposed new standards for old terms. Geological Society of America Bulletin, **87**(10), 1463-1469.
- Pandey, P., Sharma, L.N., (2019). Image Processing Techniques Applied to Satellite Data for Extracting Lineaments Using PCI Geomatica and Their Morphotectonic Interpretation in the Parts of Northwestern Himalayan Frontal Thrust. J. Indian Soc. Remote Sens. **47**, 809–820. <https://doi.org/10.1007/s12524-019-00962-2>
- Tözün, K. A., & Özyavaş, A. (2022). Automatic detection of geological lineaments in central Turkey based on test image analysis using satellite data. Advances in Space Research, **69**(9), 3283-3300. <https://doi.org/10.1016/j.asr.2022.02.026>

IDENTIFICATION OF RETENTION AREAS USING AIRBORNE LIDAR DATA. A CASE STUDY FROM CENTRAL SWEDEN

Jakub SEIDL^{1,2} 

DOI: 10.21163/GT_2023.182.12

ABSTRACT :

This paper presents a method for identifying retention areas in forest stands using publicly available ALS (Aerial Laser Scanning) data. Retention areas/trees are the cause of large inaccuracies in compartmental timber volume calculations when updated with remote sensing data. Tree height was selected as the most explanatory parameter for identification. The calculation of the threshold value for each compartment was based on data from the FMS (Forest Management System) or on the evaluation of the statistical distribution of LiDAR data in the compartment. The calculation was applied directly to the 3D point cloud, where points with the corresponding height were classified and processed into the resulting vector layer. Both methods were tested and validated on a reference dataset. The statistical approach proved to be more reliable (OA 89%) due to frequent errors or outdated data in the FMS (OA 82%). After removing dead retention trees (standing tree torsos) from the validation dataset, the OA of both methods increased (FMS approach 90%, statistical approach 94%).

Key-words: ALS, LiDAR, Retention trees, Forest Management System, Sweden

1. INTRODUCTION

With the increasing emphasis on biodiversity and sustainability, new approaches and practices have been introduced in various sectors. Forestry is undoubtedly one of them. As timber production can conflict with conservation objectives, a new concept of retention forestry (Beese et al., 2019) has been incorporated into the forest management system (Gustafsson et al., 2020). The aim is to promote biodiversity directly during timber harvesting. Retention is understood as a single tree or group of trees set aside in a logged area because it provides a home for different types of organisms (insects, fungi, etc.). They have become common practice in Scandinavian countries (Finland, Sweden, Norway) since the late 1990s and are included in national legislation and certification standards (Gustafsson et al., 2010).

Since the forest fulfills multiple roles (productive, ecological) a long-term management plan is needed to enhance or preserve it. For more detailed planning additional forest stands stratification is done (PEFC, 2016). Those areas are called compartments and present relatively homogeneous areas, which are then managed separately to achieve specific goals. For each compartment, a detailed description is provided including information about age, area, forestry objective, tree species distribution, volume, etc. These days, compartments are usually constructed with the usage of remote sensing data such as aerial or satellite images (Poso et al., 1987).

¹ Stora Enso IT, Stora Enso Wood Products Ždírce s.r.o., Nová Karolina Park, 702 00, Ostrava, Czech Republic, jakub.seidl@storaenso.com

² Department of Geoinformatics, Faculty of Mining and Geology, VSB – Technical University of Ostrava, , Ostrava, Czech Republic, jakub.seidl@vsb.cz

Forest inventory and monitoring benefit from new technologies. These make it possible to cover large areas and obtain important information on forest stands or even individual trees with less cost and effort required by traditional methods. An example of these technologies is Light Detection and Ranging (LiDAR, Pitman et al., 2004; Wandinger, 2005). Its ability to penetrate the tree canopy makes this technology almost ideal for forest mapping. There are multiple areas in forestry where LiDAR data are used these days. One of those is forest inventory and monitoring which usually incorporate techniques for tree detection, and calculation of their characteristics like height, volume (Hyyppa et al., 2001; Popescu et al., 2003; Andersen et al., 2004; Dalponte et al., 2016; Cao et al., 2016), or species classification (Heinzel et al., 2011; Yao et al., 2012). Other areas like forest ecology are interested in deriving information about biomass (Zhao et al., 2009; Gleason et al., 2012) or forest canopy structure (Zhao et al., 2011; Wang et al., 2008). Harvesting operations can also benefit from LiDAR-derived DTM that can be utilized as input for routing of forwarders (Holmström et al., 2023) or optimization of landings (Flisberg et al., 2022) to improve work efficiency and minimize environmental impact.

Regarding the tree parameters that can be derived from LiDAR data, two main approaches are usually distinguished: ABA (Area Based Approach) which is an estimate of selected parameters in some aggregation unit, and ITD (Individual Tree Detection) where all trees are tracked individually. Various techniques are utilized for ITD, such as the Watershed algorithm (Wu et al., 2019) and methods using Local Maxima Identification (Hyyppa et al., 2001), Polynomial Fitting Method (Cao et al., 2016), Individual Tree Crown Segmentation (Dalponte et al., 2016), and Point Cloud Segmentation (Li et al., 2012). Other methods use deep/machine learning (Chen et al., 2021) or graph theory (Strîmbu et al., 2015), or a combination of those methods where the result of one method serves as input into another (Wu et al., 2019).

Only a single study (Hardenbol et al., 2022) so far has dealt with the identification and classification of retention trees. The study used the ITD approach to identify and classify retention trees on ALS (Aerial Laser Scanning) data with a density of 5 points/m² in combination with not rectified CIR (color-infrared) aerial images in Finland. The basis of the ITD was CHM (Canopy Height Model) smoothing and local maxima detection in moving fixed size window. Then, tree crown boundaries were identified with the Watershed algorithm, and a height threshold was applied to keep only retention trees. The study reached a detection rate of 83.8% for living trees and 41.7% for dead trees.

This paper presents novel methods to identify retention areas using low-resolution ALS (Aerial Laser Scanning) data with a density around 2 points/m². Two methods are presented and evaluated. Both are based on ABA since forest retention is not only consisting of selected trees left after harvest but also complete small intact forest areas (Gustafsson et al., 2020). The objective of the presented work was:

- i) to create a solution for identifying retention areas from publicly available data
- ii) solution must be suitable for large areas using standard hardware

Currently, no dataset on retention areas is publicly available, although they can be beneficial for biodiversity applications and increase data accuracy in the forest management system. These systems typically include dominant tree height values at the compartment level, and retention areas can strongly influence them since the retention is usually much higher than the productivity layer.

2. DATA AND METHODS

2.1 Used data

Because of availability, sufficient detail, and coverage, publicly available LiDAR dataset from Lantmäteriet (<https://www.lantmateriet.se/>) was used as source data. Dataset covers the whole of Sweden with a minimum point density of 0.5 points/m² for all scanned surfaces and a minimum point density of 1.0 points/m² in forest areas, decreasing to 0.25 points/m² in bare mountains.

The height of flight from which scanning was realized ranged from 1700 to 2300 m above sea level (4000 m in mountains). The data acquisition was performed with a maximum scanning angle of $\pm 20^\circ$ and a lateral overlap of 10 to 20%. Absolute positional accuracy for open flat hard surfaces was 0.1 m in height and 0.3 m in plane. The data come pre-processed and classified into four categories (land, water, bridge, unclassified) and follow the SS-EN ISO 16157:2013 standard Geographic information - Data quality (Lantmäteriet, 2022).

Two areas (AOI 1, AOI 2) in Sweden (Norra Sverige, Dalarnas Län) were selected for testing the approach (**Fig. 1**). Both together cover approximately 250 km² and contain approximately 900 forest units less than 30 years old (see **Table 1** for more detailed information) which in total covers around 55 km². The main reason for age restriction is the fact, that retention forestry was implemented in the early 1990s, and therefore is no sense in processing older data. The point density was approximately 2.7 points/m² for both selected areas thus adequate for tree detection (Kaartinen et al. (2012) state sufficient point density for grown-up trees as 2 p/m²).

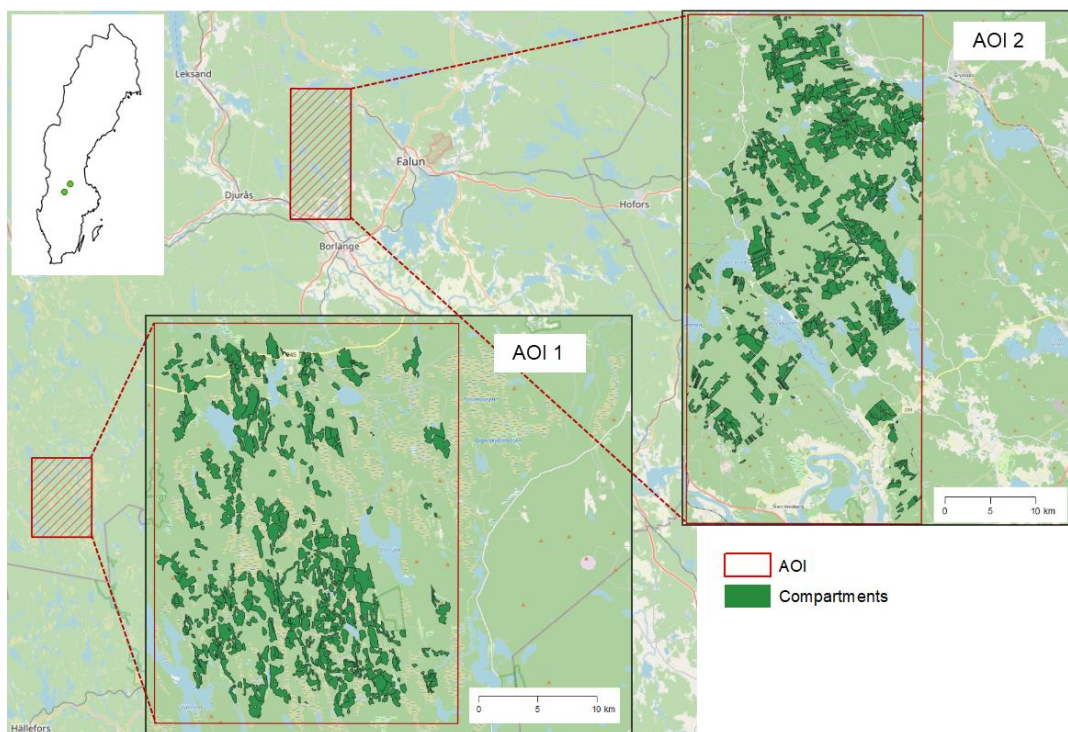


Fig. 1. Map of selected test areas.

Table 1.

Test area basic information.

	AOI 1	AOI 2
Area size (km ²)	78 km ²	189 km ²
Number of compartments	249	668
Compartment coverage (km ²)	22.7	34.5
Mean compartment size (km ²)	0.07	0.05
Year of sensing	2021	2020

2.2. Retention areas identification

To stratify the forest, forest compartments were used to divide the forest into relatively homogeneous areas. The main assumption of the presented approach was that trees in retention areas should be significantly higher than other young trees in the forest compartment (production layer). Therefore, a simple height threshold for the whole compartment was defined to detect retention. To ensure that all retention trees are significantly taller than the production layer and thus identifiable in the LiDAR data, only stands younger than 30 years were selected. Two different approaches were then used (described in the processing section) and the results were validated.

It was decided to implement both approaches directly on the point cloud data (**Fig. 2**) instead of using techniques to identify retention on the CHM (Canopy Height Model) (Hardenbol et al., 2022). The main reason was that the point cloud data allowed us to obtain the number of points in each cell and thus omit cells with significant enough height but low point counts. These could potentially also be retention regions but with much lower reliability resulting from the low number of laser pulse measurements.

The whole calculation process was implemented in Python 3.10.8 (<https://www.python.org/>) with the libraries Numpy 1.22.3 (<https://numpy.org/>), Laspy 2.3.0 (<https://laspy.readthedocs.io/>), GDAL 3.5.1 (<https://gdal.org/>), Shapely 1.8.2 (<https://shapely.readthedocs.io/>), and PDAL 3.1.2 (<https://pdal.io/en/latest/>). The first step of the workflow is to crop the LiDAR point cloud data to the extent of the given forest compartment or another stratification layer to assure some level of forest homogeneity. The compartment geometry was converted from ESRI Shapefile to JSON format to be readable by the PDAL library. Then, for all points, the Z coordinate values were normalized to HAG (Height Above Ground) based on the distance of a particular point from the ground. The ground was interpolated from points classified as ground. The next step was classifying points representing retention. For this purpose, minimum tree height thresholds were calculated separately for each forest compartment. Two methods were used. The first one used data from the forest management system and was based on the information of the expected DOM (DOMinant tree height) in the forest compartment. Based on interviews with expert forest managers, it was decided to calculate the threshold as the expected DOM + 70%. DOM itself is usually calculated as the average height of the trees with the largest diameter at breast height (Kangas et al., 2011). The 70% enlargement should guarantee that all trees higher than that are true retention.

The second method was based on a statistical approach whereby retention was identified by statistically different heights compared to other points in the compartment that were not classified as ground. To deal with the possible different distribution of data in the compartments, the height values (x) were transformed into z-score values with the usage of PDAL *filters.assign* function which enables setting the filtering rule for a specific dimension of the point cloud that is applied to all points parsed as input to the function. The nature of the z-score implies that a higher value means that the value is less likely to come from a chance. Therefore z-score (Z) values greater than 3 (p-value = 0.0013) were considered statistically significant differences (three standard deviations (σ) away from the mean (μ)) and classified as potential retention:

$$Z = \frac{x - \mu}{\sigma} \quad (1)$$

where:

- Z = the z-score
- x = the height values
- μ = the mean
- σ = the standard deviations

This approach was chosen to evaluate the possibility of identifying retention areas in localities where forest management system DOM heights are not available.

Right after, points assigned to the retention class were converted into a two-band raster with a 2 m cell size (band 1: maximum height; band 2: number of points). With these data, a new Boolean raster was created (1: retention; 0: other). The number 1 was assigned to cells whose values were calculated from a sufficient number of points (at least 4 in a cell) or had a sufficient HAG value relative to the other retention areas in that compartment.

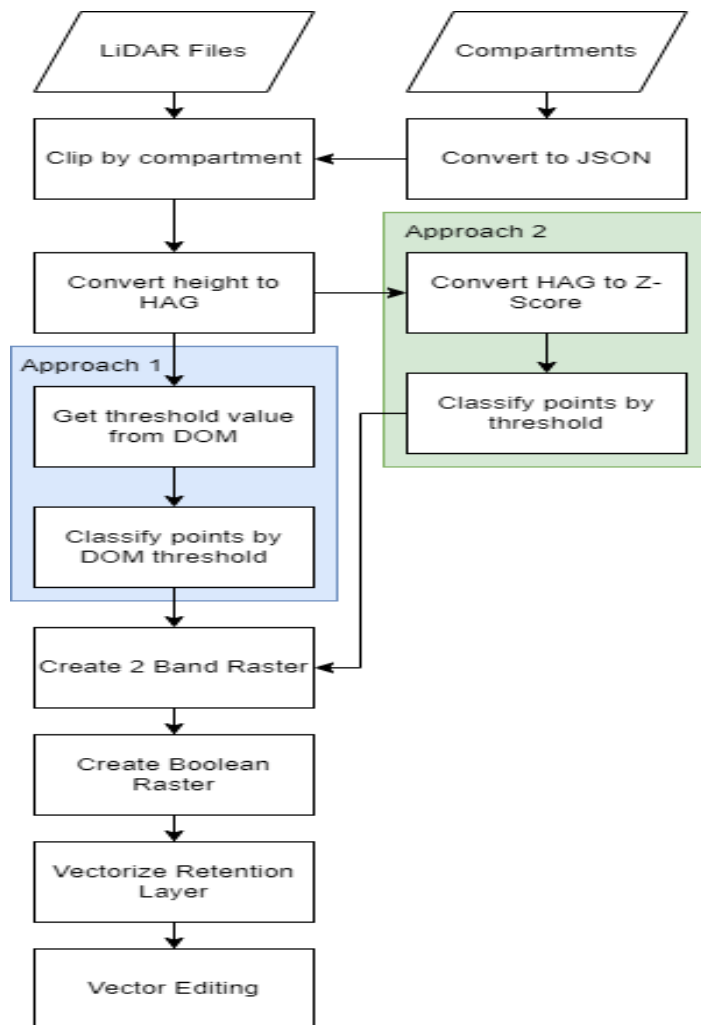


Fig. 2. Process schema.

In the last step, the Boolean raster was polygonized, and the following polygons were adjusted:

- 1) polygons smaller than 4 m² were removed to prevent false positives originating from overgrown vegetation (solo branches, etc.) or noise in the data;
- 2) polygons touching the forest compartment boundary were marked, to avoid errors originating from the boundary imprecision;
- 3) polygons that could potentially be solo trees were marked, based on the maximum area of the retention polygon and similarity to a circle (Fig.3). The area threshold was set to 160 m² = 40 pix (approximately the area of the crown with a 7 m radius).

If the polygon satisfies the area condition a circle similarity was evaluated. The area of a circle with a diameter equal to the polygon's maximum distance was compared with the retention polygon area (the polygon must cover at least 65 % of the circle).

2.3. Validation

Validation was based on orthophotos with 16 cm GSD (Ground Sample Distance) acquired in the summer of 2022. Despite the problems arising from the time lag, these data are the most recent data suitable for validation. Given that field measurements from 2023 would extend the time gap. Prominent retention trees standing in cleared areas or among young/low vegetation were marked by visual inspection in both areas and divided into two classes (tree, dead tree). All trees without green branches or without visible branches at all were considered dead since the orthophotos were captured in the middle of vegetation season. Tree shadows were very useful in this case, as can be seen in **Figure 4**. Marking of reference trees was done before the retention areas processing, therefore the reference dataset was not influenced by prior knowledge of the process result.

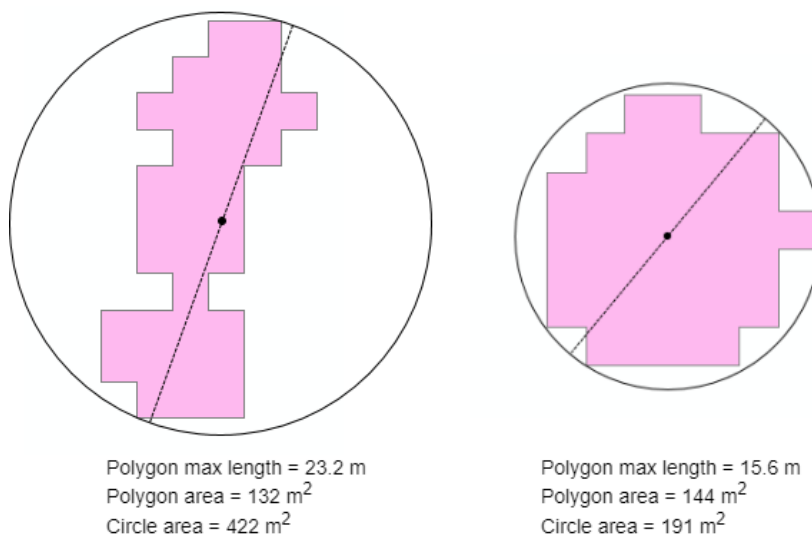


Fig. 3. Retention polygons comparison to area of circle where diameter is equal to maximum distance in given polygon.

Because of imprecision in compartment borders, all retention areas intersecting the border were not marked as a reference. Those areas were also removed from the outputs of both approaches. Polygon identification was used for a group of trees, otherwise, a point symbol was added. A straightforward validation method was then used: if the reference point feature laid within the retention polygon, then it was identified as correctly identified. In the case of reference polygons, the area coverage was compared. If the reference polygon was at least 80% covered by the retention polygon, it was considered correctly identified. In total, 874 reference points (790 trees; 94 torsos/dead trees) and 36 reference polygons were collected, covering a total area of 0.053 km².

To evaluate the accuracy in greater detail, and calculate omission and commission errors, four compartments were selected in which all the retention trees were marked (based on orthophotos). Compartments were selected by the possibility to mark all retention with high certainty, also not to interfere with previously marked reference trees. In total, 89 additional trees were marked.

3. RESULTS

Firstly, an overall statistical evaluation of results coming from both approaches was done (**Table 2**). Mean and median values were very similar for both areas. There was a difference in max coverage value in both areas (more significant in Area 1). Overall statistical parameters were calculated in relation to compartments (**Table 3**). Approaches reached very similar mean retention coverage in compartments in both test areas (around 18% in AOI 1, and 10% in AOI 2). The major difference was identified in the maximum retention coverage in the compartment achieved by Approach 1 (used height threshold from FMS). This problem originated from data in FMS. A more detailed investigation was done in areas that were almost fully covered by retention identified by Approach 1, but Approach 2 (height threshold based on the statistical difference) did not identify any retention in those areas. This occurred only three times and was due to areas that had already been logged but were still fully grown forests on the LiDAR data. As can be seen in **Table 2**, Approach 2 in both areas delivered much more stratified results as can be derived from a higher number of identified retention areas, and lower mean and median values of area size. Despite that, the overall identified area was very similar for both approaches.

The next phase was validation with reference data collected from orthophoto images, see Section 2.3. The results are provided in **Table 4**. When all reference trees were included, Approach 1 showed an OA (Overall Accuracy) of 82 % and Approach 2 had an OA of 90%. Removal of trees classified as torsos/dead resulted in an improved overall accuracy of 89 % with Approach 1 and 94 % with Approach 2. The reason for that could be that the dead trees were quite often just torsos without branches therefore much smaller targets to be hit by a laser pulse.

Table 2.
Overall statistical parameters of identified retention areas
(all retention polygons smaller than 4m² were removed).

	AOI 1		AOI 2	
	Approach 1	Approach 2	Approach 1	Approach 2
Max (m ²)	133300	12652	54180	18540
Mean (m ²)	164	117	138	120
Median (m ²)	44	40	52	44
Count	13380	17227	19519	23057
Total (km ²)	2.23	2.25	2.68	2.78

Table 3.
Overall statistical parameters of retention tree coverage for single compartment.

	AOI 1		AOI 2	
	Approach 1	Approach 2	Approach 1	Approach 2
Min (%)	0.08	0.00	0.00	0.00
Max (%)	0.93	0.53	0.64	0.78
Mean (%)	0.17	0.18	0.10	0.09
Median (%)	0.10	0.13	0.06	0.07

Table 4.
Retention tree identification overall accuracy.

	Tree count	Approach 1		Approach 2	
		Detected	OA	Detected	OA
Covered reference trees (all)	873	724	0.82	786	0.90
Ref. trees (no dead)	789	704	0.89	748	0.94

Figure 4 shows in a sample the result of the comparison between the retention areas (left) and solo retention trees (right) manually marked and retention layer.

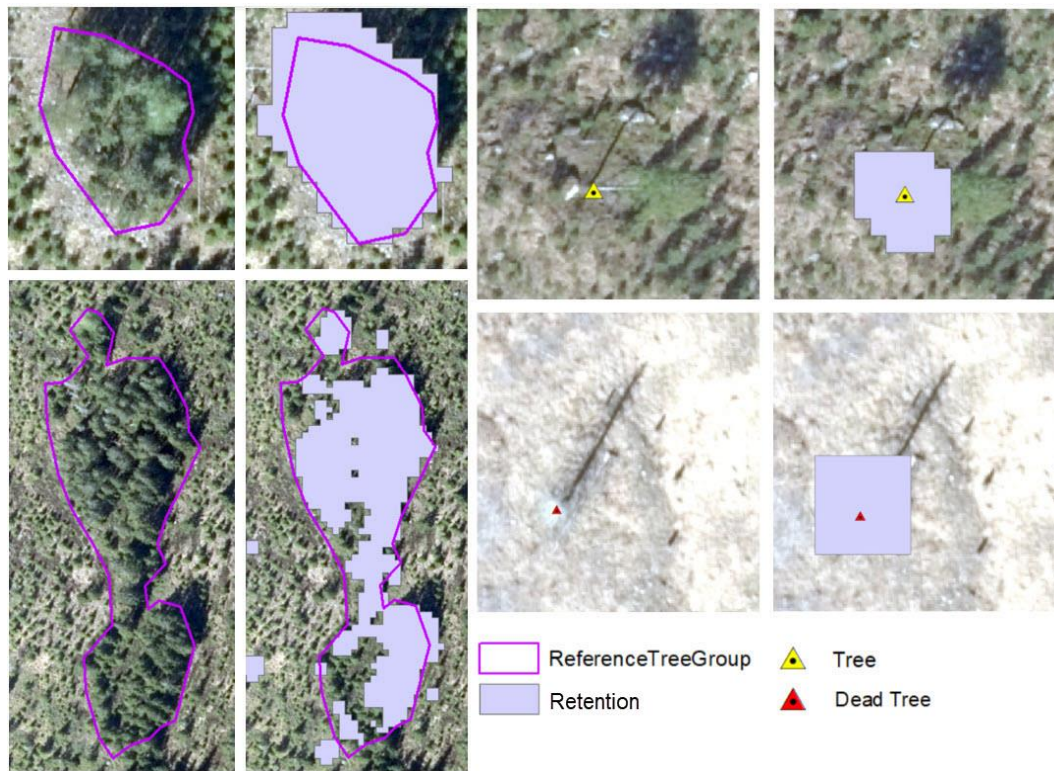


Fig. 4. Comparison of retention areas (left) and solo retention trees (right) manually marked and retention layer produced by presented approaches.

Based on the results given in **Table 5**, evaluating the accuracy of approaches in selected compartments, Approach 1 was more vulnerable to omission error.

Table 5.

Evaluation of error in compartments where all retention trees were marked as reference.

Approach 1	Number of trees	Correct	False Positive	Commission error	False Negative	Omission error
Compartment 1	33	31	1	0.03	2	0.06
Compartment 2	26	23	3	0.12	3	0.12
Compartment 3	17	15	0	0	2	0.14
Compartment 4	13	10	2	0.15	3	0.23
Total	89	79	6	0.08	10	0.14

Approach 2	Number of trees	Correct	False Positive	Commission error	False Negative	Omission error
Compartment 1	33	31	4	0.12	2	0.06
Compartment 2	26	25	5	0.19	1	0.04
Compartment 3	17	16	0	0	0	0
Compartment 4	13	11	4	0.30	2	0.15
Total	89	83	13	0.15	5	0.06

The main factor was most probably the threshold coming from FMS, therefore there was no direct relation to the data itself. As opposed to that Approach 2 resulted as more vulnerable to commission error. One possible explanation of the commission seems to be that trees fell in the time gap between orthophotos and LiDAR data capture. On multiple occasions, there were fallen trees that were still identifiable in LiDAR data but not marked on orthophotos (see **Fig. 5**).



Fig. 5. Commission error caused by trees fell between LiDAR data and orthophoto images.

Overall, (see **Fig. 5**) both retention area identification approaches delivered very similar results in many cases. This applies mostly to solo standing trees and dense groups of trees. The most divergent results were in areas of sparse retention vegetation areas inside clear-cut areas. Approach 1 with the threshold from FMS found only the taller trees in the area, while Approach 2 included also the lower part of the vegetation. This behavior was the result of differences in the bases of both applied approaches (**Fig. 6**).

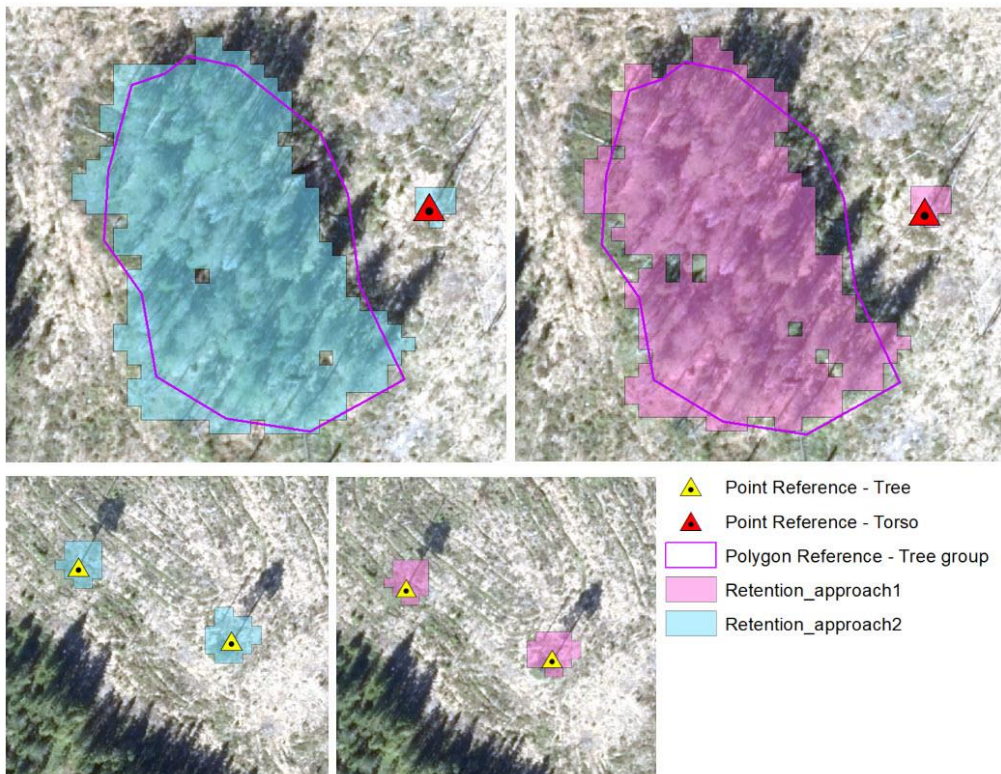


Fig. 6. Comparison of results of both presented approaches.

4. DISCUSSION

According to **Table 4** and **Table 5** given in the Results section, both proposed approaches achieved encouraging results despite some limitations. As was already mentioned, approaches were applied for forest stands younger than 30 years, where a significant difference in height between the production layer and potential retention is expected. Applying the same methods for older forests might result in an increased error therefore threshold calculation methods should be modified to minimize this. Also, a forest compartment layer is required on input. Such a layer is standardly available in forest management systems in countries all over the world. In case the forest compartment layer is not available, another stratification layer needs to be calculated (e.g. Watershed (Vincent et al., 1991), thresholding (Davis et al., 1975), region or edge-based methods (Gould et al., 2009; Wani et al., 1994; Fan, 2010; Angelina et al., 2012), etc.) and provided as input to the process.

To evaluate the robustness of the process a larger dataset covering more heterogeneous areas could be used. The validation results can be partly influenced by errors arising from reference data manual collection on orthophotos as mentioned in previous sections. Instead of them, precisely measured field data could be used, e.g. by applying GNSS Real-Time Kinematic (RTK, Teunissen and Motenbruck, 2017) or a similar approach for highly accurate positioning. Acquisition of both reference and ALS datasets should be done in a similar time period to capture the same situation in forests.

So far, only the Hardenbol et al. (2022) study dealt with the identification of retention trees. Their method was built on the ITD approach. In contrast to that, our methods utilize the ABA approach to minimize errors originating in not finding all individual trees in a scene, which could be challenging even with high-density LiDAR data. The ABA approach is also more in accordance with the goals of this paper, to identify the area covered by retention instead of identifying each retention tree likewise to keep the processing more computationally efficient. Our approaches were applied to sparser point cloud data than in the mentioned study and also did not use any additional remote sensing data. As well as in Hardenbol et al. (2022), dead trees, which are very difficult to detect with lower point cloud densities, had a significant effect on the accuracy of the presented approaches.

5. CONCLUSION

Information about retention areas in forest compartments is needed for a better understanding of overall forest conditions and for more precise forest management planning. The study presented two novel ABA methods for retention areas identification based on a low-density LiDAR point cloud from ALS. Both methods are easily applicable for computation over large areas while using a standard personal computer. During the validation, both proposed methods delivered promising results with 82% overall accuracy delivered by the first approach based on FMS data on input and 90% by the second approach based on statistical differences in height. As the second approach delivered slightly better performance and does not require additional data on the input, it can be recommended in overall. Since data from ALS with needed point density are publicly available in many countries over the world, there are no inhibitions present to apply the described methods for the creation of national retention areas datasets.

REFERENCES

- Andersen, H.-E., McGaughey, R., Reutebuch, S. (2005) Estimating Forest canopy fuel parameters using LIDAR data. *Remote sensing of Environment*, 94 (4), 441-449.
- Angelina, S., Suresh, L. P., Veni, S. H. K. (2012) Image segmentation based on genetic algorithm for region growth and region merging. In 2012 international conference on computing, electronics and electrical technologies (ICCEET), 970-974, Tamil, India, March 2012.
- Beese, W. J., Deal, J., Dunsworth, B. G., Mitchell, S. J., Philpott, T. J. (2019) Two decades of variable retention in British Columbia: a review of its implementation and effectiveness for biodiversity conservation. *Ecological Processes*, 8 (1), 1-22.
- Cao, L., Gao, S., Li, P., Yun, T., Shen, X., Ruan, H. (2016) Aboveground biomass estimation of individual trees in a coastal planted forest using full-waveform airborne laser scanning data. *Remote Sensing*, 8 (9), 729.
- Chen, X., Jiang, K., Zhu, Y., Wang, X., & Yun, T. (2021). Individual tree crown segmentation directly from UAV-borne LiDAR data using the PointNet of deep learning. *Forests*, 12(2), 131.
- Dalponte, M., Coomes, D., A. (2016) Tree-centric mapping of forest carbon density from airborne laser scanning and hyperspectral data. *Methods in ecology and evolution*, 7 (10), 1236-1245.
- Davis, L., S., Rosenfeld, A., Weska, J. S. (1975) Region extraction by averaging and thresholding. *IEEE transactions on systems, man, and cybernetics*, 3, 383-388.
- Flisberg, P., Rönnqvist, M., Willén, E., Forsmark, V., & Davidsson, A. (2022) Optimized locations of landings in forest operations. *Canadian Journal of Forest Research*, 52(1), 59-69.
- Gleason, C. J., & Im, J. (2012) Forest biomass estimation from airborne LiDAR data using machine learning approaches. *Remote Sensing of Environment*, 125, 80-91.
- Gould, S., Gao, T., Koller, D. (2009) Region-based segmentation and object detection. *Advances in neural information processing systems*, 22.
- Gustafsson, L., Bauhus, J., Asbeck, T., Augustynczyk, A.L.D., Basile, M., Frey, J., Gutzat, F., Hanewinkel, M., Helbach, J., Jonker, M., Knuff, A., Messier, C., Penner, J., Pyttel, P., Reif, A., Storch, F., Winiger, N., Winkel, G., Yousefpour, R., Storch, I. (2020) Retention as an integrated biodiversity conservation approach for continuous-cover forestry in Europe. *Ambio*, 49, 85-97.
- Gustafsson, L., Kouki, J., Sverdrup-Thygeson, A. (2010) Tree retention as a conservation measure in clear-cut forests of northern Europe: a review of ecological consequences. *Scandinavian Journal of Forest Research*, 25 (4), 295-308.
- Hardenbol, A. A., Korhonen, L., Kukkonen, M., Maltamo, M. (2022) Detection of standing retention trees in boreal forests with airborne laser scanning point clouds and multispectral imagery. *Methods in Ecology and Evolution*.
- Heinzel, J., & Koch, B. (2011) Exploring full-waveform LiDAR parameters for tree species classification. *International Journal of Applied Earth Observation and Geoinformation*, 13(1), 152-160.
- Holmström, E., Nikander, J., Backman, J., Väätäinen, K., Uusitalo, J., & Jylhä, P. (2023) A multi-objective optimization strategy for timber forwarding in cut-to-length harvesting operations. *International Journal of Forest Engineering*, 34(2), 267-283.
- Hyypä, J., Kelle, O., Lehtikoinen, M., Inkinen, M. (2001) A segmentation-based method to retrieve stem volume estimates from 3-D tree height models produced by laser scanners. *IEEE Transactions on geoscience and remote sensing*, 39 (5), 969-975.
- Kaartinen, H., Hyypä, J., Yu, X., Vastaranta, M., Hyypä, H., Kukko, A., Holopainen, M., Heipke, C., Hirschmugl, M., Morsdorf, F., Næsset, E., Pitkänen, J., Popescu, S., Solberg, S., Wolf, B.M., Wu, J.-C. (2012) An international comparison of individual tree detection and extraction using airborne laser scanning. *Remote Sensing*, 4 (4), 950-974.
- Kangas A., Päivinen R., Holopainen M., Maltamo M. (2011). *Silva Carelica 40. Metsänmittaus ja kartoitus. [Forest mensuration and mapping]*. University of Eastern Finland, School of Forest Sciences. 210 p.
- Lantmateriet, (2022-04-05), *Product Description Laser data Download, NH*, Available online at: https://www.lantmateriet.se/globalassets/geodata/geodatabrodukter/hojddata/e_pb_laserdata_nedladdning_nh.pdf, (Accessed: May 1, 2023)

- Lantmäteriet, (2022-04-05), *Quality Description Laser data*, Available online at: https://www.lantmateriet.se/globalassets/geodata/geodataprodukter/hojddata/quality_description_lidar.pdf, (Accessed: May 4, 2023)
- Li, W., Guo, Q., Jakubowski, M. K., & Kelly, M. (2012). A new method for segmenting individual trees from the lidar point cloud. *Photogrammetric Engineering & Remote Sensing*, 78(1), 75-84.
- PEFC, (2016-04-20), Programmer for The Endorsement of Forest Certification Sweden Forest Standard, PEFC SWE 002:4, Available online at: <https://cdn.pefc.org/pefc.se/media/2021-02/49cc8975-4e4e-4f6e-9c95-37f4829f869f/2c1bd611-0b7f-5c7a-b76d-137e70cfd42.pdf>, (Accessed: May 4, 2023)
- Pitman, J., Duncan, A., Stubbs, D., Sigler, R., Kendrick, R., Smith, E., Mason, J., Delory, G., Lipps, J. H., Manga, M., Graham, J., De Pater, I., Reiboldt, S., Bierhaus, E., Dalton, J. B., Fienup, J., Yu, J. (2004) Remote sensing space science enabled by the multiple instrument distributed aperture sensor (MIDAS) concept. In: Proceedings of SPIE - The International Society for Optical Engineering, 5555, pp. 301 - 311.
- Popescu, S., C., Wynne, R. H., Nelson, R. F. (2003) Measuring individual tree crown diameter with lidar and assessing its influence on estimating forest volume and biomass. *Canadian journal of remote sensing*, 29 (5), 564-577.
- Poso, S., Paananen, R., Similä, M. (1987) Forest inventory by compartments using satellite imagery. *Silva Fennica*, 21 (1), 69-94.
- Strîmbu, V. F., & Strîmbu, B. M. (2015). A graph-based segmentation algorithm for tree crown extraction using airborne LiDAR data. *ISPRS Journal of Photogrammetry and Remote Sensing*, 104, 30-43.
- Swedish Standards Institute. (2013) Information and documentation -- Principles and functional requirements for records in electronic office environments (SS-EN ISO 16157:2013). Stockholm, Sweden: Swedish Standards Institute.
- Tang, J. (2010) A color image segmentation algorithm based on region growing. In: 2010 2nd international conference on computer engineering and technology, pp. V6634-V6637, Chengdu, China, April 2010.
- Teunissen, P. J. G., Montenbruck, O., (ed.). (2017) Springer handbook of global navigation satellite systems. Cham, Switzerland: Springer International Publishing.
- Vincent, L., Soille, P. (1991) Watersheds in digital spaces: An efficient algorithm based on immersion simulations. *IEEE Transactions on Pattern Analysis and Machine Intelligence*, 13 (6), 583-598.
- Wandinger, U. (2005) Introduction to Lidar. In: Weitkamp, C. (eds) Lidar. Springer Series in Optical Sciences, 102, Springer, New York, USA.
- Wang, Y., Weinacker, H., & Koch, B. (2008) A lidar point cloud-based procedure for vertical canopy structure analysis and 3D single tree modelling in forest. *Sensors*, 8(6), 3938-3951.
- Wani, M. A., Batchelor, B., G. (1994) Edge-region-based segmentation of range images. *IEEE Transactions on Pattern Analysis and Machine Intelligence*, 16 (3), 314-319.
- Wu, X., Shen, X., Cao, L., Wang, G., Cao, F. (2019) Assessment of individual tree detection and canopy cover estimation using unmanned aerial vehicle based light detection and ranging (UAV-LiDAR) data in planted forests. *Remote Sensing*, 11, (8), 908.
- Yao, W., Krzystek, P., & Heurich, M. (2012) Tree species classification and estimation of stem volume and DBH based on single tree extraction by exploiting airborne full-waveform LiDAR data. *Remote Sensing of Environment*, 123, 368-380.
- Zhao, K., Popescu, S., & Nelson, R. (2009) Lidar remote sensing of forest biomass: A scale-invariant estimation approach using airborne lasers. *Remote Sensing of Environment*, 113(1), 182-196.
- Zhao, K., Popescu, S., Meng, X., Pang, Y., & Agca, M. (2011) Characterizing Forest canopy structure with lidar composite metrics and machine learning. *Remote Sensing of Environment*, 115(8), 1978-1996.

A ROBUST UNIFIED MODEL FOR NATIONAL STREET GAZETTEER BASED ON LAND REGISTER AND GIS FOR THE REPUBLIC OF KOSOVO

Përparim AMETI ^{1*}, Dustin SANCHEZ ^{1,2}

DOI : 10.21163/GT_2023.182.13

ABSTRACT:

A street gazetteer is a database of street names, addresses, and other relevant information that is used by various organizations, such as local governments, emergency services, and transportation agencies. A unified model for a national street gazetteer would standardize the way that this information is collected, stored, and shared across different regions or jurisdictions. This work includes a formal review process of data specification to ensure that the data model is correct and enhanced by current best practice for a unified address system. In developing countries like Kosovo, the lack of a complete and accurate base map to enable geocoding prohibits subsequent analysis of many geographic data sources for GIS (Geographic Information System) applications. One way to create a unified model for a national street gazetteer would be to base it on land, which means using geographic information to organize and categorize the streets and other features in the geodatabase. This could include using geographical coordinates, such as latitude and longitude, to pinpoint the location of each street, as well as other relevant data such as the type of terrain, land use, and environmental features.

Key-words: Unified Gazetteer model, GIS, Kosovo, Land register, Technical Geography

1. INTRODUCTION

In many developing countries, there is a lack of a unified address catalog system to mark the location of a postal address which massively disrupts capacity building for emergency services, economic, and broad social development. There has been progress made in ongoing European initiatives, such as Infrastructure for Spatial Information in Europe (INSPIRE) and existing standards for addresses (e.g. United Kingdom (UK), United States (US)), these approaches can be assessed to identify the best practices in address management. This research presents a real-world case study that existing data models are currently woefully inadequate and require major redevelopment to broadly mirror pan-European implementations for many post-communist address systematic approaches. The process of refining the data models as part of an objective data specification review to ensure client requirements are met while incorporating best practice enhancements where feasible. The process will benefit from the experience of other addressing implementations and pave the way for future interoperability between Kosovo, the European Union, and other European states.

The process of developing an address system, involves compiling accurate and complete base maps that can assign key attributes to important geographic features, such as street names, house numbers, and other land parcel attributes to ensure easy identification of people and places (Farvacque-Vitkovic & McAuslan, 2005, Davis Jr. et al., 2005, Coetzee & Cooper, 2007, Zandbergen, 2008, Yildirim et al., 2017). An effective street addressing system greatly increases the possibility of identification of a location of a parcel or dwelling in an urban area which can be utilized to facilitate service delivery, revenue generation, and emergency response services.

The aim of the study is to identify the best practices for the development of an address management system and analyze issues associated with the process and understanding the technological methods utilized for address system modernization.

¹Department of Geomatics, Geoinformation, Earth and Space Observation, University of Prishtina, Prishtine, Kosovo, perparim.ameti@uni-pr.edu

²Department of Geography and Environmental Studies, Texas State University, San Marcos, Texas, USA, dps57@txstate.edu

2. THEORETICAL BACKGROUND

2.1. INSPIRE Directive recommendation on addresses

The INSPIRE Directive is the foundational framework for address management and broader land cadastre modernization, providing an important understanding for building economic interconnectivity and development. According to the INSPIRE directives on addresses (Giff et al. 2008), the overall concept of this data specification is that an address has a “locator” that is represented as an address number that enables a user to distinguish it from the neighbor addresses; and a geographic position, which enables an application to locate the address spatially within the framework of explicit x- and y-coordinates. To identify the address unambiguously in a wider context, an address must be associated with several “address components” that define its location within a certain geographic area. Each of the address components represents a spatial identifier, such as the name of a road, district, postcode, municipality, region, or country.

The definition of spatial data themes and specifications for harmonizing the exchange of European spatial information has provided European states a roadmap for best practices in encoding postal addresses and implementing spatial data infrastructures. Despite widely different cadastral and administrative variances between EU member states, guidelines for defining address information have still been set out to benefit existing and proposed implementations.

The key standard features of the Address themes are (Giff et al. 2008):

- The implementation of spatially-enable Geographic Identifiers according to the ISO 19112 standard and the flexibility in the relationships between these identifiers in defining unique addresses for European states.
- The set of Geographic Identifiers associated with an address should distinguish a specific geographic location which unambiguously locates the address context.
- The identification of a unique locator which distinguishes itself from other addresses with similar Geographic Identifiers.

This locator is given a unique reference identifier, along with life-cycle attributes and temporal status to allow for dynamic information to be captured and incorporated. Alternative locators are also possible with different life-cycle, temporal or language frameworks. From the spatial point of view, the Address is one of many spatially referenced Geographic Identifiers which form a unique combination that definitively references a specific address. All address components are different, and many Geographic Identifiers are not prescribed or mandatory because all INSPIRE partners have the same systemic approach towards addressing requirements.

Within the Kosovo Address System, the constructs of INSPIRE Addresses should indicate the key Geographic Identifiers and how spatially enabled entities can be combined to assist in providing a framework to support geocoding unique identifiers for addresses. Providing equal importance within the system are the unique reference, life-cycle attributes, and temporal status information.

2.2. US Standards on addresses

US does not have a uniform standard of address for the whole country with the most extensive standard being developed by US Postal Service for the implementation of a mailing industry. Standardized address information enhances the processing and delivery of mail, reduces undeliverable mail, and provides mutual cost reduction opportunities through improved efficiency. The standards include uniform methods for matching addresses with the information in Address Information System (AIS) products and formats for outputting addresses on mail pieces. This standard describes how various elements appear on a mail piece or in an address record as well as the characters that constitute various address elements. The Postal Service defines a complete address as one that has all the address elements necessary to allow an exact match with the current Postal Service ZIP+4 and City State files, collated into a master address file by the Census Bureau, to obtain the finest level of ZIP+4 and delivery point codes for the delivery address.

2.3. UK Standards on addresses

The UK Land and Property Gazetteer (**Fig. 1**) specification found in the BS7666 standard is an extension of what is commonly defined as address register as it includes real-world objects called Basic Land and Property Units (BLPUs) where the INSPIRE addresses excludes them as Buildings, Cadastral Parcels, etc. However, the model has detailed specifications of addresses, streets as well as their identifiers which provide richer detail of how to create a unique and definitive address register. The uniqueness is specified in the constructs of Primary and Secondary Addressable Objects, as well as Street Identifiers with administrative attributes, with provision for alternative language entries existing alongside the primary address identifiers.

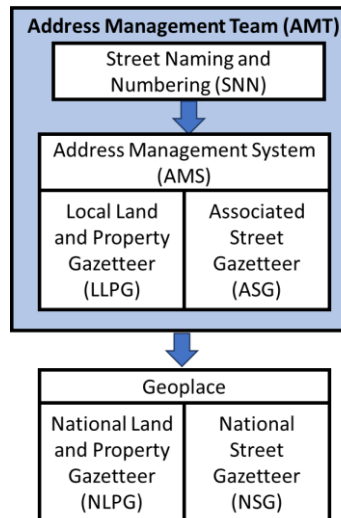


Fig. 1. The conceptual model of UK national street gazetteer.

While the INSPIRE Address theme specifies the importance of a spatially referenced ThoroughfareName (Defined as an address component which represents the name of a passage or way through from one location to another), the BS7666 standard for Addressing (current standard at BS7666:2006) further emphasizes the role of roads as a necessity for identifying unique addresses. According to the specification, the street or Unique Street Reference Number (USRN) is the spatial reference for any address identifier, referred as a Land and Property Identifier (LPI). While the underlying addressable object has a spatial attribute, this can often be different from a delivery or entry point or actual address identifier, which can always be classified as accessible via a thoroughfare access, which may be a street, footpath, waterway, etc. Real-world objects such as large buildings often have multiple entry points with different thoroughfare access points.

2.4. Non-English unification and modernization

2.4.1. Greenland

The country of Greenland, which exists as an autonomous country within the Kingdom of Denmark, had the fortune of leveraging Danish knowledge building and addressing system. Denmark struggled with creation of a unified address due to inconsistencies between business and building register information and with the governmental consolidation for authority (Coetzee et al., 2008). The model involves three separate databases: list of localities, technical base maps, and the NIN registry. The model struggles to maintain interconnect ability and making creation of a single point data address impossible (Siksnans et al., 2012).

2.4.2. Türkiye

Türkiye worked to update and unify its addressing standards in 2006, when it engaged local governments to study addressing. The discontinuity within the Turkish governments created a process where many local governments did not desire to update the system which greatly disrupted the national system unification process to build an Address Reference File (ARF). The system itself lacks continuity entirely and remains dysfunctional with a multitude of issues plaguing the implementation including no standard address format across municipalities, arbitrary changes to street names, no institutional connectivity for changes of address, no citizen participation, deficient legal frameworks for spatial information systems, no local government participation, and no creation of numerating maps. The geocoding process for this model resulted in an average location misplacement of 980m (Yomralioglu et al., 2014).

2.4.3. Poland

The most successful and well published modernization of stewardship methodological approaches was completed in Poland, which made a series of systematic updates with surveying, legal, and planning databases (Mika, Kotlarz and Jurkiewicz, 2020). These developmental goals were subsidized partially through the World Bank and occurred over a 30-year timespan. The implementation of the process was designed foundationally upon the INSPIRE Directive and aimed for Polish ascension into and connectivity with the European Union (Trystuła, Dudzińska and Żróbek, 2020). The Polish modernization experienced data deterioration problems which morphed sporadically at each stage of data consolidation (Zegar, Pęska-Siwik and Maciuk, 2023). Furthermore, the process of a more complete modernization involved broad scoped processes which posed incredibly labor-intensive solutions.

3. MATERIALS AND METHODS

The product of a formal data specification process should include the definition of the following elements:

- a) Data domain definitions,
- b) Relevant domain background information, and
- c) The context of the data domain to the specified data objects.

This may include the relationship between the data model identified specifically, as well as it could help define the interactions required between the Graphical and Address component repositories. Full data object specification including data types, range values and data integrity, including mandatory/optional, conditional, and dependent values. In addition to the data model, this specification could be used by the web-based GIS Address Register application for form validation. Data entry conventions - data entry strategies provided in the context of practical issues and scenarios to ensure conformance and best practice within the data specification. These conventions could help streamline and automate actions behind the functionality provided by the web-based GIS Address Register application. Data transfer formats - a specification of how to exchange full datasets and possibly change information to provide supporting metadata and to ensure data integrity and verify completeness. All these activities provide greater detail of purpose and usage of the Address Register which will highlight where the data model needs to support data requirements and validate the integrity and conformance of the address information.

3.1. Implementation model

To build an address data model, there are many factors to be considered, including but not limited to specification refinement, temporal period, business processes, data structures, user interface(s) and infrastructure requirements. Building a National Street Gazetteer (NSG) includes layers of requirements to ensure that the product achieved is a long-term sustainable solution for the country. The proper way to design the best solution for the NSG of Kosovo will be to choose from several different options that should be investigated through a pros and cons analysis to improve model compatibility with current municipal functionalities.

NSG Implementation models	Pros	Cons
Use available existing data		
Use one of the existing addresses lists and data available on Open Street Map to be the starting point to which additional addresses, other attributes, coordinates, classifications and managed to create a template dataset.	<ul style="list-style-type: none"> •Simple implementation •Diverse data •Community-driven data management 	<ul style="list-style-type: none"> •Difficulties with incorrect data •External data sources •Data privacy considerations •Licensing Requirements
Match and combine		
Match and combine the existing address lists to create a master list.	<ul style="list-style-type: none"> •Simple implementation •Comprehensive coverage •Increased accuracy through cross referenced data •Standardization of system 	<ul style="list-style-type: none"> •Duplicate entries from illegal buildings •Collaboration required across organizations
Ignore and collect		
Ignore the existing lists and start the collection of addresses anew using the field work.	<ul style="list-style-type: none"> •New up-to-date data •Local context •Increase quality control •Requirement specific classification 	<ul style="list-style-type: none"> •Time and resource intensive •Incomplete coverage due to illegal buildings •Human error •High maintenance cost and updates
Centralize and synchronize		
Centralize the organization and coordination of field work to build the initial list, though for the roll-out it could be that the field work is organized by each of the Municipal Offices (MO) to work with them which can be managed from with the institutional frameworks of bottom-up, top-down or hybrid approaches for best resource synchronization.	<ul style="list-style-type: none"> •Standardization •Resource Optimization •Data integration and stakeholder interoperability 	<ul style="list-style-type: none"> •Loss of local context •Implementation challenges •Resource allocation difficulties •Local municipal buy-in

According to the Kosovo law in local governments (Official Gazette, 2008), the municipality has the responsibility for resolving street name and property number issues. This information can either be designed to input directly to the NSGK using a central maintenance facility or the local government can use a local hub for verification and then input into the master NSGK database. This can be achieved by the inclusion of several key aspects. The structure is effectively the skeleton of information with many opportunities to add additional entities if the need is identified. Examples are places of worship, public conveniences, sports facilities, ATMs, statues etc. The data structure should be designed to enable applications to collect a range of additional attribute data against the entities – for example this could be the age of the property, an organization name, floor area, rental history, energy performance (Black 2010).

The resultant NSGK could enable organizations in both governments, municipal and the public/private sector, such as the utilities, to check their own lists and ensure that they are complete

and accurate. The process underpinning the NSGK ensures that the Municipality can keep the information up to date as changes take place. A facility must also be provided pertinent information so that others (users, citizens, companies) can provide feedback on environmental changes for which the Municipalities need to investigate, i.e. a large property split into flats. One of the key strengths to the proposed solution is the use of a Unique Reference Number (URN), which would be attached to every single address record to provide consistency (Black 2010). This URN can never be used twice (even after a property is destroyed), and so removes the occurrence of duplicate addresses.

Additionally, the URN approach can be used to link a set of external datasets in a different format, even if the recorded addresses vary to a degree. For example, an organization may wish to keep its own address list for a particular reason. By including the URN on address data in other systems, these numbers can be used as a comprehensive system of cross-referencing, giving confidence that all parties involved are using the same address. This framework allows for joined up working and the sharing of data with external organizations such as municipalities, public utilities and emergency services.

3.2. System Development

One of the most valuable solutions to develop a NSG should be the use of Java programming language with all source code made available through an Open-Source license. Using the OpenGeo suite with different data source architectures opens a large number of deployment possibilities. The use of Java is valuable not only because it is independent on OS but also reduce substantially the use of volume storage. Java source code does not compile directly into native machine code. Instead, Java compilation generates bytecode, which contains a high-level set of machine instructions that are general enough not to be platform-specific (Montelatici et al., 2005). The basic architectural pattern of using a database as a "single point of truth" allows a great deal of flexibility, both in supporting heterogeneous environments and evolving over time. The Software Architecture of NSG could be implemented as a multi-tier architecture with totally independent development and running software components. Multi-tier architecture has significant positive impacts and provides great advantages in factors such as costs, time, effort, and characteristics of Software Quality (complexity, usability, efficiency, reliability, integrity, adaptability, robustness, maintainability, portability, testability etc.) (Keßler et al., 2009). Open-source geospatial tools provide facilities such as cost effectiveness and it can be customized according to user needs. Also, various spatial queries can be made to assist decision making. They are helpful in monitoring various rural development schemes run by the government (Kumar, 2008).

3.3. Data Store

According to current developments in the Database (DB) technology, one of the data store solutions could be a single datastore based on Open-Source Solution PostgreSQL including Spatial Extensions PostGIS to ensure address-based data consistency at the database level. PostgreSQL is an open-source descendant of this original Berkeley code. It supports a large part of the Structured Query Language (SQL) standard and offers many modern features: complex queries, foreign keys, triggers, views, transactional integrity, multiversion concurrency control, PostGIS "spatially enables" the PostgreSQL Server (Fig. 2), allowing it to be used as backend spatial database for geographic information system (GIS), much like ESRI's SDE or Oracle's Spatial extension. At the database level, this database can be made available in 'Graphical Component' form and 'Address Registry' form, through Linked Databases and Web Services. It is certified as compliant with the Open Geospatial Consortium (OGC) "Simple Features for SQL" specification. While databases offer the strongest combination of data integrity, integrated analysis, and support for write operations. A web service can discover and invoke any service anywhere on the Web, independently of the language, location, machine, or other implementation details. The goal of Semantic Web Services is the use of richer, more declarative descriptions of the elements of dynamic distributed computation including services, processes, message-based conversations, transactions, etc. (Shalini & Seema, 2010).

3.4. User Interface

For the user interface, it is recommended that a combined Graphical and Address Register user interface can be accessed via a web browser. This idea requires further development within the Kosovo government for implementation within the proper bureaucratic process for proper implementation. This can be built in a way that will allow the Address Register to plug into the Graphical element. This will also allow the Address Register to be available as an independent Text based system if required. In **figure 2**, it is represented that the system architecture of a Web-GIS based systems when using Java and PostGIS geodatabases.

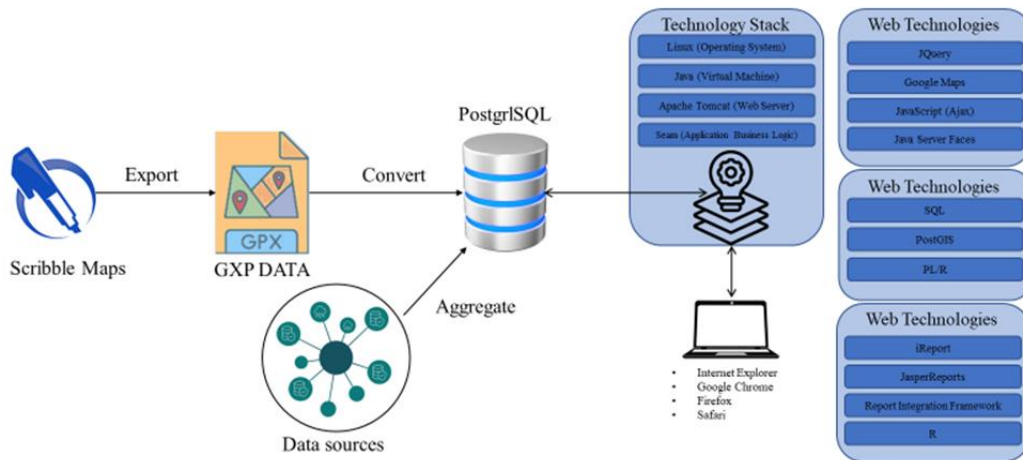


Fig 2. Open GIS System architecture.

It is highly recommended to use integration libraries with jQuery to ensure that a fully feature rich mapping interface is provided. OpenLayers makes it easy to embed a dynamic map in any web page. There are multiple objectives of map interface, with the primary of providing digitization capacity which streamlines the processes required for conversion of physical addresses into digital. Secondary objectives such as integration, interoperability, and collaboration provide strong social incentives which allow for broad development capacity. The map interface includes validation mechanisms to ensure data accuracy and integrity. It may include validation rules for address formats, consistency checks, and error detection. This creates the capacity to maintain data quality and reliability within the master address file. Incorporation of security measures designed to protect the master address file and control access to sensitive address information is imperative for mapping interface. User authentication, role-based access controls, and data encryption are implemented to safeguard data privacy and prevent unauthorized access. Functionalities for updating and maintaining the master address file are paramount for design functionality. Allowing enabled users to add new addresses, modify existing ones, and mark addresses as inactive or removed. This ensures that the address file remains up-to-date and reflects any changes or additions accurately. These processes provide for a modernized reliable map capable of safeguarding privacy for a robust unified national street gazetteer.

4. DISCUSSION

An NSG for Kosovo will involve considerable difficulties from multiple internal and external issues. Türkiye serves as an analog for governmental issues that could arise within the application, given the geopolitical likeness. Kosovo has weak government institutions and institutional corruption will dominate the process in formation of a unified model implementation. The “municipalization” of Kosovo and the creation of autonomous Serbian enclaves inside of Kosovo will create further issues

towards a systemized and unified address system. Modern technology and approaches can be utilized to mitigate aspects of systemic failures for implementation. The formulation of a ground-up strategic approach that will allow for top-down sorting of troubled municipalities can be leveraged to ease these issues. Maintaining the model at a national level will be extremely difficult given the weakness of governmental connectivity will provide considerable barriers towards data upkeep across Kosovo.

The geopolitical issues that come from the hostage-state position pose significant issues through lack of ethnic municipality cooperation. The political situation creates a necessity for adaptability in approach which gives power for strategic management approaches that engage key stakeholders while providing opportunities for different approach avenues on difficult government institutions. The need for dual language requirements increases the difficulty as both Albanian and Serbian datasets will require consistent synchronization. An open-source model provides the most reasonable method for the project but is overshadowed by regional political pressures that could cause the model to become weaponized for political gain. The political issues associated with gazetteer modernization is not well described in the literature.

A major issue that will be faced in the creation and modernization of the land and building gazetteer will be the extremely high occurrences of illegal and unregistered buildings. The strategies to overcome this can be a low-tech human survey-based solution or a high-tech deep learning approach. The utilization of data intensive deep learning algorithmic approaches to increase building location accuracy provides a baseline application for correction of the illegal and unregistered buildings which currently plagues Kosovo (Zhuo et al, 2018 & Ma et al., 2019). Major hurdles remain within the application of these methods, the capacity for multi-sensor fusion building detection has shown successes (Zhang et al., 2019 & Lai et al, 2019). The implementation advanced technological solutions towards modernization have displayed levels of success for country-wide applications for cadastre modernization in Poland (Wierzbicki, Matuk and Bielecka, 2021).

A gazetteer is a linear progression towards a more completed land and building cadaster (LBC). The LBC develops further to include ownership with increased accuracy towards geolocation through a linear progression of the modernization process (Kocur-Bera and Stachelek, 2019 & Kocur-Bera 2019 & Wierzbicki, Matuk and Bielecka, 2021 & Mika, 2020). Importantly the Polish modernization process benefited significantly from a well-organized multi-stage approach towards data collection, consolidation, and management. The modernization using existing data models requires an in-depth formal review process of data specification to include technical documentation of address data domain, data objects, and attributes. The unification process must fall within well-defined data entry conventions and data transfer protocols to facilitate information exchanges that will occur between various data formats. Each stage of data consolidation and unification of formats yields compounding errors within the resulting addressing system, these issues are multiplied as project complexity increases in complete land cadastre modernizations.

Data scarcity on road networks is a considerable roadblock towards rapid street gazetteer modernization which was solved in Ghana using service data of a service known as Trotro to provide more representative road networks (Dumedah and Eshun, 2020). Utilization of the approach of multi-agent-based addressing provides an architectural framework that shows high potential for modernization applications (Kebe, Faye and Lishou, 2021). There is considerable capacity in Pristina for data consolidation and utilization. It is clear within the literature that capitals cities with higher economic development produce data capable of rapid approaches to modernization but extending that data into rural areas appears more challenging.

There is historical precedence towards land administration systems tendency for reflecting their jurisdictions of origins (Enemark, Williamson and Wallace, 2005). A likely implementation issue that will surface for Kosovo are those which occurred within the Turkish addressing system modernization, given in part to the shared Ottoman stewardship political mechanisms that decentralize governing power of political systems required for addressing unification and modernization. These issues will largely occur within the spheres of; failure to reduce incompatibility, errors for door numbers, and mismatched addresses (Yomralioglu et al., 2014).

5. CONCLUSIONS

The modernization of an addressing system requires a high degree of planning, coordination, and cooperation from involved stakeholders. These are required to improve data quality assurance and quality control capabilities. Data issues become compounded with each progressive step towards unification of an addressing system and political dysfunction increases data dysfunction. The INSPIRE Directive is fundamental foundation for best practice modernization and open-GIS tools offers cost effective technological alternatives. The technologically advanced approaches which exist to attempt rapid modernization tend to work in isolated geographies and are difficult to scale for country wide modernization. Open GIS frameworks cover much of the technological gaps required for an effective low-cost addressing system unification, though there is a need for adequate funding and community buy-in as seen in Poland for higher degrees of success. The NSG implementation model for Kosovo will require a high degree of adaptability with significant time investment into planning to ensure best outcomes. The largest barriers for model implementation will emerge from within political institutional corruption and regional instability, as their impacts on land registry modernization is not well defined within the research.

REFERENCES

- Ameti, P. "Addressing issues in Kosovo, Current Situation" , University of Prishtina, Department of Geodesy, 2010. (Presentation paper)
- Ahlfors, R. Building up population registration system Experiences from Kosovo, 5th Conference on eServices in European Civil Registration, Berlin May 6 - 7, 2010.
- Black, A. Intelligent Addressing, London, UK, Personal communication, 2010. (Personal communication)
- Coetzee S and Cooper AK. What is an address in South Africa?, South African Journal of Science (SAJS), Nov/Dec 2007, 103(11/12), pp449-458, 2007.
- Coetzee, S., Cooper, A., Lind, M., Wells, M., Yurman, S. W., Wells, E., Griffiths, N., Nicholson, M. 2008. Towards an international address standard.
- Davis Jr., C.A., F. Fonseca, and K.A.V. Borges. A Flexible Addressing System for Approximate Geocoding. in V Brazilian Symposium on GeoInformatics, 2005.
- Dumedah, G. and Eshun, G. (2020) 'The case of Paratransit - "Trotro" service data as a credible location addressing of road networks in Ghana' , Journal of Transport Geography, 84, p. N.PAG. doi:10.1016/j.jtrangeo.2020.102688.
- Enemark, S., Williamson, I. and Wallace, J. (2005) 'Building modern land administration systems in developed economies' , Journal of Spatial Science, 50(2), pp. 51-68. doi:10.1080/14498596.2005.9635049.
- Farvacque-Vitkovic and McAuslan, P. Urban management program. Urban management and land. "Prepared for the Land Management component of the joint UNDP/World Bank/UNCHS Urban Management Program (UMP)": p. 107-114, 2005.
- Giff, GA., van Loenen, B., Crompvoets, J., & Zevenbergen, JA. (2008). Geoportals in selected European states: a non-technical comparative analysis. In J. Opadey, & B. Ramlal (Eds.), Small Island Perspectives on Global Challenges: The Role of Spatial Data in Supporting a Sustainable Future (pp. 1-14). University of the West Indies.
- Katarzyna Kocur-Bera and Marta Stachelek (2019) 'Geo-Analysis of Compatibility Determinants for Data in the Land and Property Register (LPR)' , Geosciences, 9(7), p. 303. doi:10.3390/geosciences9070303.
- Karen, L. Lee, J. Developing fully functional E-government: A four stage model, Government Information Quarterly, Volume 18, Issue 2, 2001, Pages 122-136, ISSN 0740-624X.
- Ke β ler, C., Janowicz K., and Bishr M. "An Agenda for the Next Generation Gazetteer: Geographic Information Contribution and Retrieval." International Conference on Advances in Geographic Information Systems (GIS' 09), 91-100, 2009.

- Kebe, M. A. M., Faye, R. M. and Lishou, C. (2021) "A multi-agent-based approach for address geocoding in poorly mapped areas through public company data" , *International Journal of Information Technology and Applied Sciences (IJITAS)*, 3(1), pp. 1-9. doi: 10.52502/ijitas.v3i1.14.
- Kumar, A. (2008). *Participatory GIS for e-Governance and Local Planning: A Case Study in Different Environments on Its Applicability*. Retrieved from http://www.gisdevelopment.net/proceedings/mapworldforum/poster/MMW_Poster_52.pdf
- Lai, X. et al. (2019) 'A Building Extraction Approach Based on the Fusion of LiDAR Point Cloud and Elevation Map Texture Features' , *Remote Sensing*, 11(14). doi:10.3390/rs11141636.
- Ma, L. et al. (2019) 'Deep learning in remote sensing applications: A meta-analysis and review' , *ISPRS Journal of Photogrammetry and Remote Sensing*, 152, pp. 166-177. doi:10.1016/j.isprsjprs.2019.04.015.
- Kocur-Bera, K. (2019) 'Data compatibility between the Land and Building Cadaster (LBC) and the Land Parcel Identification System (LPIS) in the context of area-based payments: A case study in the Polish Region of Warmia and Mazury' , *Land Use Policy*, 80, pp. 370-379. doi:10.1016/j.landusepol.2018.09.024.
- Mika, M., Kotlarz, P. and Jurkiewicz, M. (2020) 'Strategy for Cadastre development in Poland in 1989-2019' , *SURVEY REVIEW*, 52(375), pp. 555-563. doi:10.1080/00396265.2019.1674472.
- Mika, M. (2020) 'Modernisation of the Cadastre in Poland as a tool to improve the land management and administration process' , *SURVEY REVIEW*, 52(372), pp. 224-234. doi:10.1080/00396265.2019.1610211.
- Montelatici, R., Chailloux, E., & Pagano, B. (2005). The OCaml compiler and top level. In 3rd International Conference on. NET Technologies (pp. 109-120).
- Official Gazette, Law on local self government No. 03/L-040, Kosovo Assembly, 2008.)
- Shalini, B., & Seema, B. (2010). Review of Machine Learning Approaches to Semantic Web Services Discovery. *Journal of Advances in Information Technology*, 1(3), 146-151.
- Siksnans, J., Pirupshvarre, H. R., Lind, M., Mioc, D., & Anton, F. (2012). Towards Introducing a Geocoding Information System for Greenland. *The International Archives of the Photogrammetry, Remote Sensing and Spatial Information Sciences*, XXXVIII-4-W25, 2011.
- Trystuła, A., Dudzińska, M. and Żróbek, R. (2020) 'Evaluation of the Completeness of Spatial Data Infrastructure in the Context of Cadastral Data Sharing' , *Land*, 9(8). doi:10.3390/land9080272.
- Wierzbicki, D., Matuk, O. and Bielecka, E. (2021) 'Polish Cadastre Modernization with Remotely Extracted Buildings from High-Resolution Aerial Orthoimagery and Airborne LiDAR' , *Remote Sensing*, 13(4). doi:10.3390/rs13040611.
- Yildirim, U., Campean, F. and Williams, H. "Function modeling using the system state flow diagram" , *Artificial Intelligence for Engineering Design, Analysis and Manufacturing*, Vol. 31 No. 4, pp. 413-435, 2017.
- Yomralioglu, T. N., Nisanci, R., & Inan, H. (2014). Turkish Street Addressing System and Geocoding Challenges. *Proceeding of the Institution of Civil Engineers-Municipal Engineer*, 167(2), 99-107.
- Zandbergen, P. A comparison of address point, parcel and street geocoding techniques. *Computers, Environment and Urban Systems*, 32(3): 214-232, 2008.
- Zegar M., Peška-Siwik A. and Maciuk K. (2023) 'The problem of the modernisation of land and building register in Poland as exemplified by the village of Rejowiec' , *Budownictwo i Architektura*, 22(2). doi:10.35784/bud-arch.3219.
- Zhang, Z. et al. (2019) 'Detecting Building Changes between Airborne Laser Scanning and Photogrammetric Data' , *Remote Sensing*, 11(20). doi:10.3390/rs11202417.
- Zhuo, X. et al. (2018) 'Optimization of OpenStreetMap Building Footprints Based on Semantic Information of Oblique UAV Images' , *Remote Sensing*, 10(4), p. 624. doi:10.3390/rs10040624.

THE LATEST BATHYMETRY AND TOPOGRAPHY EXTRACTION OF LAKE LEDULU FROM MULTI-SOURCE GEOSPATIAL DATA

Atriyon JULZARIKA^{1, 2*} , Dany Puguh LAKSONO^{3, 4} , Luki SUBEHI⁵ ,
Elisa ISWANDONO⁶ , Alfred Onisimus Maximus DIMA⁷ ,
Media Fitri Isma NUGRAHA⁸ , Kayat KAYAT⁹ 

DOI: 10.21163/GT_2023.182.14

ABSTRACT:

Topography is the basic geospatial information that is used as the main reference in the extraction of thematic geospatial information. It consists of terrestrial topography (topography) and underwater topography (bathymetry). One of the problems related to topography is the availability of detailed and up-to-date topographic and bathymetry data. This research proposes the latest bathymetry and topography extraction modeling with multi-source geospatial data including PlanetScope, Sentinel-1, Landsat images, and in-situ field data. The study area is located in Lake Ledulu, Rote Island, Indonesia. Bathymetry and topography were extracted using PlanetScope imagery and in-situ field data using the least squares adjustment computation approach. The mathematical design model uses the latest DTM method, which correlated with in-situ data. Time-series Landsat and PlanetScope are used to extract the lake bank boundaries with water using the harmonic method. DEM integration method is used to integrate bathymetry and topography. The updated topography and bathymetry are performed by adding the true vertical deformation extracted from Sentinel-1 imagery using the D-InSAR method. The results obtained are the latest bathymetry and topography of Lake Ledulu in 2022 or so-called DTM₍₂₀₂₂₎. Then DTM₍₂₀₂₂₎ is tested for profile checking and vertical accuracy at the confidence level of 95 % according to the ASPRS 2014. The DTM₍₂₀₂₂₎ of Lake Ledulu has a vertical accuracy of ± 61.54 cm or according to 1:5000 – 1:10000 scale mapping. DTM₍₂₀₂₂₎ is also used to determine the dynamics of the volume of Lake Ledulu and its changes from 1985 to 2022. In 2022 (dry season) Lake Ledulu has a surface area (0.0946 km²), volume (701,688.45 m³), and perimeter (1.868 km). In 2022 (wet season), Lake Ledulu has a surface area (0.1555 km²), volume (1,116,525.9 m³), and perimeter (2.612 km). In 1985 (wet season) Lake Ledulu have surface area (0.3079 km²), volume (4,772,567.2 m³), and perimeter (3.477 km). The change in the surface area of Lake Ledulu from 1985-2022 was 0.1525 km² (decrease of 49.53%). The volume of Lake Ledulu from 1985-2022 was 3,656,041.3 m³ (decrease of 75.61%). Change in the perimeter of Lake Ledulu 1985-2022 was 0.862 km (shrinkage of 24.79%).

Key-words: Bathymetry, Topography, Lake Ledulu, Dynamics Volume, Multi-Source Geospatial Data

¹ Research Center for Geospatial-BRIN, Cibinong, Indonesia, atri001@brin.go.id ; verbhakov@yahoo.com

² Department of Earth Technology, Gadjah Mada University, Yogyakarta, Indonesia, atriyonjulzarika@mail.ugm.ac.id

³ Department of Geodetic Engineering, Gadjah Mada University, Yogyakarta, Indonesia, danylaksono@ugm.ac.id

⁴ Department of Computer Science, City, University of London, dany.laksono@city.ac.uk

⁵ Research Center for Limnology and Water Resources, Cibinong, Indonesia, luki001@brin.go.id

⁶ Natural Resources Conservation Center of East Nusa Tenggara, Ministry for Environment and Forestry (KLHK), Kupang, Indonesia, eiswandono@gmail.com

⁷ Department of Biology, Nusa Cendana University, Kupang, Indonesia, dimaonny@gmail.com

⁸ Research Center for Pharmaceutical Ingredients and Traditional Medicine-BRIN, Cibinong, Indonesia, medi005@brin.go.id

⁹ Research Center for Applied Zoology-BRIN, Kupang, Indonesia, kaya001@brin.go.id

* Corresponding author's email: atri001@brin.go.id and verbhakov@yahoo.com

1. INTRODUCTION

Topographic mapping technology is one of the geospatial technology which has developed rapidly (Wilson, 2012). Topography is the basic geospatial information that is used as the main reference in the extraction of thematic geospatial information (Julzarika & Harintaka, 2020). Topography study of the shape of the Earth's surface and other objects, including planets, natural satellites, and asteroids (Jenson & Domingue, 1988). In general, topography studies surface relief, 3-dimensional models, and the identification of land types (Julzarika & Djurdjani, 2018). Topography consists of terrestrial topography (topography) and underwater topography (bathymetry). The underwater topography is often referred to as bathymetry (Inglada & Garello, 2002). Bathymetry is divided into two types, namely seawater (marine) bathymetry, and inland water bathymetry (Julzarika et al., 2021). Seawater bathymetry uses a height reference field which refers to the lowest ebb in 1 tidal period (18.61 years) (IHB, 2006). Inland water bathymetry uses a height reference field regarding the highest tide (Julzarika et al., 2021). Inland water includes lakes, rivers, and reservoirs. Topographic data can be obtained by terrestrial surveys or by non-terrestrial surveys (Julzarika & Djurdjani, 2018). Terrestrial survey is carried out by direct measurements in the field using surveying tools such as a theodolite, leveling, total station, and terrestrial laser scanner (TLS) (Julzarika & Harintaka, 2019; Suhadha & Julzarika, 2022). Non-terrestrial surveys are carried out by mapping with satellites, planes, air balloons, Unmanned Aerial Vehicles (UAV), and Unmanned Surface Vehicles (USV) (Julzarika & Djurdjani, 2018; Suhadha & Julzarika, 2022). The results of measurements with terrestrial surveys and with non-terrestrial surveys are often presented as 3D visualization data (Fukuda et al., 2016; Nasir et al., 2015). The result of the data modeling and visualization is Digital Terrain Model (DTM). DTM is topographic or terrain modeling (bare earth) without any natural objects or features such as vegetation, buildings, and other artificial objects (Li et al., 2004). DTM can be used to predict past and future topography.

Currently, the availability of detailed terrain and underwater topographic data is a major problem in many countries (Julzarika, Aditya, Subaryono, & Harintaka, 2021). Not only detailed topographical data are mostly unavailable, but lack of up-to-date topography is also an important problem in many countries. The availability of underwater topography (bathymetry) is also a major constraint for mapping in various countries (Alpers & Hennings, 1984; Pleskachevsky et al., 2011). These detailed DTM updates can be made with the latest DTM products (Julzarika, 2021). The main problem with detailed topographic mapping and bathymetry in most countries is the expensive cost of mapping, as well as it is time consuming (Ruzgiene et al., 2015; Samboko et al., 2020; Uysal et al., 2015). The latest DTM can be an alternative solution for detailed topographic mapping and bathymetry at a low cost.

The latest DTM is a terrain and underwater topographic model with the latest conditions obtained from the integration of the DTM master with the up-to-date vertical deformation (Julzarika, Aditya, Subaryono, & Harintaka, 2021). The DTM includes topography and bathymetry (underwater topography). DTM master can be extracted by certain methods based on the type of input data (Julzarika, 2021). The input data are optical data, SAR data, microwave data, sonar data, or Light Detection and Ranging (LiDAR) data. The optical data that can be used to extract bathymetry and topography are PlanetScope, WorldView, Pleiades, etc. The SAR data that can be used to extract topography are ALOS-2, TerraSAR X, Radarsat, etc. The output of the processing of the input data is Digital Surface Model (DSM) and DTM (bathymetry and topography). The methods used to extract topography are reverse stereo, stereo model, triplet model, multiview model, and videogrammetry (Bignone et al., 2008; Julzarika & Djurdjani, 2018). The method used for Synthetic Aperture Radar (SAR), microwave, and sonar data is interferometry (Costantini, 1998; Julzarika, Aditya, Subaryono, & Harintaka, 2021; Nico et al., 2005; Rucci et al., 2012; Simons & Rosen, 2015). DTM master is obtained after the conversion of DSM to DTM.

Studies related to bathymetric extraction have been carried out. Bathymetric extraction with PlanetScope imagery in the Kemujan Island area using the Stumpf algorithm on the in-situ depth data (Sesama et al., 2021). In addition, there is also a bathymetric extraction using SPOT 7 images using the Random Forest method (Setiawan et al., 2019). The Satellite Derived Bathymetry (SDB)

method used in empirical bathymetry modeling on PlanetScope satellite imagery uses the Band Ratio algorithm in the Shallow Sea waters of Karimunjawa Island (Hambali et al., 2021). Bathymetry extraction can also be performed by correlating PlanetScope and Landsat images. In addition, research related to PlanetScope image bands is more representative of bathymetric extraction. The results of this study are linear regression which is more representative than SVR-based modeling, with the best single band modeling from the (ln) Green band and the best band ratio modeling from the ratio transformation of (ln) Blue/(ln) Green (Wulandari & Wicaksono, 2021). This paper will discuss the latest bathymetry and topography extraction modeling with multi-source geospatial data including PlanetScope, Sentinel-1, Landsat images, and in-situ field data. The novelty of this research is the bathymetry and topography modeling method of Lake Ledulu on Rote Island. This study aims to model the bathymetry and topography of Lake Ledulu with multi-source geospatial data (PlanetScope, Sentinel-1, Landsat, and in-situ data).

2. STUDY AREA

This study was carried out in Lake Ledulu, Rote Island, as can be seen in **figure 1**. Lake Ledulu is located in Rote Ndao Regency, East Nusa Tenggara Province, Indonesia. Based on the results of geo-forensics and geomodelling of the Expedition *Oe* 2017-2022, Lake Ledulu was formerly located on East Rote Island. *Oe* means water in the traditional Rote language. East Rote Island is located in the northern part of Rote Island. West Rote Island is similar to Southern Rote and East Rote Island is similar to Northern Rote. Administratively, Lake Ledulu is currently located in Landu Leko, Rote Ndao Regency (Ndao, 2021). Rote is the foremost island of Indonesia and a semi-arid area, located in the southern part area (Julzarika, et al., 2018; Ndao, 2021). There are 96 islands in Rote Ndao Regency, but only six islands are inhabited (Julzarika, et al., 2018). Rote Island is the largest island in this area and was formed from the combination of the Western Rote Island with the Eastern Rote Island at the end of the 19th century. East Rote Island is known as the Rote Dead Sea Area or previously the *Matara Maka* area (Julzarika et al., 2020). *Matara Maka* was the first inhabitant of this island who came from Australia. The *Matara* tribe is one of the lost aboriginal tribes in Northern Australia and had completely moved to Rote Island, Timor Island, South Papua, and southern Maluku. They migrated by following the *Makassarese* shipping route from Northern Australia (Kampung Jawa and Marege) to Makassar. The merger of West Rote Island with East Rote Island was caused by high vertical deformation in this area (Julzarika et al., 2021). Rote Ndao itself was formed from the Indo-Australian plate which was separated from the Australian continent due to the subduction of the Eurasian plate (Hall, 2011; Malaspinas et al., 2016; Suhadha & Julzarika, 2020).

The result of Expedition *Oe* 2017-2022 describes that the geological conditions in Rote have similarities with Australia (Julzarika, et al., 2018; Laksono et al., 2019). As an example, mud volcanoes were found at several points, especially in the confluence area of West Rote Island with East Rote Island. In addition, there are 82 lakes, 24 of which are saltwater lakes found in Rote Ndao (Julzarika, et al., 2018). The salinity of these 24 saltwater lakes are between 26 and more than 100 ppt with high contents of Kalium, Natrium, and Magnesium of the stones around the lakes. In saltwater lakes, we found seawater and freshwater flora-fauna living together. Furthermore, some of the flora and fauna in Rote are endemic such as Rote Turtle (*Chelodina Mccordi*), Rote lizard, *Matara* fish, Ledulu fish, Rote bird (*Myzomela irianawidodoae*), and Tunjung flower (Julzarika et al., 2018). On the mainland, many mangroves are found on the top of hills and far from the waters.

Lake Ledulu in Rote language means the Easternmost Lake. Lake Ledulu is a tectonic lake formed due to non-uniform uplift around East Rote. The sub-fault that forms Lake Ledulu extends from north to south. The high uplift on the west and east sides of the sub-fault forms high cliffs (50-200 m). Non-uniform uplift occurs along fault lines. As a result, freshwater pools form from rainwater sources. There are 3 sources of fresh water in Lake Ledulu, located in the northern part of the lake. The rocks in Lake Ledulu are sea corals that are uplifted with marine vegetation and fauna ecosystems. There are still many fossils of seashells and mangroves that grow around the lake and on the cliffs far from water sources. The rocks of Ledulu Lake have very high salinity, but the lake water is still relatively fresh.

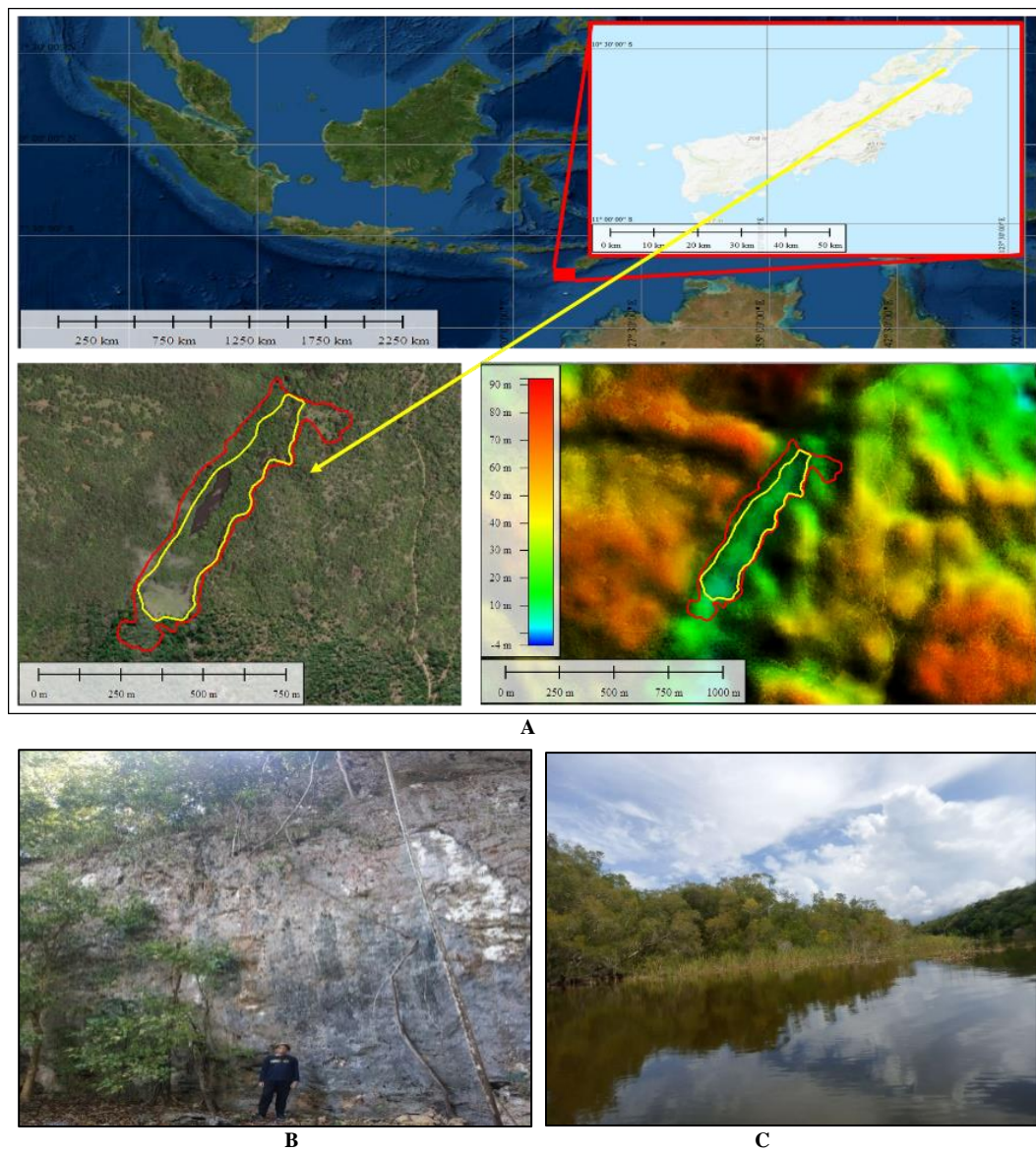


Fig. 1. A - 3D view of Lake Ledulu, located on Rote Island, Indonesia.; **B** - The fault passes through the northern part of Lake Ledulu, which is marked by steep cliffs.; **C** - The field view of Lake Ledulu.

The vegetation in Lake Ledulu and its surroundings is a mixture of terrestrial vegetation and coastal vegetation. Around the 1400s, Lake Ledulu was still a sea. At that time, it was still small islands and not yet connected as it is now, as this area was still uninhabited. Then around the 1700s, the East Rote area, where Lake Ledulu is located, became an inhabited island due to the arrival of groups of Aborigines from Australia. This sub-ethnic group that came from the Matara, a semi-arid area of the Northern Australia. The name of their leader was *Matara Maka* and made this eastern island of Rote the *Matara Maka* area. At the time of the group's arrival, the snake-necked turtles were also removed, making them an endemic species to Rote Island. All of this information was obtained from interviews with the Matara family around Lake Ledulu. Until now, Lake Ledulu and other lakes around it still belong to the Matara tribe. The East Rote area, like Lake Ledulu, has many snakes, Rote lizards, and other reptiles/amphibians that are unique and endemic.

3. DATA AND METHODS

3.1. Data

The data used are PlanetScope, Sentinel-1, Landsat, and in-situ data (bathymetry and topography measurement). PlanetScope imagery is an optical satellite belonging to the Planet company which consists of many satellites with a spatial resolution of 3 m. The details are 88 Dove satellites (February 2017) and an additional 48 Dove satellites (July 2017). The advantage of the PlanetScope satellite is that it can make acquisitions every day with 4 spectral bands (blue, green, red, NIR). In August 2021, Planet updated the satellite's original dove with the next generation of Doves. All PlanetScope images can still be acquired daily with 8 spectral bands (blue, green, red, NIR, green I, red edge, yellow, and coastal blue). NIR, blue, and coastal blue bands can be used for bathymetry extraction. The optimal red edge band is used for vegetation applications, and yellow is used for rock, soil, and mining applications. All PlanetScope bands can be utilized for extraction of DSM, DTM, vegetation height, canopies, buildings, and bathymetry. PlanetScope has derivative products in the form of PS2, PS2.SD, and PSB.SD.

Sentinel-1 is a C-band SAR satellite owned by European Space Agency (ESA) and Copernicus. Sentinel-1 is part of creating a radar observatory in Europe. The Sentinel-1 mission includes C-band imaging, operating in four proprietary imaging modes with different resolutions (up to 5 m) and ranges (up to 400 km). These conditions provide dual polarization capabilities. Sentinel-1 has a radial recording pattern making it optimal for vertical deformation applications. Sentinel-1 consists of Sentinel-1a and Sentinel-1b, each of which has a temporal resolution of 12 days. If used simultaneously, Sentinel-1 data can be obtained every 7-8 days.

Landsat is earth observation satellites for natural resources that uses optical sensors. This satellite has had 9 generations and was first launched in 1972. Landsat is owned by the United States of Geological Survey (USGS), and all data can be accessed free of charge from the USGS web. There are optical sensors on Landsat such as Coastal blue, Blue, Green, Red, NIR, SWIR, Thermal, Cirrus, and Panchromatic. Landsat spatial resolution for multispectral sensors is 30 m and 15 m spatial resolution for panchromatic sensors. Landsat and PlanetScope are optical satellites and complement each other in this research.

3.2. Methods

Bathymetry and Topography Extraction

Bathymetry and Topography are extracted with the Latest DTM method which displays the up-to-date conditions according to the conditions of the input data. This method uses the integration of the DTM master with vertical deformation (true). The input data used for bathymetry and topography are PlanetScope and vertical deformation (true) using Sentinel-1. Eq. 1 and eq. 2 is the latest DTM algorithm (Julzarika, 2021; Julzarika, Aditya, Subaryono, & Harintaka, 2021).

$$\text{The latest DTM} = \text{DTM master} \pm \text{the latest vertical deformation (true)} \quad (1)$$

$$\text{DTM master} = \text{DSM} + \text{height error correction} + \text{geoid undulation} \quad (2)$$

where DSM is extracted by InSAR (topography using SAR), reverse stereo (single optical images), LiSAR (SAR bathymetry), or SDB (optical bathymetry). Height error correction includes vegetation height, radius, and angle of view to the top of the surface object. Geoid undulation refers to the height reference field of Earth Gravitational Model (EGM) 2008.

The D-InSAR method is used to obtain vertical deformation information (uplift and subsidence) (Devanthéry et al., 2016; Herrera et al., 2013; Julzarika et al., 2022; Rucci et al., 2012; Simons & Rosen, 2015). The results of SAR extraction with D-InSAR are still in the form of vertical displacement-Light of Sight (LoS) which are the results of SAR extraction with D-InSAR. LoS correction to true is needed to convert vertical displacement (LoS) into vertical deformation (true) using equation 3 (Julzarika, 2021; Suhadha et al., 2021).

$$\text{The latest vertical deformation (true)} = \text{vertical displacement (LoS)} / \text{Cos}(\theta) \tag{3}$$

where θ is the incidence angle of SAR images

SDB is an alternative method that can replace Single-Beam Echo Sounder (SBES), Multi-Beam Echosounder (MBES), and Airborne Lidar Bathymetry (ALB) for measuring depth. This method is generally applied to relatively shallow waters. The measurement results of this method are also able to provide good correlation and accuracy values. The application of SDB requires satellite imagery as its dataset is complemented by in situ depth data. In this study, to get the SDB, the calculation is done by the least squares adjustment computation. This condition is caused by the number of measurements being greater than the number of parameters. Each pixel in satellite imagery can be predicted for its depth value after obtaining the values parameter of the design transformation model for the field measurement matrix (X). Equation (4) is a calculation of SDB by the least squares adjustment computation.

$$X = -(A^T P A)^{-1} A^T P F \tag{4}$$

X = matrix parameter transformation matrix A to matrix F.

A = design matrix of bathymetry and topography model.

F = ground measurement of bathymetry and topography matrix or approach measurement (comparison)

P = Weight matrix (using variant-covariant of bathymetry and topography from the sensor, ground, and model).

The DTM (bathymetry and topography) needs to be tested for vertical accuracy assessment. It includes the height difference test (equation 5) and the vertical accuracy test (equation 6 and 7). The height difference test aims to determine the vertical accuracy value at a certain tolerance so that it can be used to eliminate systematic errors that still exist in the height model (Julzarika, 2015). The height difference test can be useful in determining the height difference between two or more points. The method is to check at least 25 points on an area of 500 km² with a 95% confidence level (1.96 σ). The vertical accuracy test refers to the ASPRS 2014 standard (ASPRS, 2014).

$$\text{Height different test} = \Sigma (H_{n1} - H_{n0}) \tag{5}$$

where H_{n1} = the next height point in the polygon; H_{n0} = the before height point in the polygon

$$\text{Vertical accuracy test} = 1.96 * \text{RMSE}(z) \tag{6}$$

$$\text{RMSE}(z) = [(\Sigma(H_{\text{data}} - H_{\text{check}})^2/n)^{1/2}] \tag{7}$$

where H = orthometric height; n = sum of height point (minimum 25 height points in a project area (500 km²); RMSE(z)=Root Mean Square Error for Vertical

If the bathymetry and topography meet the specified standards, a cross and longitudinal profile check is carried out. Subsequently, it can be used for various mapping applications such as contour extraction, vegetation height, land subsidence, and uplift.

Integration of Bathymetry (Lake) with Topography

DEM integration is combining data by involving two or more sets of data. The combination considers cofactor values and covariance variance between data (Julzarika et al., 2021). DEM integration is a method of integrating high data and/or n-dimensional data with weighting on each data based on the covariance variance calculated by least square adjustment computation (Hoja & D'Angelo, 2010; Julzarika et al., 2021). The calculation uses the smoothing method, where the number of measurements is more than the number of parameters (Ghilani & Wolf, 2006; Z. Li et al.,

2005). The determination of the boundary of the lake is done by using the harmonic method approach (Julzarika, et al., 2019). This harmonic method is a tidal observation (inland water with the highest tide) using time series data every month (Julzarika & Harintaka, 2020). The detailed explanation regarding this harmonic method refers to Julzarika, et al., (2019).

The harmonic method is used to extract the lake bank boundaries with water. The input data used is time-series satellite imagery. The results of determining the edge of a lake or beach will be optimal if using satellite imagery for 18-19 years. This condition is similar to tidal observations for 1 period in determining the coastline. Calculations using the Harmonic method are based on a least square adjustment computation. The shoreline of the lake from 1972-2022 was monitored also using time-series Landsat images.

Calculation of surface area and volume of lakes

The surface area of the lake is calculated based on the results of the extraction of the lake's edge boundaries. Lake volume calculation using the volume formula with the cut-and-fill method (Baek & Choi, 2017; Kubla, 2019). Cut-and-fill method is a soil or ice surface work process in which several materials, both soil, ice surface, or rocks, are taken from a certain place and then moved to another place to create the desired elevation. The bottom of the layer (elevation in bathymetry and topography) act as a zero-reference plane and is used to calculate the volume based on the cut-and-fill method. The grid method is used in the volume calculation (Kubla, 2019). The volume calculation based on the cut-and-fill method is easier due to the elevation and height differences being known based on the zero-reference plane. The grid method describes a uniform grid on each soil surface that is cut and filled. Each grid will have a different elevation according to the cut and fill sections (Julzarika, 2015). The total cut and fill volume is obtained by adding each pixel together. The volume of each pixel is obtained by multiplying the depth by the pixel area or the project area (Kubla, 2019).

4. RESULTS AND DISCUSSIONS

Discussion regarding the results includes bathymetry (wet season and dry season), vertical deformation, vertical accuracy tests, and the application of the DTM₍₂₀₂₂₎ to predict past topographical conditions and future predictions. We extract the underwater topography (bathymetry) of Lake Ledulu based on the season conditions (wet and dry seasons). The height reference field of the inland water is the highest water level. The difference in the water level of the two seasons has a significant effect on the determination of the surface area and volume. Vertical deformation is also a major influence in determining the bathymetry and topography used. High uplift events affect the rise in the bottom of the lake and cause a change in its depth.

4.1. Bathymetry and topography of Lake Ledulu in dry season 2022

The dry season referred to in this study is the dry season that occurs on Rote Island. Rote Island is a semi-arid area. The dry season occurs from March to November. The peak of summer occurs in October-November which is characterized by hot temperatures ($> 40^{\circ}\text{C}$) with strong winds, general drought throughout the region, and very rare rain. **Figure 2** is a display of the surface area of Lake Ledulu in the dry season. The water leveling that occurs in Lake Ledulu during the dry season has a elevation 0.5-3 m lower” to the water level during the wet season. Based on field measurements, in 2022 the water level difference was 0.9 m between the dry season and the wet season. In 2018-2020 (before the Seroja storm), the Rote Island area experienced maximum drought, with many droughts occurring in small lakes. Medium and large lakes experienced reductions in volume. Lake Ledulu is a medium-sized lake. After June 2020 (after the Seroja storm), there was a change in rainfall and the lake water level became higher than before the storm. One of the affected lakes is Lake Ledulu. In 2022 (wet season) Lake Ledulu had a surface area of 0.0946 km² and a volume of 701,688.45 m³. The total length/perimeter of Lake Ledulu was 1.868 km.

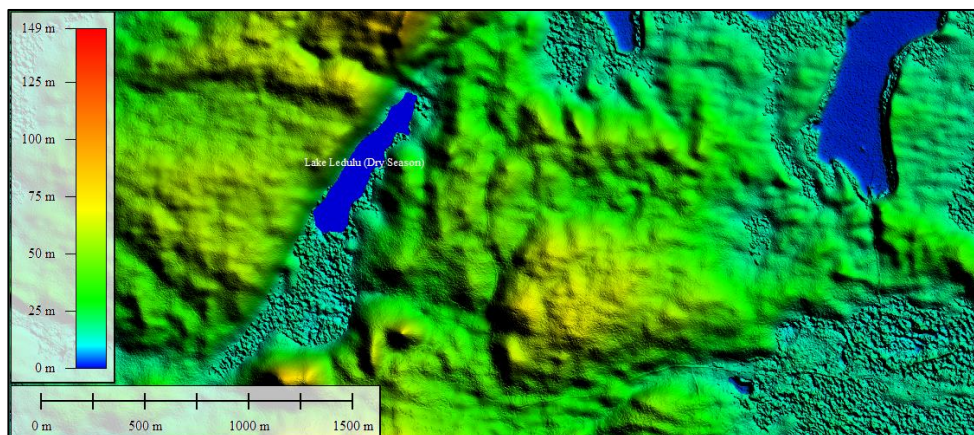


Fig. 2. Bathymetry and topography of Lake Ledulu in the dry season (2022)

4.2. Bathymetry and topography of Lake Ledulu in wet season 2022

The rainy season or wet season only occurs for 3 months on Rote Island, with the peak of the highest rainfall occurring in December. During this rainy season, the addition of water level in Lake Ledulu is 2 to 3 m. This has an impact on increasing the surface area, volume, and circumference of the lake. The surface area of Lake Ledulu in the wet season was 0.1555 km² with a volume of 1,116,525.9 m³. The total perimeter was 2.612 km. Based on these values, there is a significant addition to Lake Ledulu from the dry season to the wet season. The addition of the surface area of Lake Ledulu was 60.83%. The addition of lake volume was 62.85%. The lake perimeter addition was 71.52%. **Figure 3** is the display of bathymetry and topography in the wet season (2022).

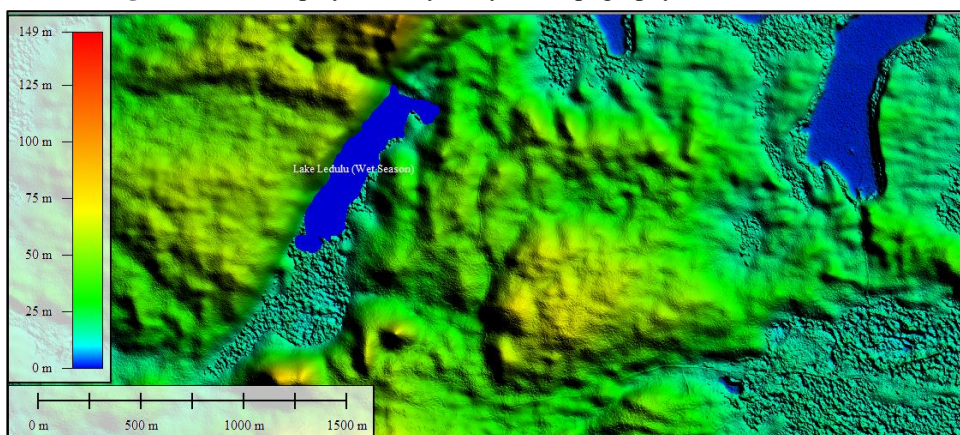


Fig. 3. Bathymetry and topography of Lake Ledulu in the wet season (2022).

4.3. Bathymetry and topography of Lake Ledulu in wet season 1985

Lake Ledulu's variations from 1985 to 2022 were carried out to establish changes in Lake Ledulu over the past 37 years. The surface area in the wet season of 1985 was used. In 1985, the surface area and volume of Lake Ledulu were still large. The dominant vertical deformation in Rote affected the reduction of the surface area and volume of Lake Ledulu. We can compare it with our last research on Rote Island. Based on measurement data from the expedition *Oe* 2017-2022, Rote Island experienced an uplift in the range of 13-25 cm/year (Julzarika et al., 2018). In this study, the uplift value in Rote was 13 cm/year. **Figure 4** is the bathymetry and topography of Lake Ledulu in the wet season (1985).

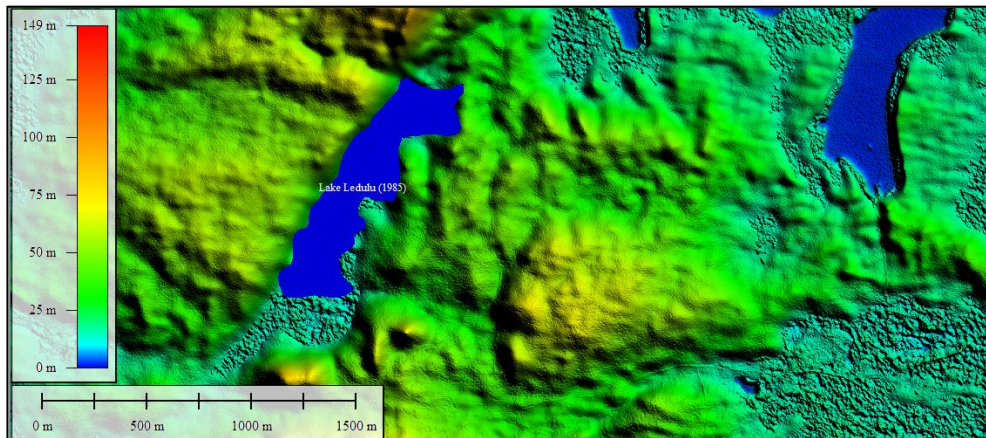


Fig. 4. Bathymetry and topography of Lake Ledulu in the wet season (1985).

DTM results (1985) can be compared in harmonic modeling and visually with Landsat imagery 1972-1985 to determine the shape of the lake shoreline. These conditions were used to extract the fixed boundaries of the shores of Lake Ledulu in that period. The fixed boundary on the shores of Lake Ledulu used is during the wet season. The surface area of Lake Ledulu in 1985 was 0.3079 km² with a perimeter of 3.477 km. Based on bathymetry data (2022), vertical deformation (1985-2022), and surface area of Lake Ledulu (1985), the volume can be calculated. The volume of Lake Ledulu was 4,772,567.2 m³. Changes in surface area and volume of Lake Ledulu (1985-2022) can be calculated based on previously available geospatial information. Changes are calculated based on the wet season.

The change in the surface area of Lake Ledulu from 1985-2022 was 0.1525 km². Changes in the surface area of Lake Ledulu experienced a decrease of 49.53%. The volume of Lake Ledulu 1985-2022 was 3,656,041.3 m³. Changes in the volume of Lake Ledulu experienced a decrease of 75.61%. Changes in the perimeter of Lake Ledulu 1985-2022, namely 0.862 km. Changes in the perimeter of Lake Ledulu experienced a shrinkage of 24.79%. The shrinkage of lake volume, lake surface area, and perimeter of the lake is caused by the dynamics of the seasons, the amount of rainfall, and the dynamics of vertical deformation. **Figure 5** is the display of the bathymetry and topography of Lake Ledulu (1985-2022).

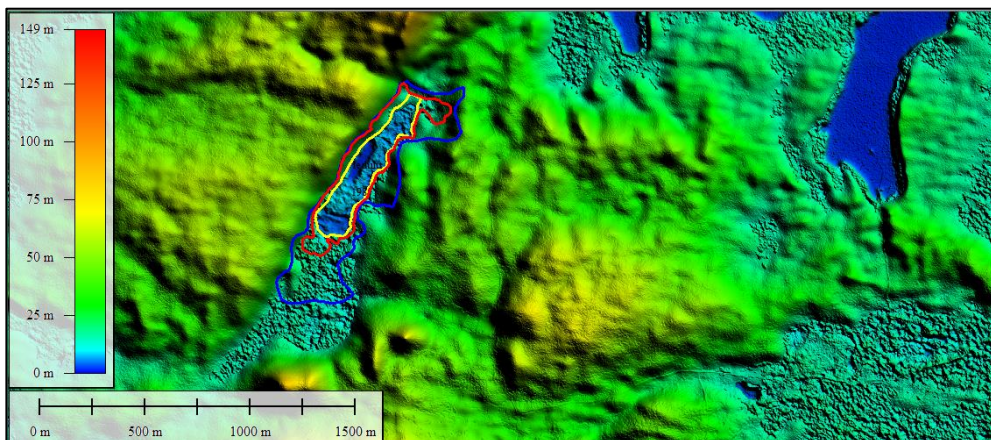


Fig. 5. Bathymetry and topography of Lake Ledulu (1985-2022).

4.4. Profile test of bathymetry and topography

The profile tests carried out consisted of cross-section profile and longitudinal profile tests.

Cross-section profile

The cross-section profile is generated in the west-east direction. The results of the cross-section profile can be seen in **figure 6**. The red line (wet season) is above the yellow line (dry season). This condition means that the water level in the wet season is higher than the water level in the dry season. The difference in water level has an impact on the depth of the lake. The depth of the lake affects the volume of the lake. The volume of the lake in the wet season is greater than the volume of the lake in the dry season.

During the dry season, the water level of Lake Ledulu is around 13 m, while during the wet season, the water level of Lake Ledulu is around 15.5 m. Based on this cross-section profile, the north and west sides of the lake are bordered by steep cliffs of hills. On the north side, it is passed by a sub-fault that divides and limits Lake Ledulu with the hills on the north side bordering the sea. The west side of the lake is hilly with dense vegetation. The hills on the west side are dominated by ocean bedrock. The eastern part of the lake is bounded by hills with a gentler slope. The vegetation on the east side is less dense and dominated by karst rocks.

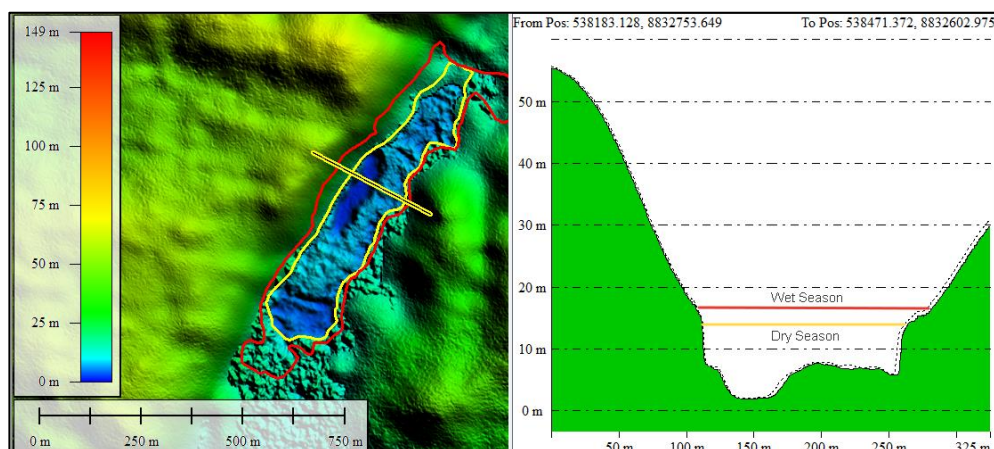


Fig. 6. The cross-section profile of Lake Ledulu in the wet and dry season.

The southern part of the lake is dominated by stretch of swamps filled with mangroves and other vegetation. About 1 km to the south of the lake, hills that have been uplifted and have a height difference of 50-100 m compared to the lakeside are found. The bathymetry of Lake Ledulu from west to east is divided into two characteristics. The western bathymetry is deeper than the eastern bathymetry. The deepest point of the western bathymetry is at an elevation of 4 m in mean sea level (MSL). In the wet season, the maximum depth is 11 m with an average depth of about 5 m. The eastern deepest point is located at an elevation of 8 m MSL or a maximum depth of 7 m with an average depth of 2 m. In dry season conditions, the maximum depth was 8.5 m with an average depth of 2.5 m in the western part of the lake. The eastern region has a maximum depth of 4.5 m with an average depth of 0.5 m. The eastern region is dominated by dense vegetation and grass with a vegetation height of around 1-5 m.

Longitudinal Profile

The next check is carried out by making a longitudinal profile from south to north. The results obtained are the appearances of various bottom topography. Two locations have deeper basins compared to other areas. The first basin is located in the south part of the lake, while the second basin is located in the middle of the lake.

The first basin area in the wet season, the deepest point is located at an elevation of 4.5 m or a depth of 11 m with an average depth of 6 m. The second basin area has the deepest point at an elevation of 3 m or a depth of 12.5 m with an average of 7.5 m. In dry season conditions, the first basin area has a depth of 8.5 m with an average depth of 3.5 m.

The second basin area has a depth of 10 m with an average of 5 m. Based on the appearance of the bathymetry of Lake Ledulu, the complex dynamics of tectonic movements can be seen. The dynamics of the tectonic movement are in the form of fault movements in the north and west of the lake which form steep cliffs. In addition, three sub-fault movements divide the lake, causing two areas that are squeezed and not completely uplifted. These two areas are the areas with maximum depth which are in the south and center of Lake Ledulu. The complex dynamics of tectonic movement with the vertical direction is one of the signs that high vertical deformation has occurred. These conditions support the results of previous studies regarding the vertical deformation value of Rote Island of 13-25 cm/year. If this high vertical deformation is constant in the future, then the potential for Lake Ledulu to become land becomes even greater. **Figure 7** is the longitudinal profile of Lake Ledulu in the wet and dry seasons.

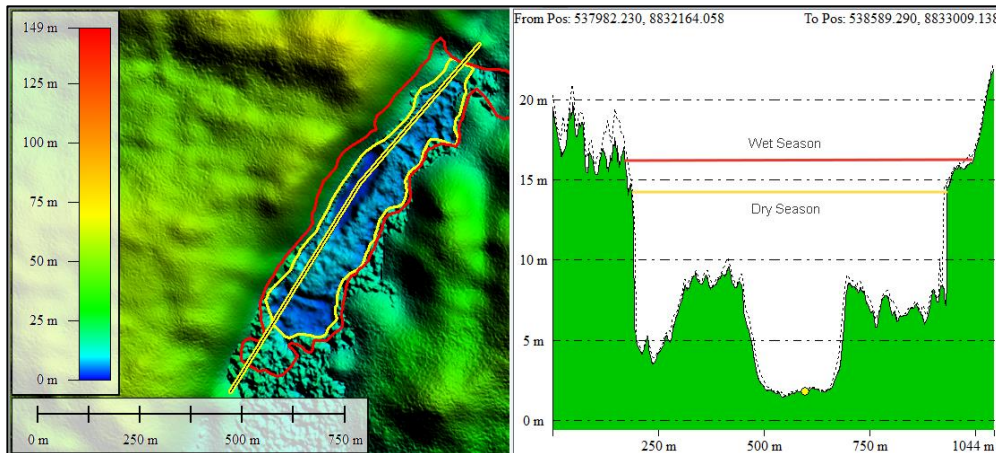


Fig. 7. The longitudinal profile of Lake Ledulu in the wet and dry seasons.

4.5. Vertical accuracy assessment of Lake Ledulu's bathymetry and topography (DTM₍₂₀₂₂₎)

The vertical accuracy test was carried out on DTM₍₂₀₂₂₎. The accuracy test was in the form of a height difference test and a vertical accuracy test. Tests were carried out using 30 points measured in the field with Global Navigation Satellite System (GNSS) with sonar depth measurements and water leveling. In the height difference test, 30 points are made into polygons and the difference in height between the points is added up.

The difference in elevation between these points refers to MSL, whereas all points in the elevation model refer to a specific datum reference plane. The results obtained in the height difference test in this study were a total height difference of ~ 0 m. The DTM₍₂₀₂₂₎ has height relative to the datum due to the points tested (closed polygon) having minimum height difference (close to zero). This condition eliminates any remaining systematic errors in the DTM₍₂₀₂₂₎. The vertical accuracy test was carried out by comparing the orthometric height of the DTM₍₂₀₂₂₎ with the orthometric height of field measurements, see **figure 8**. **Table 1** is the result of the vertical accuracy test of DTM₍₂₀₂₂₎. After checking the difference in height for each point, then check the accuracy of the difference in height at the 95% confidence level according to equation (6). The DTM used includes the detail category (spatial resolution 1 m). The results obtained are a vertical accuracy value of +61.54 cm or <1 m. This DTM can be used for 1:5000 – 1:10000 scale mapping.

Table 1.

The vertical accuracy test of DTM (2022).

No	Longitude	Latitude	H _{data} DTM(m)	Height Difference (m)	H _{check} Ground (m)	(H _{data} - H _{check}) ² (m)
1	123.348,449,709	-10.562,885,753	5.2603		5.3000	0.0016
2	123.348,985,702	-10.562,935,934	3.7694	-1.4909	3.8000	0.0009
3	123.348,245,522	-10.562,634,843	5.1122	1.3428	5.2000	0.0077
4	123.348,381,647	-10.562,275,205	5.3269	0.2147	5.4000	0.0053
5	123.348,602,850	-10.562,475,933	4.5548	-0.7721	4.5000	0.0030
6	123.348,883,608	-10.562,584,661	4.4857	-0.0691	4.6000	0.0131
7	123.349,206,906	-10.562,609,752	3.8453	-0.6404	3.8000	0.0021
8	123.349,385,570	-10.562,793,752	3.4687	-0.3766	3.3000	0.0285
9	123.349,412,039	-10.562,399,731	4.6145	1.1458	4.8000	0.0344
10	123.348,757,882	-10.562,790,035	4.4663	-0.1482	4.7000	0.0546
11	123.349,185,163	-10.563,091,127	4.9151	0.4488	5.2000	0.0812
12	123.349,480,101	-10.560,845,944	5.4670	0.5519	5.2000	0.0713
13	123.349,710,758	-10.560,548,568	2.4018	-3.0652	2.4000	0.0000
14	123.349,657,820	-10.560,344,121	2.1233	-0.2785	2.3000	0.0312
15	123.349,907,383	-10.560,280,929	2.4936	0.3703	2.9000	0.1652
16	123.349,888,477	-10.560,039,310	1.7909	-0.7027	1.5000	0.0846
17	123.350,172,071	-10.559,964,966	2.0953	0.3044	2.3000	0.0419
18	123.350,122,914	-10.559,701,044	2.0567	-0.0386	2.2000	0.0205
19	123.350,429,196	-10.559,615,548	3.0569	1.0002	3.8000	0.5522
20	123.350,240,133	-10.559,388,797	2.3891	-0.6678	2.5000	0.0123
21	123.350,485,915	-10.559,199,219	3.3532	0.9641	3.6000	0.0609
22	123.351,383,963	-10.558,760,586	6.0781	2.7249	6.4000	0.1036
23	123.351,607,057	-10.558,552,422	6.3215	0.2434	6.1000	0.0491
24	123.352,117,526	-10.557,545,051	8.2687	1.9472	8.7000	0.1860
25	123.352,257,432	-10.557,284,843	16.0103	7.7416	16.5000	0.2398
26	123.352,756,558	-10.557,630,547	15.5275	-0.4828	15.7000	0.0298
27	123.353,111,996	-10.557,593,375	15.0473	-0.4802	15.8000	0.5666
28	123.353,081,746	-10.558,002,271	16.4595	1.4122	16.1000	0.1292
29	123.350,374,368	-10.560,697,256	4.4982	-11.9613	4.1000	0.1586
30	123.348,169,897	-10.563,239,814	12.0269	7.5287	12.5000	0.2238
1	123.348,449,709	-10.562,885,753	5.2603	-6.7666		
Height Different Test				0.0000	Total (H _{data} - H _{check}) ²	2.9574
RMSE(z) (Topography) = 0.4452 m; RMSE(z) (Bathymetry) = 0.2714 m RMSE(z) (Topography and Bathymetry) = 0.3140 m						
Vertical Accuracy (Topography) = 0.872551793 m; Vertical Accuracy (Bathymetry) = 0.32012182 m Vertical Accuracy Test (Topography and Bathymetry) = 0.61538516 m						
Vertical Accuracy Test (Topography and Bathymetry) = ± 61.54 cm						

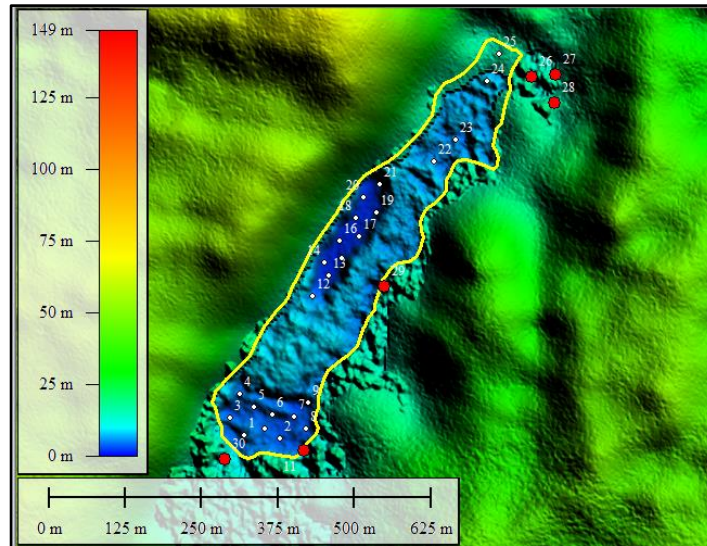


Fig. 8. The 30 measurement points in the field. Red dots were located in topography (outside the Lake Ledulu) and the white dots were located inside of Lake Ledulu. The yellow line was Lake Ledulu shoreline in dry season 2022. We measure all of the points in September-October 2022 (dry season).

6. CONCLUSIONS

The latest bathymetry and topography in Lake Ledulu can be extracted by using modeling with multi-source geospatial data. They include PlanetScope, Sentinel-1, Landsat images, and in-situ field data. The DTM₍₂₀₂₂₎ Lake Ledulu has a vertical accuracy of 61.54 cm or according to 1:5000 – 1:10000 scale mapping with confidence level (95 %) according to the ASPRS 2014. DTM₍₂₀₂₂₎ was used to determine the dynamics of the volume of Lake Ledulu and its changing from 1985 to 2022. In 2022 (dry season) Lake Ledulu has a surface area of 0.0946 km² and a volume of 701,688.45 m³. The total length/perimeter of Lake Ledulu was 1.868 km. The surface area of Lake Ledulu in the wet season (2022) was 0.1555 km² with a volume of 1,116,525.9 m³. The total perimeter was 2.612 km.

The surface area of Lake Ledulu in 1985 was 0.3079 km² with a perimeter of 3.477 km. The volume of Lake Ledulu in 1985 was 4,772,567.2 m³. The change in the surface area of Lake Ledulu from 1985-2022 was 0.1525 km². Changes in the surface area of Lake Ledulu experienced a decrease of 49.53%. The volume of Lake Ledulu between 1985-2022 was 3,656,041.3 m³ (decrease of 75.61%). The changing of Lake Ledulu perimeter in 1985-2022 was 0.862 km. Changes in the perimeter of Lake Ledulu experienced a shrinkage of 24.79%.

ACKNOWLEDGEMENTS

We would like to thank the Indonesian National Research and Innovation Agency (BRIN), Ministry for Environment and Forestry (KLHK), Nusa Cendana University, and Matara Family for supporting this research. There is no external and internal funding for this publication. All authors are the main contributors to this paper. The authors reported no potential conflicts of interest.

REFERENCES

- Alpers, W., & Hennings, I. (1984). A theory of the imaging mechanism of underwater bottom topography by real and synthetic aperture radar. *Journal of Geophysical Research: Oceans*, 89, 0529–10546. <https://doi.org/10.1029/JC089iC06p10529>
- ASPRS Accuracy Standards for Digital Geospatial Data, The American Society for Photogrammetry and Remote Sensing (2014). [https://doi.org/10.1016/S0033-3506\(98\)80082-6](https://doi.org/10.1016/S0033-3506(98)80082-6)
- Baek, J., & Choi, Y. (2017). A new algorithm to find raster-based least-cost paths using cut and fill operations. *International Journal of Geographical Information Science*, 31(11), 2234–2254. <https://doi.org/10.1080/13658816.2017.1356463>
- Bignone, F., Umakawa, H., Sensing, R., Centre, S., & Aperture, L. S. (2008). Assessment of Alos Prism Digital Elevation Model Extraction Over Japan. *The International Archives of the Photogrammetry, Remote Sensing and Spatial Information Sciences*, XXXVII, Pa, 1135–1138.
- Costantini, M. (1998). A novel phase unwrapping method based on network programming. *IEEE Transactions on Geoscience and Remote Sensing*, 36(3), 813–821. <https://doi.org/10.1109/36.673674>
- Devanthery, N., Crosetto, M., Cuevas-González, M., Monserrat, O., Barra, A., & Crippa, B. (2016). Deformation Monitoring Using Persistent Scatterer Interferometry and Sentinel-1 SAR Data. *Procedia Computer Science*, 100, 1121–1126. <https://doi.org/10.1016/j.procs.2016.09.263>
- Fukuda, T., Tokuhara, T., & Yabuki, N. (2016). A dynamic physical model based on a 3D digital model for architectural rapid prototyping. *Automation in Construction*, 72, 9–17. <https://doi.org/10.1016/j.autcon.2016.07.002>
- Ghilani, C. D., & Wolf, P. R. (2006). *Adjustment Computations Spatial Data Analyses 4th Edition*. <https://doi.org/10.1038/ni1566>
- Hall, R. (2011). Australia-SE Asia collision: Plate tectonics and crustal flow. *Geological Society Special Publication*, 355, 75–109. <https://doi.org/10.1144/SP355.5>
- Hambali, A., Santoso, A. I., Setiawan, K. T., Julzarika, A., Setiyadi, J., & K, E. S. (2021). Utilization of PlanetScope Image For Batimetry Estimation, Case Study In Shallow Sea Waters Of Karimunjawa Island, Jepara, Central Java. *Hidropilar*, 7(1), 23–30.
- Herrera, G., Gutiérrez, F., García-davalillo, J. C., Guerrero, J., Notti, D., & Galve, J. P. (2013). Remote Sensing of Environment Multi-sensor advanced DInSAR monitoring of very slow landslides : The Tena Valley case study (Central Spanish Pyrenees). *Remote Sensing of Environment*, 128, 31–43. <https://doi.org/10.1016/j.rse.2012.09.020>
- Hoja, D., & D'Angelo, P. (2010). Analysis of DEM combination methods using high resolution optical stereo imagery and interferometric SAR data. *International Archives of the Photogrammetry, Remote Sensing and Spatial Information Science, Volume XXXVIII, Part 1*, 02–05. <https://doi.org/10.1007/978-3-319-59489-7>
- IHB. (2006). *Technical Aspect of the Law of the Sea (TALOS)* (I. UNESCO, IOC, IHO (ed.)). International Hydrographic Bureau (IHB). United Nation.
- Inglada, J., & Garello, R. (2002). On rewriting the imaging mechanism of underwater bottom topography by synthetic aperture radar as a volterra series expansion. *IEEE Journal of Oceanic Engineering*, 27, 665–674. <https://doi.org/10.1109/JOE.2002.1040949>
- Jenson, S. K., & Domingue, J. O. (1988). Extracting topographic structure from digital elevation data for geographic information-system analysis. *Photogrammetric Engineering and Remote Sensing*, 54(11), 1593–1600. <http://pubs.er.usgs.gov/publication/70142175>
- Julzarika, A., & Harintaka. (2020). Utilization of DSM and DTM for Spatial Information in Lake Border. *IOP Conference Series: Earth and Environmental Science*, 535(1). <https://doi.org/10.1088/1755-1315/535/1/012034>
- Julzarika, A., Laksono, D. P., Kayat, Subehi, L., Dewi, E. K., Sofiyuddin, H. A., Nugraha, M. F. I., Anggraini, N., Setianto, A., Janwes, & Yudhatama, D. (2020). Realizing the Dead Sea Lakes Region in Rote Islands to be a geopark using multidisciplinary spatial information approach. *IOP Conference Series: Earth and Environmental Science*, 535(1). <https://doi.org/10.1088/1755-1315/535/1/012033>
- Julzarika, Atriyon. (2015). Height Model Integration Using ALOS PALSAR, X SAR, SRTM C, and IceSAT/GLAS. *International Journal of Remote Sensing and Earth Sciences*, 12(2), 107–116. <https://doi.org/nrrheum.2016.1> [pii] [r10.1038/nrrheum.2016.1](https://doi.org/10.1038/nrrheum.2016.1) [doi]

- Julzarika, Atriyon. (2021). *The Updated DTM Model using ALOS PALSAR/PALSAR-2 and Sentinel-1 Imageries for Dynamic Topography*. Universitas Gadjah Mada.
- Julzarika, Atriyon, Aditya, T., Subaryono, Harintaka, Dewi, R. D., & Subehi, L. (2021). Integration of the latest Digital Terrain Model (DTM) with Synthetic Aperture Radar (SAR) Bathymetry. *J. Degrade. Min. Land Manage*, 8(3), 2502–2458. <https://doi.org/10.15243/jdmlm>
- Julzarika, Atriyon, Aditya, T., Subaryono, S., & Harintaka, H. (2021). The latest dtm using insar for dynamics detection of semangko fault-indonesia. *Geodesy and Cartography (Vilnius)*, 47(3), 118–130. <https://doi.org/10.3846/gac.2021.12621>
- Julzarika, Atriyon, Aditya, T., Subaryono, S., & Harintaka, H. (2022). Dynamics Topography Monitoring in Peatland Using the Latest Digital Terrain Model. *Journal of Applied Engineering Science*, 20(1), 246–253. <https://doi.org/10.5937/jaes0-31522>
- Julzarika, Atriyon, Anggraini, N., Kayat, K., & Pertiwi, M. (2018). Land changes detection on Rote Island using harmonic modelling method. *J. Degrade. Min. Land Manage*, 5(53), 2502–2458. <https://doi.org/10.15243/jdmlm>
- Julzarika, Atriyon, & Djurdjani, D. (2018). DEM classifications: opportunities and potential of its applications. *J. Degrade. Min. Land Manage*, 5(53). <https://doi.org/10.15243/jdmlm>
- Julzarika, Atriyon, & Harintaka. (2019). *UTILIZATION OF SENTINEL SATELLITE FOR VERTICAL DEFORMATION MONITORING IN SEMANGKO FAULT-INDONESIA*. *Acrs*, 1–7.
- Julzarika, Atriyon, & Harintaka. (2020). Indonesian DEMNAS: DSM or DTM? *2019 IEEE Asia-Pacific Conference on Geoscience, Electronics and Remote Sensing Technology (AGERS)*, 31–36. <https://doi.org/10.1109/AGERS48446.2019.9034351>
- Julzarika, Atriyon, Laksono, D. P., Subehi, L., Dewi, E. K., Kayat, K., Sofiyuddin, H. A., & Nugraha, M. F. I. (2018). Comprehensive integration system of saltwater environment on Rote Island using a multidisciplinary approach. *J. Degrade. Min. Land Manage*, 5(53), 2502–2458. <https://doi.org/10.15243/jdmlm>
- Kubla. (2019). *How Accurate is the Grid Method For Calculating Earthworks Cut & Fill Volumes?* <https://www.kublasoftware.com/grid-method-accuracy/>
- Laksono, D., Julzarika, A., Subehi, L., Sofiyuddin, H. A., Dewi, E. K., N, M. F. I., Pekerjaan, K., Rakyat, P., & Kelautan, K. (2019). Expedition Oe : A Visual- storytelling map on Rote Island ' s Lakes. *Journal of Geospatial Information Science and Engineering*, 1(2), 87–93.
- Li, Z., Zhu, Q., & Gold, C. (2004). Digital terrain modeling: Principles and methodology. In *Digital Terrain Modeling: Principles and Methodology*. <https://doi.org/10.1201/9780203357132>
- Malaspinas, A. S., Westaway, M. C., Muller, C., Sousa, V. C., Lao, O., Alves, I., Bergström, A., Athanasiadis, G., Cheng, J. Y., Crawford, J. E., Heupink, T. H., MacHoldt, E., Peischl, S., Rasmussen, S., Schiffels, S., Subramanian, S., Wright, J. L., Albrechtsen, A., Barbieri, C., ... Willerslev, E. (2016). A genomic history of Aboriginal Australia. *Nature*, 538(7624), 207–214. <https://doi.org/10.1038/nature18299>
- Nasir, S., Iqbal, I. A., Ali, Z., & Shahzad, A. (2015). Accuracy assessment of digital elevation model generated from pleiades tri stereo-pair. *RAST 2015 - Proceedings of 7th International Conference on Recent Advances in Space Technologies*, 193–197. <https://doi.org/10.1109/RAST.2015.7208340>
- Ndao, P. K. R. (2021). *Profil Daerah Kabupaten Rote Ndao*. Pemda Kabupaten Rote Ndao. <https://rotendaokab.go.id/profil-daerah>
- Nico, G., Leva, D., Fortuny-Guasch, J., Tarchi, D., & Antonello, G. (2005). Generation of digital terrain models with a ground-based SAR system. *IEEE Transactions on Geoscience and Remote Sensing*, 43(1), 45–49. <https://doi.org/10.1109/TGRS.2004.838354>
- Pleskachevsky, A., Lehner, S., Heege, T., & Mott, C. (2011). Synergy and fusion of optical and synthetic aperture radar satellite data for underwater topography estimation in coastal areas. *Ocean Dynamic*, 61(12), 2099–2120. <https://doi.org/10.1007/s102-011-0460-1>
- Rucci, A., Ferretti, A., Monti Guarnieri, A., & Rocca, F. (2012). Sentinel 1 SAR interferometry applications: The outlook for sub millimeter measurements. *Remote Sensing of Environment*, 120, 156–163. <https://doi.org/10.1016/j.rse.2011.09.030>
- Ruzgiene, B., Berteška, T., Gečyte, S., Jakubauskiene, E., & Aksamitauskas, V. Č. (2015). The surface modelling based on UAV Photogrammetry and qualitative estimation. *Measurement: Journal of the International Measurement Confederation*, 73, 619–627. <https://doi.org/10.1016/j.measurement.2015.04.018>

- Samboko, H. T., Abas, I., Luxemburg, W. M. J., Savenije, H. H. G., Makurira, H., Banda, K., & Winsemius, H. C. (2020). Evaluation and improvement of remote sensing-based methods for river flow management. *Physics and Chemistry of the Earth*, *117*, 102839. <https://doi.org/10.1016/j.pce.2020.102839>
- Sesama, A. S., Setiawan, K. T., & Julzarika, A. (2021). Bathymetric Extraction Using PlanetScope Imagery (Case Study: Kemujan Island, Central Java). *International Journal of Remote Sensing and Earth Sciences (IJReSES)*, *17*(2), 209. <https://doi.org/10.30536/j.ijreses.2020.v17.a3445>
- Setiawan, K. T., Suwargana, N., Br. Ginting, D. N., Manessa, M. D. M., Anggraini, N., Adawiah, S. W., Julzarika, A., Surahman, S., Rosid, S., & Supardjo, A. H. (2019). Bathymetry Extraction From Spot 7 Satellite Imagery Using Random Forest Methods. *International Journal of Remote Sensing and Earth Sciences (IJReSES)*, *16*(1), 23. <https://doi.org/10.30536/j.ijreses.2019.v16.a3085>
- Simons, M., & Rosen, P. A. (2015). Interferometric Synthetic Aperture Radar Geodesy. In *Treatise on Geophysics: Second Edition* (Vol. 3). Elsevier B.V. <https://doi.org/10.1016/B978-0-444-53802-4.00061-0>
- Suhadha, A. G., & Julzarika, A. (2020). Integration of Remote Sensing and Geographic Information System for Mapping Potential Tsunami Inundation. *Proceeding - AGERS 2020: IEEE Asia-Pacific Conference on Geoscience, Electronics and Remote Sensing Technology: Understanding the Interaction of Land, Ocean and Atmosphere: Disaster Mitigation and Regional Resillience, December*, 163–167. <https://doi.org/10.1109/AGERS51788.2020.9452767>
- Suhadha, A. G., & Julzarika, A. (2022). Dynamic Displacement using DInSAR of Sentinel-1 in Sunda Strait. *Trends in Sciences*, *19*(13), 4623. <https://doi.org/10.48048/tis.2022.4623>
- Suhadha, A. G., Julzarika, A., Ardha, M., & Chusnayah, F. (2021). Monitoring Vertical Deformations of the Coastal City of Palu after Earthquake 2018 Using Parallel-SBAS. *Proceedings - 2021 7th Asia-Pacific Conference on Synthetic Aperture Radar, APSAR 2021, March*. <https://doi.org/10.1109/APSAR52370.2021.9688380>
- Uysal, M., Toprak, A. S., & Polat, N. (2015). DEM generation with UAV Photogrammetry and accuracy analysis in Sahitler hill. *Measurement: Journal of the International Measurement Confederation*, *73*. <https://doi.org/10.1016/j.measurement.2015.06.010>
- Wilson, J. (2012). Digital terrain model. *Regional Assessment of Global Change Impacts: The Project GLOWA-Danube*, *137*(1), 69–74. https://doi.org/10.1007/978-3-319-16751-0_7
- Wulandari, S. A., & Wicaksono, P. (2021). Bathymetry mapping using PlanetScope imagery on Kemujan Island, Karimunjawa, Indonesia. *The International Conference on Smart and Innovative Agriculture (IOP Conf. Series: Earth and Environmental Science 686 (2021) 012032)*, 1–11. <https://doi.org/10.1088/1755-1315/686/1/012032>

APPLICATION OF GIS TECHNOLOGY TO ASSESS THE ENVIRONMENTAL SUITABILITY FOR *RUPICAPRA RUPICAPRA* IN ROMANIAN CARPATHIANS

Sanda-Maria ROȘCA^{1,2}, Vasile CEUCA³

DOI: 10.21163/GT_2023.182.15

ABSTRACT:

The chamois (*Rupicapra rupicapra*) is one of the primary mammals on the territory of Romania that still exists nowadays, but one which has restricted its suitable living habitat to alpine and subalpine areas due to global warming and the influence of anthropic factors (poaching, excessive grazing). The main aim of the present study consists of the ecological diagnosis of the fields in the Romanian Carpathians suitable for the chamois by using tools for mapping, as well as the statistical and mathematical analysis of the GIS technology. In order to determine field favorability modelling for the chamois, we used both knowledge expert-type data and official assessments of real actual numbers of specimens, but also, a complete database regarding the main biotic factors (topographic characteristics, hydrographic network, climate characteristics); abiotic factors (the existence of pastures, shrubby and forest vegetation, as well as the presence of feeding areas during winter), and anthropic factors (grazing, mountain tourism). All the hunting grounds at the level of the mountainous area in Romania was analysed in a qualitative and quantitative manner while taking into account the favorability and restriction character of these factors. To validate the modelling results that were obtained, the data from 97 hunting grounds where the chamois is present were used. The main results highlighted the territories situated in the massifs: Rodnei, Retezat, Făgăraș, Pietrosul Maramureșului as being territories that provide the best conditions for *Rupicapra rupicapra*. With these studies at our disposal, researchers may indirectly evaluate the genetic diversity of the species that are already present as well as the repopulation of the Romanian Carpathians' most advantageous areas.

Key-words: *Rupicapra rupicapra*, Favourability, GIS, Environmental modelling.

1. INTRODUCTION

The chamois (*Rupicapra rupicapra*) was a forest animal at its origins. It used to live at the superior limit of the forest (Anderwald et al., 2020) but due to its sensitivity to noises, once human activity started to intensify, the chamois left the forest and inhabited the rocky sides of the mountainous ridges that are hardly accessible. The chamois belongs to the Animalia kingdom, Vertebrata subkingdom, Mammalia class, Ruminantia subordinate, Bovidae family, Caprinae subfamily, evolving from *Pachygazella* sp. The species originates from Central Asia (where it lived approximately 10 million years ago). The first chamois fossils identified in Europe were found about the Mid-Pleistocene (Lovari & Scala, 1980), until the end of the '80s, 10 subspecies of one species called *Rupicapra rupicapra* were described. Later, as a result of thorough studies, two Chamois species were described: *Rupicapra pyrenaica* with other three subspecies, and *Rupicapra rupicapra* - this representing other seven subspecies *R. r. asiatica*, *balcanica*, *carpatica*, *cartusiana*, *caucasica*, *rupicapra* and *tatica* (Shackleton, 1997, Pedrotti & Lovari, 1999, Anderwald et al., 2020).

At the present moment, the chamois population is under 500000 specimens (Corlatti et al., 2011). However, a part of the subspecies requires conserving measures, as their number is anticipated to decrease to 20% of the total, due to the extension of the network communication channels, hydroelectric stations situated in mountainous areas that increase the pressures on this species, together with poaching activities (Anderwald et al., 2020).

¹ Faculty of Geography, Babeș-Bolyai University, 400006 Cluj-Napoca, Romania; sanda.rosca@ubbcluj.ro

² Romanian Academy of Scientists, Ilfov 3, 050044 Bucharest, Romania

³ Faculty of Forestry and Land Survey, University of Agricultural Sciences and Veterinary Medicine Cluj-Napoca, 400372 Cluj-Napoca, Romania; vasy.ceuca@yahoo.com

In Europe, large numbers of both species exist in France (approx. 16500 specimens) (Roucher, 1987), a migration of the species towards lower areas from the Low Tatra Mountains can be identified (Corti, 2012; Barboiron et al., 2018), in the Cantabrian Mountains (approx. 19000 specimens) (Alados, 1985), in the Abruzzo National Park, in Italy (approx. 650 specimens) (Pellicoli, 2019), in the Tatra Mountains (640 specimens), in the Carpathians (9000 specimens) (Shackleton, 1997), as well as a hybridization of the subspecies *Rupicapra tatrica* in *Rupicapra rupicapra* (Zemanová, 2015). There are major differences between populations from different countries. In some, an increase in the number of specimens was registered (Vogt et al., 2019; Willisch et al., 2013, Reimoser & Reimoser, 2019), whereas in others, there is a decreasing tendency (in Switzerland, from 96000 specimens existing in 2008, the number decreased to 91000 in 2018) (Anderwald et al., 2020). However, a decrease in the number of counted or hunted specimens does not directly reflect a decline of the species (Vogt et al., 2019). At the same time, the differences may also be influenced by the frequency of inventories, economic resources or the number of people that are involved (Forsyth, 2000; Loison et al., 2006; Chantreau et al., 2019). The chamois is an important game species as trophies are highly valued by passionate hunters. Hunting them offers hunters increased satisfaction due to the remarkable landscape provided by the areas situated above the forest limits, but the adventure itself is also satisfying, as the chamois has an excellent sense of sight and it can notice a person in motion from large distances. In order to maintain equilibrium in the mountainous areas with numerous specimens, as in the case of the Alps, approx. 20% of the spring population is harvested (Shackleton, 1997). However, in the Romanian Carpathians, taking into consideration the number of species in the field and their living conditions, the harvesting rates are established depending on the actual numbers of specimens, optimal numbers of specimens at the level of each hunting ground, their natural population growth, but also the necessity of achieving selection for maintaining the best specimens from the genotypic and phenotypic points of view.

At the present moment, in order to determine the ecological diagnosis of the areas where the chamois is present, the rating method is used. With this, we determine a specific score for one area that comprises the surface of the alpine terrain and one surface that is the same with it from the bordering forest for biotic factors (the presence of pastures and shrubby vegetation in the alpine area, the composition of the bordering forest vegetation present in the alpine area, the existence of feeding areas during winter), abiotic factors (the percentage of the area occupied by rocks and heavily rugged terrains, the average temperature between April 25th - June 10th, the quantity of precipitations between April 25th - June 10th, the density of the hydrographic network, the average thickness of the snow cover) and cynegetic factors (the density of the sources of salt, the numerical control of specific predators, the density of dogs and the load on the pastures). To these, we may add negative anthropic factors that consist in poaching (number of cases/year), the density of stray dogs/1000 hectares, as well as the intensity of tourist activities in the area (Law 393/2000).

By applying traditional methodology, all these factors receive one generalized value at the level of a hunting ground. Thus, this implies a specific level of generalization, as well as a specific level of score mediation. Considering this result, we resorted to specific modelling tools and GIS spatial and mathematical statistical analysis techniques in order to attain the objectives of the present study.

One main objective consists in favorability modelling in order to achieve the minimal conditions of existence for the chamois at the level of the Carpathian mountainous area in Romania, while using expert knowledge and official data obtained from the central public authority representatives who are responsible for forestry, like the ministry, specialists in forest administration, NMA structures (National Meteorological Administration), NAEP (National Agency for Environmental Protection), cynegetic hunting ground managers (public or private) and the custodians of the protected natural areas where this specimen is present.

In order to attain this objective, the emphasis will be put creating the databases for the determinant factors and on the analysis of all environmental factors, topographic characteristics (elevation, slope angle, fragmentation), climatic characteristics that include the quantity of precipitation and the air temperature between April 25th - June 10th, as well as the thickness of the snow cover.

At the same time, the land use classes will be analyzed. This time, the emphasis will be put on identifying the shrubby vegetation classes, the fields with pastures, the bordering forest vegetation in alpine areas that provide feeding areas also in winter. Given the high sensibility level of this species regarding noise, a database will be created that will consist of tourist tracks in the Carpathian area, but also of the transport infrastructure that has lately developed in the mountainous area through transmountain roads. This has led to an exceeding anthropic pressure, taking into account the fact that the living habitat of the species is represented by tourist mountainous areas that are highly attractive for mountain tourism.

2. STUDY AREA

The study area is represented by the Romanian Carpathians (a surface of 66286 km² which represents 27.8% of Romania). Due to their morphometric characteristics (elevation, slope angle, slope orientation, etc.), these determine an overlap of vegetation with the beech level (600-1200 m), Norway spruce level (1200-1800 m), mountain pine level (1600/1800-2200 m) and with the alpine grassy-vegetation level (over 2200 m) (Coldea, 19990), the last two being the ones we are mostly interested in for the present study (**Fig. 1**). In Romania, the chamois belongs to the category of protected species as it was declared “a monument of nature” even back in 1933. This moment represented an important step in the evolution of this species on a national level. In Romania, the chamois is present in the following massifs: Căpățâni, Retezat, Făgăraș, Bucegi, Țarcu, Piatra Craiului, Parâng, Rodnei, Suhard (Ionescu, 2002; Spiess, 2005).

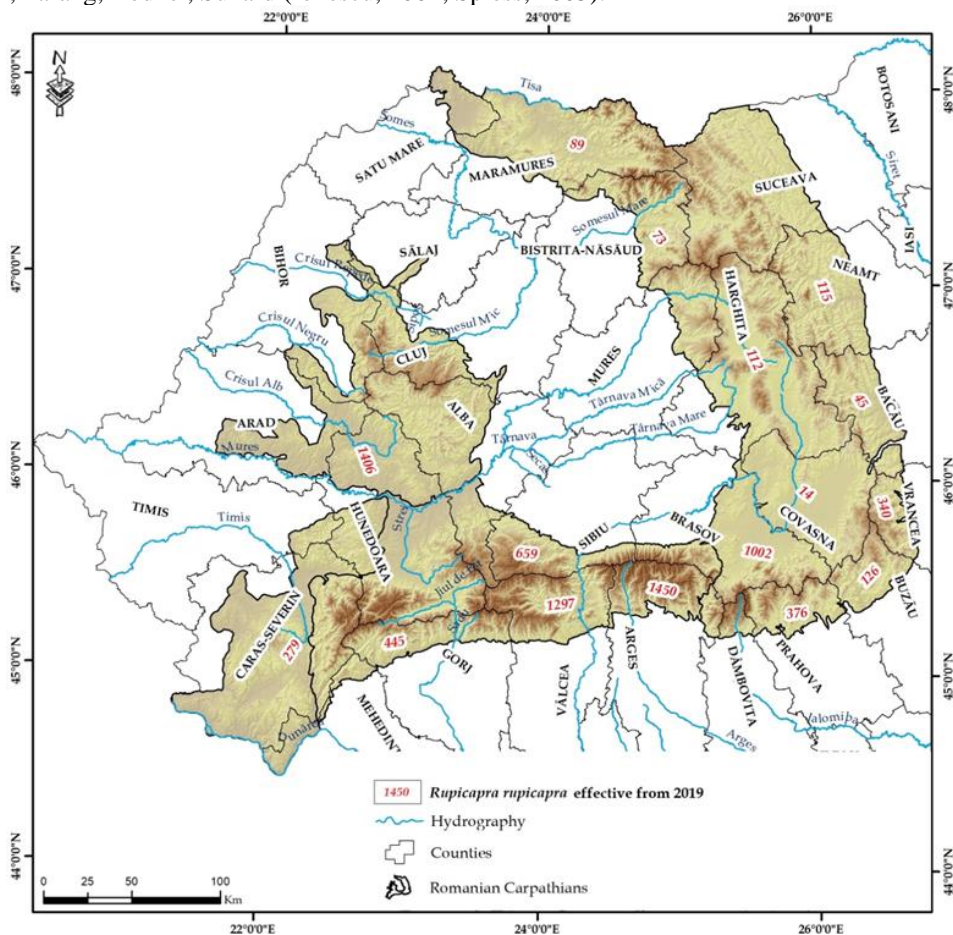


Fig. 1. The geographical position of the study area and the real number of chamois specimens in 2019.

A proportion of 70% of the chamois females reach sexual maturity by the third year of life, whereas the other 30% reach it in their second year. The female chamois reaches maturity quicker than the male chamois by 1-1.5 years (Rughetti & Festa-Bianchet; Anderwald, 2020). The mating period takes place from the middle of October to the middle of November. At lower elevation, the mating period could start one week earlier. At the same time, this period may vary by 1-2 weeks depending on the weather (cold weather quickens mating). The sociability of the chamois is highly pronounced as they generally live in herds. The leading of the herd is taken by a female chamois that already gave birth to one calf; it is usually a more mature female, one that has experience. In Romania, herds of chamois were observed to consist of females and calves, females without calves and males over one year of age. Males between 2-3 years old usually constitute separate herds, whereas the mature ones are generally solitary. The size of the herd increases depending on the density of its number, with the possibility of reaching 10, 20 or even more specimens. In Romania, an average size of such a herd is estimated to be made of 8 specimens.

The food of the chamois is exclusively vegetal, consisting of graminaceae, stems, buds and mainly lichens (*Festuca*, *Poa*, *Carex* and *Trifolium* species are very important for the alimentation of the chamois). and from the category of shrubs and subshrubs feeding on species such as: *Coryllus avellona*, *Juniperus communis*, *Ribes grossularia*, *Ribes nigrum*, *Crataegus monogyna*. Salt also has an important role together with the water they consume when eating. They are active during the day - feeding before noon and afternoon - lying down at midday.

3. DATA AND METHODS

The chamois is a forest animal that is truly a glacial relict, living with predilection along the superior limit of the forest in the least accessible rocky and steep areas. The presence of the inaccessible steep rocks, intercalated by scrublands of mountain pine and grey alder with rare tree vegetation, then by alpine plains that provide water sources, are mandatory conditions for its existence. Being aware of the requirement of this species for the environmental factors represents the necessary database for the implementation, the processing and the calibration of the current model.

In order to classify the mountainous territory of Romania on favorability classes for the chamois, the creation of a GIS complex database with high resolution is necessary for such interdisciplinary studies, but this must cover the entire Carpathian mountain range. Thus, a complex database was made, consisting of both vector databases (meteorological stations, hydrographic network, cynegetic areas, county limits, land use, etc.) and raster databases (precipitation grid, temperature grid, thickness of snow cover, etc.) which influence individually and cumulatively the favorable and restrictive conditions for the analyzed species (**Table 1**).

It is also necessary to analyze the thickness of the snow cover for the entire Carpathian mountainous range. In this sense, the database consisting of the thickness of snow cover is used for the period 1960-2010, available online for the entire Carpathian Mountain range (Szalai et al., 2013).

The analysis of climatic data is extremely important. Both the precipitation grid and the average annual temperature grid at the level of the Carpathian mountainous range will be used. These databases resulted from generating the specific grids for each parameter while using GIS spatial interpolation techniques and correlation equations between the point values of these parameters and the elevation of the meteorological stations that monitor the Carpathian mountain area, as well as those situated in its proximity, in order to guarantee the continuity of the databases. These climatic data are included in the analysis, as they cause the mortality of some young specimens, predominantly male (because when winter comes, they are already weak as a result of the mating period).

The density of the elementary hydrographic network and its equal distribution in the mountainous area represents an element of favorability, as it provides places with water supply for the chamois. Considering these aspects, the hydrographic network was digitized by using topographic maps for the entire Carpathian area, as the density of the hydrographic network is one of the parameters that was included in the final model of favorability.

Table 1.

Used database.

N o.	Database	Type of database	Format	Result
1	Meteorological stations	primary	Vector (point)	Vectorization
2	Precipitation grid in the period April 25th – June 10th (mm)	modelled	Raster (GRID)	Modelled by using as data source: carpatclim
3	Air temperature grid in the period April 25th – June 10th (degrees Celsius)	modelled	Raster (GRID)	Modelled by using as data source: carpatclim
4	The thickness of the snow cover	modelled	Raster (GRID)	Modelled by using as data source :carpatclim
5	Hydrographic network	primary	Vector (line)	Vectorization
6	Land use	primary	Vector (polygon)	Corine Land Cover 2018 Database, v.20, European Environment Agency (EEA) - Copernicus Land Monitoring Service
7	Digital Elevation Model (m)	modelled	Raster (GRID)	Derived from DEM
8	Geodeclivity (slope angle of the terrain)	derived	Raster (GRID)	Interpolation of point values from the terrain
9	Mountain tourist tracks	primary	Vector (line)	Open Street map database
10	Hunting grounds with chamois specimens	primary	Vector (polygon)	Digitization
11	Real number of chamois specimens	primary	attributes	Attribute tables
12	Bordering forest vegetation in alpine area	derived	Vector (polygon)	Corine Land Cover 2018 Database, v.20, European Environment Agency (EEA) - Copernicus Land Monitoring Service
13	Pastures	derived	Vector (polygon)	Corine Land Cover 2018 Database, v.20, European Environment Agency (EEA) - Copernicus Land Monitoring Service
14	Shrubby vegetation in the alpine area	derived	Vector (polygon)	Corine Land Cover 2018 Database, v.20, European Environment Agency (EEA) - Copernicus Land Monitoring Service
15	Rocky landform unit (% from the occupied area)	derived	Vector (polygon)	Corine Land Cover 2018 Database, v.20, European Environment Agency (EEA) - Copernicus Land Monitoring Service
16	The limits of landform units	primary	Vector (polygon)	Geo-spatial.org

At the same time, from the category of limitative factors of anthropic nature, we can notice the degradation of habitats preferred by the chamois, as the touristic activities can determine the fragmentation of living habitats, the change of diet or even the disappearance of sheltering places for the chamois. In this sense, we will use the shapefile of tourist tracks in the Romanian Carpathians by using Open Street Map national database. In order to identify biotic parameters that influence the living habitat for the chamois, we will use Corine Land Cover 2018 database, v.20, European Environment Agency (EEA) - Copernicus Land Monitoring Service. Thus, the polygons will represent the shrubby vegetation, the rocky areas with exposed rock, but at the same time, we will extract the territories with forest vegetation from nearby alpine grasslands from this database, and this will be used in the final modelling of favorability.

The influence of the snow coverage, low temperatures and unavailability of food in the cold season are the main factors that induce morbidity around the mountain ungulates in the Alps where losses of over 6500 chamois specimens were identified within a period of 13 years due to the snow layer and the avalanches (Jonas et al., 2008). The most favorable territories that were identified are those exposed to the sun where accumulations of snow are more reduced (Gonzales & Crampe, 2001). For this kind of studies, the spatial and temporal analysis of the pursued causality are highlighted (Johnson et al., 2008; Boyce et al., 2003, Hysa et al., 2021, Bilașco et al., 2022, Hyka et al., 2022).

The temperature intervenes in the quantity of consumed food, fecundity, growing speed, the arrival to the stage of reproduction, thus influencing the vital processes. Low temperatures, especially when they are correlated with the increase of humidity, may cause losses among the offspring of some game species. Values higher than 4 degrees Celsius for the analyzed period are classified using the best rating notes in the classical methodology as well. This is because the available food resource is extremely important in this period for the female specimens found in their gestation period, while the direct influence of the climatic factors (minimal temperature especially corroborated with high values of mixed precipitation at the beginning of the period) and the environmental conditions are very important for the calf. At lower elevations, where extreme temperatures have little effects and the quantity of precipitation is reduced, greater natural growth of the population can be identified than at the level of territories where these factors induce inadequate conditions, especially in the first days of the life of the calf when the incidence of illnesses is higher. To these inadequate development conditions, we can also add the accentuated parasitism or the existence of a large number of predators (Șelaru, 2000). Heavy rains, snow, floods or droughts influence the life of the game in multiple ways, either by the direct losses they produce or by restricting the access to food. The animals get the water they need to survive directly by drinking or through the food they consume. It is known that there is an interdependence between the faunistic species and the forest vegetation. Thus, the richer the variety of wooden species, the better food and sheltering conditions for the game species. The sum of climatic, edaphic, ecological and anthropic factors may have numerous influences on the health of forests and on the game species from the economic, social or structural organization points of view.

From the category of biotic factors, the factors that are linked to the available food source for the studied species were included in the model by knowing the fact that this species feeds on lichens, grasses and shrubbery, buds, stems, moss, depending on the season (Dumitrescu et al., 2019, Curovic et al., 2020). The role of vegetation in the life of the game is to provide shelter and food. In this sense, the forest vegetation provides the herbaceous plants, shrubs and young species of trees as food source.

The noise produced as a result of traffic is a stress factor for various animal species, such as the bear, the stag, the boars or the chamois (Shackleton, 1997; Switalski & Nelson, 2011). This is the reason why major investments are made in order to carry out the creation of passages for wild animals (Mata et al., 2008) some studies also highlighting the possibility of using drainage culverts (Brunen et al., 2020). Due to disturbances caused by mountain tourism and excessive grazing, a longer movement of the chamois in search for food was signaled which altered the animals' accustomed daily and seasonal pattern of home range use (Hamr, 1988), as the magnitude of avoiding areas with a dense road network increased together with the increase of pressure caused by hunting (Laurance et al., 2006). The attention was drawn to the negative effects induced by the dense system of roads that also infiltrates in the natural protected areas. The reason why this is brought up is the negative potential of reducing the biodiversity that is directly proportional with the extension of the road network that serves rural areas continuously expanding. In this sense, the roads participate at the over-fragmentation of terrains and at a reduction in the quality of landscapes. The level of stress during the season was identified through the concentration of fecal cortisol metabolites (FCM) which in the studies carried out in the Tatra Mountains highlighted higher values in the territories with greater frequency of tourism compared to the protected areas situated at higher distances from the tourist tracks and the road network (Szijacz-Kosica et al., 2013). Thus, the level of stress may reduce immunocompetence and the reproductive output (Apanius, 1998; Mullner et al., 2004). To all these factors, the influence of human beings on the existence of the game is added, as this is felt under multiple aspects, such as the intense hunting, which could lead to the decrease or the disappearance

of some game species. The intervention of the human being is reflected through selective harvesting of trophies. Eliminating the mature specimens leads to the structure alteration of a population. Massive deforestation, agricultural practice, intense mechanization and chemicalization have important effects on living habitats, causing imbalance among the game species. All these factors are important to be included in the analysis, but, due to nonuniformity and variable availability at the level of the entire Carpathian mountainous range, these were not included in the assessment in order to avoid local overestimations (Cota et al., 2001).

By applying the GIS geospatial modelling techniques, this GIS database will allow the implementation of a quantitative model of classification on classes of favorability for the chamois, both at the level of mountainous massifs and at the level of detail. Thus, the statistical analysis and the interrogation of the database and of the final result are possible at any moment. The first methodological stage consists in acquiring the previously mentioned databases directly, through vectorization from different data sources, and indirectly, by modelling and spatial analysis, while using specific techniques of conversion and rating. The second aspect consists in the actual analysis of the obtained submodels and the applying of techniques of rating scores for favorability and restriction for every class of each factor included in the model, as well as the result of favorability classes cumulated for the entire analyzed area. Building a complex, interdisciplinary database that includes ecological determinants for the species under analysis, landform characteristics, climatic characteristics, food resources, snow cover thickness is a challenge both for small study areas and for a mountain range as in this case.

4. RESULTS AND DISCUSSIONS

The results obtained from applying the GIS model were materialized in a collection of thematic maps (Fig. 2 - 9) which implicitly led us to the possibility of classifying on favorability categories all the hunting grounds from the Romanian Carpathians, as well as at the level of major landform subunits from the analyzed territory. From the category of anthropic factors that influence the living conditions of the analyzed species, rock distribution and slope angles were analyzed, as this species prefers territories where over 50% of the surface of the hunting grounds is represented by with rocks and cliffs with slope angles over 35 degrees. These surfaces will be classified within the present model in the very high favorability class which is found on 32.2% from the studied area (Fig. 2). To these, the territories that consist of surfaces occupied by rocks and cliffs up to 40-50%, and the slope angle ranges between 20-35, are added. These are territories that are classified in the high favorability class.

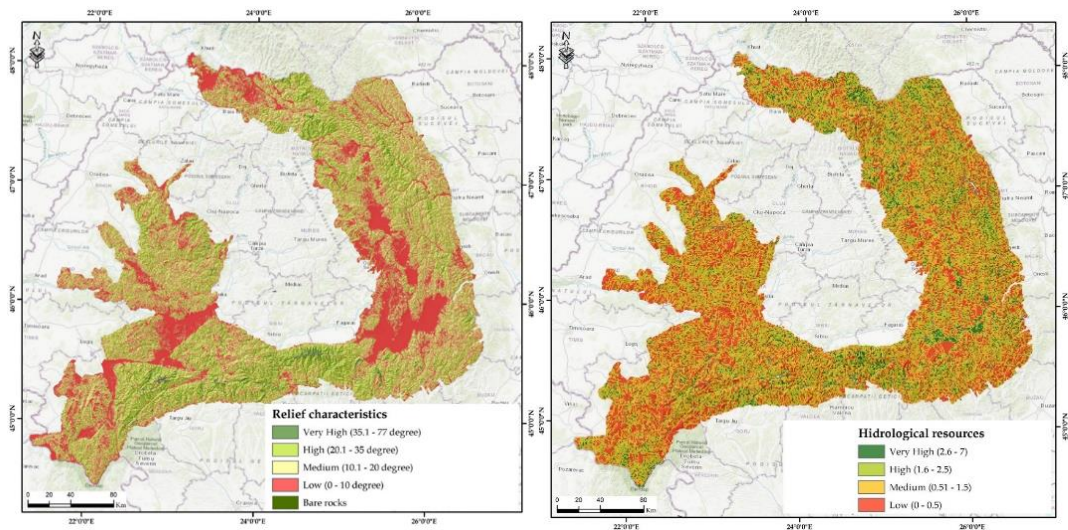


Fig. 2. Favourability for *Rupicapra rupicapra* according to topographic characteristics (left) and according to hydrological resources (right).

The areas with medium conditions are represented by territories characterized by cliffs where rocks occupy up to 30-40% of the territory, and the slope angle is between 10-20.

In order to discover the most favorable territories for *Rupicapra rupicapra*, the water supply available for this species was analyzed at the level of the entire Carpathian mountainous range. Thus, by using G.I.S. spatial analysis techniques, the density of the hydrographic network (km/km^2) determined. This consists of values between 0-4.37 km/km^2 , territories with a higher density than 2.6 km/km^2 as well as territories where natural and anthropic lakes are found. These are classified as belonging to the very high favorability class. In this sense, we can notice the compensation provided in the high mountainous area on the surfaces where the hydrographic network does not cover the necessary water supply by the 642 glacial, natural and anthropic lakes.

In order to discover the influence of the snow cover on living conditions for the chamois, the CARPATCLIM database (Szalai et al., 2013) was used. This was used through a process-related snow cover model based on pre-finished CARPATCLIM grids, the application of the snow cover model was not divided among the project members according to their national domains but collectively, by the project associate member ZAMG. Pre-finished CARPATCLIM daily grids of mean air temperature [$^{\circ}\text{C}$], precipitation sum [mm] and relative air humidity [%] were used as input (**Fig. 3**). For the territory of the Romanian Carpathians, the average of the thickness of snow cover was obtained for the period between October and March. This varies between 6-193 cm thickness, with the highest values being characteristic for the areas present at a higher elevation (**Fig. 3, left**). The territories with the snow cover thicker than 60 cm are classified in the low favorability areas for *Rupicapra rupicapra* because it makes their movement and resistance difficult in the face of their natural predators. The areas with the thickness of the snow cover between 40 and 60 centimeters are classified in the medium favorability area whereas the areas characterized by the thickness of the snow cover between 20-40 or the territories with snow less thick than 20 cm are classified in the areas with the highest favorability for the studied species. Regarding the air temperature between April 25th and June 10th, we may notice that, in the studied area of the Romanian Carpathians, the values of this indicator are classified in the range between 1.8-16 $^{\circ}\text{C}$ (**Fig. 3, middle**). Temperature levels were classified by using Natural Breaks classification, higher temperatures corresponding to better favorability classes. From the point of view of the quantity of precipitation, we can notice the fact that the entire Romanian Carpathian Mountain range benefits from quantities of precipitation between 9.48-39.12 mm for the analyzed time period (April 25th – June 10th) (**Fig. 3, right**). This precipitation range is not restrictive according to the classic rating norms, but in our study case it was, so the territories that receive more than 30 mm of precipitation for the critical period are included in the low favorability class. Indeed, it is interesting to analyze the quantity of precipitation for the entire Carpathian Mountain range in Romania for the entire year, as this varies between 557-1620 mm/an (Rosca et al., 2019) because the quantity of precipitation will influence the development of herbaceous, shrubby and forest vegetation that constitutes the main food source for the chamois.

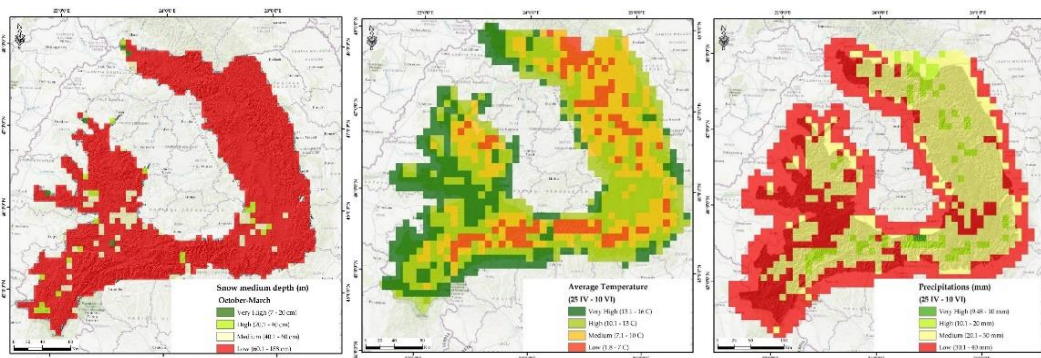


Fig. 3. Favourability for *Rupicapra rupicapra* according to average snow thickness between October and March (left), to average temperature in the period 25 IV – 10 VI (middle), to precipitation in the period 25 IV (right).

By using CorineLandCover database (CLC), we extracted the territories classified in the category of pastures; the territories classified in the category of areas occupied by shrubby vegetation (scrub and/or herbaceous vegetation associations according to CLC, 2018) – these being extended on 2108 km² within the analyzed area. To these, we add the areas classified in the category of subalpine vegetation (moors and heathland according to CLC, 2018) that are extended on 739 km², 5141 km² represented by pastures and 5107 km² represented by natural grasslands (Fig. 4).

Various studies have highlighted the tendencies of increasing pressure on living habitats, especially in the context of future changes regarding land use (Powers & Jetz, 2019). To these factors, the analysis of the afforested areas at the level of the Romanian Carpathians was added. In this sense, the database was used in order to highlight the forests situated in the proximity of the alpine area with a greater consistency than 30%, thus with a stand of trees that presents rare consistency (31-60%), almost full consistency (71-90%) and full consistency (90-100%). Thus, the areas of alpine pastures with bordering forest are classified in the high-est favorability class, as they offer both food source and shelter; the area of alpine pastures and sub-shrubby vegetation is classified in the high favorability class, the bordering forests in the alpine area are classified in the medium favorability class, and the forests situated at elevation lower than 1800 m, together with the pastures situated at medium and low elevation are classified in the low favorability class (Fig. 4).

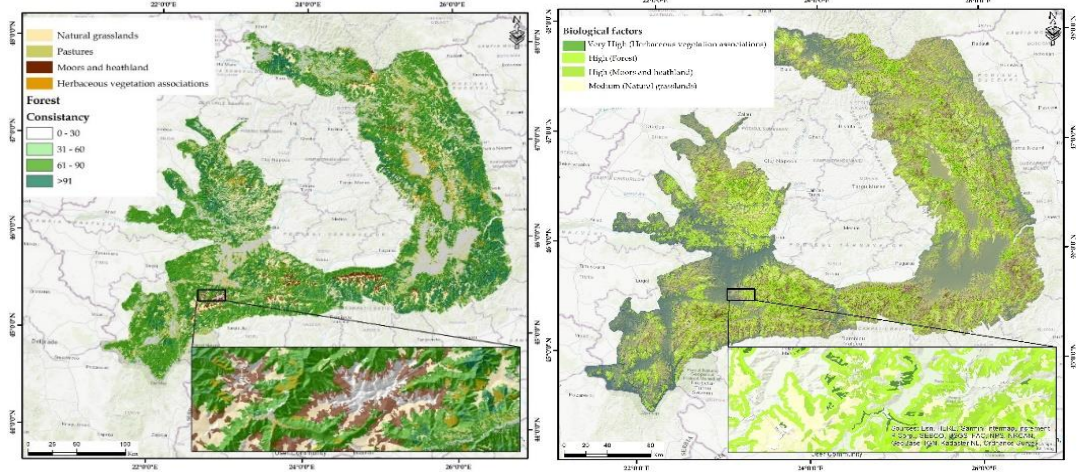


Fig. 4. Favourability for *Rupicapra rupicapra* according to biological factors.

The analyzed species is found in mountainous massifs with rugged landforms, steep slopes (the Făgăraș, Rodnei and Bucegi Mountains), but this species also looks for shelter against unfavorable meteorological conditions and natural pests. Therefore, in areas such as the Retezat Mountains, where the topography offers both morphometric and morphologic diversity, the presence of glacial valleys and lakes, as well as the abundant subalpine vegetation led to a greater number of specimens (Georgescu, 1989; Ionescu, 2002; Sapies, 2005; Dumitrescu et al., 2016). The adaptation of the species to high slopes is well-known, as their hooves are big and cloven and these allow them to move with relative lightness on the rocky areas with high slopes (Ionescu, 2002; Spiess, 2005). The analysis of the behavior of the species is extremely important within these types of analyses. Previously, tendencies of higher frequency among the male specimens on sectors with exposed high slopes were identified, unlike the female specimens with calves that avoid exposed slopes as they are rather looking for shelter (Boschi & Nievergelt, 2003). However, the areas with high slopes and vegetation are used as escape places, meaning that the female specimens are more sensitive than the male ones (Hamr, 1988).

Taking into consideration the influence of the transportation network on the comfort of mammal species within the mountainous areas, the factor related to the road network, railroad system and tourist tracks was added as a mostly limitative factor for the studied species (Fig. 5). By using the Euclidean distance analysis, the studied territory was classified on favorability and restriction classes, while taking into consideration the influence of the road network on the studied species.

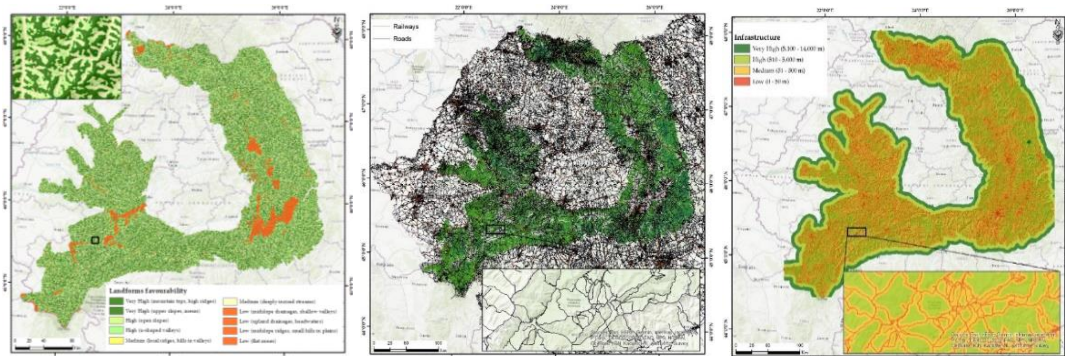


Fig. 5. Favorability for *Rupicapra rupicapra* according to landforms (left), according to the density of the roads (middle and right).

Territories situated in the immediate proximity (up to 50 m) of them, are classified in the most restrictive class, those situated between 51-500 m from it are part of the medium favorability area, those situated between 501-5000 m are part of the high favorability class, whereas the areas situated at higher distances than 5 km present the best living conditions for the chamois (**Fig.5**).

All ecological conditions found under “proper functioning” conditions – food abundance, quietness in the environment of each species, as well as human intervention restricted only to help game species in critical moments, such as epidemic diseases, water and food shortages, or the presence of pests, with no accentuated involvement in the forest ecosystem – may lead to good results in order to have specimens that are healthier and more reliable from a genetic point of view.

5. DISCUSSION

The use of the GIS technology in order to classify the Romanian sector of the Carpathians depending on the level of favorability or restriction for the chamois represents an element of novelty for the spatial modelling studies. However, due to the possibility of integration of spatial databases regarding the accumulation of biotic and abiotic factors that take part in guaranteeing living habitat conditions for the chamois, this is constituted through a modern means, innovative for the interdisciplinary analysis.

As a result of applying the G.I.S. complex spatial analysis model after taking into account the provided input based on expert knowledge-type information regarding the ecological necessities for the analyzed species, the entire Romanian Carpathian mountainous range was classified on favorability classes for the chamois (**Fig. 6**). Thus, the 7900.8 km² that represent 20.9% of the analyzed territory are highlighted, as these represent the territories situated in the very high (3848.5 km²) and high (4052.3 km²) favorability classes, which provide good living conditions from the point of view of abiotic factors (topography, climate) and biotic factors (mainly represented by an adequate food source). There is also a reduced anthropic pressure from the point of view of reduced density of transportation network, as well as reduced practice of winter sports and tourist activities.

At the opposite pole, territories with high anthropic pressure are identified at a lower elevation in marginal and intramountainous depressions where environmental characteristics rather induce limitative and restrictive conditions for the chamois, but good living conditions for their natural enemies. It is the case of 9000.2 km² (23.9 % of the analyzed territory) which are classified in the low (36.6 %) and very low (11.2 %) favorability classes. The advantages of the G.I.S. technology and the cumulated spatial analyses with expert knowledge-type information are successfully used in studies related to the movement of animals (Hooge & Eichenlaub, 1997). As a result of applying the proposed quantitative model, we obtained a global classification of the entire Romanian Carpathians Mountain range on favorability classes for the chamois (**Table 2**) taking into consideration the correlative influence of environmental factors, topographic characteristics, forest, shrubby and herbaceous vegetation, as well as anthropic influences on this species.

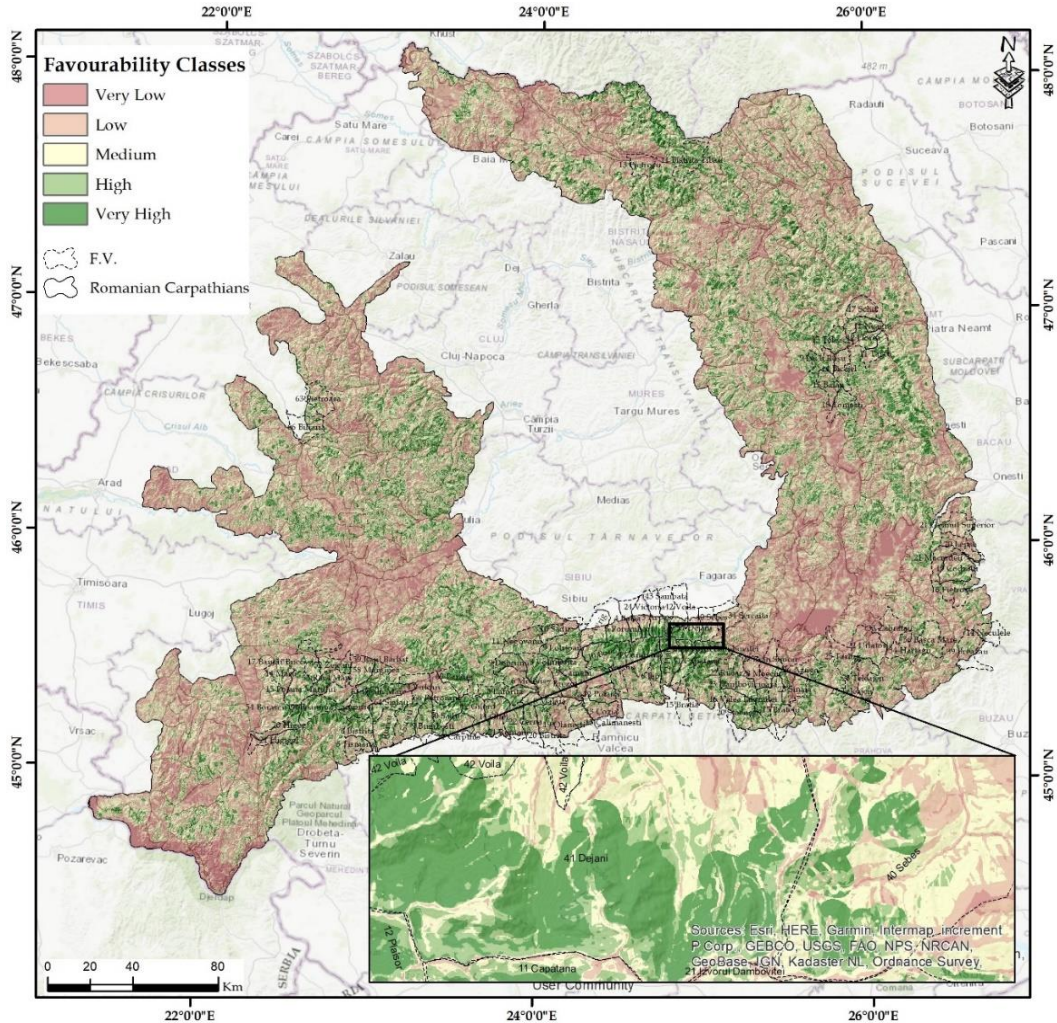


Fig. 6. Favorability map for *Rupicapra rupicapra* in the Romanian Carpathians.

The advantages of using these models, in the detriment of the classic method based on the diagnosis keys for the chamois, mainly consist in maintaining the variability of factors at the level of each hunting ground, for every analyzed factor, as well as for the territorial surfaces found at different levels. At the same time, there is the possibility of carrying out comparative analyses between different massifs which could help us within the regional and national projects and politics, but also within the exchange of information between institutions for an efficient implementation of conservation strategies for the chamois in Romania.

As a result of carrying out this analysis, the hunting grounds were identified as hotspots providing the best developing conditions of the studied species (Fig. 7). Thus, hunting grounds are situated in the Retezat Mountains where previous studies have analysed the food resources (raw protein, etheric extract and raw fiber) and high-lighted areas like Gorganu, Negru and Secări (Dumitrescu et al., 2019) or other territories belonging to the Rodnei National Park (Iușan & Filipoiu, 2010). We may notice the fact that, as a result of modeling, extended areas within the well-known hunting grounds in Romania were classified in the very high and high favorability classes due to the high number of chamois specimens. For instance, at the level of the hunting ground 12 Plăișor in Argeș county, 394 chamois specimens were registered in the inventory; the hunting ground in Dejeani presented 231 specimens and 170 chamois specimens were registered in the inventory at the level of the hunting ground 54 Borascu Godeanu in the Retezat Mountains.

Table 2.

Classification on high favourability classes of mountainous massifs with the most extended surfaces that provide favourable conditions for the chamois.

Massif	Favorability classes					
	Very High		High	Medium		
	Km ²	%	Km ²	%	Km ²	%
The Țarcaului Mountains	215.7	10.2	135.1	10.7	331.1	31.3
Rodna Massif	183.1	25.3	155.2	15.9	321.8	38.9
The Călimani Mountains	172.2	19.3	207.9	16.4	616.8	34.0
The Goșmanu Mountains	90.9	10.4	88.7	12.5	252.9	37.1
Fâncel Mountain	87.8	13.3	83.8	13.0	262.8	37.1
Pietrosul Maramureșului Peak	86.8	12.6	44.3	12.0	99.3	37.7
The Țibles Mountains	78.0	25.0	68.7	12.8	169.8	28.6
The Neamțului Mountains	74.7	19.4	83.4	16.4	211.9	39.0
Cearcanu Peak	70.6	12.2	45.5	13.6	68.5	34.5
Mount Cucu	65.0	29.6	83.9	19.0	205.1	28.7
Toroioaga Peak	64.7	10.8	44.3	14.0	102.5	34.2
Hășmaș Massif	63.6	21.4	62.7	14.6	120.7	33.8
The Corbului Mountains	59.8	17.8	43.2	17.6	73.1	33.8
The Suhard Mountains	58.6	26.7	50.4	19.3	95.3	32.7
Mount Saca	58.4	19.2	82.0	16.5	173.4	31.2
The Șumuleu Mountains	56.1	11.1	74.4	15.6	146.2	33.0
Grintiesul Mare Massif	55.4	12.2	44.9	16.2	125.3	31.7
The Bodoc Mountains	54.3	18.9	49.7	15.3	139.8	42.8
The Farcău Mountains	49.3	24.8	34.6	15.3	73.7	35.3
Mount Mădăraș	46.2	16.9	87.8	15.8	203.1	39.7
The Bârgăului Mountains	43.0	6.5	75.9	12.3	342.7	28.5
Nemira Peak	42.4	4.9	36.0	8.7	97.1	39.2
Budacu Massif	39.7	13.8	29.3	12.9	92.4	34.5
Viscolului Peak	36.1	19.1	36.7	14.1	73.5	44.4
Rarău Massif	35.9	13.5	41.5	13.7	137.2	27.5
Giumalău Massif	35.5	8.5	32.2	9.8	74.0	32.5
Tatarcii Peak	35.4	14.6	37.4	13.2	97.7	30.4
Ceahlău Massif	34.8	11.2	35.2	11.8	92.7	30.8

Regarding the determination of the level of predictability for the proposed model within the present study, the value of the ROC curve was determined for the territories at the level of which there are hunting grounds where *Rupicapra rupicapra* specimens are known to live. In this case, the sensitivity of the model represents the true positive rate, meaning that there is the possibility that the studied species benefits from good developing conditions and this can be validated in the field through the direct observations carried out during the inventories.

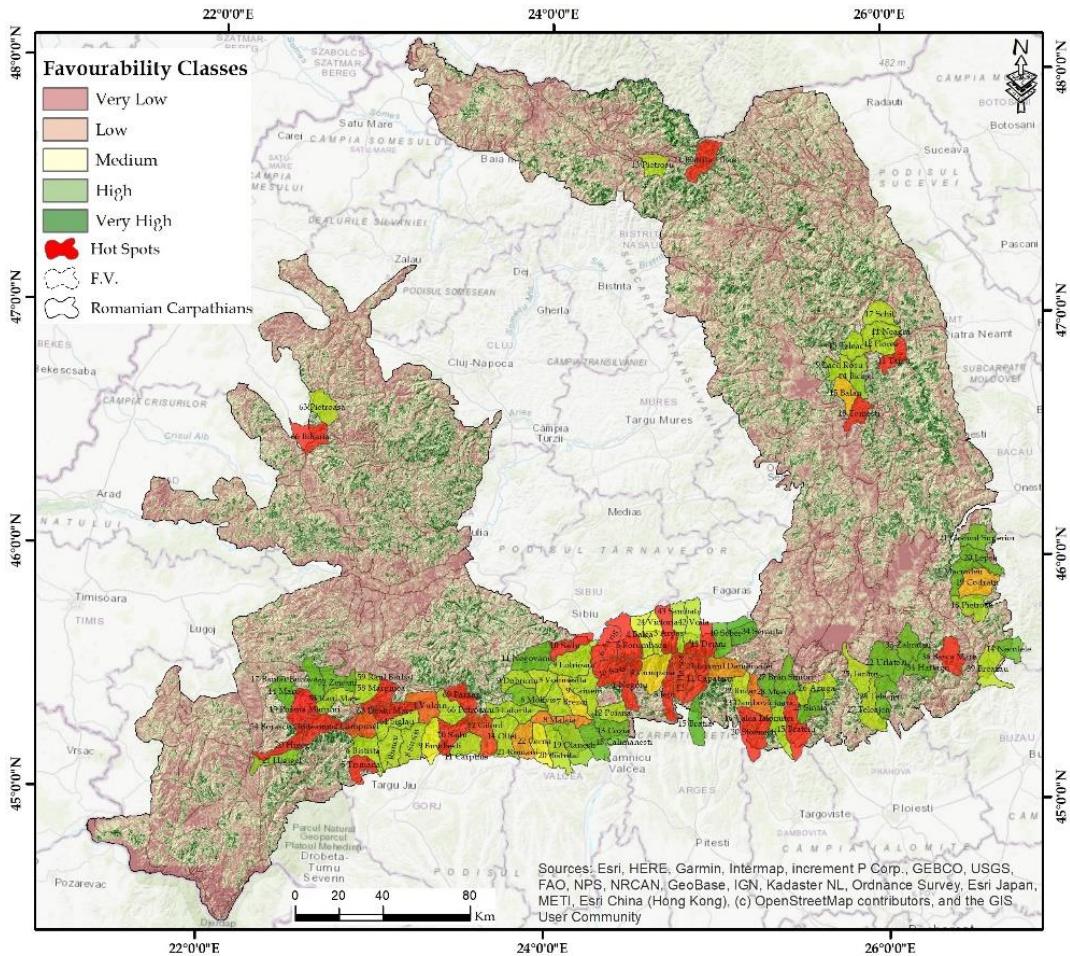


Fig. 7. Hotspot analysis at the level of hunting ground with *Rupicapra rupicapra* herds.

The specificity of the model consists in the probability that the result of the modeling is negative through the invalidation in the field of the existence of the chamois at the level of the areas which are classified by the model in high classes of its existence. Thus, the calculated value under the ROC curve (Relative Operational Curve) is 0.819 (AUC=0.819, 95% confidence interval: 0.71-0.87, $p<0.001$) (Fig. 8).

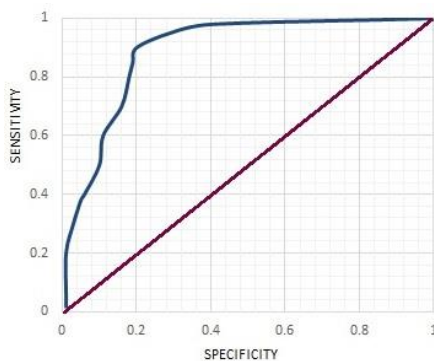


Fig. 8. ROC curve for the model.

This was calculated because we tried to identify the accuracy level of the present model. Thus, a higher value than 0.8 of the area under the ROC curve and its graphical position near the left corner of the system of coordinates indicate a high value of sensitivity and a reduced true positive rate. Thus, we may conclude that the implemented model to determine favorable and restrictive areas for the chamois at the level of the Romanian Carpathian territory has a satisfying precision of the obtained results.

In order to discover the correspondence between the favorability classes provided by each category of factors for *Rupicapra rupicapra* and the modelled classification of cumulated favorability, modelled within the present study, we extracted point values randomly distributed within the hunting grounds where the inventory of the real number of chamois specimens was carried out (Fig. 9). Thus, we can notice the enlarged patch for biological factors due to their diversity at the level of the validation area, as well as a high validation rate of the influence of topographic characteristics, especially for the high and very high favorability classes. Indeed, improvements can be brought at the level of the database used in modelling by adding the factors linked to the spatial distribution of natural enemies, the numerical control of specific predators (lynx and wolf) or to the negative influence of poaching. These are aspects that may be improved in future studies on territories that have a reduced surface, so that the generation these high-quality databases may be realistically carried out.

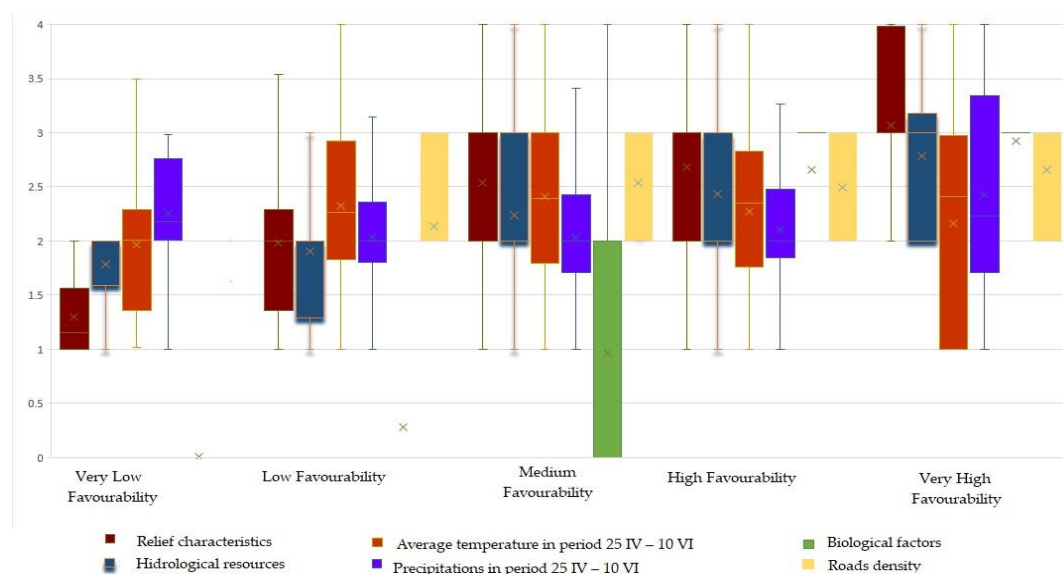


Fig. 9. Comparative box plot of used factors.

6. CONCLUSIONS

The studies that were carried out regarding the number of chamois specimen highlight periods of time when the species faced important losses in the number of specimens, as well as periods when the population increased and the discrepancy between sexes was present. Therefore, we draw attention on the necessity of conserving the numbers of chamois specimens, especially in the places where strict protection is provided to natural predators as well, such as the lynx or the wolf, and on the necessity of identifying those territories that provide good living and developing conditions for the natural growth of the species with respect to repopulation. The constant monitoring of the specimens by using modern investigation methods and by presenting the evolution of the real number of chamois specimens in the Romanian Carpathians may also serve for the sensibilization of various target groups in order to bring awareness regarding the negative effects that overgrazing and anthropic interventions have on this species. Thus, this serves at educating the population and it implicitly promotes conservation activities for the species considered to be a symbol for the high mountainous territories. The current strategy applied for the management of *Rupicapra rupicapra* implies measures taken from the administrative offices of the natural parks, the managers of hunting grounds or authorities in such a way that a durable conservation of the species is achieved.

Thus, the present study supports the measures of repopulation/relocation of specimens in areas that provide the best developing conditions for the chamois. To these, stricter regulations are added. These regard overgrazing in the high mountainous areas, the control of natural pests and predators, active involvement in managing the hunting grounds and the involvement of volunteers to create special areas for food and salt sources, as well as the creation of limitative temporary niches for tourist activities in the living habitats of the chamois - aspects that can also be carried out by using modern techniques of spatial analysis and G.I.S. The creation of national GIS databases for the hunting grounds, together with the number of chamois specimens, also represents a strength, thus allowing the updating of databases regarding numbers of specimens, the calculation of density (per hectare, per hunting ground or massif) and, last but not least, it allows the possibility to create some detailed databases regarding the morphometric characteristics of the individuals, their health condition, the presence of illnesses, etc. that may be available for all institutions involved in protecting and conserving this species in Romania. The access to the databases that induce favorability or restriction to the species is extremely important when we aim at the repopulation or revigoration of the species in areas where the chamois population is declining (it is necessary to be repopulated with specimens coming from massifs with similar characteristics), but at the same time when it is necessary to identify potential living habitats for this species. The variables are intrapopulation. In order to reduce errors in the favorability modeling for *Rupicapra rupicapra* and to calibrate the favorability for black goats according to their actual numbers for territories where their numbers are known, we draw attention to the quality of the databases used in the modeling. Future studies aim at carrying out additional measurements for all chamois populations that live in the Romanian Carpathians in order to identify the influence of the level of favorability of different types of habitats on the quality of trophies and the maintenance of genetic diversity of populations.

REFERENCES

- Alados CL. (1985) An analysis of vigilance in the Spanish IbeX (*Capra Pyrenaica*), *Z. Tierpsychol.* :58-64.
- Anderwald, P., Ambarli, H., Avramov, S., Ciach, M., Corlatti, L., Farkas, A., Jovanovic, M., Papaioannou, H., Peters, W., Sarasa, M., Šprem, N., Weinberg, P., Willisch, C. (2020) *Rupicapra rupicapra*. The IUCN RedList of Threatened Species: e. T39255A22149561. Available online: <https://dx.doi.org/10.2305/IUCN.UK.2020-3.RLTS.T39255A22149561.en>.
- Apanius, V. (1998) Stress and immune defense, *Adv Stud Behav*, 27:133-153.
- Banu, Gh., Banu, E. Capra Neagra (*Rupicapra rupicapra*) la o jumătate de secol de ocrotire Rezervația naturală Pietrosul Rodnei la 50 de ani, 1977, Cluj Napoca (in Romanian).
- Barboiron, A., Saint-Andrieux, C., Garel, M., Calenge, C., Guibert, B. (2018) Inventaire des populations françaises d'ongulés de montagne, mise à jour 2016. *Faune Sauvage* 320: 35-44.
- Bilașco, Ș., Hognogi, G. G., Roșca, S., Pop, A. M., Vescan, I., Fodorean, I., Sestras, P. (2022). Flash flood risk assessment and mitigation in digital-era governance using unmanned aerial vehicle and GIS spatial analyses case study: Small river basins. *Remote Sensing*, 14(10), 2481.
- Boschi, C., Nievergelt, B. (2003) The spatial patterns of Alpine chamois (*Rupicapra rupicapra rupicapra*) and their influence on population dynamics in the Swiss National Park. *Mamm. Biol.*, 68: 16-30.
- Brunen, B., Daguët, C., Jaeger, JAG. (2020) What attributes are relevant for drainage culverts to serve as efficient road crossing structures for mammals? *J Environ Manage.* 15(268): 110-423. doi: 10.1016/j.jenvman.2020.110423. Epub 2020 May 14. PMID: 32510423.
- Chantreau, F., Gaudry, W. (2019) Synthèse des acquis et du fonctionnement du site OGFH de la Chartreuse., Observatoire grande faune et habitats - ONCFS.
- Cheroiu, G., (2003), A history of Romanian hunting literature, Ed. Cynegis, Romania (in Romanian).
- Coldea Gh., (1990) Rodna Mountains. Geobotanical study, Edit. Academiei Române, Bucuresti, Romania, (in Romanian).

- Corlatti, L., Herrero, J., Ferretti, F., Anderwald, P., García-González, R., Hammer, S., Nores, C., Rossi, L., Lovari, S. (2011) Chamois, *Rupicapra* spp. In: Zachos, F.E. & Corlatti, L. (ed.), *Terrestrial Cetartiodactyla*, Springer.
- Corti, R. (2011) Le chamois des Alpes *Rupicapra rupicapra rupicapra*. Pages 4-19, Inventaire des populations françaises d'ongulés de montagne - Mise à jour 2011. Inventaire des populations françaises d'ongulés de montagne - Mise à jour 2011, pp. 4-19. Réseau Ongulés Sauvages ONCFS-FNC-FDC.
- Cota, V., Bodea, M.ș Micu, I. (2001) Hunting and hunting in Romania, Editura Ceres (in Romanian).
- Crestanello, B., Pecchioli E., Vernesi C., Mona S., Martinkova N., Janiga M., Hauffe H. C., Bertorelle G. (2009) The Genetic Impact of Translocations and Habitat Fragmentation in Chamois (*Rupicapra*) spp., *Journal of Heredity*, vol. 100.
- Curovic, M., Spalevic, V., Sestras, P., Motta, R., Dan, C., Garbarino, M., Urbinati, C. (2020). Structural and ecological characteristics of mixed broadleaved old-growth forest (Biogradska Gora-Montenegro). *Turkish Journal of Agriculture and Forestry*, 44(4), 428-438.
- Dumitrescu, V., Borlea, F., Tîrziu, E., Hotea, I., Ilie, M., Colibar, O. (2019) Researches Regarding the Feeding of the Black Goat (*Rupicapra Rupicapra*). *Lucrări Științifice*, 45.
- Dumitrescu, V., Borlea, G. F., Dumitrescu, A., Țenche-Constantinescu, A. M. (2016) Nature protection and sustainable conservation of *Rupicapra rupicapra* L. in the Retezat National Park area. *Journal of Horticulture, Forestry and Biotechnology*, 20(2), 112-117.
- Forsyth, D.M. (2000) Habitat selection and coexistence of the Alpine chamois (*Rupicapra rupicapra*) and Himalayan tahr (*Hemitra gusjehlahicus*) in the eastern Southern Alps, New Zealand, *J. of Zoology*, 252 (2), 215-225.
- Georgescu, M. (1989) Wild mammals in Romania, Ed. Albatros, 1989, (in Romanian).
- Hamr, J. (1988) Disturbance behaviour of chamois in an Alpine tourist area of Austria. *Mt. Res. Dev.*, 8: 65-73.
- Hooge, P.N., Eichenlaub, B. (1997) Animal Movement Extension to Arcview, Ver. 1.1. Geological Survey; Alaska Science Center—Biological Science Office, USA Geological Survey: Anchorage, AK, USA.
- Hyka, I., Hysa, A., Dervishi, S., Solomun, M. K., Kuriqi, A., Vishwakarma, D. K., & Sestras, P. (2022) Spatiotemporal Dynamics of Landscape Transformation in Western Balkans' Metropolitan Areas. *Land*, 11(11), 1892.
- Hysa, A., Spalevic, V., Dudic, B., Roșca, S., Kuriqi, A., Bilașco, Ș., & Sestras, P. (2021). Utilizing the available open-source remotely sensed data in assessing the wildfire ignition and spread capacities of vegetated surfaces in Romania. *Remote Sensing*, 13(14), 2737.
- Ionescu, O., (2002) Eco-Ethology of the black goat in Bucegi, PhD Thesis, Transilvania University, Brașov, Romania (in Romanian)
- Iușan, C., Filipoiu, T. (2010) The Dynamics of the Chamois (*Rupicapra Rupicapra Carpathica*) In Rodna Mountains National Park (Biosphere Reserve).
- Laurance, W.F., Croes, B.M., Tchignoumba, L., Lahm, S.A., Alonso, A., Lee, M.E., Campbell, P., Ondzeano, C. (2006) Impacts of roads and hunting on central African rainforest mammals. *Conserv. Biol.*, 20:1251-1261.
- Loison, A., Appolinaire, J., Jullien, J.-M., Dubray, D., (2006) How reliable are total counts to detect trends in population size of chamois *Rupicapra rupicapra* and *R. pyrenaica*? *Wildlife Biology*, 12: 77-88.
- Lovari, S., Scala, C. Revision of *Rupicapra* Genus. I. (1980) A statistical re-evaluation of Couturier's data on the morphometry of six chamois subspecies, *Bollettino di zoologia*, 47:1-2, 113-124, DOI: 10.1080/11250008009440328.
- Mata, C., Hervás, I., Herranz, J., Suárez, F., Malo, J.E. (2008) Are motorway wildlife passages worth building? Vertebrate use of road-crossing structures on a Spanish motorway. *J Environ Manage.* 88(3):407-15. doi: 10.1016/j.jenvman.2007.03.014. Epub 2007 Apr 30. PMID: 17467145.
- Mullner, A., Linsenmair, K.E., Wikelski, M. (2004) Exposure to ecotourism reduces survival and affects stress response in hoatzin chicks (*Opisthocomus hoazin*). *Biol Conserv*, 118:549-558
- Order no. 418 of June 2, 2005 for the approval of the methodology for evaluating game trophies, in accordance with the methodology of the International Council for Hunting and Game Protection, Issued by the Ministry of Agriculture, Forests and Rural Development, Published in the OFFICIAL GAZETTE no. 548 of June 28, 2005 (in Romanian).

- Order of the Ministry of Agriculture, Forests and Rural Development no. 393/2002 has as its object the approval of the keys and the optimal densities for the species red deer, red deer, deer, black goat, wild boar, bear, rabbit, pheasant, partridge, mountain rooster, lynx, wolf and wild cat and for the determination of the optimal numbers, on hunting grounds, for these species of wild fauna of hunting interest (in Romanian)
- Pedrotti, L., Lovari, S. (1999) *Rupicapra rupicapra*. In: A. J. Mitchell-Jones, G. Amori, W. Bogdanowicz, B. Kryštufek, P.J.H. Reijnders, F. Spitzenberger, M. Stubbe, J.B.M. Thissen, V. Vohralfk, and J. Zima (eds), The Atlas of European Mammals, Academic Press, London, UK.
- Pelliccioli, L. (2019) Indagine sulla stima di consistenza e sul prelievo di ungulati selvatici sull' arco alpino italiano (2009-2014), Quaderno UNCZA studi e ricerche n° 2/2019. Ed. Fidc.
- Powers, R.P., Jetz, W. (2019) Global habitat loss and extinction risk of terrestrial vertebrates under future land-use-change scenarios. *Nat. Clim. Chang.*, 9: 323-329.
- Reimoser, S., Di, I.R., Reimoser, F. Lebensraum und Jagdstrecke - Abschussdichtenverschiedener Wildarten in den österreichischen Bezirken seit (1955). - 1. Teil: Gamswild. In Weidwerk, 2019. 11: 20-22.
- Roșca, S., Șimonca, V., Bilașco, Ș., Vescan, I., Fodorean, I., Petrea, D. (2019) The Assessment of Favourability and Spatio-Temporal Dynamics of *Pinus Mugo* in the Romanian Carpathians Using GIS Technology and Landsat Images. *Sustainability* 11, 3678. <https://doi.org/10.3390/su11133678>
- Roucher, F. (1987) Chamois de Chartreuse, plan de gestion cynotique en vue de restaurer la population. Groupement d' interet cynegetique de Chartreuse - Is&e. 52 pp
- Rughetti, M., Festa-Bianchet, M. (2011) Seasonal changes in sexual size dimorphism in northern chamois., *J. Zool.*, 284, 257-264. 24.
- Șelaru N., (2000) Hunting trophies, A.R.E.D., București, (in Romanian).
- Shackleton, D.M. (1997) Wild Sheep and Goats and Their Relatives: Status Survey and Conservation Action Plan for Caprinae. IUCN/SSC Caprinae Specialist Group, Gland, Switzerland and Cambridge, UK.
- Spieß, A., (2005) Black goats in Retezat massif, Ed. Hora, Romania (in Romanian).
- Switalski, T.A., Nelson, C.R. (2011) Efficacy of road removal for restoring wildlife habitat: Black bear in the Northern Rocky Mountains, USA. *Biol. Conserv.* 144, 2666-2673.
- Szalai, S., Auer, I., Hiebl, J., Milkovich, J., Radim, T., Stepanek, P., Zahradnicek, P., Bihari, Z., Lakatos, M., Szentimrey, T., Limanowka, D., Kilar, P., Cheval, S., Deak, Gy., Mihic, D., Antolovic, I., Mihajlovic, V., Nejedlik, P., Stastny, P., Mikulova, K., Nabyvanets, I., Skyryk, O., Krakovskaya, S., Vogt, J., Antofie, T., Spinoni, J. (2013) Climate of the Greater Carpathian Region. Final Technical Report. www.carpatclim.eu.org.
- Vogt, K., Signer, S., Ryser, A., Schaufelberger, L., Nagl, D., Breitenmoser, U., Willisch, C. (2019) Einfluss von Luchsprädatoren und Jagd auf die Gämse - Teil 1 und 2. Bericht in Zusammenarbeit mit dem Jagdinspektorat des Kantons Bern, KORA Bericht Nr. 84. KORA, Muri bei Bern, Schweiz.
- Willisch, C.S., Bieri, K., Struch, M., Franceschina, R., Schnidrig-Petrig, R., Ingold, P. (2013) Climate effects on demographic parameters in an un hunted population of Alpine chamois (*Rupicapra rupicapra*). *Journal of Mammalogy*, 94: 173-182.
- Zemanová, B., Hájková, P., Hájek, B., Martínková, N., Mikulíček, P., Zima, J., Bryja, J. (2015) Extremely lowgenetic variation in endangered Tatra chamois and evidence for hybridization with an introduced alpinepopulation. *Conservation Genetics*, 16: 729-741.
- Zwijacz-Kozica, T., Selva, N., Barja, I., Silván, G., Martínez-Fernández, L., Illera, J. C., Jodłowski, M. (2013) Concentration of fecal cortisol metabolites in chamois in relation to tourist pressure in Tatra National Park (South Poland). *Acta theriologica*, 58(2), 215-222.

CHATEAU BROWNFIELDS IN SELECTED LAU1 REGIONS OF THE CZECH REPUBLIC: SEARCHING FOR REMARKABLE FEATURES WITHIN DESCRIPTIVE LOCALIZATION ANALYSIS

Kamila TURECKOVA¹ 

DOI: 10.21163/GT_2023.182.16

ABSTRACT:

The Czech Republic, like many other European countries, is characterised by a large number of chateau buildings and sites. Historical events of the last century have caused that in the countries of the so-called Eastern Bloc the original use of these buildings was largely interrupted and the overall management of these properties was neglected. This, together with other factors, led to the creation of a large number of chateau brownfields, which are still visible in the Czech Republic today. The aim of this paper is to determine on the background of a descriptive analysis the key characteristics of chateau brownfields associated in particular with their localization and to reveal any similarities and differences that result from their location within selected LAU1 regions. The analysis is based on the primary research of 367 chateau buildings in 4 NUTS3 regions of the Czech Republic and is unique in its concept.

Key-words: *Brownfield, chateau, Chateaufield, region, Czech Republic, Analysis.*

1. INTRODUCTION

Chateau brownfields are a specific type of brownfields that have been created by the abandonment of a property that was primarily built as a chateau. Alker et al. (2000) or Yount (2003) define brownfield as a real estate property that is insufficiently utilized, neglected and might be also contaminated. A brownfield is also defined as a property that is or has been only partially used (Ferber, 2006 or Martinat et al, 2016). As such, brownfields can be the remains of industrial, agricultural, military, transport, religious, housing and other activities (e.g. public amenities), whether in the form of land or buildings (sites), located anywhere in the cadastral area of towns and cities (Krzysztofik et al., 2013 or Tang & Nathanail, 2012). Contamination is not assumed to occur in chateau brownfields. However, if it does, it was most likely created ex post as part of the activities that followed in the chateaux after they lost their primary function (Turečková, 2023).

Manor houses, chateaux, aristocratic estates, manorial or manorial residences have been an integral part of the European cultural landscape since the early modern period (since the 16th century) and refer to their administrative, economic, representative and residential functions (see also Magnussen, 2018 or Pluskowski et al., 2019). Like other real estate, chateau buildings are exposed to the risk of losing their purpose, abandonment and devastation, which in the Central European space has been intensified by the events of the last century, in particular the formation of independent republics after World War I, the onset of fascism and World War II, the political turbulence and the onset of communism after its end, and finally the collapse of the so-called Eastern Bloc after 1989. All these events significantly affected the property-ownership relations to the chateau residences and forcibly interrupted their current use (Turečková, 2022 and Turečková et al., 2022).

This paper focuses on a relatively new object of research - chateau brownfields (alt. chateaufields) and builds on the research topic developed last year. It is an issue that has not been systematically investigated before and from this point of view it is necessary to proceed with its solution on the one hand analogically with other studies in terms of inspiration in the determination of the research areas and research methodology, but on the other hand also intuitively and inductively. This corresponds to

¹ School of Business Administration in Karvina, Silesian University in Opava, Univerzitní Nam. 1934/3, 733 40 Karvina, Czech Republic, tureckova@opf.slu.cz

the stated objective of this article, which is to determine the key characteristics of chateau brownfields associated with their location in particular and to reveal any similarities and differences resulting from their location within the selected LAU1 regions, against the background of descriptive analysis. We are interested in whether any causalities and similarities of a general and logical nature can be found in the simplified data on the characteristics of 367 chateau buildings in the four NUTS3 regions of the Czech Republic. It was not the intention here to use a complex statistical apparatus, but mainly to characterize the set of chateau brownfields in each territorial unit and to determine logical links, if any. In a way, the paper and the presented analysis can also be seen as a description of regional differences in the localization of chateau brownfields in Moravia and Silesia in the Czech Republic.

Due to the thematic "novelty" of the object of research, the literature search of other scientific sources related to chateaux brownfields is also limited.

2. METHODOLOGY AND DATA

The presented and analysed data is based on research in the field of chateau brownfields on the territory of the Czech Republic which required the identification of all chateau buildings in the given regions according to the set criteria (see below) and the search for their required characteristics and attributes. The analysed chateaux and chateau brownfields are located within the Czech Republic in two macro-regions of the Czech Republic (Moravia and the Czech part of Silesia) and 4 NUTS3 regions (Moravian-Silesian Region, Olomouc Region, Zlín Region and South Moravian Region). In this territorial area, 367 chateaux were found within 22 LAU1 regions (**Fig. 1**), 153 of which had or still have brownfield status (see **Appendix**). It should be noted here that despite the precision with which the objects in the territory were located it cannot be guaranteed that the list is absolute. Let us add that the actual database of chateau buildings has 30 characteristics for each chateau, which had to be individually traced.

In order to be included in the research, the chateau had to (A) still have a physical form (we abstracted from chateaux that no longer exist, i.e. they were "razed to the ground") and (B) it had to be continuously habitable and fulfil a certain practical function (i.e. it did not only fulfil a beautification function). Whether the chateau was abandoned and without use and was therefore a brownfield was only determined for the period since 1900. In the case of determining whether a particular chateau was a brownfield and this was not entirely clear from the information obtained, the following rules were laid down: (1) if various activities or targeted reconstruction and restoration were systematically carried out in the building, the chateau was not a brownfield; (2) the same applies in the case of restitution, where the intention of subsequent use of the chateau was known during the period of the ongoing restitution proceedings, or the original activities were 'catching up' there; (3) However, if it was clear that the chateau had been abandoned for some time, but it was not possible to ascertain the exact information (in particular the exact period for which it had been a brownfield), a combination of deductive, intuitive and analogical approaches was followed and the information was "guessed". This approach was used for a maximum of 10% of the objects. A chateau was classified as a brownfield if it was (4) currently (spring 2023) without use and intended for sale, and is or has been used (5) only partially, more or less marginally (e.g. in a situation where only 20% of the chateau was used and the rest was dilapidated). The term regenerated brownfield refers to a chateau brownfield that has a new economic function after a period of disuse and dilapidation. 107 reclaimed chateau brownfields have been identified, the remaining 46 are still abandoned and are still waiting for their new meaningful use.

The sources of information included publicly accessible internet portals and websites, the data of which were critically confronted with each other and the aim was to provide information on the chateaux as accurately as possible. The sources of information included in particular (1) the websites of the municipalities in whose cadastre the chateaux are located; (2) the websites of the chateaux themselves or of the institutions that are housed in them, if available; (3) the website of the National Heritage Institute; and (4) other websites and portals, e.g. hrady.cz; denik.cz; rozhlas.cz; prazdnedomy.cz; mizejicipamatky.cz; mapy.cz and others.

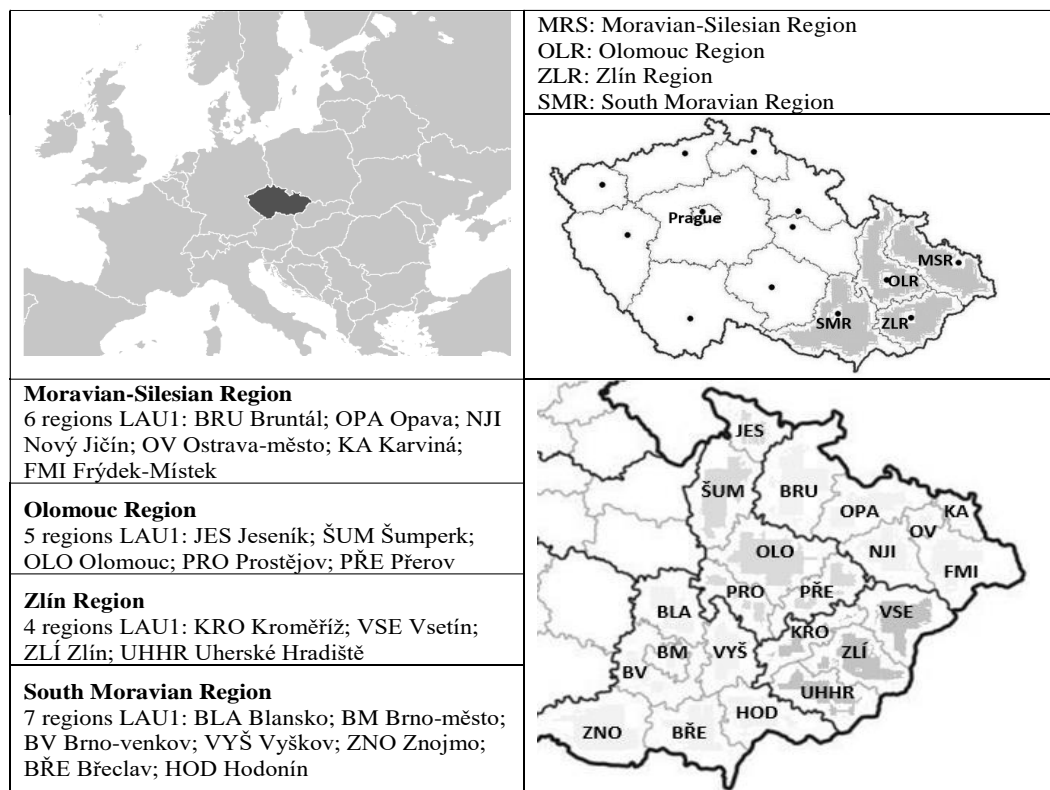


Fig. 1. Analysed LAU regions of the Czech Republic from the point of view of chateau brownfields (Source: own).

With regard to the stated aim of the paper, i.e. to determine the key attributes of chateau brownfields within the LAU1 regions in order to uncover the underlying similarities or differences in their location within the framework of the descriptive analysis, due to the amount of primary data, only some characteristics and features relating to chateaux and chateau brownfields were selected and are presented and commented upon in the following section. These are summarised by LAU1 regions and are presented, according to the logic of the matter, either as an average or through a mode, either by a specific number, a word or a summary category. The analysis and description of these data is preceded by a brief analysis of selected indicators at NUTS3 level. Due to the relatively large amount of data, only some of the nuances and points of interest resulting from the regional location of chateaux and chateau brownfields are highlighted in the text of the following chapter. Selected relationships between the indicators were subjected to correlation analysis to confirm or refute possible causality (using Pearson coefficient ($r \in [-1, +1]$). Thus, it applies that the closer the value of the coefficient is to one (+1), the higher the correlation between the two variables—indicators (Nevima, 2014; Meloun, 1994)). A verbal assessment of the measured causality is presented in **Tab. 1**.

In order to make the localization of chateau brownfields in LAU1 regions more comparable and to make the data more easily visualized, two ratio coefficients were created: Ratio I and Ratio II. Ratio I (R_I) represents the ratio of unregenerated chateau brownfields to regenerated ones. For this ratio, the lower its value is, the more successful is the process of regeneration of chateau brownfields. If all chateau brownfields in the area are regenerated, this indicator has a value of zero. The second ratio indicator (Ratio II; R_{II}) expresses the proportion of chateaux per chateau brownfield. This indicator has a parallel in the percentage of chateau brownfields to the total. For this indicator, the lower the value of the coefficient, the higher the representation of chateau brownfields relative to the total number of chateaux in the region. If its value is 1, then all the chateaux in LAU1 of the region had brownfield status.

3. ANALYSIS OF CHATEAU BROWNFIELDS IN THE REGIONS OF THE CZECH REPUBLIC

Before we focus on the determination of the factors of chateau brownfields at the level of LAU1 regions, we comment on the occurrence of chateaux in Moravia and Silesia within 4 NUTS3 regions. As can be seen in the table below (**Tab. 1**) the largest number of chateaux was located in the South Moravian Region (123), which corresponded to the largest number of identified chateau brownfields (48), of which 34 have been regenerated and the remaining 14 are still abandoned and awaiting their new use. The smallest number of chateaux is in the Zlín Region (54), which is the smallest in terms of area and population.

Table 1.
Dependence between variables (correlation analysis, Pearson coefficient).

Value of Pearson Coefficient (<i>r</i>)	Type of Dependence
0.70 or higher	Very strong positive relationship
0.40 to 0.69	Strong positive relationship
0.30 to 0.39	Moderate positive relationship
0.20 to 0.29	Weak positive relationship
0.01 to 0.19	No or negligible relationship
0	No relationship, no correlation
-0.01 to 0.19	No or negligible relationship
-0.20 to 0.29	Weak negative relationship
-0.30 to 0.39	Moderate negative relationship
-0.40 to 0.69	Strong negative relationship
-0.70 or higher	Very strong negative relationship

Relative indicators in the second part of the table provide more relevant information: (1) in terms of municipalities, the largest number of chateaux is in the Moravian-Silesian Region, where it is one chateau per 3.3 municipalities, while in the Zlín Region, it is one chateau per 5.7 municipalities; (2) 39% of chateaux in the South Moravian and Zlín Regions were brownfield, while in the Olomouc and Moravian-Silesian Regions it was 44% of the total number of chateaux. (3) The largest number of regenerated chateau brownfields in their total number was in the Zlín Region (76%), while in the Olomouc Region, 34% of the buildings are still abandoned and dilapidated. (4) The concentration of chateaux in the territory of the regions is lowest in the Zlín Region, where on average one chateau occurs in an area of 73.4 km² and one chateau brownfield in an area of 188.7 km². The highest number of inhabitants (5) per chateau is in the Moravian-Silesian Region (12835), as is the case for the chateau brownfield (29200).

In the case of the Olomouc Region it is interesting that while the concentration of chateaux in the territory is the highest (1 chateau per 53.2 km²), the number of inhabitants per 1 chateau is the lowest (6292). The same is true in the indicator of the number of inhabitants per chateau brownfield (14158). If we take into account that the largest number of brownfield chateaux not yet regenerated is located here, one may wonder whether the number of abandoned and dilapidated chateaux is not directly related to the area of the territory and indirectly to the number of inhabitants. There would be a logic to this. At the same time, in **table 2** we see that there is a de facto causality between the total number of chateaux and the number of chateau brownfields, while there is no causality between the number of chateau brownfields and the number of their regeneration.

In the following, we will focus on the analysis of the basic characteristics of chateaux and chateau brownfields at the regional level of districts (LAU1), see **table 3**. Due to the already large amount of information, only the most interesting ones will be selected (also valid for further presentation and description of the data), first separately within a given region, then across all LAU1 regions and finally, some causalities that emerge from the analysis and are interesting from the point of view of presentation of the results will be highlighted.

Table 2.

Characters of selected NUTS3 regions of the Czech Republic in the context of chateaux and chateau brownfields.

Region (NUTS3)	Number of municipalities (LAU2)	Area (km ²)	Number of LAU1 regions	Population (as of 1.1.2022)	Total number of chateaux	of which chateau brownfields	of which regenerated chateau brownfields
South Moravian	673	7195	7	1184568	123	48	34
Zlín	307	3963	4	572432	54	21	16
Olomouc	399	5267	5	622930	99	44	29
Moravian-Silesian	300	5425	6	1167989	91	40	28
total	1679	21850	76	3547919	367	153	107
Region (NUTS3)	Number of municipalities per 1 chateau	The share of chateau brownfields in the whole	Share of regenerated CHBs in the total number of CHBs	Area of the region (km ²) per 1 chateau	Area of the region (km ²) per 1 chateau brownfield	Number of inhabitants of the region per 1 chateau	Number of inhabitants of the region per 1 chateau brownfield
South Moravian	5.5	39%	71%	58.5	149.9	9631	24679
Zlín	5.7	39%	76%	73.4	188.7	10601	27259
Olomouc	4.0	44%	66%	53.2	119.7	6292	14158
Moravian-Silesian	3.3	44%	70%	59.6	135.6	12835	29200
average	4.6	42%	70%	59.5	142.8	9840	23824

Note: CHBs – chateau brownfields.

In the South Moravian Region, the largest number of chateaux is located in the Znojmo district (32), of which 13 have the status of brownfield, followed by the Brno-venkov district with 24 chateau buildings including 10 brownfields. The highest share of chateau brownfields in the total number of chateaux is in the Blasnko district (47%, also R_II has the lowest value of 2.1), the most successful in regeneration is, apart from the Brno-město district, where both identified chateau brownfields have been regenerated (R_I has a value of 0), the Blansko and Břeclav districts with 86% success rate of the regeneration process. The Znojmo district is the worst-performing district in terms of regeneration of chateau brownfields (54%). This is confirmed by the R_I ratio, which is the highest in the whole region for this district. The district of Breclav has (apart from the extreme Brno-město) the densest concentration of chateaux per number of municipalities (3.9), i.e. one chateau per less than 4 municipalities. The Znojmo district has the lowest number of inhabitants per chateau (3,546), while the highest number is in Brno-město (4,733). The concentration of chateaux in the area of districts is the densest in Brno-město (28.8), while the highest number of chateaux is in Hodonín (99.9).

The Zlín Region has 4 districts and only 54 chateaux have been traced on its territory, 21 of which were previously abandoned and 5 of which are still waiting for new use. The largest number of chateau brownfields is in the Vsetín district (every second chateau is or was a brownfield; R_II = 2). For the Uherské Hradiště district, on the other hand, the R_II indicator has a value of 4.5, i.e. there is a total of 4.5 chateaux per one chateau brownfield. Successful in regeneration are the Kroměříž district (8 out of 9 brownfields have been regenerated) and the Uherské Hradiště district with a 100% success rate (R_I = 0). The worst performing district in the regeneration of chateau brownfields is Zlín, which has only a 50% success rate (R_I reaches the highest value in this district of the Zlín Region). The most frequent encounter with a chateau is in the Kroměříž region, where there is a chateau in every fourth municipality and there is also the lowest number of inhabitants per chateau (5172), similarly with the occurrence of chateaux in the territory, where the highest concentration of them is in the Kroměříž district (1 chateau is located in the territory of less than 40 m2).

Table 3.

Characters of selected LAU1 regions of the Czech Republic in the context of chateaux and chateau brownfields.

NUTS3	LAU1	Number of municipalities (LAU2)	Area (km ²)	Total number of chateaux	of which CHBs	of which regenerated CHBs	The share of CHBs in the whole	Share of regenerated CHBs in the total number of CHBs	Number of municipalities per 1 chateau	Number of inhabitants of the region per 1 chateau	Area of the region (km ²) per 1 chateau	Ratio I (number of unregenerated CHBs to regenerated)	Ratio II (number of chateaux per 1 CHB)
South Moravian Region	Blansko	116	863	15	7	6	47%	86%	7.7	7194	57.5	0.17	2.1
	Brno-město	1	230	8	2	2	25%	100%	0.1	47433	28.8	0.00	4.0
	Brno-venkov	187	1499	24	10	7	42%	70%	7.8	9396	62.5	0.43	2.4
	Břeclav	63	1038	16	7	6	44%	86%	3.9	7175	64.9	0.17	2.3
	Hodonín	82	1099	11	4	3	36%	75%	7.5	13736	99.9	0.33	2.8
	Vyškov	80	876	17	5	3	29%	60%	4.7	5430	51.5	0.67	3.4
	Znojmo	144	1590	32	13	7	41%	54%	4.5	3546	49.7	0.86	2.5
	Total/Average	673	7195	123	48	34	39%	71%	5.5	9631	58.5	0.41	2.6
Zlín Region	Kroměříž	79	796	20	9	8	45%	89%	4.0	5172	39.8	0.13	2.2
	Uherské Hradiště	78	991	9	2	2	22%	100%	8.7	15537	110.1	0.00	4.5
	Vsetín	59	1142	12	6	4	50%	67%	4.9	11681	95.2	0.50	2.0
	Zlín	91	1034	13	4	2	31%	50%	7.0	14537	79.5	1.00	3.3
		Total/Average	307	3963	54	21	16	39%	76%	5.7	10601	73.4	0.31
Olomouc Region	Jeseník	24	719	18	9	4	50%	44%	1.3	2042	39.9	1.25	2.0
	Olomouc	96	1620	20	7	3	35%	43%	4.8	11679	81.0	1.33	2.9
	Prostějov	97	770	23	11	9	48%	82%	4.2	4677	33.5	0.22	2.1
	Přerov	104	845	23	9	8	39%	89%	4.5	5505	36.7	0.13	2.6
	Šumperk	78	1313	15	8	5	53%	63%	5.2	7893	87.5	0.60	1.9
		Total/Average	399	5267	99	44	29	44%	66%	4.0	6292	53.2	0.52
Moravian-Silesian Region	Bruntál	67	1536	15	8	6	53%	75%	4.5	5970	102.4	0.33	1.9
	Frydek-Místek	72	1208	12	5	2	42%	40%	6.0	17696	100.7	1.50	2.4
	Karviná	17	356	12	7	3	58%	43%	1.4	19193	29.7	1.33	1.7
	Nový Jičín	54	882	15	5	5	33%	100%	3.6	9995	58.8	0.00	3.0
	Opava	77	1113	30	8	6	27%	75%	2.6	5792	37.1	0.33	3.8
	Ostrava-město	13	331	7	7	6	100%	86%	1.9	44586	47.3	0.17	1.0
		Total/Average	300	5426	91	40	28	44%	70%	3.3	12835	59.6	0.43

In the Olomouc Region, 44% of all 99 identified chateaux are brownfields. In absolute terms, the largest number of brownfields is located in the Prostějov district (11) and the smallest in the Olomouc district (7), while in relative terms the largest number of brownfields is determined in Šumperk (53%) and Jeseník (50%) districts (also the lowest values of indicator R_II). Jeseník, together with Olomouc, is also the least successful in the regeneration of chateau brownfields (the R_I indicator is the highest for these districts). In Jeseník, 5 brownfields out of 9 are still without meaningful use (only 44% of the original buildings are regenerated) and in Olomouc, 4 chateaux out of 7.

In contrast, in Přerov, the regeneration process is 89% successful, with 8 chateau brownfields regenerated out of 9 ($R_I = 0.13$ and is the lowest). In Jeseník district there is one chateau per 1.3 municipalities, i.e. chateaux are located in almost every one of them. This district also has the lowest number of inhabitants per occurrence of one chateau (2042). The highest territorial density of chateau occurrence is in the Prostějov district (one chateau for every 33.5 km²), while the least number of chateaux in the territory is in the Šumperk district (87.5).

Nový Jičín in the Moravian-Silesian Region together with the Ostrava-City district is very successful in the regeneration of chateau brownfields, as all the brownfields were regenerated here ($R_I = 0$), in Ostrava-City it was 6 objects out of 7 in total. Interestingly, in Ostrava-town all 7 chateaux had brownfield status ($R_{II} = 1$). A large proportion of brownfields in all chateaux is also found in the Karviná (58%), Bruntál (53%) and Frýdek Místek (42%) districts. The least regenerated chateaux are located in the Karviná (4 out of 7) and Frýdek Místek (3 out of 5) districts, which is also evidenced by the values of the R_I ratio, which are the highest for the whole region. In the Karviná region, there is one chateau per 1.4 municipalities, but due to the large number of inhabitants, there are less than 20 thousand inhabitants per chateau. In the Karviná region, chateaux are also the most frequent in the territory, because they are concentrated there the most in relation to the area of the region.

If we select the most significant data across all LAU1 regions, then the most chateaux are located in the Znojmo (32) and Opava (30) districts, and the least in the Ostrava-město (7) and Brno-město (8) districts, while the chateau brownfields are in absolute terms most represented in the Znojmo (13), Prostějov (11) and Brno-venkov (10) districts, and the least in the Brno-město (2) and Uherské Hradiště (2) districts. The largest share of chateau brownfields in the total number of chateaux (R_{II}) is in Ostrava-město, Karviná, Bruntál (all Moravian-Silesian Region) and Šumperk. The most successful in brownfield regeneration are the districts of Brno-město, Uherské Hradiště and Nový Jičín, where all previously abandoned buildings have been regenerated. The worst districts are Frýdek-Místek (only 40% success rate in the regeneration of chateau brownfields), Olomouc (43%), Karviná (43%) and Jeseník (44%).

Table 4 shows the selected indicators with the assumption of certain causality and the size of the correlation coefficient. Apart from the two cases of mutual causality, the Pearson Coefficient values were very low and correlation across indicators was not confirmed (this is also evident directly from the data in **Table 3**). A further measure of correlation between all indicators was also carried out, but the results were around zero. A Pearson coefficient of 0.41 was found between the area of the site and the number of unregenerated chateau brownfield sites. We could find logic here, it is likely that the larger the area of the territory, the more chateau brownfields there will be ($r=0.32$). Interestingly, a much smaller correlation value came out between the area of the territory and the number of chateaux in general ($r=0.25$), so the claim that the number of chateaux is directly related to the area of the territory is not very strong. The second interesting result is in the case of the link between population and the number of chateau brownfields ($r=-0.4$). In the preceding text, when analysing NUTS3 regions, the idea was raised whether the number of abandoned and dilapidated chateaux is directly related to the size of the territory and indirectly related to the population. This reasoning was confirmed on the data from LAU regions, as both coefficients represent a strong relationship.

Table 4.

Selected results of correlation analysis of data from Table 3.

Selected variable indicators	Value of Pearson Coefficient (r)
area and number of chateaux	0.25
area and number of chateau brownfields	0.32
R_I and area of the region (km ²) per 1 chateau	0.12
area and number of unregenerated chateau brownfields	0.41
number of inhabitants and number of unregenerated chateau brownfields	-0.2
number of chateau brownfields and number of inhabitants of the region	-0.4

In the last part of the analysis of chateau brownfields, selected characteristics directly related to chateau brownfields in individual LAU regions will be presented, see **table 5**). These data take the form of an average or a mode. The most common original use of chateau brownfield sites was housing, but due to the gradual devastation of these buildings, they were gradually displaced and the buildings fell into disrepair. Devastation is also the most common reason for the abandonment of chateau estates, coupled with problems with the definition of property rights and disagreements between owners.

Table 5.**Selected indicators of chateau brownfields for LAU1 regions.**

NUTS3	LAU1	Number of chateau brownfields	Ratio number I	Area chateau brownfields in m ² (average)	Distance in km from the center of the municipalities (average)	Distance in km from the center of the NUTS3 region (average)	Economic sector of previous use (mode)	The cause of chateau brownfields (mode)	Time without use in years (average)
South Moravian Region	Blansko	7	0.17	2783	0.95	41	housing	devastation/search for purpose	17
	Brno-město	2	0.00	3574	0.66	11	housing	search for purpose	10
	Brno-venkov	10	0.43	1592	0.79	28	agriculture/housing	devastation/ownership issues	21
	Břeclav	7	0.17	2499	1.99	50	agriculture/housing	devastation	21
	Hodonín	4	0.33	1880	0.8	68	housing	ownership issues	15
	Vyškov	5	0.67	1394	1.19	46	public services /agriculture	change of ownership/ devastation	19
	Znojmo	13	0.86	1991	0.39	65	public services /agriculture	ownership issues/ search for purpose	22
Zlín Region	Kroměříž	9	0.13	2347	0.49	42	public services	ownership issues	17
	Uherské Hradiště	2	0.00	1837	1.05	28	housing	search for purpose	5
	Vsetín	6	0.50	1524	0.2	43	housing	conscious abandonment	23
	Zlín	4	1.00	3952	0.97	27	housing	ownership issues	21
Olomouc Region	Jeseník	9	1.25	1092	1.2	121	agriculture	devastation	33
	Olomouc	7	1.33	1773	1.72	25	public services	devastation	20
	Prostějov	11	0.22	2201	0.34	29	housing/ public services	devastation/search for purpose	15
	Přerov	9	0.13	2312	0.44	36	housing/ education	devastation/ ownership issues	15
	Šumperk	8	0.60	3645	0.92	59	agriculture/housing	devastation	37
Moravian-Silesian Region	Bruntál	8	0.33	2271	2.13	78	public services	devastation	20
	Frydek-Místek	5	1.50	685	0.25	30	public services	financial problems/ conscious abandonment	39
	Karviná	7	1.33	1252	1.74	22	housing/ offices of institutions	devastation	30
	Nový Jičín	5	0.00	982	0.4	34	housing	devastation/ conscious abandonment	30
	Opava	8	0.33	990	0.69	32	housing/ public services	devastation	36
	Ostrava-město	7	0.17	1080	0.43	10	offices of institutions /housing	devastation	23

Chateau brownfields were also originally used for agricultural purposes (especially in the South Moravian Region), mainly as warehouses or as part of agricultural cooperatives, and often also temporarily housed libraries, health facilities, nurseries, municipal offices etc. (public services). Let's add here that the original use of chateau buildings in the given region reflects the representation of economic sectors (Turečková, 2014). The manor house (the main building) covered an average area of less than 2,000 m², was less than one kilometre from the centre of the village (the municipal office) and had not been used for 22 years. The longest abandoned chateaux were in the Moravian-Silesian region (on average more than 29 years) while in the Zlín region, it was only 16 years.

From the data in **table 5**, it can be seen that there is no link between the original use, the reason for abandonment and other indicators. The selected causalities and their significance are summarized in **table 6**. In this context, we can mention that the success of regeneration (measured by the coefficient R_I) depended on the length of abandonment of the object, i.e. regions were more successful in regenerating chateau brownfields for objects that were without use for a shorter period of time ($r = 0.55$). We also found that the smaller the size of the chateau brownfield object, the longer it took to decay ($r = -0.38$). This suggests that the gradual regeneration of chateau brownfields was more likely to involve larger objects. Surprisingly, distance from both the village centre and the centre of the NUTS3 region did not seem to affect the success of the regeneration process, nor did the size of the chateau site.

Table 6.

Selected results of correlation analysis of data from Table 5.

Selected variable indicators	Value of Pearson Coefficient (r)
R_I and area chateau brownfields	-0.22
R_I and distance from the center of the municipalities	0.22
R_I and time without use	0.55
area chateau brownfields and time without use	-0.38
distance from the center of the municipalities and time without use	-0.05

4. CONCLUSION

The presented paper is a continuation of last year's publications, which were devoted to the entry into the issue of chateau brownfields in the sense of elaboration of their theoretical concept and determination of the reasons for their creation in relation to their current use. This paper takes the topic further by examining the distribution of chateaux and chateau brownfields in the space of selected regions of the Czech Republic and looking for basic connections between them. It was found that the larger the area of the territory, the more brownfields are located in it (however, this is not true for chateaux as such) and more brownfields are located in areas with lower population density. The spatial success of chateau regeneration depends on the length of dilapidation, where the shorter the period of dereliction, the greater the chances of regeneration. Objects larger in area have been more successfully regenerated. Other links were not demonstrated in the analysis carried out, so it cannot be argued that chateau buildings located closer to the centre of the village etc. have a better chance of regeneration. The fact remains, and it does not invalidate our results, that the analysis carried out was mainly based on average data for the LAU1 due to the amount of data. The next steps in the investigation of this issue will therefore lead to the analysis of individual transformed data within factor or correspondence analysis. There is also the possibility of using panel regression. Subsequently, it will be interesting to compare these results with the findings presented in this paper.

The performed analysis can also represent an argument for channeling aid for the restoration of chateaux brownfields. On the one hand, we know in which regions it is necessary to provide increased attention to regeneration (Olomouc region), because compared to other regions there is still a large proportion of neglected and abandoned buildings, and also which buildings to focus on in terms of their characteristics.

Naturally, "young" and "large" chateaux brownfields due to their area are better restored. Supportive regeneration assistance schemes should thus concern chateaux buildings that deteriorate over a long period of time and are smaller in scope.

The contribution for further research is the refinement of the research object and the definition of conditions for determining the brownfield status for a chateau building, the compilation of two ratio indicators (R_I and R_II), which simplify the interpretation of data and the presented overall overview of the occurrence of chateau brownfields in the territory of Moravia and Silesia. If we take into account that 153 out of 367 chateaux had the status of brownfield and only 107 were successfully regenerated, then there is still significant room for increasing the development potential of the territory within the framework of future regeneration of the remaining 46 chateaux that are still dilapidated. Determining the benefits of regenerated chateau buildings for the development of the area will also be one of the future directions of research.

ACKNOWLEDGMENT

This paper (research) was supported by the project SGS/29/2023 "Regeneration potential of brownfields in the Czech Republic with reference to public sector activities".

REFERENCES

- Alker, S., Joy, V., Roberts, P. & Smith, N. (2000) The definition of brownfield. *Journal of Environmental Planning and Management*, 43 (1), 49-69. ISSN: 0964-0568. DOI 10.1080/09640560010766.
- Ferber et al. (2006) Sustainable brownfield regeneration: CABERNET network report. Nottingham: University of Nottingham.
- Krzystofik, R., Kantor-Pietraga, I. & Spórna, T. (2013) A Dynamic Approach to the Typology of Functional Derelict Areas (Sosnowiec, Poland). *Moravian Geographical Reports*, 21 (2), 20-35.
- Magnussen, S. 2018: Form Follows ‚Fürst‘? A Study on the Uses of Analogies in Castle Research by Reference to Valdemar I and Erik VI of Denmark. In MAGNUSSEN, S. and KOSSACK, D. ed. *Castles as European Phenomena. Towards an international approach to medieval castles in Europe. Contributions to an international and interdisciplinary workshop in Kiel. Frankfurt am Main (Peter Lang)*, 177–195.
- Meloun, M. (1993) Statistické zpracování experimentálních dat v chemometrii, biometrii, ekonometrii a dalších oborech přírodních, technických a společenských věd. Praha: Plus.
- Nevima, J. (2014) Konkurenceschopnost regionů Visegrádské čtyřky (teoretické a empirické přístupy k vymezení, měření a hodnocení). Praha: Professional Publishing.
- Pluskowski, A., Banerjea, R. & García-Contreras, G. (2019) Forgotten Castle Landscapes: Connecting Monuments and Landscapes through Heritage and Research. *Landscapes*, 20(2), 89-97. DOI: <http://dx.doi.org/10.1080/14662035.2020.1857909>.
- Tang, Y. T. & Nathanail, C. P. (2012) Sticks and Stones: The Impact of the Definitions of Brownfield in Policies on Socio-Economic Sustainability. *Sustainability*, 4 (5), 1-23. DOI: <https://doi.org/10.3390/su4050840>.
- Turečková K. 2023. The Causes of the Occurrence and Spheres of Restoration of Chateau Brownfields: A Search for Causality on the Example of Properties in the Moravian-Silesian Region, Czech Republic. *Land*, 12(1): 251. <https://doi.org/10.3390/land12010251>.
- Turečková, K. 2014. Rozšířená sektorová struktura regionů České republiky v kontextu produktivity práce. In: *Sborník příspěvků Mezinárodní vědecké konference Region v rozvoji společnosti 2014*. Brno: MU Brno, s. 921-931. ISBN 978-80-7509-139-0.
- Turečková, K., 2022. Categorizing the Causes of Occurrence of Chateau Brownfields: A Case Study on the Czech Republic. *Geographia Technica*, 17(2), 220-227. ISSN 2065-4421. DOI: 10.21163/GT_2022.172.18.
- Turečková, K., Nenička, L. & Glacová, K. (2022) Chateau brownfields: Causes of their formation in the context of the historical specificities of the Czech Republic. In: *Mezinárodní vztahy 2022: Aktuální otázky světové ekonomiky a politiky (Zborník vedeckých prác z 23. medzinárodnej vedeckej konferencie)*. Bratislava: EUBA, pp. 596-606. ISBN 978-80-225-5034-5.
- Yount, K. R. (2003) What are brownfields? Finding a conceptual definition. *Environmental Practice*, 5 (1), 25-33. DOI: <https://doi.org/10.1017/S1466046603030114>.

Appendix

Chateaux in LAUI regions of Moravia and Silesia in the Czech Republic.

NUTS3	LAUI	Chateaux without brownfield status	Chateau brownfields (regenerated and non-regenerated)
South Moravian Region	Blansko	Adamov; Boskovice; Křetín; Křtiny; Kunštát; Lhota Rapotína; Lysice; Šebetov	Blansko; Borotín; Černá Hora; Lamberk; Letovice; Rájec nad Svitavou; Velké Opatovice
	Brno-město	Bauerův zámek; Brněnské Ivanovice; Kociánka; Letohrádek Mitrovských; Medlánky; Řečkovice	Belcredi (Zámek Líšeň); Chrlice
	Brno-venkov	Cvrčovice (Petersova Vila); Hrubšice; Kuřim; Loděnice; Lomnice; Podolí (Podolí); Pozořice; Prštice; Rosice; Sokolnice; Šlapanice; Těšany; Vohančice; Židlochovice	Branišovice; Dolní Kounice; Hajany; Kupařovice; Leopoldsdruhe (Leopoldov); Lesní Hluboké; Oslavany; Paarův zámek; Troubsko; Vlasatice
	Břeclav	Diváky; Hraniční zámek; Lednice; Lovecký zámek; Lednice; Pohansko; Valtice; Velké Němčice; Velké Pavlovice; Lanžhot	Břeclav; Drnholec; Klobouky u Brna; Lány (Břeclav); Letohrádek Portz Insel; Mikulov; Pouzdřany
	Hodonín	Čejkovice; Hodonín; Kyjov; Milotice; Svatobořice; Žďánice; Žeravice	Bzenec; Dolní Moštěnice; Strážnice; Veselí nad Moravou
	Vyškov	Bohdalice; Bučovice; Čechyně; Drnovice; Habrovany; Hrušky; Nové Hvězdilice; Nové Zámky; Slavkov; Troyerstein; Vážanský zámek; Vyškov	Ferdinansko; Chvalkovice na Hané; Ivanovice na Hané; Komorov; Račice
	Znojmo	Allein (České Křídlovce); Bohunice; Bohutice; Březany; Emin zámek; Hostim; Lechovice; Mikulovice; Miroslav; Plaveč; Skalice (Skalice); Slatina (Slatina); Starý zámek Jevišovice; Tavikovice; Tulešice; Uherčice; Únanov; Višňové; Vranov nad Dyjí	Boskovštejn; Dyjákovice; Dyje (Milfron); Horní Dunajovice; Hrušovany nad Jevišovkou; Jaroslavice; Kravsko; Miroslavské Knínice; Moravský Krumlov; Nový zámek Jevišovice; Rešice; Tvořihráz; Újezd
Zlín Region	Kroměříž	Bystřice pod Hostýnem; Chropyně; Koryčany; Kroměříž; Kvasice; Pačlavice; Střílky; Věžky; Zborovice (Nový); Zborovice (Starý); Žeranovice	Cetchevovice; Dřínov; Holešov; Litenčice; Morkovice; Přilepy; Uhrice; Zdislavice; Zdounky
	Uherské Hradiště	Březolupy; Buchlovice; Nezdenice; Ořechov; Lovecký zámek; Strání; Uherský Brod; Uherský Ostroh	Bílovice; Nový Světlov
	Vsetín	Branky (Starý); Hovězí; Hošťálková; Choryně; Kinských Valašské Meziříčí; zámek Žerotínů ve VM	Branky (Nový); Kelč; Lešná; Liptál; Loučka; Vsetín
	Zlín	Klečůvka; Lešná; Napajedla (Starý); Návojná; Zlín; Pohořelice; Tlumačov; Velký Ořechov; Vizovice	Hrádek na Vlárské dráze; Luhačovice; Napajedla; Slavičín (zámek Wichterle)
Olomouc Region	Jeseník	Bernartice; Dolní Červená Voda; Hradec; Jánský vrch; Jeseník; Kobylá nad Vidnavkou; Rittneerův zámek; Široký Brod; Vlčice	Bílá Voda; Černá Voda; Horní Fořt; Hukovice (Velká Kraš); Kohout; Tomíkovice; Vápenná; Velké Kunčice; Vidnava
	Olomouc	Bores; Červenka; Dolní Dlouhá Loučka; Dolany; Drahanovice; Haňovice; Náklo; Náměšť na Hané (Dolní); Náměšť na Hané (Horní); Nové zámky u Litovle; Velká Bystřice; Velký Týnec; Vsisko	Bílá Lhota; Horní Dlouhá Loučka; Chudobín; Nenakonice; Nové Valterčice; Tršice; Žerotín (Žerotín)
	Prostějov	Brodek u Prostějova; Hluchoy; Hrubčice; Jesenec; Konice; Nezamyslice; Oborský Dvůr (Híršperk); Plumlov; Víceměřice; Vrchoslavice; Výšovice	Čechy pod Košířem; Dobromilice; Doloplazy; Krakovec; Kralice na Hané; Laškov; Mořice; Prostějov; Přemyslovice; Ptení; Vřesovice
	Přerov	Čitov; Čekyně; Dřevohostice; Horní Moštěnice; Hustopeče nad Bečvou; Kovalovice; Lipník nad Bečvou; Malhotice; Polkovice; Přerov; Rokytnice (Přerov); Říkovice; Veselíčko; Želatovice	Hranice; Kunzov; Lhotsko; Pavlovice u Přerova; Potštát; Přestavky; Skalička (Zábřeh); Tovačov; Všechnovice
	Šumperk	Bludov; Mohlenice; Sobotín; Šumperk; Velké Losiny; Zábřeh na Moravě; Žádlovce	Doubravice; Kolštejn; Lechovice; Loučná nad Desnou; Maršíkov; Ruda nad Moravou; Třemešek; Úsov

Moravian-Silesian Region	Bruntál	Branice; Grohmann (Vrbno pod Pradědem); Hošťalkovy; Hynčice (Nový zámek Albrechtice); Jindřichov; Krmov; Lovecký zámek Hubertov	Brantice; Bruntál; Dívčí hrad; Rýmařov (Janovice); Linhartovy; Slezské Pavlovice; Slezské Rudoltice; Staré Heřminovy
	Frydek-Místek	Bílá; Dolní Tošanovice; Frydek (Místek); Horní Tošanovice; Konská; Lovecký zámek Hartisov (Bílá); Třinecký zámek	Hnojník; Hukvaldy; Paskov; Ropice; Střítež
	Karviná	Bludovice; Fryštát (Karviná); Horní Suchá; Larischův zámek (Těrlicko); Letohrádek Těrlicko	Dolní Lutyně; Doubrava; Chotěbuz; Petrovice u Karviné (Prstná); Rychvald; Šumbark (Havířov); Životice
	Nový Jičín	Bartošovice; Bílovec; Hukovice; Jeseník nad Odrou; Nová Horka; Pustějov; Slatina; Spálov; Studénka; Trnávka	Bravantice; Fulnek; Kunín; Sedlnice; Žerotínský zámek Nový Jičín
	Opava	Albertovec; Bolatice; Dolní Životice; Hlavnice; Hradec nad Moravicí; Chuchelná; Jedzkovice; Kyjovice; Loděnice (Holasovice); Melč; Mladecký Dvůr; Oldřišov; Raduň; Radkov (Dubová); Slavkov; Sosnová; Stěbořice; Šilheřovice; Štěplovec; Velké Heraltice; Velké Hoštice; Závada	Jakartovice (Deštné); Dolní Benešov; Hlučín; Hrabyně; Kravaře; Litultovice; Neplachovice; Štářblovce
	Ostrava-město	x	Hošťálkovice; Klimkovice; Polanka nad Odrou; Poruba; Rothschildův empírový zámek (Vítkovice); Stará Ves nad Ondřejnicí; Zábřeh

(Source: own survey, November 2022 – June 2023).

CHANGES AND TRENDS IN IDEAL HOLIDAY PERIOD BASED ON HOLIDAY CLIMATE INDEX APPLIED TO THE CARPATHIAN BASIN

Zsolt MAGYARI-SÁSKA¹ , Attila MAGYARI-SÁSKA²

DOI: 10.21163/GT_2023.182.17

ABSTRACT:

The Holiday Climate Index (HCI) is a well-known and valued index for assessing the weather suitability of outdoor recreational activities. As a composite index, it takes into account many aspects of the weather, all of which affect the well-being of tourists. With the accentuation of climate change, the HCI plays an important role in the organization and planning of tourist activities. These plans must take into account not only the individual values of the index for different destinations, but also the sequence of days with certain expected values of the index. The aim of our research was to create a software module in R that would allow the analysis and identification of periods of consecutive days in which the HCI is above a certain minimum threshold and also has a minimum average value for that period. We applied this module to the analysis of historical (1970-2004) and present and near-future (2005-2040) HCI values in the EC-EARTH climate model, identifying for each year and location in the Carpathian Basin the starting day of the climatically best seven-day period. To obtain a time series for each location, we aggregated the values for the two periods using the mean, median, standard deviation and trend calculation. The analysis shows that the ideal time to start a holiday is not only changing, it is becoming increasingly unpredictable. Whereas in the 1970-2004 period there was a well-observed decreasing trend in the starting day, for the 2005-2040 period we see a trend-free situation in most of the area. Even where trends do appear, we find them in opposite directions in nearby areas, making it difficult to plan the ideal time to start a holiday.

Key-words: *Holiday Climate Index, Carpathian Basin, ideal touristic period, R Cran, automatized analysis*

1. INTRODUCTION

The Carpathian Basin comprises diverse natural and man-made landscapes, making it a favoured tourist destination. Sustainable tourism development is a crucial factor in the region's efforts to maintain and expand tourist activities (Dávid & Szűcs, 2009). A key element of sustainability concerns climate change, which affects the region owing to its location at the intersection of multiple climatic zones. The region generally encounters a continental climate marked by warm summers and chilly winters. Nevertheless, over the last few decades, the climate within the locality has significantly fluctuated (Rakonczai, 2011; Magyari, 2022; Mezősi et. al, 2014), rendering it one of the most fragile territories in Europe (Csete & Szécsi, 2012).

Tourism satisfaction depends on the climate, as demonstrated by previous studies (Gomez, 2005; Amelung et al., 2007) and the suitability of climate for tourist activities can be assessed using either the Tourism Climate Index (TCI) or the Holiday Climate Index (HCI). TCI, which was created by Mieczkowski in 1985, has been found to have limitations in recent years (Dubois et al., 2016). As a result, the new Holiday Climate Index (Scott et al., 2016) has been developed, which provides several advantages over TCI. The HCI takes into account six meteorological factors: average temperature, maximum temperature, minimum temperature, hours of sunshine, rainfall, and humidity. This

¹ Babes-Bolyai University, Faculty of Geography, Gheorgheni University Extension, RO-535500 Gheorgheni, zsolt.magyar@ubbcluj.ro

² Babes-Bolyai University, Faculty of Mathematics and Informatics, RO-400084 Cluj-Napoca, magyari.saska.attila@gmail.com, attila.magyar@stud.ubbcluj.ro

includes all three aspects of tourism satisfaction in relation to the climate: comfort, aesthetics, and physical effects. The HCI is subsequently calculated as a weighted average of these six elements.

Due to the anticipated impact of climate change on tourism (Scott et al., 2012), the significance of the HCI has grown in the context of climate change. It allows for the evaluation of the vulnerability of tourism destinations to climate change and the formulation of strategies for adaptation (Yu et al., 2022).

HCI has gained popularity and its adaptation to different tourism segments, including beach, urban and winter sports tourism, has been pursued (Demiroglu et al., 2021). This renders it a significant contribution to research of specific tourism types, given the numerous studies that use it in diverse locations globally (Demiroglu et al., 2020; Amiranashvili et al., 2021; Yu et al., 2021; Saygili Araci et al., 2021, Samarasinghe et al., 2023).

Research in our study area focuses on HCI and is concentrated in two research groups, one located in Romania and the other in Hungary. In Romania, Velea et al. (2022) studied the correlation between tourist flow and urban HCI values from 2010 to 2018, finding a clear link between the two. In a near future period of 2021-2040, Velea et al. (2023) examined the climate suitability of various cities and rural tourist destinations for each season. The study estimated the impact of climate change on overnight stays. For research conducted in Hungary (Kovács et al., 2017; Kovács & Király), the TCI was enhanced to account for differences in seasonal thermal perception. This allowed for the calculation of the index's spatial distribution for various annual periods and months, thus enabling an interpretation of its evolution on a district level.

Climate-influenced tourism is significant for both the supply and demand sides (Öztürk & Gömal, 2018). Individuals wish to select an optimal consecutive period for their holiday based on weather conditions. Our study aims to create an automated data processing module that investigates the emergence and variation over time of the ideal seven-day period for vacation planning in the Carpathian Basin.

2. DATA AND METHODS

Our study is based on the Holiday Climate Index (HCI) which was accessible from the Copernicus Database (<https://climate.copernicus.eu/climate-suitability-tourism>). This index was obtainable as historical data, covering the time span from 1970 to 2004, and as climate model data, extending from 2005 to 2100. The research employed the EC-EARTH Global Climate Model combined with the intermediate scenario RCP4.5. The data format was NetCDF, with each downloadable file featuring data at a daily resolution for a period of five years. The dataset includes four variables per location per year: the daily index, the number of fair days, good days, and unfavorable days. It's noteworthy that the last three indices lack temporal linkage; we are uncertain about their timing and distribution. Our research aims to address this information gap. **Table 1** presents the index values and interpretation.

Table 1.

HCI index values and their interpretation.

HCI score	Interpretation	Copernicus variable
0-20	Dangerous	Unfavorable
20-40	Unacceptable	
40-50	Marginal	
50-60	Acceptable	Fair
60-70	Good	
70-80	Very good	Good
80-90	Excellent	
90-100	Ideal	

The initial phase involved extracting the study region from every datafile and merging the results to produce a single NetCDF file. The CDO (Climate Data Operator) tool was employed to accomplish this task, utilizing *sellonlatbox* and *mergetime* commands (Schulzweida, 2022). The full data processing procedure was developed in R through R Studio. Three additional extension packages were required to process the data: *raster* (Hijmans, 2023) for managing the HCI index raster layers, *ncdf4* (Pierce, 2022) for accessing the NetCDF raw data files, and *wql* (Jassby & Cloern, 2022) for determining trend significance.

The data processing algorithm contains the following steps (Fig. 1):

- for each year present in the dataset
 - extract of one year data
 - descale the extracted data
 - for each location in the study area
 - identify the best consecutive days having given thresholds for minimum HCI value and minimum mean HCI value through those days.

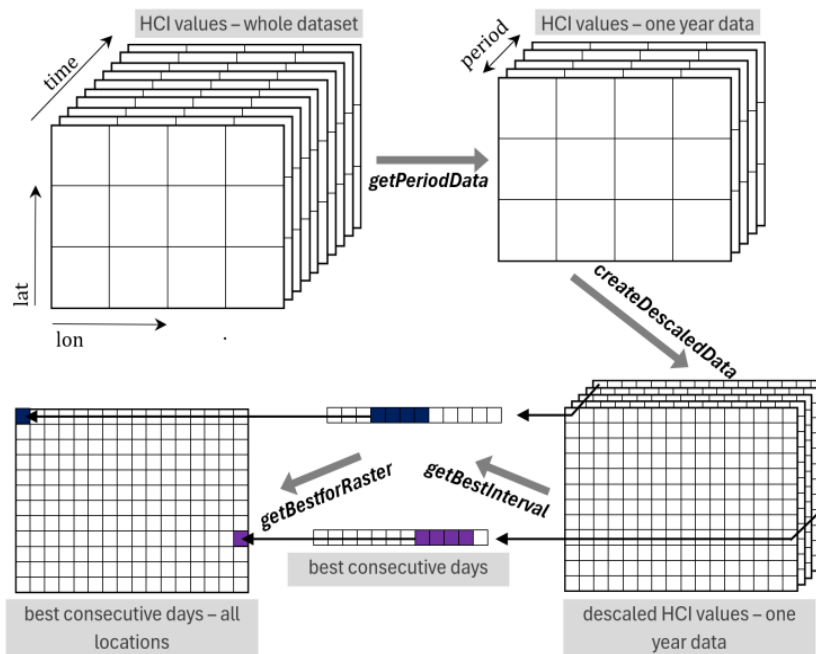


Fig. 1. Visual illustration of the data processing algorithm with the name of developed R functions.

The role of each function used in the algorithm is described below mentioning its role and parameters. The *getPeriodData* function returns the desired time period from a dataset (Fig. 2). The function's input parameters: *dataset* – original dataset with full data, *firstDate* – date of the first data in the whole dataset, *startDate* and *endDate* – date for the desired extraction period. The *createDescalcedData* function returns the 1 km² spatial resolution variant of the raw dataset for a selected year (Fig. 3). The initial spatial resolution of the Copernicus dataset is 0.11°. With this function data descaling was realized on the fly only for the actually processed year by this saving memory which is important issue for such huge datasets.

```
getPeriodData <- function(dataSet, firstDate, startDate, endDate)
{
  startIdx <- startDate - firstDate + 1
  endIdx <- endDate - firstDate + 1
  return (dataSet[, startIdx:endIdx])
}
```

Fig. 2. R code of the *getPeriodData* function.

```

createDescaledData <- function(hci,firstDate,year)
{
  values <- ncvr_get(hci,"hci-proj")
  fullStartDate <- as.Date(paste(year,"-01-01",sep=""))
  fullEndDate <- as.Date(paste(year,"-12-31",sep=""))
  selSet <- getPeriodData(values,firstDate,fullStartDate,
                          fullEndDate)

  lon <- ncvr_get(hci,"lon")
  lat <- ncvr_get(hci,"lat")
  nr <- nrow(selSet)
  nc <- ncol(selSet)
  l <- length(selSet[1,1,])
  finalSet <- array(0,dim=c(nr*8,nc*8,l))
  for(i in 1:l)
  {
    lyr <- raster(t(selSet[, ,i]), xmn=min(lon), xmx=max(lon),
                  ymn=min(lat), ymx=max(lat), crs="+proj=longlat")
    lyr <- disaggregate(lyr,fact=8,method='bilinear')
    finalSet[, ,i] <- getValues(lyr)
  }
  finalSet
}

```

Fig. 3. R code of the createDescaledData function.

The function's input parameters: *hci* – netCDF identifier resulted on file opening, *firstDate* – date of the first data in the whole dataset, *year* – the desired year for which data descaling has to be made.

The **getBestInterval** function returns the first day index as day number inside a year which respects the imposed restrictions/thresholds for consecutive day (Fig. 4). In case of more suitable periods that with the highest average will be returned. The function's input parameters: *dataVector* – daily HCI data for a year for a single spatial location, *minValue* – minimum accepted HCI value for consecutive days, *minAvgValue* – minimum accepted HCI mean value for consecutive days, *minLength* – minimum length of consecutive days.

```

getBestInterval <- function(dataVector,minValue,
                           minAvgValue, minLength)
{
  dataVector[dataVector<minValue] <- 0
  maxAvg <- 0
  idx <- 0
  for(i in 1:(length(dataVector)-minLength))
  {
    values <- dataVector[i:(i+minLength-1)]
    if (sum(values==0,na.rm=TRUE)==0)
    {
      currentAvg <- mean(values,na.rm=TRUE)
      if (!is.na(currentAvg) & !is.nan(currentAvg))
      if (currentAvg > minAvgValue & maxAvg < currentAvg)
      {
        maxAvg <- currentAvg
        idx <- i
      }
    }
  }
  idx
}

```

Fig. 4 – R code of the getBestInterval function.

The **getBestforRaster** function creates the raster layer as a file for a given year considering the imposed thresholds (Fig. 5). The function's input parameters: *hci* - netCDF identifier resulted on file opening, *firstDate* – date of the first data in the whole dataset, *minValue* – minimum accepted HCI value for consecutive days, *minAvgValue* – minimum accepted HCI mean value for consecutive days, *minLength* – minimum length of consecutive days.

```

getBestforRaster <- function(hci,firstDate,year,
                             minValue,minAvgValue, minLength)
{
  dData <- createDescalData(hci,firstDate,year)
  nc <- ncol(dData[, ,1])
  nr <- nrow(dData[, ,1])
  startIdx <- array(0,dim=c(nr,nc))
  for(i in 1:nr)
  {
    for(j in 1:nc)
      startIdx[i,j] <- getBestInterval(dData[i,j,],minValue,
                                       minAvgValue,minLength)
  }
  lon <- ncvr_get(hci,"lon")
  lat <- ncvr_get(hci,"lat")
  lyr <- raster(t(startIdx), xmn=min(lon), xmx=max(lon),
                ymn=min(lat), ymx=max(lat), crs="+proj=longlat")
  lyr <- flip(lyr)

  writeRaster(lyr,paste("HCI_",year,"_Min",minValue,"_Avg",
                       minAvgValue,"_L",minLength,".tif",sep=""),overwrite=TRUE)
}

```

Fig. 5. R code of the **getBestforRaster** function.

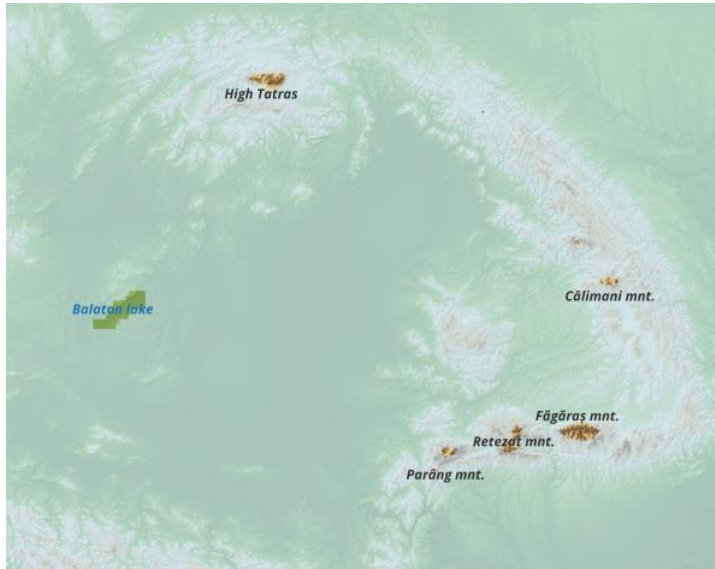
In addition to the aforementioned functions, two others were defined to aid in automating data processing. The **getAllYears** function requires no parameters and is responsible for generating raster layers for every year. Subsequently, a new function was required to aggregate data for each location from all the raster layers containing the starting day of the most appropriate seven consecutive days. Data was aggregated using indices of central tendency, specifically the mean and median, along with two variations indices: standard deviation and interquartile range. The **createMaps** function was utilized, which compiles all files that correspond to the set pattern and within the designated time frame, to produce four raster layers displaying the mean, median, standard deviation and trend significance for each location. Its parameters consist of two variables: *Limit*, which is the minimum HCI value utilized as the exclusive identifier for the files generated by the **getBestforRaster** function, and *first* and *Last*, denoting the index of the file set to be taken into account.

3. RESULTS AND DISCUSSION

The objective of the R software module development was to identify the optimal seven-day period in each calendar year. This is defined as the period in which the minimum HCI value for each day reaches or exceeds a predetermined threshold and with the highest overall average. Additionally, the mean value must also be at a minimum. Initially, we utilized two threshold pairs. For the first scenario (SCEN75), the acceptable minimum value for the consecutive day's HCI was 75, which lies in the mid-range of the "Very good" category. Additionally, the mean should be at least 85, which is also in the mid-range of the "Excellent" category. The second scenario (SCEN80) considers higher values, with a 5-point increase for the aforementioned thresholds. The minimum daily HCI is 80, while the minimum mean HCI is 90, which represents the lowest value in the "Ideal" category.

Throughout the entire 71 years period from 1970-2040, the mean HCI of SCEN75 shows that only the close neighborhoods of the highest mountains lacked appropriate periods. These locations

are situated in High Tatras, Retezat, Parâng, Făgăraș and Călimani Mountains, all of which have peaks over 2000m (**Fig. 6a**). For SCEN80, additional areas beside the expanded locations of SCEN75 have been identified. These spots appear in the Apuseni Mountains as well as in the Rodnei or Bucegi Mountains and other locations with altitudes down to 1500-1600m (**Fig. 6b**). The areas that do not meet the desired criteria are 4.74 times larger than those for SCEN75. The study also included an analysis of two subperiods: the first spans 35 years between 1970-2004, while the second covers 36 years from 2005-2040. In both scenarios, the first subperiod reveals larger areas failing to reach minimum requirements. These findings suggest that more areas will become applicable for outdoor activities. A comparison of the ratio of these inadequately met areas between SCEN80 and SCEN75 shows 74% and 67%, respectively, in favor of the former.



a – SCEN75 scenario.



b – SCEN80 scenario.

Fig. 6. Regions which don't meet minimum scenario thresholds considering whole analysis period.

The percentage of the area gained is significantly lower when applying the highest HCI thresholds, implying an irregular increase in appropriate locations. The analysis undertaken for SCEN75 aimed to identify and examine the characteristics of the optimal seven-day periods. For each year, the most suitable seven-day periods were identified based on their starting day within the year. The resulting data series were then aggregated and analyzed for the entire period and the two sub-periods for each location. Based on the central tendency values of mean and median, it is clear that July and August are the most appropriate months for the entire analysis period (Fig. 7).

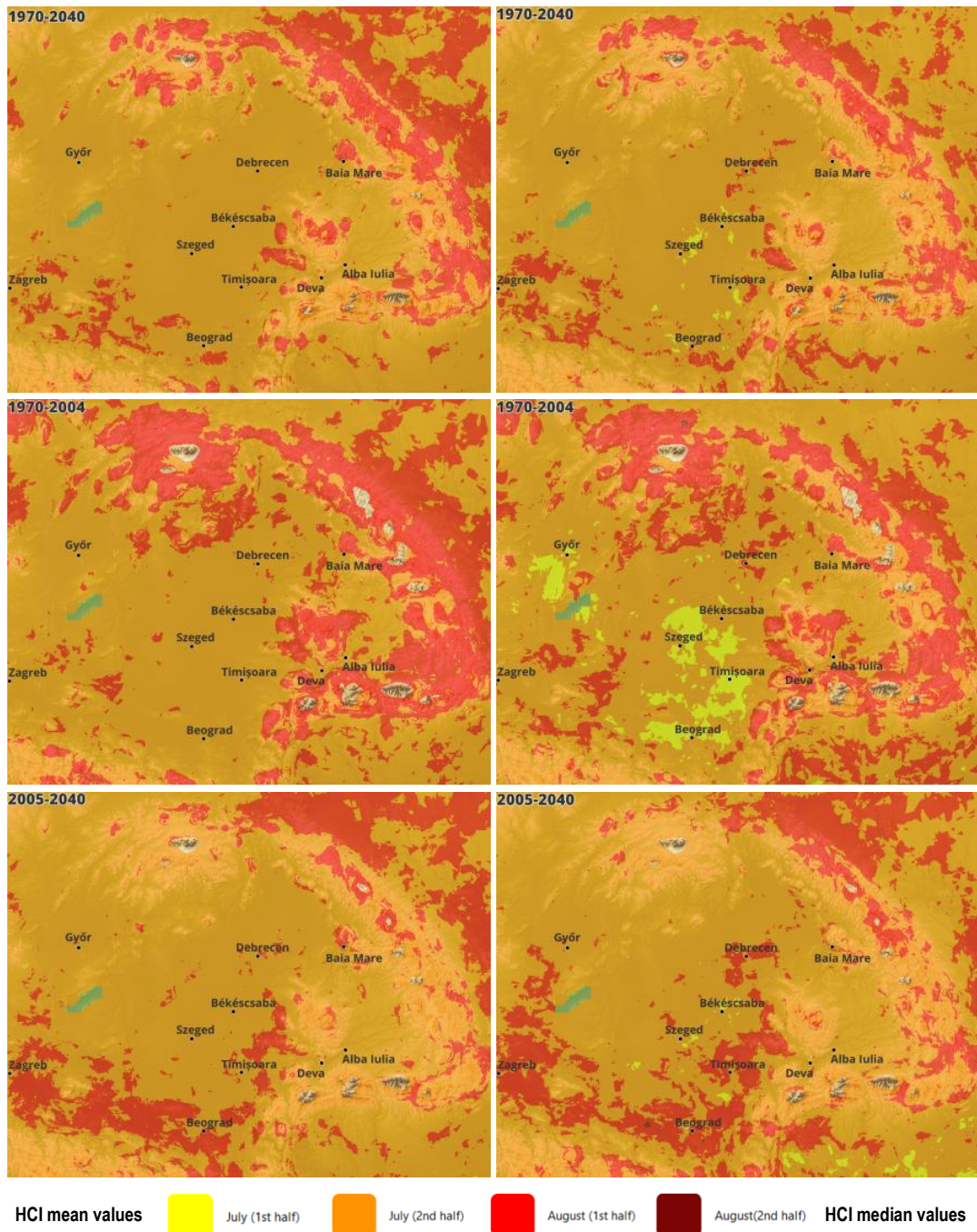


Fig. 7. Ideal seven-days period starting time

Specifically, for the mean value, only the latter half of July and early August are present. However, when considering the median value, the first half of July is also present in certain central-southern areas encompassing the Békéscsaba, Szeged, Timișoara, and Beograd regions. The first half of August is more prevalent in mountainous regions, whereas inside the Carpathian Basin, the second half of July is overwhelmingly preferred. After comparing the mean values of the two subperiods, it is clear that the most suitable period for future holidays starts in August, particularly in the Carpathian Mountains. However, for vast areas, the most suitable seven-day holiday starts in the second half of July instead of August. The first half of August is more beneficial in the southern part of the study area along the Zagreb-Beograd axis.

The median value reinforces previous findings, but with some refinements. In the first subperiod (1971-2004), the middle-south region and north Balaton Lake areas favoured the first half of July for outdoor tourism, while in the Győr region, the same period was optimal. However, in the second subperiod (2005-2040), these regions have shifted towards the second half of July or the first half of August. It is noteworthy that, for certain areas to the west and south of Belgrade, the optimal time for holidays has shifted to the latter half of August. The first few weeks of July are now only considered an ideal vacation period in a few isolated locations. Moreover, both the mean and median indicate a significant southern influx occurring in the first half of August along the Belgrade-Timișoara-Debrecen axis.

Changes between the two sub-periods are apparent, but they differ across different regions. In the southern, western, and central areas of the Carpathian Basin, the most appropriate period for outdoor tourist activities is delayed by 1-2 weeks. However, in the northern and eastern regions, the starting days' mean value is advanced by 1 week (Fig. 8). The same findings, but with pronounced values, are seen in the median values. Generally, two interlocking U shapes can be observed. The inverted U denotes regions where the ideal period is advanced, while the upright U indicates a delay in the ideal period.

The minor disparities between the mean and median values of the data series hint at noteworthy variations in the starting day across different years. Since the central tendency values are generic, collective values, the deviation inside the data series also holds significance. To this end, we computed the standard deviation and the interquartile range expressed in days for the entire period and the two subperiods.

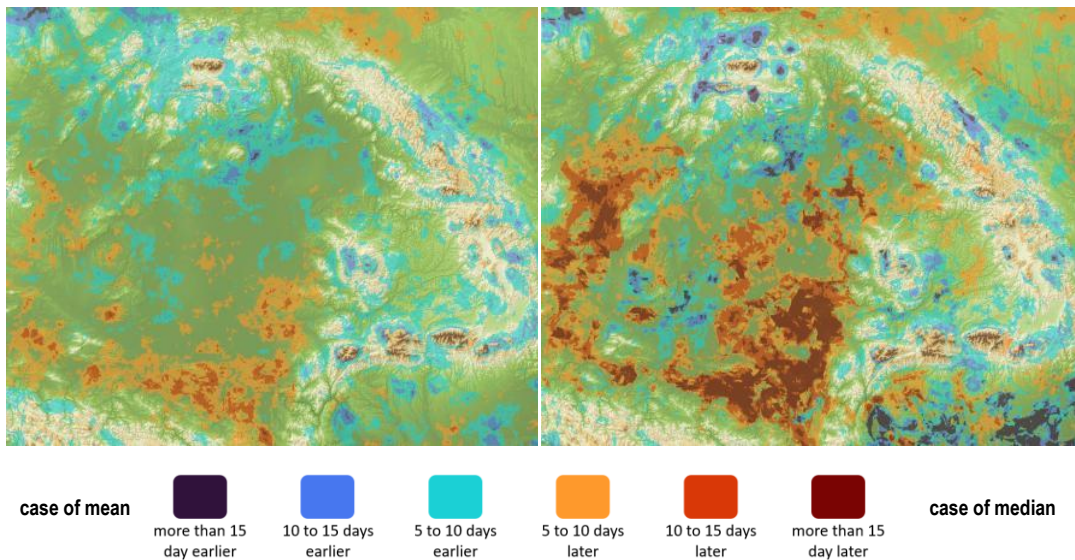


Fig. 8. Differences between 1970-2004 and 2005-2040 subperiods for the starting day for ideal seven-day holiday.

Both indices demonstrate a consistent pattern throughout the analysis period, with greater reduction in variation in the northern and eastern regions compared to the southern and western areas (Fig. 9). While a strong correlation exists between the two indices indicating internal deviation, an anomalous situation is evident during the first subperiod near Timișoara. Based on the standard deviation, a mid-value is recorded according to the legend. Additionally, the interquartile range shows that the dispersion of values falls within the low and very low categories.

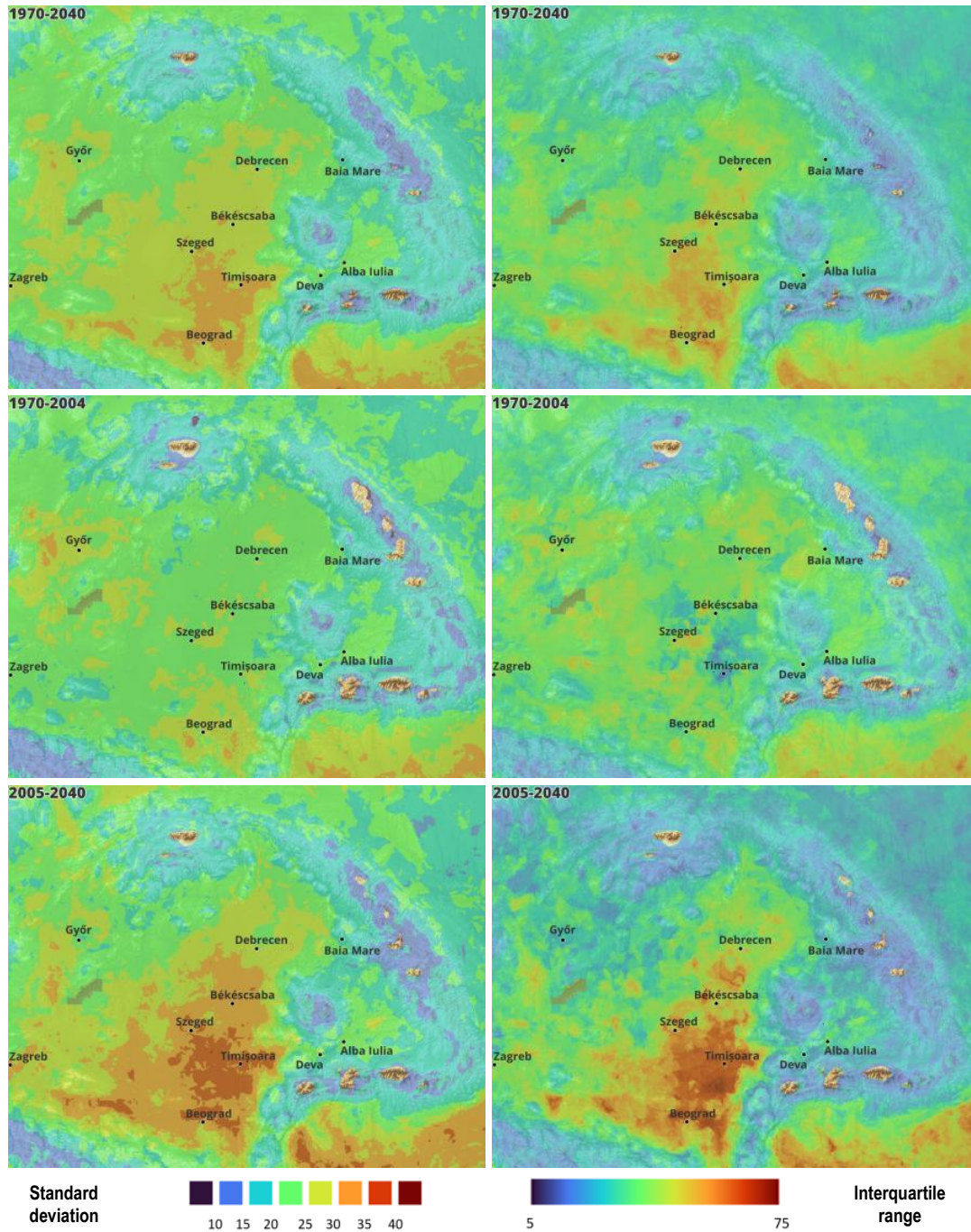


Fig. 9. Internal deviation of data series.

This indicates that around half of the values exhibit significant deviations in both directions, while for other locations, the distribution of values is more balanced, even if the values themselves are high.

Over the initial 35 years of the first subperiod, variations were less pronounced compared to those of the second subperiod. In the present and near future, it is improbable to generalize as to when it is worthwhile to commence holidays in the Beograd-Timişoara vicinity, given that deviations exceed a month. Upon assessing the stability of mean values, we conducted a trend analysis to determine the optimal starting day for each location.

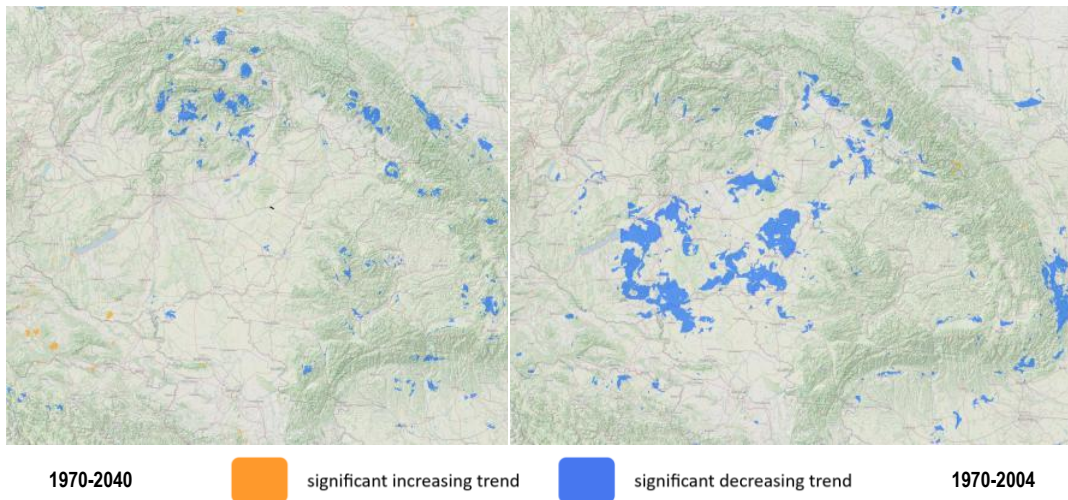


Fig. 10. Trends in ideal seven-day log holiday starting day.

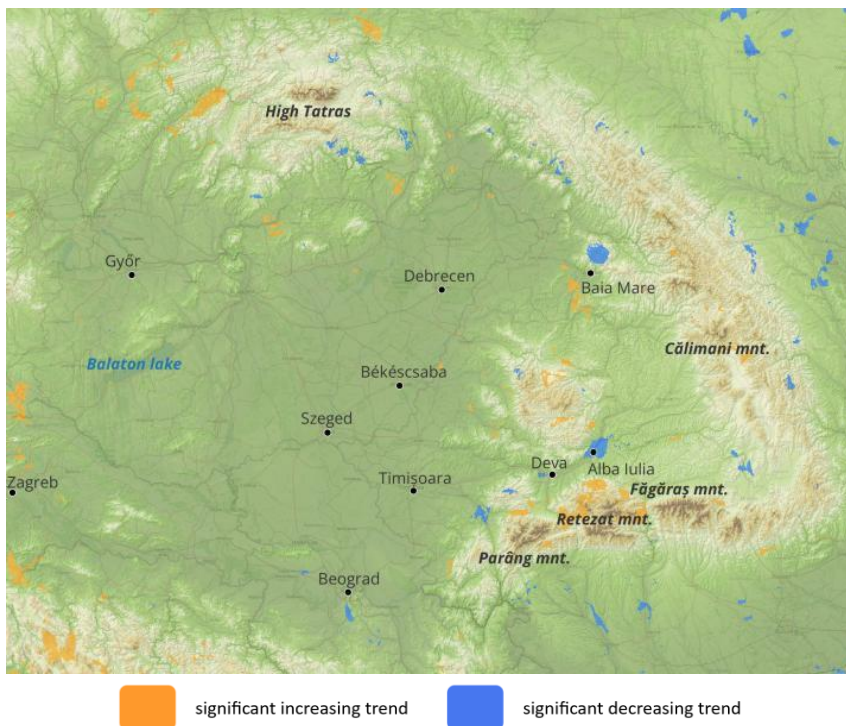


Fig. 11. Trends in ideal seven-day log holiday starting day for the 2005-2040 period.

While many locations do not exhibit a statistically significant trend in their data series values, other locations clearly do. The analysis of trend significance was based on the Mann-Kendall test (Fang et al., 2016).

Throughout the analysis period, it has been observed that there are certain locations displaying a significant decreasing trend. This suggests that the most favorable seven-day long period is moving earlier over the past 71 years (**Fig. 10**). These areas are mainly situated in the Carpathian Mountains. Additionally, an overall increasing trend can be noted to the east of Zagreb, indicating a consistent shift towards the end of the year in terms of the most desirable holiday period.

The two subperiods demonstrate significant differences in trends. During the first subperiod (1971-2004), decreasing trends were observed primarily in the interior territories of the Carpathian Basin. These areas became known for their early start to the ideal holiday season (**Fig. 10**). However, this trend is no longer evident in the second subperiod. Based on HCI values from the past 36 years, there are no clear trends present in the main part of the Carpathian Basin (**Fig. 11**). Although interesting situations can be observed locally, it is noteworthy that the northern areas of Baia-Mare exhibit a significant decreasing trend, while the southern areas show an increasing trend. Furthermore, Alba Iulia and Deva, both towns with high tourist potential, experience a significant decreasing trend in the starting day of the ideal tourist period. Conversely, important areas over the valley in the Retezat Mountains exhibit an increasing trend.

4. CONCLUSIONS

Climate change affects many aspects of everyday life, including recreational activities. Our study examined how the Holiday Climate Index (HCI), developed specifically for urban and nature-based tourism, will evolve based on the EC-EARTH climate model for the Carpathian Basin. We have also developed a parametrizable R software module for data processing to support further similar investigations. Our research is focused on identifying the optimal seven-day period of each year where the HCI index exceeds a certain threshold, considering both the minimum and mean values. For this study, the minimum value was set at 75 (denoting a very good rating), while the mean was set at 85 (indicating an excellent rating).

The results obtained cover three distinct aspects. Firstly, it has been determined that there are areas within high mountainous regions that fail to meet the imposed requirements. These locations are therefore unsuitable to be utilized as tourist destinations for a minimum of seven consecutive days.

Secondly, by examining historical data between 1970 and 2004 as well as modelled data from 2005 to 2040, we have compared past and forecasted future trends according to two sub-periods. Based on the mean and median values, the most suitable time to begin a seven-day holiday appears to be during the latter half of July. This trend is consistent even in mountainous areas where the optimal starting day was previously in the first half of August during the first subperiod. Furthermore, a new development is the occurrence of the first half of August being the optimal starting time in mid-southern locations, which was previously the first half of July during the first subperiod.

Finally, the trend analysis indicates that the previous noteworthy decline in the central area of the Carpathian Basin has ceased, and distinct significant trends emerge in the peripheral regions. These differing trends may or may not be linked to altitude, and though they are in close proximity to each other, they have the potential to coexist in several square kilometers.

All of the above findings show how climate change impacts outdoor recreational activities, indicating that it will become increasingly difficult to determine the best time to plan a holiday based on ideal weather conditions.

ACKNOWLEDGMENT

The presented research was supported by the DOMUS scholarship program of the Hungarian Academy of Sciences.

REFERENCES

- Amelung, B., Nicholls, S. & Viner, D. (2007). Implications of Global Climate Change for Tourism Flows and Seasonality. *Journal of Travel Research*, 45, pp. 285-296
- Amiranashvili, A.G., Kartvelishvili, L.G., Kutaladze, N.B., Megrelidze, L.D., & Tatishvili, M.R. (2021). Holiday Climate Index in Some Mountainous Regions of Georgia. *Journals of Georgian Geophysical Society*, 24(2). doi: 10.48614/ggs2420213327
- Csete, M. & Szécsi, N. (2015) The role of tourism management in adaptation to climate change – a study of a European inland area with a diversified tourism supply, *Journal of Sustainable Tourism*, 23:3, pp. 477-496, doi: 10.1080/09669582.2014.969735
- Dávid, L. & Szűcs, C. (2009), Building of networking, clusters and regions for tourism in the Carpathian Basin via Information and Communication Technologies, *Netcom*, 23-1/2, pp.63-74.
- Demiroglu, O.C., Saygili-Araci, F.S., Pacal, A., Hall, C.M. & Kurnaz, M.L. (2020), Future Holiday Climate Index (HCI) Performance of Urban and Beach Destinations in the Mediterranean, *Atmosphere*, 11(9):911. <https://doi.org/10.3390/atmos11090911>
- Demiroglu, O.C., Turp, M.T., Kurnaz, M.L. & Abegg, B. (2021) The Ski Climate Index (SCI): fuzzification and a regional climate modeling application for Turkey, *Int J Biometeorol.* 65(5):763-777. doi: 10.1007/s00484-020-01991-0
- Dubois, G., Ceron, J.P., Dubois, C., Frias, M.D. & Herrera, S. (2016), Reliability and usability of tourism climate indices, *Aerth Perspectives*, 3(2), doi: 10.1186/s40322-016-0034-y
- Fang, S., Qi, Y., Han, G., Li, Q. & Zhou, G. (2016), Changing Trends and Abrupt Features of Extreme Temperature in Mainland China from 1960 to 2010. *Atmosphere*. 2016; 7(2):22. doi: 10.3390/atmos7020022
- Gómez, M. (2005). Weather, Climate and Tourism. A Geographical Perspective. *Annals of Tourism Research*, 32(3), pp. 571-591.
- Hijmans, R. (2023). *raster: Geographic Data Analysis and Modeling*. R package version 3.6-14, <<https://CRAN.R-project.org/package=raster>>.
- Jassby, A.D. & Cloern, J.E. (2022). *wq: Some tools for exploring water quality monitoring data*. R package version 1.0.0. <https://cran.r-project.org/package=wq>
- Kovács, A., Németh, Á., Unger, J. & Kántor, N. (2017) Tourism climatic conditions of Hungary – present situation and assessment of future changes. *Időjárás*, 121(1). pp. 79-99
- Kovács, A., & Király, A. (2021). Assessment of climate change exposure of tourism in Hungary using observations and regional climate model data. *Hungarian Geographical Bulletin*, 70(3), pp. 215-231. <https://doi.org/10.15201/hungeobull.70.3.2>
- Magyari-Sáska, Zs. (2022), How the Climate Migrates. Case Study for four Locations in the Carpathian Basin, *Geographia Technica*, 17(2), pp.97-106, doi: 10.21163/GT_2022.172.09
- Mezősi, G., Bata, T., Meyer, B.C., Blanka, V. & Ladányi, Zs. (2014), Climate Change Impacts on Environmental Hazards on the Great Hungarian Plain, Carpathian Basin. *Int J Disaster Risk Sci* 5, pp.136-146 doi: 10.1007/s13753-014-0016-3
- Mieczkowski, Z. (1985) The Tourism Climatic Index: A Method of Evaluating World Climates for Tourism. *The Canadian Geographer*, 29, pp. 220-233. doi: 10.1111/j.1541-0064.1985.tb00365.x
- Öztürk, A. & Göral, R.(2018), Climatic Suitability in Destination Marketing and Holiday Climate Index, *GJETeMCP*, 4(1), pp 619-629
- Pierce, D. (2022). *_ncdf4: Interface to Unidata netCDF (Version 4 or Earlier) Format Data Files*. R package version 1.20, <<https://CRAN.R-project.org/package=ncdf4>>.

- Rakonczai, J. (2011), Effects and Consequences of Global Climate Change in the Carpathian Basin, in *Climate Change – Geophysical Foundation and Ecological Effect* ed. Juan A. Balnco and Houshang Kheradmand, p. 536, ISBN 9533074191
- Samarasinghe, J.T., Wickramarachchi, C.P., Makumbura, R.K., Meddage, P., Gunathilake, M.B., Muttill, N. & Rathnayake, U. (2023), Performances of Holiday Climate Index (HCI) for Urban and Beach Destinations in Sri Lanka under Changing Climate. *Climate* 11(48). doi: 10.3390/cli11030048
- Saygili Araci, F. S., Demiroglu, O. C., Pacal, A., Hall, C. M., & Kurnaz, M. L. (2021) Future Holiday Climate Index (HCI) Performances of Urban and Beach Destinations in the Mediterranean, *EGU General Assembly 2021, online*, doi: 10.5194/egusphere-egu21-13217
- Schulzweida, U. (2022). *CDO User Guide (2.1.0)*. Zenodo. <https://doi.org/10.5281/zenodo.7112925>
- Scott, D., Gössling, S. & Hall, C.M. (2012), International tourism and climate change, *WIREs Climate Change*, 3(3), pp.213-232
- Scott, D., Ruttly, M., Amelung, B. & Tang, M. (2016) An Inter-Comparison of the Holiday Climate Index (HCI) and the Tourism Climate Index (TCI) in Europe. *Atmosphere*. 2016; 7(6):80. doi: 10.3390/atmos7060080
- Velea, L., Gallo, A., Bojariu, R., Irimescu, A., Craciunescu, V., & Puiu, S. (2022), Holiday Climate Index: Urban—Application for Urban and Rural Areas in Romania. *Atmosphere*. 13(9):1519. doi: 10.3390/atmos13091519
- Velea, L., Bojariu, R., Irimescu, A., Craciunescu, V., Puiu, S. & Gallo (2023) A Climate Suitability for Tourism in Romania Based on HCI: Urban Climate Index in the Near-Future Climate. *Atmosphere*, 14(6), doi: 10.3390/atmos14061020
- Yu, D.D., Ruttly, M., Scott, D. & Li, S. (2021) A comparison of the holiday climate index:beach and the tourism climate index across coastal destinations in China. *Int J Biometeorol* 65, pp. 741-748, doi: 10.1007/s00484-020-01979-w
- Yu, D.D., Matthews, L., Scott, D., Li, S. & Guo, Z.Y. (2022) Climate suitability for tourism in China in an era of climate change: a multiscale analysis using holiday climate index, *Current Issues in Tourism*, 25:14, pp. 2269-2284, doi: 10.1080/13683500.2021.1956442

INVESTIGATION OF CHLOROPHYLL-A VARIABILITY IN RED SEA USING SATELLITE-BASED METEOROLOGY AND OCEANOGRAPHY DATA

Anton Satria PRABUWONO¹, KUNARSO^{2,3*}, Anindya WIRASATRIYA^{2,3}
Satria ANTONI^{4,5}

DOI: 10.21163/GT_2023.182.18

ABSTRACT :

The Red Sea has a special geographical feature because it is situated in the tropical and subtropical zones. The uniqueness of the Red Sea makes a variability of oceanography data (Chlorophyll-a (Chl-a), current, Salinity, etc.) and meteorological data (Precipitation, Wind Speed, etc.). However, investigations of differences interaction of oceanography and meteorology are less studied in of the Red Sea. Satellites and modeling make it possible to observe oceanographic and meteorological data over a long period of time. This study first demonstrates that there are three major areas along the Red Sea that represent the different Chl-a concentrations during the rainy season. The month of July has the highest Chl-a concentration in the south (1.3 mg/m³) and the lowest Chl-a concentration in the north (0.18 mg/m³). The southern part of the Red Sea has a different generation mechanism from the northern part of the Red Sea in terms of increasing and decreasing Chl-a concentrations. The existence of surface runoff in this area may result in the supply of anthropogenic organic compounds and fresh water to coastal waters. This may increase the supply of nutrients at the peak of the rainy season, and finally increase the concentration of Chl-a in the southern part. In the middle part, the variability of Chl-a is mainly affected by wind speed. Meanwhile, the high salinity in the northern part may limit the growth of phytoplankton and keep the Chl-a concentration low.

Key-words: *Chlorophyll-a, Precipitation, Salinity, Surface Runoff, Red Sea.*

1. INTRODUCTION

Chlorophyll-a (Chl-a) is a phytoplankton biomass indicator present in practically every aquatic habitat (Smith et al., 2005). As the top trophic level, it is crucial to the marine food chain. Chl-a is an important food for fish and other organisms in coral reef ecosystems (Smith et al., 2005; Zainuddin et al., 2017). The positive correlation between Chl-a and fish productivity can be seen from the lower of Chl-a corresponding to the lower fish catch. Smith et al. (2005), reported a significant positive relationship between the skipjack catches and the concentration of chlorophyll in the Gulf of Bone-Flores Sea. Furthermore, Hunt et al. (2021), reported that the Red Sea's fish catch potential is split into two areas, with the south having the highest potential and the north having the lowest. Chl-a variability characteristics in an area are essential in increasing fish catches. Furthermore, we also need to understand Chl-a variability to understand fisheries management.

The Red Sea is one of the most important marine economic and environmental assets in the Middle East (Daqamseh et al., 2019). The Red Sea is a semi enclosed waters, lies between the Asian and African continental shelves and has a complex bathymetry and topography. The Red Sea's

¹ Faculty of Computing and Information Technology in Rabigh, King Abdulaziz University, Jeddah 21589, Saudi Arabia; aprabuwono@kau.edu.sa

² Department of Oceanography, Faculty of Fisheries and Marine Sciences, Diponegoro University, Semarang 50275, Indonesia; anindyawirasatriya@lecturer.undip.ac.id; Correspondence: kumarso@lecturer.undip.ac.id.

³ Center for Coastal Disaster Mitigation and Rehabilitation Studies, Diponegoro University, Semarang 50275, Indonesia

⁴ Marine Geology Department, Faculty of Marine Sciences, King Abdulaziz University, Jeddah 21589, Saudi Arabia; suddin@stu.kau.edu.sa

⁵ Centre of Artificial Intelligence, University of Insan Cita Indonesia, Jakarta, Indonesia; satriaantoni@uici.ac.id

southern region has numerous islands and shallow bathymetry. In contrast, the northern and middle regions have fewer islands and deeper bathymetry (Raitsos et al., 2013). It can cause variations in oceanographic and meteorological variability (Munandar et al., 2023; Figa-Saldaña et al., 2002). This feature makes the Red Sea an essential region for many marine species, some of which are endemic (Belkin, 2009). Another essential feature of the Red Sea lies in the uniqueness of the coral reef ecosystem that survives with the highest salinity in the world [Nassar et al., 2014; Raitsos et al., 2011]. The range of salinity that coral reefs can survive is 28.7–40.4 ppt (Wilkinson, 2008), and the Red Sea has a salinity range of 36–40 ppt (Mezger et al., 2016). The Red Sea has the highest diversity of coral communities outside of the southeast Asian "coral triangle," with a 0.12 percent global coral reef ecosystem (Wilkinson, 2008; DeVantier et al., 2000). The water can influence the natural environment of phytoplankton communities (Mezger et al., 2016; Sew and Todd, 2020; Sugie et al., 2020; Redden and Rukminasari, 2008). Changes in salinity are the result of runoff from the mainland and the balance between precipitation and evaporation (Al-Najjar et al., 2007; Lee and Hong, 2019).

Precipitation is one of the most important climate variables that influence the variability of chlorophyll in marine ecosystems (Shou et al., 2022; Kim et al., 2014). Increased precipitation triggers a rise in nutrient supply (NO_3^-), which plays an essential role in the increase of Chl-a in coastal waters (Baker et al., 2007; Maslukah et al., 2019). Meanwhile, the variability of chlorophyll-a in offshore areas is more dominated by upwelling, downwelling, and vertical mixing caused by wind speed variability (Munandar et al., 2023; Wirasatriya et al., 2019; Siswanto et al., 2020; DeCarlo et al., 2021). The mechanisms of upwelling, downwelling, and vertical mixing can be triggered by Ekman transport, Ekman pumping, cyclonic and anticyclonic eddy, etc. (Wang and Tang, 2014). These mechanisms influence the movement of nutrients from the deep ocean to the surface and from the surface to the deep ocean (Munandar et al., 2023; Wirasatriya et al., 2019; Wirasatriya et al., 2020). The variability of nutrients in surface water can influence the growth of phytoplankton (Maslukah et al., 2019). Consequently, it is necessary to determine to what extent these parameters affect the variability of Chl-a as a representative of phytoplankton in these waters.

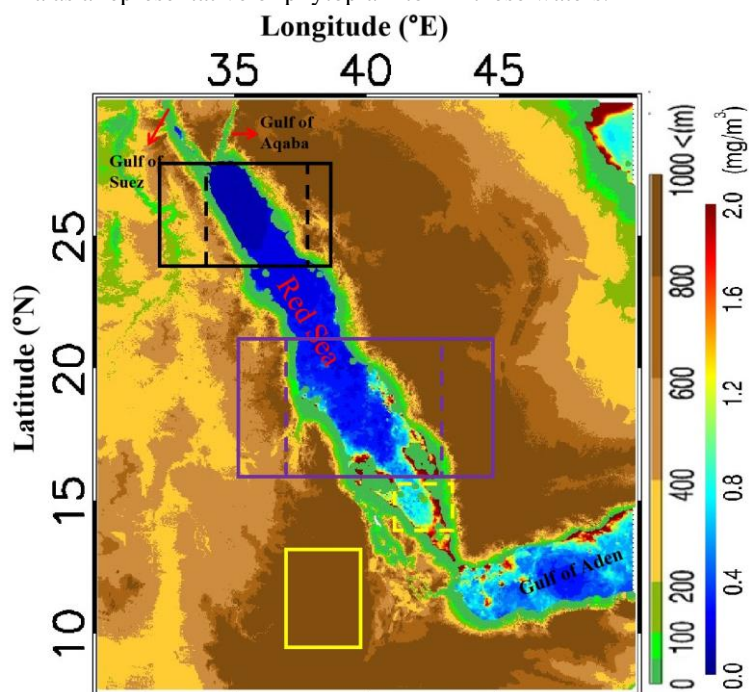


Fig. 1. Location area research with topography and Chl-a in Summer (July). Sampling areas for time series analysis (Fig. 3, 4) are denoted by the boxes. The yellow, purple and black boxes (dotted line) represent the region of the southern, middle and northern Red Sea with the highest, medium and lowest Chl-a concentration, respectively. The area for extracting the value of surface runoff and precipitation are extended into land (solid line).

Therefore, we observed the seasonal variations of Chl-a concentration in the whole area along the Red Sea. In addition, data on surface wind, surface current, current curl, precipitation, and salinity are used to comprehend the mechanisms responsible for the occurrence of these phenomena. In the present study, the analysis data came from satellite and model observation for 17 years of recording (from 2003 to 2020). In Section 2.1, we explain all remote sensing and modeling data used in this research. Furthermore, all data is averaged into seasonal variations to investigate time series and spatial variations.

2. STUDY AREA

Our study area is located at the Red Sea and the area of interest was limited for the Red Sea area bordered by 30°E - 50°E and 8°N -30°N (**Fig. 1**). The Red Sea is one of the most important marine economic and environmental assets in the Middle East (Daqamseh et al., 2019). The Red Sea is a semi enclosed waters, lies between the Asian and African continental shelves and has a complex bathymetry and topography.

3. DATA AND METHODS

3.1. Data

The data used in this study are Chl-a, surface wind, surface current, current curl, surface salinity, surface runoff and precipitation with the observation period from 2003-2020. We observed the distribution of Chl-a concentrations in the Red Sea using products from a multi-satellite collaboration of the European Space Agency (ESA) and the National Aeronautics and Space Administration (NASA). This collaboration resulted in a more accurate product, the Ocean Color-Climate Change Initiative (OC-CCI) (<http://marine.copernicus.eu/>). To create this data, the OC-CCI product used a multi-ocean-color satellite platform that included the Sea-viewing Wide Field-of-View Sensor (SeaWiFS GAC+LAC), the Medium Resolution Imaging Spectrometer (MERIS), the Moderate Resolution Imaging Spectro-radiometer (MODIS-A), and the Visible Infrared Imaging Radiometer Suite (VIIRS) (Sathyendranath et al., 2019). All satellite platforms are combined using the space-time interpolation method (Wirasatriya et al., 2019). This product has a spatial resolution of 4 km.

For investigating the surface current, we used the ocean physics reanalysis data distributed through the Copernicus Marine Environment Monitoring Service (CMEMS), i.e., GLOBAL-REANALYSIS-PHY-001-030

(https://data.marine.copernicus.eu/product/GLOBAL_MULTIYEAR_PHY_001_030/description). The grid interval of this dataset is $0.083^\circ \times 0.083^\circ$ (Drévilion et al., 2022). From surface ocean current, we calculated surface ocean curl to represent the existence of eddies.

The Advanced Scatterometer (ASCAT) is produced by the European Organization for the Exploitation of Meteorological Satellites (EUMETSAT) and has more accuracy for coastal waters compared to other products (Figa-Saldaña et al., 2002). ASCAT is a semi-daily surface wind product with a resolution of 14 km (<http://marine.copernicus.eu/>).

The precipitation data product from ERA-5 reanalysis is widely used for hydrological monitoring (<https://cds.climate.copernicus.eu/cdsapp#!/dataset/reanalysis-era5-single-levels?tab=form>). ERA5 precipitation data is generated using a combination of modelling and data assimilation systems (Lavers et al., 2022). ERA5 output is provided hourly, and the resolution of this dataset is 30 km. Data on sea surface salinity were obtained from Remote Sensing Systems' Soil Moisture Active Passive (SMAP) version 2.0 (<https://www.remss.com/missions/smap/salinity/>). The resolution of SMAP 2.0 is 70 km, but the 70 km product is resampled into 0.25° . The accuracy product, SMAP 2.0, is higher if compared with SMAP 1.0 (AlJassar et al., 2022).

The surface runoff data is obtained from ERA5 data which is the fifth generation European Centre for Medium-Range Weather Forecasts (ECMWF) reanalysis for the global climate and weather for the past 8 decades. This is hourly data with grid interval of $0.25^\circ \times 0.25^\circ$ (<https://cds.climate.copernicus.eu/cdsapp#!/dataset/reanalysis-era5-single-levels?tab=overview>).

3.2. Method

The data in this study were collected over various time periods of observation (hourly, semi-daily, daily, and monthly), so all data needs to be averaged into monthly climatological data to facilitate analysis. To composite the data, we used the formula described in (Wirasatriya et al., 2017).

$$\bar{X}(a, b) = \frac{i}{m} \sum_{i=1}^m x_i(a, b, t) \quad (1)$$

where (a, b) is the monthly climatology at a, b , and $x_i(a, b, t)$ is the i -th data value at position a (longitude), b (latitude), and t (time). Furthermore, m is the number of time periods of observation for the monthly climatology calculation. Additionally, the Not a Number (NaN) data is excluded from the calculation of the monthly climatology calculation.

We analyzed the spatial distribution of all data by season i.e. winter, spring, summer and autumn as represented by January, April, July, and October, respectively.

To investigated the influence of eddies forcing on chlorophyll-a in the Red Sea, we convert surface current data into *current curl* (Wang and Tang, 2014):

$$\text{Current Curl} = \frac{\partial V}{\partial x} - \frac{\partial U}{\partial y} \quad (2)$$

where V is wind stress from meridional component and U is wind stress from zonal component.

4. RESULTS AND DISCUSSIONS

4.1. Spatial Distribution of Chl-a, Current Curl, Surface Current, and Surface Wind

The results of the spatial distribution of the monthly climatology of Chl-a in the Red Sea in January, April, July, and October (**Fig. 2**) and the Chl-a concentration detected appear in three areas (**Fig. 1**). The three locations studied have low (northern part), medium (middle part), and high (southern part) Chl-a concentrations, respectively. In the northern part, Chl-a concentrations reach 0.18 mg/m^3 in October and 0.28 mg/m^3 in February (**Fig. 3**). In the middle part, Chl-a concentrations reach 0.4 mg/m^3 in April and 0.8 mg/m^3 in July (**Fig. 3**). In the southern part, Chl-a concentrations reach 0.5 mg/m^3 in May and 1.3 mg/m^3 in July (**Fig. 3**). The difference in Chl-a concentration in the Red Sea is clearly seen, and it is indicated that the Red Sea has different mechanisms to generate increases and decreases in Chl-a concentration. The variability of the Chl-a concentration in the on-shore and off-shore areas can be triggered by wind, current, tide, run-off from the mainland, etc. (Munandar et al., 2023; Kim et al., 2014; Wirasatriya et al., 2020; Wang and Tang, 2014).

To investigate the Chl-a variability mechanisms, we examined the relation between Chl-a and surface wind. In the southern part, surface winds reached 5.5 m/s (November) and 1 m/s (May), surface winds in the middle part reached 3.5 m/s (July) and 1.5 m/s (October), and in the northern part, surface winds reached 4.25 m/s (June and September) and 3.25 m/s (April) (**Fig. 3**). Previous studies found that strong surface winds mostly influence the increasing Chl-a (Wirasatriya et al., 2019; Iwasaki, 2020; Liu et al., 2020). In the middle part, the relationship between surface wind and Chl-a has the same pattern. It is indicated that surface wind can generate vertical mixing and become the primary process for increasing Chl-a in the middle part of the Red Sea. However, we found an inconsistent relationship between wind speed and Chl-a in the southern and northern parts of the Red Sea. The variability of Chl-a does not follow the variation of surface wind. In the southern part, the increasing surface wind increases Chl-a a little from the previous month (September–October) from 0.8 to 1 mg/m^3 , but not higher than July (1.3 mg/m^3). In the northern part, the strong wind speed does not influence the increase of Chl-a. Munandar et al. (2023) found that in the Sulu Sea, surface wind is not the primary data to trigger high Chl-a, but tide is the primary process to trigger high Chl-a. Thus, surface wind in the northern and southern parts of the Red Sea has less influence on the variability of Chl-a in the Red Sea and indicates a different mechanism for the variability of Chl-a in the Red Sea.

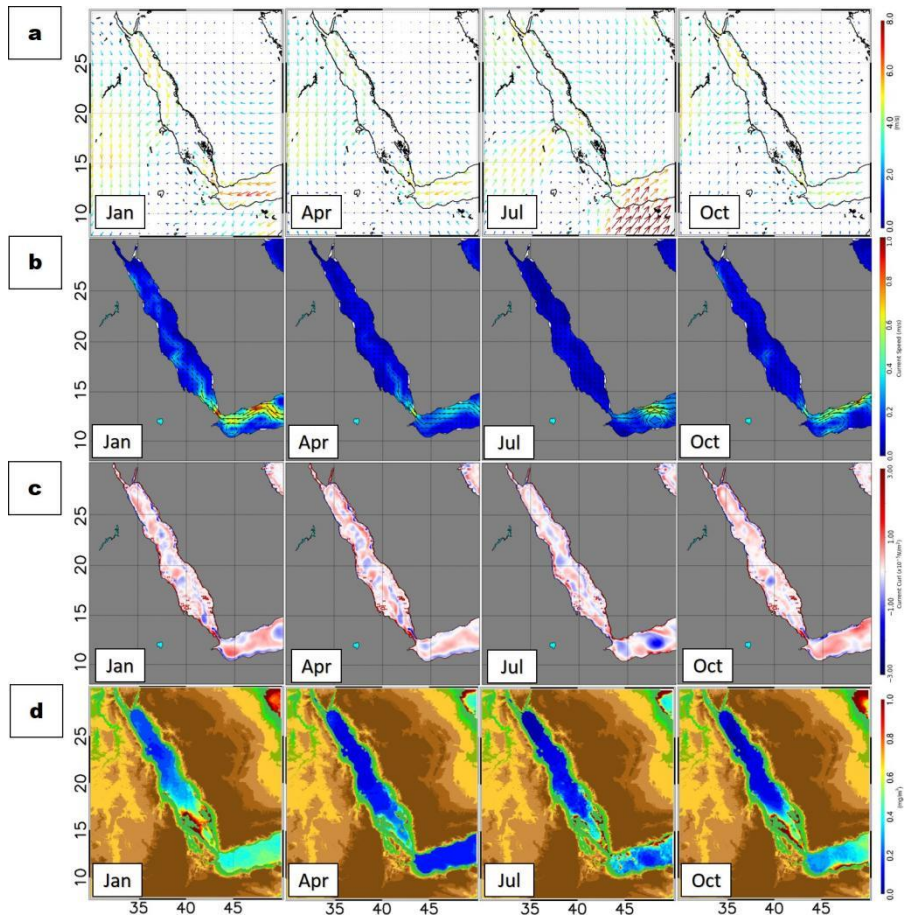


Fig. 2. The spatial distribution of the monthly climatology of (a) Surface wind, (b) Surface current, and (c) Curl current and (d) Chl-a along the Red Sea in January, April, July and October (2003–2020).

We also investigate the relation between Chl-a and current speed, the current speed is high in the southern part (0.6 m/s) in January and lower on the other. Raitsos et al. (2013) indicate that the existence of cyclonic and anticyclonic eddies along the Red Sea contributes to the variability of Chl-a. To represent the variability of eddy, we convert current speed to current curl, and compare it to Chl-a (**Fig. 2 c, d**). The existence of cyclonic and anticyclonic eddies along the Red Sea is indicated by positive and negative curl, respectively. The distribution of surface current and current curl do not show that there are strong cyclonic and anticyclonic eddies in the Red Sea. Interestingly, the cyclonic and anticyclonic eddies are stronger in the Gulf of Aden (southern part of the Red Sea). In the Gulf of Aden, strong anticyclonic eddies occur in July and cause Chl-a decrease. Furthermore, cyclonic eddies detected in October, and their occurrences increases Chl-a. In contrast, the curl pattern in the Red Sea as not as clear as the Gulf of Aden. Thus, eddy currents are not the primary processes that trigger increasing Chl-a in the Red Sea but the play important role to distribute Chl-a in the Red Sea as mentioned by Raitsos et al. (2013). This indicates a different mechanism for the generating factor of increasing Chl-a in the Red Sea.

4.2. Time Series investigation of Chl-a, Surface Wind, and Precipitation

The previous analysis found that surface wind and current do not play a significant role in chlorophyll variability in the northern and southern parts of the Red Sea. We investigated the time series variability of precipitation and Chl-a to investigate the inconsistency of the relationship

between wind speed and Chl-a in the southern Red Sea. Kim et al. (2014) and Wirasatriya et al. (2021) found that precipitation plays an important role in increasing Chl-a in the on-shore area. The precipitation extraction area was expanded in order to observe mainland runoff in the southern Red Sea (Figure 1). In the southern part, the intensity of precipitation is 14–30 times higher (14 mm/day) than precipitation in the northern and middle areas (Fig. 3). Higher precipitation in the southern part occurs in July, at the same time as the peak of Chl-a concentration (1.3 mg/m³). Precipitation can influence the variability of Chl-a in on-shore areas because, during the rainy season, it can change the amount of nutrients coming from runoff on the mainland. Increased runoff water from the mainland has an impact on the nutrients (phosphate, nitrate, etc.) in coastal waters and becomes an important material for phytoplankton to conduct photosynthesis (Baker et al., 2007; Maslukah et al., 2019; Gittings et al., 2018).

To investigate the evidence of high runoff from land during high rainfall, we analyzed surface runoff in the southern part of the Red Sea. The peak of surface runoff reached $150 \times 10^3 \text{ m}^3/\text{s}$ in July and decreased in the next month. It has the same pattern with precipitation and Chl-a in the southern part. The influx of mainland runoff is characterized by an increase in surface runoff in July, as well as the occurrence of Chl-a and precipitation peaks (Fig. 4). This indicates that precipitation is the primary process contributing to the variability of Chl-a in the southern part of the Red Sea.

Nevertheless, the precipitation in the northern part reaches only 0,18 mm/day, which is lower than in other parts. This reinforces the fact that wind speed and precipitation are not the primary processes that trigger the variability of Chl-a in this area. This indicates another factor influences the occurrence of variability in Chl-a concentration in the northern part of the Red Sea.

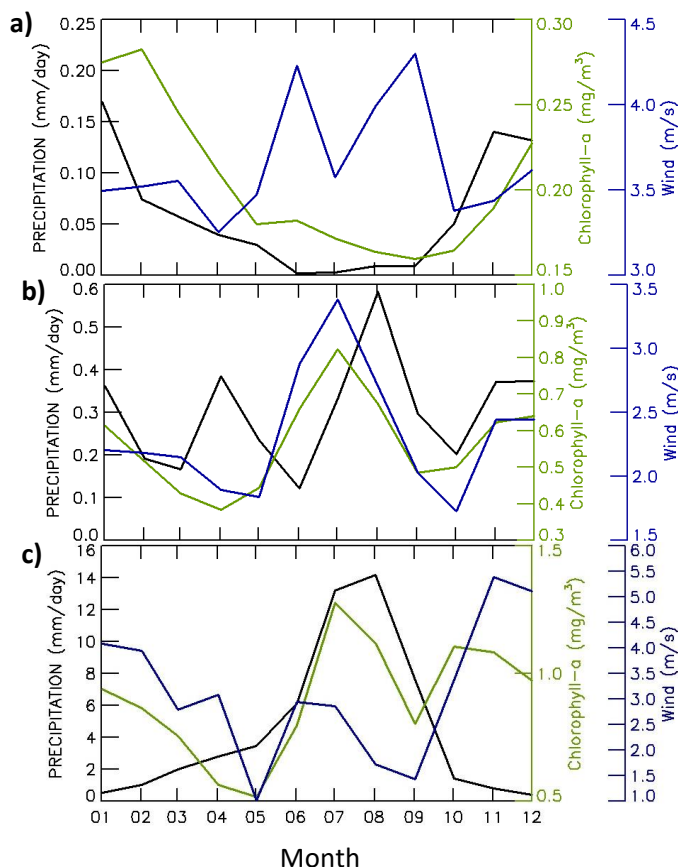


Fig. 3. Time series data of the monthly climatology of Chl-a, surface wind speed, and precipitation in three areas (a= northern, b= middle, c= southern).

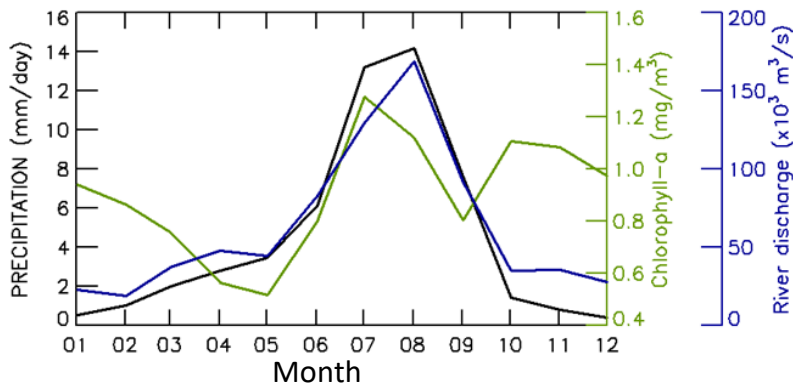


Fig. 4. Time series data of Chl-a, surface runoff, and precipitation in the southern part of Red Sea.

4.3. Time Series investigation of Chl-a, Surface Wind, and Salinity

In the northern part of the Red Sea the variability of Chl-a does not match with the wind speed and precipitation (**Fig. 3a**). In this area, the wind speed increases between the May - September reach 3.4 – 4.4 m/s and precipitation increase between the November - January reach 0.05 – 0.18 mm/day. Wind speed values in the northern is not lower than other areas, but the value of Chl-a in the northern is lower compared to other areas.

As shown earlier, Chl-a in the north was lower than in other areas and this could be because the northern part has higher salinity. Moreover, the northern part is included in the sub-tropical region. To investigate more about this phenomenon, we analyze the meridional propagation of salinity, Chl-a and surface wind along the Red Sea. We took 14 sample areas in $0.5^\circ \times 0.5^\circ$ bins and the plot the monthly climatology of salinity, Chl-a and surface wind speed in Hovmöller diagram as shown in **Fig. 5**. In the middle and southern parts, the salinity reaches 35-38 ppt and in the north it reaches >38.5 ppt. the high salinity in the northern area may become the limiting factor for several organisms including phytoplankton in the sea to survive and grow. Ismael (2015) reported a gradual decrease in phytoplankton richness from the southern Red Sea to the Gulf of Suez.

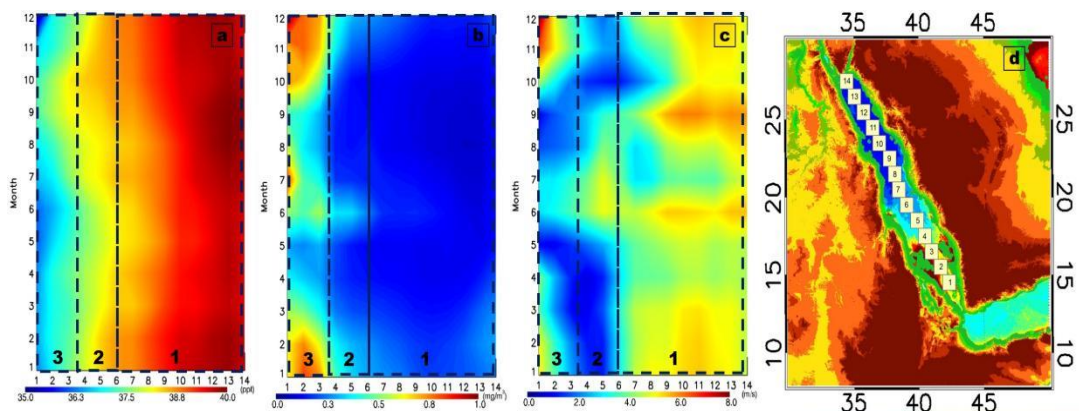


Fig. 5. Hovmöller diagram of monthly climatology of (a) salinity, (b) Chl-a, and (c) surface wind (C) with bin number at x-axis. The bins with numbers used for creating Hovmöller are shown in (d). Dashed black box donates the area of observation 1 (northern), 2 (middle), 3 (southern).

The high (low) salinity impact to low (high) Chl-a.

5. DISCUSSION

According to previous research, the Red Sea is known for having high Chl-a concentrations during the winter (December-March) and low concentrations during the summer (May-September) (Raitsos et al., 2013; Raitsos et al., 2015). An essential mechanism for influencing the high Chl-a in the Red Sea found by [Raitsos et al., 2013; Gittings et al., 2021] is eddy current and vertical mixing, which supply nutrients from deeper waters. We discovered the time difference and the mechanism causing the increase and decrease of Chl-a concentration in the Red Sea. This vertical mixing may occur in winter because wind speeds are higher in the Red Sea from November to December. However, higher wind speeds are unrelated to increased Chl-a concentration (July) in the Red Sea. More clearly affecting the increase in Chl-a are salinity and precipitation in the northern and southern parts of the Red Sea, respectively. Vertical mixing is shown in the middle part of the Red Sea, even though the wind speed values are lower compared to other areas. Furthermore, the impact of wind speed in the southern affects the increase in Chl-a in October, but not higher than precipitation in July (Fig. 3c).

The climatological and meteorological analysis determine the essential factors that influence the increase in Chl-a in the Red Sea (Acker et al., 2008). As presented in this study, the southern part of the Red Sea clearly shows that precipitation can affect the variability of Chl-a caused by mainland runoff. In accordance with the result of Racault et al. (2015), the highest Chl-a occurs during summer and we found that it occurs under the condition of highest precipitation and surface runoff. As found by (Kim et al., 2014; Wirasatriya et al., 2017; Wang and Tang, 2014; Iwasaki, 2020; Kunarso et al., 2019), the increases in wind speed and precipitation greatly affect the variability of Chl-a. The mainland runoff may supply nutrients to coastal areas and can be part of the items for the photosynthesis mechanism. Therefore, this finding completes the results of Dreano et al. (2016) and Triantafyllou et al. (2014), who found the subsurface intrusion from the Gulf of Aden that plays a key role in the development of the southern Red Sea phytoplankton blooms during winter. However, the use of satellite imagery to analyze the effect of precipitation on Chl-a needs to be done carefully because the total suspended matter factor in the waters can affect the accuracy of the data. The periodic collection of field observations needs to be done to improve the accuracy of satellite imagery by creating an algorithm suitable for the Red Sea conditions. Future research is required to improve and extend this task.

The different conditions in the northern part of the Red Sea, where salinity is a limiting factor in the growth of phytoplankton. As summarized by (Mezger et al., 2016; Sew and Todd, 2020; Putland and Iverson, 2007), in areas with four seasons the salinity value suitable for the growth of phytoplankton ranges from 20-30 ppt. Sugie et al. (2020) found that waters with low to moderate salinity or in the upper reaches had higher levels of Chl-a. Furthermore, research in the laboratory conducted by Yun et al. (2019) revealed that increased salt levels in the waters affect the growth of phytoplankton. The high salinity in the northern part of the Red Sea can be affected by lower precipitation, so that the surface runoff in this area becomes less. The lower surface runoff can influence the high salinity in the water (Sew and Todd, 2020; Sugie et al., 2020; Redden and Rukminasari, 2008; Fisher et al., 1988), respectively. However, a more thorough analysis is needed regarding the types of phytoplankton that live in the Red Sea because some phytoplankton have different salinity tolerances. Future research is required to improve and extend this task.

6. CONCLUSIONS

Utilizing satellite observations, Chl-a variability in the Red Sea is characterized by highest, medium and lowest concentration in the southern, middle, and northern parts, respectively. In the southern part, the highest Chl-a (i.e., 1.3 mg/m³) occurs during summer as a result of high precipitation that may bring nutrient from land via surface runoff. In the middle part, the highest Chl-a (i.e., 0.8 mg/m³) also occurs during summer. However, wind speed play more important role to control the variability of Chl-a than precipitation. In the northern part, the Chl-a concentration is very low, even during the peak in winter, the concentration is only 0.28 mg/m³. The high salinity (> 38.5 ppt) in the northern part may become the limiting factor for phytoplankton to survive and grow.

ACKNOWLEDGMENTS

We are thankful for the data provided by NASA, ESA, EUMETSAT, and other stakeholders for this article. This research was funded by Institutional Fund Projects under grant no. (IFPIP:1424-830,1442). Therefore, authors gratefully acknowledge technical and financial support from the Ministry of Education and King Abdulaziz University, DSR, Jeddah, Saudi Arabia. Thanks to Bayu Munandar and Ardiansyah Desmont Puryajati for their contributions to this article.

REFERENCES

- Acker, J., Leptoukh, G., Shen, S., Zhu, T., & Kemple, S. (2008). Remotely-sensed chlorophyll a observations of the northern Red Sea indicate seasonal variability and influence of coastal reefs. *Journal of Marine Systems*, 69, 191-204. <https://doi.org/10.1016/j.jmarsys.2005.12.006>.
- AlJassar, H., Temimi, M., Abdelkader, M., Petrov, P., Kokkalis, P., AlSarraf, H., Roshni, N., & Al Hendi, H. (2022). Validation of NASA SMAP Satellite Soil Moisture Products over the Desert of Kuwait. *Remote Sensing*, 14, 3328. <https://doi.org/10.3390/rs14143328>.
- Al-Najjar, T., Badran, M. I., Richter, C., Meyerhoefer, M., & Sommer, U. (2007). Seasonal dynamics of phytoplankton in the Gulf of Aqaba, Red Sea. *Hydrobiologia*, 579, 69–83. <https://doi.org/10.1007/s10750-006-0365-z>.
- Baker, A. R., Weston, K., Kelly, S. D., Voss, M., Streu, P., & Cape, J. N. (2007). Dry and wet deposition of nutrients from the tropical Atlantic atmosphere: Links to primary productivity and nitrogen fixation. *Deep Sea Res. Part I*, 54, 1704–1720. <https://doi.org/10.1016/j.dsr.2007.07.001>.
- Belkin, I. M. (2009). Rapid warming of large marine ecosystems. *Progress in Oceanography*, 81, 207–213. <https://doi.org/10.1016/j.pocean.2009.04.011>.
- Daqamseh, S. T., Al-Fugara, A., Pradhan, B., Al-Oraiqat, A., & Habib, M. (2019). MODIS Derived Sea Surface Salinity, Temperature, and Chlorophyll-a Data for Potential Fish Zone Mapping: West Red Sea Coastal Areas, Saudi Arabia. *Sensors*, 19, 2069. <https://doi.org/10.3390/s19092069>.
- DeCarlo, T. M., Carvalho, S., Gajdzik, L., Hardenstine, R. S., Tanabe, L. K., Villalobos, R., & Berumen, M. L. (2021). Patterns, Drivers, and Ecological Implications of Upwelling in Coral Reef Habitats of the Southern Red Sea. *Journal of Geophysical Research: Oceans*, 126, e2020JC016493. <https://doi.org/10.1029/2020JC016493>.
- DeVantier, L., Turak, E., Al-Shaikh, K., & De'ath, G. (2000). Coral communities of the central-northern Saudi Arabian Red Sea. *Fauna of Arabia*, 18, 23–66.
- Dreano, D., Raitos, D.E., Gittings, J., Krokos, G., & Hoteit, I. (2016). The Gulf of Aden Intermediate Water Intrusion Regulates the Southern Red Sea Summer Phytoplankton Blooms. *PLoS One*, 11, 1–20. <https://doi.org/10.1371/journal.pone.0168440>.
- Drévilion, M., Fernandez, E., & Lellouche, J. M. (2022). Copernicus Marine Service PUM for GLOBAL_MULTIYEAR_PHY_001_030 (<https://catalogue.marine.copernicus.eu/documents/PUM/CMEMS-GLO-PUM-001-030.pdf>).
- Figa-Saldaña, J., Wilson, J. J. W., Attema, E., Gelsthorpe, R. V., Drinkwater, M. R., & Stoffelen, A. (2002). The Advanced Scatterometer (ASCAT) on the Meteorological Operational (MetOp) Platform: A Follow on for European Wind Scatterometers. *Canadian Journal of Remote Sensing*, 28, 404–412. <https://doi.org/10.5589/m02-035>.
- Fisher, T. R., Harding Jr., L. W., Stanley, D. W., & Ward, L. G. (1988). Phytoplankton, nutrients, and turbidity in the Chesapeake, Delaware, and Hudson estuaries. *Estuarine Coastal and Shelf Science*, 27, 61–93. [https://doi.org/10.1016/0272-7714\(88\)90032-7](https://doi.org/10.1016/0272-7714(88)90032-7).
- Gittings, J. A., Raitos, D. E., Krokos, G., & Hoteit, I. (2018). Impacts of warming on phytoplankton abundance and phenology in a typical tropical marine ecosystem. *Scientific Reports*, 8, 2240. <https://doi.org/10.1038/s41598-018-20560-5>.
- Gittings, J. A., Raitos, D. E., Brewin, R. J. W., & Hoteit, I. (2021). Links between Phenology of Large Phytoplankton and Fisheries in the Northern and Central Red Sea. *Remote Sensing*, 13, 231. <https://doi.org/10.3390/rs13020231>.
- Hunt, B. P. V., Espinasse, B., Pakhomov, E. A., Cherel, Y., Cotte, C., Delegrange, A., & Henschke N. (2021). Pelagic food web structure in high nutrient low chlorophyll (HNLC) and naturally iron fertilized waters in

- the Kerguelen Islands region, Southern Ocean. *Journal of Marine Systems*, 224, 103625. <https://doi.org/10.1016/j.jmarsys.2021.103625>.
- Ismael, A. A. (2015). Phytoplankton of the Red Sea: In: Rasul, N., Stewart, I. (eds) *The Red Sea*. Springer Earth System Sciences. Springer, Berlin, Heidelberg. https://doi.org/10.1007/978-3-662-45201-1_32.
- Iwasaki, S. (2020). Daily Variation of Chlorophyll-A Concentration Increased by Typhoon Activity. *Remote Sensing*, 12, 1259. <https://doi.org/10.3390/rs12081259>.
- Kim, T., Najjar, R. G., & Lee, K. (2014). Influence of Precipitation Events on Phytoplankton Biomass in Coastal Waters of the Eastern United States. *Global Biogeochemical Cycles*, 28, 1–13. <https://doi.org/10.1002/2013GB004712>.
- Kunarso, Wirasatriya, A., Irwani, Satriadi, A., Helmi, M., Prayogi, H., & Munandar, B. (2019). Impact of Climate Variability to Aquatic Variability and Fisheries Resources in Jepara Waters. In Proceedings of 4th International Conference on Tropical and Coastal Region Eco Development. *IOP Conference Series: Earth and Environmental Science, Semarang, Indonesia*. 30-31 October 2018, 246, 012021. <https://doi.org/10.1088/1755-1315/246/1/012021>.
- Lavers, D. A., Simmons, A., Vamborg, F., & Rodwell, M. J. (2022). An evaluation of ERA5 precipitation for climate monitoring. *Quarterly Journal of the Royal Meteorological Society*, 148, 3071-3427. <https://doi.org/10.1002/qj.4351>.
- Lee, E., & Hong, S. -Y. (2019). Impact of the Sea Surface Salinity on Simulated Precipitation in a Global Numerical Weather Prediction Model. *Journal of Geophysical Research: Atmospheres*, 124, 441-1193. <https://doi.org/10.1029/2018JD029591>.
- Liu, Y., Tang, D., Tang, S., Morozov, E., Liang, W., & Sui, Y. (2020). A case study of Chlorophyll a response to tropical cyclone Wind Pump considering Kuroshio invasion and air-sea heat exchange. *Science of the Total Environment*, 741, 140290. <https://doi.org/10.1016/j.scitotenv.2020.140290>.
- Maslukah, L., Zainuri, M., Wirasatriya, A., & Salma, U. (2019). Spatial Distribution of Chlorophyll-a and Its Relationship with Dissolved Inorganic Phosphate Influenced by Rivers in the North Coast of Java. *Journal of Ecological Engineering*, 20, 18–25. <https://doi.org/10.12911/22998993/108700>.
- Mezger, E. M., de Nooijer, L. J., Boer, W., Brummer, G. J. A., & Reichart, G. J. (2016). Salinity controls on Na incorporation in Red Sea planktonic foraminifera. *Paleoceanography and Paleoclimatology*, 31, 1562-1582. <https://doi.org/10.1002/2016PA003052>.
- Munandar, B., Wirasatriya, A., Sugianto, D. N., Susanto, R. D., Purwandana, A., & Kunarso. (2023). Distinct mechanisms of Chlorophyll-a blooms occur in the Northern Maluku Sea and Sulu Sill revealed by satellite data. *Dynamics of Atmospheres and Oceans*, 102, 101360. <https://doi.org/10.1016/j.dynatmoce.2023.101360>.
- Nassar, M. Z., Mohamed, H. R., Khiray, H. M., & Rashedy, S. H. (2014). Seasonal fluctuations of phytoplankton community and physico-chemical parameters of the north western part of the Red Sea, Egypt. *Egyptian Journal of Aquatic Research*, 40, 395–403. <http://dx.doi.org/10.1016/j.ejar.2014.11.002>.
- Putland, J. N., & Iverson, R. L. (2007). Phytoplankton Biomass in a Subtropical Estuary: Distribution, Size Composition, and Carbon: Chlorophyll Ratios. *Estuaries and Coasts*, 30, 878–885. <https://doi.org/10.1007/BF02841341>.
- Raitsos, D. E., Hoteit, I., Prihartato, P. K., Chronis, T., Triantafyllou, G., & Abualnaja, Y. (2011). Abrupt warming of the Red Sea. *Geophysical Research Letters*, 38, L14601. <https://doi.org/10.1029/2011GL047984>.
- Raitsos, D. E., Pradhan, Y., Brewin, R. J. W., Stenchikov, G., & Hoteit, I. (2013). Remote Sensing the Phytoplankton Seasonal Succession of the Red Sea. *PLoS ONE*, 8, e64909. <https://doi.org/10.1371/journal.pone.0064909>.
- Raitsos, D. E., Yi, X., Platt, T., Racault, M. F., Brewin, R. J. W., Pradhan, Y., Papadopoulos, V. P., Sathyendranath, S., & Hoteit, I. (2015). Monsoon oscillations regulate fertility of the Red Sea. *Geophysical Research Letters*, 42, 855–862. <https://doi.org/10.1002/2014GL062882>.
- Racault, M. F., Raitsos, D. E., Berumen, M. L., Brewin, R. J. W., Platta, T., Sathyendranath, S., & Hoteit, I. (2015). Phytoplankton phenology indices in coral reef ecosystems: Application to ocean-color observations in the Red Sea. *Remote Sensing of Environment*, 160, 222-234. <http://dx.doi.org/10.1016/j.rse.2015.01.019>.
- Redden, A. M., & Rukminasari, N. (2008). Effects of increases in salinity on phytoplankton in the Broadwater of the Myall Lakes, NSW, Australia. *Hydrobiologia*, 608, 87–97. <https://doi.org/10.1007/s10750-008-9376-2>.

- Sathyendranath, S., Brewin, R. J. W., Brockmann, C., Brotas, V., Calton, B., Chuprin, A., Cipollini, P., Couto, A. B., Dingle, J., Doerffer, R., Donlon, C., Dowell, M., Farman, A., Grant, M., Groom, S., Horseman, A., Jackson, T., Krasemann, H., Lavender, S., Martinez-Vicente, V., Mazeran, C., Mélin, F., Moore, T. S., Müller, D., Regner, P., Roy, S., Steele, C. J., Steinmetz, F., Swinton, J., Taberner, M., Thompson, A., Valente, A., Zühlke, M., Brando, V. E., Feng, H., Feldman, G., Franz, B. A., Frouin, R., Gould Jr, R. W., Hooker, S. B., Kahru, M., Kratzer, S., Mitchell, B. G., Muller-Karger, F. E., Sosik, H. M. Voss, K. J., Werdell, J., & Platt, T. (2019). An Ocean-Colour Time Series for Use in Climate Studies: The Experience of the Ocean-Colour Climate Change Initiative (OC-CCI). *Sensors*, 19, 4285. <https://doi.org/10.3390/s19194285>.
- Sew, G. & Todd, P. (2020). Effects of Salinity and Suspended Solids on Tropical Phytoplankton Mesocosm Communities. *Tropical Conservation Science*, 13, 1–11. <https://doi.org/10.1177/1940082920939760>.
- Shou, C. –Y., Tian, Y., Zhou, B., Fu, X. –J., Zhu, Y. –J., & Yue, F. –J. (2022). The Effect of Rainfall on Aquatic Nitrogen and Phosphorus in a Semi-Humid Area Catchment, Northern China. *International Journal of Environmental Research and Public Health*, 19, 10962. <https://doi.org/10.3390/ijerph191710962>.
- Siswanto, E., Horii, T., Iskandar, I., Gaol, J. L., Setiawan, R. Y., & Susanto, R. D. (2020). Impacts of Climate Changes on the Phytoplankton Biomass of the Indonesian Maritime Continent. *Journal of Marine Systems*, 212, 103451. <https://doi.org/10.1016/j.jmarsys.2020.103451>.
- Smith, V. H., Foster, B. L., Grover, J. P., Holt, R. D., Leibold, M. A., & deNoyelles, F. (2005). Phytoplankton species richness scales consistently from laboratory microcosms to the world's oceans. *PNAS*, 102, 4393–4396. <https://doi.org/10.1073/pnas.0500094102>.
- Sugie, K., Fujiwara, A., Nishino, A., Kameyama, S., & Harada, N. (2020). Impacts of Temperature, CO₂, and Salinity on Phytoplankton Community Composition in the Western Arctic Ocean. *Frontiers in Marine Science*, 6, 821. <https://doi.org/10.3389/fmars.2019.00821>.
- Triantafyllou, G., Yao, F., Petihakis, G., Tsiaras, K. P., Raitsos, D. E., & Hoteit, I. (2014). Exploring the Red Sea seasonal ecosystem functioning using a three-dimensional biophysical model. *Journal of Geophysical Research: Oceans*, 119, 1791–1811. <https://doi.org/10.1002/2013JC009641>.
- Wang, J. J., & Tang, D. L. (2014). Phytoplankton patchiness during spring intermonsoon in Western Coast of South China Sea. *Deep-Sea Res. II*, 101, 120–128. <https://doi.org/10.1016/j.dsr2.2013.09.020>.
- Wilkinson, C. (2008). Status of coral reefs of the world: 2008. Global Coral Reef Monitoring Network and Reef and Rainforest Research Centre, Townsville, Australia, 296 p.
- Wirasatriya, A., Setiawan, R. Y., & Subardjo, P. (2017). The Effect of ENSO on the Variability of Chlorophyll-a and Sea Surface Temperature in the Maluku Sea. *IEEE Journal of Selected Topics in Applied Earth Observations and Remote Sensing*, 10, 5513–5518. <https://doi.org/10.1109/JSTARS.2017.2745207>.
- Wirasatriya, A., Sugianto, D.N., Helmi, M., Setiawan, R. Y., & Koch, M. (2019). Distinct Characteristics of SST Variabilities in the Sulawesi Sea and the Northern Part of the Maluku Sea During the Southeast Monsoon. *IEEE Journal of Selected Topics in Applied Earth Observations and Remote Sensing*, 12, 1763 – 1770. <https://doi.org/10.1109/JSTARS.2019.2913739>.
- Wirasatriya, A., Setiawan, J. D., Sugianto, D. N., Rosyadi, I.A., Haryadi, Winarso, G., Setiawan, R. Y., & Susanto, R.D. (2020). Ekman Dynamics Variability along the Southern Coast of Java Revealed by Satellite Data. *International Journal of Remote Sensing*, 41(21), 8475–8496. <https://doi.org/10.1080/01431161.2020.1797215>.
- Wirasatriya, A., Susanto, R. D., Setiawan, J. D., Ramdani, F., Iskandar, I., Jalil, R., Puryajati, A.D., Kunarso, K., & Maslukah, L. (2021). High Chlorophyll-a Areas along the Western Coast of South Sulawesi-Indonesia during the Rainy Season Revealed by Satellite Data. *Remote Sensing*, 13, 4833. <https://doi.org/10.3390/rs13234833>.
- Yun, C. –J., Hwang, K. –O., Han, S. –S., & Ri, H. –G. (2019). The Effect of Salinity Stress on the Biofuel Production Potential of Freshwater Microalgae *Chlorella Vulgaris* YH703. *Biomass and Bioenergy*, 127, 105277. <https://doi.org/10.1016/j.biombioe.2019.105277>.
- Zainuddin, M., Farhum, A., Safruddin, S., Selamat, M. B., Sudirman, S., Nurdin, N., Syamsuddin, M., Ridwan, M., & Saitoh, S. (2017). Detection of Pelagic Habitat Hotspots for Skipjack Tuna in the Gulf of Bone-Flores Sea, Southwestern Coral Triangle Tuna, Indonesia. *PLoS One*, 12, e0185601. <https://doi.org/10.1371/journal.pone.0185601>.
-

Aims and Scope

Geographia Technica is a journal devoted to the publication of all papers on all aspects of the use of technical and quantitative methods in geographical research. It aims at presenting its readers with the latest developments in G.I.S technology, mathematical methods applicable to any field of geography, territorial micro-scalar and laboratory experiments, and the latest developments induced by the measurement techniques to the geographical research.

Geographia Technica is dedicated to all those who understand that nowadays every field of geography can only be described by specific numerical values, variables both of time and space which require the sort of numerical analysis only possible with the aid of technical and quantitative methods offered by powerful computers and dedicated software.

Our understanding of **Geographia Technica** expands the concept of technical methods applied to geography to its broadest sense and for that, papers of different interests such as: G.I.S, Spatial Analysis, Remote Sensing, Cartography or Geostatistics as well as papers which, by promoting the above mentioned directions bring a technical approach in the fields of hydrology, climatology, geomorphology, human geography territorial planning are more than welcomed provided they are of sufficient wide interest and relevance.

Targeted readers:

The publication intends to serve workers in academia, industry and government. Students, teachers, researchers and practitioners should benefit from the ideas in the journal.

Guide for Authors

Submission

Articles and proposals for articles are accepted for consideration on the understanding that they are not being submitted elsewhere.

The publication proposals that satisfy the conditions for originality, relevance for the new technical geography domain and editorial requirements, will be sent by email to the address editorial-secretary@technicalgeography.org.

This page can be accessed to see the requirements for editing an article, and also the articles from the journal archive found on www.technicalgeography.org can be used as a guide.

Content

In addition to full-length research contributions, the journal also publishes Short Notes, Book reviews, Software Reviews, Letters of the Editor. However the editors wish to point out that the views expressed in the book reviews are the personal opinion of the reviewer and do not necessarily reflect the views of the publishers.

Each year two volumes are scheduled for publication. Papers in English or French are accepted. The articles are printed in full color. A part of the articles are available as full text on the www.technicalgeography.org website. The link between the author and reviewers is mediated by the Editor.

Peer Review Process

The papers submitted for publication to the Editor undergo an anonymous peer review process, necessary for assessing the quality of scientific information, the relevance to the technical geography field and the publishing requirements of our journal.

The contents are reviewed by two members of the Editorial Board or other reviewers on a simple blind review system. The reviewer's comments for the improvement of the paper will be sent to the corresponding author by the editor. After the author changes the paper according to the comments, the article is published in the next number of the journal.

Eventual paper rejections will have solid arguments, but sending the paper only to receive the comments of the reviewers is discouraged. Authors are notified by e-mail about the status of the submitted articles and the whole process takes about 3-4 months from the date of the article submission.

Indexed by: **CLARIVATE ANALYTICS**
SCOPUS
GEOBASE
EBSCO
SJR
CABELL

ISSN: 1842 - 5135 (Print)
ISSN: 2065 - 4421 (Online)

